



UNIL | Université de Lausanne

Unicentre

CH-1015 Lausanne

<http://serval.unil.ch>

Year : 2022

Integrated approach to evaluate rock mass stability by means of remote sensing techniques and conventional geotechnical and geomechanical surveys

Loiotine Lidia

Loiotine Lidia, 2022, Integrated approach to evaluate rock mass stability by means of remote sensing techniques and conventional geotechnical and geomechanical surveys

Originally published at : Thesis, University of Lausanne

Posted at the University of Lausanne Open Archive <http://serval.unil.ch>

Document URN : urn:nbn:ch:serval-BIB_AD6B328A9F3A9

Droits d'auteur

L'Université de Lausanne attire expressément l'attention des utilisateurs sur le fait que tous les documents publiés dans l'Archive SERVAL sont protégés par le droit d'auteur, conformément à la loi fédérale sur le droit d'auteur et les droits voisins (LDA). A ce titre, il est indispensable d'obtenir le consentement préalable de l'auteur et/ou de l'éditeur avant toute utilisation d'une oeuvre ou d'une partie d'une oeuvre ne relevant pas d'une utilisation à des fins personnelles au sens de la LDA (art. 19, al. 1 lettre a). A défaut, tout contrevenant s'expose aux sanctions prévues par cette loi. Nous déclinons toute responsabilité en la matière.

Copyright

The University of Lausanne expressly draws the attention of users to the fact that all documents published in the SERVAL Archive are protected by copyright in accordance with federal law on copyright and similar rights (LDA). Accordingly it is indispensable to obtain prior consent from the author and/or publisher before any use of a work or part of a work for purposes other than personal use within the meaning of LDA (art. 19, para. 1 letter a). Failure to do so will expose offenders to the sanctions laid down by this law. We accept no liability in this respect.



UNIL | Université de Lausanne

Faculty of Geosciences and Environment
Institute of Earth Sciences

INTEGRATED APPROACH TO EVALUATE ROCK MASS STABILITY BY MEANS OF REMOTE SENSING TECHNIQUES AND CONVENTIONAL GEOSTRUCTURAL AND GEOMECHANICAL SURVEYS

Ph.D. Thesis

Presented at the

Faculty of Geosciences and Environment of the University of Lausanne

by

Lidia Loiotine

To obtain the grade of
Ph.D. in Earth Sciences

Prof. Michel Jaboyedoff
Prof. Mario Parise
Prof. F. Agliardi
Dr. Marc-Henri Derron
Prof. Marie-Elodie Perga

Jury

Thesis director
Thesis director
Expert
Expert
Jury president

Lausanne 2022

IMPRIMATUR

Vu le rapport présenté par le jury d'examen, composé de

Président de la séance publique :	Mr le Professeur Prof. Roberto Sulpizio
Présidente du colloque :	Mme la Professeure Marie-Elodie Perga
Co-directeur de thèse :	M. le Professeur Michel Jaboyedoff
Co-directeur de thèse :	M. le Professeur Mario Parise
Expert interne :	M. le Docteur Marc-Henri Derron
Expert externe :	M. le Professeur Federico Agliardi

Le Doyen de la Faculté des géosciences et de l'environnement autorise l'impression de la thèse de

Madame LIDIA LOIOTINE

*Titulaire d'un
Master of Geological and Geophysical Sciences
de l'Università degli Studi di Bari « Aldo Moro »*

intitulée

**INTEGRATED APPROACH TO EVALUATE ROCK MASS STABILITY BY
MEANS OF REMOTE SENSING TECHNIQUES AND CONVENTIONAL
GEOSTRUCTURAL AND GEOMECHANICAL SURVEYS**

Lausanne, le 3 août 2022



Pour le Doyen de la Faculté des géosciences et de
l'environnement

Professeure Marie-Elodie Perga

Acknowledgements

I would like to express my heartfelt gratitude to those who, even indirectly, supported the success of this challenging journey.

Particularly, I would like to thank my supervisors Prof. Gioacchino Francesco Andriani, Prof. Michel Jaboedoff and Prof. Mario Parise: you have all believed in my skills, even when I doubted of myself; with your feedback and your enigmatic silences (have to disclose this) you brought out the best of me. A warm thanks goes also to Dr. Marc-Henri Derron and Prof. Federico Agliardi, for sharing their academic knowledge of the remote sensing technologies and offering me proper hints to interpret apparently mysterious results, and to Prof. Monica Ghirotti for her support during the final steps of the thesis defense.

I thank my friends and colleagues of University of Bari Marco La Salandra and Dr. Giuseppe Diprizio for their contribution and personal support. I extend my sincere thanks to Dr. Antonella Marsico, Prof. Vincenzo Festa, Giovanni Barracane and Francesco De Giosa for their practical help on field.

A special thanks goes to the University of Lausanne Risk Analysis Group, that I consider a second family: Charlotte Wolff, Valérie Baumann, Amalia Gutiérrez, Meriam Ben Hammouda, Nasrin Amini Tehrani, Li Fei, Tiggi Choanji, Chunwei Sun, Antoine Guerin, François Noël, Emmanuel Wyser and Federico Franzosi. They all welcomed me warmly in Lausanne and I am glad having shared the good and the (fortunately few) bad moments with you. I thank so much Dr. Antoine Guerin for his suggestions to carry out my research and for his never-ending patience!

I sincerely thank Dr. Teresa Gracchi for helping me to solve all the papers issues related to the co-tutorship and for her precious suggestions for continuing this journey in the fascinating city of Lausanne.

Moreover, I would like to thank Peppino Campanella, Vito Pellegrini, the Tecno-Lab company (Altamura, Italy) and all the community of Polignano a Mare (Italy) for the immense aid and support to perform the remote sensing surveys on field, together with the execution of laboratory tests on the collected samples.

My gratefulness goes to my family for believing in me and encouraging me even if at hundreds of kilometers away, I would not have realized myself without you. I thank my dearest friend and colleague Riccardo Bellomira for continuously sharing his enthusiasm for life with me, even though our paths have temporarily gone apart. Finally, my heartfelt gratitude goes to my partner Daniele, for his excellent problem-solving skills, for moving the entire world to reach me and to overcome the difficulties we have all been facing these sad historical times and, most of all, for keeping me “hydrated” and alive while writing this manuscript! I couldn’t thank you enough for everything you have done for me.

Abstract

Rock mass failures pose significant hazards and risks to society and can seriously damage the anthropogenic infrastructures or the natural, cultural or historical heritage of protected sites and, most of all, human lives, even when they involve small volumes of rock. Although large volumes are typically mobilized in mountainous areas, several episodes sporadically occur in coastal cliffs, also as a consequence of the on-going climate changes. The risk is particularly high when instability processes take place in urban or tourist area.

Both traditional and most advanced methods for landslide hazard assessment in rock slopes necessitate a full understanding of the overall rock mass behavior and of the on-going endogenic and exogenic processes. Given the anisotropic, inhomogeneous, discontinuous, and non-elastic nature of rock masses, stability analyses necessarily require appropriate rock mass characterization. Discontinuities play a key role in the mechanical behavior of rock masses, and their detection and quantitative description represent one of the most challenging aspects of hazard assessment.

Several remote sensing techniques have been introduced in geoscience to support the conventional, dangerous and time-consuming field surveys, and their application is increasing exponentially. However, because of the intrinsic complexity of rock masses, a comprehensive standard procedure for rock mass characterization and hazard assessment, involving both conventional field surveys and remote sensing techniques, has not yet been proposed.

The main goal of this PhD thesis is to investigate the applicability of remote sensing methods for rock mass characterization in complex environments, with focus on their integration with the irreplaceable conventional geosstructural and geomechanical surveys, in order to set-up advanced geomechanical models for sophisticated stability analyses.

- The first part of this manuscript is of informative type and provides a solid background of the techniques and methods (e.g. discontinuity characterization, rock mass classification systems, failure mechanisms, and application of remote sensing techniques) faced throughout the document, as well as an outline of the research approach.
- The second part of this thesis concerns the testing, validation and optimization of different remote sensing techniques for rock mass characterization, and presents an innovative digital tool for 2-D analyses of discontinuities.

More in detail, the first topic addressed in this part is a critical review of the most used remote sensing techniques for rock slope investigation in complex conditions: Terrestrial Laser Scanning (TLS), terrestrial and Unmanned Aerial Vehicle (UAV) Structure from Motion techniques, and InfraRed Thermography (IRT). A coastal case study affected by complex morphology, with intense development of karst and weathering processes, presence of Mediterranean vegetation, in a context heavily frequented by tourists, was selected to carry out these researches. In detail, a quantitative comparison of the first three methods for rock slope characterization from point clouds, with particular reference on their accuracy for discontinuity extraction and characterization, as well as for rock slope monitoring, is presented. It was found out that point clouds generated from terrestrial or UAV-based photogrammetry are prone to “distortions” if control points cannot be evenly distributed on the field because of morphological constraints. As concerns the accuracy, terrestrial photogrammetry by means of common digital cameras can be used for a preliminary characterization, whilst TLS and UAV

have similar accuracies. The use of one technique rather than the other for monitoring purposes depends on the objectives of the survey: whilst TLS provides more accurate deformation measurements and rockfalls volume estimations, UAV systems cover larger area, and allow an easier interpretation by direct comparison with high-resolution photos. This aspect is important in rock masses where shrubs are not easily recognizable on the point clouds. As concern the discontinuity characterization, the three point clouds provided approximately the same results, however the UAV technique was found to be more reliable because it was not affected by occlusions (shadow areas). This part of the manuscript presents a critical analysis of the advantages and limitations not only of different remote sensing techniques, but also of different platforms (e.g. hand-held cameras or UAV systems). Although some papers on the use of remote sensing techniques for rock mass characterization are reported in the literature, this part of the thesis focuses on their quantitative comparison and on their optimization in carbonate and coastal environments, which are subjected to particular issues.

The second analysis concerns the applicability of IRT technique for rock slope characterization. A 24-hours monitoring was carried out on the case study, and coupled with UAV systems to detect discontinuities and voids. In addition, the air-rock temperature profiles extracted from the thermograms were aligned to high-resolution photos to directly obtain information on the topography, lithology, jointing degree and Geological Strength Index of the rock mass. This section offers new insights on a technique still in development and proposes a methodology to detect some useful information (although with limitations) even if the on-site conditions are not favourable, with the possibility of using IRT techniques for the characterization of inaccessible areas.

The last section of the second part of the thesis is devoted to the 2-D analyses of discontinuity traces from ortho-rectified photos derived from remote sensing techniques. Bi-dimensional analyses are recommended for low-relief, sub-horizontal or sub-vertical rock slope, because the extraction of discontinuities from point cloud is affected by undersampling. However, despite several advances were made for 3-D characterization from point clouds, 2-D analyses are stuck to the time-consuming methods proposed in the literature some decades ago. Recent digital implementations are not publicly available, or do not provide a comprehensive discontinuity characterization. Hence, the methods proposed in the literature were adapted to a digital environment to perform faster quantitative discontinuity characterization. To this aim, a publicly-available MATLAB routine was developed, which is able to classify the discontinuity traces into discontinuity sets and calculate their mean orientation, spacing, trace length, and persistence, as well as their probabilistic distributions. In addition, information on the fracture network is provided by means of intensity, density and trace length estimators, block volume, and block shape. The routine was built on a synthetic dataset, then applied on the discontinuity map of the case study and validated by means of conventional geostructural and geomechanical field surveys on the same area.

- In the third part of this manuscript, the overall objective of the PhD research is achieved. A comprehensive methodology for rock mass stability assessment through the integration of remote sensing techniques and conventional geostructural and geomechanical surveys is proposed and applied to the case study. An advanced 3-D geomechanical model was generated, based on the results of the point clouds processing and interpretation, field surveys and laboratory tests for the physical and mechanical characterization of the rock materials. Kinematic analyses allowed a first assessment of the potential failures of the case study, then the typical failure mechanisms were detected by means of field and remote sensing inspections. Later on, the geomechanical model was used to perform 3-D and 2-D numerical stability analyses. At this stage, the Finite Element Method (FEM), which is commonly used because of its versatility to model a broad range of continuous and discontinuous

rock masses without assumptions on the failure mechanisms, was used to validate the developed methodology by direct comparison with the failure mechanisms observed on the field. Two different approaches were tested and compared to each other, both for the current conditions and by simulating surface processes observed in the field. This study was targeted to evaluate the effect of discontinuity implementation in FEM methods by means of a stochastic approach. However, given the complexity of the failure mechanisms of the study site, further researches are suggested as future perspective. This final part of the manuscript integrates all the investigations carried out on the study area and illustrates how different data can be combined to achieve reliable stability analyses. The importance of the input data, as well as the difficulties in producing and interpreting the results are outlined and discussed.

Résumé

Les ruptures de masses rocheuses représentent des aléas et des risques importants pour la société et peuvent gravement endommager les infrastructures ou le patrimoine naturel, culturel ou historique des sites protégés et, surtout, des vies humaines, même lorsqu'elles concernent de petits volumes de roche. Bien que de grands volumes soient généralement mobilisés dans les zones montagneuses, des événements se produisent sporadiquement dans les falaises côtières, également en raison des changements climatiques en cours. Le risque est particulièrement élevé lorsque les processus d'instabilité se produisent dans des zones urbaines ou touristiques.

Les méthodes traditionnelles et les plus avancées d'évaluation des risques de chutes de blocs dans les pentes rocheuses nécessitent une compréhension complète du comportement global de la masse rocheuse et des processus endogènes et exogènes en cours. Étant donné la nature anisotrope, inhomogène, discontinue et non élastique des masses rocheuses, les analyses de stabilité nécessitent nécessairement une caractérisation appropriée de la masse rocheuse. Les discontinuités jouent un rôle clé dans le comportement mécanique des masses rocheuses, et leur détection et leur description quantitative représentent l'un des aspects les plus difficiles de l'évaluation des risques.

Plusieurs techniques de télédétection ont été introduites dans le domaine des géosciences pour faciliter les investigations de terrain conventionnelles, souvent dangereuses et longues, et leur application augmente de façon exponentielle. Cependant, en raison de la complexité intrinsèque des masses rocheuses, une procédure standard complète pour la caractérisation des masses rocheuses et l'évaluation des risques, impliquant à la fois des enquêtes de terrain conventionnelles et des techniques de télédétection, n'a pas encore été proposée.

L'objectif principal de cette thèse de doctorat est d'étudier l'applicabilité des méthodes de télédétection pour la caractérisation des masses rocheuses dans des environnements complexes, en mettant l'accent sur leur intégration avec les irremplaçables études géostructurales et géomécaniques conventionnelles, afin d'établir des modèles géomécaniques avancés pour des analyses de stabilité sophistiquées.

- La première partie de cette thèse est informative et fournit un arrière-plan solide des techniques et méthodes (par exemple, caractérisation de la discontinuité, systèmes de classification des masses rocheuses, mécanismes d'instabilité et application des techniques de télédétection) abordées dans la thèse, ainsi qu'une illustration de la démarche de recherche.

- La deuxième partie de cette thèse est consacrée à une revue critique des techniques de télédétection les plus utilisées pour l'investigation des pentes rocheuses dans des conditions complexes : Le Terrestrial Laser Scanner (TLS), la Structure from Motion terrestre et réalisée par Unmanned Aerial Vehicle (UAV) et la thermographie infrarouge (IRT). Pour réaliser cette recherche, un cas d'étude côtier affecté par une morphologie complexe, avec un développement intense de processus karstiques et d'altération, la présence de végétation méditerranéenne, dans un contexte fortement fréquenté par les touristes, a été sélectionné.

En détail, une comparaison quantitative des trois premières méthodes de caractérisation des falaises rocheuses à partir de nuages de points, avec une attention particulière apportée à leur précision pour l'extraction et la caractérisation des discontinuités, ainsi que pour la surveillance des falaises rocheuses, est présentée. Il a été constaté que les nuages de points générés par la photogrammétrie terrestre ou par drone sont sujets à des "distorsions" si les points de contrôle ne peuvent pas être répartis uniformément sur le terrain en raison de contraintes morphologiques. En ce qui concerne la précision, la photogrammétrie terrestre au moyen d'appareils photo numériques courants peut être utilisée pour une caractérisation préliminaire,

sachant que le TLS et le drone ont des précisions similaires. L'utilisation d'une technique plutôt que l'autre à des fins de surveillance dépend des objectifs de l'étude : alors que le TLS fournit des mesures de déformation plus précises et des estimations du volume des éboulements, les systèmes UAV couvrent une plus grande surface et permettent une interprétation plus facile par comparaison directe avec des photos à haute résolution. Cet aspect est important dans les masses rocheuses où les arbustes ne sont pas facilement reconnaissables sur les nuages de points. En ce qui concerne la caractérisation des discontinuités, les trois nuages de points ont fourni approximativement les mêmes résultats, cependant la technique UAV s'est avérée plus fiable car il n'était pas affecté par les occlusions. Cette partie du manuscrit présente une analyse critique des avantages et des limites non seulement des différentes techniques de télédétection, mais aussi des différentes plateformes (ex. caméras au sol ou systèmes UAV). Bien que quelques travaux soient rapportés dans la littérature sur l'utilisation des techniques de télédétection pour la caractérisation des massifs rocheux, cette partie de la thèse porte sur leur comparaison quantitative et leur optimisation en milieu carbonaté et côtier, soumis à des problématiques particulières.

La deuxième analyse concerne l'applicabilité de la technique IRT pour la caractérisation des pentes rocheuses. Une surveillance de 24 heures a été effectuée sur l'étude de cas, et couplée à des systèmes de drones pour détecter les discontinuités et les vides. En outre, les profils de température air-roche extraits des thermogrammes ont été alignés sur des photos haute résolution afin d'obtenir directement des informations sur la topographie, la lithologie, le degré de jointure et l'indice de résistance géologique (GSI) de la masse rocheuse. Cette section offre de nouvelles perspectives sur une technique encore en développement et propose une méthodologie innovante pour acquérir des informations utiles (quoiqu'avec certaines limites) même si les conditions sur site ne sont pas favorables, avec la possibilité d'utiliser des techniques IRT dans des zones inaccessibles.

La dernière section de cette partie de la thèse est consacrée aux analyses bidimensionnelles de traces de discontinuités à partir de photos orthorectifiées issues de techniques de télédétection. Les analyses bidimensionnelles sont recommandées pour les pentes rocheuses à faible relief, subhorizontales ou subverticales, car l'extraction des discontinuités à partir de nuages de points est affectée par le sous-échantillonnage. Cependant, malgré plusieurs progrès réalisés pour la caractérisation 3D à partir de nuages de points, les analyses 2D restent identiques aux méthodes fastidieuses proposées dans la littérature il y a quelques décennies. Les implémentations numériques récentes ne sont pas accessibles au public ou ne permettent pas une caractérisation complète des discontinuités. Par conséquent, les méthodes proposées dans la littérature ont été adaptées à un environnement numérique afin de réaliser une caractérisation quantitative plus rapide des discontinuités. À cette fin, une routine MATLAB accessible au public a été développée, capable de classer les traces de discontinuité en ensembles de discontinuité et de calculer leur orientation moyenne, leur espacement, la longueur des traces et leur persistance, ainsi que leurs distributions probabilistes. En outre, des informations sur le réseau de fractures sont fournies au moyen d'estimateurs de l'intensité, de la densité et de la longueur des traces, du volume de bloc et de la forme de bloc. La routine a été construite sur un ensemble de données synthétiques, puis appliquée sur la carte de discontinuité de l'étude de cas et validée au moyen d'études de terrain géostrucuturales et géomécaniques conventionnelles sur la même zone.

- Dans la troisième partie de ce manuscrit, l'objectif global de la recherche doctorale est atteint. Une méthodologie complète d'évaluation de la stabilité des masses rocheuses par l'intégration de techniques de télédétection et d'études géostrucuturales et géomécaniques conventionnelles est proposée et appliquée à l'étude de cas. Un modèle géomécanique 3D avancé a été généré, basé sur les résultats du traitement et de l'interprétation des nuages de points, des enquêtes de terrain et des tests de laboratoire pour la caractérisation physique et mécanique des matériaux rocheux. Les analyses cinématiques ont permis une première évaluation des ruptures potentielles sur le site d'étude, puis les mécanismes de rupture typiques ont été détectés au moyen d'inspections sur le terrain et de télédétection. Par la suite, le modèle géomécanique a été

utilisé pour effectuer des analyses numériques de stabilité en 3 et 2 dimensions. À ce stade, la méthode des éléments finis (FEM), qui est couramment utilisée en raison de sa polyvalence pour modéliser une large gamme de masses rocheuses continues et discontinues sans hypothèses sur les mécanismes de rupture, a été utilisée pour valider la méthodologie développée par comparaison directe avec les mécanismes de rupture observés sur le terrain. Deux approches différentes ont été testées et comparées l'une à l'autre, à la fois pour les conditions actuelles et en simulant les processus de surface observés sur le terrain. Cette étude avait pour but d'évaluer l'effet de la mise en œuvre de discontinuités dans les méthodes FEM au moyen d'une approche stochastique. Cependant, étant donné la complexité des mécanismes de rupture du site étudié, des recherches supplémentaires sont suggérées comme perspectives futures. Cette dernière partie de la thèse intègre toutes les investigations menées sur la zone d'étude et illustre comment différentes données peuvent être combinées pour obtenir des analyses de stabilité fiables et avancées, soulignant l'importance des données d'entrée et les difficultés de production et d'interprétation des résultats.

Sintesi

I fenomeni di instabilità in ammassi rocciosi costituiscono un rischio significativo per la società e possono causare danni ingenti alle infrastrutture antropiche o al patrimonio naturale, culturale o storico di siti protetti e, soprattutto, mettere in pericolo la popolazione, anche nel caso di volumi coinvolti limitati. Sebbene i volumi maggiori siano tipicamente mobilitati in aree montuose, diversi episodi si verificano sporadicamente lungo le falesie costiere, anche come conseguenza dei cambiamenti climatici in corso. Il rischio idrogeologico è particolarmente elevato qualora i processi di instabilità avvengano in zone urbane o turistiche.

Sia i metodi tradizionali che quelli più avanzati per la valutazione della pericolosità da frana dei versanti in roccia necessitano di una comprensione completa del comportamento complessivo degli ammassi rocciosi e dei processi endogeni ed esogeni in corso. A causa della natura anisotropa, disomogenea, discontinua e non elastica degli ammassi rocciosi, le analisi di stabilità richiedono necessariamente un'adeguata caratterizzazione dell'oggetto in esame. Inoltre le discontinuità hanno un ruolo chiave sul comportamento meccanico degli ammassi rocciosi e la loro individuazione e descrizione quantitativa rappresentano uno degli aspetti più impegnativi nella valutazione della pericolosità.

Diverse tecniche di *remote sensing* sono state introdotte nelle Geoscienze per supportare i rilievi geostrutturali e geomeccanici convenzionali, spesso dispendiosi e caratterizzati da un'elevata difficoltà, tanto da risultare in un aumento esponenziale della loro applicazione negli ultimi anni. Tuttavia, a causa della complessità intrinseca degli ammassi rocciosi, non è stata ancora proposta una procedura standard completa per la caratterizzazione degli ammassi rocciosi e la valutazione della pericolosità da frana, che combini sia i rilievi convenzionali sul campo che le tecniche di *remote sensing*.

La presente tesi di dottorato ha come obiettivo principale lo studio dell'applicabilità delle tecniche di *remote sensing* per la caratterizzazione degli ammassi rocciosi in ambienti complessi, con particolare riferimento alla loro integrazione con i metodi geostrutturali e geomeccanici convenzionali, al fine di realizzare modelli geomeccanici avanzati per sofisticate analisi di stabilità.

- La prima parte di questa tesi è di tipo informativo e fornisce un solido background delle tecniche e dei metodi (es. caratterizzazione della discontinuità, sistemi di classificazione degli ammassi rocciosi, meccanismi di instabilità ed applicazione delle tecniche di *remote sensing*) affrontati nella dissertazione, nonché un'illustrazione dell'approccio di ricerca.
- La seconda parte del manoscritto riguarda i test, la validazione e l'ottimizzazione di diverse tecniche di *remote sensing* per la caratterizzazione degli ammassi rocciosi e presenta un tool digitale innovativo per l'analisi 2-D delle discontinuità.

Nello specifico, il primo argomento riguarda un esame critico delle tecnologie di *remote sensing* più utilizzate per lo studio di pendii in roccia in condizioni complesse: *Terrestrial Laser Scanning* (TLS), fotogrammetria terrestre e da sistemi *Unmanned Aerial Vehicle* (UAV) e *InfraRed Thermography* (IRT). A tal fine, è stato individuato un caso di studio in ambiente costiero interessato da morfologia complessa, processi carsici, *weathering*, presenza di vegetazione mediterranea ed attività antropiche.

Nello specifico, è riportato un confronto quantitativo dei primi tre metodi citati per la caratterizzazione degli ammassi rocciosi da nuvole di punti, con particolare riferimento alla loro accuratezza per l'estrazione e la caratterizzazione delle discontinuità ed al monitoraggio dei versanti. È stato osservato che le nuvole di punti generate dalla fotogrammetria terrestre o da tecnologie UAV sono soggette a "distorsioni" se i punti di controllo non possono essere distribuiti uniformemente sul campo a causa di limitazioni morfologiche. Per quanto riguarda l'accuratezza, la fotogrammetria terrestre condotta tramite comuni fotocamere digitali può essere utilizzata per una caratterizzazione preliminare, mentre i metodi TLS e UAV hanno maggiori accuratezze, simili tra loro. La preferenza di utilizzo di una determinata tecnica, piuttosto che di un'altra ai fini del monitoraggio, dipende dagli obiettivi del rilievo: mentre il TLS fornisce misure più accurate di deformazione e stime dei volumi mobilitati, i sistemi UAV coprono un'area più ampia e permettono una più facile interpretazione dei risultati mediante il confronto diretto delle foto ad alta risoluzione. Questo aspetto è fondamentale per lo studio di versanti rocciosi interessati dalla presenza di arbusti difficilmente riconoscibili sulle nuvole di punti. Per quanto concerne la caratterizzazione delle discontinuità, le tre nuvole di punti hanno fornito sommariamente gli stessi risultati, tuttavia la tecnica UAV è risultata più affidabile in quanto non affetta da occlusioni (zone d'ombra). Questa parte del manoscritto presenta un'analisi critica dei vantaggi e dei limiti non solo delle diverse tecniche di remote sensing, ma anche delle diverse piattaforme (es. fotocamere da terra o sistemi UAV). Sebbene in letteratura siano riportati alcuni lavori sull'uso delle tecniche di remote sensing per la caratterizzazione degli ammassi rocciosi, questa parte della tesi si concentra sul loro confronto quantitativo e sulla loro ottimizzazione in ambienti carbonatici e costieri, soggetti a particolari problematiche.

La seconda analisi riguarda l'applicabilità della tecnica IRT per la caratterizzazione degli ammassi rocciosi. Al fine di identificare le discontinuità e le cavità presenti nel caso di studio, è stato eseguito un monitoraggio di 24 ore supportato dai sistemi IRT ed UAV. I profili di temperatura all'interfaccia ariarocchia estratti dai termogrammi sono stati allineati con foto ad alta risoluzione per estrarre informazioni su topografia, litologia, grado di fratturazione e *Geological Strength Index* (GSI) dell'ammasso roccioso. Questa sezione offre nuovi spunti su una tecnica ancora in sviluppo e propone una metodologia innovativa per acquisire informazioni utili (sebbene con alcuni limiti) anche se le condizioni in sito non sono favorevoli, con la possibilità di utilizzare tecniche IRT in aree inaccessibili.

L'ultima sezione di questa parte della tesi è dedicata alle analisi 2-D delle tracce delle discontinuità da ortofoto generate tramite *remote sensing*. Le analisi bidimensionali sono indispensabili per ammassi rocciosi a basso rilievo, sub-orizzontali o sub-verticali, in quanto l'estrazione delle discontinuità dalle nuvole di punti è soggetta a sotto-campionamento. Nonostante siano disponibili diversi metodi per la caratterizzazione 3-D dalle nuvole di punti, le analisi 2-D, proposte in letteratura alcuni decenni fa, sono obsolete e richiedono tempi lunghi. Alcuni progressi sono stati raggiunti tramite l'implementazione dei metodi classici in ambiente digitale, ma tali prodotti non sono accessibili liberamente e/o non forniscono una caratterizzazione completa delle discontinuità. Di conseguenza, nell'ambito di questa tesi, i metodi proposti in letteratura sono stati adattati ad un ambiente digitale per eseguire caratterizzazioni quantitative delle discontinuità più rapide ed avanzate. A questo scopo è stata sviluppata una routine MATLAB disponibile al pubblico, in grado di classificare le tracce in set di discontinuità e calcolare, per ognuno di essi, i valori medi di orientazione, spaziatura, lunghezza della traccia e persistenza, oltre a riportare le distribuzioni probabilistiche di tali proprietà. Inoltre, la routine fornisce informazioni sul *fracture network* per mezzo di estimatori di intensità, densità e lunghezza delle tracce, volume e forma dei blocchi. Tale routine è stata implementata utilizzando un dataset sintetico

e successivamente applicata alla mappa delle discontinuità di un settore del caso studio. La procedura è stata infine validata per mezzo di indagini geostrutturali e geomeccaniche convenzionali *in situ* nella stessa area analizzata digitalmente.

- Nella terza parte di questo manoscritto viene raggiunto l'obiettivo principale della ricerca. Nel dettaglio, è riportata una procedura per la valutazione di stabilità di ammassi rocciosi mediante l'integrazione di tecniche di *remote sensing* e di rilievi convenzionali geostrutturali e geomeccanici, sviluppata nel caso di studio. Sulla base dei risultati inerenti l'elaborazione e l'interpretazione delle nuvole di punti, le indagini sul campo e le conseguenti prove di laboratorio per la caratterizzazione fisica e meccanica dei materiali rocciosi, è stato prodotto un modello geomeccanico 3-D sofisticato. Una prima valutazione dei potenziali fenomeni di instabilità del caso studio è stata effettuata applicando delle analisi cinematiche, seguite dall'individuazione dei tipici meccanismi di instabilità tramite indagini *in situ* e studi dei prodotti restituiti dal *remote sensing*. In seguito, il modello geomeccanico è stato utilizzato per eseguire analisi di stabilità 3-D e 2-D di tipo numerico. In questa fase, il Metodo degli Elementi Finiti (FEM), comunemente usato per la sua versatilità nel modellare diversi ammassi rocciosi continui e discontinui, senza presupposti sui meccanismi di rottura, è stato utilizzato per validare la metodologia sviluppata attraverso un confronto diretto con i processi di instabilità individuati sul campo. Sia le condizioni attuali del caso di studio, sia processi superficiali osservati in campagna, sono stati simulati mediante due diversi approcci (continuo e discontinuo), successivamente confrontati tra loro. Questa procedura è stata eseguita per valutare l'effetto dell'implementazione della discontinuità nei metodi FEM generate con un approccio stocastico. Tuttavia, considerando la complessità dei meccanismi di instabilità del caso di studio, potrebbero essere opportune ulteriori ricerche sono suggerite come prospettive future. Questa parte finale della dissertazione integra tutte le indagini svolte sull'area di studio e illustra come diversi dati possano essere combinati per ottenere analisi di stabilità affidabili e avanzate, sottolineando l'importanza dei dati di input e le difficoltà nel produrre ed interpretare i risultati.

Contents

Acknowledgements	i
Abstract	iii
Résumé	vii
Sintesi	xi
Contents	xv
PART 1 - BACKGROUND	
Chapter 1 Introduction	1
1.1. Scope and problem definition.....	1
1.2. Project history.....	2
1.3. Thesis outline.....	2
Chapter 2 Methods and research approach	7
2.1. Discontinuities	7
2.1.1. Definition	7
2.1.2. Types of discontinuities and field sampling techniques.....	7
2.1.3. Quantitative discontinuity characterization.....	9
2.1.4. Additional properties	16
2.2. Use of discontinuity information for rock mass characterization	18
2.2.1. Rock Quality Designation (RQD)	18
2.2.2. Rock Mass Rating (RMR) and Slope Mass Rating (SMR).....	18
2.2.3. Q-System	19
2.2.4. Geological Strength Index (GSI)	21
2.2.5. Rock Mass index (RMi).....	20
2.3. Rock slope failure mechanisms	22
2.4. Remote sensing background	24
2.4.1. Introduction	24
2.4.2. LiDAR technique.....	25
2.4.3. SfM technique.....	28
2.4.4. IRT technique	35
2.5. Use of point clouds for rock mass characterization	39
2.5.1. Rock mass characterization	40
2.6. Methods for stability analyses in rock slopes.....	45
2.6.1. Conventional methods: Kinematic analyses and Limit Equilibrium techniques ...	45
2.6.2. Numerical methods	47
2.6.3. Recent advances in geomechanical modelling: Discrete Fracture Network	51
2.7. Research approach	53

Chapter 3	Case study	53
3.1.	Geological and geomorphologic setting.....	55
3.2.	Geostructural setting	57
3.3.	Hydrogeological setting	58
3.4.	Marine erosion and meteo-marine conditions	58
3.5.	Lama Monachile and Pietra Piatta sites	60
	3.5.1. Lama Monachile site	60
	3.5.2. Pietra Piatta site.....	64
3.6.	Choice of the case study	65
PART II – REMOTE SENSING		
Chapter 4	Comparison of Remote Sensing techniques for geostructural analysis and cliff monitoring in coastal areas of high tourist attraction: the case study of Polignano a Mare (southern Italy).....	69
4.1.	Introduction	69
4.2.	Case Study.....	72
4.3.	Materials and Methods.....	74
	4.3.1. Remote Sensing Acquisition and Processing.....	74
	4.3.2. Quality Assessment of the Point Clouds	78
	4.3.3. Comparison of Point Clouds.....	78
	4.3.4. Extraction of Discontinuities from Point Clouds	79
	4.3.5. Rockfall Detection by Means of Multi-Temporal Acquisitions	80
4.4.	Results and Discussion	81
	4.4.1. Quality Assessment of the Point Clouds	81
	4.4.2. Comparison of Point Clouds.....	83
	4.4.3. Extraction of Discontinuities from Point Clouds	86
	4.4.4. Rockfall Detection by Means of Multi-Temporal Acquisitions	89
4.5.	Main Outcomes and Conclusions.....	92
4.6.	Supplementary materials.....	97
Chapter 5	Evaluation of InfraRed Thermography Supported by UAV and Field Surveys for Rock Mass Characterization in Complex Settings	101
5.1.	Introduction	101
5.2.	Materials and Methods.....	104
	5.2.1. Case study: Polignano a Mare (southern Italy)	104
	5.2.2. UAV and IRT surveys	107
	5.2.3. IRT data processing and correlation with UAV data.....	109
5.3.	Results and discussion	110
	5.3.1. Environmental conditions and rock temperature curves.....	110

5.3.2.	Time series and correlations with rock mass properties.....	111
5.3.3.	Detection of discontinuities in thermal images	114
5.4.	Main outcomes and conclusions.....	117
5.5.	Supplementary Materials.....	119
Chapter 6	QDC-2-D: A Semi-Automatic Tool for 2-D Analysis of Discontinuities for Rock Mass Characterization	123
6.1.	Introduction	123
6.2.	Materials and Methods.....	125
6.2.1.	Study Site	125
6.2.2.	Generation of the Digital Outcrop Model (DOM)	126
6.2.3.	Field Characterization of Discontinuity Sets	128
6.2.4.	Manual Mapping of the Fracture Traces.....	130
6.2.5.	Methodological Approach for the Digital 2-D Quantitative Analysis of Discontinuities	130
6.2.6.	Workflow of the MATLAB Routine.....	132
6.3.	Results.....	139
6.3.1.	Results of the Synthetic Dataset	139
6.3.2.	Application to the Case Study	142
6.4.	Discussion	146
6.5.	Conclusions.....	149
PART III	- INTEGRATION OF REMOTE SENS-ING AND CONVENTIONAL SUR-VEYS FOR STABILITY ANALYSES	
Chapter 7	Multidisciplinary approach for stability analyses of rock masses: integration of field surveys, remote sensing techniques and numerical modelling.....	153
7.1.	Introduction	153
7.2.	Methodology overview	156
7.3.	Case study: Polignano a Mare (southern Italy)	158
7.3.1.	Geological and morphologic setting	158
7.3.2.	Physical and mechanical characterization of the rock materials	159
7.3.3.	Conventional geostructural and geomechanical surveys.....	162
7.3.4.	UAV surveys.....	166
7.3.5.	Geostructural analysis from orthophotos/point clouds.....	169
7.3.6.	Kinematic analyses.....	174
7.3.7.	Instability mechanisms	176
7.3.8.	Finite Element Method analyses.....	180
7.4.	Conclusion.....	197
a.	Supplementary materials.....	199

Chapter 8	Conclusion and future perspectives	213
References	217
Publication list	245

PART I

BACKGROUND

Chapter 1 Introduction

1.1. Scope and problem definition

Rock slope stability analyses are fundamental to design functional interventions in civil applications and for hazard assessment of natural and artificial slopes, as well as to understand the processes and mechanisms driving potential instabilities. At present, several approaches (e.g. kinematic analyses, limit equilibrium techniques, sophisticated numerical methods) exist to perform stability analyses depending on the site conditions and on the scale of the problem (Edelbro 2003), but they all aim at the following main objectives (Eberhardt 2003):

- To determine the rock slope stability conditions;
- To investigate potential failure mechanisms;
- To evaluate the effect of different processes on slope stability;
- To test and compare different support and stabilization measures;
- To design optimal excavated slopes in terms of safety, reliability and economics.

Undoubtedly, efficient stability analyses require a proper conceptualization of the examined slope, which concerns the definition of the strength properties of the rock materials, the identification and characterization of structural features (e.g. faults, joints, bedding planes), and of the endogenic and exogenic processes which can perturbate the system. In this perspective, it is evident that, whatever the chosen technique, a comprehensive rock slope characterization is fundamental to achieve reliable results.

In the last decades, remote sensing techniques such as Light Detection and Ranging (LiDAR), terrestrial or Unmanned Aerial Vehicle (UAV)-supported Photogrammetry, and InfraRed Thermography (IRT) were introduced in the field of rock slope investigation to collect geological data over large areas and in relatively short time. The integration of remote sensing techniques allows geoscientists and engineers to overcome most of the limitations which the traditional field methods are subjected to (e.g. large areas, adverse weather conditions, inaccessibility, safety issues). Current technologies are able to provide high-resolution 3-D models of rock slopes that are widely used for rock slope characterization, focusing on the extraction of discontinuities and of their properties.

Despite several technologies and methods for rock slope investigation were introduced in the scientific community, some gaps emerged from a detailed literature review of the traditional and remote-sensing approaches for rock mass characterization, as well as of different stability analysis techniques. It is believed that a comprehensive state of the art of the different topics discussed in this thesis (Chapter 2) should be accomplished before outlining the specific objectives of this research, which are described in Section 2.7.

In summary, the main gaps delineated in the literature review are the following:

- Only a few studies dealt with the quantitative comparative analysis of different remote sensing techniques, in order to assess if they are interchangeable, or which ones are more appropriate according to the site conditions.
- Being the use of IRT techniques for rock mass characterization quite recent and still under development, further investigations should be performed to explore its applicability in complex conditions (e.g. urban or rural areas).
- When dealing with low-relief or sub-vertical outcrops, the quantitative characterization of discontinuities from point clouds is limited to a few sampled surfaces, as most of them are visible in the form of discontinuity traces. However, although many methods for discontinuity characterization from 3-D models exist, notorious 2-D approaches are stuck to about twenty years ago, and need to be updated in a digital system.
- Finally, even if sophisticated 3-D models can be provided through the combination of traditional field surveys and remote sensing products, as well as accurate quantitative discontinuity characterization, their integration to set up advanced geomechanical models for sophisticated stability analyses is still little explored.

Based on these observations, the main goal of this PhD thesis is to develop a methodology to assess rock mass stability through the integration of conventional geostructural and geomechanical surveys and remote sensing techniques.

1.2. Project history

This PhD thesis started in November 2018 and was carried out in the form of co-tutorship under the supervision of University Aldo Moro of Bari (Italy) and University of Lausanne (Switzerland). Whilst the first year of PhD was dedicated to the literature review, choice of the case study, and the management of bureaucratic issues related to the co-tutorship modality, the second year was devoted to the field work and data processing. During the third year, in addition to the processing refinement, a critical phase of results interpretation was performed and continuously updated, until developing the methodology proposed in the final section.

1.3. Thesis outline

This PhD thesis is divided into three main parts and comprises 8 chapters. All chapters belonging to Part II and Part III, which are preceded by an introductory section (Part I), were set up to be self-contained and were designed for international journals. Among them, Chapter 4, Chapter 5 and Chapter 6 have been published whilst Chapter 7 is going to be submitted in the form of two papers. Parts I-III are followed by the last chapter (Chapter 8) which reports the conclusion and future perspectives. The thesis outline is as follows (Figure 1.1):

- **PART I:** Background

Following this introduction chapter, Part I comprises:

- **Chapter 2:** Methods and research approach

This section covers the literature review and the methodological background of the themes discussed throughout the dissertation. Since a specific introductory section is provided for each of the following

chapters, dealing with different topics, this section provides a general overview. The first section reports a review of the methods for quantitative characterization of discontinuities and of their use for rock mass characterization, as well as a summary of the failure mechanisms of rock slopes. The second section deals with the principles of remote sensing techniques (LiDAR, Photogrammetry, IRT) and on the methods for rock slope characterization using point clouds and triangulated surfaces. The third section illustrates the most used methods for rock mass stability analysis, from traditional limit equilibrium approaches to the most advanced numerical techniques.

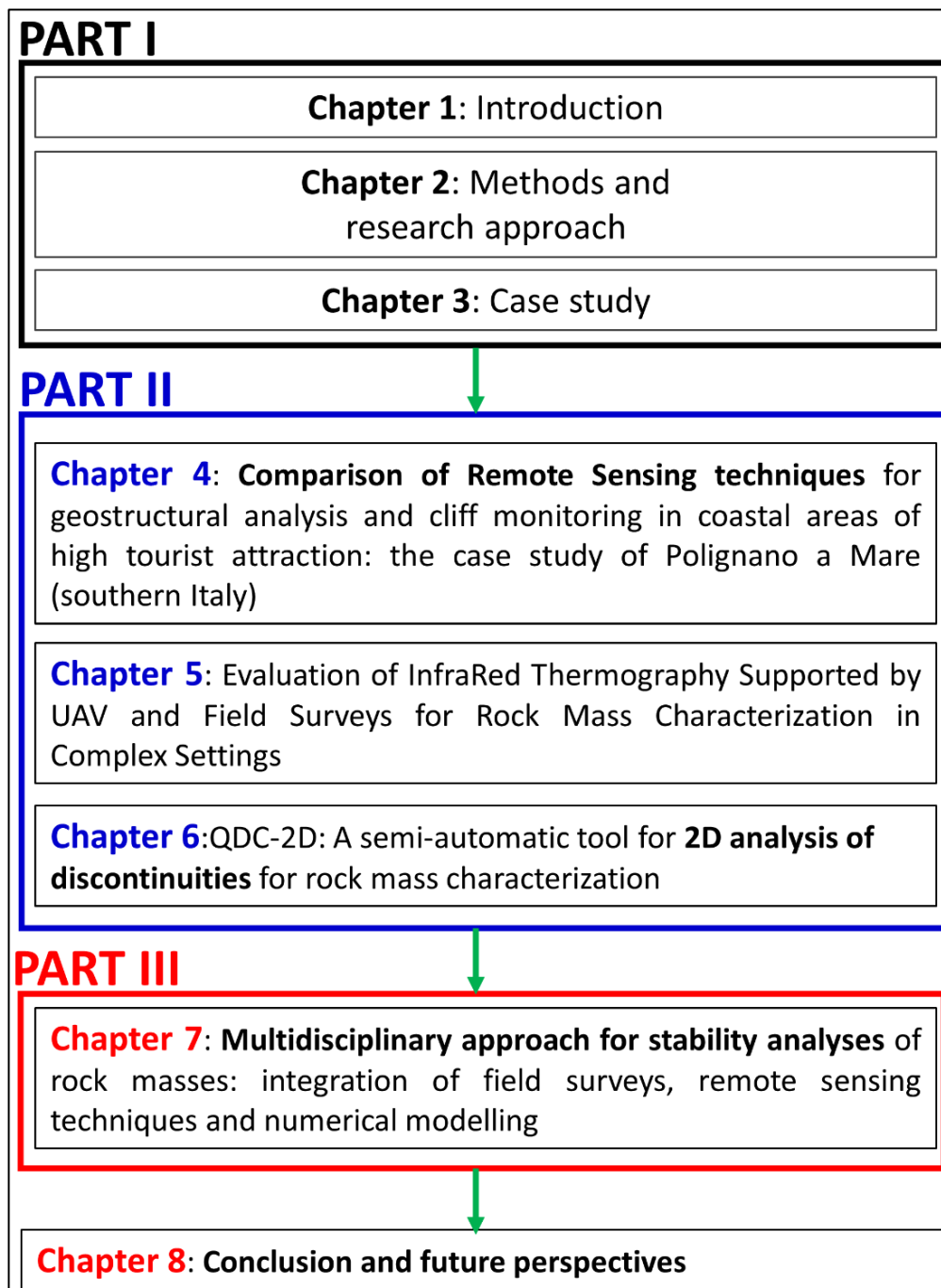


Figure 1.1: Flowchart of the thesis structure.

The last part of this chapter provides a detailed summary of the questions and potential improvements arose during the literature review and of the specific goals of the thesis.

- **Chapter 3:** Case study

In this chapter, a comprehensive description of the case study is given. The final section explains the reasons that led to the choice of the site to conduct the research. It is remarked that each chapter in Part II and Part III presents a study carried out on the same site, which was analyzed from different perspectives to achieve different goals. For this reason, this manuscript may be redundant with regard to the site description. However, it is specified that each chapter, which is supposed to be self-contained, reports only the information relevant to address the discussed topic, whilst Chapter 4 provides an overall description to contextualize the case study in a broader context.

- **PART II:** Remote Sensing

This part aims at investigating the application of remote sensing approaches for rock slope characterization, with focus on the questions posed in Chapter 2. More in detail, this part comprises three chapters, which are described below.

- **Chapter 4:** *Comparison of Remote Sensing techniques for geostructural analysis and cliff monitoring in coastal areas of high tourist attraction: the case study of Polignano a Mare (southern Italy)*

This chapter, which was published as a technical note in *Remote Sensing – Special Issue Remote Sensing for Rock Slope and Rockfall Analysis* in December 2021, compares Terrestrial Laser Scanning (TLS), terrestrial and UAV-based photogrammetry and IRT techniques for rock slope geostructural analyses and monitoring. Particular emphasis was given to the quantitative assessment of the generated point clouds, to application of two semi-automatic methods to extract and characterize the discontinuities, and to detection of rockfalls by means of multi-temporal acquisitions. After the validation by means of conventional geostructural field surveys, the pros and cons of each method were outlined.

- **Chapter 5:** *Evaluation of InfraRed Thermography Supported by UAV and Field Surveys for Rock Mass Characterization in Complex Settings*

In this chapter, which was published as a communication in *Geosciences* in March 2022, the use of IRT technique for carbonate rock mass characterization in complex conditions (e.g. poor accessibility, vegetation, human interventions) is discussed. Specific investigations are reported to assess the IRT applicability, what type of information can be collected, and what are its main advantages and limitations.

- **Chapter 6:** *QDC-2D: A semi-automatic tool for 2D analysis of discontinuities for rock mass characterization*

This chapter was published as an original article in *Remote Sensing – Special Issue 3D Point Clouds in Rock Mechanics Applications* in December 2021 and deals with the development of a publicly available MATLAB routine to perform quantitative discontinuity characterization by means of stochastic analyses of discontinuity traces. The time-consuming methods presented in the literature since the eighties were implemented in a digital environment to speed up the process and analyze more data,

hence achieving statistical significance. This chapter illustrates in which cases the proposed routine is preferred to point clouds or meshes analyses, as well as the procedures to pre-process the Digital Outcrop Models (DOMs) in order to carry out the 2-D analysis.

- **PART III:** Integration of remote sensing and conventional surveys for advanced stability analyses

This part aims at linking the different themes faced in Part II and to combine them with the conventional geostuctural and geomechanical methods for rock slope stability analysis. It is formed by the penultimate chapter of this manuscript.

- **Chapter 7:** Multidisciplinary approach for stability analyses of rock masses: integration of field surveys, remote sensing techniques and numerical modelling.

This chapter reports the developed procedure for rock slope stability analyses based on the combination of traditional field surveys, remote sensing data, 2-D and 3-D numerical modelling by means of stochastic approaches. Given the large amount of data due to interdisciplinary character of this study, this chapter is divided in two smaller sections (sections 7.3-7.7 and section 7.8) for submission to an international journal. The first part of the method describes the set-up of an innovative 3-D geomechanical model which includes the results of the previous chapters, as well as the physical and mechanical properties of both rock materials and discontinuities. The second part concerns the stability analyses carried out using the geomechanical model by means of 2-D and 3-D numerical modelling, with focus on the effects of discontinuity implementation with respect to continuum-based approaches. In addition, different surface processes detected by means of conventional and remote sensing surveys were simulated to observe the stability of the case study in different scenarios, and to observe the failure mechanisms.

- **Chapter 8:** Conclusion and future perspectives

Since Chapters 4-7 individually present a discussion section, this last chapter summarizes the major findings of this study in relation to the research rationale, and discusses future developments for the proposed methodology.

Chapter 2 Methods and research approach

2.1. Discontinuities

2.1.1. Definition

Rock slope discontinuities play a key role in strength, deformability and permeability of rock masses, and exhaustive understanding of their properties is crucial to assess the stability of the medium (Hoek and Bray 1981; Hudson and Harrison 2000). As described by Priest (1993), discontinuities are all significant mechanical breaks or fractures of negligible tensile strength, low shear strength and high fluid conductivity in rocks, regardless of their age, geometry and origin.

2.1.2. Types of discontinuities and field sampling techniques

The types and properties of discontinuities are discussed in many books, to which reference is made for more extensive information (Fookes and Denness 1969, 2015; Piteau 1973; Attewell and Farmer 2012; Baecher and Lanney 1978; ISRM 1978; Priest and Hudson 1981; Blyth and De Freitas 1984, 2017; Priest 1993; Wyllie 1999, 2017; Hills 2012; Price 2016).

According to their origin, discontinuities can be classified as:

- Bedding planes: extensive discontinuities in sedimentary rock masses determined by interruptions in the sedimentation. Bedding planes are generally parallel to each other but can be folded during the deformation processes.
- Faults: discontinuities with identifiable relative displacements on the opposite sides of the fault plane.
- Joints: discontinuities with no visible relative displacement, often arranged in groups of parallel or subparallel structures, to form joint sets. Joints are the result of several geological processes related to the stresses induced, for instance, by rapid cooling of basaltic lava flows (columnar joints), diurnal temperature changes, geologic uplift or tectonic processes.
- Foliation: planar surfaces produced by the recrystallization and parallel alignment of platy minerals during metamorphism.
- Fractures and cracks: in the literature, these terms are related to brittle mechanisms, but they do not have a unique definition. According to Priest (1993), the words “fracture” and “crack” are used as synonyms of the term “discontinuity” in general and colloquial speech.

In common practice, quantitative characterizations of discontinuities are carried out following the International Society for Rock Mechanics recommendations (ISRM 1978), aimed at determining 10 attributes (Figure 2.1):

1. *Orientation*: it represents the attitude of a discontinuity in space and is measured by means of geologic compass and clinometer. In this PhD thesis, it will be defined by means of strike

and dip direction/dip for in plan (top view imagery) and 3-D datasets (point clouds and triangulated surfaces), respectively.

2. *Set spacing*: normal distance between two adjacent discontinuities belonging to the same discontinuity set.
3. *Persistence or continuity*: length of the trace of a discontinuity observed in an exposure.
4. *Roughness*: degree of asperity of the discontinuity surface at different scales.
5. *Wall strength*: compressive strength of the exposed surface of a discontinuity.
6. *Aperture*: orthogonal distance between the two opposite sides of an open discontinuity, filled by air or water.
7. *Infilling*: material separating the two rock walls of a discontinuity. It can be made up of weaker (*i.e.* soil, weathered material) or more resistant material (*i.e.* cement, veins).
8. *Water seepage*: presence of water inside a discontinuity or the whole rock mass.
9. *Number of discontinuity sets*: number of sets in which the discontinuity network is arranged.
10. *Block size*: dimensions of the rock blocks determined by intersecting discontinuities.

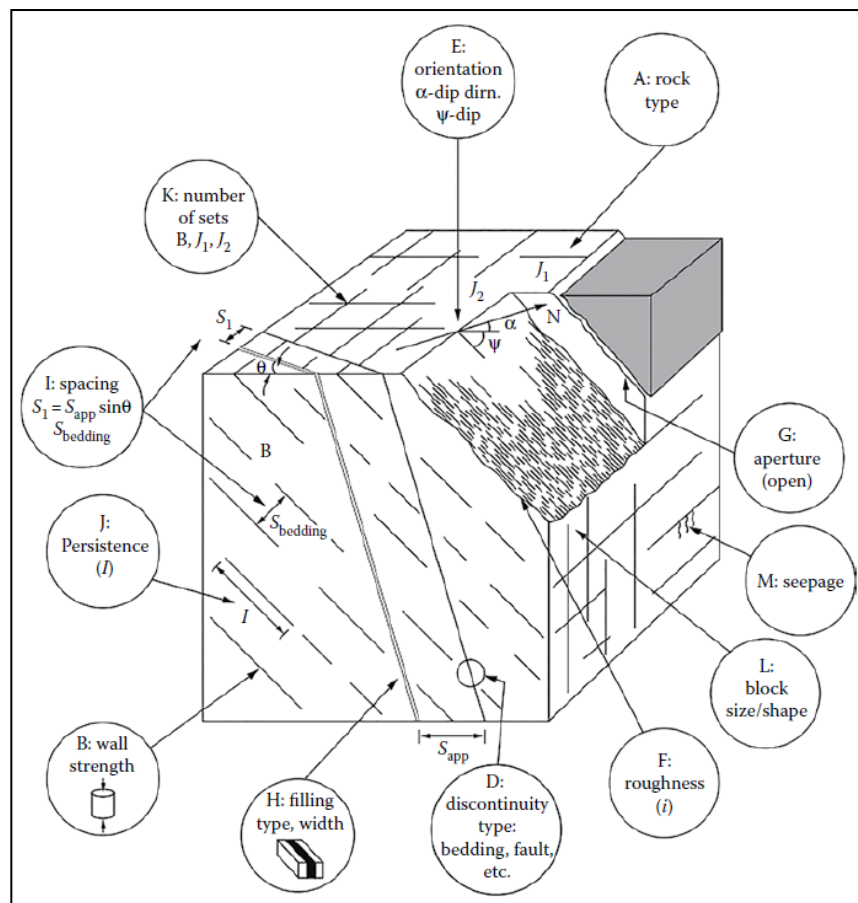


Figure 2.1: Sketch illustrating the discontinuity properties to be collected for rock mass characterization (after Wyllie 1999).

The two most applied sampling strategies to collect information on discontinuities in the field are the *scanline* and the *window* surveys. The first approach consists in placing an imaginary or physical line on an exposed rock face representative for the study area and acquiring data on all the discontinuity traces that intersect the line. According to Priest (1993), 150-350 discontinuities, of which half with

at least one termination visible, should be analyzed in order to obtain statistical significance. The scanline should be long enough compared to size and spacing of the discontinuities. For instance, Priest and Hudson (1976) suggest that the length of the linear sample should be at least 50 times the mean discontinuity set spacing. With regards to the number of scanlines, it is recommended to apply at least three sampling lines orthogonal to each other (Priest, 1993). Further description and discussions on scanlines are reported by La Pointe and Hudson (1985), Villaescusa (1992), Priest (1993) and Windsor (1997).

The window sampling is a bi-dimensional analysis aimed at collecting information on the discontinuities whose traces intersect or are located in a rectangular window. As for the scanline, the size of the window should be appropriate, so that at least 30-100 discontinuities intersect each side (Priest, 1993). To avoid under-sampling of the discontinuities parallel to the sampled surface, a second window should be placed perpendicularly to the first one.

2.1.3. Quantitative discontinuity characterization

2.1.3.1. Orientation

After the data collection, the orientations of the sampled discontinuities are commonly plotted on stereonet with the support of specific softwares. Stereographic projections allow to represent a planar surface as a point in the circle of geographical azimuth directions, with the north generally corresponding to azimuth=0° (Phillips 1955; Goodman 1976; Kalkani and von Frese 1980; Duncan 1981). Contouring plots help to identify the main discontinuity sets by individuating group of poles (clusters) by eye. Several clustering algorithms were introduced in the literature to avoid personal biases in order to identify the discontinuity sets in a more objective way (Miller 1983; Mahtab and Yegulalp 1984; Harrison 1992; Kulatilake 1993). The orientation of a discontinuity can also be expressed in vectorial form by converting the dip direction and dip in the Cartesian components u_x , u_y , u_z of the discontinuity normal (pole) (Figure 2.2).

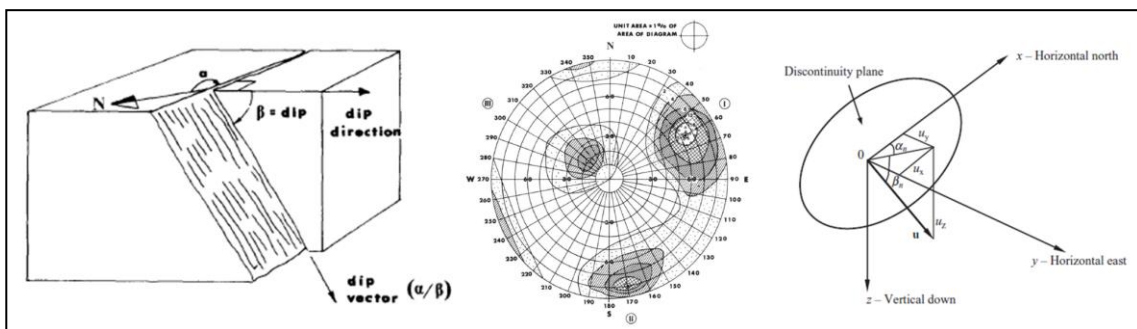


Figure 2.2: Discontinuity orientation. (a) measurement of dip/dip direction of a discontinuity (after ISRM 1978); (b) contour pole of three discontinuity sets by means of stereographic projections (after ISRM 1978); (c) vectorial representation of a discontinuity (after Zhang 2016).

With regards to measurements of the orientations along a scanline, several authors pointed out that any sampling line has a major probability of intersecting discontinuity traces perpendicular to its direction, and a probability of intersecting parallel discontinuities close to zero (Baecher 1983; Kulatilake and Wu 1984b). This issue is less problematic for the window sampling technique, in which all the traces partially located in the sampling area are recorded. For mono-dimensional analyses,

Terzaghi (1965) proposed to compensate this effect, known as *orientation bias*, by multiplying the vector of each discontinuity by a correction factor w :

$$w = \frac{1}{\cos\delta} \quad (\text{for } \delta < 90^\circ) \quad \text{Eq. 2.1}$$

where δ is the acute angle between the discontinuity normal and the scanline (Figure 2.3).

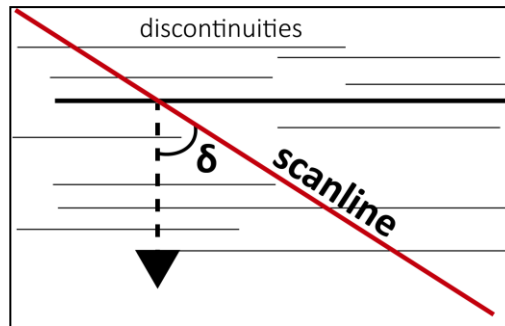


Figure 2.3: Application of Terzaghi's correction factor to correct orientation biases (modified after Terzaghi 1965).

Geostatistic approaches are traditionally applied to derive the probability distribution of the orientation of a dataset. The simplest and most used probability function is represented by the Fisher's model, which is based on the assumption that the orientations of a discontinuity set are symmetrically distributed around a mean value:

$$f(\theta) = \frac{K \sin\theta e^{K\cos\theta}}{e^K - e^{-K}} \quad \text{Eq. 2.2}$$

where θ is the angular deviation from the mean vector and K is the *Fisher constant*. This parameter gives an estimation of the degree of clustering: a small value of K is attributable to a large cluster and therefore to more dispersed orientations. Asymmetric datasets can be better defined using more complex probability distributions, such as bivariate Fisher, Bingham, bivariate normal and bivariate normal distribution (Shanley and Mahtab 1976; Kulatilake 1985, 1986). However, Einstein and co-workers (Einstein et al. 1979) performed goodness-of-fit tests on different distributions and demonstrated that not all the datasets agree with the current analytical models. As pointed out by Zhang (2016), empirical distributions might be a reasonable compromise for orientations that do not fit well with the models proposed so far.

2.1.3.2. Spacing

Generally speaking, the discontinuity spacing is the distance between two adjacent discontinuities along a scanline. Priest (1993) specifies that this parameter can be named *set spacing* if the measurement is carried out along discontinuities belonging to the same set, and *normal set spacing* if it is calculated along a scanline perpendicular to the mean orientation of the set. If the sampling line is not perpendicular to the mean direction of the discontinuity set, an apparent value S_d will be obtained. The normal set spacing S_n can be calculated by applying Terzaghi's correction:

$$S_n = S_d \cos\delta \quad \text{Eq. 2.3}$$

The classification of the discontinuity spacing proposed by ISRM (1978) is illustrated in Table 2.1.

Table 2.1: Classification of discontinuity spacing according to ISRM (1978).

Description	Spacing (mm)
Extremely close spacing	<20
Very close spacing	20-60
Close spacing	60-200
Moderate spacing	200-600
Wide spacing	600-2000
Very wide spacing	2000-6000
Extremely wide spacing	>6000

Since discontinuity spacings do not have a unique value, many authors investigated their distribution by plotting histograms in order to determine their probability density distribution. The most common distribution forms used in the literature for homogeneous and isotropic materials are the lognormal and the negative exponential (Rives et al. 1992). The negative exponential form, implicating that most discontinuities are closely spaced whilst widely spaced discontinuities are less common, was introduced by Priest and Hudson (Priest and Hudson 1976; Hudson and Priest 1979) who tested several varieties of sedimentary rocks, and was later supported by Wallis and King (1980) and Einstein and Baecher (1983), who worked respectively on porphyritic granites and on igneous, sedimentary and metamorphic rocks. For instance, Figure 2.4 illustrates the discontinuity spacing histogram and the fitted negative exponential law for the scanline strategy applied in a tunnel in Lower Chalk at Chinnor, UK (Priest and Hudson 1976).

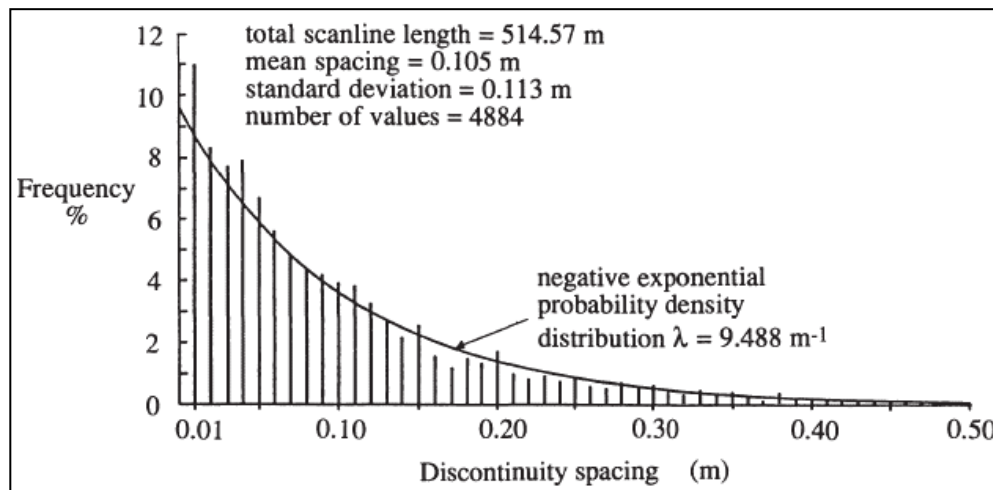
The frequency $f(x)$ for a given discontinuity spacing value s is given by:

$$f(x) = \frac{1}{\bar{x}} (e^{-x/\bar{x}}) \tag{Eq. 2.4}$$

and the associated cumulative probability $F(x)$ that a given spacing value will be less than the dimension x is given by:

$$F(x) = 1 - (e^{-x/\bar{x}}) \tag{Eq. 2.5}$$

where x is the measured value of spacing and \bar{x} is the mean spacing.



obscured if the endpoints are located outside the rock exposure (*persistent discontinuities*) (ISRM 1981; Ulusay 2015). The termination index T_i proposed by the ISRM (1978) is given by:

$$T_i = \frac{100 N_i}{N_i + N_a + N_o} \% \tag{Eq. 2.6}$$

where N_i , N_a and N_o are the number of discontinuities with terminations in intact rock (non-persistent discontinuities), at other discontinuities (abutting) and obscured, respectively. The higher is T_i , the higher is the number of discontinuities.

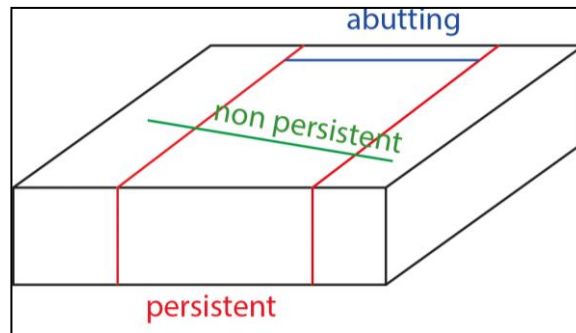


Figure 2.6: Examples of discontinuity persistence (modified after ISRM 1978).

Discontinuity persistence is one of the most difficult parameters to estimate in the field (Einstein et al. 1983) and therefore it is common practice to approximate the discontinuity set persistence from their modal lengths, as suggested by ISRM (1978). Discontinuity persistence can be classified according to the system reported in Table 2.2.

Table 2.2: Classification of discontinuity persistence according to the modal trace length (after ISRM 1978).

Description	Modal trace length (m)
Very low persistence	<1
Low persistence	1-3
Medium persistence	3-10
High persistence	10-20
Very high persistence	>20

2.1.3.5. Trace lengths

The trace lengths of discontinuities are fundamental to estimate the discontinuity size from scanline or window mapping techniques, thus performing bi-dimensional analyses. For limited extent out-crops it is common practice to measure the lengths of discontinuities located above or below the scanline, referred as *semi-trace lengths* (Figure 2.7). Whether dealing with trace lengths or semi-trace lengths, several authors illustrated sources of errors in their estimation (Baecher and Lanney 1978; Einstein et al. 1979; Priest and Hudson 1981; Kulatilake and Wu 1984a; Priest 1993; Mauldon 1998; Zhang and Einstein 1998; Zhang and Ding 2010). The sampling biases affecting these parameters are:

- Size bias: the probability that a scanline intersects a discontinuity trace is directly proportional to its trace length. For this reason, shorter traces tend to be undersampled.

- Trimming bias: traces smaller than a certain threshold are difficult to be identified. The terms *truncation* and *trimming* refer respectively to the fact that the number of ignored traces is recorded or not.
- Curtailment bias: long discontinuities are probable to terminate beyond the visible exposure and their measurement is subjected to a cut-off (c_m in Figure 2.7).

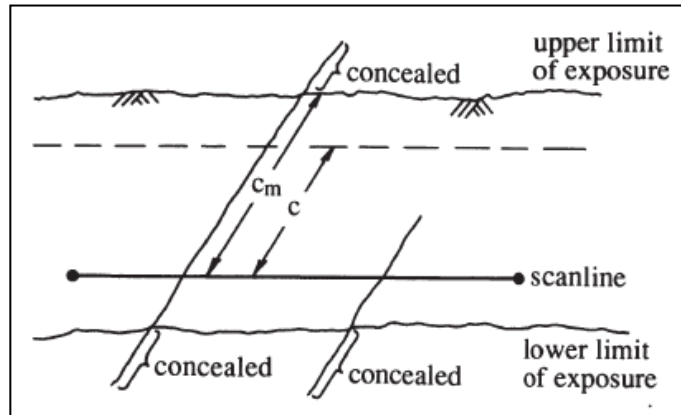


Figure 2.7: Curtailed trace-lengths due to a limited extent of the outcrop (after Priest and Hudson 1981).

To avoid the curtailment bias, Priest (1993) proposed the following formula to derive the corrected trace length, which is in agreement with that presented by Warburton (1980):

$$\mu_{iL} = \int_0^c \frac{l h(l) dl}{H(c)} \quad \text{Eq. 2.7}$$

where μ_{iL} is the theoretical length, $h(l)$ is the probability density distribution and $H(c)$ is a constant depending on $h(l)$. The author emphasizes that this approach can be applied only if the density distribution is known; formulas to derive μ_{iL} for uniform, triangular and negative exponential distributions are presented in his paperwork. However, the topic of the trace length probability distribution is still subject of debate and other researchers support lognormal and exponential models (Cruden 1977; Einstein et al. 1979; Baecher 1983; Kulatilake 1993) (Figure 2.8).

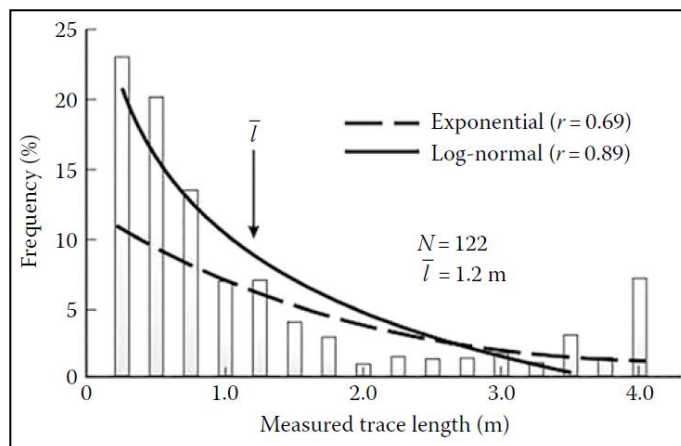


Figure 2.8: Histogram of discontinuity trace lengths, with best-fit exponential and lognormal curves (after Priest and Hudson 1981).

A method to estimate the corrected trace length independently from the type of distribution was reported by Pahl (1981) and is based on the geometrical relationship between the discontinuities and a rectangular sampling window (Figure 2.9). According to the author’s definition, the discontinuities are said to be *contained* if they have both terminations inside the sampling window, *dissecting* if only one termination is located inside the window and *transecting* if both the terminations are located outside the window. The mean trace length is calculated as:

$$\mu_L = \frac{w h (n_{tot} + n_0 - n_2)}{(w \cos \phi + h \sin \phi) (n_{tot} - n_0 + n_2)} \tag{Eq. 2.8}$$

where w and h are the length and height of the window, n_0 , n_2 and n_{tot} are the number of transecting, contained, and total discontinuities, respectively, and ϕ is the acute angle between the discontinuities and the height side of the window. As remarked by Priest (1993), the method is unsuitable when all the discontinuities transect the window and when no discontinuities are contained in the window. In the first case, since $n_{tot}=n_0$, the mean trace length would be infinite, whilst in the second case ($n_{tot}=n_2$) the mean trace length would be zero.

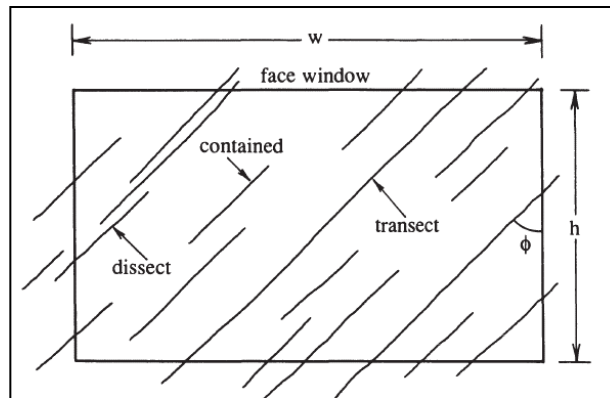


Figure 2.9: Estimation of the corrected trace length by means of Pahl’s method (1981).

2.1.3.6. Block size

The size of blocks is determined by the number of discontinuity sets, discontinuity spacing and persistence. Where relatively regular discontinuity patterns exist, Dearman’s system (Dearman 1991) can be used to determine the block shape (Figure 2.10). A method to classify the rock blocks according to their volume was proposed by Palmstrøm (1996b) by means of the Block volume parameter V_b (Table 2.3).

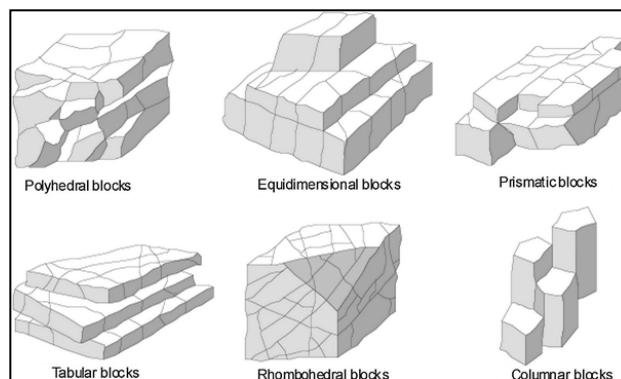


Figure 2.10: Examples of block shapes (after Dearman 1991).

Table 2.3: Classification of block size by means of the Block volume parameter (after Palmstrøm 1996a).

Description	Block volume V_b
Extremely small	<10 cm ³
Very small	10-200 cm ³
Small	0.2-10 dm ³
Moderate	10-200 dm ³
Large	0.2-10 m ³
Very large	10-200 m ³
Extremely large	>200 m ³

2.1.4. Additional properties

Non-geometrical properties of discontinuities such as filling, seepage and weathering are fundamental to achieve a thoroughgoing discontinuity characterization. Since a large part of this manuscript is dedicated to the characterization of the discontinuities by analysing data obtained by means of remote sensing techniques, non-geometrical properties and millimetric scale geometrical properties (*i.e.* roughness and aperture) will be briefly summarised.

2.1.4.1. Roughness

Discontinuity roughness represents the surface irregularity both on a small scale (*i.e.* waviness) and on a large scale (*i.e.* unevenness) (Figure 2.11) and strongly influences the shear strength of the discontinuity itself (Patton 1966; Rengers 1970). Both types of roughness are estimated by means of different methods, such as profilometers (Barton and Choubey 1977) and straight edge (Stimpson 1982). Large scale (several centimetres) and intermediate scale (several metres) roughness can be classified following the ISRM system (1978) by comparing the roughness profile with standardized profiles (Table 2.4).

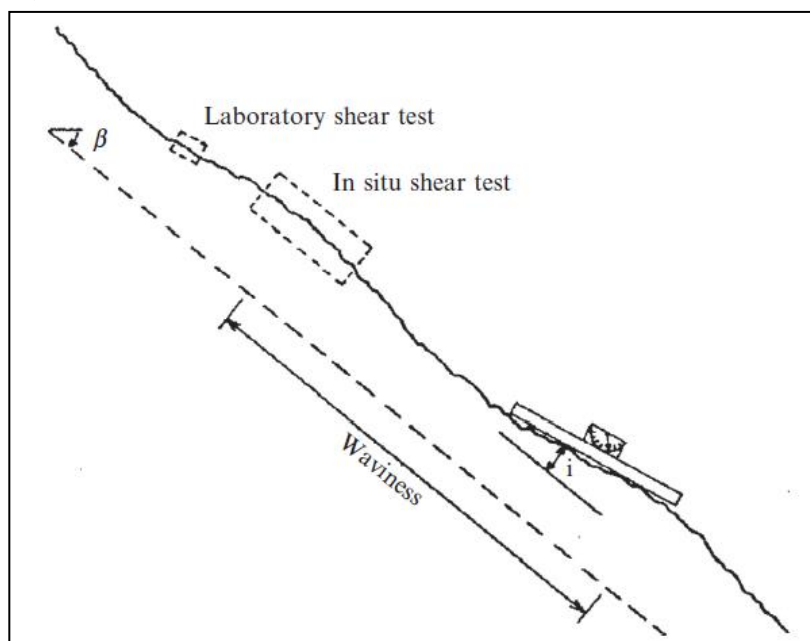
**Figure 2.11:** Different scales of discontinuity roughness (after ISRM 1978).

Table 2.4: Large and intermediate scale classification of discontinuity roughness (after ISRM 1978).

Class	Description
I	Rough, stepped
II	Smooth, stepped
III	Slickensided, stepped
IV	Rough, undulating
V	Smooth, undulating
VI	Slickensided, undulating
VII	Rough, planar
VIII	Smooth, planar
IX	Slickensided, planar

2.1.4.2. Aperture

Discontinuity aperture is the result of shear displacement of rough surfaces, outwash of filling material, tensile opening and solution processes. The aperture of a discontinuity influences its deformability, shear strength and hydraulic conductivity. The ISRM aperture classification system (1978) is reported in Table 2.5.

Table 2.5: Classification of discontinuity aperture (after ISRM 1978).

Description	Aperture (mm)	
"Closed features"	Very tight	<0.1
	Tight	0.1-0.25
	Partly open	0.25-0.5
"Gapped" features	Open	0.5-2.5
	Moderately wide	2.5-10
	Wide	>10
"Open" features	Very wide	10-100
	Extremely wide	100-1000

2.1.4.3. Wall strength

The compressive strength of discontinuities is a fundamental component of the shear strength and is especially relevant for unfilled surface. This property is commonly measured by means of *Schmidt hammer* tests.

2.1.4.4. Infilling, seepage and weathering

When dealing with filled discontinuities, the physical and mechanical properties of the infilling should be determined in order to correctly define the discontinuity mechanical behaviour. In addition, care should be taken to the presence of water within the discontinuity system, karstification processes and weathering. With regards to the weathering, mechanical disintegration and chemical alteration like solution can significantly reduce discontinuity strength and deformability, especially near the ground surface. In addition, any karst processes should be considered because soluble rock solution can develop through the main discontinuity systems and lead to the formation of conduits and caves, thus causing anisotropy and significantly influencing the rock mass behaviour (Andriani and Parise 2015, 2017). Despite karst processes are not described in the ISRM guidelines for discontinuities

quantitative analyses, in this manuscript it is strongly recommended to take them into account, as karst occurs in around 20% of the emerged Earth's surface (Parise et al. 2015a).

2.2. Use of discontinuity information for rock mass characterization

This section will briefly illustrate how discontinuity properties are integrated in the most popular rock mass classification systems used for the characterization of rock masses and the design of engineering rock structures such as tunnels and underground excavations.

2.2.1. Rock Quality Designation (RQD)

The RQD system was introduced by Deere (1964) and is based on the estimation of the RQD index, which can be determined from drill core logs or indirectly by using correlations such as the discontinuity frequency (Priest and Hudson 1976). For instance, Palmstrøm (1996b) suggested the following relationship to evaluate the RQD from the number of discontinuities per unit volume when no core is available, but discontinuity traces are well visible in rock exposures:

$$RQD = 115 - 3.3J_v \quad \text{Eq. 2.9}$$

where J_v is the volumetric joint count (see Chapter 6).

As pointed out by Hoek (2007), the use of the volumetric joint count to determine the RQD index can help reducing its direction dependence from the borehole orientation.

The rock mass quality is classified in 5 classes according to the RQD value (Table 2.6). As stated by Zhang (2006), when considered alone the RQD index is not sufficient to achieve a comprehensive understanding of the rock mass behaviour, because it does not take into account the discontinuity properties. As a matter of fact, the RQD index is nowadays used as input parameter in other classification systems.

Table 2.6: Rock Mass Quality according to the RQD System (after Deere 1964).

RQD (%)	Rock Mass Quality
<25	Very poor
25-50	Poor
50-75	Fair
75-90	Good
90-100	Excellent

2.2.2. Rock Mass Rating (RMR) and Slope Mass Rating (SMR)

The Rock Mass Rating system proposed by Bieniawski (1973, 1976, 1989) was developed for tunnels and successively extended to rock slopes and foundations (Romana 1985). It is based on the estimation of the RMR index which depends on the strength properties of the intact rock, as well as on the discontinuity conditions:

$$RMR_b = R_s + RQD + R_{dj} + R_{cj} + R_w \quad \text{Eq. 2.10}$$

where R_s is the compressive strength of the intact rock, R_{dj} is the joint spacing, R_{cj} refers to the joint conditions and R_w represents the groundwater conditions. The rock mass quality is classified in 5 classes, as illustrated in Table 2.7.

Table 2.7: Rock mass classification according to the RMR system (after Bieniawski 1973).

RMR	Rock Mass Quality
100-81	Very good
80-61	Good
60-41	Fair
40-21	Poor
<20	Very poor

The RMR system was modified by means of the Slope Mass Rating (SMR) proposed by Romana (1985) to achieve more realistic rock mass quality assessment in view of stability assessment:

$$SMR = RMR_b + (F_1 \cdot F_2 \cdot F_3) + F_4 \tag{Eq. 2.11}$$

where RMR_b is the basic RMR index resulting from Bieniawski’s classification, F_1 depends on the parallelism between discontinuity strike and slope face strike, F_2 refers to joint dip angle in the planar mode of failure., F_3 depends on the relationship between discontinuity dip and slope face dip and F_4 is a correction factor related to the excavation method. Five rock mass stability classes, ranging from completely unstable (SMR <20) to completely stable (SMR<81), were proposed according to the SMR value (Table 2.8).

Table 2.8: Rock mass classification according to the SMR system (after Romana 1985).

SMR	Rock Mass Quality
100-81	Very good
80-61	Good
60-41	Normal
40-21	Bad
<20	Very bad

2.2.3. Q-System

The Q-system was presented by Barton (1974) for tunnel and underground excavations and successively extended to other applications in rock masses (Barton 2002). The rock mass quality is estimated by means of the Q index, which takes into account the discontinuity properties:

$$Q = \frac{RQD}{J_n} \frac{J_r}{J_a} \frac{J_w}{SRF} \tag{Eq. 2.12}$$

where J_n is the number of joint sets, J_r is the joint roughness parameter, J_a is the joint alteration parameter, J_w is the joint water parameter and SRF is the Stress Reduction Factor. In detail, the first quotient refers to the structure of the rock mass, the second is related to properties of the discontinuities (roughness and alteration of the walls) and the third expresses the stress conditions. Further information on the estimation of the parameters can be found in specific tables presented by Barton

and co-workers (Barton et al. 1974). Depending on the Q value, the rock mass can be classified in 9 classes (Table 2.9).

Table 2.9: Rock mass classification according to the Q system (after Barton 1974).

Q	Rock Mass Quality
1000-400	Exceptionally good
400-100	Extremely good
100-40	Very good
40-10	Good
10-4	Fair
4-1	Poor
1-0.1	Very poor
0.0-0.01	Extremely poor
0.01-0.001	Exceptionally poor

2.2.4. Rock Mass index (RMI)

The Rock Mass index (RMI) introduced by Palmstrøm (1996a) classifies rock masses taking into account the properties of the discontinuity which tend to reduce their strength.

The RMI is expressed as:

$$RMI = \sigma_c JP \quad \text{Eq. 2.13}$$

where σ_c is the uniaxial compressive strength of the intact rock and JP is the jointing parameter, which expresses the strength reduction of the intact rock caused by the joints.

The jointing parameter is composed of the joint condition factor (jC) and the block volume (V_b), according to the following relation:

$$JP = 0.2 \sqrt{jC} V_b^D \quad \text{Eq. 2.14}$$

where D is a constant.

More in detail, the joint condition factor is given by:

$$jC = j_R \frac{j_L}{j_A} \quad \text{Eq. 2.15}$$

where j_R , j_L and j_A are, respectively, the joint roughness factor, the joint size and continuity factor, and the joint alteration factor.

All the attributes needed to determine the RMI are illustrated in Figure 2.12.

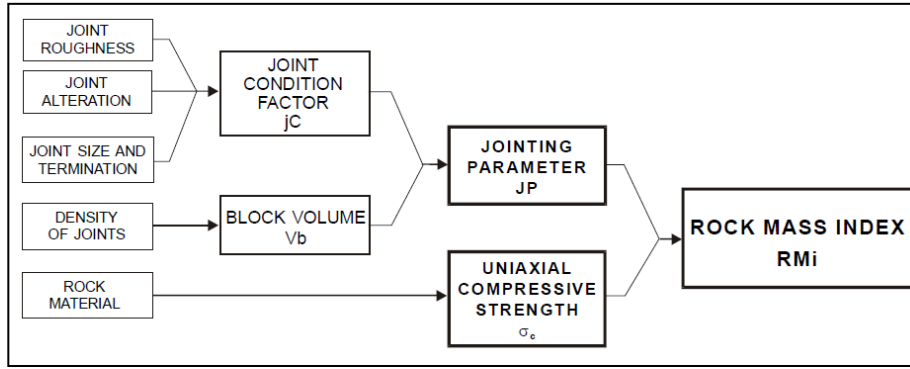


Figure 2.12: Discontinuity properties used for the RMI classification system (after Palmstrøm 1996a).

Table 2.10: Rock mass classification according to the RMI system (after Palmstrøm 1996a).

RMI	Rock Mass Quality
<0.001	Extremely weak
0.001-0.01	Very weak
0.01-0.1	Weak
0.1-1	Medium
1-10	Strong
10-100	Very strong
>100	Extremely strong

Several authors presented correlations to predict the mentioned classification indexes from one system to another. Specific equations, tables and discussions are reported by Zhang (2016).

2.2.5. Geological Strength Index (GSI)

The GSI classification system was proposed by Hoek and Brown (1997) and relies on the Hoek-Brown strength criterion for rock masses. Originally, this criterion was formulated for the intact rock (Hoek & Brown 1980a, 1980b) as:

$$\sigma'_1 = \sigma'_3 + \sigma_{ci} \left(m_i \frac{\sigma'_3}{\sigma_{ci}} + 1 \right)^{0.5} \quad \text{Eq. 2.16}$$

where σ_1 and σ_3 are the major and minor principal stresses, respectively, σ_{ci} is the unconfined compressive strength and m_i is a material constant for the intact rock.

The criterion was later adapted to rock masses by means of the generalized Hoek-Brown strength criterion (Hoek & Brown 1997), defined through the following equation:

$$\sigma'_1 = \sigma'_3 + \sigma_{ci} \left(m_b \frac{\sigma'_3}{\sigma_{ci}} + s \right)^\alpha \quad \text{Eq. 2.17}$$

where m_b , s , and α are constants defined for the rock mass material.

The GSI classification system provides a qualitative evaluation of the rock mass quality by means of the GSI index, which is determined by the rock mass structure (ranging from intact to disintegrated)

and the discontinuity conditions (from very good to very poor). Since the estimation of the GSI is rather subjective, Hoek and Brown suggested to identify a range of GSI rather than a single value. The original GSI classification system is reported in Figure 2.12. However, the system has been recently adapted to different types of rock masses and several charts are reported in the literature (Hoek and Marinos 2000; Hoek et al. 2002; Hoek and Brown 2019).

GEOLOGICAL STRENGTH INDEX FOR JOINTED ROCKS (Hoek and Marinos, 2000) From the lithology, structure and surface conditions of the discontinuities, estimate the average value of GSI. Do not try to be too precise. Quoting a range from 33 to 37 is more realistic than stating that GSI = 35. Note that the table does not apply to structurally controlled failures. Where weak planar structural planes are present in an unfavourable orientation with respect to the excavation face, these will dominate the rock mass behaviour. The shear strength of surfaces in rocks that are prone to deterioration as a result of changes in moisture content will be reduced if water is present. When working with rocks in the fair to very poor categories, a shift to the right may be made for wet conditions. Water pressure is dealt with by effective stress analysis.		SURFACE CONDITIONS				
STRUCTURE		VERY GOOD	GOOD	FAIR	POOR	VERY POOR
		Very rough, fresh unweathered surfaces	Rough, slightly weathered, iron stained surfaces	Smooth, moderately weathered and altered surfaces	Slickensided, highly weathered surfaces with compact coatings or fillings or angular fragments	Slickensided, highly weathered surfaces with soft clay coatings or fillings
		DECREASING SURFACE QUALITY →				
DECREASING INTERLOCKING OF ROCK PIECES ↓	 INTACT OR MASSIVE - intact rock specimens or massive in situ rock with few widely spaced discontinuities	90			N/A	N/A
	 BLOCKY - well interlocked undisturbed rock mass consisting of cubical blocks formed by three intersecting discontinuity sets	80	70			
	 VERY BLOCKY- interlocked, partially disturbed mass with multi-faceted angular blocks formed by 4 or more joint sets		60	50		
	 BLOCKY/DISTURBED/SEAMY - folded with angular blocks formed by many intersecting discontinuity sets. Persistence of bedding planes or schistosity			40	30	
	 DISINTEGRATED - poorly interlocked, heavily broken rock mass with mixture of angular and rounded rock pieces				20	
	 LAMINATED/SHEARED - Lack of blockiness due to close spacing of weak schistosity or shear planes	N/A	N/A			10

Figure 2.13: Characterization of rock masses by means of GSI system (after Hoek and Marinos 2000).

2.3. Rock slope failure mechanisms

In most cases, rock mass failures are controlled by geological structures, and their kinematics depend on the geometrical relationship between the slope and the discontinuities (Stead and Wolter 2015). Four main types - planar sliding, wedge sliding, rotational sliding and toppling - are described in many works as typical failure mechanisms (Hoek and Bray 1981; Goodman and Shi 1985; Giani 1992; Cruden 2003; Hoek 2007). However, supplementary types of failure were recognised based on the description of the phenomena rather than on the spatial orientation of the slope and of the joints (Jaboyedoff et al. 2001; Hantz et al. 2003; Hungr and Evans 2004; Hungr et al. 2014).

According to the classification systems proposed by Jaboyedoff and co-workers (Jaboyedoff et al. 2001) and by Hantz and co-workers (Hantz et al. 2003), the main failure modes in rock masses are:

- Planar sliding (Figure 2.14a): translational movement of a rock block along a plane dipping out of the slope. This mechanism occurs along a discontinuity striking parallel or nearly parallel to the slope and less steep than the slope dip. The failure surface can be persistent, connected by rock bridges or connected to a tension crack.
- Wedge sliding (Figure 2.14b): translational movement of a rock block defined by two discontinuities striking obliquely to the slope face and dipping out of it. The wedge can slide along the line of intersection of the two discontinuities, or along the plane with the most favourable attitude. Wedge sliding mechanisms were analyzed by many authors among which Goodman (1964), Londe and co-workers (Londe et al. 1969), John (1970) and Hoek (2007).
- Rotational sliding/double wedge slide (Figure 2.14c): typical failure mechanism of homogeneous weak or weathered rock masses along a circular sliding surface. If the sliding rock block is delimited by three discontinuity planes, the sliding is referred as *double wedge slide* (Goodman and Shi 1985).
- Overhang failure (Figure 2.14d): failure of protruding blocks due to the exceeding of the tensile strength along a sub-horizontal or sub-vertical discontinuity.
- Toppling (Figure 2.14e): rotation of columns or blocks delimited by sub-vertical discontinuities dipping into the slope; flexural toppling involves continuous columns with limited thickness which progressively bend forward (Goodman and Bray 1976; Hoek and Bray 1981; Sagaseta 1986; Adhikary et al. 1997).
- Column failure at the foot (Figure 2.14f): failure of a rock column determined by a sub-vertical discontinuity along its base.
- Buckling (Figure 2.14g): failure of banks with deep angle $>45^\circ$ favoured by the presence of orthogonal joints.

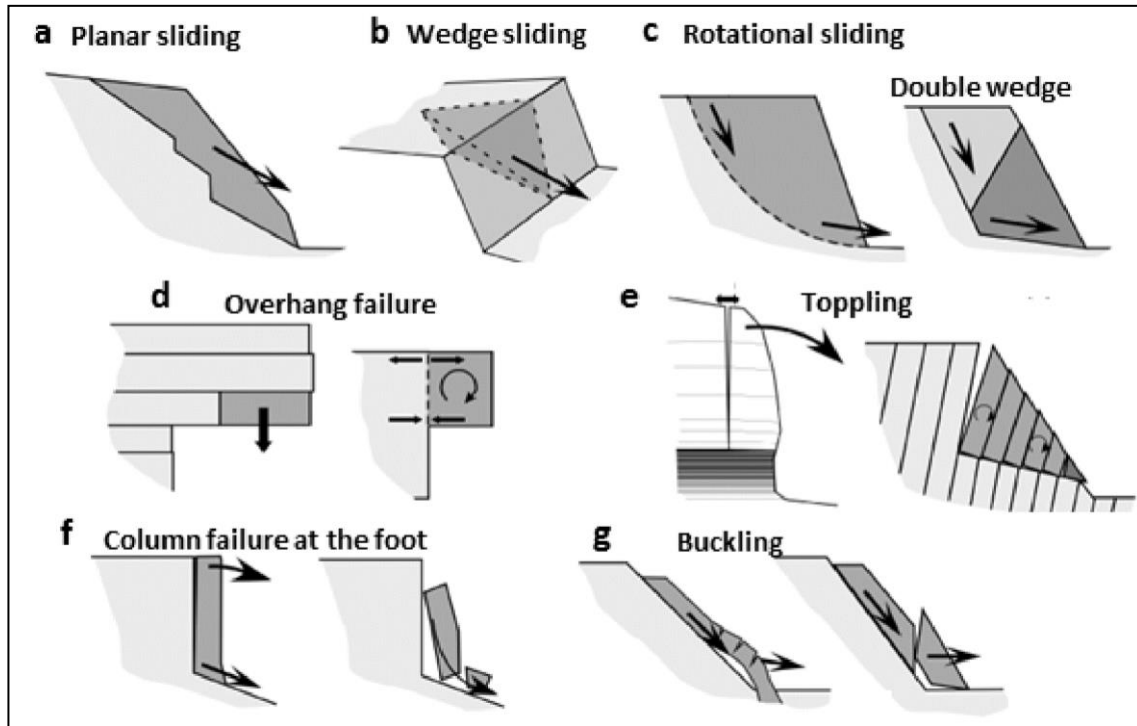


Figure 2.14: Typical failure mechanisms in rock masses (modified after Hantz et al. 2003).

It has to be remarked that the illustrated mechanisms are simplified models which are more likely to occur on large scale instability processes. Large volume phenomena are often the result of combined failure types acting simultaneously or successively, as pointed out by many authors (Sagaseta 1986; Adhikary et al. 1997; Sartori et al. 2003; Martin 2007; Gischig et al. 2011; Böhme et al. 2013; Moh-tarami et al. 2014; Bassa et al. 2014; Stead and Wolter 2015; Alejano et al. 2019; Alejano 2021). Furthermore, it is specified that, in some circumstances, the properties of the rock mass and the scale of the problem (e.g. discontinuity spacing in the domain) are compatible with global failures (i.e. circular slipping surfaces) rather than with the mobilization of single blocks. Indeed, instability processes of rock masses can result in a series of mechanisms ranging between the mentioned extreme conditions, respectively related to a continuum and discontinuum behaviour of the medium (Hoek 2007; Hoek & Bray 1981; Jing 2003; Jing & Hudson 2002).

2.4. Remote sensing background

2.4.1. Introduction

The last two decades have witnessed an impressive progression of geospatial technologies such as differential Global Positioning Systems (DGPS) and robotic devices which has led to a modernized approach to geosciences, thanks to the possibility to acquire and process large datasets.

Regardless of the field of study, remote sensing approaches can be classified as *passive* and *active* (Schowengerdt 2006).

Passive techniques like satellite imaging, photography and InfraRed Thermography enable to collect information using the natural radiation (e.g. sunlight) emitted or reflected by an object. On the other hand, active techniques such as LiDAR (Light Detection And Ranging) or Radar provide an impulse

that hits the target and is measured by the instrument after being reflected. With regard to rock slope investigations, if on the one hand remote sensing techniques can solve several issues typically faced during field surveys, on the other hand the large number of available technologies may be intimidating. In this perspective, the most important step for the choice of the appropriate technique consists in identifying the advantages and limitations of each method (Derron et al. 2011). An attempt to solve these uncertainties was made by Petrie and Toth (2018), who compared the two most used methods for rock slope investigation, namely laser scanning and photogrammetry (Figure 2.15). In addition, the characteristics of the investigated area (e.g. extension, morphology, meteorological conditions), the goals of the surveys (e.g. needed resolution, accuracy, ease of reproducibility), time availability and budget should be all considered in attempt to find the most suitable solution.

Photogrammetric Weaknesses, Contrasted with LiDAR Strengths	
LiDAR Pros	Photogrammetric Cons
Dense information along homogeneous surfaces	Almost no positional information along homogeneous surfaces
Day or night data collection	Day time data collection only
Direct acquisition of 3D coordinates	Complicated and sometimes unreliable matching procedures
The vertical accuracy is better than the planimetric accuracy	The vertical accuracy is worse than the planimetric accuracy
<hr/>	
LiDAR Weaknesses, Contrasted with Photogrammetric Strengths	
Photogrammetric Pros	LiDAR Cons
High redundancy	No inherent redundancy
Rich in semantic information	Positional information; difficult to derive semantic information
Dense positional information along object space break lines	Almost no positional information along break lines
The planimetric accuracy is better than the vertical accuracy	The planimetric accuracy is worse than the vertical accuracy

Figure 2.15: Advantages and limitations of photogrammetry and laser scanning techniques (after Petrie and Toth 2018).

2.4.2. LiDAR technique

2.4.2.1. Introduction

Laser scanners enable to collect 3-D data of large areas in relatively short time, with unprecedented accuracy. Albeit laser scanners were invented in the 1960s, the introduction of direct georeferencing technologies and progresses in computer technology of the mid-1990s have been the crucial factors for the effective development of this technology (Petrie and Toth 2018). With regards to the application of LiDAR methods for slope investigations, early laser scanners were mounted on aerial platforms, while ground-based laser scanner appeared later (Large and Heritage 2009).

2.4.2.2. LiDAR fundamentals

LiDAR surveys are carried out by means of instruments able to measure distances with high degree of accuracy, based on the Light Amplification by Stimulated Emission of Radiation (LASER) technique. Laser scanners are optical devices constituted by a transmitter/receiver of highly collimated, directional, coherent and in-phase electromagnetic radiation and a scanning device. Depending on the

position of the instrument, laser scanners are classified as *Airborne Laser Scanners* (ALS) and *Terrestrial Laser Scanners* (TLS). The formers are typically used to scan large areas and achieve decimetrical accuracies and resolutions (Baltsavias 1999). For this reason, ALS techniques are carried out to map regional structures (Matasci et al. 2011; Loye et al. 2012; Humair et al. 2013), obtain Digital Elevation Models (DEMs) for small-scale landslide modelling and susceptibility assessment (Chigira et al. 2004; Haneberg et al. 2009; Dietrich et al. 2011; Michoud et al. 2012) and to identify active areas by means of surface change detection (Lato et al. 2014; Okyay et al. 2019). Conversely, TLS systems work on static positions and several scans are usually acquired from different locations to obtain an overall representation of the investigated area, but might be limited by topographic constraints (Lato et al. 2014). Ground-based laser scanners are recommended for sub-vertical or overhanging slopes, which are not adequate to ALS methods (Oppikofer et al. 2009; Stock et al. 2011; Bremer and Sass 2012), provided that they can be placed at relatively short distance from the target.

For both techniques, the measurement of distance or range can be carried out using one of the two main methods:

- *Time of flight* (TOF): a very short and intense pulse of radiation is emitted by the laser scanner towards the target object and reflected back to the instrument (Figure 2.16). The time taken by the pulse emitted at the position A to hit the object located at position B and return to the laser scanner allows to measure the distance according to the following formula:

$$R = \frac{vt}{2} \quad \text{Eq. 2.18}$$

where R is the distance between the instrument and the object, v is the speed of the electromagnetic radiation (speed of light) and t is the measured time interval.

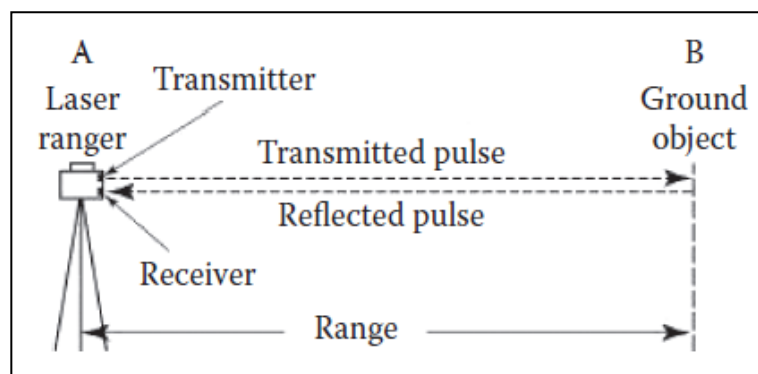


Figure 2.16: Range measurement by means of Time Of Flight laser scanner (after Petrie and Toth 2018).

- *Phase pulse*: the laser scanner emits a continuous beam of laser radiation rather than a pulse. The distance of the object is measured from the phase difference between the transmitted and the received sinusoidal wave of the beam (Petrie and Toth 2018) (Figure 2.17):

$$R = \frac{M\lambda + \Delta\lambda}{2} \quad \text{Eq. 2.19}$$

where M is the integer number of wavelengths, λ is the known value of the wavelength and $\Delta\lambda$ is the fractional part of the wavelength ($=\varphi/2\pi$, with φ being the phase angle).

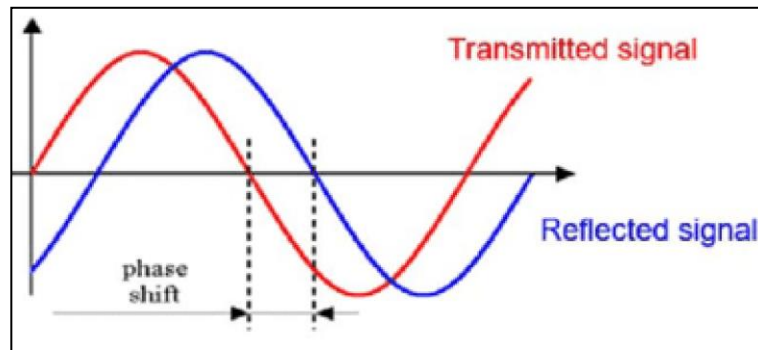


Figure 2.17: Range measurements by means of phase-based laser scanner (after Wang et al. 2019).

As pointed out by Petrie and Toth (2008, 2018), phase-based laser scanners provide more accurate distance measurements but are limited to short ranges (up to 100 m). For this reason, these techniques are restricted to specific situations such as displacement monitoring, whilst TOF techniques, which allow to measure larger distances, are typically used for Earth surface observations (Baltsavias 1999b; Wehr and Lohr 1999). With regards to ground-based laser scanners, motion in azimuth direction is performed to measure a series of elevation profiles (closely spaced points along a line) around the vertical axis of the device. On the other hand, airborne systems scan the target area by means of profile measurements in the direction perpendicular to the flight line. The scanned area is equal to the laser beam projected on the target object and increases as the distance between the device and the object increases because of the divergence effect (Petrie and Toth 2008, 2018). Knowing the orientation of the laser beam (LOS, Line Of Sight) and the attitude of the instrument, it is possible to determine the position Δx , Δy , Δz of the target object relative to the instrument (Jaboyedoff et al. 2012). In practice, GPS systems, if not integrated in the laser scanners, are additionally used during the surveys to accurately define attitude and position of the laser scanner, and to successively georeference the acquired data in a global coordinate system. Both methods provide the position and elevation of thousands of points representing a 3-D model of the scanned object, also called LiDAR point cloud.

In addition to providing information on the position of the scanned object, laser rangefinders provide its *reflectivity*, which is defined as the ratio of the incident radiation on the surface to the radiation reflected by the same surface. “Hard surfaces” such as rocks and buildings are characterized by diffuse reflectivity scattering into a hemispherical pattern, with the maximum intensity perpendicular to the target (Figure 2.18). The reflectivity is influenced by the colour, roughness and humidity of the target area, as well as the wavelength emitted by the device, the laser ranger-target distance and the incident angle of the laser beam (Petrie and Toth 2008, 2018; Jaboyedoff et al. 2012; Lato et al. 2013; Carrea et al. 2016).

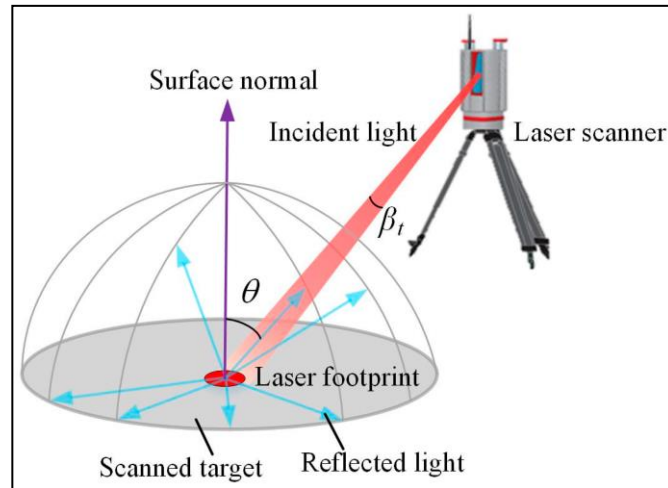


Figure 2.18: Reflectivity of a diffuse target; the maximum reflection takes place perpendicular to the target plane (after Xu et al. 2017).

Laser scanner *resolution* is commonly used to describe the ability to detect small objects in a point cloud or, in other words, the level of detail that can be observed within a point cloud (Pesci et al. 2011). Resolution is commonly interpreted as equivalent of the point spacing, which depends on the survey settings such as laser scanner-target distance and angular spacing between adjacent scanlines (Optech 2009). In addition, the effective resolution is also influenced by the dimension of the laser footprint: a wide diameter causes a higher point spacing and consequently a lower resolution (Abellán et al. 2014).

In a more specific context, the term *accuracy* is used to indicate the range of error inherent to the measurement (*i.e.* the degree of closeness of a range measurement to the actual distance; Abellán et al. 2014). It is divided in range accuracy and angular accuracy (Kamerman 1993; Lichti and Jamtsho 2006; Jaboyedoff et al. 2012). The term *range accuracy* refers to the ability of a laser scanner to resolve two objects on the same line of sight, whilst the term *angular accuracy* is referred to the ability of resolving two objects on adjacent lines of sights. Laser scanner accuracy decreases with increasing range, surface roughness and angle of incidence (Ingensand 2006; Lichti 2007; Voegtli et al. 2008; Abellán et al. 2009), and is influenced by environmental conditions like temperature, humidity and interfering radiations (sunlights, lamps; Boehler et al. 2003).

Although early laser scanners could provide an accuracy of $\pm 5\text{-}15$ cm for airborne systems (Habib 2018) and ± 1.5 cm for ground-based systems at a distance of 300 m (Oppikofer 2009; Jaboyedoff et al. 2012), new generation technologies allow to reach, respectively, a few centimeters and a few millimeters (Jaboyedoff and Derron 2020).

2.4.3. SfM technique

2.4.3.1. Introduction

Structure from Motion (SfM) is a technique based on the application of photogrammetry by means of terrestrial, UAV or aircraft platforms developed from advances in computer vision and traditional photogrammetry, initially developed for multimedia applications (Doorn and Koenderink 1991; Shashua 1994; Beardsley et al. 1997). SfM has been introduced in the Earth Sciences relatively

recently, but its application is constantly gaining popularity thanks to the opportunity of producing high-quality point clouds of landforms at different scales, with relative low cost (Remondino and El-Hakim 2006; Matthews 2008; Fraser and Cronk 2009; Westoby et al. 2012; Carrivick et al. 2016; Anderson et al. 2019; Eltner and Sofia 2020). Traditional photogrammetric methods allowed to reconstruct 3-D scenes from photographs taken by compact and single lens reflex (SLR) cameras by means of triangulation processes. However, the precise knowledge of the camera location and pose needed to be known *a priori*. Alternatively, the precise location of control points on the surveyed area could be used to determine the camera positions (*resectioning* process). Early 1990s progress in computer vision (e.g. Boufama et al. 1993; Spetsakis and Aloimonos 1991; Szeliski and Kang 1994) and feature-matching algorithm development (e.g. Förstner 1986; Harris and Stephens 1988) led to the introduction of techniques able to automatically solve the geometry of the scene, camera positions and orientations, without the need of knowing the control points' positions, by matching features in multiple images (Turner et al. 2012; Westoby et al. 2012; Lucieer et al. 2014). Thus, highly redundant, iterative bundle adjustment procedures (Snavely et al. 2008) are used in SfM techniques to estimate the positions of several features by overlapping the photographs acquired from a moving sensor.

Since points of known coordinates belonging to the real scene are not required to perform the SfM technique, the resulting point clouds are located in a relative "image-space" coordinate system (Turner et al. 2012; Westoby et al. 2012; Fonstad et al. 2013; James and Robson 2014). For this reason, the generated point cloud or polygonal surface will not be georeferenced and scaled, contrarily to the traditional photogrammetric methods (Favalli et al. 2012; Carrivick et al. 2016; Clapuyt et al. 2016). Roto-translation matrixes can be applied on the point cloud to orient and scale the model into an absolute coordinate system with the help of Ground Control Points (GCPs) of known coordinates.

2.4.3.2. Typical workflow

Nowadays, several commercial softwares (e.g. Agisoft Metashape (Agisoft 2020), Pix4D (Pix4DMapper 2017), Zephyr (3-Dflow 2018)) are available to perform SfM technique with standard desktop computers on photos collected by hand-held cameras or more advanced UAV systems. Although some commands may change, the overall process follows the workflow described below (Figure 2.19).

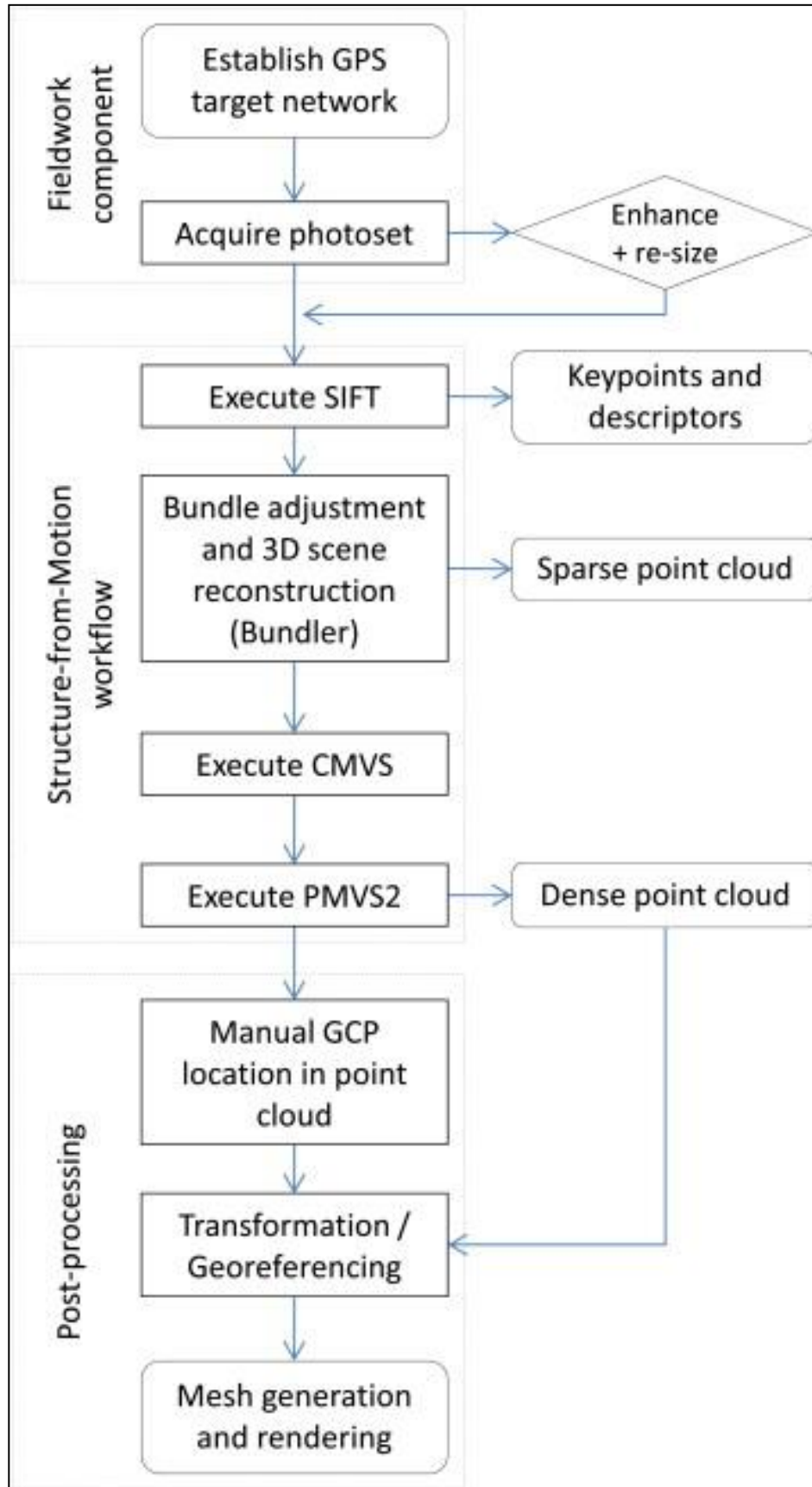


Figure 2.19: Typical SfM workflow (after Westoby et al. 2012).

a. Image acquisition

The very first step to obtain a 3-D reconstruction of the target is the acquisition of photos, which should be taken with sufficient overlap (ideally 80-90%) and from different positions and/or angles (James and Robson 2012; Lucieer et al. 2014). As regards the acquisition platform, ground-based systems are appropriate to investigate large-scale and steep areas, whilst aerial platforms are more indicated to acquire data on large and low-relief zones (Westoby et al. 2012).

b. Keypoints detection and matching

The *processing* of the acquired images starts with the image matching, through which common features are identified in different photos (Figure 2.20). These features, called *keypoints*, can be points, edges or characteristic patterns (Lowe 2004; Bay et al. 2008; Calonder et al. 2010; Strecha et al. 2012) and should be invariant to changes in scale, orientation and illumination conditions (Carrivick et al. 2016). The keypoints are automatically extracted and matched in each image by means of specific algorithms such as the Scale Invariant Feature Transform (SIFT) proposed by Snavely (2008) or the Random Sample Consensus (RANSAC) by Fischler and Bolles (1981).

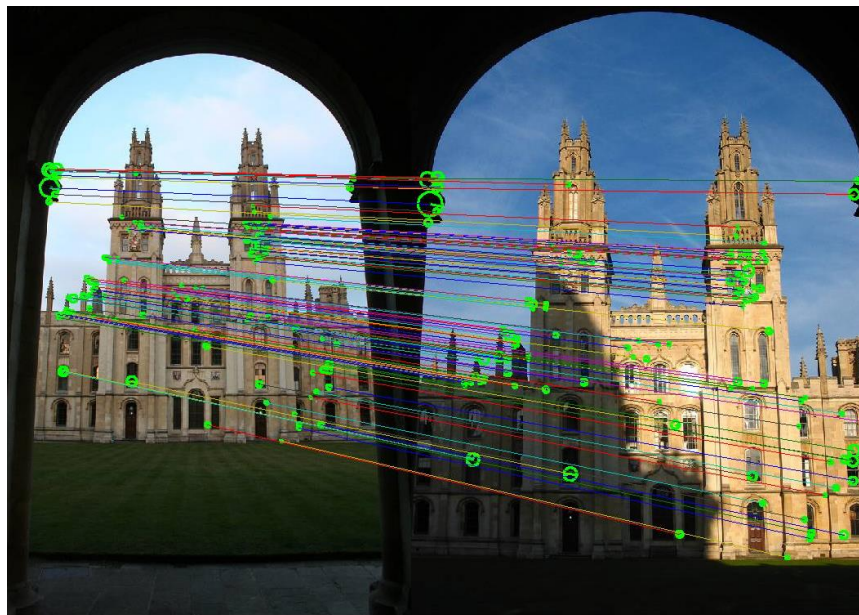


Figure 2.20: Example of feature detection and matching (retrieved from <https://blog.ekbana.com>).

c. Collinearity, bundle adjustment and sparse point cloud

Before the 3-D reconstruction begins, the paths between specific keypoints are linked to remove disturbances, like objects moving on the scene during the surveys (Snavely et al. 2008). In fact, although the keypoints located on moving objects are recognised in different photos, the distances from the other features are constantly changing, and therefore the disturbance can be filtered using visibility and regularisation constraints (Furukawa and Ponce 2008).

A set of equations is used to reconstruct a 3-D scene from 2-D photographs so that collinearity is maintained (Liu et al. 2006; Roncella et al. 2011; Fonstad et al. 2013). The collinearity equation

establishes that a point belonging to the surveyed object, its representation in an image, and the camera optic centre are aligned along a straight line (Figure 2.21).

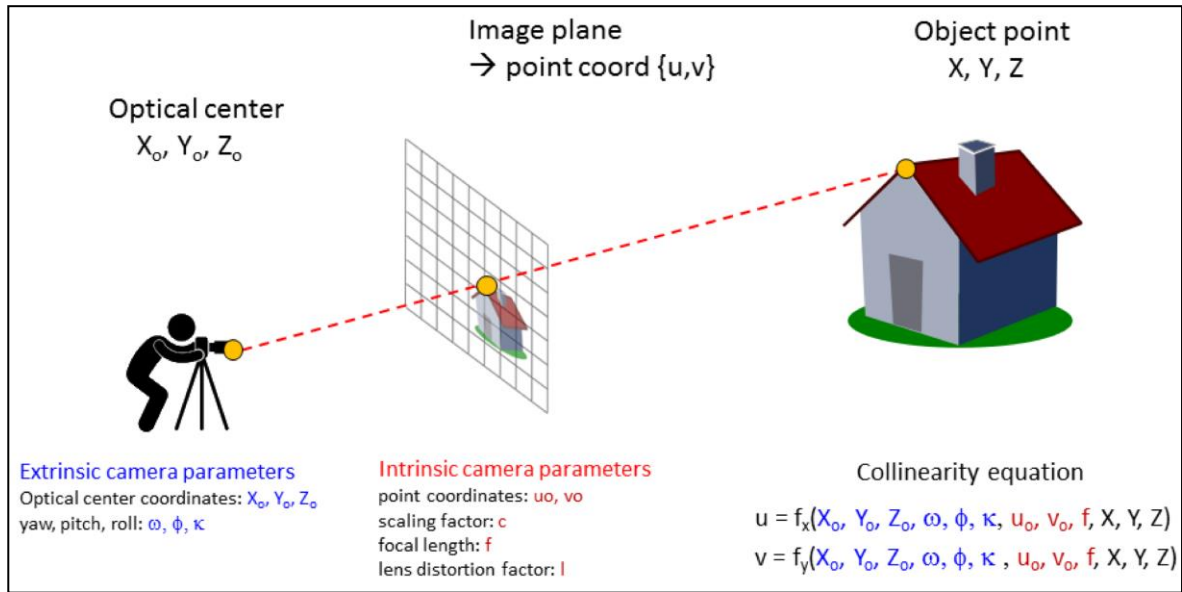


Figure 2.21: Sketch showing the relationships between the extrinsic and intrinsic camera parameters, the collinearity equations and the projection line (content provided by M.-H. Derron).

One of the main objectives of photogrammetry is to transform the coordinates of the point in the picture (in pixels) into geographic coordinates, therefore obtaining a 3-D scene. To this aim, the extrinsic and intrinsic camera parameters need to be known. The extrinsic camera parameters are the optic centre coordinates (X_o, Y_o, Z_o) and the orientation of the instrument (yaw ω , pitch ϕ , roll κ). The intrinsic camera parameters are the point's coordinates in the image (u_o, v_o) , the scaling factor k , the focal length f and the lens distortion factor l . The collinearity equation expresses the coordinates of the point in the image in function of the geographic coordinates of the same point (Mikhail et al. 2001):

$$\begin{cases} u = f_x(X_o, Y_o, Z_o, \omega, \phi, \kappa, u_o, v_o, f, X, Y, Z) \\ v = f_y(X_o, Y_o, Z_o, \omega, \phi, \kappa, u_o, v_o, f, X, Y, Z) \end{cases} \quad \text{Eq. 2.20}$$

The collinearity equation can be expressed in matrix form as:

$$\begin{bmatrix} u - u_o \\ v - v_o \\ f \end{bmatrix} = k M \begin{bmatrix} X - X_o \\ Y - Y_o \\ Z - Z_o \end{bmatrix} \quad \text{Eq. 2.21}$$

where k and M are the scaling factor and the rotation matrix taking into account the orientation of the camera, respectively. More in detail, the rotation matrix is:

$$M = \begin{bmatrix} \cos\phi\cos\kappa & \cos\omega\sin\kappa + \sin\omega\sin\phi\cos\kappa & \sin\omega\sin\kappa - \cos\omega\sin\phi\cos\kappa \\ -\cos\phi\sin\kappa & \cos\omega\cos\kappa - \sin\omega\sin\phi\sin\kappa & \sin\omega\cos\kappa + \cos\omega\sin\phi\sin\kappa \\ \sin\phi & \sin\omega\cos\phi & \cos\omega\cos\phi \end{bmatrix} = \begin{bmatrix} m_{11} & m_{12} & m_{13} \\ m_{21} & m_{22} & m_{23} \\ m_{31} & m_{32} & m_{33} \end{bmatrix} \quad \text{Eq. 2.22}$$

After development, the following relationships are obtained:

$$\begin{cases} u - u_0 = -f \frac{m_{11}(X - X_0) + m_{12}(Y - Y_0) + m_{13}(Z - Z_0)}{m_{31}(X - X_0) + m_{32}(Y - Y_0) + m_{33}(Z - Z_0)} \\ v - v_0 = -f \frac{m_{21}(X - X_0) + m_{22}(Y - Y_0) + m_{23}(Z - Z_0)}{m_{31}(X - X_0) + m_{32}(Y - Y_0) + m_{33}(Z - Z_0)} \end{cases} \quad \text{Eq. 2.23}$$

The problem remains indeterminate because the number of equations is less than the number of unknowns (X, Y, Z). Moreover, for every other point in the analyzed image, there will be 2 more equations and 3 more unknowns. The Structure from Motion technique enables to solve the problem and obtain the 3-D coordinates of the target point by using multiple views: if more photos containing the same point are examined, the 3 unknown coordinates will be the same, but the number of equations will increase (for every image, 2 more equation will be given) (Figure 2.22). Since the number of equations will largely exceed the number of unknowns, it will be possible to create a 3-D scene by analysing all keypoints.

More in detail, for N_v images the collinearity equation will be solved by having a minimum number of keypoints (N_p) equal to:

$$N_p = \frac{6N_v + 3}{3N_v - 3} \quad \text{Eq. 2.24}$$

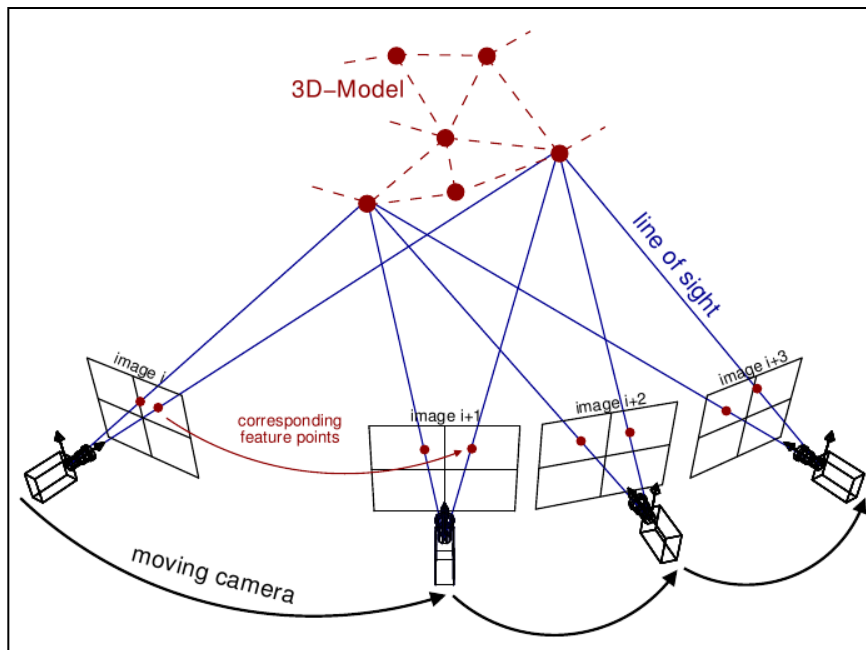


Figure 2.22: Structure from Motion principles. The 3-D scene is reconstructed by estimating camera positions and orientations acquired from a moving sensor. Several features are detected and matched on multiple photos by means of specific algorithms to produce a point cloud (after Van Riel 2016).

In practice, the common SfM softwares automatically solve the collinearity equations for each detected keypoint and for each photograph introduced within the model by means of least-square

bundle adjustment (Brown 1976; Triggs et al. 1999; Snavely et al. 2008; Fonstad et al. 2013; Lucieer et al. 2014). Thus, the extrinsic and intrinsic camera parameters, as well as the XYZ coordinates of the feature points, are calculated, allowing to accurately position the photos (Ohnishi et al. 2006; Turner et al. 2012; Favalli et al. 2012). As a result, a sparse (low-density) point cloud with RGB colours obtained from the photographs is generated.

d. Absolute registration

Since the points of known coordinates belonging to the real scene are not required to perform the SfM technique, the resulting point clouds are located in a relative “image-space” coordinate system (Turner et al. 2012; Westoby et al. 2012; Fonstad et al. 2013; James and Robson 2014). For this reason, the generated point cloud or polygonal surface will not be georeferenced and scaled, contrarily to the traditional photogrammetric methods (Favalli et al. 2012; Carrivick et al. 2016; Clapuyt et al. 2016). Roto-translation matrixes can be applied on the point cloud to orient and scale the model into an absolute coordinate system with the help of ground-control-points (GCPs) of known coordinates. It is common practice to place clearly visible elements (targets) on the surveyed area before the image acquisition and to collect their coordinates by means of GPS systems. The control points should be distributed throughout the area to avoid errors during the 3-D scene reconstruction (James and Robson 2012c). The GCPs are semi-automatically identified on the images during the processes and their coordinates are assigned in the software to scale and orient the point cloud in an absolute reference system. Although 3 GCPs with XYZ coordinates are theoretically enough to locate the scene in a 3-D environment, it is recommended to use more targets (5-7) evenly distributed in the area, to reduce deformations related to camera lens distortions (*doming shape deformations*) (James and Robson 2014; Eltner et al. 2016).

e. Dense 3-D reconstruction

A higher resolution point cloud is produced by means of dense matching process using the Multi-View-Stereo (MVS) algorithms, which increase the point cloud density by at least two orders of magnitude (Smith et al. 2016). According to Eltner and co-workers (Eltner et al. 2016), the most common MVS algorithms used in geosciences are the Patch-based Multi-view Stereo (PMVS) algorithms (Furukawa and Ponce 2008) and the depth-map merging method (e.g. Li et al. 2010, Agisoft 2020). The PMVS technique reconstructs the 3-D scene from clusters of manageable size, while the second method is based on the distances between the camera location and the 3-D scene (depth maps). Patches or depth maps are matched and grown around the sparse point cloud to produce a dense point cloud. Once the 3D model is rotated and scaled, the quality of the final result can be evaluated by analyzing the residuals of the Bundle Adjustment: the smaller are the reprojection errors, (i.e. the distance between the projections of each key point and its observations), the better is the accuracy.

f. Polygonal surface and orthophotos

A polygonal surface (mesh) can be generated from the point cloud or dense map, with the possibility of choosing filters (e.g. vegetation removal), face counts and quality. A texture generated from the photos can be added to the mesh. Additionally, orthophotos and Digital Elevation Models (DEMs) can be produced.

It should be specified that the SfM technique must be coupled with the MVS algorithm to obtain dense point clouds and eventually their derivative products. Therefore, the term *SfM-MVS* is more appropriate when addressing the overall process (from photo acquisition to point clouds/meshes generation - Figure 2.23). However, *SfM* is commonly used in the literature also to refer to the data produced after the dense matching. The term SfM will be generally used in this manuscript to avoid misunderstandings, but is referred to the SfM-MVS coupling.

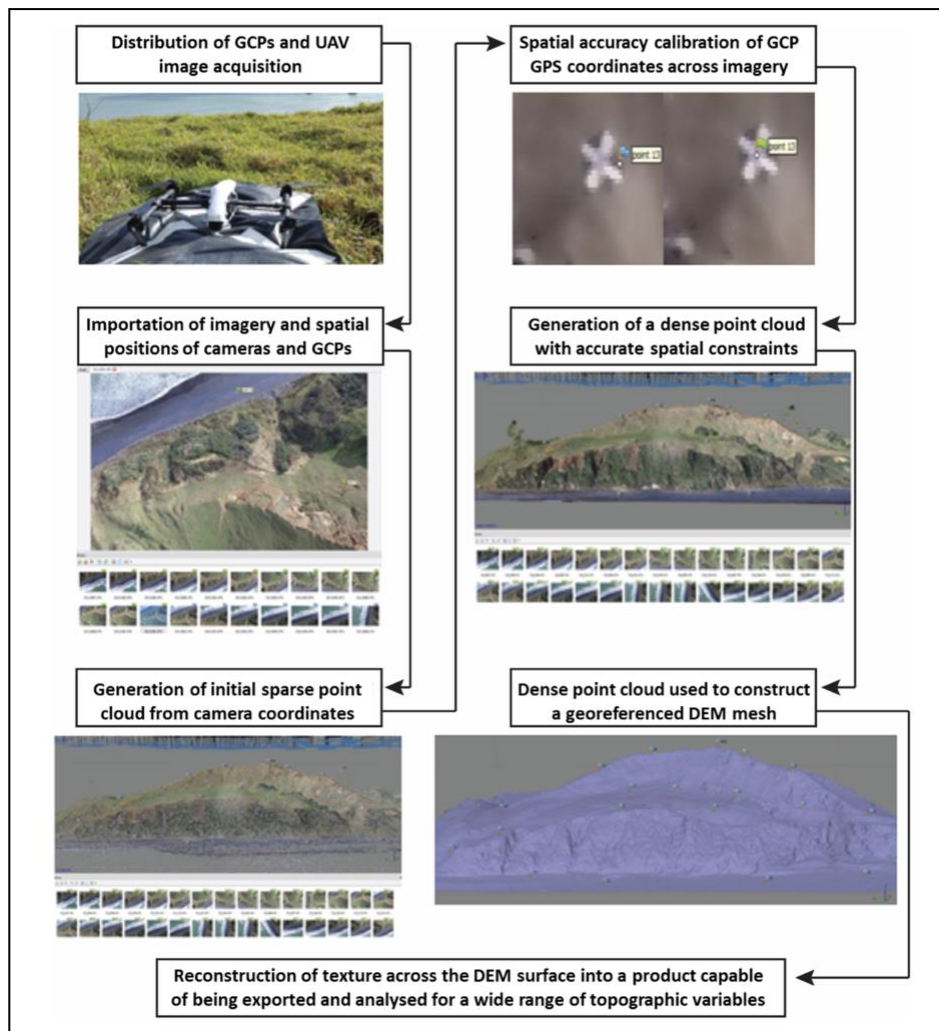


Figure 2.23: Illustrated example of SfM-MVS workflow (after Bevan et al. 2017).

2.4.4. IRT technique

2.4.4.1. Introduction

Modern InfraRed Thermography (IRT) was discovered in 1800 by the physicist Herschel during his search for new optical materials. Herschel studied the heating effect of the colour spectrum formed by passing sunlight through a prism and noticed a consistent increase of temperature from the violet to the red end. The temperature increased even more going beyond the red end, into the “dark heat” zone of the spectrum, nowadays called *infrared spectrum*. Several scientists (e.g. Nobili, Melloni,

Kirchoff, Maxwell, Svanberg, Stefan, Boltzmann, Planck, Holst) followed this discovery and, after a few decades, the IRT technique was employed for surface temperature mapping.

Thermal radiation operates in the portion of the electromagnetic spectrum with wavelengths falling in the range of 0.78-1000 μm (Wolfe et al. 1985; Dewitt and Nutter 1988; FLIR 2014) (Figure 2.24). Five main sub-bands form the infrared spectral band: Near Infrared (NIR, 0.75-1.4 μm), Short Wavelength Infrared (SWIR, 1.4-3 μm), Medium Wavelength Infrared (MWIR, 3-8 μm), Long Wavelength Infrared (LWIR, 8-15 μm) and Far Infrared (FIR, 15-20 μm).

IR thermography is a non-contact technique recording and visualizing thermal radiation emitted by objects, aimed at analysing surface temperature distributions (Vavilov and Burleigh 2020). IRT surveys use thermographic cameras, which are devices working in the spectral band of wavelengths ranging between 7.5 and 14 μm that measure radiations emitted by objects and convert them into temperatures (Shannon et al. 2005). This wavelength range allows to measure temperatures from -60°C to +100°C (Bramson 1968; Holst 2000).

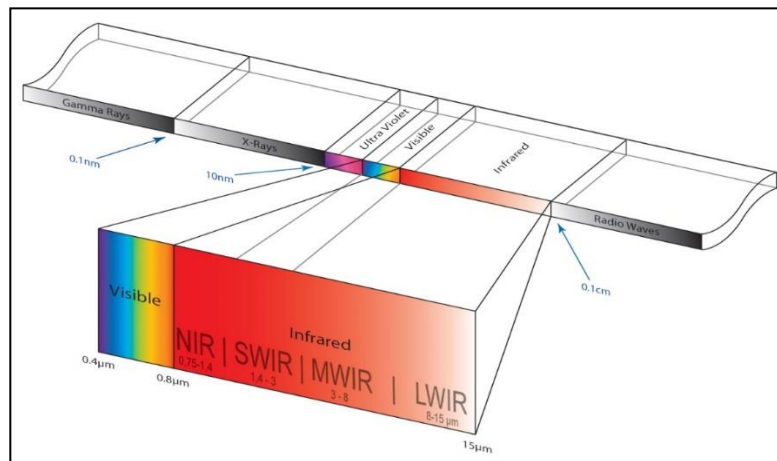


Figure 2.24: Schematic representation of the InfraRed spectrum (retrieved at: <https://www.ametek-land.com/pressreleases/blog/2021/june/thermalinfraredrangeblog>).

2.4.4.2. IRT fundamentals

InfraRed Thermography technique is based on the physic principle that all objects at temperatures above absolute zero emit radiation because of their kinetic energy (Modest 2013). The radiation is transferred in the form of electromagnetic waves, depending on the temperature and properties of the object. A blackbody is a medium that absorbs all incident radiations, without reflecting them (Kirchhoff 1860). According to Planck's radiation law, the energy E_b emitted for each wavelength λ by a black body at temperature T is given by:

$$E_b = \frac{C_1}{\lambda^5 e^{C_2/\lambda T} - 1} \quad \text{Eq. 2.25}$$

where C_1 and C_2 are the Planck constant and the Boltzman constant, respectively. The spectral radiance, expressed in $\text{Watt}\cdot\text{sr}^{-1}\cdot\text{m}^{-3}$, is represented by a group of curves in which, for each temperature, a maximum of radiant power appears at a particular wavelength (Figure 2.24). These wavelengths increase as the temperature decrease, implicating that radiant power drastically decays with lower temperatures. The maxima of the Planck function are given by the Wien displacement law:

$$\lambda_{\max} = \frac{A}{T} \quad \text{Eq. 2.26}$$

where A is a constant equal to $2.898 \mu\text{m}\cdot\text{K}$. Figure 2.25 illustrates how the spectral radiance is related to the visible light spectrum: the Sun has a temperature of $5777 \text{ }^\circ\text{K}$ and emits yellow light peaking at $0.5 \mu\text{m}$ of the light spectrum, while for ambient air temperature ($300 \text{ }^\circ\text{K}$) the peak of radiation has a maximum wavelength of about $10 \mu\text{m}$, corresponding to the far infrared band.

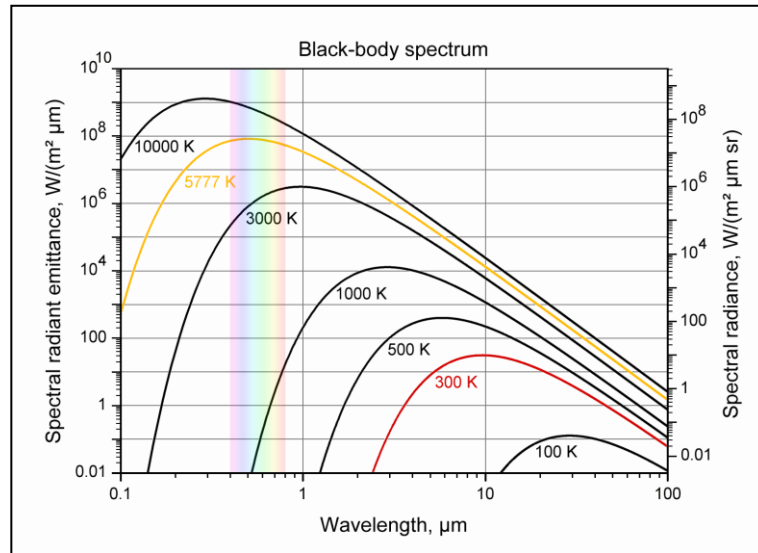


Figure 2.25: Spectral radiance according to wavelengths for different temperatures (from www.commonswiki-media.org).

The total radiant exitance is obtained by integrating Planck's law over the entire spectrum ($\lambda = 0 - \infty$):

$$J = \sigma T^4 \quad \text{Eq. 2.27}$$

This relation, known as the Stefan-Boltzmann law, shows that the total energy (J) emitted by a black-body depends on the fourth power of its surface temperature (T) and is proportional to the Stefan-Boltzmann constant σ ($=5.6 \cdot 10^{-8} \text{ Wm}^2\text{K}^{-4}$).

Real materials (*i.e.* greybodies) rarely behave as blackbodies because they absorb only a fraction of the incident radiations, while the remaining radiations are transmitted and/or reflected (Kirchhoff 1860). For real materials, the total energy is reduced in proportion to the value of their emissivity (ϵ), which is the ratio between the radiation emitted by the object at a given temperature and the radiation emitted by a blackbody at the same temperature (Gaussorgues 1994; Incropera 2007). Thus, the Stefan-Boltzmann's law can be re-adapted for grey-bodies as:

$$J = \epsilon \sigma T^4 \quad \text{Eq. 2.28}$$

Emissivity ranges between 0 and 1 and represents the ability of an object to emit heat energy (Shannon et al. 2005). Rocks have emissivities close to 0.9, whereas metals have lower emissivities, about 0.1 (Jensen 2007; Monchau 2013). Emissivity of natural objects depends on their colour, chemical composition, humidity and roughness (Holst 2000).

2.4.4.3. Thermal imaging

Thermal imagers do not directly measure temperatures, but the energy emitted by the surface of an object during a time period. Nevertheless, the signal received by the thermal camera is not uniquely provided by the target object, but is the sum of signals deriving from more sources (Figure 2.26). In detail, in outdoor settings thermal imagers receive signals from the target object (J_{obj}), the surrounding environment (ground, vegetation) reflected by the surface of the object (J_{env}) and from the “atmosphere” located between the target and the instrument (J_{atm})(Rees 2012; Gero et al. 2013; FLIR 2014). Therefore, the total radiation received by the camera is given by (FLIR 2014):

$$J_{tot} = \tau (J_{obj} + J_{env}) + (1 - \tau) J_{atm} \quad \text{Eq. 2.29}$$

where τ is the transmittance of the atmosphere. The energy received by the device is then converted into electrical voltage or current. As output, thermal imagers provide thermograms: matrixes of pixels representing the surface temperatures, which can be further processed in specific software according to the aim of the survey (e.g. detect cold or hot sources).

To derive the surface temperature of the object, a calibration protocol needs to be applied during the processing of the thermograms, taking into account parameters such as emissivity of the material, distance thermal camera-target, atmospheric temperature, relative humidity and reflected temperature (Spampinato et al. 2011; FLIR 2014).

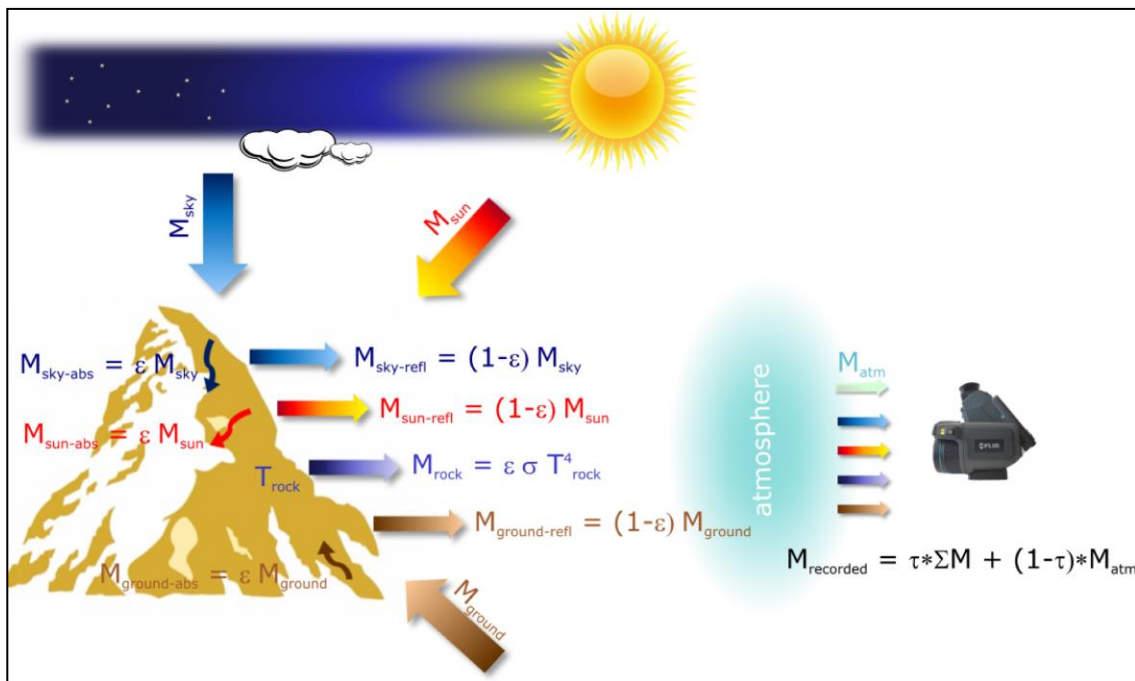


Figure 2.26: Main sources of thermal radiation detected by thermal cameras (content provided by M-H. Deron). The recorded radiant exitance is the sum of the radiant exitance emitted by the object and the radiant exitance of sky, Sun and ground reflected by the object itself. A part of radiation emitted by the ground and Sun is absorbed by the atmosphere.

Concerning the application of IRT for rock slope investigation, it should be specified that the amount of radiant energy reaching a rock surface (e.g. from the Sun) depends on its geometry and on the

orientation of its facets with respect to the direction of radiation. Shadow zones or multiple reflections can be produced depending on the orientation of the outcrop relative to the camera (incidence angle), sky, ground and Sun (Figure 2.27). For instance, lower than actual temperatures may be recorded for incidence angles greater than 60° (Howell et al. 2021). With regards to the orientation of the outcrop with respect to the sky, Guerin and co-workers point out that flat areas may return lower temperatures because they reflect the cold radiations from the sky (-60°C for a clear sky), whereas reflections from the ground are less relevant because of temperatures similar to those of the rock mass above (Guerin et al. 2019). With regard to the Sun radiation, more illuminated zones and shadows can be produced according to the topography and the elevation angles of the Sun.

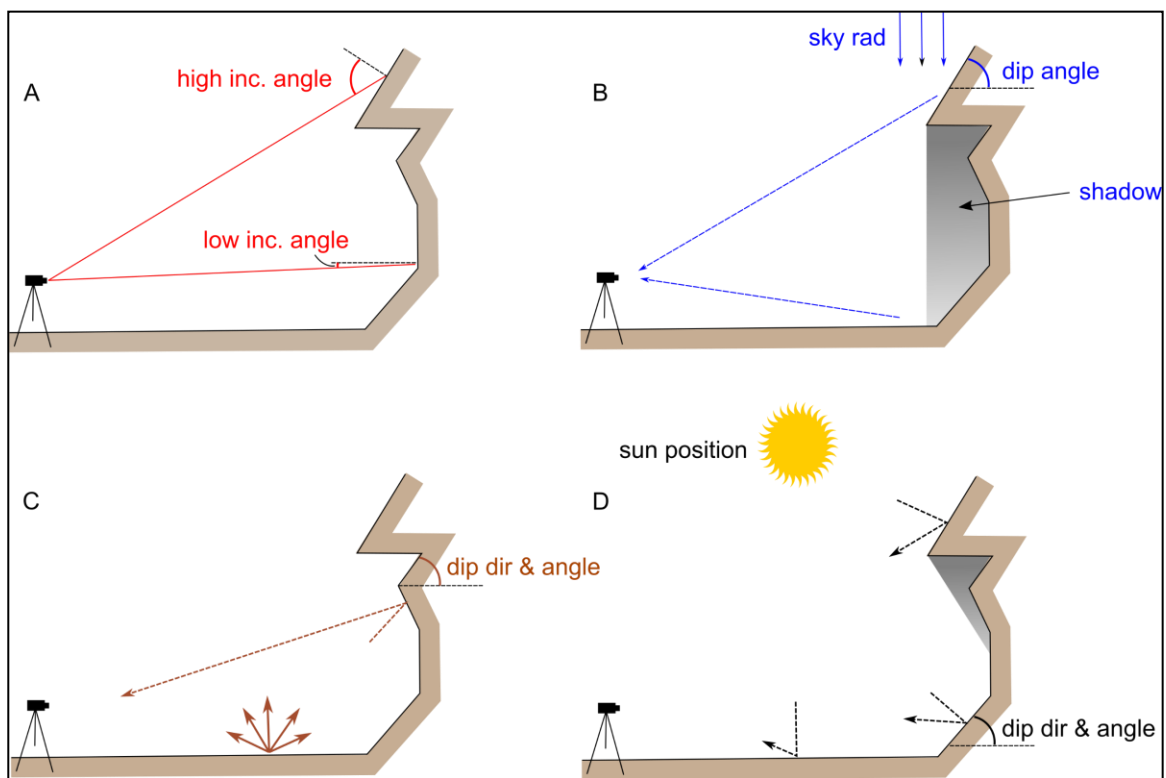


Figure 2.27: Effect of outcrop geometry and orientation for IRT (content provided by M-H. Derron). (a) effect of the incident angle camera-outcrop; (b) effect of the outcrop orientation relatively to the sky; (c) effect of the outcrop orientation relatively to the ground; (d) effect of the outcrop orientation relatively to the Sun.

2.5. Use of point clouds for rock mass characterization

Remote sensing techniques such as LiDAR and SfM are increasingly being used for rock slope investigation to support conventional geospatial and geomechanical field surveys, thanks to the possibility of generating high-resolution virtual outcrops across a wide range of spatial and temporal scales. Despite laser scanners were the main acquisition tool for deriving virtual outcrops in the last decade (Pringle et al. 2006; Buckley et al. 2008; Jones et al. 2009), availability of light weight and less expensive UAV platforms suitable for SfM technique has aroused growing interest among engineering and structural geologists. Another key factor for the choice of SfM technique for rock slope investigations is the possibility of carrying out the surveys without the need to gain specific knowledge and experience, as in the case of LiDAR techniques (James and Robson 2012). A detailed review of the

application of different remote sensing technique to achieve advances for geostructural investigations, as well as their advantages and limitations, was provided by Cawood and co-workers (Cawood et al. 2017). However, it must be remarked that remote sensing techniques are not intended to be used individually, but as support for on-site geostructural and geomechanical surveys. As a matter of fact, their application increases the productivity when dealing with rock mass characterization, but it does not allow to collect all the data necessary for a comprehensive description of the target. Direct measures on the field are essential to determine many properties like the wall strength, roughness, nature of filling and seepage conditions of discontinuities (Ferrero et al. 2009; Gigli and Casagli 2011, Martino and Mazzanti 2014).

2.5.1. Rock mass characterization

Surface measurement from point clouds or triangulated surfaces (meshes) were introduced to overcome the limitations of conventional geostructural and geomechanical techniques, such as sample representativity, accessibility, operators' safety, human bias and measurements inaccuracies (Feng et al. 2001; Ferrero et al. 2009). At present, orientation, spacing, persistence and roughness of discontinuities can be extracted from point clouds or meshes by means of different methods.

2.5.1.1. Orientation

Measurements on virtual outcrops solve many problems related to errors made during conventional field surveys. For instance, shallow-dipping joints can be incorrectly measured using a traditional compass (Herda 1999) and consistent skills are needed to measure undulated surfaces, whose orientation varies with space (Sturzenegger and Stead 2009). As remarked by Abellán and co-workers and Battulwar and co-workers, manual and semi-automatic (with different degree of automation) methods allow to detect the discontinuity sets (Abellán et al. 2014; Battulwar et al. 2021). Figure 2.28 shows some examples of the different methods proposed in the literature to extract discontinuities and orientations.

- Manual methods consist in manually delimiting a sub-region of point cloud or mesh considered representative for a discontinuity and to measure the orientation by means of least squares best-fitting plane (Fernández 2005; Oppikofer et al. 2008; Sturzenegger and Stead 2009).
- Some semi-automatic methods are carried out calculating the normal vector of each facet of a mesh (Slob and Hack 2004; Kemeny et al. 2006; Jimenez-Rodriguez and Sitar 2006; Olariu et al. 2008; Lato and Vöge 2012). However, the accuracy of the results strongly depends on the quality of the triangulated surface (Lato et al. 2009), which in turn depends on the previous data acquisition and processing, as well as on the operator's skills. Alternative methods (among which Jaboyedoff et al. 2007, Ferrero et al. 2009, García-Sellés et al. 2011, Gigli and Casagli 2011) were proposed to overcome this limitation and rely on the measurement of orientations directly from the point clouds. For instance, the commercial software *Coltop3D* (Terranum 2020) computes the dip direction/dip by means of eigenvalue analysis of the covariance matrix of a local neighbourhood (Jaboyedoff et al. 2007). Each point is coloured according to the measured dip direction/dip using a Hue-Saturation-Intensity method, allowing the user to semi-automatically identify the discontinuities. Riquelme and co-workers introduced the *Discontinuity Set Extractor* software (Riquelme et al. 2014) to detect discontinuities

by means of kernel density estimation and to classify them into discontinuity sets by applying the DBSCAN algorithm (Ester et al. 1996). Recently, a method to overcome human bias introduced in clustering algorithms by means of fast search and find of density peaks (CFSDP) algorithm (Rodriguez and Laio 2014) was presented by Kong and co-workers (Kong et al. 2020).

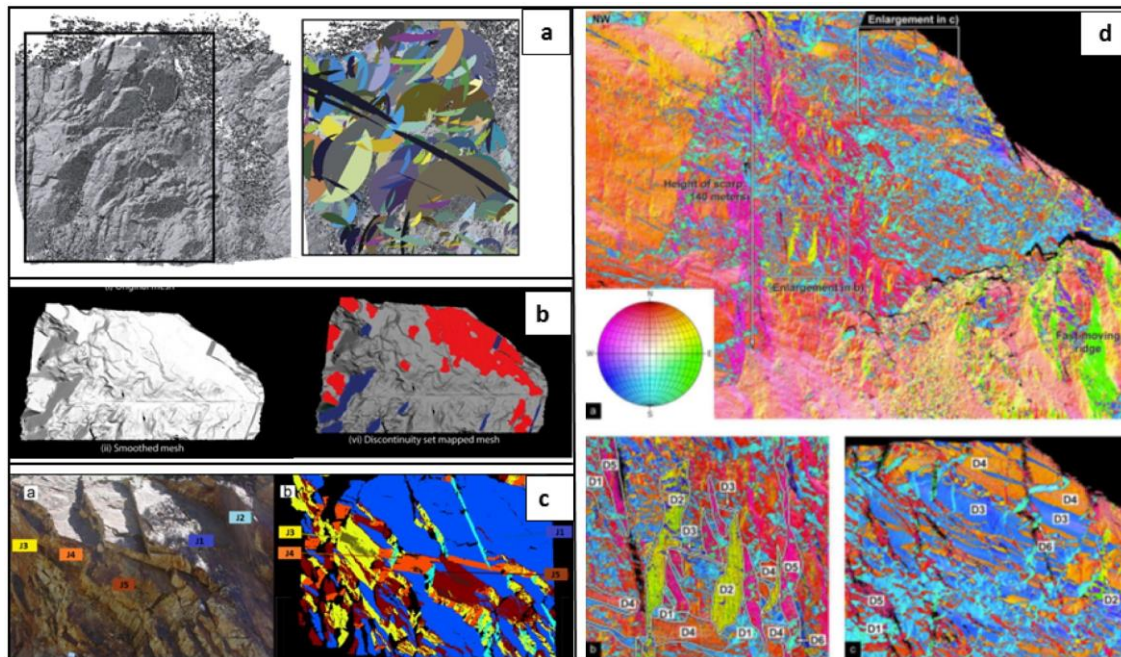


Figure 2.28: Different approaches to extract discontinuity sets from point clouds. (a) manual method by fitting planes (after Sturzenegger and Stead, 2009). (b) semi-automatic extraction on a mesh (after Vöge et al. 2013); (c) semi-automatic extraction from the point cloud by means of *Discontinuity Set Extractor* software (after Riquelme et al. 2014); (d) semi-automatic extraction from the point cloud by means of *Coltop3D* software (after Stead et al. 2012).

2.5.1.2. Spacing and persistence

Discontinuity spacing is estimated from point clouds by means of cluster analysis: points close to each other and with similar normal vectors are grouped into clusters for each of which the plane equation is calculated. The discontinuity set spacing is then computed as the normal distance between adjacent and parallel planes (Figure 2.29a) (Slob and Hack 2004; Slob et al. 2005; Riquelme et al. 2015; Wichmann et al. 2018; Kong et al. 2020). Gigli and Casagli (2011) introduced a method to identify all discontinuities belonging to one set using a virtual cylinder, to calculate the spacing from the intersections between the cylinder and the discontinuities. Sturzenegger and Stead (2009) proposed an approach to estimate discontinuity persistence by manually fitting circular planes to individual discontinuities and calculating their trace length. Moreover, a method to determine the persistence by applying convex hull algorithms to fit polygons on individual discontinuities was presented by Gigli and Casagli (2013). A schematic view to calculate discontinuity trace lengths from polygons is reported in Figure 2.29b. The software *Discontinuity Set Extractor* calculates the persistence from point clouds by merging groups of points belonging to the same discontinuity into a cluster and applying a coordinate system transformation based on the dip direction/dip of the cluster. Later, the persistence is measured along dip direction and dip, resulting in the extraction of the length of the maximum chord and the area of the convex hull (Riquelme et al. 2018).

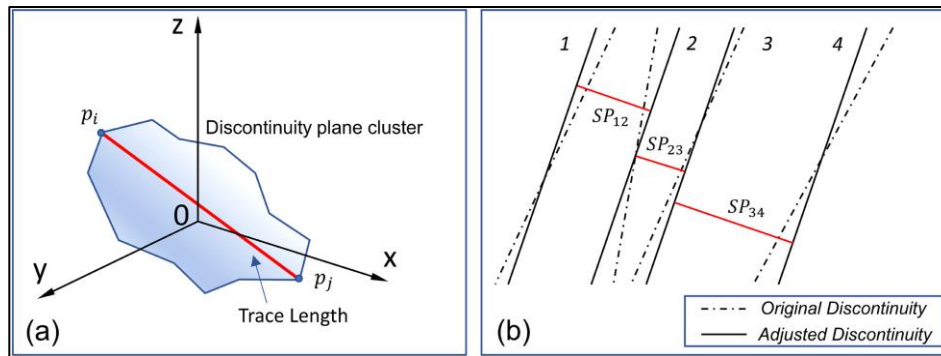


Figure 2.29: Schematic view of a 3-D point cloud for trace length and spacing calculation (after Kong 2020). (a) trace length calculated as the maximum distance between points of a discontinuity surface (polygon); (b) normal set spacing, calculated as the distance between two adjacent parallel discontinuity planes.

2.5.1.3. Roughness

Discontinuity roughness is approximately quantified by fitting planes on the discontinuities and computing the differences between the same surface and the plane (Sturzenegger and Stead 2009) or drawing cross-sections and comparing them to Joint Coefficient Roughness (JRC) profiles (Haneberg 2007; Oppikofer et al. 2011; Pollyea and Fairley 2011). Fardin and co-workers proposed a technique to estimate the roughness from the fractal parameters of discontinuity surfaces (Fardin et al. 2004). Moreover, Gigli and Casagli proposed to move a searching cube with different dimensions along a discontinuity and fitting a plane in each sector; the roughness at different scales is then estimated from the scattering degree of the resulting stereoplot (Gigli and Casagli 2011). More recently, Li and co-authors presented a technique to calculate the JRC of a discontinuity by tracing planes with a fixed step along its dip direction (Figure 2.30) (Li et al. 2019). More in detail, for each plane a profile of the intersection with the discontinuity is obtained; the JRC is calculated as a function of the root mean square of the first derivative of the profile.

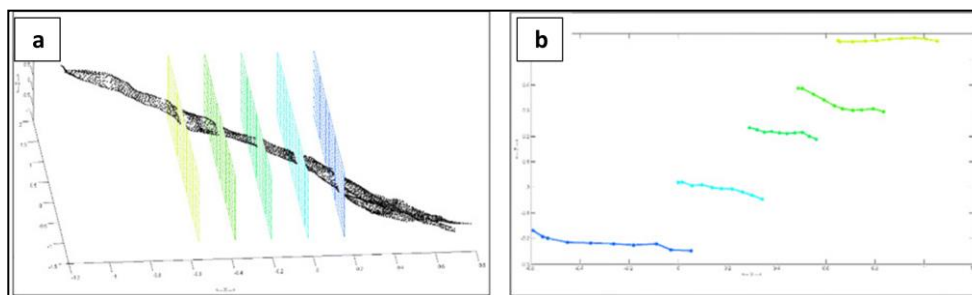


Figure 2.30: Discontinuity roughness calculation (after Li et al. 2019). (a) the discontinuity is plotted in a dip direction-strike frame and some planes are traced along the dip direction; (b) the intersections between the planes and the surfaces are plotted as profiles to derive JRC by means of mathematical relationships.

The accuracy of the roughness estimated from point clouds is affected by the spatial resolution and by the intrinsic noise associated with remote sensing tools. More in detail, an underestimation of the discontinuity roughness can be caused by a low spatial resolution (smoothing effect), whilst an overestimation of the roughness may be the result of a noisy point cloud (Bitenc et al., 2019).

2.5.1.4. Rockfall identification

Multi-temporal remote sensing acquisitions are of paramount importance to detect failures in rock slopes by means of sequential point clouds comparison, and ensure exceptional levels of accuracy (Rosser et al. 2005; Oppikofer et al. 2008; Abellán et al. 2011; Royán et al. 2013). Rock slope monitoring from virtual outcrops provide more evenly distributed measurements compared to traditional instruments like crack-metres, dilatometers and survey prisms, which are typically used in smaller areas (Oppikofer et al. 2009; Prokop and Panholzer 2009; Jaboyedoff et al. 2012, 2018).

Rockfall detection is achieved through the comparison of successive acquisitions, aimed at identifying changes between meshes or 2.5D surfaces oriented parallel to the strike of the slope. Three techniques are typically carried out to identify displacements: displacement vectors calculation, point clouds comparison, and rigid body transformation by means of roto-translation matrix.

The first approach is based on manually identifying and tracking common features within the point clouds (Monserrat and Crosetto 2008; Travelletti et al. 2008; Oppikofer et al. 2008; Teza et al. 2008; Pesci et al. 2011; Carrea et al. 2012). According to Abellán and co-workers (Abellán et al. 2014), the most employed method to detect displacements is the point cloud comparison: the scanned area is partitioned in smaller sub-regions and an Iterative Closest Point (ICP) algorithm is run to find the local displacement vector between successive point clouds. In practice, differences between the compared surfaces are calculated, and their values are interpreted to understand the failure mechanism. The computed differences can be positive or negative, depending on whether the given point is located above or below the reference dataset (Figure 2.31). According to Oppikofer and co-workers, positive differences are associated to sliding, buckling, rotation, toppling, flexure, swelling or debris mechanisms, while negative differences correspond to subsidence, shrinkage or rock failures (Oppikofer et al. 2009).

However, this technique does not consider potential rotations between couples of sub-regions and supposes rigid bodies. This issue was solved by Reshetyuk (2009) using a 3-D similarity transformation to deal with more complex deformations. In practise, a roto-translation matrix between the data and the reference point cloud is calculated to detect the displacements (Teza et al. 2007; Monserrat and Crosetto 2007; Oppikofer et al. 2008).

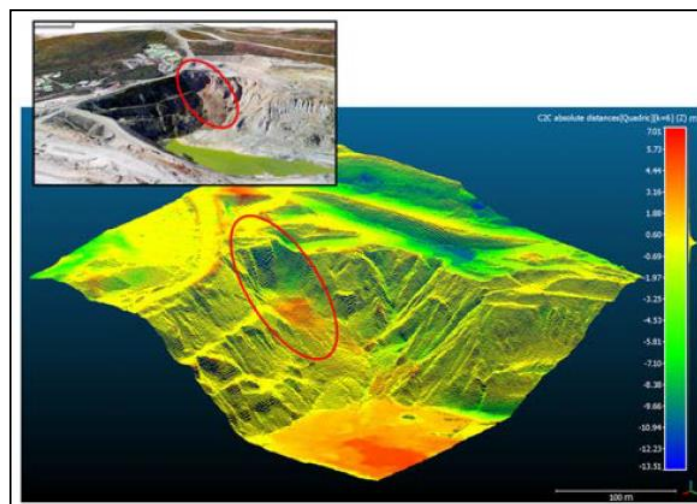


Figure 2.31: Detection of surface changes through the distance computation between two consecutive point clouds (after Vanneschi et al. 2017).

2.5.1.5. Rockfall volume calculation

As stated by Abellán and co-workers (Abellán et al. 2014), once a rockfall is identified, it is possible to measure not only 2-D geometric surface changes along the failure surface (height, width, area, shape), but also 3-D volumes (e.g. Lim et al. 2005; Rosser et al. 2005; Rabatel et al. 2008; Oppikofer et al. 2008; Carrea et al. 2015; Loye et al. 2016; Benjamin et al. 2018; Bonneau et al. 2019). A first approach to quantify failed volumes from point clouds is based on the rasterization of the point clouds to generate 2.5 D grids. The volumes are then calculated from the differences between the grids (Olsen et al. 2015; Williams et al. 2018). However, Bonneau and co-workers and Di Francesco and co-workers explained that the accuracy of the volume estimation is strongly affected by the resolution of the 2.5 D grid, which depends on the user-defined cell size (Bonneau et al. 2019; Di Francesco et al. 2020). More accurate estimations can be accomplished through the generation of a high-resolution triangulated surface from the point clouds acquired previously and successively to the failure (Figure 2.32) (Guerin et al. 2017). In detail, the failed volume is isolated by segmenting and merging the failure surface (visible in the point cloud acquired after the failure) and the sub-region of points corresponding to the failed mass (visible in the point cloud acquired before the rockfall). Then, a 3-D feature is generated from the point cloud of the isolated mass by means of Poisson Surface Reconstruction (Kazhdan and Hoppe 2013), and the volume is calculated as the sum of the elements' volumes of which the feature is composed.

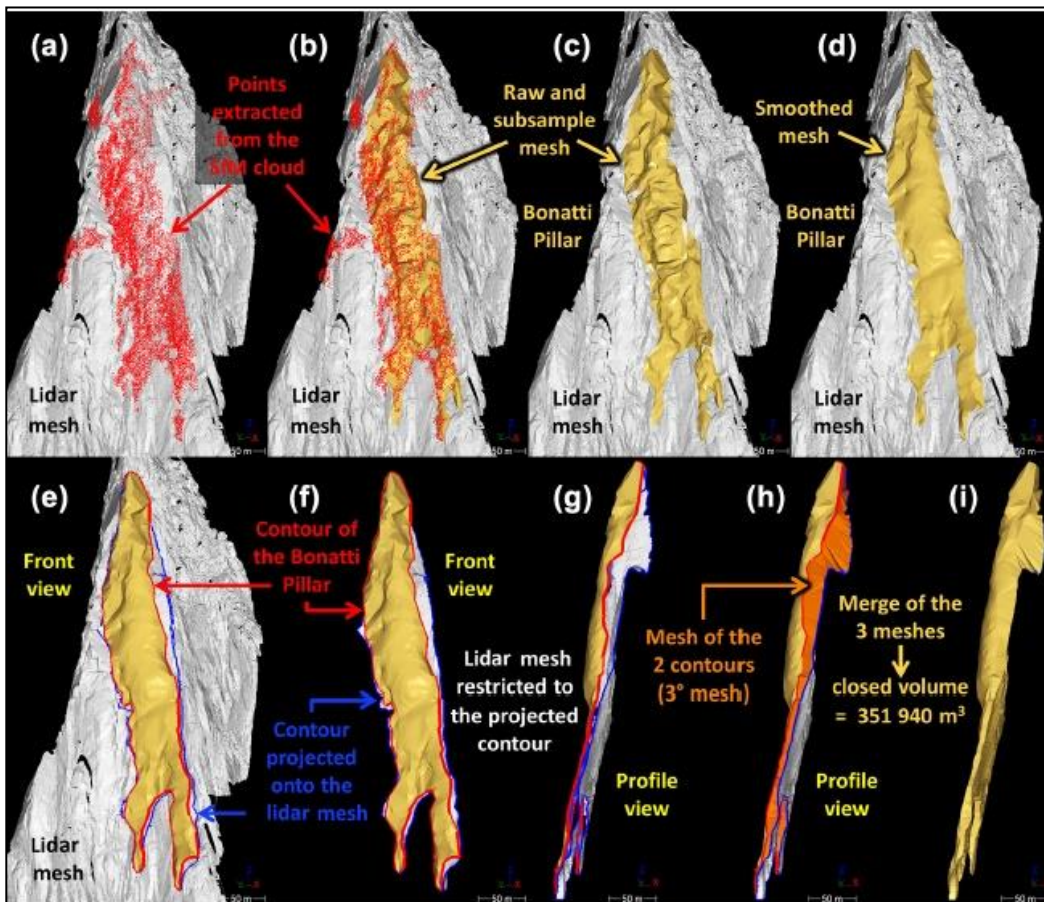


Figure 2.32: Volume calculation method (after Guerin et al. 2017). (a) detection of the failed mass by means of comparison of multi-temporal TLS and photogrammetry acquisitions; (b-d) raw and smoothed “open” mesh of the failed volume; e-i) generation of a closed mesh and calculation of the failed volume.

2.5.1.6. *Rockfall prediction*

Rock slope monitoring by means of remote sensing technique introduced recent advances in attempt to predict failures in rock slopes. Imminent failures may be revealed through precursory rockfall evidences (Sartori et al. 2003, Cruden and Martin 2007). Novel researches illustrated how the dilation of joints and small volume precursory rockfalls (detected from point clouds) accelerated before the larger failure (Rosser et al. 2005, 2007; Abellán et al. 2010; Royán et al. 2013; Kromer et al. 2015, 2017). Coherently, Pedrazzini and co-workers found out that the rate of small rockfalls decreased as the study area was progressively stabilizing (Pedrazzini et al. 2010). Precursory rockfalls can be interpreted as an increase of internal stresses within the slope, with progressive displacements over time. This process, known as *progressive failure*, is related to the consecutive tensile or shear strength reduction of rock bridges, and their consequent failure (Lawn 1993; Eberhardt et al. 2004, 2017; Scholtes and Donzé 2012; Scavia 2015). Thus, the detection of small volume rockfalls can help to predict larger instabilities and plan mitigation measures.

2.6. Methods for stability analyses in rock slopes

When dealing with rock slope stability investigations, the data collected during *in situ* geostructural and geomechanical surveys are used as input for stability analyses, which are carried out to evaluate the rock slope stability conditions, potential failure mechanisms and to assess the effect of different processes and interventions. Both the conventional and innovative approaches for stability analyses are reviewed in the following sections. The main characteristics, advantages and limitations of each method are reported in Figure 2.33.

method	parameters		
Stereographic and kinematic	Critical slope and discontinuity geometry; representative shear strength characteristics.	Simple to use and show failure potential. Some methods allow analysis of critical key-blocks. Can be used with statistical techniques to indicate probability of failure and associated volumes.	Suitable for preliminary design or for non-critical slopes, using mainly joint orientations. Identification of critical joints requires engineering judgement. Must be used with representative joint/discontinuity strength data.
Limit equilibrium	Representative geometry, material/joint shear strength, material unit weights, groundwater and external loading/support conditions.	Much software available for different failure modes (planar, circular, wedge, toppling, etc.). Mostly deterministic but some probabilistic analyses in 2-D and 3-D with multiple materials, reinforcement and groundwater profiles. Suitable for sensitivity analysis of FoS to most inputs.	FoS calculations must assume instability mechanisms and associated determinacy requirements. In situ stress, strains and intact material failure not considered. Simple probabilistic analyses may not allow for sample/data covariance.
Rockfall simulation	Representative slope geometry and surface condition. Rock block sizes, shapes, unit weights and coefficients of	Practical tool for siting structures and catch fences. Can utilize probabilistic analysis. 2-D and 3-D codes available.	Limited experience in use relative to empirical design charts.

Figure 2.33: Characteristics, advantages and limitations of the conventional and numerical approaches for stability analyses in rock slopes (modified after Stead et al. 2006).

2.6.1. Conventional methods: Kinematic analyses and Limit Equilibrium techniques

In a first phase, deterministic or probabilistic stability assessments can be performed by means of kinematic analyses using stereographic projections. Kinematic feasibility tests (e.g. Markland 1972) are carried out to identify potential failure mechanisms, as well as the movement direction, on the

basis of the spatial orientation of both the rock slope and the discontinuities. Several commercial software like *Dips* (Rocscience 2021a) and *DipsAnalyst* (Admassu and Shakoor 2013) are available to run kinematic analyses for different failure types, such as planar sliding, wedge sliding, direct and oblique toppling.

Limit Equilibrium methods are specifically used to study the stability of rock slopes affected by planar or circular failure surfaces. The slope is treated as a rigid body whose stability is defined by the *factor of safety*, which is the ratio between the resisting force along a well-defined failure surface (ultimate stress) and the driving force acting on the same surface (working stress). For all shear-type failures, the resisting and working stresses are expressed in terms of shear strength τ (Wyllie 2017):

$$FS = \frac{\text{Ultimate stress}}{\text{Working stress}} = \frac{\tau}{\tau_s} \quad \text{Eq. 2.30}$$

where τ and τ_s are the resisting shear strength and the displacing shear strength along the sliding surface, respectively. The limit equilibrium condition is reached when the driving forces equal the resisting forces, *i.e.* when $FS=1$. Many Limit Equilibrium methods were reported in the literature and differ on the investigated failure mechanism and on the hypotheses assumed to make the problem statistically determined (Figure 2.34). For instance, mechanisms involving circular and non-circular failure surfaces were discussed by Fellenius (1936), Bishop (1955) and Janbu (1973). Later, inter-slice forces were considered by Morgenstern-Price (1965), Spencer (1967) and Sarma (1973).

Methods	Equilibrium conditions satisfied	Slip surface	Use
Ordinary Method of Slices (Fellenius, 1927)	Moment equilibrium about center of circle	Circular slip surface	Applicable to non-homogeneous slopes and c- ϕ soils where slip surface can be approximated by a circle. Very convenient for hand calculations. Inaccurate for effective stress analyses with high pore water pressures.
Bishop's Modified Method (Bishop, 1955)	Vertical equilibrium and overall moment equilibrium	Circular	Applicable to non-homogeneous slopes and c- ϕ soils where slip surface can be approximated by a circle. More accurate than Ordinary Method of slices, especially for analyses with high pore water pressures. Calculations feasible by hand or spreadsheet.
Janbu's Generalized Procedure of Slices (Janbu, 1968)	Force equilibrium (vertical and horizontal)	Any shape	Applicable to non-circular slip surfaces. Also for shallow, long planar failure surfaces that are not parallel to the ground surface.
Morgenstern & Price's Method (Morgenstern & Price's, 1965)	All conditions of equilibrium	Any shape	An accurate procedure applicable to virtually all slope geometries and soil profiles. Rigorous, well established complete equilibrium procedure.
Spencer's Method (Spencer, 1967)	All conditions of equilibrium	Any shape	An accurate procedure applicable to virtually all slope geometries and soil profiles. The simplest complete equilibrium procedure for computing factor of safety.

Figure 2.34: Main Limit Equilibrium methods (after Duncan 1996).

Commercial computer programs such as *RocPlane* (Rocscience 2021b), *Swedge* (Rocscience 2021c), *Slide3* (Rocscience 2021d) and *CLARA-W* (Hungry 2001) allow to apply these methods relatively fast and to perform sensitivity analyses to estimate the factor of safety with discontinuity parameters varying in a range, rather than assuming unique values. However, these softwares are limited to simple blocks simulations and are not suitable to more complex geometries and conditions. In fact, as pointed out by Stead and co-workers (Stead et al. 2006), limit equilibrium methods and related computer codes do not account for non-persistent failure planes, although some attempts were made by numerous researchers (Jennings 1970; Baczynski 2000; Kemeny 2003), and do not allow to simulate

progressive failures (Bjerrum 1967; Chowdhury and A-Grivas 1982) or internal deformation of the rock mass.

2.6.2. Numerical methods

2.6.2.1. Introduction

Numerical methods have considerably evolved in the last 25 years to overcome some of the limitations to which the Limit Equilibrium methods are subjected, and are currently the most practised techniques in engineering geology to investigate landslides in soil and rock slopes. Recent developments in computing techniques allowed faster and extensive application of these methods to predict the mechanical behaviour of rock slopes in a more realistic context, since it is possible to set different parameters such as *in situ* stresses, water levels, different constitutive laws and boundary conditions for complex geometrical surfaces.

According to Lorig and Varona (2004), the key points of numerical methods can be summarised as follows:

- Numerical models can predict the failure mechanism as well as the most unfavourable failure surface.
- Oversimplification of the modelled slope can be overcome by integrating complex geologic and hydrologic conditions (*i.e.* folds, faults, weathered zones, groundwater), thus obtaining more realistic results.
- Numerical approaches can describe complex mechanical behaviour of rock slopes.
- Different failure mechanisms, topographies and design options can be investigated in relatively short computational times.

In practice, the model of the study object is divided (*discretized*) into zones to which the corresponding material and constitutive law are independently assigned to describe the material behaviour in different stress conditions (Read and Stacey 2009). The computation is performed by simulating different processes (*i.e.* excavations, seismic activity, changes of the water level, application of loads) using advanced algorithms. The mechanical response of the rock mass is given in the form of graphic outputs showing parameters like stresses and displacements that help to evaluate if the stability is achieved despite the simulated process, or to identify the mechanisms in case of failure.

2.6.2.2. Factor of safety

The stability of rock slopes by means of numerical methods is assessed by means of the *factor of safety* (FS), defined as the ratio of the actual shear strength to the minimum shear strength required to prevent failure (Wyllie 2017a). Numerical methods allow to define the factor of safety of a slope by means of the Shear-strength Reduction method (SSR) (Zienkiewicz et al. 1975; Hammah et al. 2005; Hammah and Yacoub 2006), which consists in gradually reducing the shear strength properties (*i.e.* cohesion c and friction angle ϕ) of the rock materials by a trial factor of safety f until the collapse occurs. For each iteration, the reduced cohesion and friction angle are:

$$c_{\text{trial}} = \left(\frac{1}{f}\right) c \quad \text{Eq. 2.31}$$

$$\phi_{\text{trial}} = \arctan\left(\frac{\tan\phi}{f}\right) \quad \text{Eq. 2.32}$$

When failure is achieved, the factor of safety is equal to the trial factor of safety:

$$FS=f \quad \text{Eq. 2.33}$$

2.6.2.3. Continuum, discontinuum and hybrid approaches

Nowadays, the most common codes for numerical stability analyses are based on continuum, discontinuum and hybrid methods. Early codes were introduced in the form of *continuum approaches* through which the model is discretised into a finite number of elements whose behaviour is approximated by simpler mathematical descriptions with finite degrees of freedom. The sub-domains must satisfy both the governing differential equations of the problem and the continuity condition at their interfaces with adjacent elements (Jing 2003). Continuum codes are based on *Finite-Element (FEM)*, *Finite Difference (FDM)* and *Boundary Element (BEM)* methods, which solve the same equations using different computational techniques (*i.e.* time-steps, matrixes) (Wyllie 2017). Both the techniques are based on the principle that at all points of the domain, the material cannot be broken into pieces, therefore all the material points originally in the neighbourhood of a certain point will remain in the same neighbourhood throughout the deformation process (Jing 2003).

These procedures are typically used for slopes constituted by soils, weak rocks or rock masses where failure is controlled by the deformation of the intact material or where a few discontinuities are present (Hoek et al. 1991; Coggan et al. 1998; Stead et al. 2006). Major structural features such as faults can be represented as interfaces between regions of continuum behaviour. Early numerical analyses by means of continuum approaches were performed to assess the stability of rock cuts and open pits (e.g. Krahn and Morgenstern 1976; Kalkani and Piteau 1976; Carranza-Torres et al. 1997; Bye and Bell 2001; Stacey et al. 2003; Guadagno et al. 2003). In recent years, advanced continuum-approach softwares able to carry out three-dimensional stability analyses were introduced. Some of the most used software are *RS3* (Rocscience 2021e), *FLAC3-D* (Itasca 2019) and *Plaxis3-D* (Bentley 2013). The advantages and limitations of finite-element methods and finite-difference methods are discussed by Hoek and co-workers (Hoek et al. 1991) and Jing (2003).

On the other hand, discontinuum approaches are commonly adopted to model rock slopes where the potential failure is controlled by persistent discontinuity sets, and allow to characterize both the intact rock and the discontinuities. The fractured medium is represented as an assemblage of blocks formed by connected fractures. At present, discontinuum methods are classified as *Distinct Element Methods (DEM)*, *Discontinuous Deformation Analysis (DDA)* and *Bounded Particle Method (BPD)*. For each technique, the medium is considered to be formed by rigid or deformable blocks (discrete elements) that interact with each other and can be exposed to gravity or external loads. The equations of motions are solved throughout the analysis considering the contacts between the blocks. Exhaustive description of the methodologies and computational techniques are reported by Jing (2003) and Bobet and co-workers (Bobet et al. 2009). Some applications of discontinuum approaches were proposed as solutions to study the stability and kinematics of large landslides (Sitar and MacLaughlin 1997; Eberhardt et al. 2005; Gischig et al. 2011; Gigli et al. 2011), quarries (Costa et al. 1999), and mines (Hutchison et al. 2000), to investigate the effect of the geometry of non-persistent joints on the stability of rock slopes (Kulatilake et al. 1992; Bahrani et al. 2014), and to study hydraulic fracturing (Damjanac and Cundall 2016). Despite the use of these methods for three-dimensional analyses is limited due to practical and economic reasons (Stead et al. 2006), some pioneering works were introduced in the literature to explore the potentialities of 3-D discontinuous approaches using *3-DEC*

(Itasca 2020) (e.g. Adachi et al. 1991; Zhu et al. 1996; Corkum and Martin 2002; Kalenchuk et al. 2011; Spreafico et al. 2016) and *Yade* (Boon et al. 2014).

Recently, hybrid models (continuum/discontinuum methods) were proposed as innovative approaches to analyze complex situations involving progressive failures associated to internal dilation and fracturing (Eberhardt et al. 2004; Vyazmensky et al. 2010; Lollino and Andriani 2017), which are typical of slopes constituted by blocky rock masses where instability is achieved through the progressive failure of rock bridges.

A sketch of the continuum, discontinuum and hybrid methods, a short description and their advantages and limitations are provided in Figure 2.35 and Table 2.11. In-depth descriptions, applications and reviews of these methods are reported in Sharma and co-workers (Sharma et al. 1999), Jing (2003) and Bobet (2010).

Unquestionably, the choice of the numerical approach depends on the physical and mechanical characteristics of the rock mass in question and on the considered scale (Edelbro 2003). Aimed at preliminarily assessing the appropriate numerical technique and at focusing on the critical parameters that should be further explored, Brideau and co-workers (Brideau et al. 2009) suggested some relationships among the GSI and the expectable failure mechanisms. More in detail, 5 zones were identified on the GSI chart depending on the structure of the rock mass and the surface conditions, each of which can be approached using a specific method (Figure 2.36).

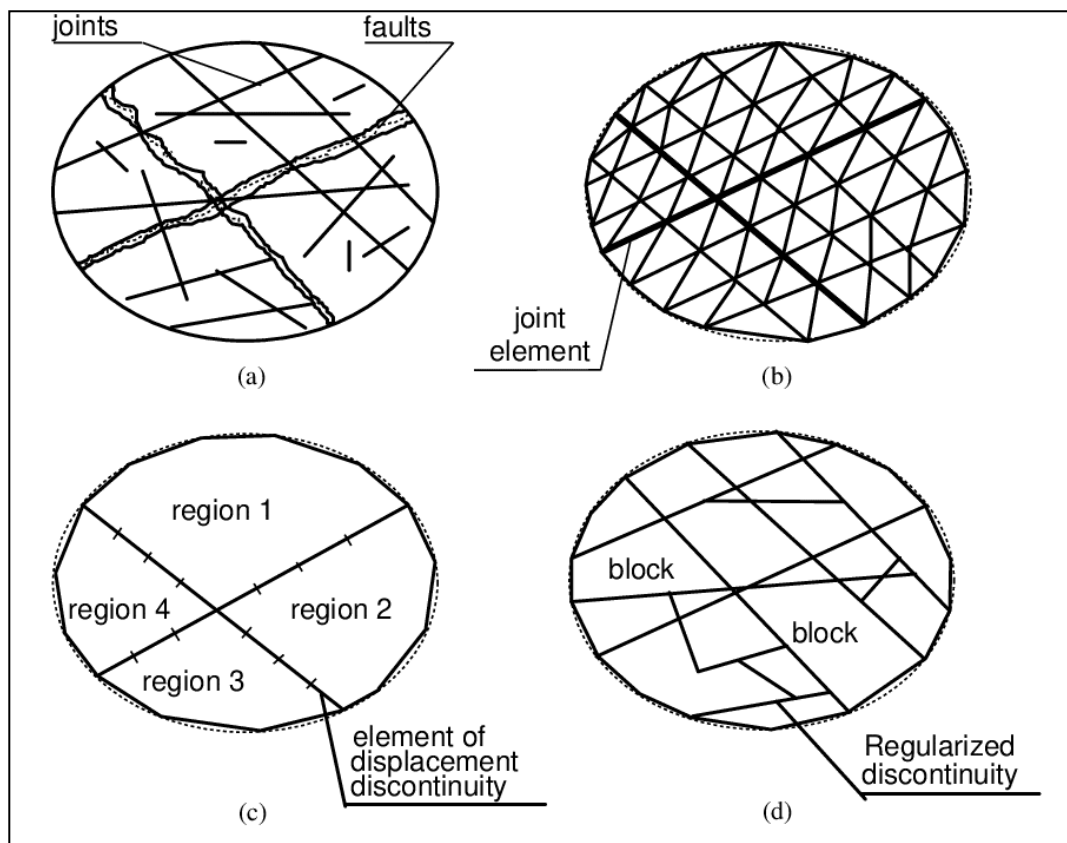


Figure 2.35: Representation of a rock mass using different numerical approaches (after Jing 2003). (a) sketch of the rock mass; (b) discretisation by means of Finite Difference Method or Finite Element Method; (c) discretisation by means of Boundary Element Method; (d) discretisation by means of Discrete Element Method.

Table 2.11: Summary of the main numerical methods commonly adopted for rock slope investigations (modified after Stead et al. 2006).

Analysis method	Critical input parameters	Advantages	Limitations
CONTINUUM MODELLING (e.g. finite element, finite difference, boundary)	Representative slope geometry; constitutive criteria, groundwater characteristics; shear strength of surfaces; in situ stress state.	Allows for material deformation and failure, including complex behaviour and mechanisms, in 2-D and 3-D with coupled modelling of groundwater. Can assess effects of critical parameter variations on instability mechanisms.	Users should be well trained, experienced, observe good modelling practice and be aware of model/software limitations. Input data generally limited, and some required inputs are not routinely measured.
DISCONTINUUM MODELLING (e.g., distinct element, DDA)	Slope and discontinuity geometry; intact constitutive criteria; discontinuity stiffness and shear strength; groundwater and in situ stress conditions.	Allows for block deformation and movement of blocks relative to each other. Can model complex behaviour and mechanisms (combined material and discontinuity behaviour, coupled with hydro-mechanical and dynamic analysis).	As above, experienced users needed. General limitations similar to those listed above. Need to simulate representative discontinuity geometry (spacing, persistence, etc.). Limited data on joint properties available (e.g., joint stiffness, jkn and jks).
HYBRID FINITE-/DISCRETE-ELEMENT CODES	Combination of input parameters for both continuum and discontinuum; damping factors; tensile strength and fracture energy release rate for fracture simulation.	Combines advantages of both continuum and discontinuum methods. Coupled finite-/discrete-element models able to simulate intact fracture propagation and fragmentation of jointed and bedded media.	Complex problems require high memory capacity. Comparatively little practical experience in use.

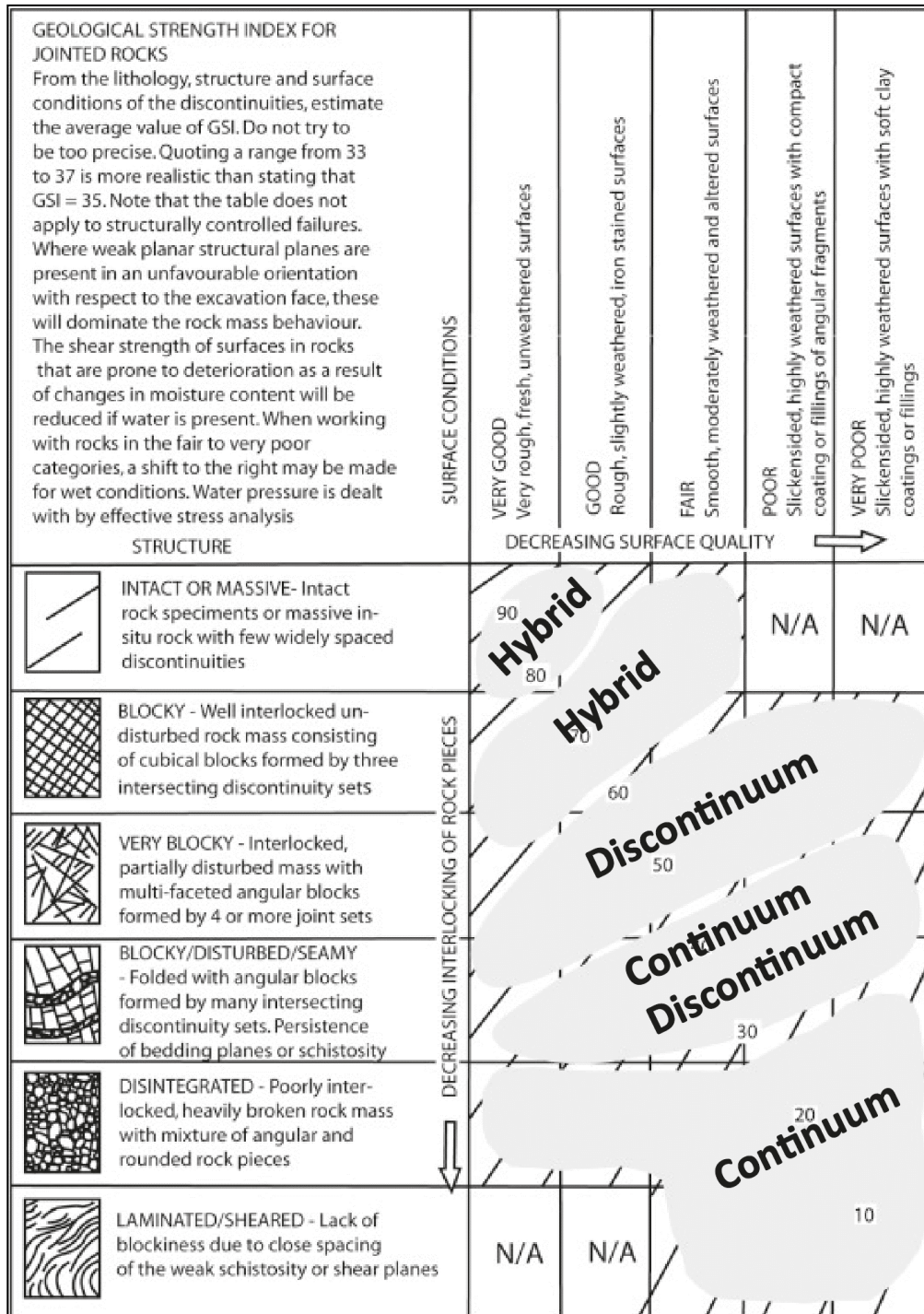


Figure 2.36: Numerical methods suggested according to the GSI (after Brideau et al. 2009).

2.6.3. Recent advances in geomechanical modelling: Discrete Fracture Network

Significant progresses were made in rock engineering through the implementation of Discrete Fracture Networks (DFNs) techniques for rock slope modelling. The application of DFNs was promoted in the late nineties by several research groups (Long et al. 1982; Baecher 1983; Andersson et al. 1984; Dershowitz and Einstein 1988; Staub et al. 2002; Elmo 2006), but they have been gaining popularity only in the last few years with the advent of specific advanced commercial softwares. The principle

of DFNs in rock slope characterization consists in treating the discontinuities and their properties such as location, orientation, persistence, spacing, termination mode and intensity as random variables with inferred probability distributions (Xu and Dowd 2010; Wyllie 2017). At present, 3-D geomechanical modelling codes such as *FracMan* (Dershowitz et al. 1994; Golder Associates 2018), *Resoblock* (Merrien-Soukatchoff et al. 2012) and *Fracas* (Xu and Dowd 2010) are provided with DFN generators that allow to produce more realistic models and to investigate the effect of the size and space variability of discontinuities on slope stability. Novel research proposed the implementation of fracture networks obtained by means of DFNs approaches in codes for numerical modelling, as shown by Havaej and co-workers (Havaej et al. 2016) and Montiel and co-workers (Montiel et al. 2020), who used the discontinuum method code *3-DEC* to understand the effects of the stochastic nature of geologic structures on the stability of a slate quarry and of an open pit mine, respectively (Figure 2.37).

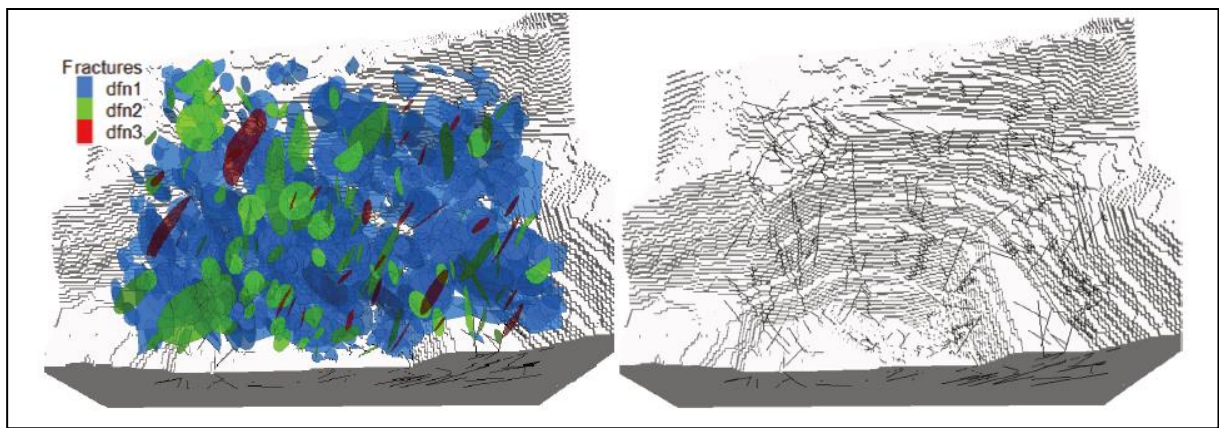


Figure 2.37: Integration of discontinuities generated by means of DFNs method in numerical modelling to perform stability analyses in an open pit mine (after Montiel et al. 2020).

2.7. Research approach

The main objective of this PhD thesis is to elaborate a workflow for rock slope stability analyses based on the integration of field surveys, geotechnical investigations, remote sensing techniques and 3-D numerical modelling. However, before achieving the final goal, the detailed literature review that was carried out throughout the doctorate activity brought to arise some questions and to propose some implementations during the research.

A. Remote sensing technologies were introduced for rock slope characterization to overcome the main limitations of conventional geotechnical surveys, such as low accessibility, safety risk, instrument and human bias. However, although many researches (most of them at the laboratory scale) were carried out to outline the main advantages and limitations of TLS, traditional photogrammetry and UAV methods, it appears that they were not directly compared to each other to assess their reliability. More specifically, the following questions emerged after the literature review:

- 1. From a practical standpoint, is there any difference among TLS, terrestrial-SfM and UAV-SfM techniques, in terms of accuracy, site conditions, required time and economical resources?**
- 2. Does the choice of the survey technique influence the results of rock slope characterization and monitoring from point clouds or triangulated surfaces?**
- 3. Moreover, when dealing with the extraction and characterization of discontinuity sets from point clouds, regardless of the survey technique, does the chosen method provide different results with respect to the others proposed in the literature?**

To answer these questions, the abovementioned remote sensing techniques were carried out in an appropriate case study and quantitatively compared to each other to assess their quality by considering different factors. In addition, two methods with different degree of automation for discontinuity extraction and characterization from each point cloud were tested and compared to the results of conventional geotechnical and geomechanical surveys to answer questions number 2 and 3. This research approach is illustrated in Chapter 4.

B. InfraRed Thermography (IRT) in Geosciences is relatively recent and very few researches addressed its application for rock mass characterization. For this reason, further investigations were carried out during this PhD, with the purpose to answer the following questions:

- 4. Is the IRT technique useful for rock mass characterization at a relatively large scale for sites characterized by lithological units with similar diffusivity, mild climate, dense vegetation and anthropogenic disturbances?**
- 5. Are other survey techniques needed to interpret the thermal response of rock masses?**

Aimed at evaluating the applicability of IRT techniques in these conditions, a 24 hours thermal monitoring was performed in a complex study area and the acquired thermograms were analyzed to solve the raised questions (see Chapter 5).

C. As outlined in section 2.5, many methods to perform rock mass characterization from three-dimensional datasets were introduced in the last decades. Nevertheless, this approach can be challenging to investigate sub-vertical and low-relief areas, since only a limited number of discontinuities can be extracted in the form of planar surfaces, with the risk of obtaining improper results (e.g. set

spacing overestimation). At present, bi-dimensional analyses, which are more accurate in these cases, require the application of conventional field surveys or in any case the analysis of discontinuity trace maps by means of complex and time-consuming techniques (see section 2.1).

- 6. To solve these limitations, methods and formulas proposed in the literature were adapted to a digital environment by developing and validating a specific MATLAB routine for quicker and more efficient 2-D discontinuity analysis from orthophotos collected by means of remote sensing techniques.**

The last phase of the study focused on summing up the different research activities to achieve the main objective of the PhD thesis:

- 7. How can the data obtained by means of remote sensing techniques and conventional geostructural and geomechanical surveys be optimally combined to perform sophisticated rock slope stability analyses?**

As a matter of fact, the most common approaches to carry out stability analyses by means of numerical modelling (considering software availability and costs) do not fully exploit the results of rock mass characterization from Digital Elevation Outcrops (DOMs), with the consequence that large part of the work is not implemented in geomechanical models. For this reason, many tests were carried out to generate a realistic geomechanical model of the case study by combining the 3-D model with the results of the geostructural and geomechanical characterization (from point clouds and from site investigations) and with the physical and mechanical properties of the rock materials. All the tests allowed the execution of advanced stability analyses by means of 3-D and 2-D Finite Element Method optimized through the implementation of the discontinuity sets, as well as the identification of potential triggering factors and carry out specific simulations in order to assess the rock slope stability in different scenarios.

Finally, a complete procedure to evaluate rock mass stability by means of remote sensing techniques and conventional geostructural and geomechanical surveys was set up. This subject was addressed in Chapter 7, where numerical models were used to validate the proposed methodology and to evaluate the effects of the discontinuities in the study site, as well as to perform a preliminary stability assessment.

Chapter 3 Case study

3.1. Geological and geomorphologic setting

The study sites are located in the urban area of the municipality of Polignano a Mare (Bari province), southern Italy, along the Adriatic side of the Apulian coast (Figure 3.1).

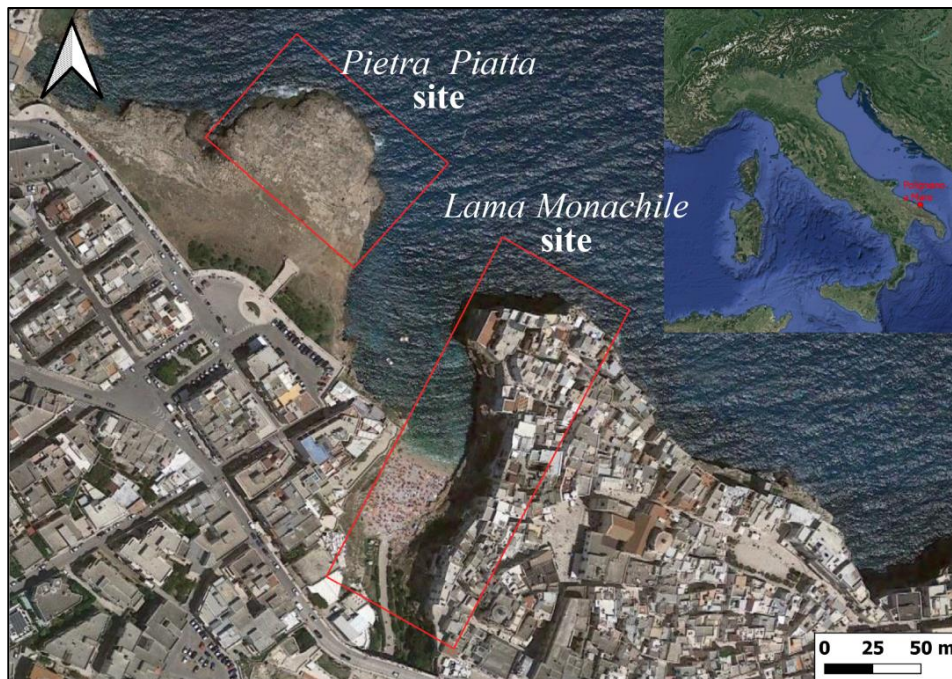


Figure 3.1: Geographic location of the study area.

The area falls at the northern part of *Sheet no. 190 Monopoli* of the Geological Map of Italy, at scale 1:100.000. The geologic setting is represented by an about 3 km-thick Cretaceous carbonate bedrock belonging to the Calcare di Bari Fm., unconformably overlain by Plio-Pleistocene calcarenite deposits attributable to the Calcarenite di Gravina Fm. From a geodynamic standpoint, during the Late Cenomanian and Turonian, the Cretaceous succession related to a wide carbonate platform was subjected to temporary emergence of some sectors, including the Murge Plateau, to which the study area belongs, as consequence of the Alpine orogenesis (Mindszenty et al. 1995). Such emergence brought to the first occurrence of karst processes on the exposed carbonate outcrops, and the development of karst systems (Sauro 1991; Parise 2011). The collision between the African and European Plates started in the Oligocene originated the opposite-vergence Apennininic and Dinaric chains (Ricchetti et al. 1988; De Alteriis and Aiello 1993; Argnani et al. 1993), of which the Murge Plateau, together with other zones, constituted the foreland (Figure 3.2). The Miocene-Early Pleistocene migration of the South Apennine system towards the east led to the arching of the Adriatic plate and the consequent development of faults on both the Apennine and Dinaric sides (Ricchetti and Mongelli 1980;

Ricchetti et al. 1988). The Apenninic through, namely *Bradanic Through*, which was delimited on the east and west sides by the Apenninic Chain and the emerged sectors of the Apulian foreland, respectively, was filled by allochthonous deposits deriving from the erosion of the Apennines (Casnedi et al. 1982). To the east, the subsidence of the Apulian foreland led to the erosion of the Cretaceous bedrock and consequent deposition of the Calcarenite di Gravina Fm. During the Early Pleistocene, a drastic change of the geodynamic setting led to a slow regional uplift of both the Apulian Foreland and the Bradanic Through (Ciaranfi et al. 1983; Doglioni et al. 1994, 1996) that, together with absolute sea level changes, determined the sea regression up to the current level and the formation of marine terraces degrading toward the present sea level (Ricchetti et al. 1988).

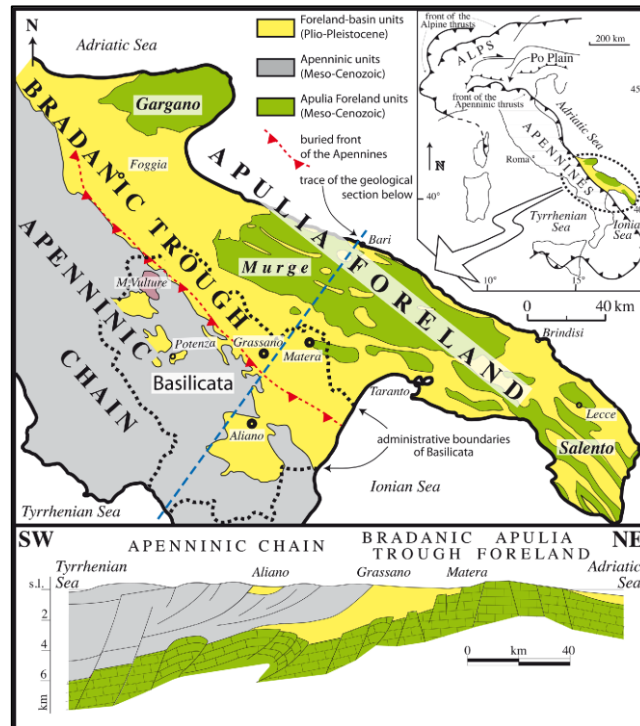


Figure 3.2: (a) Geologic sketch of Apulian Foreland and Bradanic Through (modified after Pieri et al. 1997); (b) geologic section of southern Italy (modified after Sella et al. 1988).

The marine terraces are visible in the form of relatively flat terrains, parallel to the coastline and slightly dipping toward the Adriatic Sea, linked by sub-vertical steps, which represent the paleo-coastlines (Bruno et al. 1995; Dini et al. 2000; Mastronuzzi and Sansò 2002). Several karst incisions, locally named *lame*, cross the marine terraces until reaching the Adriatic Sea. *Lame* are slightly incised and flat-bottomed generally dry valleys, but they can channel waters during intense rainy events, thus originating flash floods in the Apulian karst environments (Parise 2003; Mossa 2007; Martinotti et al. 2017; Gentile et al. 2020).

The rock coast of the neighbouring zones is formed by promontories and inlets gently dipping toward the sea, locally interrupted by *pocket beaches* made up by coastal erosion materials, where *lame* reach the sea. Locally, the coast is constituted by sub-vertical and plunging cliffs reaching altitudes up to 20 metres, as in the case of *Lama Monachile* site. Karst landforms like karrens, conduits and caves are widespread in the study area (Favale and Sauro, 1994; Parise et al., 2013; Rudnicki, 2003) and are predominantly related to the continental phase, which lasted for large part of the Tertiary, determined by the Apenninic orogenesis.

3.2. Geostructural setting

The Murge area is formed by a monoclinical structure slightly dipping toward S-SW (up to 15°), with trend compatible with the Apennine fold-and-thrust belt system (Lavecchia et al. 2003) probably influenced, at the regional scale, by a gentle regional fold named *Anticlinale di Monte Acuto* in the northern area and by a gentle anticline with ESE plunging hinge line trending close to the Adriatic Sea (Ricchetti 1980; Ciaranfi et al. 1988; Ricchetti et al. 1988). The Murge area is characterized by prevailing brittle tectonic structures developed during the Tertiary as a consequence of the genesis of the Apenninic and Dinaric chains. Two major fault systems are present at the regional scale: high-angle normal faults striking in the range EW-N140, dipping mostly toward NNE (Apenninic system) and high-angle faults striking in the range NS-N050, mostly dipping toward NW (anti-Apenninic system) (Pieri et al. 2012). Gentle anticlinal and synclinal folds with axes oriented parallel to the Apenninic system, as well as *horsts* and *grabens*, are related to the first system, whose origin is prior to the deposition of the Quaternary calcarenites. According to Festa (1999, 2003), the normal faults striking EW-N140 are partly constituted by ancient re-activated structures whose strain ellipse is compatible with the NE-SW directed extension that was active at least from Late Cretaceous (Figure 3.3). On the other hand, the orthogonal system is thought to be more recent, as it locally interrupts folds and faults belonging to the first system. As a matter of fact, the activity of the NS-N050 faults, related to strike-slip cinematics associated with Apenninic thrusts (Doglioni et al. 1994, 1996), is dated back to the time span from the Early Pleistocene to the present. The Quaternary tectonic activity of Apulia region is also demonstrated by the presence of alluvial terraces, which progressively formed at lower elevations as the Apulia region was subjected to uplifting.

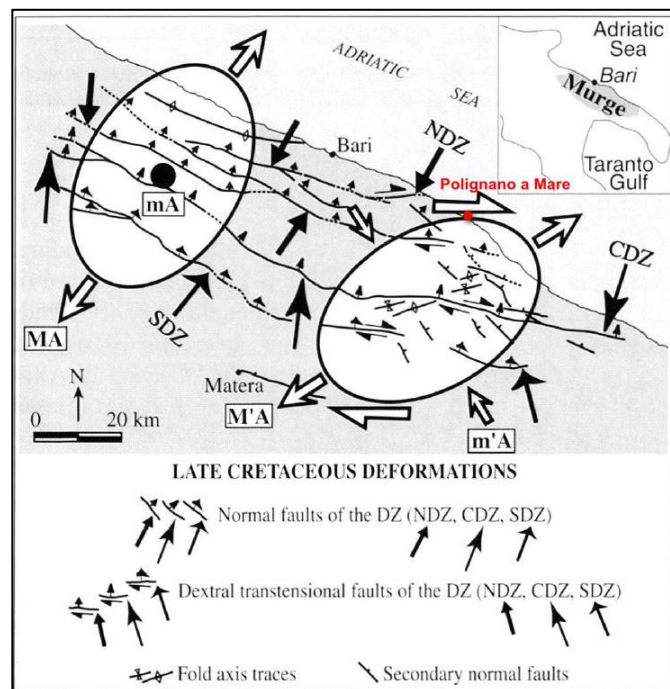


Figure 3.3: Resuming sketch of the late Cretaceous brittle deformation of the Murge area (modified after Festa 2003), mA and MA indicate the minor and major strain axes, respectively. The study area is located in the Northern Deformation Zone (NDZ). Mesoscopic and macroscopic structures are represented by NNW-SSE trending normal faults, E-W trending right trans-tensional mesoscopic faults, ENE-WSW trending sub-vertical axial plane traces of macroscopic open folds and sub-horizontal NW-SE directed tectonic stylolite peaks.

3.3. Hydrogeological setting

From a hydrogeological standpoint, the Murge area is characterized by the karst aquifer of the Mesozoic carbonate units of the Apulian platform. The groundwater recharge area is located landwards, up to 40 km from the coast, where the calcareous units crop out continuously and karst landforms favour infiltration (Parise 2011; Pieri et al. 2012). Groundwater flows under pressure, with head gradient of 0.1-0.5%, towards the base level corresponding to the sea (Grassi and Micheletti 1972; Cotecchia et al. 1983, 2001; Cotecchia 2014). More in detail, the hydrogeological domain of the study sites is related to the permeability of the Calcarene di Gravina and Calcare di Bari Fm.s, which are characterized by different hydraulic conductivity k , related to the pore size and distribution. More in detail, pores in the rock particle system of the calcarenite units are usually interconnected and continuous (high open primary porosity), contrarily to the limestone units, characterized by isolated voids (secondary porosity) (Andriani and Walsh 2003; Cherubini et al. 2018; Andriani et al. 2021). At a smaller scale, infiltration occurs by means of secondary porosity through the system of fractures and karst voids diffused in the study area (Andriani and Walsh 2007; Parise et al. 2020; Liso et al. 2020), with k values up to 10^{-1} - 10^{-2} cm/s. Several springs are located along the coast, especially where calcarenites crop out (Liso and Parise 2020). Freshwater lies above the seawater and intense karst processes take place in the mixing zone (Rudnicki 1973; Sauro 1991), where the hydraulic conductivity is particularly high. In addition, Polignano a Mare locality is affected by marine water intrusion that is favoured by the ongoing excessive overexploitation of Apulian groundwater resources, as in many other towns of Apulia region (Cotecchia et al. 1997, 2005). The water table is located at 15-25 m below the topography and the groundwater flows toward N-NNE, while direct discharge in the sea occurs by means of a coastal spring in proximity of the cave named *Grotta Palazzese* (Figure 3.4). As outlined above, the surface-water flow follows the karst incisions crossing the Murge area toward the Adriatic Sea.

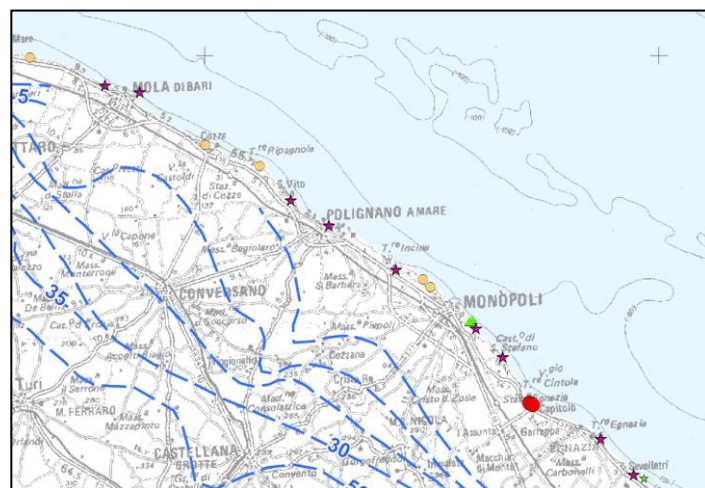


Figure 3.4: Isopiezic map of the karst aquifer of the Murge area (from Piano di Tutela delle Acque (PTA) of Apulia region, available at www.sit.puglia.it).

3.4. Marine erosion and meteo-marine conditions

Marine erosion occurs at the toe of the cliffs diffuse along the coast by means of hydraulic and mechanical action on the exposed face. Hydraulic processes simultaneously operate through

compression, tension, shearing and explosive forces. Compressive forces act perpendicular to the rock face when assailing waves break in front of the rock cliff, tension forces are caused by receding waves, shearing occurs when masses of water are thrown against the cliff and generate tangential stresses (Sunamura 2015). In addition, strong waves splashing against the rock cliff push compressed air inside the fractures and voids, generate compressive stresses and further rock mass degradation (explosive force). On the other hand, mechanical action is represented by wearing, grinding or scraping of the cliff face caused by loose materials transported by the wave motion and thrown against the cliff during intense storms (abrasion). As pointed out by Sunamura (2015), erosion takes place when the wave assailing forces exceed the rock mass resisting forces, which depend on the rock material strength properties and geological structures such as discontinuities. However, rock mass resisting forces tend to be reduced over time as incessant stresses caused by marine action (cyclic loading) generate crack initiation and propagation. This concept, known as *fatigue*, was investigated by many authors, among which Brossard and Duperret (2004) and Adam and co-workers (Adams et al. 2005).

Undoubtedly, knowledge of the local meteo-marine conditions of the study site, with particular reference to winds and sea storms, is fundamental to estimate the wave motion in attempt to assess landslide susceptibility. For this reason, anemometric and ondametric data (collected by the Italian Air Force-Aeronautica Militare) of the measurement stations close to the study area were analyzed. The most frequent annual winds registered at Bari Palese (about 35 km NW from the study area) come from W, SSW, WSW and S, with frequencies of 13.1%, 10.1%, 9.8% and 7.2% (Figure 3.5). With regards to the wind intensity, 48.5% of the wind population belongs to classes I-II of the Beaufort scale ($v \leq 11$ km/h; $v < 7$ nodes), 30.5% is represented by classes III and IV ($v = 12-29$ km/h; $8 < v < 17$ nodes) and only 2.5% is characterized by higher velocities, mostly corresponding to winds coming from N, NNW and S.

Data recorded by the ondametric station in Monopoli (about 8 km SW from the study area) were observed to estimate the annual frequency of occurrence of sea storms. As shown in Figure 3.6, intense sea storms come mostly from NNW (25.5%), corresponding to the greatest fetch, and are followed by storms coming from N (17.2%), ESE (15.2%), E (14.6%), ENE (12.0%) and NNE (10.5%). About half of the events are characterized by significant wave heights smaller than 0.5 m, while 31.5% and 2.5% are represented by significant wave heights of 0.5-1m and 2-3 m, respectively. The maximum wave amplitude (4.0 m) recorded close to the coastline came from the N and NNE (Maracchione et al. 2001).

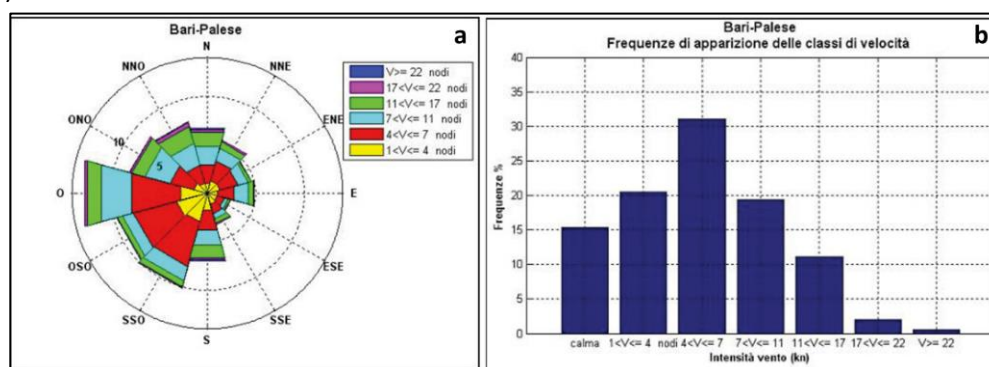


Figure 3.5: Rose plot (a) and histogram (b) of the annual wind frequencies registered by the anemometric measurement station in Bari-Palese (from Piano Regionale delle Coste (PCR) of Apulian Region www.sitpuglia.it).

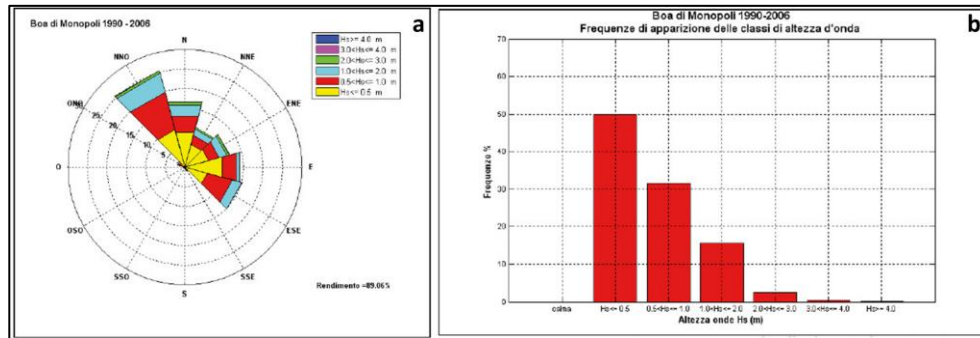


Figure 3.6: Rose plot of the annual sea storm frequencies (a) and histogram of the significant wave height (b) registered by the ondametric measurement station in Monopoli (from Piano Regionale delle Coste (PCR) of Apulian Region www.sitpuglia.it).

3.5. *Lama Monachile and Pietra Piatta sites*

3.5.1. *Lama Monachile site*

Lama Monachile site belongs to the above-mentioned karst incisions crossing large part of the Murge area until reaching the Adriatic Sea. The incision, oriented SSW-NNE, crosses the town of Polignano a Mare for about 250 m, developing from an altitude of 25 m to the sea level, where an about 1900 m² wide *pocket beach*, constituted by loose materials derived mainly from the coastal erosion, is set. A series of alluvial terraces related to the glacio-eustatic sea level changes are visible along both sides of the *lama*. The NNE sector of *Lama Monachile* is set in a plunging cliff (Figure 3.7) up to 20 m high, with sub-vertical walls steeply passing down into deep nearshore water (Bird 2011). The top of the cliff is famous all over the world for the historic centre of Polignano a Mare, which attracts many tourists throughout the year and hosts international sport competitions (Figure 3.8).

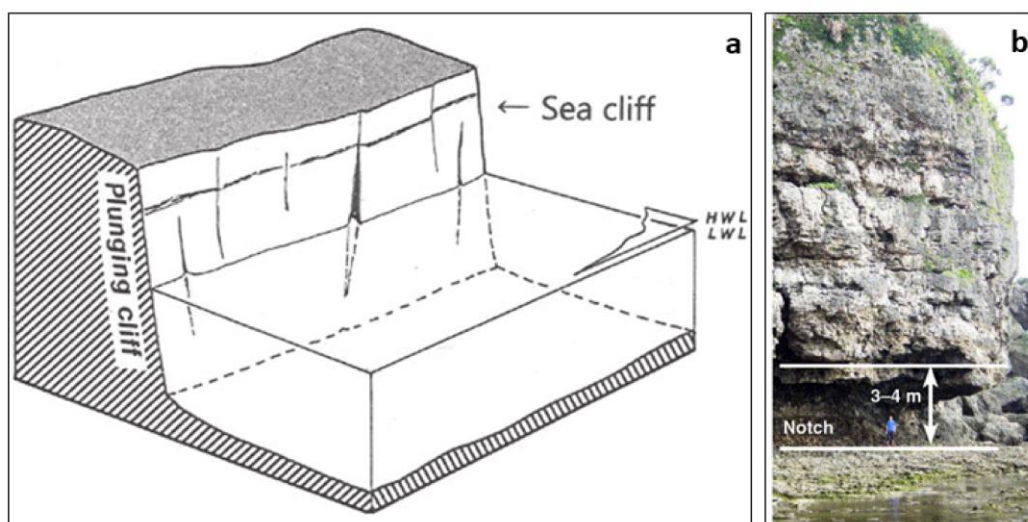


Figure 3.7: Plunging cliff sketch (a) (after Sunamura 1992) and marine notch (b) (after Kogure et al. 2006).



Figure 3.8: Panoramic view of *Lama Monachile* site (photo taken on 20/10/2021). Note the anthropogenic modifications along the hydrographic network, the buildings located at the top of the cliff and the presence of people also in an Autumn weekday afternoon.

The karst incision is set in both the *Calcare di Bari* and the *Calcarenite di Gravina* Formations and offers a 3-D exposure of the geology of the area. The presence of alluvial and anthropogenic terraces facilitates the observation of the macroscopic and microscopic fabric of the outcropping facies, as well as the collection of information on the stratigraphic relations. However, it has to be noted that human interventions like excavations and building constructions mostly obliterated the original calcarenite structure, and strongly complicate the on-site recognition. The *Calcare di Bari* Fm. is formed by alternating thin (*Calcari a chiancarelle*) to medium bedded micritic and dolomitic levels, for a total height of 18 metres. The whitish micritic facies has a mud-supported fabric with grains mostly constituted by bioclasts, which are not visible in the greyish-brownish dolomitic facies, in which the dolomitization process obliterated the original texture. The *Calcare di Bari* Fm. has a monocline structure, with generally sub-horizontal layers, locally folded (maximum dipping 10°). Sub-vertical discontinuities are widespread in the limestone and dolostone levels, and locally cause an intense jointing degree of the rock mass. The *Calcarenite di Gravina* Fm., which at *Lama Monachile* site has a maximum thickness of 8 metres, overlies the Cretaceous bedrock through an angular erosional unconformity. This unit has a massive appearance and is made up of yellowish-greyish coarse to medium size bioclasts such as fragments of lamellibranchs, brachiopods, gastropods and serpulids.

The rock mass is characterized by sub-vertical joints and thin-to-medium bedded layers whose intersections determine the formation of potential unstable blocks with variable volumes. As a matter of fact, several boulders and rock fragments, mobilized from the cliff, are occasionally visible below the sea level (Figure 3.9b). The majority of these blocks belongs to the *Calcarenite di Gravina* Fm and is related to simple structurally-controlled failures (i.e. toppling, sliding). However, potential instabilities related to complex mechanisms involving several rock blocks belonging to both formations are well visible along the cliff (Figures 3.9a, c).

It must be remarked that the instability processes observed at *Lama Monachile* site, although controlled by its geomorphological, lithological and structural setting, are the result of the jointed action of different factors such as marine erosion, chemical solution, biological, subaerial processes, and human activity.

In detail, waves breaking against the coast, together with biochemical-biophysical erosion by algae, bacteria, molluscs, benthic foraminifers and echinoids (Neumann 1997), contribute to form a notch along the cliff at the sea level (Figure 3.9a).

Moreover, being a carbonate rock mass, chemical processes play a key role for the cliff evolution. As a matter of fact, epigeal and hypogean karst landforms such as corrosion voids and cavities, due to the dissolution of the carbonate rocks by carbon dioxide rich waters, are widespread in both geological units. Chemical dissolution is particularly active in the mixing area between fresh water and sea water, as demonstrated by several karst caves formed in the *Calcare di Bari* Fm. at the sea level (Figure 3.9c). Wave undercutting causes deepening of the notch, with consequent loss of support of the overlying levels and localized failures. Furthermore, bedding surfaces and joints developed especially in the limestone and dolostone units favour the circulation of chemically aggressive waters, producing cave expansion and progressive collapses to achieve stability through arc-shaped structures (Diederichs and Kaiser 1999; Waltham et al. 2005; Parise 2010).

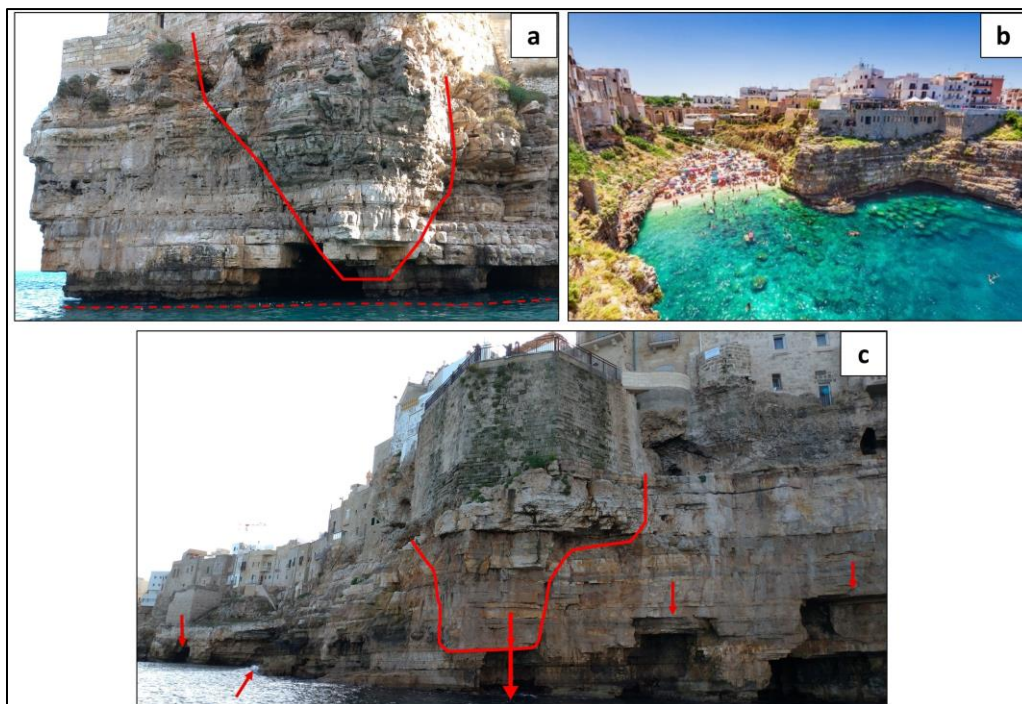


Figure 3.9: Different factors contributing to cliff retreat; (a) notch at the sea level formed by the interaction of mechanical wave erosion, chemical alteration and bioerosion; (b) boulders occasionally visible below the sea level related to localized failures of the rock mass and densely populated beach at the base of the cliff (retrieved from www.appulia.net); (c) karst caves produced by dissolution of limestones and dolostones.

In addition to physical erosion by sea waves and chemical dissolution, subaerial weathering also contributes to the rock mass deterioration. In the study area, subaerial weathering is mainly caused by salt crystallization determined by marine spray, which transports sea salt particles in the atmosphere

(Blanchard and Woodcock 1980; Zezza and Macrì 1995). Aerosol particles are removed from the air by dry (gravity) or wet deposition (wash-out and rain-out) and salt crystallization takes place on the exposed rock surfaces (Torfs and van Grieken 1997). Crystals deposited within the pores and cavities of the rock materials can grow or be hydrated, changing their volume, as consequence of relative air humidity changes (Amoroso and Fassina 1983). This process causes stresses within the pores, disaggregation and crumbling of the surfaces, with consequent rock mass degradation, especially in the more porous Calcarene di Gravina Fm.

Moreover, anthropogenic modifications of the coast morphology by means of excavations and building structures especially in the easily workable calcarenites, contribute to rock mass degradation, as in many sites of the Apulian territory (Andriani and Walsh 2007; Lollino et al. 2013; Gutiérrez et al. 2014; Andriani and Loiotine 2020).

All the mentioned factors act together to reduce the rock mass strength and represent a serious hazard for the cliff stability (Parise et al. 2015; Vennari et al. 2020). Considering the historical heritage of the town located on the top of the cliff and the high population density of the beach at its base for large part of the year, even small-size potential instabilities may cause severe consequences. Indeed, in relation to the presence of elements at risk and to high landslide and hydraulic hazard (the latter along the karst incision), *Lama Monachile* site and the adjacent east coast have been mapped by local authorities as areas of high hydro-geomorphological risk (Figure 3.10).

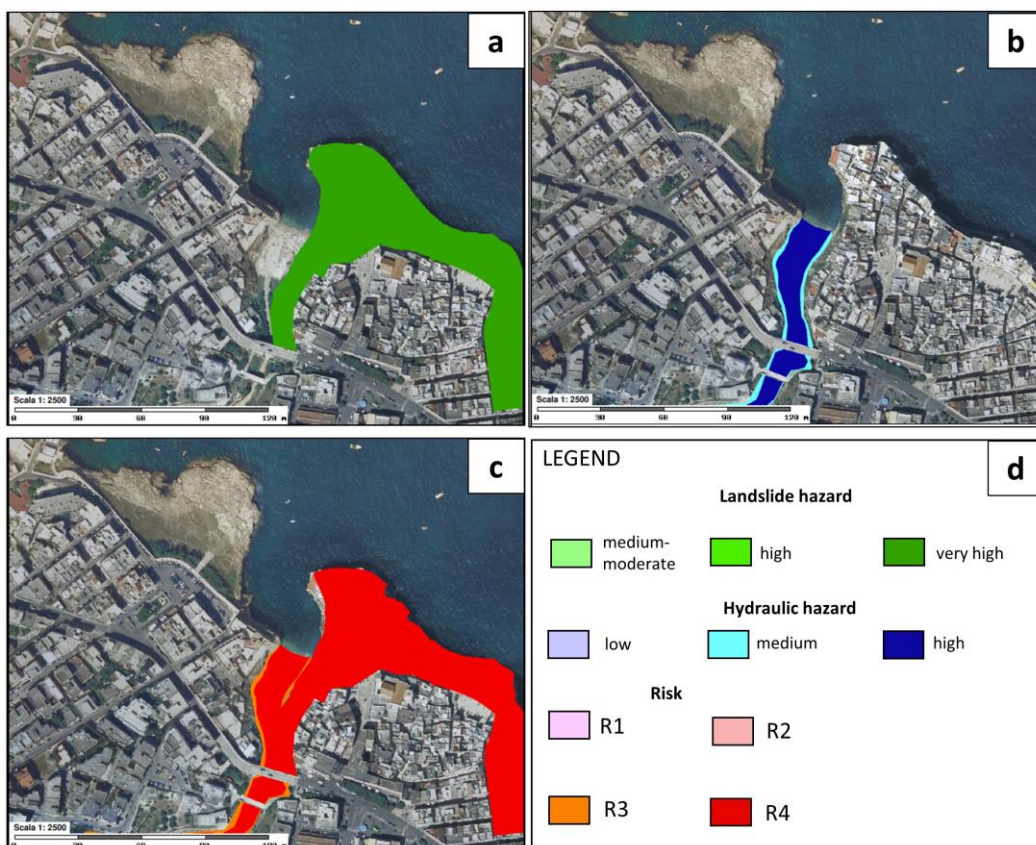


Figure 3.10: Identification of landslide hazard (a), hydraulic hazard (b) and risk (c) zones in the study area according to Piano d'Assetto Idrogeologico (PAI) of Apulia region (available at <http://webgis.adb.puglia.it/>). (d)

Legend of the hazard and risk maps. *Lama Monachile* site is located in high landslide and hydraulic hazard zones and falls in the highest risk category (R4).

3.5.2. *Pietra Piatta* site

Pietra Piatta site is a 6400-m², low-relief platform developing from 10 m above the sea level to the current coastline. The area is located about 90 m west of the axis of *Lama Monachile* site and it is surrounded by the sea except for the SW zone, through which it is connected to the inland. The platform reaches a maximum length and width of 135 m and 90 m, respectively, and stepped scarps with height ranging between 0.5 and 2 m are located in the eastern side. Due to erosional processes, the Calcarene di Gravina Fm. crops out only in the external zone, whilst the central area offers a detailed view of the Calcare di Bari Fm. Also in this site, the limestone unit is formed by alternating thin to medium bedded whitish micritic and greyish-brownish dolomitic levels, whose stratigraphic relationships are visible along the highest steps. The Calcare di Bari Fm. has a monocline structure, with generally sub-horizontal layers (dipping maximum 5°). The lack of vegetation and of man-made structures offers a detailed view of the rock mass fracturing conditions. Several discontinuity traces, arranged in a specific fracture pattern (see Chapter 6), can be observed on the flat surfaces of the rock mass and, together with the bedding surfaces, determine the formation of discrete blocks.

Given the lack of significant relief and the presence of extended flat surfaces, this outcrop is less subjected to instabilities with respect to *Lama Monachile* site. However, several on-going failures are located along the perimeter of the outcrop where the continuous wave action, combined with biological activity, karst and subaerial weathering, contributes to the opening of the major fractures (Figure 3.11) and to the toppling and sliding of large blocks.

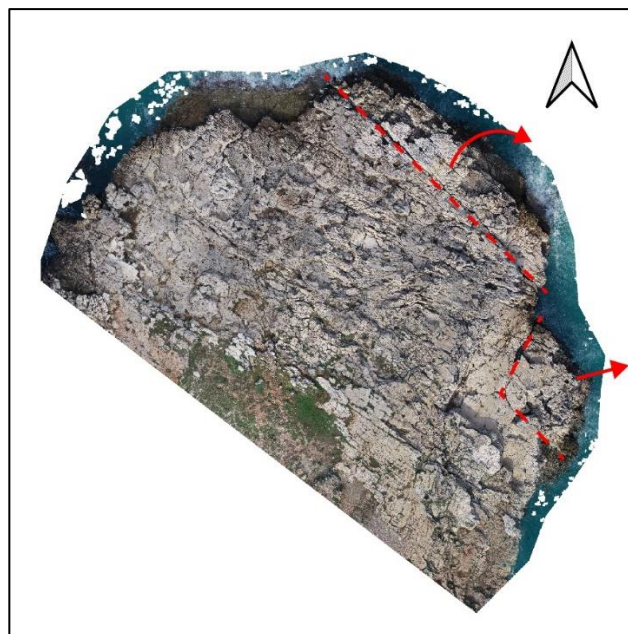


Figure 3.11: Toppling and sliding mechanisms at *Pietra Piatta* site caused by the geostuctural setting and the combined action of wave assault, biological activity, chemical dissolution and weathering. The 3-D model used to illustrate the failures was obtained by means of Structure from Motion (see Chapter 6).

Although the failures are localized along the borders of the outcrop and there are no infrastructures, the site is no risk-free because the described area is quite busy throughout the year. As a matter of fact, many people visit the outcrop to enjoy the spectacular view on the sea and the statue of Domenico Modugno, one of the greatest exponents of Italian music, who was born at Polignano, located just a few meters above the platform.

3.6. Choice of the case study

As pointed out in the previous sections, *Lama Monachile* is a typical morpho-structure of the Apulian territory, with thousands of tourists visiting both the beach and the old town of Polignano a Mare, located respectively at the toe and at the top of the rock slope in which it is carved. Despite no landslide events were ever reported by the local news, except for small collapses of anthropogenic structures (which, however, may have been triggered by rock mass degradation), it is evident that several failures occurred over time (e.g. Figure 3.9b) and it cannot be excluded that other events will take place, as rock cliffs naturally retrocede through progressive localized failures. Indeed, some worrying structural cracks on the buildings in the immediate proximity of the cliff border are well visible from photographic inspections, so that support structures were set to prevent collapse.

Rock slope geostructural and geomechanical characterization is of paramount importance to identify potential failures, as well as kinematics and likely volumes of detaching blocks, and to contribute to the planning of prevention and mitigation measures. Since aim of this PhD is to test and optimize the use of remote sensing techniques for rock mass characterization and stability assessment, the rock slope at Polignano a Mare was considered appropriate, also in the perspective to contribute to the protection of its natural and cultural heritage, as well as of the infrastructures and the people's safety. Other factors that played an important role for the choice of this study area are the dense Mediterranean vegetation, the karst caves, different lithologies, weathering of the materials, anthropogenic structures, high people transit and local regulations, all factors that can disturb/cause difficulties during the planning, acquisition, processing and interpretation phases of data collected by means of remote sensing techniques. Moreover, it was chosen to survey the east side of *Lama Monachile* site and of the adjacent coast since there more element at risk are located (historically relevant buildings and a major tourist density) and for the possibility to perform TLS, UAV and IRT surveys more efficiently and with less risk to damage the instruments. With regards to *Pietra Piatta* site, the rock mass was considered pertinent to characterize the discontinuities affecting the Calcere di Bari Fm. from their traces, because they are only partly visible at *Lama Monachile* site, as the formation is overlain there by the calcarenite units.

PART II
REMOTE SENSING

Chapter 4 Comparison of Remote Sensing techniques for geostructural analysis and cliff monitoring in coastal areas of high tourist attraction: the case study of Polignano a Mare (southern Italy)

Abstract

Rock slope failures in urban areas may represent a serious hazard for human life, as well as private and public property, even on the occasion of sporadic episodes. Prevention and mitigation measures indispensably require a proper rock mass characterization, which is often achieved by means of time-consuming, costly and dangerous field surveys. In the last decades, remote sensing devices such as high-resolution digital cameras, laser scanners and drones have been widely used as supplementary techniques for rock slope analysis and monitoring, especially in poorly accessible areas, or in sites of large extension. Although several methods for rock mass characterization by means of remote sensing techniques have been reported in specific studies, there are very few contributions that focused on comparing the different methods in an attempt to establish their advantages and limitations. With this study, Terrestrial Laser Scanning and terrestrial/UAV Structure from Motion were performed on a cliff located in a popular tourist attraction site, characterized by complex geological and geomorphological settings, as well as by disturbance elements such as vegetation and human activities. For each point cloud, geostructural analyses by means of semi-automatic methods were applied and then multi-temporal acquisitions were compared for cliff monitoring. By quantitative comparison of the results and validation by means of conventional geostructural field surveys, the pros and cons of each method were outlined in attempt to depict the conditions and goals the different techniques seem to be more suitable for.

4.1. Introduction

Local to global failures in urbanized steep rock coasts represent a serious threat to the natural landscape, infrastructure and human activities. Cliff retreat is the cumulative result of several marine and subaerial processes acting at different temporal and spatial scales, which were described and simulated by several authors (Rosen 1980; Pilkey and Davis 1987; Trenhaile 1987, 2010; Sunamura 1992, 2015; Walkden and Dickson 2008; Bernatchez and Dubois 2008; Castedo et al. 2012; Martino and Mazzanti 2014) in an attempt to understand and predict the geomorphologic evolution of rock coasts. Given the interaction between geo-environmental processes and material properties, hazard assessment and planning of prevention or mitigation measures in coastal areas require a full understanding of the specific site conditions, with particular emphasis on the mechanical behavior of the rock mass, as well as the failure volumes, time frequency and modes. All of the above need to be carefully evaluated in relationships with the human infrastructures and activities present in the area, as a crucial step in the definition of the related risk.

At a preliminary stage, environmental engineering solutions are planned by means of rock mass classification systems that have been proposed since the 1950s in the international literature (Barton et al. 1974; Bieniawski 1979, 1989, 1993; Marinos and Hoek 2000). At a more detailed level, geotechnical models should be produced: they are 2-D or 3-D simplified and schematic representations of the geomorphologic, geostructural and hydrogeological setting of the study site, and of the physical and mechanical properties of the rock materials (Fookes 1997; Miroshnikova 1999; Stavropoulou et al. 2007). Particular attention should be given in conceptualizing primary (i.e., bedding planes) or secondary (i.e., joints, faults) discontinuities within the models, since they cause anisotropy of rock masses and influence their mechanical behavior (Goodman 1976; Priest 1993; Bieniawski 1993; Hudson and Harrison 2000; Wyllie 2017). Numerical simulations are carried out on the geotechnical models to predict the location and kinematics of potential instabilities by adopting the appropriate technique (Barla and Barla 2000; Jing and Hudson 2002; Jing 2003; Lisjak and Grasselli 2014). Based on these considerations, the success in numerical modelling and in susceptibility assessment depends on the quality of the geotechnical model, which necessarily requires a proper rock mass characterization.

However, traditional field surveys are particularly complex and unsafe in near-vertical outcrops, with the drawback of collecting information only at the few accessible areas, which are not always representative of the whole study site. Alternative techniques for rock slope investigations were proposed in the last decades with the advent of technologies such as high-resolution digital cameras, laser scanners and drones to overcome the notorious limits of conventional geostructural and geomechanical surveys, highlighted by several authors (Barton et al. 1974; Franklin et al. 1988; Slob et al. 2005). For instance, Fardin and co-workers and Pollyea and Fairley proposed a method to determine joint surface roughness from point clouds obtained by means of Terrestrial Laser Scanning (TLS) (Fardin et al. 2004; Pollyea and Fairley 2011), Teza and co-workers introduced a method to monitor landslides by detecting displacement from multi-temporal TLS acquisitions (Teza et al. 2007), Viero and co-workers monitored a Deep-Seated Gravitational Slope Deformation by means of TLS methods (Viero et al. 2010) and Mavrouli and co-workers performed rockfall investigation on Digital Elevation Models (DEM) generated from TLS point clouds, with particular reference to kinematically unstable surfaces and block size distribution (Mavrouli et al. 2015). In other cases, TLS and Structure-from-Motion (SfM) methods were applied, respectively, for cliff retreat (Rosser et al. 2005) and erosion monitoring (James and Robson 2012). The principles of these technologies, as well as their main advantages, limitations and applications to rock slopes, are illustrated in several articles (Slob and Hack 2004; Westoby et al. 2012; Tofani et al. 2013; Abellán et al. 2014; Abellan et al. 2016).

Nowadays, TLS, terrestrial SfM and Unmanned Aerial Vehicle (UAV) SfM techniques are widely used to detect, characterize, model and monitor processes in rock slopes. A very popular issue in the application of remote sensing techniques for rock slope investigations concerns the quantitative characterization of discontinuities from point clouds. As described by Slob and co-workers, discontinuities can be extracted from point clouds by means of semi-automatic or fully automated approaches (Slob et al. 2007). The first method makes it possible to calculate the orientation (i.e., dip direction/dip) of discontinuities by calculating the best-fit plane on a geological feature manually marked by the operator in the 3-D point cloud. The automatic method requires less interaction and is based on direct segmentation or surface reconstruction. With the direct segmentation method, all the points of the raw dataset distributed along planar surfaces are selected and classified into discontinuities, each one constituted by a mathematical expression. Afterwards, the poles of the main discontinuity sets

are identified on stereo plots. The surface reconstruction methods require an initial 3-D reconstruction of the point cloud; for example, by means of Triangular Irregular Networks (TINs). All the facets' orientations are plotted on stereonet, allowing the automatic identification of the discontinuity sets. Several authors proposed different algorithms and software solutions for the automatic extraction of fractures from raw or processed point clouds, with all of them being based on the principles outlined above. For instance, some examples of direct segmentation techniques were presented by means of the RANSAC iterative method (Jaboyedoff et al. 2007; Olariu et al. 2008; Gigli and Casagli 2011; García-Sellés et al. 2011; Riquelme et al. 2014; Buyer and Schubert 2016; Palma et al. 2017). On the other hand, triangulation techniques were introduced by many researchers (among which Slob et al. 2005; Lato and Vöge 2012; Vöge et al. 2013; Li et al. 2016). Recently, the semi-automatic or automatic techniques for the extraction of discontinuities in point clouds were optimized with the aim of conducting rock mass classification (Riquelme et al. 2016) or identifying additional properties such as discontinuity spacing, persistence, trace length, frequency, intensity, block size and shape (Gigli and Casagli 2011; Sturzenegger et al. 2011; Oppikofer et al. 2011; Riquelme et al. 2015, 2018; Buyer and Schubert 2017, 2018; Kong et al. 2020, 2021). A detailed review of the methods for structural analyses from point clouds was presented by Battulwar and co-workers (Battulwar et al. 2021).

The potential of remote sensing techniques for rock slope characterization is widely recognized and includes the ability to acquire data of large areas in reasonably short time periods and under safe conditions, as well as the creation of permanent databases (Feng and Röshoff 2004; Haneberg and Findley 2006; Jaboyedoff et al. 2008; Sturzenegger and Stead 2009).

Despite remote sensing techniques represent a powerful solution when dealing with rock mass characterization, they are subjected to some serious limitations that do not allow a full understanding of the target object, if used individually. As a matter of fact, shadow areas, low spatial resolution, uncorrect georeferencing or significant noise in the point clouds can cause the undersampling of the discontinuities and the incorrect estimation of some attributes (e.g. orientation, density, spacing, roughness of the discontinuity sets, and block volume). In addition, geostructural analyses require information on the physical properties of the intact rock and of the discontinuities (i.e. aperture, seepage, wall strength, and filling), which can be collected only through direct access to the rock mass. For these reasons, it is strongly recommended to carefully plan the remote sensing surveys and to always integrate them with on-site geostructural and geomechanical surveys (Ferrero et al. 2009; Oppikofer et al. 2012; Gigli et al. 2014; Pagano et al. 2020).

With regard to carbonate systems, in addition to presence of discontinuities and other deformations in the rock mass, they are particularly prone to dissolution, weathering and karstification processes (Steidtmann 1911; Ford and Williams 2013; Andriani et al. 2015; Palmer 2017). In this case, the interpretation of data from remote sensing techniques might be challenging because of the presence of irregular geometries, especially when dealing with karst or paleo-karst landforms (i.e., weathered materials, karst conduits and cavities), which can affect the accuracy of the automatic methods for rock mass characterization. Due to karst areas being particularly complex and heterogeneous (Walsham 2002; Parise et al. 2015a), specific multidisciplinary on-site investigations are recommended to avoid erroneous geotechnical modelling, estimation of failure susceptibility and planning of intervention strategies (Milanovic 2002; Andriani and Parise 2015, 2017; Andriani et al. 2015), especially in places of high tourist attraction, characterized by higher geological risk due to the presence of people and infrastructure.

Remote sensing techniques in steep carbonate coastal areas are powerful tools to overcome the limits of conventional techniques. However, some practical questions may arise:

- 1) What is the best technique in terms of costs and benefits for structural analyses and monitoring?
- 2) Does the type of technology used affect the results of the geostructural characterization and surface-change detection from point clouds?

In the current literature, few contributions have been presented to answer these questions. For instance, Rosser and co-workers, by direct comparison with TLS data, pointed out that the SfM technique can provide results of acceptable accuracy (although not as high as from TLS) in 20% of the time used to collect TLS data (Rosser et al. 2005; 2012). Moreover, Sturzenegger and Stead (2009) compared the stereonets obtained by means of field scanline, TLS and terrestrial SfM techniques on rock cuts of different lithologies, while Pagano and co-workers compared the results of TLS and UAV surveys in carbonate environments to illustrate their main advantages and drawbacks (Pagano et al. 2020). However, it appears that a quantitative and complete comparative analysis of the different remote sensing techniques commonly used for rock mass investigations in coastal areas has not yet been reported.

With this study, point clouds were acquired on a carbonate cliff of high tourist attraction using TLS, terrestrial SfM and UAV-based SfM techniques to quantitatively estimate their quality and assess their applicability for rock mass characterization and monitoring by means of semi-automatic techniques.

Because of the presence of disturbance elements such as shrubs and human activities, two segmentation software applications (Coltop3D (Terranum 2020) and DSE-Discontinuity Set Extractor (2020)) were preferred to triangulation methods to avoid incorrect connection between the points and incorrect surface triangulation (Ferrero et al. 2009). Moreover, the pros and cons of each technique, as well as the chosen platform for SfM (hand-held camera vs UAV system) are presented in attempt to depict the conditions and goals the different techniques are more suitable for.

4.2. Case Study

The study area is a 20 m high rock cliff facing the Adriatic Sea located at *Lama Monachile* site, in the municipality of Polignano a Mare (southern Italy), in the Apulia region. The site belongs to the eastern part of the Murge area, which is a structural relief of the Apulian carbonate platform formed in Tertiary and overlain by Quaternary deposits (Parise 2011) (Figure 4.1). The Apulia region represents the foreland of the Apenninic Chain and has been subjected to tectonic uplift since the middle Pleistocene (Ciaranfi et al. 1988; Doglioni et al. 1994). A series of stepped scarps dipping to NE developed up to the current configuration as a result of the interactions between the tectonic uplift and the absolute sea-level changes (Bruno et al. 1995; Mastronuzzi and Sansò 2002; Parise 2006). The marine terraces are crossed by a karst network of slightly incised valleys, locally named *lame* (Parise et al. 2003), to which the study site belongs, terminating towards the Adriatic Sea and often difficult to recognize because the waters flow only during exceptional rainfall events, causing flash floods that are typical of karst landscapes (Parise 2003; Parise et al. 2015b; Martinotti et al. 2017). The site is made up of whitish to greyish limestones belonging to the Calcare di Bari Formation, unconformably overlain by transgressive calcarenites belonging to the Calcarenite di Gravina Formation. A pocket beach

constituted by loose materials derived mainly from the coastal erosion is located at the base of the cliff in correspondence of the inlet. The rock mass is characterized by sub-vertical joints and thin-to-medium bedded layers whose intersections determine the formation of potential unstable blocks with variable volumes. In addition, notches and karst caves, formed due to wave erosion and dissolution at the interface between fresh groundwater and sea water (Rudnicki 1973; Sauro 1991), are well visible along the coastline (Andriani and Pellegrini 2014). Mechanical, chemical and biological processes

contribute to degradation of the rock mass and influence predisposing instability processes such as toppling, rockfalls, wedge slides and cave failures. Moreover, anthropogenic activities such as artificial cavities in the calcarenites, and terraces and buildings partially carved in the rock mass perturbate the stability conditions of the site, as is also the case for many other towns of Apulia (Lollino et al. 2013). All these factors represent a serious hazard for the population and infrastructure. Both the old town of Polignano a Mare at the top of the cliff and the beach located at *Lama Monachile* attract many locals and tourists, especially during summer, given the exceptional beauty of the area and the large number of cultural events and sports competitions.

For these reasons, a contribute to the assessment of the stability conditions at the site by means of rock mass characterization and monitoring was given in this research. Furthermore, the complex geological and geomorphological setting was exploited to test different technologies in order to answer to the above questions about the applicability of remote sensing techniques in coastal areas. Different factors, such as scarce accessibility and GPS signal, karst caves, weathered rock materials, Mediterranean vegetation, local regulations and dynamic disturbances (i.e., sea waves and human activities) were of paramount importance to validate the advantages and limitations of remote sensing techniques in complex environments.



Figure 4.1: Geographic location of the study area (base map retrieved from Google Satellite). The compared area (Figure 4.2) is highlighted in red.



Figure 4.2: Final point clouds acquired by means of remote sensing techniques: (a) Terrestrial Laser Scanning point cloud (24,196,954 points and 6852 points/m² density); (b) Terrestrial SfM point cloud (6,701,071 points and 1507 points/m² density); (c) UAV-SfM point cloud (21,849,920 points and 5244 points/m² density).

4.3. Materials and Methods

4.3.1. Remote Sensing Acquisition and Processing

4.3.1.1. Terrestrial Laser Scanning

The Terrestrial Laser Scanning point cloud was acquired on 12 December 2019, by means of a Riegl VZ 400 laser scanner, from one scan position located on the opposite side of the cliff (Figure 4.1), at a 35 m distance. According to the manufacturer's specifications, the laser scanner has a 5 mm accuracy at a range up to 600 m, a measurement rate up to 120,000 points per second and a 360° horizontal field of view (Riegl 2017). The coordinates of 4 targets placed in different locations of the study site (4 tripods were set on the beach located at the foot of the cliff) were acquired using a Stonex SIII Differential Global Positioning System for accurate georeferentiation of the point cloud. The dataset was imported in CloudCompare software (version 2.12. alpha 2021) and converted from a local to a global WGS84/UTM 33 N metric coordinate system. Successively, points generated by sea reflections and part of the buildings located on the top of the cliff were removed using the segmentation tool. The point cloud was sub-sampled with a 1 cm minimum distance between points to better manage the raw dataset (about 68 million points) on a standard laptop. The resulting point cloud was constituted by more than 24 million points, about 6800 points/m² density and 1.2 cm mean point spacing (Figure 4.2a, Table 4.4).

4.3.1.2. Structure-from-Motion

Terrestrial SfM Image Acquisition

Terrestrial SfM was applied on 26 October 2019, using a common digital camera with 4000 × 3000 pixels resolution and 35 mm focal length. The technical specifications of the used camera and the location of the views are reported in Table 4.1 and Figure 4.3, respectively. One hundred and nine digital photographs with a 1.41 pix/cm mean ground resolution were captured from different points of view from the opposite side and the base of the cliff, following detailed recommendations (Agisoft 2020). Since the site accessibility was limited, the photos were taken following the trajectory shown in Figures 4.1 and 4.3, with camera–target distances in the range of 20–100 m. It is outlined that this type of survey was carried out to test the efficacy of low-cost tools, which are easily available on the market, to perform rock slope geostructural analyses and monitoring.

Table 4.1: Details of the terrestrial (left) and UAV (right) SfM technique, on-board camera and photogrammetric surveys.

TERRESTRIAL PLATFORM	
Camera model	
Body type	Compact
Max resolution	4000 x 3000
Effective pixels	12 megapixels
Sensor size	1/2.3" (6.17 x 4.55 mm)
Sensor type	BSI-CMOS
ISO	Auto, ISO 100-12800
Focal length (equiv.)	25–100 mm
Max aperture	F2–4.9
Max shutter speed	1/2000 sec
SURVEY DETAILS	
Acquisition mode	manual
Ground Sampling distance (cm/pix)	1.41
Coverage area (m ²)	4850
Frontal distance from the cliff (m)	18
Number of photos	109
Number of tie-points	311,111
Number of projections	1,017,611
Reprojection error (pix)	0.599
GCPs XY error (m)	0.022
GCPs Z error (m)	0.005
Total GCPs error (m)	0.028

UAV PLATFORM	
UAV device	DJI Inspire 2
Maximum take-off weight (g)	4250 g
Maximum flight time (min)	27
Gimbal stabilization	3-axis (pitch, roll, yaw)
ON-BOARD CAMERA PARAMETERS AND SETTING	
Camera model	Zenmuse X5S
Supported lens	DJI MFT 15 mm 1.7 ASPH
Sensor	CMOS, 4/3" Effective Pixels: 20.8 MP
FOV	72°
Photo resolution (pix)	5280 × 3956
SURVEY DETAILS	
Flight mode	manual
Ground Sampling distance (cm/pix)	0.41
Coverage area (m ²)	5460
Frontal distance from the cliff (m)	18
Number of photos	130
Front overlap (%)	75
Side overlap (%)	85
Frame shooting interval (s)	1.5
Number of tie-points	311,321
Number of projections	2,290,325
Reprojection error (pix)	0.541
GCPs XY error (m)	0.097
GCPs Z error (m)	0.001
Total GCPs error (m)	0.010

Unmanned Aerial Vehicle (UAV) Image Acquisition

The Unmanned Aerial Vehicle surveys required preliminary planning of the flight mission to achieve optimal coverage of the area, in terms of the function of the morphology of the site, weather conditions and exposition to the sunlight. A manual flight mission with side and frontal overlap,

respectively, of 75% and 85% was set for the survey campaign, which was carried out on December 12, 2019. One hundred and thirty frontal photos were acquired using a quadcopter platform DJI Inspire 2, equipped with a 20.8 Megapixel resolution camera, an integrated Global Navigation Satellite System (GNSS) and a remote flight controller, at horizontal distance of 18 m from the cliff (Figure 4.1). Further details of the UAV system and surveys are reported in Table 4.1 and Figure 4.3.

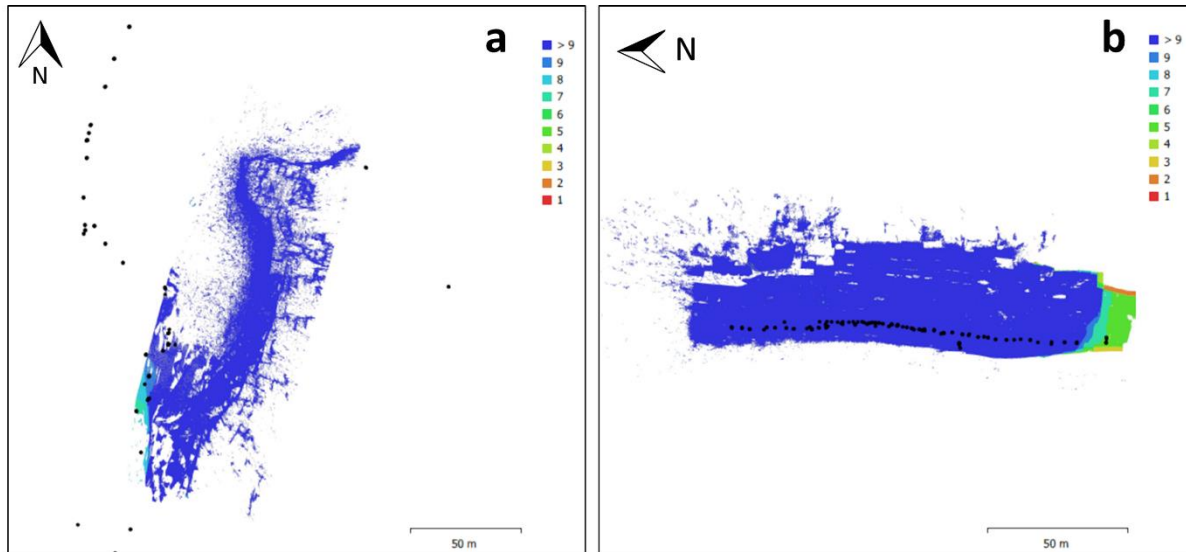


Figure 4.3: camera location and image overlap of the surveys carried out by means of compact digital camera (left) and UAV systems (right).

Processing

The images collected by means of terrestrial SfM and the UAV SfM were processed by means of the Structure-from-Motion (SfM) technique following the workflow of Agisoft Metashape Professional software (Agisoft 2020):

- Image inspection, importation, and conversion of the coordinates into the WGS84/33 N metric coordinate system.
- Insertion of Ground Control Points (GCP): points whose coordinates were taken from the TLS point cloud on well-recognizable surfaces were added to the photos as constraints to roughly georeference the SfM model. Due to the low resolution, only 3 GCPs were identified on well-recognizable elements (i.e., building structures) of the terrestrial SfM point cloud, whilst 5 GCPs, evenly distributed in the 3-D scene, were detected on the higher-resolution UAV point cloud. The GCP projection errors of the terrestrial and UAV SfM point clouds are, respectively, summarized in Tables 4.2 and 4.3. For each GCP, the horizontal (E_x , E_y) and vertical (E_z) reprojection errors correspond to the Root Mean Square Error ($RMSE$) calculated over all the photos where it was visible. The total error for each GCP is given by: $RMSE = \sqrt{E_x^2 + E_y^2 + E_z^2}$. In addition, some reference points (check points) of known coordinates, which were not used for the alignment process, were checked to assess the accuracy of the absolute registration of the 3-D scene. The total error of the check points are 0.73 cm and 4.2 cm for the UAV and terrestrial point clouds, respectively. It is remarked that a finer registration was carried out

Comparison of Remote Sensing techniques for geostructural analysis and cliff monitoring in coastal areas of high tourist attraction: the case study of Polignano a Mare (southern Italy)

in a second phase to detect surface changes among consecutive point clouds (see section 4.4.4).

- c) High-accuracy camera alignment by means of sparse bundle adjustment algorithm (Snavely et al. 2008).
- d) High-quality depth maps calculation and generation of the dense point clouds.
- e) Refinement of the dense point cloud by means of subsampling (minimum distance between points of 1 cm for the UAV point cloud) and direct segmentation.

The final point cloud of the terrestrial SfM consisted of more than 6 million points, with 1507 points/m² density and 2.5 cm mean point spacing (Figure 4.2b, Table 4.4), whilst the point cloud generated by means of UAV SfM was formed by about 22 million points, with a density of 5244 points/m² and a mean point distance of 1.3 cm (Figure 4.2c, Table 4.4).

Table 4.2. Root Mean Square Errors (RMSE) of the Ground Control Points used to georeference the point cloud generated by means of terrestrial SfM. The total error in the last row represents the population’s standard deviation.

GCP ID	Number of Images	Horizontal Errors (cm)		Vertical Errors (cm)	Total Error	
		X	Y	Z	cm	pix
GCPa	49	-0.41	1.26	-0.17	1.33	2.45
GCPb	55	0.27	-3.09	0.69	3.18	1.15
GCPc	48	0.14	1.84	-0.52	1.91	0.94
Total		0.29	2.20	0.51	2.28	1.64

Table 4.3. Root Mean Square Errors (RMSE) of the Ground Control Points used to georeference the UAV point cloud.

GCP ID	Number of Images	Horizontal Errors (cm)		Vertical Errors (cm)	Total Error	
		X	Y	Z	cm	pix
GCP1	18	0.76	-0.96	0.15	0.12	1.27
GCP2	29	0.00	0.63	0.04	0.63	0.68
GCP3	57	0.04	0.10	0.03	0.11	0.40
GCP4	29	-0.44	0.63	0.15	0.79	0.24
GCP5	49	-0.35	0.70	-0.51	0.94	0.23
Total		0.42	0.80	0.29	0.95	0.56

Table 4.4. Summary of the point clouds generated by means of terrestrial SfM, TLS and UAV SfM techniques.

Acquisition Method	Number of Scans	Number of Aligned Photos	Number of Targets/GCPs	Image Pixel Size	Total Reprojection Error of the GCPs	Number of Points in the Point Cloud	Surface Density of the Point Cloud	Average Point Spacing	Number of Points after Sub-Sampling and Cleaning
Terrestrial SfM	/	109/109	3	1.41 cm/pix	2.28 cm	20,457,182	1507 points/m ²	2.5 cm	6,701,071
TLS	1	/	5	/	/	62,861,985	6852 points/m ²	1.2 cm	24,196,954
UAV SfM	/	125/125	5	0.95 cm/pix	0.95 cm	52,363,336	5244 points/m ²	1.3 cm	21,849,920

4.3.2. Quality Assessment of the Point Clouds

Buildings located at the top of the cliff were used to estimate the quality of the point clouds generated with different techniques. Six planes (3 m² rectangles) were fit in the form of meshes on each point cloud on low-roughness facades of the buildings, evenly distributed in the study area (Figure 4.4). Then, each point cloud was segmented to obtain six sub-point clouds in correspondence of the planar surfaces. The CloudCompare Cloud-to-Mesh (CtM) algorithm was run to calculate the distances between each sub-point cloud (compared entity) and the corresponding plane (reference entity), and to determine the type of distribution, as well as the mean and standard deviation values. High values of the standard deviation for the normal distribution of the cloud-mesh distances would imply a particular roughness of the point cloud in a clearly flat zone, related to noise, and therefore, would indicate scarce quality.

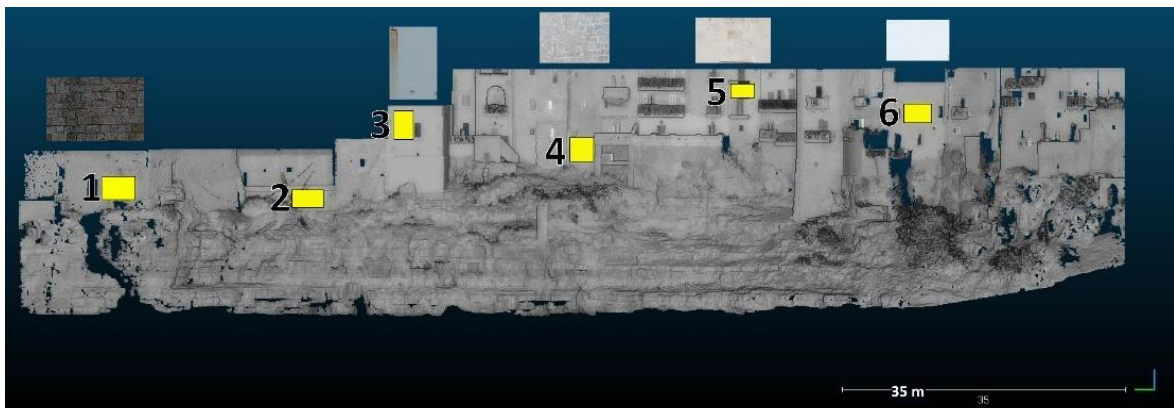


Figure 4.4: Segmentation of 6 rectangles (numbers 1-6) on the facades (photos above) of the buildings for estimating the quality of the three point clouds obtained by means of TLS, terrestrial and UAV SfM.

4.3.3. Comparison of Point Clouds

With the aim of ascertaining the reliability among the different point clouds, and of testing their combined use for a variety of purposes, the acquired point clouds were compared at couples by means of the Cloud-to-Cloud (CtC) distance computation tool available in CloudCompare. To avoid differences caused by different extents of the surveyed area for each acquisition technique, the three original point clouds were segmented together. The TLS and terrestrial SfM point clouds were compared, selecting the first as the reference entity and the second as the compared entity. Since the two surveys were not performed on the same day, part of the vegetation was removed by direct segmentation to avoid high values of the scalar field caused by vegetation changes. Further, for the comparison between the TLS and UAV point clouds, that from the laser scanner was kept as a reference. As regards the terrestrial and UAV SfM distance computation, the latter was used as a reference. The default values of the algorithm (i.e., octree level, multi-thread and neighboring points) were used for all the calculations. Visual inspection of the generated scalar field, represented by an appropriate color scale, allowed the identification of zones characterized by higher difference values. More precise details were obtained by overlapping the high values of the scalar field, filtered from the dataset, on the TLS point cloud colored by a grey color scale. In addition, the type of distribution, mean distance and standard deviation of the CtC difference were determined.

4.3.4. Extraction of Discontinuities from Point Clouds

The structural analysis was performed independently on each point cloud using Coltop3D software (Jaboyedoff et al. 2007; Terranum 2020). Since the study site is characterized by flat surfaces (terraces) and sub-vertical steps, few planar surfaces could be detected on the point cloud due to their scarce exposition. Thus, a smaller area of the point clouds, where joint sets could be detected as planes (instead of traces), was segmented. The bedding surfaces were not analyzed in this study because the sampled area is not suitable for an appropriate detection, as many surfaces are present in the form of traces along the sub-vertical steps. As regards the 2-D geostructural analyses of discontinuity traces, which is out of the scope of this research, a specific methodology was recently proposed by Loiotine and co-workers (Loiotine et al. 2021b – see Chapter 6). For each point cloud, after importing the coordinates file, the software automatically computed the point normals and produced a point cloud represented by a Hue Saturation Intensity color scale (HSI) through which the dip direction and the dip of the normals (poles) were represented, respectively, by the hue and saturation values. This graphical representation helps the user to identify the mean discontinuity sets in a point cloud according to their color and saturation. After manually selecting a few polygons that were representative of the main discontinuity sets, Coltop3D automatically detected the parallel surfaces, with a certain tolerance (in this case, a value of 30° was considered to be appropriate for the study site). The coordinates and dip direction/dip of the points belonging to each discontinuity set were imported in CloudCompare and the respective point clouds were overlapped on the original point cloud (with RGB colors) to validate the results by visual inspection. Dip direction/dip data were then represented on lower-hemisphere Schmidt equal-angle stereographic projections to identify the mean orientation, dispersion and weight of the discontinuity sets.

In a second step, a similar process was carried out using the DSE software (Riquelme et al. 2014, 2015, 2018). After the estimation of the normal vectors with 30 nearest neighbors and a 20% tolerance for the coplanarity test, a density-based analysis (number of bins = 64, minimum angle between principal poles = 10°) identified clusters of points with similar orientations, which therefore belonged to the same discontinuity set. Based on previous on-site geostructural characterization and literature data in nearby areas (Andriani and Walsh 2007), a maximum number of 4 discontinuity sets was set as a threshold. Successively, the mean orientation of each set was calculated and the points were assigned to the respective discontinuity set according to their orientation (setting a 30° maximum angle between the normal vector of a point and of the discontinuity set). Percentages of 20.08%, 13.97% and 20.76% of the points, respectively, remained unclassified for the TLS, terrestrial SfM and UAV SfM point clouds. The final cluster analysis determined individual discontinuities belonging to each discontinuity set by detecting clusters of points using the DBSCAN algorithm (Ester et al. 1996). Therefore, every point belonging to one discontinuity set was assigned to the corresponding cluster. In addition, the persistence and mean spacing for persistent and non-persistent discontinuities were calculated for each discontinuity set using the DSE integrated module.

Specific on-site geostructural and geomechanical surveys were carried out at *Lama Monachile* site by means of scanlines to validate and compare the results of the semi-automatic extraction from point clouds.

4.3.5. Rockfall Detection by Means of Multi-Temporal Acquisitions

The accuracy of the TLS and UAV techniques in terms of the detection of potential rockfalls was tested by means of multi-temporal acquisitions with both methods. Two successive surveys were performed using a laser scanner and a drone, in July 2020 and December 2020, respectively. The same operations described in Sections 4.3.1.1. and 4.3.1.3. were carried out during the processing phase. Rockfall detection from the two types of datasets was performed according to the method developed by Guerin and co-workers (Guerin et al. 2017, 2020). The second point cloud from the TLS survey was roughly aligned on the former by homologous-point pair picking on well-recognizable entities (i.e., anthropogenic elements). The point clouds were segmented together in order to have two datasets of the same area, thus avoiding differences related to missing or additional zones during the comparison. Successively, a fine registration was applied by means of the Iterative Closest Point (ICP) algorithm (Besl and McKay 1992). In detail, the original point clouds were split into 6 couples of subsets, and each subset of the second TLS acquisition was finely registered on the corresponding point cloud of the first TLS subset (used as a reference). This operation was iteratively carried out until the roto-translational matrix used to align the compared point cloud on that of the reference became an identity matrix, meaning that the computational limit was reached. The described method made it possible to minimize the Root Mean Square Error of the fine registration (RMSE = 41 mm). Moreover, the TLS point cloud of December 2019 was transformed into a reference triangular mesh using the Poisson Surface Reconstruction plugin (Kazhdan and Hoppe 2013). The comparison between the registered and the reference point clouds was carried out using the Cloud-to-Mesh (CtM) distance computation algorithm, which calculates the shortest distance of each point of the cloud from the nearest triangle of the mesh (Guerin et al. 2017, 2020). The calculated scalar value was represented by means of a color scale showing negative surface changes (loss of material) and positive surface changes (gain of material) in blue and red, respectively (Figure 4.5a).

The same process was used to compare the December 2019 and December 2020 UAV point clouds. To avoid misalignments of the second point cloud, due to insufficient GCPs and “doming deformations” generated from the SfM technique (Rosnell and Honkavaara 2012; Javernick et al. 2014; James and Robson 2014; Ruggles et al. 2016), the point clouds were segmented in more parts and each subset was registered by means of the ICP algorithm, setting the scaling option. This procedure independently aligns each sub-point cloud on the reference one, and “undeforms” the point cloud. A total RMSE of 79 mm was achieved during this step. The CtM algorithm was run using the mesh of the 2019 point cloud as a reference (Figure 4.5b).

For both datasets, positive and negative surface changes were compared with digital photographs acquired during the surveys to verify that they were caused by failures of the rock mass and not by vegetation changes or anthropogenic activities. Aiming at detecting source areas of probable rockfalls, greater attention was given to the negative values. The volume of material not detected during the successive acquisition was estimated by merging the reference and compared point clouds, thus isolating the missing rock blocks. At last, the volume was calculated on the mesh obtained by means of the Poisson Surface Reconstruction plugin.

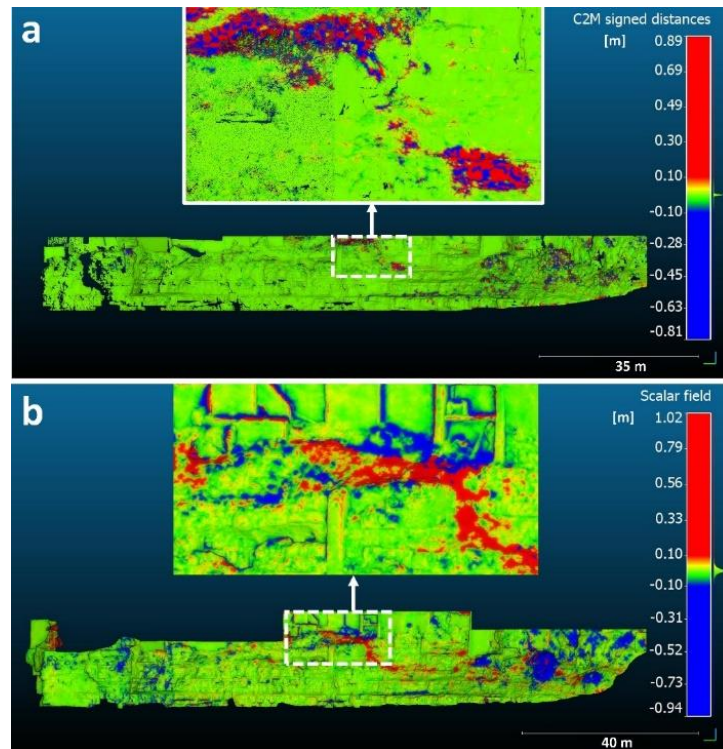


Figure 4.5: Positive and negative surface changes calculated by means of the Cloud-to-Mesh algorithm in consecutive point clouds acquired by different remote sensing techniques. Positive and negative surface changes are colored in red and blue, respectively. (a) Differences (in meters) between the December 2019 and July 2020 TLS point clouds; (b) differences between the December 2019 and December 2020 UAV point clouds.

4.4. Results and Discussion

4.4.1. Quality Assessment of the Point Clouds

The scalar values obtained in the distance computation between the sub-sets of the point clouds and the planes fitted on the facades of buildings showed a Gaussian distribution, with peaks on the mean distance (Figure 4.6). As concerns the terrestrial SfM technique, the CtM scalar value in correspondence of plane 3 had a bi-modal distribution, suggesting that the points aligned along two surfaces rather than one. In addition, the measured dip/direction and dip of the six sub-sets of terrestrial SfM, TLS, and UAV point clouds along the planes differed by up to one degree (Table 4.5), implicating that orientation measurements for geometrically simple surfaces (i.e., building facades or walls) are not influenced by the acquisition technique. Although the mean distances of the different types of point clouds along all planes were near to zero, the most significant parameter in terms of usefulness in quantitatively estimating the quality of the datasets was the standard deviation, which indicated the point clouds' dispersion on flat surfaces. Despite similar accuracies of the three techniques being detected for plane 1 and 4, some differences were found for the other datasets. In detail, for each plane except no. 1, the smallest value of the standard deviation of the CtM distances was related to the laser scanning acquisition technique. Slightly higher values, but in the same order of magnitude (mm), were attributable to the UAV-supported SfM technique, while terrestrial SfM showed values of up to 4 cm (plane 3). Based on the outcomes of the analysis, it can be deduced that the best quality was provided by the TLS and UAV-based SfM techniques, followed by the terrestrial SfM, which might

be inappropriate when dealing with complex natural surfaces, especially for in-depth geosstructural analyses. However, it must be remarked that the lower accuracy of the Structure from Motion technique is linked to the platform used during the surveys. As a matter of fact, the terrestrial SfM, which provided the less accurate results, was performed using a common-low cost digital camera and, because of the complex topography, the photos were taken from different distances. Indeed, the use of professional tools and longer lenses could have provided higher resolution photos and denser point clouds, leading to results comparable to those returned by the TLS and the UAV Structure from Motion

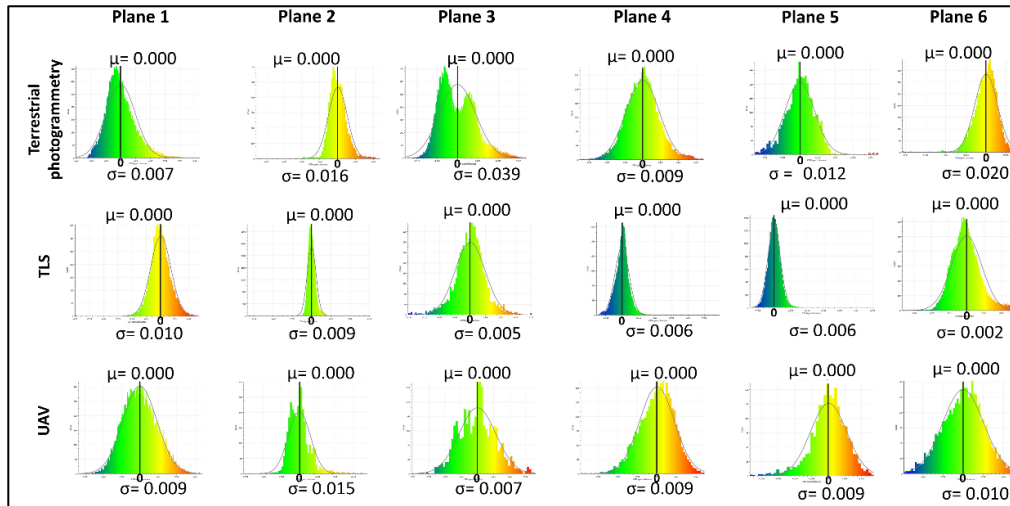


Figure 4.6: Cloud-to-Mesh distance computation on the 6 planar surfaces for the estimation of the point cloud quality obtained from TLS, terrestrial and UAV SfM. μ and σ represent the mean and standard deviation of the distribution of the distances, respectively. High resolution Figures are reported in the Supplementary Materials (Figures S4.6 a–f).

Table 4.5. Measured dip direction/dip, mean and standard deviation of the calculated Cloud-to-Mesh distances on the 6 planar surfaces for the estimation of the quality of the point clouds. The mean distances of the subsets of the point clouds from the planar surfaces close to 0 show a good quality for the three datasets. However, higher values of the standard deviation of the cloud from terrestrial SfM indicate major irregularity and noise with respect to the other datasets.

PLANE 1			
Type of Point Cloud	Measured dip direction/dip	Mean CtM distance (m)	Mean st. dev. (m)
Terrestrial SfM	291/87	0.000	0.007
Terrestrial Laser Scanning	291/86	0.000	0.010
Unmanned Aerial Vehicle SfM	291/86	0.000	0.009
PLANE 2			
Type of Point Cloud	Measured dip direction/dip	Mean CtM distance (m)	Mean st. dev. (m)
Terrestrial SfM	78/89	0.000	0.016
Terrestrial Laser Scanning	78/88	0.000	0.009
Unmanned Aerial Vehicle SfM	78/88	0.000	0.015

Comparison of Remote Sensing techniques for geostructural analysis and cliff monitoring in coastal areas of high tourist attraction: the case study of Polignano a Mare (southern Italy)

PLANE 3			
Type of Point Cloud	Measured dip direction/dip	Mean CtM distance (m)	Mean st. dev. (m)
Terrestrial SfM	99/88	0.000	0.039
Terrestrial Laser Scanning	98/88	0.000	0.005
Unmanned Aerial Vehicle SfM	97/87	0.000	0.011
PLANE 4			
Type of Point Cloud	Measured dip direction/dip	Mean CtM distance (m)	Mean st. dev. (m)
Terrestrial SfM	283/86	0.000	0.009
Terrestrial Laser Scanning	283/86	0.000	0.006
Unmanned Aerial Vehicle SfM	284/86	0.000	0.009
PLANE 5			
Type of Point Cloud	Measured dip direction/dip	Mean CtM distance (m)	Mean st. dev. (m)
Terrestrial SfM	104/89	-0.000	0.012
Terrestrial Laser Scanning	104/88	-0.000	0.006
Unmanned Aerial Vehicle SfM	104/87	-0.000	0.009
PLANE 6			
Type of Point Cloud	Measured dip direction/dip	Mean CtM distance (m)	Mean st. dev. (m)
Terrestrial SfM	307/84	-0.000	0.020
Terrestrial Laser Scanning	307/84	-0.000	0.002
Unmanned Aerial Vehicle SfM	306/84	0.000	0.010

4.4.2. Comparison of Point Clouds

As regards the comparison between the TLS and the terrestrial SfM point clouds by means of Cloud-to-Cloud distance computation, high values (up to 186 cm) of the scalar field were detected in the southern part of the model (Figure 4.7). This anomaly was caused by a bad alignment of the compared point clouds, probably caused by a deformation (doming effect) of the terrestrial SfM point cloud (Rosnell and Honkavaara 2012; Javernick et al. 2014; James and Robson 2014; Ruggles et al. 2016) resulting from images taken from near-parallel directions and from non-optimal survey design (i.e. heterogeneous picture overlay, variable camera-object distances, different focal lengths), in turn related to difficult logistics. Indeed, if the site conditions had been less restrictive, a better survey design or, alternatively, a network of GCPs would have made it possible to give more constraints during the alignment phase and to solve the doming effect.

To fix this issue, the ICP algorithm was used to separately align couples of sub-point clouds to optimize the comparison. The mean absolute distance and standard deviation between compared and reference point clouds were 7 and 11 cm, respectively. Ninety percent of the difference values were smaller than 16 cm. Figure 4.8 shows the results of the CtC distance computation after the fine registration process, with values higher than 10 cm colored in red. Although some misalignment issues were solved, a small portion of the point cloud at the southern sector remained problematic. The red zones that were evenly distributed in the model were related to vegetation changes, human artifacts caused by people moving on the cliff for works during the TLS acquisition, and to TLS occlusions. In

fact, the remaining 10% of the distances (with values in the range of 16–186 cm) were detected on elements that were not surveyed from the laser scanner, due to the scan position, located in the areas exposed to NNW and on horizontal surfaces at higher altitudes with respect to the laser scanner.

Although the UAV point cloud misalignments were not consistent, the fine registration was applied to detect the differences related only to the acquisition techniques. The mean and standard deviation values of the CtC differences between the TLS and UAV point clouds were 7 cm and 15 cm, respectively. Since the surveys were carried out at the same time, human activities did not interfere significantly in the differences. For the same reason, vegetation changes were not detected, except for some elements that moved with the wind. Ninety percent of the difference was below 16 cm, while the remaining 10% was up to 186 cm. As shown in Figure 4.9, the highest values of the differences were detected in areas that were not surveyed by the laser scanner, such as windows and balconies whose surfaces were acquired by the drone flying at higher altitudes with respect to the laser scanner position. Moreover, not all the sub-horizontal surfaces were acquired from the laser scanner, and in some sectors, the high incidence angle caused reflections on the windows located on the buildings in front of the scanner.

To isolate the differences between the point clouds from the reported factors, and to detect only surface changes that occurred due to the reconstruction technique, some cross sections were traced perpendicularly to the previously fitted planes, and the CtC algorithm was run successively. For instance, Figure 4.10 illustrates a section drawn perpendicularly to plane 6: the mean distance and standard deviations were 2.4 cm and 2.8 cm, while the highest value was 28 cm. Ninety percent of the data were below 5 cm, and higher values were recognized on indented surfaces not acquired by the laser scanner and on the vegetation whose surface was smoothed during the generation of the point cloud by means of the SfM technique.

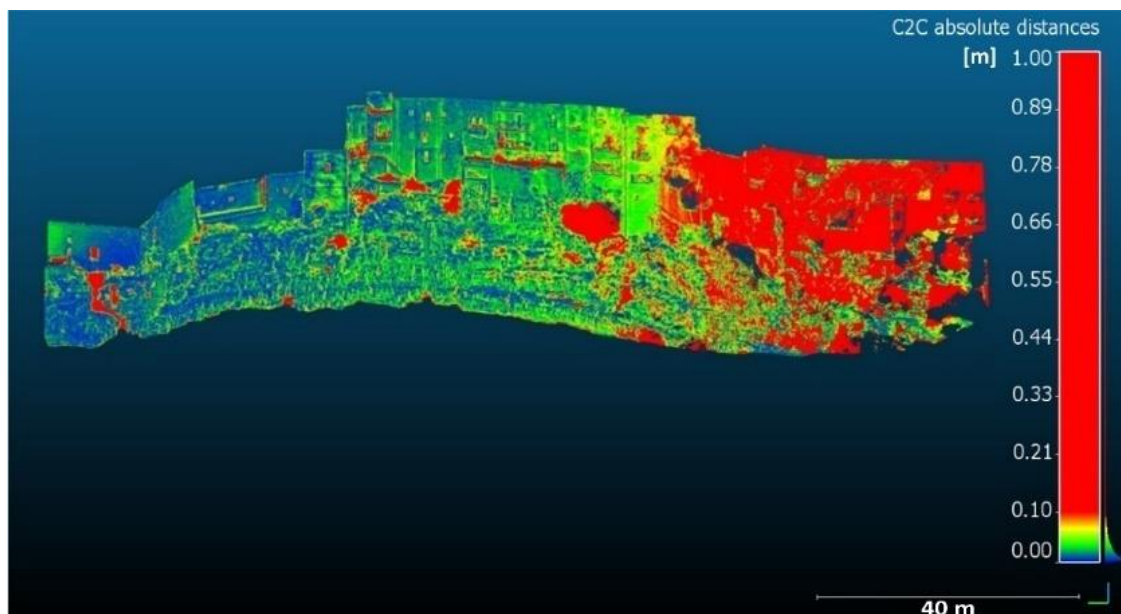


Figure 4.7: Comparison between the point clouds from terrestrial SfM (compared) and TLS (reference): Cloud-to-Cloud distance computation in CloudCompare. The greater distances are located in the right part, corresponding to a non-optimal alignment of the compared point cloud due to dome-shaped bias.

Comparison of Remote Sensing techniques for geostructural analysis and cliff monitoring in coastal areas of high tourist attraction: the case study of Polignano a Mare (southern Italy)

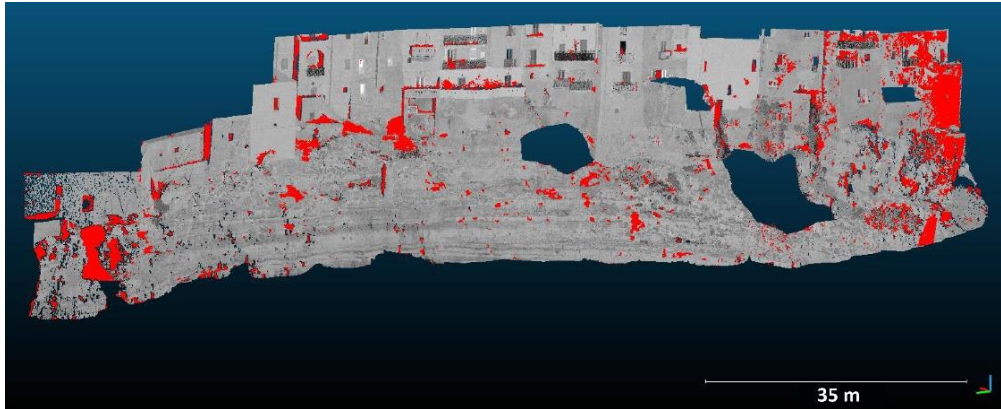


Figure 4.8: Cloud-to-Cloud distance computation between the point clouds from terrestrial SfM and TLS (reference) after the fine registration of the first point cloud by means of the Iterative Closest Point (ICP) algorithm. A small part (on the right) of the point cloud obtained by means of terrestrial SfM was not optimally aligned. Differences higher than 20 cm, corresponding to occlusions, vegetation and human artifacts, are colored in red.

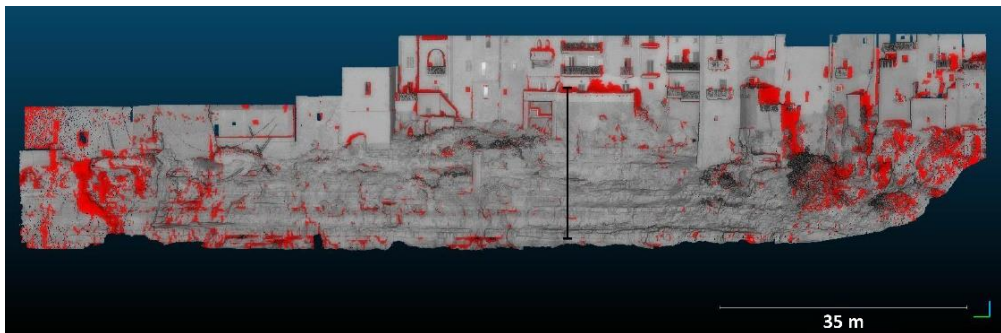


Figure 4.9: Cloud-to-Cloud distance computation between the point clouds from UAV SfM and TLS (reference). The differences higher than 10 cm (red points) were related to occlusions of the TLS technique. The details along the cross section (black segments) are illustrated in Figure 4.10.

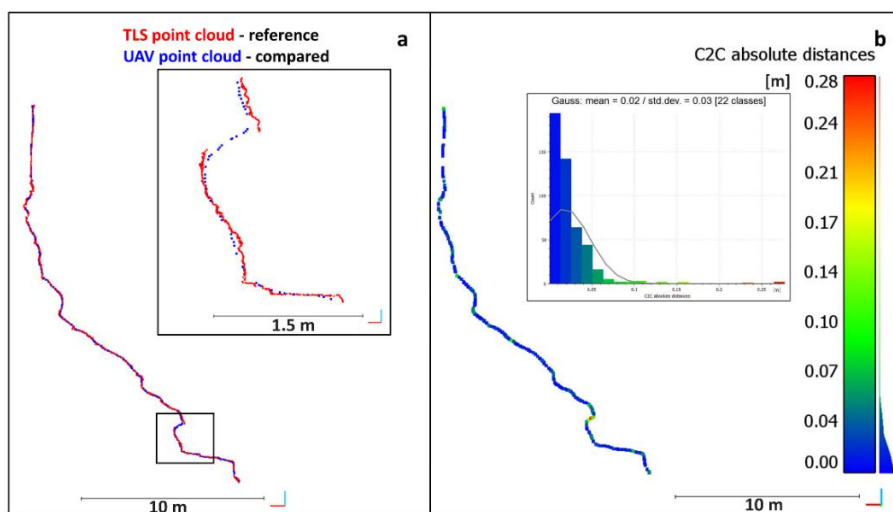


Figure 4.10: (a) Cross sections (see Figure 4.9) of the TLS (reference, in red) and UAV (compared, in blue) point clouds along plane 4. (b) A mean distance of 2.4 cm and a standard deviation of 2.8 cm between the two point clouds were detected.

4.4.3. Extraction of Discontinuities from Point Clouds

In agreement with on-site investigations, two joint sets were detected on the terrestrial SfM, the TLS and the UAV-SfM point clouds using Coltop3D. The best-fit great circles and poles of JS1 and JS2 were reported on equal-angle stereographic projections to determine their mean orientation (Figure 4.11). Table 4.6 reports the mean strike, dip, dispersion (Fisher's K parameter) and weight of JS1 and JS2 extracted from the different point clouds, as well as the data collected during conventional geosstructural and geomechanical field surveys. With regard to point clouds, the dip direction and dip of the two main joints sets were very similar, with a maximum difference of 4° for the JS2 dip direction measured on the TLS and the terrestrial SfM point cloud. The Fisher's k parameter was similar for the three datasets, but slightly higher values were obtained from the terrestrial SfM. This indicates a minor dispersion of the pole orientation, which might be related to the lower accuracy and density of the point cloud. Similar weight percentages for JS1 and JS2 were detected from the TLS point cloud (49% for JS1 and 51% for JS2, respectively), while the other datasets detected a major weight for JS1 (67% vs. 33% for the terrestrial SfM point cloud, and 58% vs. 42% for the UAV point cloud). As stated in the previous section, an underestimation of the weight of JS2 from the laser scanner might have been caused by missing data corresponding to occlusions (due to the position of the laser scanner) along the surfaces exposed to NNW, and thus, with directions parallel to JS2. Field measurements were used to validate the results (Figure 4.11c). The highest orientation difference was found for JS2: a difference of 8° between the field measurements and the terrestrial SfM was detected. It is remarkable that the ratios between the weights of JS1 and JS2 for these datasets were inverted. The weight percentages of the joint sets detected on the field were also different from the data extracted from the TLS and UAV point clouds. This discrepancy was attributable to scarce accessibility on the field, which did not allow the sampling of a representative number of surfaces belonging to JS1, leading to its underestimation. However, many fractures belonging to JS2, detected from their traces in the field, were not extracted from the point clouds because of the poor exposition of planar surfaces. In addition, the Fisher's k parameter determined from the field surveys showed a much lower dispersion of the data, probably related to a lower number of measurements, performed on small sectors of the discontinuities. As a matter of fact, field measurements taken by means of a compass-clinometer are representative of small areas and, therefore, they are less affected by undulation and discontinuity planes with respect to remote sensing techniques, which provide measurements of the entire length of the exposed surface.

The DSE software identified two additional discontinuity sets with respect to the previous method, corresponding to the bedding and the ground surface. Since the aim of the analysis was to detect whether the acquisition technique could influence the detection of joint sets, bedding and topography were not considered in the comparison. The main differences between the discontinuity sets extracted using Coltop3D and DSE are illustrated in Figure 4.12 and further discussed in Section 4.5. Tables 4.7 and 4.8 summarize the data extracted for JS1 and JS2, respectively, as well as the differences between the pairs of point clouds. A maximum strike difference of approximately 5 degrees was found for JS1 and JS2 in all datasets, but the mean dip direction of JS1, estimated from the UAV point cloud, was opposite with respect to the dip direction extracted from the other point clouds. As regards the dip values, a considerable difference was obtained for JS1: while sub-vertical surfaces were detected from the UAV and TLS point clouds, the terrestrial SfM technique provided less steep values, with a difference of about 16°. The ratios of weight percentages between JS1 and JS2 were similar for the TLS and UAV point clouds, while major differences were found in the dataset from

terrestrial SfM; however, all detected a greater weight of JS1. Acceptable differences were found for the persistence estimation for JS2, but not for JS1: the maximum persistence estimated from the terrestrial SfM point cloud differed by about 3 m from the other datasets. A possible explanation for this difference is that more discontinuities were grouped together into a single cluster because of the lower resolution of the terrestrial SfM point cloud, thus leading to an overestimation of the persistence (see blue discontinuities in Figure 4.12a).

With regard to spacing, considering both persistent and non-persistent joints as described by Riquelme and co-workers (Riquelme et al. 2015), the results of the UAV and TLS point clouds (which are similar) were much lower than those calculated from the terrestrial SfM technique, which in some cases showed values that were 10 times higher.

Based on the outcomes of the two approaches to detect and characterize the discontinuity sets from point clouds, it was found that the most accurate results were detected from the UAV point cloud, which made it possible to overcome the limitations of the TLS technique (occlusions could not have been avoided because of scarce accessibility at the study site) and of the geostructural and geomechanical surveys. Instead, an inappropriate characterization resulted from the terrestrial SfM survey. The mean orientations of the discontinuity sets extracted from the three point clouds by means of Coltop3D and DSE, together with the results of field surveys, are reported in Table 4.9. An important point concerns a limitation of the remote sensing techniques with respect to geostructural and geomechanical surveys on the field. For all the remote sensing point clouds, an appropriate detection of the bedding of the rock mass was not possible because of the orientation biases related to frontal acquisitions. Indeed, the bedding represents a major discontinuity sets in the study site, as it is characterized by a large persistence and contributes to the occurrence of potential instabilities. In this perspective, it must be stressed that whatever is the adopted remote sensing technique, the results must be compared and integrated with field-surveys.

Since the survey design and the site conditions were not optimal for the identification of the bedding, the comparative analysis reported in this chapter was focused on the sub-vertical joint sets. Further investigation on the detection of the bedding by means of combined approaches are illustrated in Chapter 7 (sections 7.3.3 and 7.3.5).

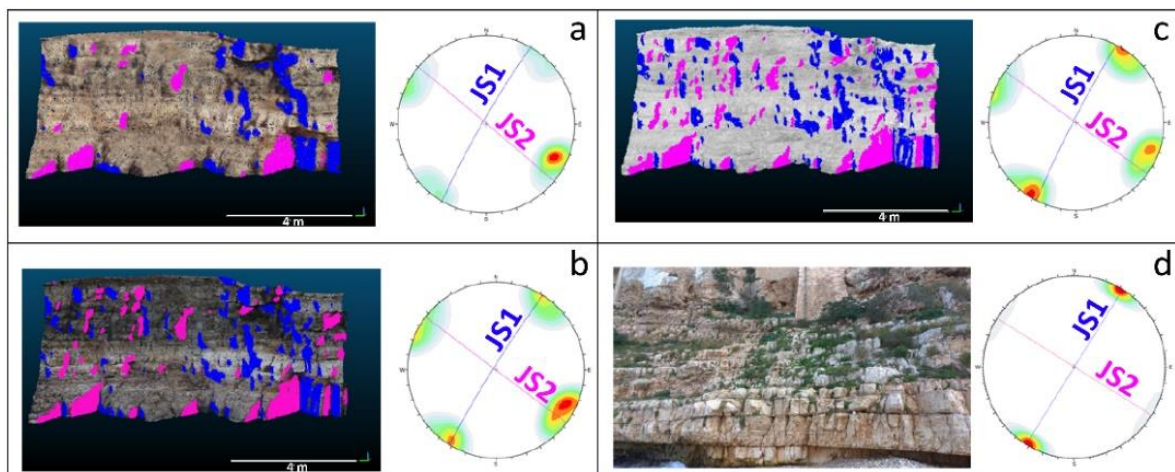


Figure 4.11: Semi-automatic identification of the main joint sets from the point clouds in a representative area of the rock mass with Coltop3D (a–c) and validation by means of field surveys (d). (a) Point cloud and stereonet from terrestrial SfM; (b) point cloud and stereonet from Unmanned Aerial Vehicle SfM; (c) point cloud and

stereonet from terrestrial Laser Scanning; (d) photo and stereonet from field surveys. The stereonet shows the best-fit great circles and poles of the main joint sets, and high lower-hemisphere Schmidt equal-angle stereographic projections.

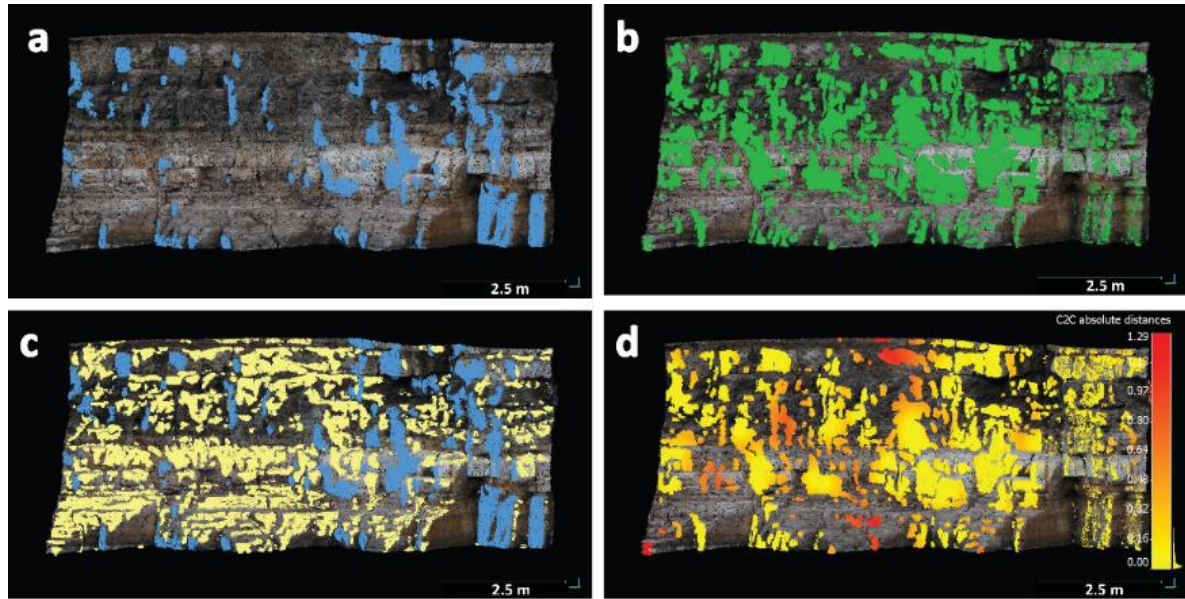


Figure 4.12: JS1 extracted from Coltop3D (a) and DSE (b). (c) Some points of the topography (in yellow) were not separated from JS1 (blue) by DSE and interfered with the estimation of the JS1 dip direction. (d) Differences in J1 between the point clouds from Coltop3D and DSE: red areas correspond to points belonging to the topography that were considered by the DSE for the extraction of JS1.

Table 4.6. Main orientation, Fisher’s K parameter and weight of the main discontinuity sets detected from the terrestrial-SfM, TLS and UAV-SfM techniques by means of Coltop3D, and results of the field surveys.

Acquisition Technique	JS1				JS2			
	Dip Direction	Dip	Fisher’s K	Weight %	Dip Direction	Dip	Fisher’s K	Weight %
TLS (21,828 poles)	301	86	40	48.55	216	90	41	51.45
terrestrial SfM (8690 poles)	300	85	42	66.60	40	89	48	33.40
UAV SfM (16,697 poles)	302	86	37	57.62	217	90	44	42.38
Field measurements (216 poles)	301	90	59	33.93	212	90	216	66.07

Table 4.7. Characterization of JS1 by means of Discontinuity Set Extractor (DSE) on point clouds acquired from Terrestrial-SfM, TLS and UAV-SfM (top) and calculated differences (bottom).

Technique	Data from geostructural analysis							
	Dip dir. °	Dip °	Density	%	Persistence (m)		Spacing (m)	
					mean	max	persistent	non-persistent
TLS (24,779 poles)	282.73	87.14	0.70	30.86	0.34	2.05	0.14	0.04
terrestrial SfM (4784 poles)	283.28	70.69	1.79	39.87	0.68	5.37	0.62	0.40
UAV SfM (17,123 poles)	108.17	86.84	0.37	26.59	0.42	2.61	0.19	0.06

Comparison of Remote Sensing techniques for geostructural analysis and cliff monitoring in coastal areas of high tourist attraction: the case study of Polignano a Mare (southern Italy)

Differences								
Compared dataset	Dip dir. °	Dip °	Density	%	Persistence (m)		Spacing (m)	
					mean	max	persistent	non-persistent
TLS- terrestrial SfM	0.55	16.45	1.09	9.01	0.35	3.32	0.48	0.36
TLS-UAV SfM	174.56	0.30	0.34	4.27	0.08	0.56	0.05	0.02
UAV SfM- terrestrial SfM	175.11	16.15	1.42	13.28	0.27	2.77	0.44	0.34

Table 4.8. Characterization of JS2 by means of Discontinuity Set Extractor (DSE) on point clouds acquired from terrestrial-SfM, TLS and UAV-SfM (top) and calculated differences (bottom). The persistence and mean spacing are calculated over the area shown in Figure 4.11.

Data from geostructural analysis								
Technique	Dip dir. °	Dip °	Density	%	Persistence (m)		Mean spacing (m)	
					mean	max	persistent	non-persistent
TLS (16380 poles)	31.18	87.96	1.08	20.40	0.34	2.02	0.20	0.08
terrestrial SfM (578 poles)	35.24	86.97	0.42	6.96	0.50	1.64	0.62	0.40
UAV SfM (9325 poles)	29.35	90.00	0.48	14.48	0.40	1.92	0.27	0.13
Differences								
Compared dataset	Dip dir. °	Dip °	Density	%	Persistence (m)		Mean spacing (m)	
					mean	max	persistent	non-persistent
TLS- terrestrial SfM	4.06	0.99	0.66	13.44	0.16	0.38	0.42	0.32
TLS-UAV SfM	1.83	2.04	0.60	5.92	0.06	0.10	0.07	0.05
UAV- terrestrial SfM	5.89	3.03	0.07	7.52	0.10	0.28	0.35	0.27

Table 4.9. Orientation of the discontinuity sets extracted by means of Coltop3D and DSE on the three datasets.

	JS1				JS2			
	Dip direction		Dip		Dip direction		Dip	
	COLTOP3D	DSE	COLTOP3D	DSE	COLTOP3D	DSE	COLTOP3D	DSE
TLS	301	283	86	87	216	31	90	88
terrestrial SfM	300	283	85	71	40	35	89	87
UAV SfM	302	108	86	87	217	29	90	90
Field measurements	301		90		212		90	

4.4.4. Rockfall Detection by Means of Multi-Temporal Acquisitions

Positive and negative surface changes between pairs of point clouds acquired using the same technique in different periods were analyzed in detail.

All positive changes, both for the UAV and TLS pairs of point clouds, were related to the growth of vegetation after the first acquisition (Figure 4.13). It is specified that an initial attempt to semi-automatically filter the vegetation in both point clouds was made by means of the Canupo plugin (Brodu and Lague 2012). However, shrubs and bushes grown in the fractures and cavities of the rock mass were not correctly identified because of their similarity in shape and color (with respect to the darker lithofacies) to the rocks. As consequence, not all the vegetation was segmented out of the point clouds and some areas of the rock slope were removed as well (especially in indented areas), causing several surface changes to be detected by the Cloud-to-Mesh distance computation. For this reason,

the vegetation was kept during the point cloud comparison process and identified by means of visual inspection during the interpretation phase.

The negative surface changes in the TLS point clouds were more difficult to interpret: although some were clearly determined by human activity and changes in the vegetation cover (Figure 4.14a), the low resolution of the photos taken by the laser scanner during the acquisitions did not make it possible to distinguish whether the points missing in the successive point cloud were related to the loss of material or vegetation, which, in some cases, is very similar in color and shape to the darker lithofacies. On the contrary, interpretation of the negative deviations was much accurate for the UAV point clouds: loss of vegetation and of man-made elements could be detected by comparing the high-resolution photos (Figure 4.14b–d). However, the fine registration of the successive UAV point cloud to the reference one was not as precise as the one of the TLS point clouds because of the SfM limitations. In fact, due to the impossibility of acquiring photos during the second flight from the same position and perspective of the first flight, not all the points could be matched during the ICP registration. As a consequence, more surface changes were observed with respect to the laser scanner point clouds, and more time was necessary for the interpretation. In addition, the detection threshold (4 cm) for surface changes was higher than the TLS one (1.5 cm), meaning that only changes higher than 4 cm could be detected from the UAV point cloud. Only one probable rockfall was identified from the two datasets (Figure 4.15). The estimated volumes were 0.038 m^3 and 0.066 m^3 for the TLS and UAV point clouds, respectively. A Cloud (UAV) to Mesh (TLS) distance computation of the point clouds acquired on the same day in December 2019 from the drone and from the laser scanner allowed the detection of the main differences (Figure 4.16). The positive surface changes (red points in Figure 4.16a) were located on the indented surface of the rock block (which failed 6 months later) because of inaccurate reconstruction of the point cloud from the SfM technique. Smoother surfaces caused the generation of a larger mesh by means of Poisson Surface Reconstruction with consequent overestimation of the failed rock block volume (Figure 4.16b–c). Although an anthropogenic cause of the failure cannot be excluded, as directly observed on the field to validate these results, the applied method shows that the TLS data were more accurate in terms of the estimation of the rockfall volume.

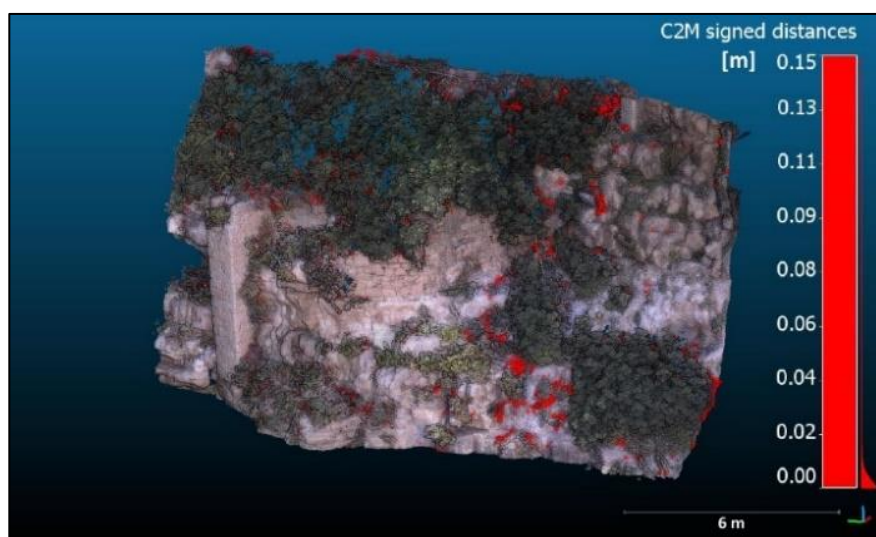


Figure 4.13: Comparison between the point clouds obtained by means of the TLS technique in December 2019 and July 2020: the positive deviations correspond to the growth of vegetation after the first acquisition.

Comparison of Remote Sensing techniques for geostructural analysis and cliff monitoring in coastal areas of high tourist attraction: the case study of Polignano a Mare (southern Italy)

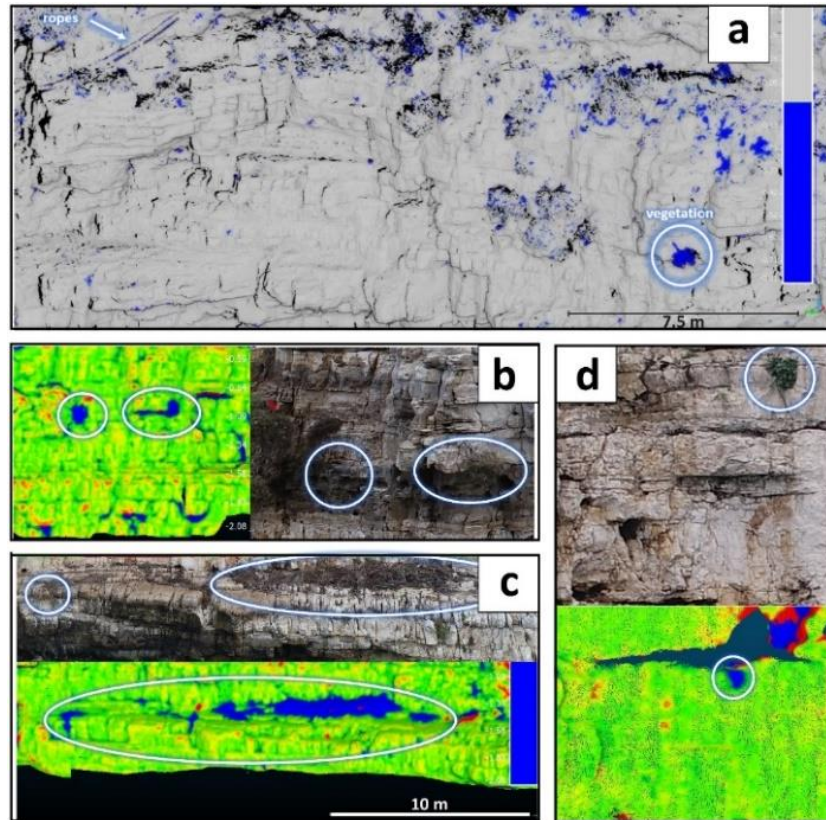


Figure 4.14: Negative surface changes detected in the TLS and the UAV point clouds. (a) The negative deviations of the TLS point clouds were mostly related to the loss of vegetation and removal of human artifacts (i.e., ropes) after the first acquisition. (b–d) The negative deviations of the UAV point clouds were identified directly on the high-resolution photos acquired by the drone and correlated to the loss of vegetation, whose color and shape could be easily confused with portions of the rock mass in the point clouds.

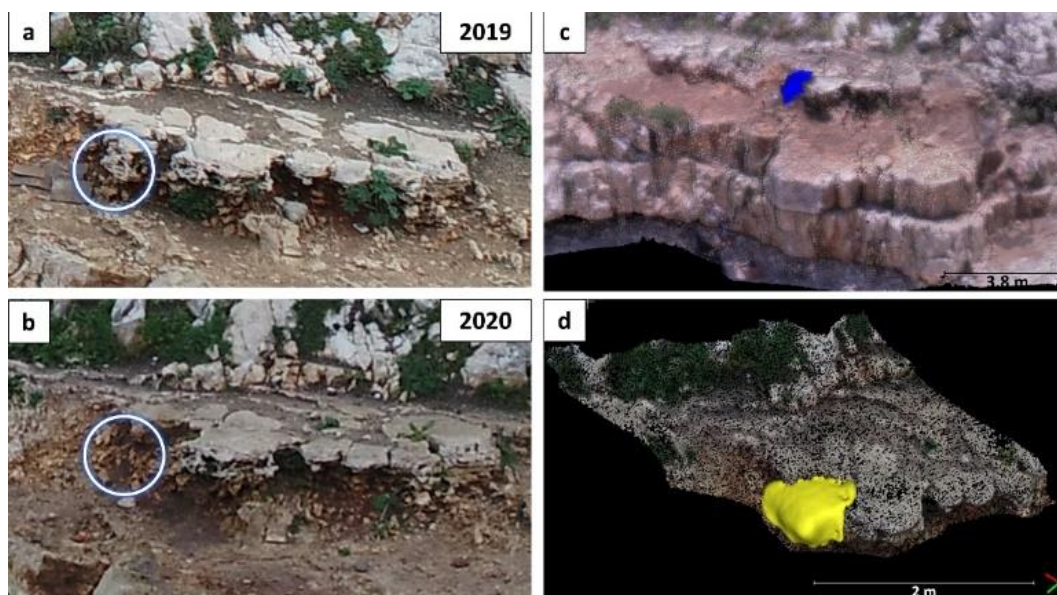


Figure 4.15: Rockfall occurred between the 2019 (a) and the 2020 (b) acquisitions, detected in the form of negative deviation from the TLS (c) and UAV (d) point clouds.

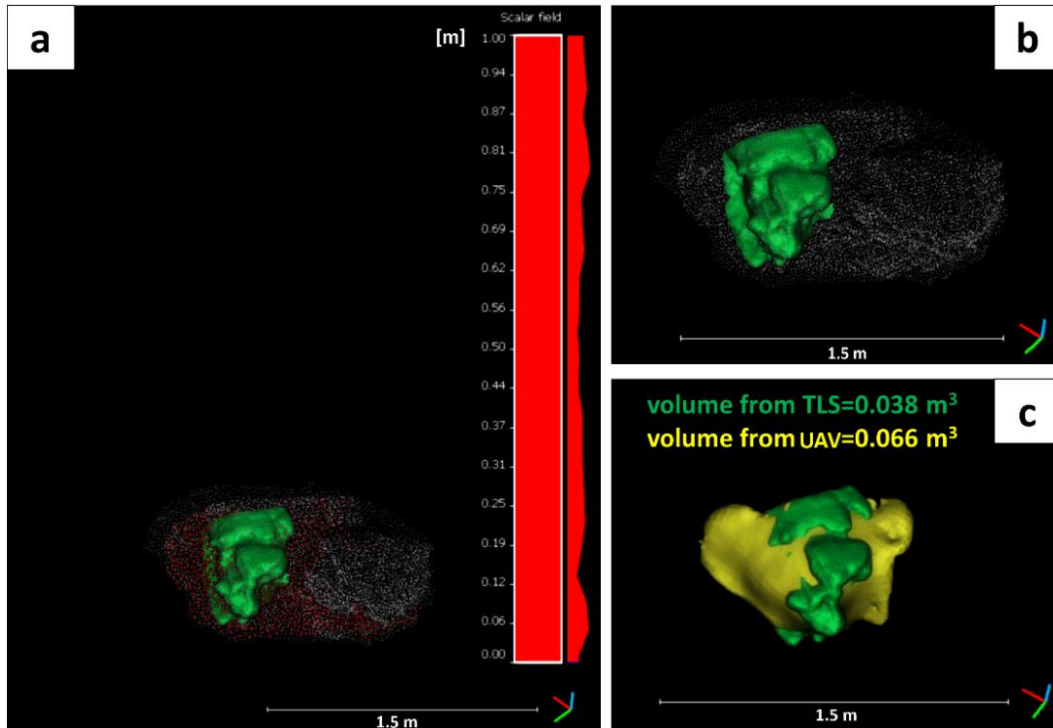


Figure 4.16: Details of the rockfall detected in the point clouds from the UAV and TLS acquisitions' comparisons. (a) Cloud (UAV) to Mesh (TLS) distance computation of the point clouds acquired on the same day in December 2019, with the positive deviations highlighted in red; (b) mesh of the rockfall detected in the TLS point clouds; (c) comparison between the volumes of the meshes calculated using the TLS (green) and UAV (yellow) techniques. The higher volume of the rockfall, as detected from the UAV technique, was due to a limitation of the SfM technique, which was not able to produce a detailed reconstruction of the surface in the fissures of the rock mass. Therefore, the smoother surface led to an overestimation of the volume of the detected rockfall.

4.5. Main Outcomes and Conclusions

Remote sensing techniques are of paramount importance to overcome the limitations of conventional field methods for rock slope investigations, especially when dealing with poorly accessible areas of large size and with unsafe conditions. Since several technologies have been introduced in recent decades, the question as to which method is more appropriate for a particular case study may arise. It is evident that the choice of technique depends on the geologic, morphological and environmental conditions of the target, as outlined by Stead and co-workers (Stead et al. 2019). With this study, a comparative analysis of point clouds obtained by means of TLS, terrestrial SfM and UAV SfM was performed, after validation by means of conventional geotechnical and geomechanical surveys, in order to evaluate the advantages and limitations of each technique for slope investigations in complex coastal areas, which are of high interest in terms of the tourist economy.

The TLS methods allowed the acquisition of detailed point clouds in a relatively short time at distances of up to hundreds of meters, depending on the laser scanner used. Conversely, the UAV-SfM technique required a preliminary mission-planning phase to achieve the best coverage area with the most appropriate ground resolution. Furthermore, permission from the authorities may be mandatory in flight-restricted areas. Adverse weather conditions such as rain, wind or fog do not affect laser scanner acquisitions as much as terrestrial and UAV SfM surveys, for which the quality of the photos might be seriously compromised, in addition to the risk of instrument damage. For terrestrial SfM, partially

cloudy weather is preferred to sunny conditions (Javernick et al. 2014) to avoid shadows and sea reflections, which can cause uneven textures and areas with low density or artifacts in the processed point cloud. However, UAV techniques require less effort in terms of costs and logistics, which can be an issue for TLS methods in poorly accessible and steep sites, due to difficulties in carrying the laser scanner and targets. TLS can be inadequate for vertical or sub-vertical slopes if the scan positions are limited by the site morphology. As a matter of fact, occlusions along the bedding and surfaces exposed to NNW in the case study were caused by the impossibility of higher positioning of the laser scanner, and occurred further north with respect to the scan position. However, as stated by Pagano and co-workers, TLS techniques are generally able to acquire data in vegetated areas, depending on the type of vegetation, which can be an issue for SfM surveys (Pagano et al. 2020). Terrestrial SfM is not the best solution in poorly accessible areas as well; for instance, a sector of the terrestrial SfM point cloud (right part of Figure 4.7) appeared distorted when compared to the TLS dataset because of the lack of good camera locations and the consequent misalignment during the SfM procedure. In addition, if the camera positions are constrained by terrain morphology, a change of the distance from the outcrop can cause differences in the ground resolutions in the 3-D model.

As regards the processing phase, SfM techniques are more time-consuming with respect to the TLS method, because more steps are necessary to carry out the SfM procedure, which can take some hours of work (from image inspection to software computation) depending on the number of photos to process and the desired resolution. In addition, a lack of sufficient Ground Control Points or a low GPS signal of the UAV system may cause deformations and incorrect georeferentiation, with unreliable results consequently being obtained in the geostructural analyses, especially if the sectors of the point clouds are mutually shifted.

Moreover, the cleaning phase of the photogrammetric technique requires greater efforts from the operator because of numerous unwanted objects such as the background and dynamic disturbances (i.e., sea waves) affecting the point cloud of the presented case study. It is remarkable that such elements had to be manually segmented out because the classification algorithms available in Agisoft Metashape and CloudCompare also removed points belonging to the rock mass in sectors with similar colors. On the other hand, the TLS point cloud appeared much less disturbed from reflections and scatter points, but in some cases, dynamic disturbances affected the quality of the point cloud. Specifically, the TLS point cloud was locally affected by noisy points caused by people moving on the study area; the same obstacles were easily removed when implementing the SfM technique by applying masks. Based on these considerations, it is specified that, although SfM techniques can reduce the data collection times by about 80% (James and Robson 2012), the same amount of time is spent in producing and cleaning the final point cloud. However, if the surveyed area is affected by dynamic disturbances, SfM techniques may provide a better solution in terms of accuracy and time.

As shown in Figure 4.6 and Table 4.5, the TLS and UAV techniques performed at short distance from the target provided point clouds with similar accuracies: for the less accurate zones (i.e., plane 1 for TLS and plane 2 for UAV), 1.3% of the points were at 3 and 4.5 cm from the reference plane ($\mu \pm 3\sigma$). In non-occluded areas, the TLS point cloud was able to provide details of very small features (i.e., building elements) and of zones below the vegetation, which were not observable from the UAV dataset. Conversely, for plane 3 of the terrestrial SfM point cloud (Table 4.5), 1.3% of the points were at a distance of 12 cm from the reference plane ($\mu \pm 3\sigma$). Although the same plane orientations were estimated from the three datasets, the low quality of the terrestrial SfM point cloud might represent a limitation when dealing with complex morphologies.

With regard to the geostructural analysis, it was found that the extracted main discontinuity sets had almost the same orientation and that only their weight was differently estimated because of occlusions specific to the analyzed dataset. The similarity of the results from geostructural characterization from TLS and terrestrial SfM along rock cuts was reported by Sturzenegger and Stead (2009). The discontinuities were sub-vertical; therefore, the estimated dip direction could be towards one direction or the opposite one. The variation of polarity for steep discontinuities, related to undulated patterns, was also outlined by Pagano and co-workers (Pagano et al. 2020). In summary, the main differences of the geostructural analysis do not depend on the point cloud type, but on the approach used. Specifically, a difference of almost 20° was found for the J1 orientation from Coltop3D and DSE. Through a detailed analysis it was assessed that the DSE did not manage to separate JS1 from the ground surface; therefore, some points belonging to the mean orientation of the cliff (N–S) were merged with the DS and its mean strike was more oriented towards N–S with respect to the results of Coltop3D (JS1 was properly isolated in Coltop3D by means of the operator’s validation). In other words, some secondary structures generated from discontinuities of larger scale belonging to JS1 and JS2 were attributed to a third discontinuity set from the DSE, which was not accurately separated from JS1 (Figures 4.12 and 4.17). Based on these observations, it is believed that automatic methods should be performed on UAV point clouds rather than on TLS point clouds in order to easily validate the results by means of visual inspection of more detailed textures or high-resolution photos.

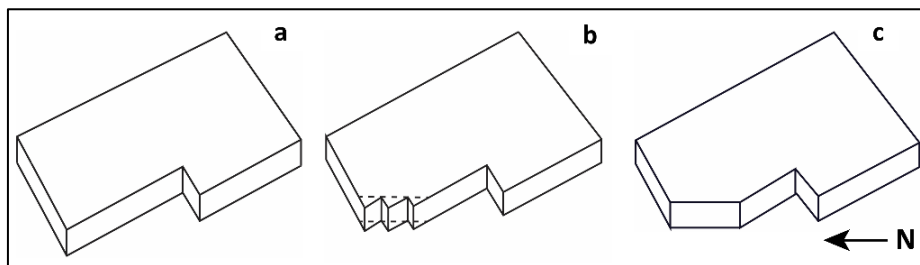


Figure 4.17: Large-scale orthogonal discontinuities (b) developed in the bedding (a) were eroded over time and led to the formation of sub-vertical discontinuities striking N–S (c) that were not correctly separated from the joint set JS1 by DSE software. For this reason, the mean dip direction of JS1, calculated by means of DSE, was about 20° closer to the North with respect to that calculated by means of Coltop3D software.

The results of multi-temporal acquisitions obtained by means of the TLS and UAV techniques showed that major accuracy, in terms of monitoring, can be achieved from the first one, given the lower threshold limit to detect surface changes. Indeed, the TLS instrumental errors are small enough to ensure the detection of millimetric deformations when comparing consecutive point clouds (Abellán et al. 2009). Interpretation of the UAV results was more complex because of the presence of more anomalies, which were due to differences in shadow zones depending on the trajectory of the drone during the two acquisitions. However, the origin of the surface change was less uncertain with respect to the TLS method because the vegetation was easily recognizable from the high-resolution photos. In addition, UAV systems allow the monitoring of larger zones compared to the laser scanner, whose field of view can be limited in poorly accessible zones. The main issues involved in using UAV techniques for rockfall detection and cliff monitoring are related to the poor coverage of the SfM in the indented areas, which, in this study, caused an overestimation of the failed block volume. This limitation should be taken into account when planning protection measures such as nets.

As a general observation, it is specified that the method carried out to align and finely register the compared point clouds required a large amount of time because many sub-sets of point clouds had to be manually segmented and aligned several times by means of ICP algorithm. For future developments, a code could be implemented to semi-automatically split the original point clouds in a grid and independently align each part to the reference one, as illustrated in Guerin and co-authors (Guerin et al. 2017), thus achieving optimal results in a relative short time.

Based on the main outcomes of the comparative analysis, terrestrial SfM can be used to perform only preliminary slope investigations in complex environments. However, professional cameras with longer focal lengths could be used to obtain higher-resolution photos and larger ground resolution. More detailed geostructural analyses and monitoring can be obtained using both the TLS and UAV methods. Each technique has its own advantages and drawbacks, but the authors agree with the statements made by Stead and co-workers, where it was stated that accessibility is the first factor to consider in order to choose the most appropriate technique (Stead et al. 2019). If accessibility is ensured, the most suitable technique is TLS, in terms of both accuracy and time.

Being complementary to each other, both methods can be combined to fully characterize the examined area. Specifically, TLS surveys can be carried out to generate accurate and geo-referenced point clouds to use as references. Successive UAV acquisitions are recommended to increase the observation area with less effort, collect data in the occlusions of the TLS point clouds (if present) and detect large-scale surface changes. If surface changes are detected, specific TLS surveys can be applied to the instable area to correctly estimate the volume of the failed blocks.

Finally, it is remarked that remote sensing techniques are powerful tools for rock slope characterization and help to significantly reduce the time needed to carry out conventional surveys in safe conditions. However, field surveys remain irreplaceable in the collection of information on the mechanical behavior of rock masses and should be combined with the described technologies to achieve deep knowledge of the investigated area.

4.6. Supplementary materials

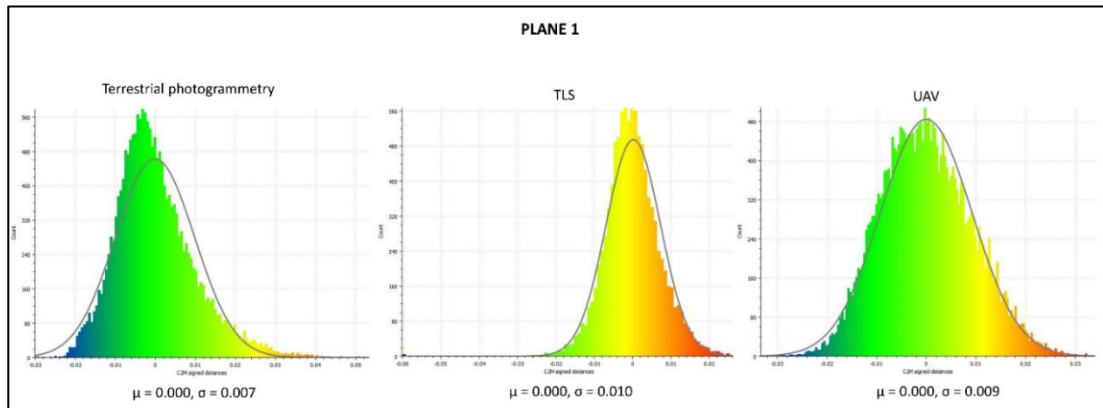


Figure S4.6a: Cloud-to-Mesh distance computation on plane 1 for the estimation of the point cloud quality obtained from TLS, terrestrial and UAV SfM. μ and σ represent the mean and standard deviation of the distribution of the distances, respectively.

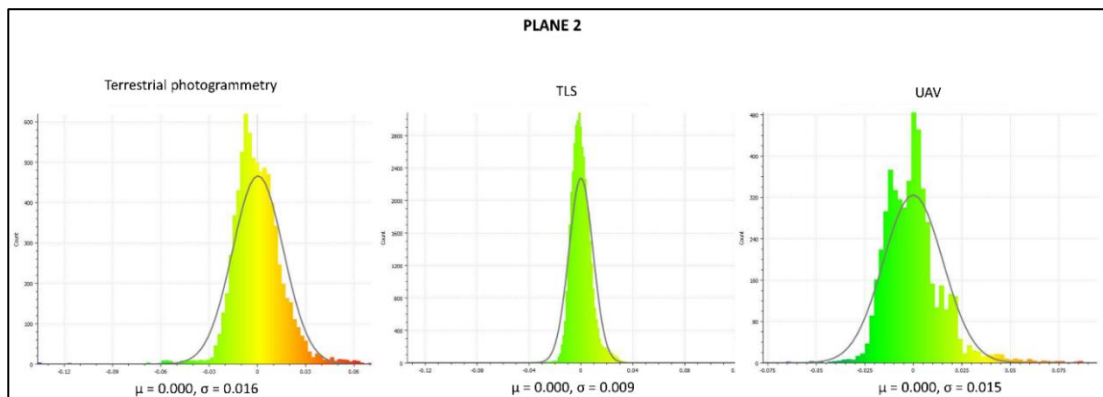


Figure S4.6b: Cloud-to-Mesh distance computation on plane 2 for the estimation of the point cloud quality obtained from TLS, terrestrial and UAV SfM. μ and σ represent the mean and standard deviation of the distribution of the distances, respectively.

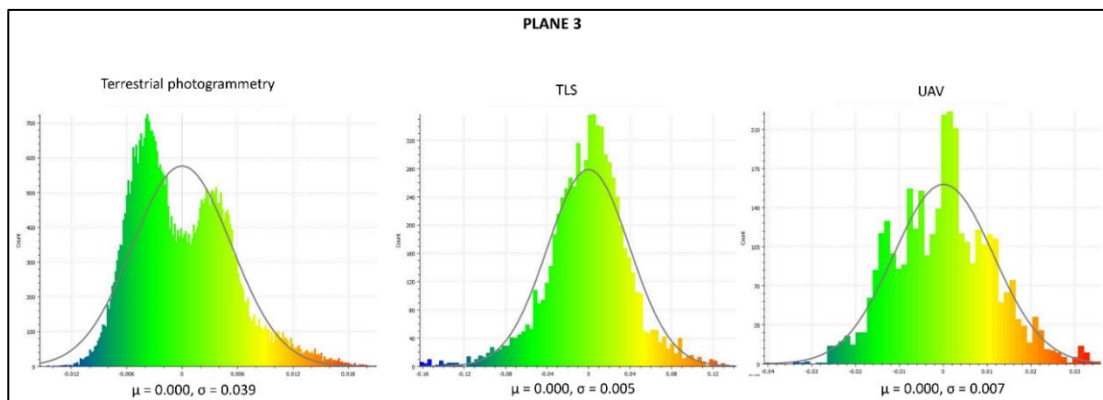


Figure S4.6c: Cloud-to-Mesh distance computation on plane 3 for the estimation of the point cloud quality obtained from TLS, terrestrial and UAV SfM. μ and σ represent the mean and standard deviation of the distribution of the distances, respectively.

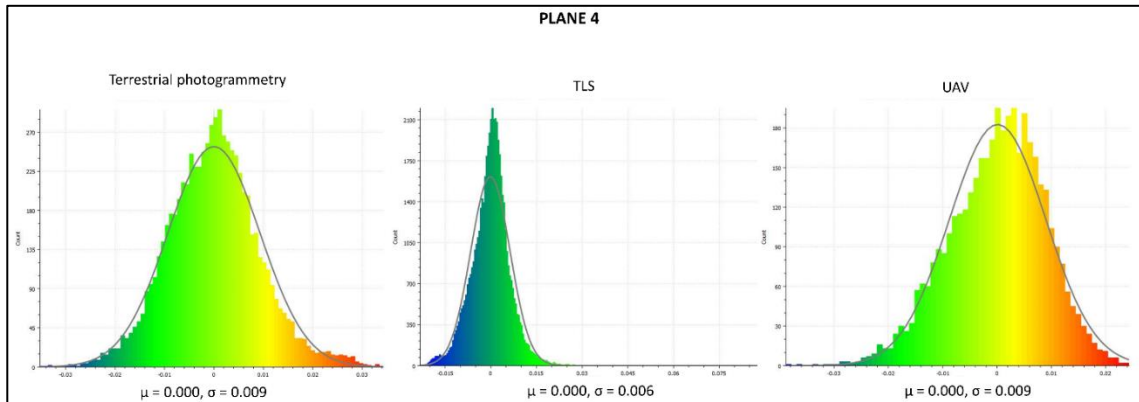


Figure S4.6d: Cloud-to-Mesh distance computation on plane 4 for the estimation of the point cloud quality obtained from TLS, terrestrial and UAV SfM. μ and σ represent the mean and standard deviation of the distribution of the distances, respectively.

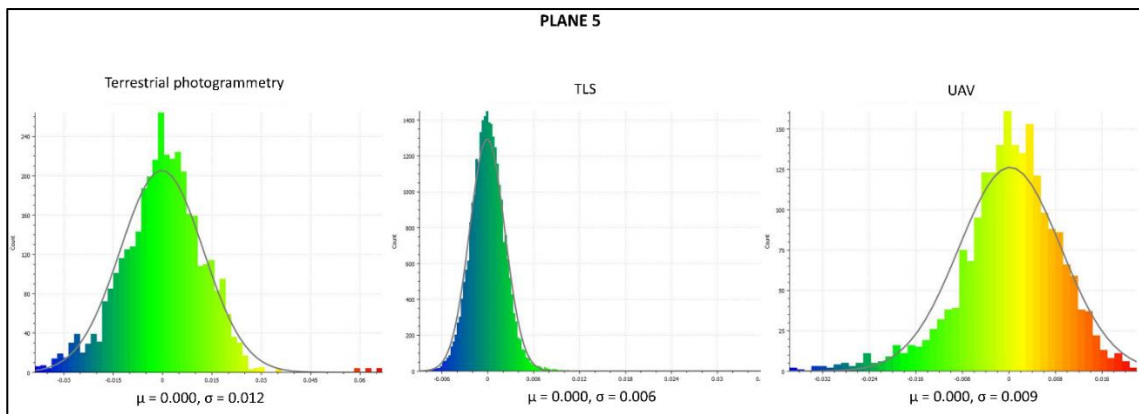


Figure S4.6e: Cloud-to-Mesh distance computation on plane 5 for the estimation of the point cloud quality obtained from TLS, terrestrial and UAV SfM. μ and σ represent the mean and standard deviation of the distribution of the distances, respectively.

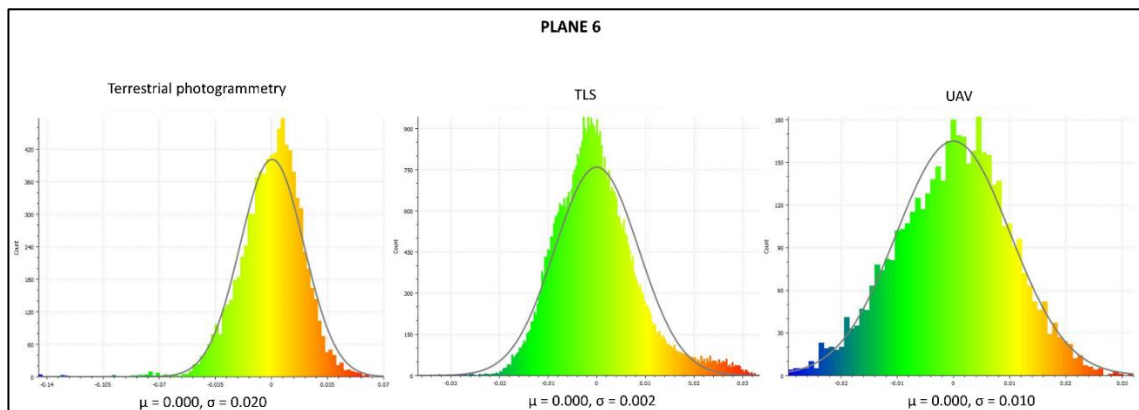


Figure S4.6f: Cloud-to-Mesh distance computation on plane 6 for the estimation of the point cloud quality obtained from TLS, terrestrial and UAV SfM. μ and σ represent the mean and standard deviation of the distribution of the distances, respectively.

Comparison of Remote Sensing techniques for geostructural analysis and cliff monitoring in coastal areas of high tourist attraction: the case study of Polignano a Mare (southern Italy)

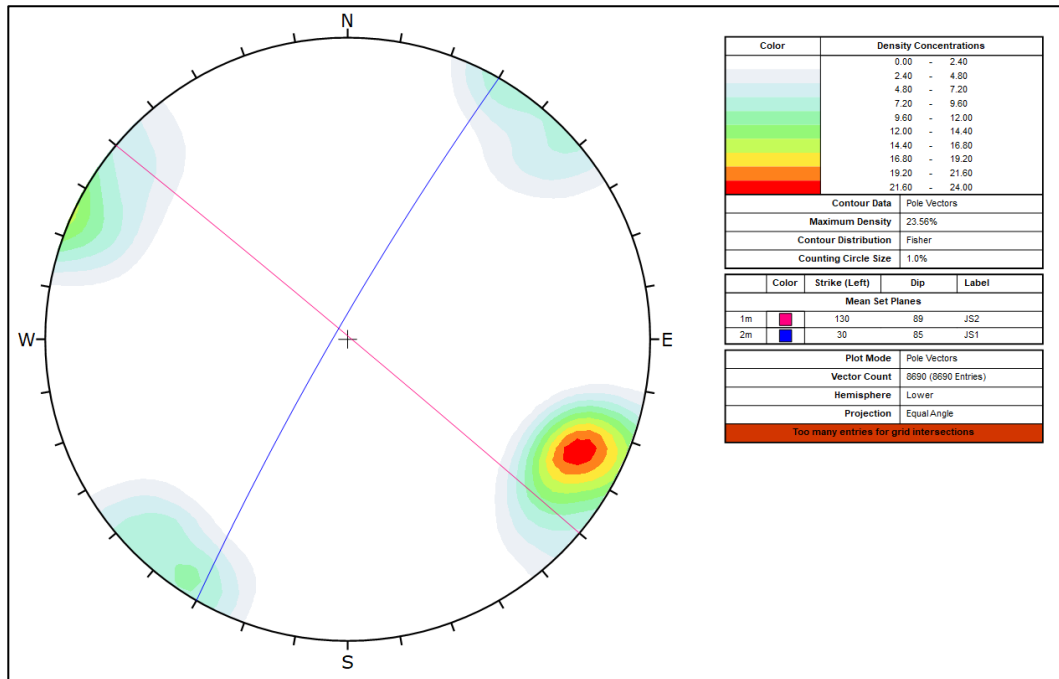


Figure S4.11a: Stereonet and contour plots from terrestrial SfM data; high lower-hemisphere Schmidt equal-angle stereographic projections.

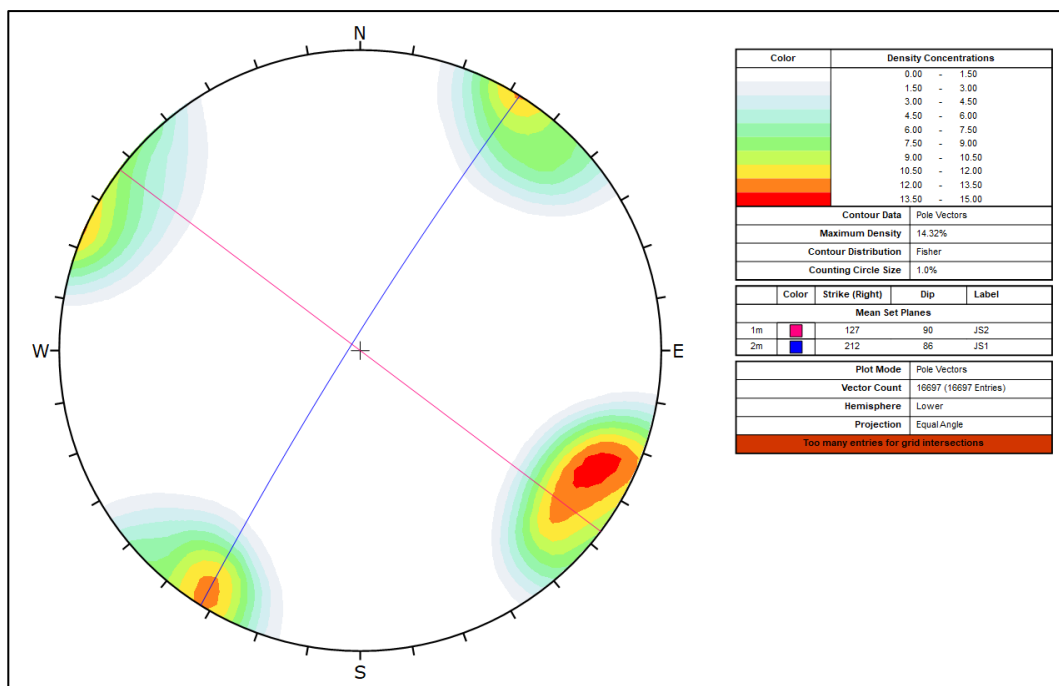


Figure S4.11b: Stereonet and contour plots from UAV data; high lower-hemisphere Schmidt equal-angle stereographic projections.

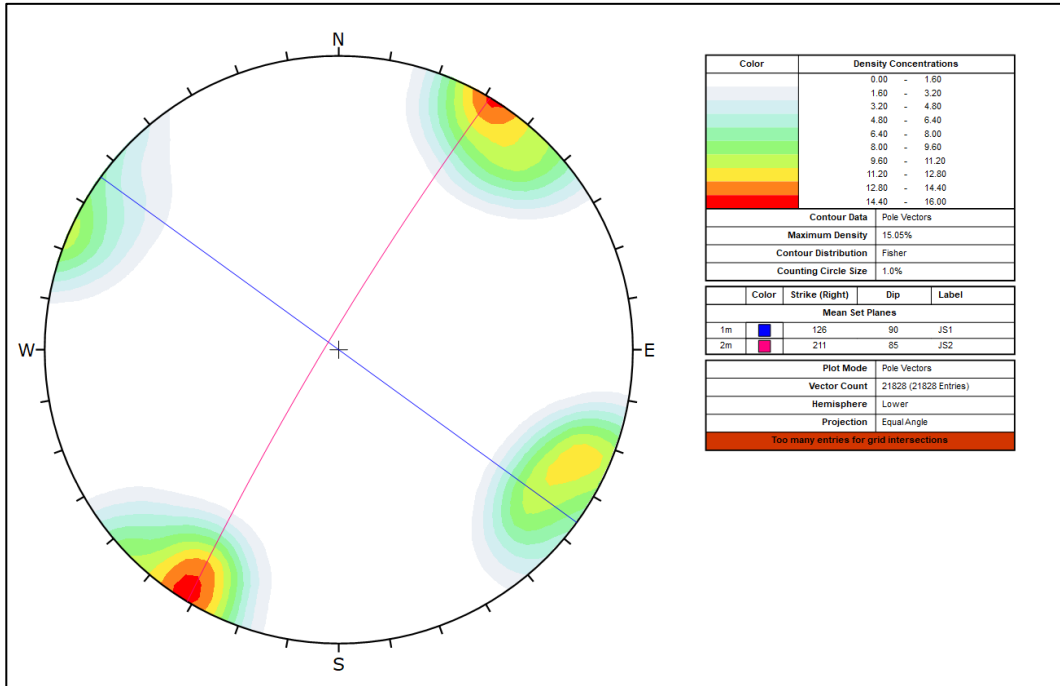


Figure S4.11c: Stereonet and contour plots from TLS data; high lower-hemisphere Schmidt equal-angle stereographic projections.

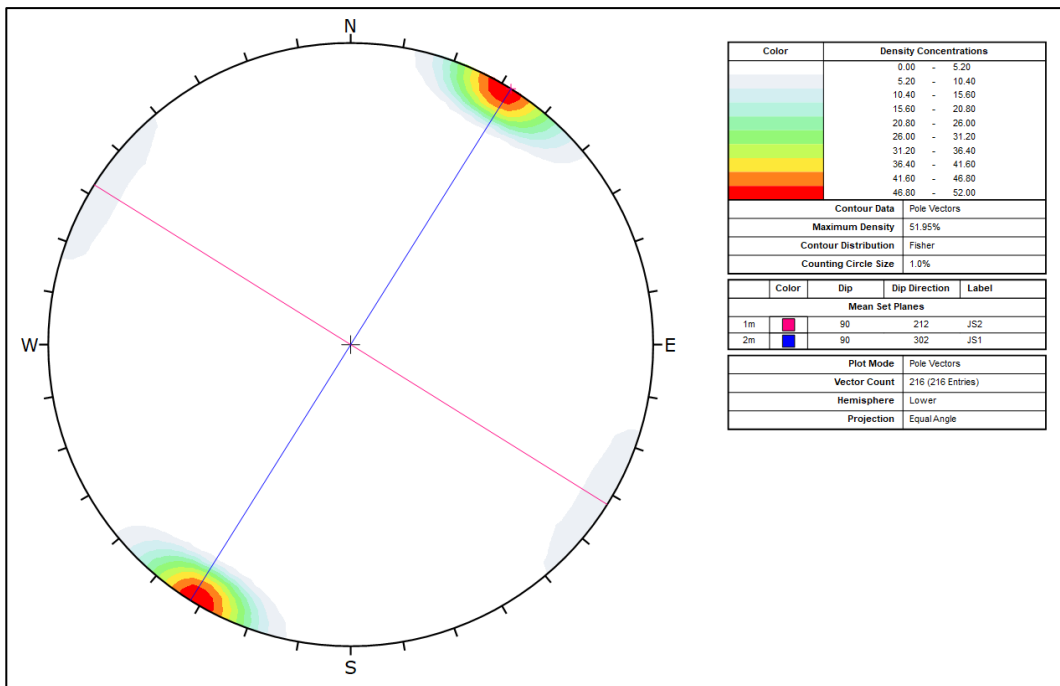


Figure S4.11d: Stereonet and contour plots from conventional field surveys data; high lower-hemisphere Schmidt equal-angle stereographic projections.

Chapter 5 Evaluation of InfraRed Thermography Supported by UAV and Field Surveys for Rock Mass Characterization in Complex Settings

Abstract: The InfraRed Thermography (IRT) technique is gaining increasing popularity in the geosciences. Although several studies on the use of this technique for rock mass characterization were reported in the literature, its applicability is challenging in complex environments, characterized by poor accessibility, lithological heterogeneity, karst features and disturbances, such as vegetation and human activities. This chapter reports the results of specific tests carried out to explore the application of IRT methods, supported by UAV surveys, for rock mass characterization in complex conditions. In detail, a 24-h monitoring was performed on an appropriate case study to assess which type of information can be collected and what issues can be expected. The results of the thermograms were compared with data reported in the literature and discussed. A novel method to detect correlations between the temperature profiles at the air-rock interfaces and the rock mass properties is presented. The main advantages, limitations and suggestions in order to take full advantage of the IRT technique in complex conditions are reported in the final section.

5.1. Introduction

InfraRed Thermography (IRT) is a contactless and non-invasive technique measuring the infrared radiations emitted by objects in the form of electronic signal (Wolfe et al. 1985) that has recently been gaining popularity in geosciences. Thermal radiation operates in the portion of the electromagnetic spectrum with wavelengths falling in the range of 0.78–1000 μm (Wolfe et al. 1985; Dewitt and Nutter 1988; FLIR 2014) (Figure 5.1). Thermographic cameras are devices working in the wavelength range of 7.15 to 14 μm that measure radiations emitted by objects and convert them into temperatures. The objects investigated by means of IRT techniques provide radiations proportionally to their emissivity ϵ , which is defined as the ability of an object to emit heat energy (Shannon et al. 2005). Since the target object itself can reflect radiations emitted by the surrounding objects, part of the total radiation can be dispersed and emitted by the atmosphere (Shannon et al. 2005; Prendes-Gero et al. 2013; FLIR 2014). Hence, the radiation U_{obj} emitted by the target object and received by a thermographic camera is defined as (FLIR 2014):

$$U_{\text{obj}} = \frac{1}{\epsilon\tau} U_{\text{tot}} - \frac{1 - \epsilon}{\epsilon} U_{\text{refl}} - \frac{1 - \tau}{\tau\epsilon} U_{\text{atm}} \quad \text{Eq. 5.1}$$

where ϵ is the emissivity, τ is the transmittance of the atmosphere, U_{tot} is the total energy received by the thermograph, U_{refl} is the reflected radiation, and U_{atm} is the radiation emitted by the atmosphere.

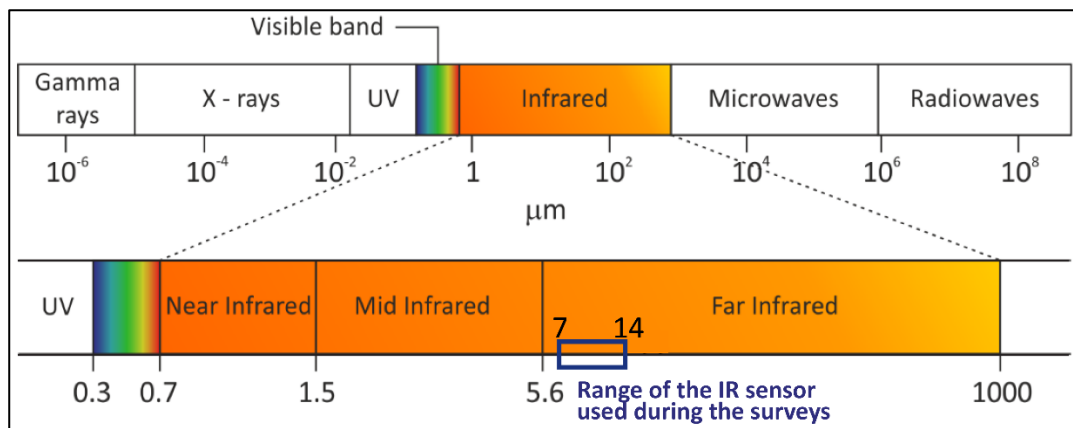


Figure 5.1: Schematic representation of the InfraRed spectrum (modified after Mineo and Pappalardo, 2021).

In the last decade, there has been a significant increase in the application of terrestrial and airborne IRT technique, supported by other remote sensing technologies, in geosciences. For instance, thermal cameras, often coupled with LiDAR (Light Detection And Ranging) or UAV (Unmanned Aerial Vehicle) systems, were used to map thermal anomalies of volcanic systems to monitor and predict potential changes (Moxham et al. 1965; Mongillo et al. 1995), for landslide mapping (Baroñ et al. 2012; Frodella et al. 2015, 2017b; Pappalardo et al. 2018) and to detect the rock bridges contributing to cliff stability (Guerin et al. 2019). In addition, thermal cameras were used in mining engineering and cave exploration to identify loose rock blocks, open cracks, tension fractures, high-stress zones, and potential rockfall source areas (Rinker 1975; Liu et al. 2011; Baroñ et al. 2012; Mineo and Pappalardo 2021). Recently, the IRT technique has been widely used for rock mass characterization to study the thermal behavior of rocks under heating and cooling conditions (Squarzoni et al. 2008; Mineo et al. 2015a; Fiorucci et al. 2018), to detect discontinuity planes, weathered and intensely jointed zones, unstable protruding blocks and water seepage (Adorno et al. 2009; Teza et al. 2012; Gigli et al. 2014; Frodella et al. 2014; Mineo et al. 2015a, b; Pappalardo et al. 2016; Frodella et al. 2017b, a; Pappalardo and Mineo 2019; Chicco et al. 2019), according to the contrast of the emitted thermal energy. Thermal devices were coupled with the GPR (Ground Penetration Radar) technique to identify eroded caves behind shotcrete-protected slopes (Wu et al. 2005). Being a non-destructive technique, the IRT was used during post-rockfall emergency surveys to evaluate potential reactivations through the detection of fractures and caves (Pappalardo et al. 2020) and as support for landslide mapping (Frodella et al. 2015), monitoring and early warning (Casagli et al. 2017).

The use of infrared thermography was also extended to geotechnical applications: for instance, the relation between the cooling index of rocks and the compressive strength of rock blocks was identified by coupling IRT and Schmidt Hammer tests (Loche et al. 2021). In addition, methods to estimate the porosity of rock samples (Mineo and Pappalardo 2019), to predict cracks development (Deng et al. 2021), wedge indentation (Liu et al. 2018) and to detect microstructural changes (Junique et al. 2021) at the laboratory scale were recently proposed.

The generation of 3-D thermal point clouds by means of Structure from Motion (SfM) approaches was introduced in a few studies (Grechi et al. 2021; Mineo et al. 2022) and, despite the low resolution of thermal images compared to other remote sensing techniques, the outputs provided accurate measurements of the rock temperatures for rock mass monitoring. In addition, the inspection of georeferenced 3-D thermal models allows geoscientists not only to extract the main discontinuity sets of rock masses, but also to estimate geomechanical parameters, such as fracture aperture, persistence and weathering degree of rock masses, as demonstrated by Mineo and co-workers (Mineo et al. 2022).

All of the above illustrate several methodologies to perform rock mass characterization at different scales by combining the infrared thermography with other remote sensing technologies (mostly LiDAR and terrestrial SfM). However, success in large-scale investigations is not guaranteed in poor-accessible sites, especially when only a few shooting points are available. In these circumstances, the field of view and the spatial resolution of the surveyed area are subjected to logistical constraints (Frodella et al. 2014; Mineo et al. 2015b; Pappalardo et al. 2016) and the acquisition of thermal images from short distances and different perspectives to produce high-resolution point clouds is not always possible.

This study reports the results of a 24-h monitoring by means of infrared thermography on a rock cliff located in an urban, highly touristic, coastal site, characterized by vertical and lateral lithological heterogeneity, as well as by the presence of karst features. As a matter of fact, the mentioned factors proved to be disturbance elements during previous studies carried out on the same area by means of Terrestrial Laser Scanning (TLS) and UAV platforms for rock mass characterization and rockfall detection (Loiotine et al. 2021a). At the same time, the shrubs diffused throughout the rock mass, the artificial cavities and walls, as well as people moving in the field of view, perturbate the thermal outputs of the target in the form of thermal anomalies.

This research is aimed at further investigating the applicability of the IRT technique for large-scale rock mass characterization and to assess whether, in complex conditions, it is possible to derive the information presented in the literature. Indeed, the lithological heterogeneity and the abovementioned disturbance elements represent a challenge for the success in IRT surveys because of the limited spatial resolution related to the site morphological constraints. Although from a distance sensor-target of 35 m, the ground resolution of the thermal outputs was 2.4 cm, the low resolution of the RGB integrated camera (5 Mpixels) did not allow an appropriate interpretation of the thermal outputs. For this reason, UAV data, field surveys and laboratory tests were carried out to support the IRT processing and interpretation, by directly inspecting the high-resolution photos and the point cloud, and taking into account the material properties (e.g., porosity).

The results of the thermal outputs (both derived from the thermograms and from direct measurements by means of k-type thermocouples) are in agreement with scientific research carried out on other case studies. A novel methodology to directly correlate the air-rock temperatures and the geomorphological, lithological and geostructural setting of rock masses through the alignment of profiles extracted from thermal images and point clouds is presented.

5.2. Materials and Methods

5.2.1. Case study: Polignano a Mare (southern Italy)

The study area is a 20-m high rock cliff facing the Adriatic Sea at the *Lama Monachile* site, a high-impact tourist destination at Polignano a Mare (southern Italy) (Figure 5.2). From a geologic standpoint, the site is constituted by a 3-km-thick Cretaceous bedrock, related to a wide carbonate platform, discontinuously overlain by transgressive quaternary deposits associated with shallow and agitated marine waters (Ricchetti et al. 1988; Tropeano and Sabato 2000). Morphology of the area is represented by a series of marine terraces parallel to the current coastline, which are the result of the superimposition of the regional uplift of Apulia started during the Lower Pleistocene and of glacio-eustatic sea level changes (Ciaranfi et al. 1988). *Lama Monachile* is part of the network of karst valleys which crosses the marine terraces until reaching the Adriatic Sea, and takes its name from local terms describing the main types of karst incisions in Apulia (Parise 2011; Parise et al. 2016). In detail, lame are generally dry and slightly incised valleys with a flat bottom, in which the water flows during exceptional rainfall events, often originating flash floods in the karst environment, with severe negative effects (Bonacci et al. 2006; Parise 2010; Del Prete et al. 2010; Gutiérrez et al. 2014; Parise et al. 2016).

Two geologic units crop out along the sides of *Lama Monachile*: limestones and dolostones belonging to the Calcare di Bari Fm. (Valanginian–late Cenomanian) and biocalcarenites belonging to the Calcarenite di Gravina Fm. (upper Pliocene–early Pleistocene). Petrographic examination with transmitted light was performed on thin sections of representative samples, using optical polarizing microscopy. The Calcare di Bari Fm., which is formed by sub-horizontal thin to thick bedded layers (0.05–1 m), for a total thickness of 15 m, is constituted by two main lithofacies, whitish-greyish micritic limestones and grey-brown dolostones, alternating in the carbonate succession. The Calcarenite di Gravina Fm. overlies the Cretaceous bedrock through an angular erosional unconformity and reaches a total thickness of about 8 m in the study site, although the upper boundary is not well visible because of the buildings located at the top of the cliff. It is made up of poorly cemented, yellowish-greyish coarse to medium-grained calcarenites.



Figure 5.2: Location of the study area (base map retrieved from Google Satellite). The thermal imager is represented by the yellow marker.

For both formations, dry density, saturated density, porosity, water absorption and degree of saturation were defined according to standard procedures (ISRM 1979; Ulusay 2015) (Table 5.1). The Calcare di Bari Fm. has mean porosity values of approximately 9% and 4% for the micritic and dolomitic facies, respectively. The water absorption is 1–5% for the micritic facies and 0–2% for the dolomitic facies, while the degree of saturation varies in the range 36–100% and 50–90% for the micritic and dolomitic facies, respectively. The Calcare di Gravina samples are characterized by higher porosity (41%) and water absorption (18–30%). A degree of saturation of about 100% indicates that the pores in the rock particle are usually interconnected and continuous (high open primary porosity), in agreement with tests carried out on the same unit, in different Apulian sites (Andriani and Walsh 2003; Andriani et al. 2021). By contrast, the Calcare di Bari Formation is characterized by isolated voids (secondary porosity), as demonstrated by the lower degree of saturation.

Table 5.1: Physical properties of the materials cropping out at the study site.

Property	Calcare di Gravina			Calcare di Bari Micritic Facies			Calcare di Bari Dolomitic Facies		
	Min	Max	Mean	Min	Max	Mean	Min	Max	Mean
Dry density (Mg/m ³)	1.48	1.72	1.60	2.44	2.52	2.47	2.47	2.72	2.62
Sat. density (Mg/m ³)	1.88	2.06	1.97	2.49	2.57	2.52	2.52	2.73	2.64
Porosity, <i>n</i> (%)	36.13	45.16	40.75	6.81	11.48	9.03	0.68	9.74	4.47
Water absorption, <i>w_a</i> (%)	18.29	29.69	23.06	1.00	4.79	2.69	0.21	1.96	1.03
Degree of saturation, <i>S_r</i> %	73.91	99.77	89.98	36.06	99.84	70.90	49.74	89.61	70.84

From a geostructural point of view, the Calcare di Bari Fm at Polignano a Mare is characterized by sub-horizontal bedding surfaces (S0) and two orthogonal subvertical joint sets striking NNE-SSW (J1) and ESE-WNW (J2), respectively (Figure 5.3a). Slight variation of the attitude of the discontinuities are locally determined by folds interpreted as the effects of transtensional and transpressional deformations (Andriani and Pellegrini 2014). The geostructural and geomechanical setting of the study site, determined by means of conventional geostructural and geomechanical surveys (ISRM 1988) and point cloud inspection, is summarized in Table 5.2. The mean discontinuity persistence was estimated according to the geometric relationships between the discontinuity traces and specific sampling windows, following the method proposed by Pahl (1981). The discontinuity surfaces are hardly recognizable in the calcarenite unit, which shows a massive structure (Figure 5.3b).

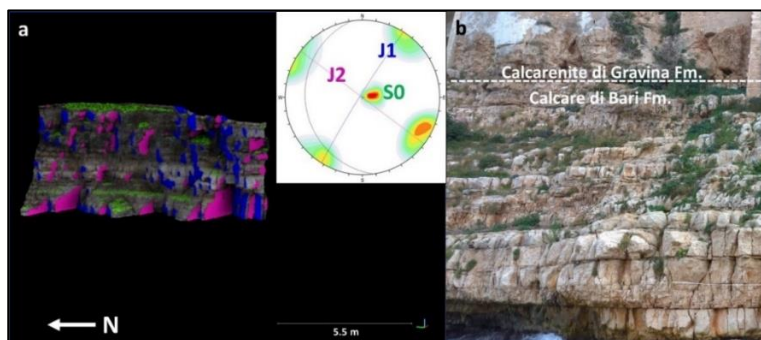


Figure 5.3: Geostructural setting of the study site; (a) sub-vertical joint sets (J1, J2) and bedding surfaces (S0) detected in the Calcare di Bari Fm. by means of field surveys and UAV point cloud inspection; (b) details of the fracture network in the Calcare di Bari Fm. and of the massive structure of the Calcare di Gravina Fm.

Table 5.2: Main geostructural and geomechanical parameters of the Calcare di Bari Fm.

DS	Type	Mean Dip Dir. °	Mean Dip °	Weight %	Spacing (m)	Persistence (m)	Aperture (cm)	Water Conditions	Filling	JRC
J1	Joint	122	88	50	0.12–1.00	0.22	Up to 0.5	Dry to damp	Generally absent	V–VII
J2	Joint	33	84	20	0.08–0.30	1.99	Up to 1.5	Dry to damp	Generally absent	V–VII
S0	Bedding	224	5	30	0.05–1	>20	Up to 1.5	Dry to damp	Generally absent	VIII

The rock mass is affected by heavy physical and chemical weathering, the effects of which are visible in the form of voids and cavities caused by karst processes, salt crystallization, wetting and drying cycles and biological activity, all factors potentially predisposing to detachment of rocks (Lollino et al. 2013; Parise et al. 2015).

Despite the presence of subvertical rock walls, bushes and shrubs of the Mediterranean vegetation are diffuse over the rock mass (Figure 5.3b) and tend to grow with their root systems inside the fractures and voids, thus favoring aperture of the discontinuities. In addition, human works, such as terraces, excavation of artificial cavities and buildings partially carved, especially in the porous and soft calcarenites, modified the overall morphology, locally contributing to reduction of the strength properties. As a result, the structure of the rock mass and the surface conditions of the discontinuities are laterally and vertically variable. Based on these observations, a geological strength index (Marinos and Hoek 2000; Marinos 2017; Hoek and Brown 2018) varying between 43 and 60 according to the local conditions was assigned to the rock mass at the *Lama Monachile* site. In detail, the GSI values of the limestone units were determined considering type “B” (thin to medium-bedded) and type “D” (blocky) structures and good– fair conditions of the discontinuities, on the basis of field and photograph inspection (Marinos 2017).

Regarding the calcarenite unit, a lower average GSI (43) was assigned to take into account the weathered surfaces.

The geomorphologic evolution of the cliff is represented by cliff recession through sporadic and localized instabilities, such as slides, topples, rockfalls and sea cave failures, mainly due to direct wave action on the Cretaceous limestone, and to strength decay of the calcarenite lithofacies at places enhanced by uncontrolled urbanization.

Although no landslides have been reported so far, it is evident that episodic failures, probably triggered by violent storms, even if involving small volumes, represent a serious risk for the community, considering the high frequency of tourists, both the historical center of Polignano a Mare, at the top of the cliff, and at the seaside at its toe during the summer season.

5.2.2. UAV and IRT surveys

UAV surveys were carried out on the study site to support the interpretation of the IRT data taking advantage of the high-resolution photos and point cloud, to check if the thermal anomalies were related to the rock mass properties or to disturbance elements. The surveys were performed by means of a quadcopter platform DJI Inspire 2 equipped with a 20.8 megapixels (5280 × 3956 pixels) resolution camera and an integrated Global Navigation Satellite System (GNSS). Sixty-eight frontal photos were taken at 9 m from the rock wall, with side and frontal overlap of 85 and 75%, respectively. The Structure from Motion technique (Westoby et al. 2012; Carrivick et al. 2016; Eltner and Sofia 2020) was performed using Agisoft Metashape Professional software (Agisoft LLC, St. Petersburg, Russia) and following the built-in workflow:

- Photo inspection, importation and conversion of the coordinates into WGS84/33 N metric coordinate system.
- High-accuracy camera alignment by means of sparse bundle adjustment algorithm (Snavely et al. 2008).
- High-quality depth maps calculation, generation of the dense point cloud (about 51 million points) and direct segmentation to remove unwanted objects.

In a second phase, the dense point cloud was aligned on a TLS point cloud previously georeferenced using a Stonex SIII Differential Global Positioning System (Stonex SRL, Monza, Italy). This step was necessary because of the impossibility to install enough ground control points during the UAV survey to correctly georeference the point cloud and avoid doming deformations (Rosnell and Honkavaara 2012; Javernick et al. 2014; James and Robson 2014; Ruggles et al. 2016). The point clouds were split at couples in more sub-point clouds and independently aligned using the Iterative Closest Points (ICP) algorithm (Besl and McKay 1992) until reaching a final root mean square Error of 43 mm. The final point cloud of the area addressed to the IRT surveys is constituted by about 16 million points and a surface density of 13,391 points/m², corresponding to a mean point spacing of 9 mm (Figure 5.4). Thermal data were acquired on the study site for 24 h starting from 21 December 2020 at 17:45 Central European Time (CET) using a FLIR T-660 thermal imager (Teledyne FLIR LLC, Wilsonville, Oregon, USA) mounted on a fixed tripod to ensure immobility of the camera. The FLIR T-660 camera has 5 MP built-in RGB camera and manufacturer-specified temperature measuring range of -40→+150 °C, measurement accuracy of ±1% of T °C, infrared spectral range of 7.5–14.0 μm, image resolution of 640 × 480 pixels, field of view (FOV) 25° × 19°, and focal length of 25 mm. The thermal sensitivity or noise equivalent temperature difference (NETD) is the apparent temperature difference between an object and its environment producing a signal equal to the noise of the system (Gaussorgues 1994). In other words, the NETD is the smallest temperature difference that can be detected by the thermal camera, whose value is less than 0.02 °C at 30 °C for the FLIR T-660. Seventy-three thermal images (thermograms) were acquired with a regular time-interval of 20 min. In addition, three type-K thermocouple sensors were positioned on three different lithofacies to compare and validate the surface temperatures recorded by the thermal camera. To avoid direct solar radiation on the sensors, the thermocouples were installed inside small cavities (dissolution voids deep up to 1–2 cm) of the rock wall (Figure 5.5d). The recorded data are reported in the supplementary materials (Table S5.1).

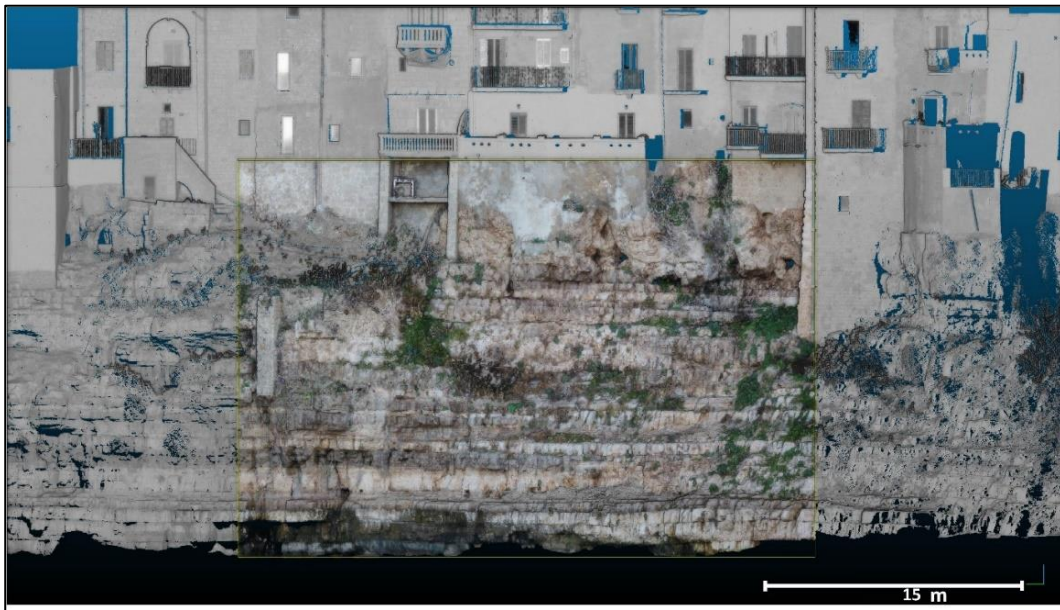


Figure 5.4: Final high-resolution point cloud (RGB colors) of the study site obtained by means of UAV-based SfM and aligned on a georeferenced TLS point cloud (in gray) to avoid doming deformations. The UAV point cloud has a surface density of 13391 points/m², corresponding to a mean point spacing of 9 mm.

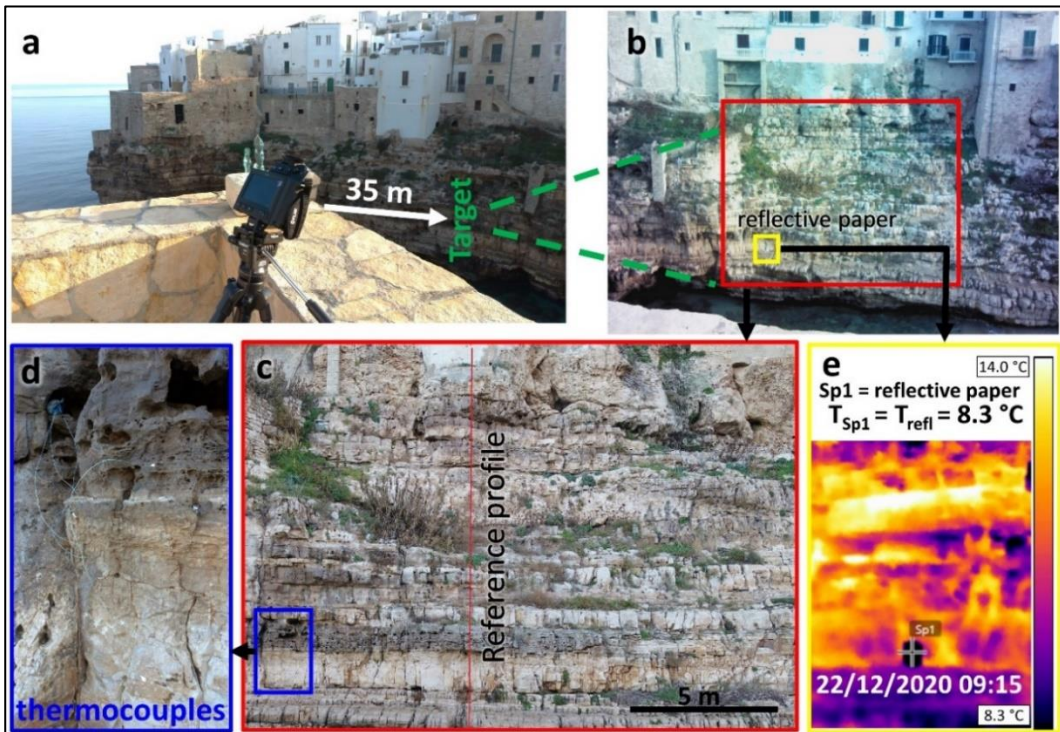


Figure 5.5: Setup of the IRT acquisition. (a) Location of the FLIR T-660 thermal camera and perspective view of the target; (b) frontal view of the target area and position of the reflective paper (yellow square); (c) zoom of the investigated area and scanline for the extraction of the thermal and lithologic profile; (d) location of the thermocouples for the temperature monitoring of the lithofacies; (e) example of measurement of the reflected temperature using the reflector method.

To correct the apparent temperatures and derive values close to the real ones, all factors that influence the results were recorded. Air temperature and relative humidity were measured before each thermal acquisition by means of a pocket-size digital thermohydrometer (Temperature measurement range = -25 ± 180 °C, humidity measurement range = 0–100%). A 35-m distance between the IRT camera and the target area was measured from point clouds obtained by means of Terrestrial Laser Scanning and Structure from Motion techniques. An emissivity coefficient equal to 0.92 was assumed from reference tables (Hudson 1969; FLIR 2014). The reflector method (Hudson 1969; FLIR 2014; Usamentiaga et al. 2014) was used to measure the reflected temperature by placing an aluminium foil-covered cardboard at the base of the cliff (Figure 5.5b). Since the aluminium foil is an almost ideal reflector (emissivity = 0.05), the temperature measured on it (Figure 5.5e) corresponds to the ambient thermal radiations reflected by the reflector itself.

5.2.3. IRT data processing and correlation with UAV data

After the acquisition phase, the thermograms were processed using the FLIR Tools software (FLIR Teledyne 2015). In detail, the object emissivity, air temperature, relative humidity, reflected temperature and distance from the cliff were entered as input in the software, which automatically calculated the real temperatures by subtracting the radiation reflected from the ambient sources and emitted from the atmosphere to the total radiation received by the thermal imager. Successively, the range of the colour scale was adjusted for each thermogram to better detect cold and hot thermal anomalies.

The surface temperatures were extracted from all thermograms along a vertical profile positioned in a low-disturbed area (to avoid vegetation and anthropogenic elements) by means of a specifically compiled algorithm. After identifying the most appropriate profile, the developed algorithm automatically extracted, in all the thermograms, the temperature of the pixels crossed by the traced line. The data were processed in a spreadsheet to determine and plot the recorded temperatures, minimum, maximum, range, mean, median and standard deviation values for each pixel along the profile. Surface temperatures on the same vertical profile were plotted in a temperature-pixel frame to obtain the time-series with a 4 h sampling interval. In addition, a topographic profile was extracted from the point cloud along the same section to identify potential thermal anomalies caused by the topography of the rock face. The geological strength index (GSI) (Marinos and Hoek 2000; Marinos 2017; Hoek and Brown 2018) and fracture frequency (i.e., number of fractures per unit length) for each layer were determined by means of measurements and qualitative observations on the point cloud and on the high resolution photos acquired by the UAV system. Specifically, the GSI was estimated by defining the rock mass structure and the discontinuity conditions (i.e., roughness and weathering) for each layer, while the fracture frequency was calculated through linear scanlines, perpendicular to the main discontinuity sets, both in the field and from high resolution georeferenced point clouds. Finally, the plots were aligned to identify correlations among the surface temperatures and topography, lithology and degree of fracturing of the layers.

5.3. Results and discussion

5.3.1. Environmental conditions and rock temperature curves

The use of the pocket-size thermo-hydrometer allowed the definition of the typical daily thermal cycles of sunny days in winter at *Lama Monachile* site, as well as the rock mass thermal response (Figure 5.6). In detail, the air temperature is in the range of 8.5–30.5 °C, with a maximum daily thermal excursion of 22 °C. The highest and lowest temperatures were recorded at midday and early morning, respectively. The relative humidity was in the range 39–96%, with a maximum variation of 57% (Figure 5.6). The rock mass is subjected to heat transfer determined by conduction, air convection and radiation processes (Robertson 1988). The temperatures of the three lithofacies, directly measured by means of K-type thermocouple sensors in areas not affected by direct solar radiation, follow the air temperature curve, although with delay due to the natural low diffusivity of rocks (Figure 5.6). The heating phase (phase H in Figure 5.6) starts at dawn (7:12 CET): the rock mass heats up by direct solar radiation until reaching the peak temperature at about 15:30 CET. Later on, a first fast cooling phase (C1) is determined by the progressive shadowing of the cliff until the sunset (at 16:26 CET), followed by a slower nocturnal cooling phase (C2). With regards to the thermal behavior of the lithofacies cropping out, they show very similar temperature curves, especially for the micritic and micritic-dolomitic facies. The major difference was detected for the dolomitic facies, darker in color and characterized by a major number of voids, during the peak solar radiation hours (13:30–15:30 CET), when it reached a temperature 4 °C higher with respect to the other facies. The analyzed curves show that the heating phase is shorter than the cooling phase and is related to a fast rise of the rock temperature because of direct solar radiation. These outcomes are in agreement with the results of rock temperature direct (thermocouples) and indirect (IRT) measurements carried out in the Mediterranean area (Fiorucci et al. 2018).

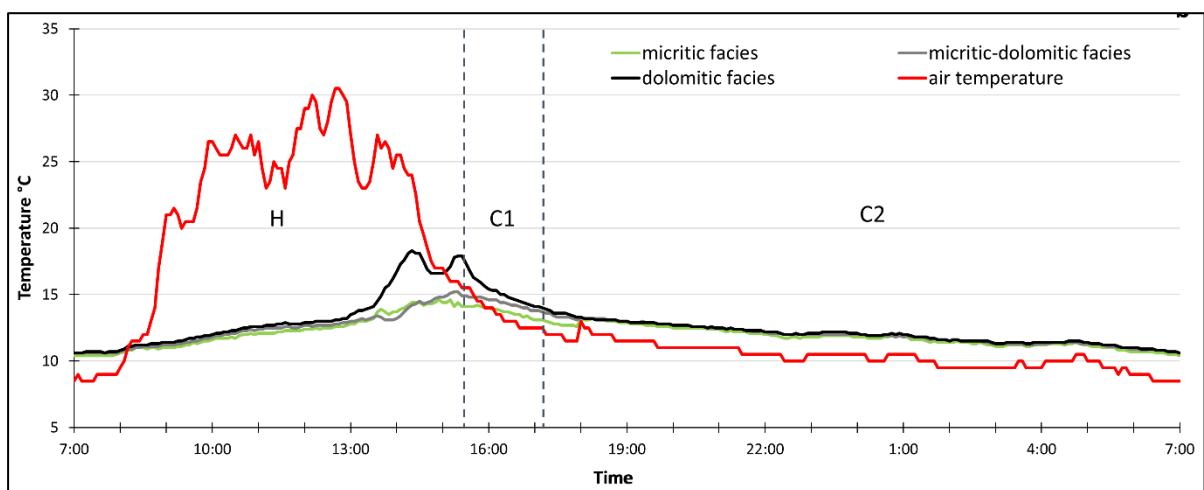


Figure 5.6: Air temperature and rock temperature directly measured on the outcropping lithofacies during the IRT monitoring by means of K-type thermocouples. H: fast heating phase, the rock materials reach the peak temperature at about 15:30; C1: first cooling phase, the progressive shadowing of the outcrop causes a drop of the rock temperatures; C2: a slower cooling phase occurs during the night.

5.3.2. Time series and correlations with rock mass properties

The alignment of the temperature profiles along the reference section with those of the rock mass properties (e.g., topography, lithology, GSI, and fracture frequency) allowed the detection of some correlations (Figure 5.7). The disturbance elements such as vegetation and man-made structures (e.g., walls), which were detected as warm thermal anomalies in the thermograms acquired during the heating phase (Figure 5.8c), were removed from the temperature profiles. It must be remarked that, due to the high horizontal and vertical heterogeneity of the rock mass properties in terms of color, porosity (at the centimetric scale) and jointing degree, very close peaks characterized the temperature profiles, making the correlation phase quite complex. In addition, because of the large-scale irregularities and of the different local orientation of the slope sectors, the rock mass was not uniformly heated during the daytime. For this reason, the extracted temperature profiles along the reference section, which appeared unclear, were further processed to distinguish the thermal response of the target during the cooling and the heating phases. It is specified that the clearest correlations were obtained by analyzing the temperature profiles during the cooling phase (time range between 17:35 of 21 December 2020 and 6:55 of 22 December 2020, Figure 5.7), to avoid the effects of Sun radiation. The correlations between the surface temperature profiles and the rock mass properties during the heating phase (time range between 6:55 and 15:35 of 22 December 2020) are reported in the Supplementary Materials (Figure S5.7). The mentioned properties contribute together, in different proportions along the reference profile, to the definition of the rock mass thermal response. The prevalence of one property over the others was marked along the plots illustrated in Figure 5.7 (cooling phase) and validated by comparing the 2-D thermograms:

- Correlation temperature-topography: lower temperatures (minimum, maximum, median, mean temperature per layer), larger standard deviations and larger difference values were detected along indented surfaces on the reference section like tight bedding planes, which were shadowed also during the daytime, and in correspondence of jutting blocks (Figure 5.7, Figure S5.7—marker “a”). On the contrary, higher temperatures, lower standard deviations and lower differences were found for the open discontinuities and the hollow sectors below the jutting blocks, in which the warm air was preserved. However, a jutting block (rectangle marker in Figures 5.8a and 5.9c) was identified in the form of positive thermal anomaly during the nighttime. This discrepancy is probably related to the different attitude of the identified rock block that, being oriented parallel to the direction of the solar radiation, gained more heat during the daytime with respect to the other sectors of the rock mass.
- Correlation temperature-rock color: darker levels corresponding to the dolomitic facies are characterized by higher temperatures (minimum, maximum, median, mean temperature per layer) and lower values of the standard deviation and difference, related to a more constant distribution of the temperature during the day (e.g., Figure 5.7, Figure S5.7—marker “b”, Figure 5.8b).
- Correlation temperature-jointing degree/GSI: higher temperature (minimum, maximum, median, mean temperature per layer) values were detected on the highly jointed layers (number of discontinuities/m and karst voids), characterized by lower GSI values (e.g., Figure 5.8a). However, the interpretation of the standard deviation and difference curves is uncertain: in

some cases, they show negative peaks (Figure 5.7, marker c1 inside orange layer), while in others they show oscillating peaks (Figure 5.7, Figure S5.7—marker “c” inside orange layer). A possible explanation could be related to the discontinuity aperture: the layers represented by the marker c1 are formed by close joints, while that marked by c2 corresponds to a very fine laminated layer, with centimetric discontinuity apertures (*Calcari a Chiancarelle*). Moreover, the vegetation grown in the voids of the *Calcari a Chiancarelle* unit may have caused disturbances, too. As a matter of fact, the vegetation disturbed the thermograms acquired during the daytime and the nighttime, respectively, in the form of warm and cold thermal anomalies (Figure 5.8c).

The direct proportionality between the air-rock temperature and the fracturing degree of rock masses, observed through the correlations along the reference profile, is in accordance with the results proposed in the literature based on the analysis of thermograms (Squarzoni et al. 2008; Pappalardo and Mineo 2019; Chicco et al. 2019; Mineo et al. 2022).

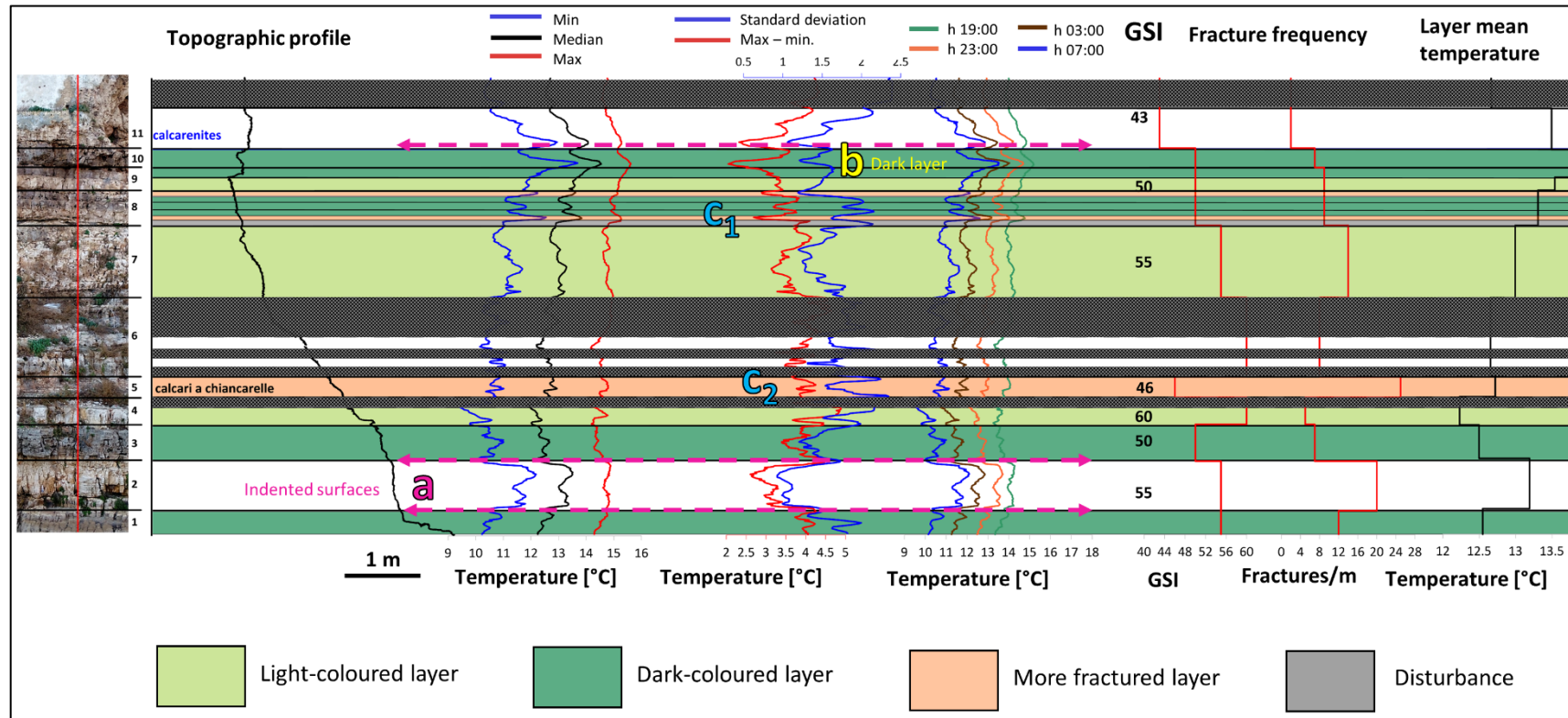


Figure 5.7: Composite plot illustrating how the surface rock temperatures detected from the IRT camera along the section during the cooling phase were determined by the interaction of different factors. The areas covered by vegetation (in gray) were filtered out during the analysis. (a) Lower temperatures and higher temperature standard deviation and differences were identified in correspondence with the indented surfaces (i.e., layer interfaces and tight discontinuities) and jutting blocks; (b) darker levels (dolomitic facies, in dark green) show higher temperatures and lower standard deviation and differences with respect to the lighter levels (micritic limestones, in light green); (c1,c2) higher temperatures are associated to levels with a higher fracture frequency and/or more dissolution voids (low GSI). The standard deviation and difference values in correspondence of moderately jointed layers were generally detected in the form of negative peaks.

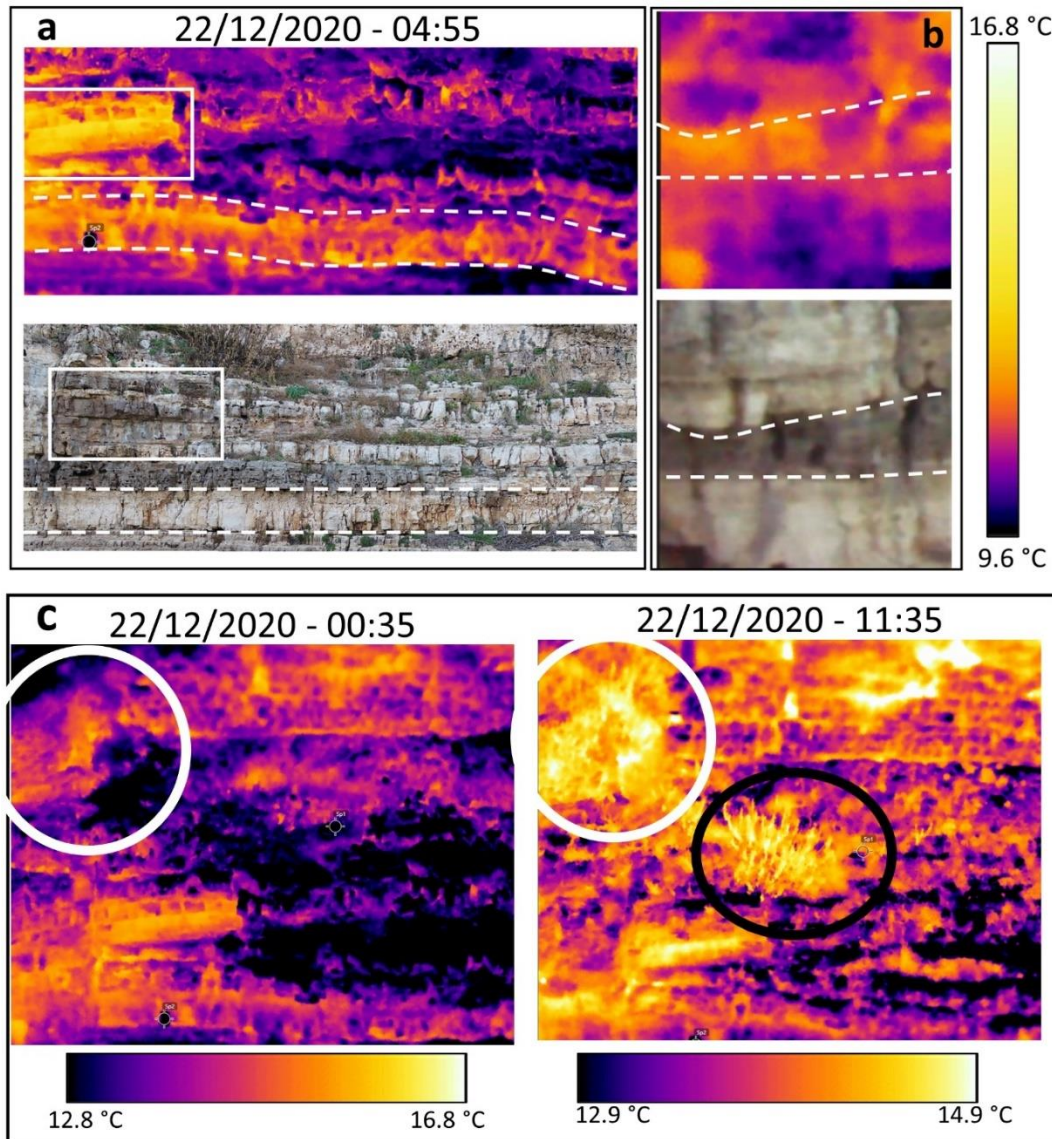


Figure 5.8: Correlation temperature-rock mass properties on the thermograms and RGB photos; (a) higher temperatures (yellow) detected on jutting blocks (white rectangle) and intensely jointed layers (white dotted line); (b) higher temperatures identified on darker levels (dolomitic facies); (c) disturbance produced by man-made structures (walls, white circle) and vegetation (black circle) especially during the daytime acquisitions.

5.3.3. Detection of discontinuities in thermal images

Cooling phase

The discontinuities, voids and hollow zones are visible in the thermograms acquired during the evening in the form of warmer anomalies (Figure 5.9a,b). As a matter of fact, while the intact rock gets colder during the cooling phase, warmer air is preserved in the discontinuity system (Mineo et al. 2015a). The best moment to detect the geosstructural features is late at night, when neither solar radiation or artificial lights disturb the acquisition (Figure 5.9c). This is consistent with data reported in many paperworks (Teza et al. 2012; Mineo et al. 2015a; Pappalardo et al. 2016; Fiorucci et al. 2018; Pappalardo and Mineo 2019; Chicco et al. 2019; Mineo and Pappalardo 2019), but a discrepancy was detected with regards to the thermal behavior of jutting blocks. Mineo et al. (2015a) and Pappalardo

et al. (2016) detected jutting blocks in the form of negative thermal anomalies in thermal images acquired during the night because of the higher exposure to ventilation. However, a jutting block of the study site was characterized by higher temperatures in all the thermograms (red rectangle in Figure 5.9). A possible explanation for this discrepancy is that the described block was more exposed to the solar radiation during the day because of its different attitude (SW, parallel to the direction of the sunrays during the peak hours) with respect to the overall aspect of the target area (NS). It is remarked that the discontinuities belonging to the bedding (S0) detected in the thermal outputs are clearer than those of the sub-vertical joint sets (J1, J2) because of the larger persistence driving a greater heat flow (Frodella et al. 2014).

Heating phase

In the early morning, the fractured and voided levels are heated by the solar radiation more quickly than the intact rock, which has a low thermal diffusivity. Thus, these structures are still visible in the form of positive thermal anomalies, but their contours are not well defined throughout the thermal image (Figure 9e). An interesting result of the IRT acquisition at early morning is that the calcarenite unit, which is in contact with the limestone unit, is not easy to define in the field and on high-resolution photos because of anthropogenic disturbances and weathered material, can be easily defined in the thermograms. This is due to the higher porosity and a high connectivity of the pore system, which allows the lithofacies to get warmer with respect to the other rock materials. Conversely, the Calcare di Bari Fm. showed a larger thermal inertia, as the warm air difficultly circulated in the pore system made up of isolated pores. However, moderately-intensely jointed layers in the limestone unit have temperatures comparable with those of the Calcare di Gravina Fm because of the warm air circulating inside the open fractures, which are represented by warm thermal anomalies, in agreement with the literature (Baroň et al. 2012; Gigli et al. 2014; Mineo et al. 2015a, 2022; Pappalardo et al. 2016; Casagli et al. 2017; Pappalardo and Mineo 2019). By analyzing the thermograms of the two formations of the study site, a discrepancy was found with respect to this aspect. As a matter of fact, the calcarenite unit generally shows higher temperatures with respect to the less porous limestone units, also during the nighttime (Figure 5.9a–c), implicating a lower cooling rate. A possible explanation is that the Calcare di Bari Fm., even if less porous, gets colder than the Calcare di Gravina Fm. because the heat is released through the discontinuity systems.

Later on, their identification of jointed and voided levels gets more uncertain because the vegetation, directly heated by the Sun, becomes much warmer and disturbs the thermal images. In addition, areas of the rock mass are differently illuminated depending on the daily solar path, until sunrise. Consequently, protruding sectors of the slope facing the direction of the solar radiation gain more heat and project their shadows on the indented and inner parts, which are represented by lower temperatures in the thermograms. These outcomes are in agreement with the results reported by many authors (Mineo et al. 2015a; Pappalardo et al. 2016; Fiorucci et al. 2018; Pappalardo and Mineo 2019; Loche et al. 2021). For instance, Figure 5.9f illustrates that at 13:55 the sector of the rock mass with slightly different aspect (dipping SW) are warmer compared to the other zones as an effect of the solar radiation. In this case, it is not possible to detect discontinuities in the form of positive anomalies. This is consistent with data reported in the literature (Mineo et al. 2015a; Pappalardo et al. 2016; Pappalardo and Mineo 2019). When the cooling phase is reached, the detection of discontinuities is again facilitated.

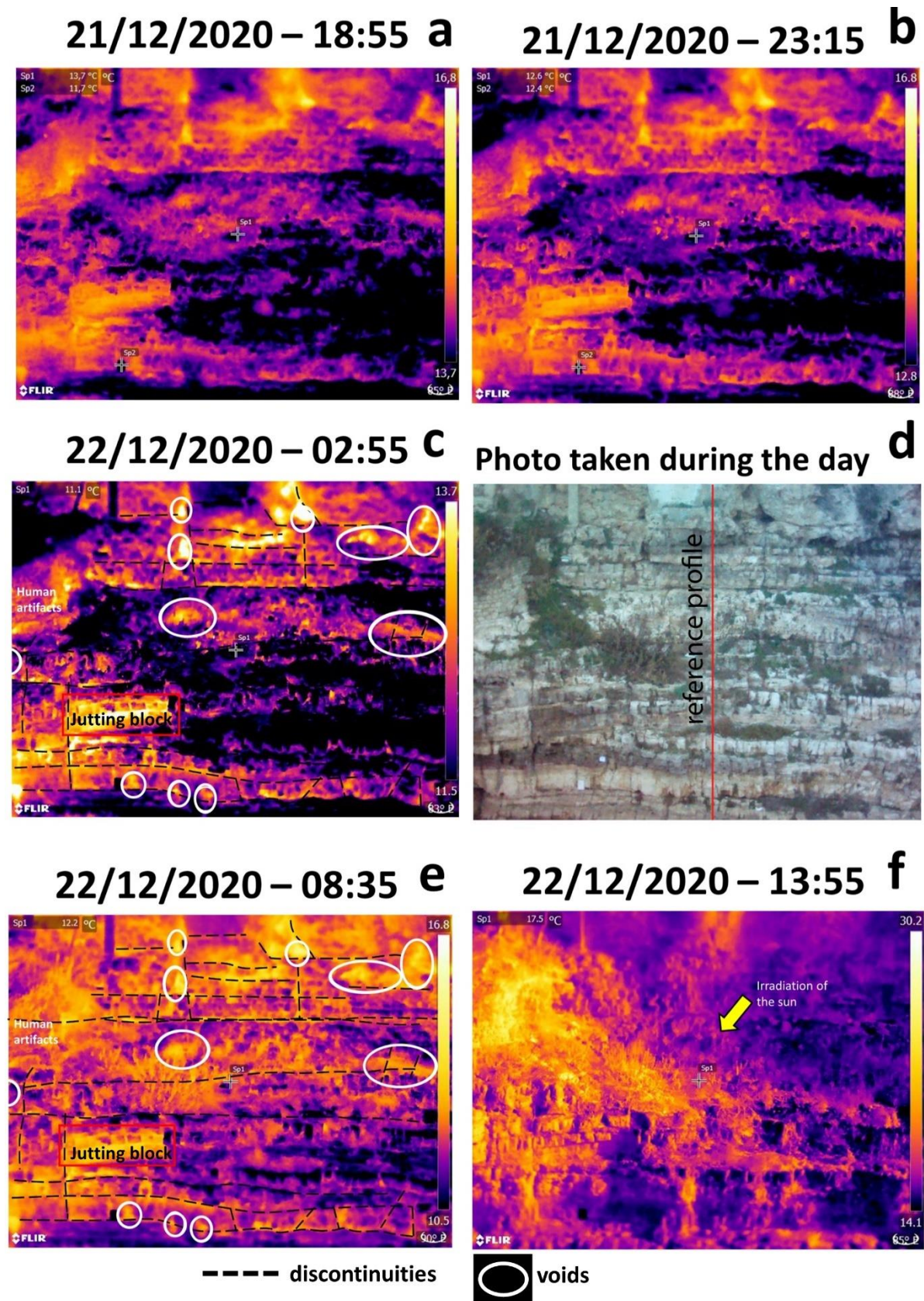


Figure 5.9: Detection of discontinuities and voids in the thermal images acquired during the 24-h monitoring. (a–c) Cooling phase: the discontinuities and voids were identified as warmer anomalies, in contrast with the intact rock which was colder; (d) RGB photo acquired by the thermal imager during the day; (e,f) heating phase:

the discontinuities and voids gain more heat than the intact rock (low thermal diffusivity), but their contours are less defined. (e) The more porous calcarenite facies is identified in the form of warm thermal anomaly; (f) the discontinuities and voids cannot be detected because of the effects of direct solar radiation on the rock mass.

5.4. Main outcomes and conclusions

With this research, the infrared thermography technique is tested in a coastal area characterized by a humid mesothermal climate with mild winters and anthropogenic disturbances. The rock mass of the study area is made up of vertical and lateral heterogeneous facies, characterized by different fabric, fracturing conditions, weathering and karst features. The aim of this study was to assess whether IRT technique in such a complex setting could be of support to the geomechanical characterization of rock masses and if it could provide additional information with respect to other remote sensing technologies, like laser scanners and drones.

By analyzing the rock temperatures, it was found out that, with a daily thermal excursion of more than 20 °C, the lithofacies reached values of temperature differences up to 4–8 °C. In addition, as outlined by Fiorucci and co-workers (Fiorucci et al. 2018), it was observed that the heating phase is faster than the cooling phase (Figure 5.6) and that it is caused by short and intense solar radiation. Detailed information on topography, lithology and fracturing conditions can be collected by aligning longitudinal profiles extracted from the thermograms, topographic profiles and high-resolution photos of the investigated area.

In addition, despite the low emissivity of the rock mass, the effect of solar radiation at the rock-air interface allowed the detection of geostructural information from the thermal images at a detailed scale. As a matter of fact, discontinuities, such as joints and bedding planes, karst voids and more fractured layers, were identified as positive thermal anomalies in the thermograms acquired at night-time, since they preserve the heat absorbed during the day.

With regard to the optimal time to acquire the IRT images, it was outlined that the night time represents the best conditions, since the detection of discontinuities and voids in the form of warm thermal anomalies is not affected by disturbances produced by vegetation, diurnal human activities and parasite radiations produced by the natural lights, in agreement with many researches (Teza et al. 2012; Frodella et al. 2014; Mineo et al. 2015a, b; Pappalardo et al. 2016; Fiorucci et al. 2018; Pappalardo and Mineo 2019; Chicco et al. 2019). Conversely, thermograms obtained during the peak solar radiation do not allow the identification of weaker zones because the different illumination conditions give information only on the attitude of the sectors of the rock mass. For this reason, IRT surveys aimed at the detection of fractured and voided zones are not recommended when the angle of incidence of the sunrays is high. However, some IRT applications took advantage of the direct solar radiation to explore the three-dimensionality of rock slopes, to detect protruding or recessed blocks (Mineo et al. 2015a) and to identify discontinuities facing the Sun direction as low thermal anomalies (Frodella et al. 2014).

Concerning the limitations of IRT techniques, the logistics and complexity of the examined area represented the main issue. In detail, considering the high lateral and vertical heterogeneity of the lithofacies, as well as the presence of thin bedded and intensely jointed layers, success of IRT monitoring can be achieved only by means of high-resolution thermal images. In other words, if the survey is aimed at identifying more fractured zones or laminated levels, the pixel size must be smaller than the fracture spacing or the layer thickness. Nevertheless, the resolution of the thermograms is related to

the distance between the IRT camera and the target area, which is often constrained to morphology conditions (Frodella et al. 2014; Grechi et al. 2021). The issues related to the low-detailed thermal outputs can be solved by using IRT sensors with higher resolution. In addition, time-series plotted to find correlations between the surface rock temperatures and the rock mass properties along a longitudinal profile are sensitive to the position of the profile itself: when the peaks of the temperature-pixel curves are very close to each other (i.e., succession of heterogeneous facies), a bad alignment of the profiles extracted at different times may affect the results. It is thus recommended to ensure immobility of the thermal imager during the acquisition.

Furthermore, the interpretation of thermograms acquired in complex environments can be challenging because the resolution of the RGB photos taken by the thermal camera is not always sufficient to examine small-sized thermal anomalies. In this case, UAV-based Structure from Motion techniques might be of paramount importance to zoom on the anomaly, locate the thermogram in a broader area and detect potential correlations with other geostructural features.

This study highlights how infrared thermography can be of support for geostructural analyses in rock masses, even in areas with mild climate, disturbance elements and characterized by heterogeneous successions made up of lithofacies with similar emissivity and not always clear contacts, due to different degrees of degradation even at a large scale and with the support of high-resolution photos. The integration of IRT results with field observations and other remote sensing technologies might be fundamental for the identification of overhanging sectors of rock masses defined by persistent and open joints, subjected to major thermal stresses and susceptible to failure over time.

5.5. Supplementary Materials

Table S5.1: Calibration parameters measured during the acquisition process (21–22 December 2020) for the correction of the apparent temperatures. The ambient air temperature and relative humidity were measured by means of a pocket-size digital thermo-hydrometer, and the reflected temperature was calculated using a reflective target at the base of the cliff to calculate the real temperatures (Hudson 1969; Usamentiaga et al. 2014; FLIR 2021).

Time of thermogram acquisition CET	Ambient air temperature °C	Relative humidity %	Reflected apparent temperature °C
17:45	15	72	13.4
18:05	12.5	83	13.1
18:25	12	86	13.7
18:45	11.5	88	13.4
19:05	11.5	89	11.7
19:25	11.5	90.5	12.4
19:45	11	91	11.7
20:05	11	92	13
20:25	11	92	12.8
20:45	11	92	12.3
21:05	11	92.5	10.7
21:25	11	93	9.7
21:45	10.5	93.5	10
22:05	10.5	94	10.2
22:25	10	94	12.3
22:45	10	94.5	12.1
23:05	10.5	94.5	11.9
23:25	10.5	94.5	12.4
23:45	10.5	94	12.6
0:05	10.5	94	9.9
0:25	10	95	11.5
0:45	10.5	94.5	12.3
1:05	10.5	94	10.2
1:25	10	95	8.4
1:45	9.5	95	10.7
2:05	9.5	95	10.8
2:25	9.5	95	10.6
2:45	9.5	96	8.9
3:05	9.5	95.5	7.6
3:25	9.5	95.5	10.2
3:45	9.5	95	10
4:05	10	95	11.7
4:25	10	95	11.6
4:45	10.5	94.5	10.9
5:05	10	94	7.6
5:25	9.5	95.5	7.5
7:05	9	95.5	6.6

Time of thermogram acquisition CET	Ambient air temperature °C	Relative humidity %	Reflected apparent temperature °C
5:45	9.5	96	8.2
6:05	9	96	7.7
6:25	8.5	95.5	7.4
6:45	8.5	96	6.6
7:25	8.5	95.5	6.5
7:45	9	94.5	8.4
8:05	10	94.5	11
8:25	11.5	90	11.1
8:45	14	88	8.4
9:05	21	65.5	8.4
9:25	20.5	63	8.2
9:45	23.5	54	8.7
10:05	26	48.5	8
10:25	26	48.5	8.5
10:45	26	48	8.9
11:05	24.5	49.5	8.7
11:25	24.5	50	9.9
11:45	25.5	48	8.9
12:05	29	41	10.3
12:25	27	44	9.6
12:45	30.5	39	10.8
13:05	25	47	11.8
13:25	23.5	52.5	11.4
13:45	26.5	47	11.6
14:05	25.5	47	13.3
14:25	22.5	52	12.9
14:45	17.5	64	12.3
15:05	16.5	68	11.7
15:25	15.5	71	11.6
15:45	14.5	74	11
16:05	14	77	9.5
16:25	13	80	10
16:45	12.5	82.5	10.4
17:05	12.5	83	10.3
17:25	12	83.5	10
17:45	11.5	84	10.6

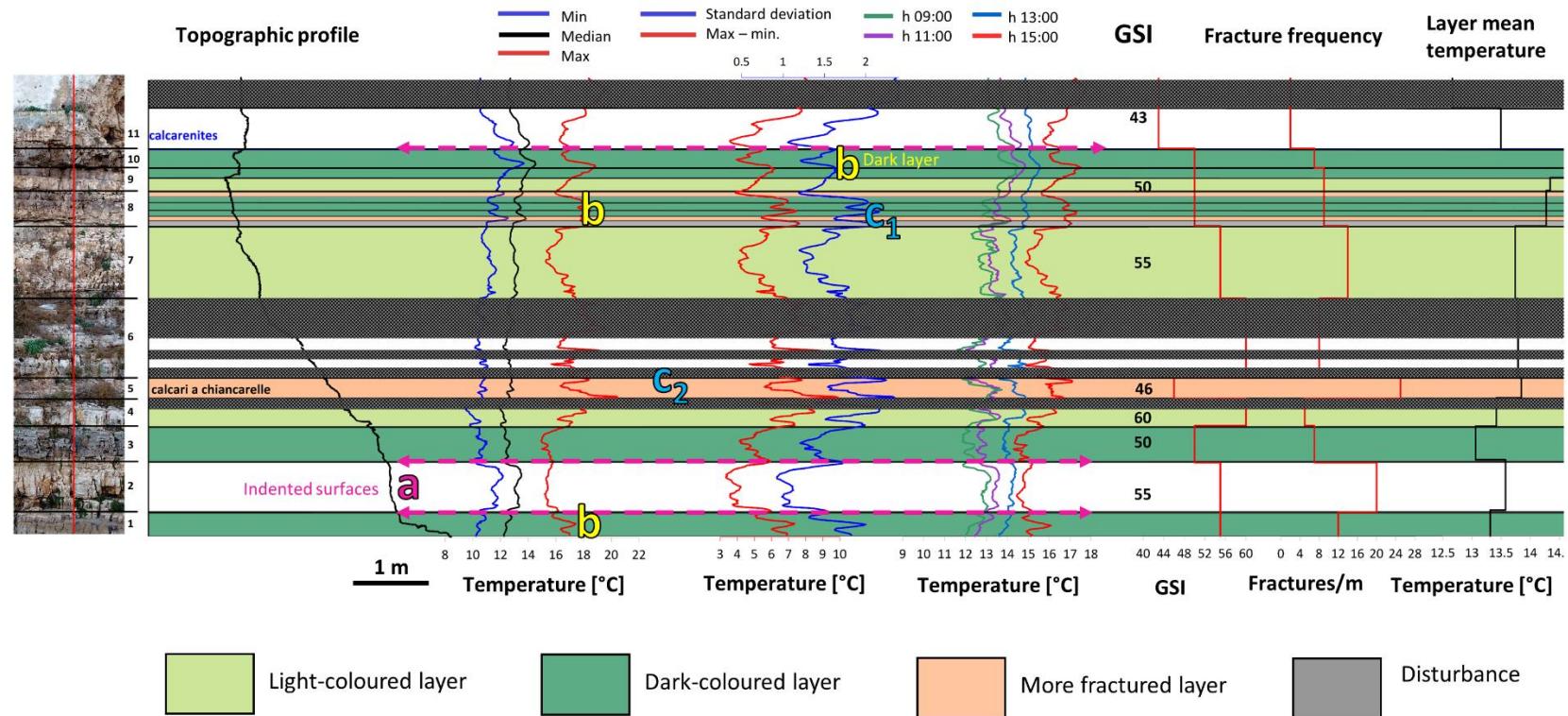


Figure S5.7: Composite plot illustrating how the surface rock temperatures detected from the IRT camera along the section during the heating phase were determined by the interaction of different factors. It is remarked that the correlations between the air-rock surface temperatures and the rock mass properties are less clear than those of the cooling phase because of the effects of Sun radiation and irregular surfaces. (a) Lower temperatures and higher temperature standard deviation and differences were identified in correspondence of the indented surfaces (i.e., layer interfaces and tight discontinuities). Conversely, open discontinuities and karst voids are represented by higher temperatures, as the warm air circulates within the discontinuity system; (b) darker levels (dolomitic facies, in dark green) show higher temperatures and lower standard deviation and differences with respect to the lighter levels (micritic limestones, in light green); (c1, c2) higher temperatures are associated with levels with a higher fracture frequency and/or more dissolution voids (low GSI). The standard deviation and difference values in correspondence of moderately jointed layers were generally detected in the form of negative peaks.

Chapter 6 QDC-2-D: A Semi-Automatic Tool for 2-D Analysis of Discontinuities for Rock Mass Characterization

Abstract: Quantitative characterization of discontinuities is fundamental to define the mechanical behavior of discontinuous rock masses. Several techniques for the semi-automatic and automatic extraction of discontinuities and their properties from raw or processed point clouds have been introduced in the literature to overcome the limits of conventional field surveys and improve data accuracy. However, most of these techniques do not allow characterizing flat or sub-vertical outcrops because planar surfaces are difficult to detect within point clouds in these circumstances, with the drawback of undersampling the data and providing inappropriate results. In this case, 2-D analysis on the fracture traces are more appropriate. Nevertheless, few methods to perform quantitative analyses on discontinuities from orthorectified photos are publicly available and do not provide a complete characterization. The scanline and window sampling strategies were implemented in a digital environment to characterize rock masses affected by discontinuities perpendicular to the bedding from trace maps, thus exploiting the potentiality of remote sensing techniques for sub-vertical and low-relief outcrops. The routine, named QDC-2-D (Quantitative Discontinuity Characterization, 2-D) was compiled in MATLAB by testing a synthetic dataset and a real case study, from which a high-resolution orthophoto was obtained by means of Structure from Motion technique. Starting from a trace map, the routine semi-automatically classifies the discontinuity sets and calculates their mean spacing, frequency, trace length, and persistence. The fracture network is characterized by means of trace length, intensity, and density estimators. The block volume and shape are also estimated by adding information on the third dimension. The results of the 2-D analysis agree with the input used to produce the synthetic dataset and with the data collected in the field by means of conventional geostructural and geomechanical techniques, ensuring the procedure's reliability. The outcomes of the analysis were implemented in a Discrete Fracture Network model to evaluate their applicability for geomechanical modeling.

6.1. Introduction

In the last two decades, remote sensing techniques have become widespread and have attracted many researchers for their application on rock mass investigations. The main goal is to overcome the limits of the conventional geostructural and geomechanical surveys to characterize rock masses, related to logistics, limited access, vegetation, adverse weather conditions, and human and instrument errors (Barton et al. 1974; Franklin et al. 1988; Slob et al. 2005; Slob 2010). In this perspective, terrestrial/aerial laser scanning and photogrammetry are widely accepted because of their capability to acquire high-resolution point clouds in a reasonable time and in safe conditions, with relatively low costs (Westoby et al. 2012; Tofani et al. 2013; Palma et al. 2017). Great attention has been paid to discontinuities in 3-D models, given the key role they play in the mechanical behavior of rock masses and in affecting their stability (Goodman 1976; Priest 1993; Hudson and Harrison 2000; Jaboyedoff et al. 2009; Kainthola et al. 2015; Cardia et al. 2021). With regards to engineering problems, the results of slope stability assessments by means of numerical modelling in discontinuous rock masses

(Lisjak and Grasselli 2014) depend on the reliability of the fracture characterization, which is fundamental to elaborate the rock mass conceptual model (Jing and Hudson 2002; Jing 2003).

In the last decades, several methods were introduced in the literature to automatically or semi-automatically extract the discontinuity sets (DSs) affecting rock masses, as well as their properties, from raw or processed data derived from Light Detection and Ranging (LiDAR) (Fardin et al. 2004; Slob and Hack 2004; Jaboyedoff et al. 2007; Vöge et al. 2013; Mavrouli et al. 2015), Structure from Motion techniques (Roncella et al. 2005; Voyat et al. 2006; Westoby et al. 2012; Buyer and Schubert 2016, 2017, 2018), or their combination (Sturzenegger and Stead 2009; Lato and Vöge 2012). As stated by Gigli and Casagli (2011), the extraction of the geometrical properties of discontinuities can be achieved by direct segmentation on point clouds (Voyat et al. 2006; Jaboyedoff et al. 2007; Slob et al. 2007; Ferrero et al. 2009; Gigli and Casagli 2011; Riquelme et al. 2014, 2018; Kong et al. 2021) or by processing surfaces like Triangulated Irregular Networks (TINs) (Slob et al. 2005; Oppikofer et al. 2011; Vöge et al. 2013; Li et al. 2016). Each technique has its advantages and limits, which are highlighted by Battulwar (2021) in a detailed review of the different methods for the extraction of discontinuities and their properties from remote sensing products.

Nevertheless, flat or sub-vertical topographies in low-relief areas or in man-made excavations do not allow a proper detection of the planar surfaces developed within rock masses from 3-D models, since only the traces of the discontinuities are visible. As a result, information on mean direction, spacing, length, and persistence of the discontinuity sets could be misinterpreted and could lead to an improper characterization. In these circumstances, 2-D analyses should be carried out on the traces of the discontinuities from orthophotos obtained utilizing LiDAR or SfM techniques.

Although methods to perform 2-D analyses on discontinuities were published during the second half of the last century, it appears that they were not fully revised and implemented into a digital environment. As a consequence, the data are usually collected in the field by means of time-consuming, locally dangerous, conventional geostructural and geomechanical surveys.

Some progress on this topic was achieved by means of commercial software/tools like ShapeMetrix 3-D (3GSM) or DiAna 2-D (Gigli and Casagli 2011) that require a license or are not available to the public. Concerning the open-source software and freeware, an estimation of the spacing and persistence of sets of discontinuities can be obtained using the Mattercliff software (CREALP) on a photo by drawing straight lines (not polylines), while the up-to-date FracPaQ2-D (Healy et al. 2017) is a useful tool to determine the strike and lengths of the traces, as well as the fracture intensity and density. In addition, Martinelli and co-workers proposed a method to characterize Digital Outcrop Models (DOMs) by means of scan-line and scan-area analyses, which can be used as outcrop analogues to model reservoirs (Martinelli et al. 2020). This procedure identifies fracture parameters such as length, strike, intensity, density, and topology and enables localizing damage zones.

It is outstanding that, despite different techniques being introduced in the literature, a procedure for complete rock mass characterization has not yet been achieved (Lyman et al. 2008; Cai 2011; Tuckey and Stead 2016; Buyer and Schubert 2018; Elmo et al. 2018, 2021; Elmo and Stead 2020).

To this aim, a user-friendly, adjustable, and repeatable MATLAB routine was developed to characterize the discontinuity sets and the fracture network of low-relief areas on DOMs by introducing the well-known formulas of the literature in a digital environment. Starting from an orthophoto, or a file with digitized traces, the routine calculates the trace orientations (strikes), lengths, spacing, and persistence; defines the fracture intensity and density; and estimates the block volume and shape, allowing the characterization of the investigated area in a few minutes. An innovative feature of the

MATLAB routine consists of the semi-automatic identification of the discontinuity sets by means of two methods and the consequent classification of the traces, which can be chosen and validated by the user.

The routine was built on a synthetic dataset, which was specifically created, and validated on the orthophoto of a case study generated by applying the SfM on a dataset collected by means of Unmanned Aerial Vehicle (UAV) systems.

Finally, the results obtained from the case study were used to generate a 3-D geomechanical model of an adjacent and scarcely accessible sub-vertical rock cliff to assess the potentiality of the 2-D analysis for engineering problems such as stability analyses. More in detail, a stochastic Discrete Fracture Network (DFN) method was used to explicitly represent the discontinuity sets of the case study using the probability distributions of their orientation, spacing, length, and persistence obtained with the MATLAB routine. The DFN model creation shows how the proposed routine can be used to further investigate the geomechanical and hydrological behavior of rock masses through more realistic approaches. Further information on the DFN techniques, commercial codes, and numerical methods that integrate DFN techniques, which are out of the scope of this research, are reported in specific review papers (Cacas et al. 1990; Lei et al. 2017).

6.2. Materials and Methods

6.2.1. Study Site

The study area used to validate the routine is located in Polignano a Mare, on the Adriatic side of the Apulian coast (SE Italy) (Figure 6.1).

Geomorphology of the area is characterized by a series of marine terraces subparallel to the coastline (Bruno et al. 1995; Dini et al. 2000), gently dipping to NE and linked by small scarps. They are, at places, carved by water ways locally called lame (Parise 2003): slightly incised in the limestone bedrock and flat-bottomed, typically dry, valleys that constitute the main drainage network during exceptional rainfall events. The mentioned morpho-structures are the result of the superimposition of the tectonic uplift of the Apulian platform and the absolute sea-level changes, starting from the middle Pleistocene (Ciaranfi et al. 1988). Platforms and cliffs form the coast up to 20 m high, linked by embayments constituted by coastal erosion deposits (pocket beaches).

From a geologic standpoint, the site belongs to the eastern part of the Murge plateau, an emerged block of the Apulian foreland characterized by a 3-km-thick Cretaceous succession related to a wide carbonate platform, overlain by upper Pliocene to Lower Pleistocene transgressive deposits of shallow marine waters (Ricchetti et al. 1988; Tropeano and Sabato 2000). The lithofacies cropping out in the study area are composed of whitish to greyish limestones and dolostones belonging to the Calcare di Bari Fm., which are discontinuously overlain by yellowish calcarenites belonging to the Calcarenite di Gravina Fm. While the latter has a massive structure, the former lithofacies is constituted by thin to medium bedded layers, crossed by a network of sub-vertical discontinuities and locally folded.

The fracture pattern, together with the marine and karst processes (Sauro; Parise 2011) strongly modelling this sector of Apulia, contributes to the geomorphologic evolution of the coastal area: detachment niches along the sub-vertical walls of the cliffs and boulders at their base, occasionally visible below the sea level, indicate local failures of the rock mass, and further potential instabilities

cannot be excluded. These are among the most frequent geological hazards in coastal karst settings and are partly favored by the diffuse presence of karst conduits and caves, further weakening the carbonate rock mass (Parise 2010, 2015c; Gutiérrez 2010; Gutiérrez et al. 2014).

Thus, a geostructural-geomechanical characterization of the site, with particular emphasis on the identification and characterization of the discontinuity sets and the estimation of the rock block shape, size, and volume, as well as the failure modes, is crucial for the management of prevention and mitigation measures at Polignano a Mare, one of the most important touristic sites of Apulia.

The rock mass considered for the 2-D analysis is a 6400-m², low-relief platform developing from 10 m above the sea level to the current coastline, locally named *Pietra Piatta*. The choice of this area to perform the study was dictated by the lack of the Mediterranean vegetation and of anthropogenic elements as well, considering the disturbance produced by the residential center and by the vegetative area in nearby sectors. Due to erosional processes, the calcarenite facies crops out only in the external part of *Pietra Piatta*; therefore, a detailed view of the fracture traces in the Calcare di Bari Fm., which is generally covered by the Plio-Pleistocene deposits, is available at the site. In addition, 0.5- to 2-m steps located in the eastern side of the rock mass were found to be essential for the characterization of the bedding surfaces, which contribute to the formation of potentially unstable discrete blocks. Further, before implementing the study, field surveys were carried out to ensure that *Pietra Piatta* site was representative of the whole study area.

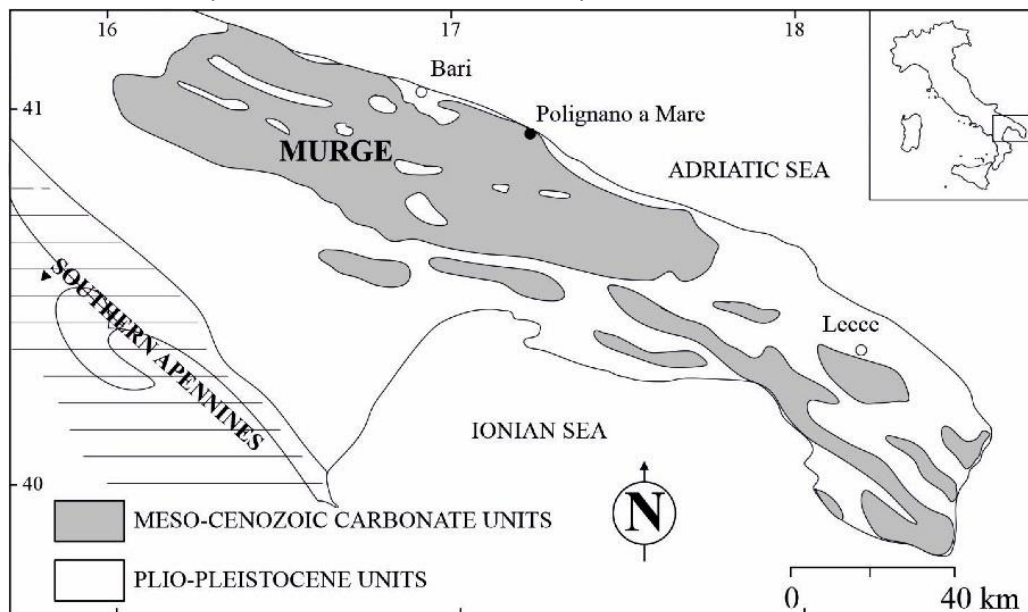


Figure 6.1: Geographic location of the study area.

6.2.2. Generation of the Digital Outcrop Model (DOM)

A DOM of the study site was produced by means of Unmanned Aerial Vehicle (UAV) acquisition and Structure from Motion (SfM) processing techniques. The UAV survey at the study site was carried out in five steps:

1. flight mission planning;
2. positioning and coordinates' acquisition of Ground Control Points (GCPs);
3. flight and image collection;

4. Structure from Motion (SfM) processing and generation of the dense point cloud; and
5. building of the orthomosaic.

To achieve the optimal coverage of the investigated area, an automatic flight mode, with front and side overlap of 75% and flight altitude of 18 m, was set in the planning phase. The nadir photogrammetric survey was performed on 12 December 2019, at early morning, in order to avoid sunlight reflections from the sea, using a quadcopter platform DJI Inspire 2 equipped with a 20.8-Megapixel (MP) resolution camera, an integrated satellite positioning system, and a remote flight controller. The system’s specifications and the details of the survey are summarized in Table 6.1. In addition, three GCPs were manually positioned on the terrain before the flight such that they could be easily detected on the photos, and their coordinates were acquired by means of a Stonex SIII Differential Global Positioning System.

Table 6. 1. Details of the UAV system, on-board camera, and photogrammetric survey.

UAV system	
UAV device	DJI Inspire 2
Maximum takeoff weight (g)	4250 g
Maximum flight time (min)	27
Gimbal stabilization	3-axis (pitch, roll, yaw)
On-board camera parameters and setting	
Camera model	Zenmuse X5S
Supported lens	DJI MFT 15mm 1.7 ASPH
Sensor	CMOS, 4/3"
FOV	Effective Pixels: 20.8 MPx
Photo resolution (mm)	72°
Survey details	
Flight mode	automatic
Ground Sampling distance (cm/pix)	0.41
Coverage area (km ²)	0.836
Flight altitude (m)	18
Number of photos	248
Front overlap (%)	75
Side overlap (%)	75
Frame shooting interval (s)	1.5
Ground resolution (mm/pix)	4.71
Number of tie-points	311,321
Number of projections	2,290,325
Reprojection error (pix)	0.541
GCPs XY error (m)	0.010
GCPs Z error (m)	0.001
Total GCPs error (m)	0.010
Orthomosaic pixel size (mm/px)	4.71

The SfM technique was carried out using Agisoft Metashape Professional (Agisoft 2020) to process the images and obtain a 3-D rock mass model. During the photo importation phase, the software automatically detected the camera calibration and location parameters (camera focal length,

coordinates of the image principal point, and lens' distortion coefficients). The images were georeferenced in a WGS84/UTM 33 N metric coordinate system. The three GCPs were semi-automatically identified on the photos and their position was validated by the operator. Taking into consideration potential imprecisions in the acquisition of the GPS coordinates from the drone, these GCPs were used as a constraint to optimize the georeferencing of the model. The Root Mean Square Errors of the GCPs are reported in Table 6.2.

Table 6.2. Root Mean Square Errors (RMSE) of the Ground Control Points used for the georeferencing optimization of the model.

GCP ID	Number of Images	Horizontal Errors (cm)		Vertical Errors (cm)	Total Error	
		X	Y	Z	cm	pix
GCP1	32	-0.78	-0.03	0.02	0.78	3.065
GCP2	22	1.19	0.74	0.21	1.42	0.744
GCP3	18	-0.40	-0.71	0.14	0.83	3.374

Successively, the SfM algorithm recognized multiple key points in each picture and matched them in the overlapping photos. Then, 248/248 photos were aligned with the “high-accuracy” alignment option and optimized by means of sparse bundle adjustment algorithm (Snavely et al. 2008), while the key point matches (tie points) were positioned in a 3-D environment, thus obtaining a sparse point cloud. Later, a Multi-View Stereo (MVS) algorithm was applied to generate a “high-quality” 3-D dense point cloud (98,375,478 points). The dense point cloud was cleaned of unwanted elements such as points belonging to the sea water moving on the borders of the model, and objects used to perform the photogrammetric surveys, by means of segmentation process. The disturbance was removed in this phase because the creation of masks on the unwanted elements in the preliminary phase of the SfM processing would have required a large amount of time, considering the high number of photos. The final step consisted of the generation of a mesh of the model, using the “high-quality” option available in Agisoft Metashape (9,785,754 faces) and in the extraction of a 2-D orthomosaic from the mesh, with a 4.71-mm pixel size.

6.2.3. Field Characterization of Discontinuity Sets

Geostructural and geomechanical surveys were performed at *Pietra Piatta* site on 4 November 2020 to carry out a quantitative analysis of the discontinuities in the Calcare di Bari Fm. Window sampling strategies were preferred to scanlines to avoid orientation biases, since discontinuities subparallel to the scanline are difficult to detect (Terzaghi 1965; Priest 1993). A preliminary visual inspection in the field helped to estimate the main joint sets. It is specified that, since the scope of this chapter is to carry out 2-D analyses of flat outcrops based on top-view images, the information on bedding surfaces (visible along cross-sections) was not included in this study.

Two 100-m²-wide squares were created on the rock mass with a tape, to collect information on the discontinuities intersecting or contained in the survey window, following specific recommendations (ISRM 1988). These areas, corresponding to two of the five sectors later analyzed with the MATLAB routine (sectors A and C in Figure 6.2), were selected for the presence of easily recognizable planar surfaces. Moreover, for each joint belonging to the analyzed discontinuity set, the strike, spacing, persistence, opening, and filling were measured by means of a Wilkie-type compass and a measuring

tape. Roughness and wall strength were estimated using, respectively, a profilometer (Barton Comb) and a sclerometer (L-type Schmidt hammer). The strike data of the detected discontinuities were processed using the Dips software (Rocscience 2021) by means of equal-angle stereographic projections (lower hemisphere) to identify the main DSs and calculate their statistical parameters. Successively, the geometrical data (i.e., spacing and trace length) collected in the field were processed on spreadsheets (Figure 6.3).

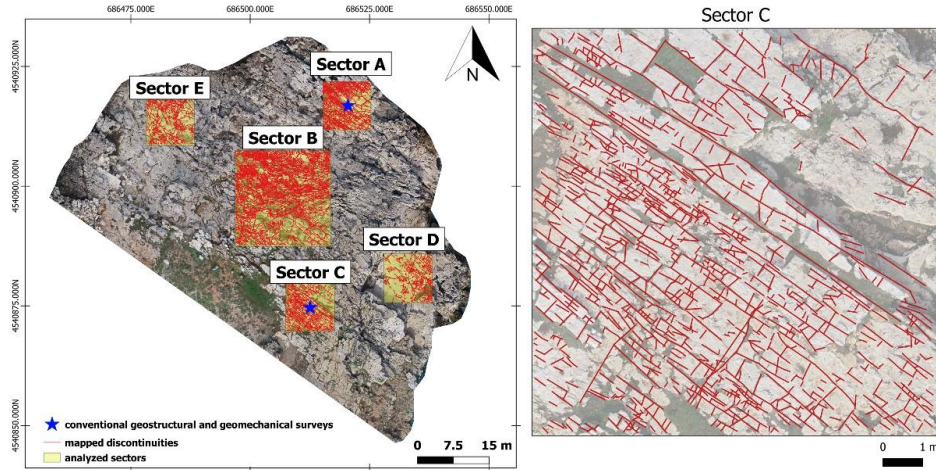


Figure 6.2: Sectors investigated by means of field geostructural and geomechanical surveys and traces digitized in the orthophoto.

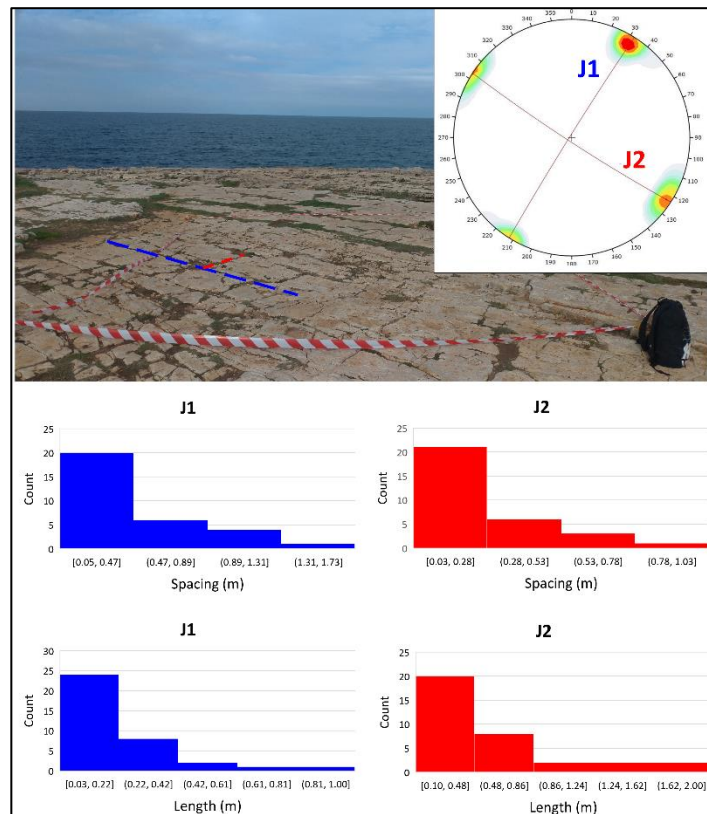


Figure 6.3: Identification of the main discontinuity sets on the field and calculation of the joint spacing and trace length distributions.

6.2.4. Manual Mapping of the Fracture Traces

The high-resolution orthophoto (1.25-GB-sized TIF image) produced by means of SfM technique was imported into a GIS environment by means of QGIS open source software, in a WGS 84/UTM 33N metric coordinate system. After a meticulous visual inspection of the model, five sectors were considered to be representative of the rock mass; therefore, a vector layer made up of five square windows was created on the orthophoto. Successively, for each sector, the traces of the discontinuities were manually drawn as polylines keeping the same scale, which was established according to the resolution of the orthophoto, in order to reduce sampling biases in the different windows. The traces drawn on each polygon are reported in Table 6.3. The nodes of the polylines were extracted using the “extract vertices” geometry tool available in QGIS, and their coordinates were obtained through the field calculator in the attribute table. The “clip” vector algorithm (input: layer of the traces, overlay layer = square window) allowed the extraction of the traces of each sector, as well as their nodes coordinates. Finally, the five layers were exported into CSV format and converted to text files with a spreadsheet.

Table 6.3. Number of traces drawn for each sector of the *Pietra Piatta* rock mass.

Sector	Area (m ²)	Number of Traces
A	100	1472
B	400	5961
C	100	1018
D	100	818
E	100	1044

6.2.5. Methodological Approach for the Digital 2-D Quantitative Analysis of Discontinuities

The code for the 2-D quantitative analysis of discontinuities was written in MATLAB environment after a preliminary literature review of the discontinuity properties that must be defined for geostructural and geomechanical characterization of rock masses and of the methods to define them as well. According to ISRM (1988), the quantitative description of the discontinuities requires the determination of their orientation, spacing, persistence, roughness, wall strength, aperture, filling, and seepage, as well as the number of discontinuity sets and the block size. In this study, focus was given to the determination of the geometrical properties and on the number of discontinuity sets from orthophotos, derived from remote sensing techniques by implementing the methods presented in the literature in a digital environment. The parameters taken into account to perform the 2-D analysis, the methods, and the source publications of the formulas are summarized in Table 6.4.

Table 6.4. Properties defined by the developed routine, applied methods, and relevant references.

Property	Orientation	Normal Spacing	Frequency	Persistence	Trace Length Estimator	Intensity Estimator P ₂₁	Density Estimator P ₂₀	Block Volume	Block Shape
Method	Histogram Rose diagram	Scanline		Window mapping	Circular window			From joint sets' spacing	
Reference	(Priest 1993)			(Pahl 1981)	(Dershowitz and Herda 1992; Mauldon et al. 2001)			(Palmstrøm 1996a; Palmstrøm 2001)	

A synthetic dataset was created to gradually build the code. Three discontinuity sets (consisting of about 300 traces, in order to achieve statistical stability) were generated with strike and length following a normal distribution and a negative exponential law, respectively. The details of the synthetic dataset are illustrated in Figure 6.4. Successively, the 2-D quantitative analysis was performed on the trace map (more than 1000 traces in sector C) of the case study and validated by comparing the results of the conventional geosstructural and geomechanical surveys. To this aim, 50 discontinuities measured in the field in the same area were reported in Dips software (Rocscience 2021) and classified into two main joint sets by means of stereographic projections (lower hemisphere). For each discontinuity set, the measurements of the spacings and trace lengths were elaborated in a spreadsheet to derive their mean values (Figure 6.3).

To test the potentiality of the 2-D analysis for geological modelling, a Discrete Fracture Network model was generated on a 20-m-high cliff located at *Lama Monachile* site, about 90 m east from the study site. The top of the rock cliff is not visible because of the presence of the Calcarenite di Gravina Fm. and the overlying buildings. For this reason, the fracture pattern of the Calcare di Bari Fm. analyzed at *Pietra Piatta* site was used as an analogue model to generate the fracture sets by means of the FracMan software (Golder Associates 2018), after validation in the field of its representativeness for the cliff. The volume (grid) was generated from the top and bottom surfaces of the mesh of the rock mass using a stochastic distribution of the bedding surfaces, which was determined from measurements on a vertical scanline on the point cloud and validated on the field. Successively, for each discontinuity set, the mean strike, standard deviation, minimum, maximum, mean spacing, and trace length derived from the MATLAB routine were used to generate the fractures in the DFN model.

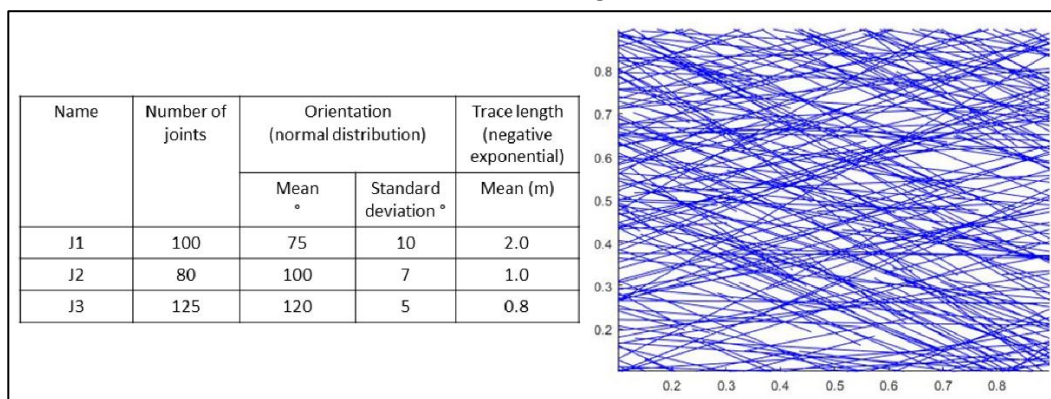


Figure 6.4: To the left, table illustrating the experimental dataset used to create the routine; to the right, graphical representation of the three joint sets.

6.2.6. Workflow of the MATLAB Routine

The MATLAB routine performs the 2-D quantitative analysis on orthophotos by combining digital scanline and areal sampling methods. In detail, rectangular/square windows (Pahl 1981; Priest 1993) are applied to identify the main discontinuity sets according to the orientation of the discontinuities, and to estimate their trace length and persistence as well. Circular windows (Mauldon et al. 2001; Rohrbaugh et al. 2002) are performed to characterize the fracture network by identifying the mean trace length, intensity, and density estimators of the whole dataset. Areal sampling is preferred to scanlines to avoid sampling inaccuracies such as orientation and length biases. In particular, orientation bias consists of the underestimation of the intensity of discontinuities, which are not perpendicular to a scanline (Terzaghi 1965; Priest 1993; Mauldon and Mauldon 1997), and length bias refers to the undersampling of short discontinuities with respect to the longer ones (Baecher and Lanney 1978; Einstein and Baecher 1983; La Pointe et al. 1985). Since areal measures allow analyzing larger areas than scanlines (Watkins et al. 2015), curtailment bias caused by the loss of information of discontinuities extending beyond the sampling windows (Priest 1993) is also reduced. However, scanlines are indispensable to define 1D properties, such as normal spacing and fracture frequency of the discontinuity sets (Priest and Hudson 1981; Priest 1993).

Aimed at creating a tool for a 2-D quantitative analysis of discontinuities, available to the scientific community and easily reproducible on different case studies, the MATLAB routines are accessible through an editable template (Figure 6.7).

The 2-D quantitative analysis is achieved in four steps (Figure 6.6):

1. graphical representation of the discontinuities;
2. semi-automatic classification of the discontinuity sets;
3. characterization of one discontinuity set; and
4. characterization of the fracture network.

The routine reads the first line of the template, in which the “STEP” command is defined. This allows performing the analyses described in Sections 2.6.1 and 2.6.2, by simply adding 1, 2, 3, or 4 next to “STEP”. Precise instructions for the users are in the help and instruction files (Supplementary Material).

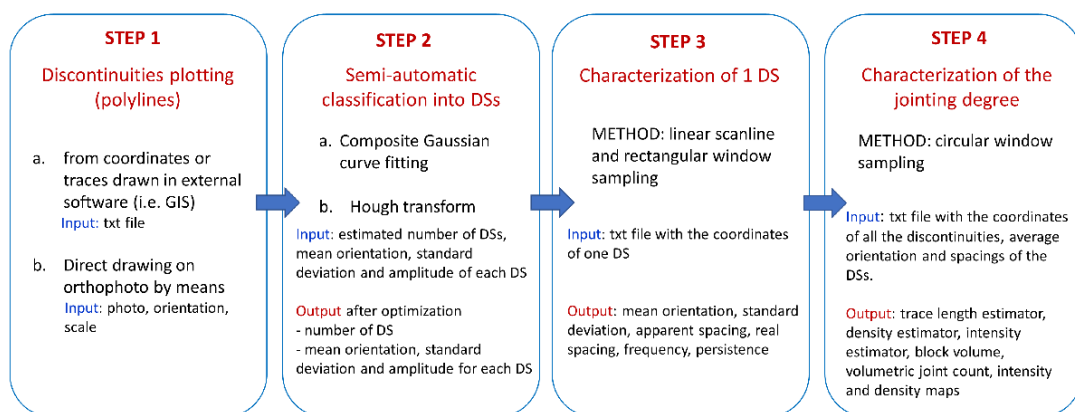


Figure 6.5: Step 1: workflow of the MATLAB routine developed for the 2-D analysis of the discontinuities.

Two methods are used to identify and classify the discontinuity sets according to the orientation of the traces.

- Method 1: fitting of the composite Gaussian curve

The orientations of the polylines are calculated from the strike of their segments and weighted according to their lengths by means of a square/rectangular window applied on the selected dataset. The number of discontinuity sets is identified by means of an innovative method, which semi-automatically plots the strike distribution of the traces on an appositely developed Graphic User Interface (GUI) (Figure 6.7). The MATLAB routine automatically extracts the distribution of each discontinuity set, with peaks corresponding to their mean strike. Three sliders allow adapting the strike distributions of each discontinuity set by interactively changing their mean, standard deviation, and amplitude. A line parallel to the x axis is used to filter out the “noise”, derived from random discontinuities, which might be present in traces from real rock masses. After the manual adjustment of the curves, an optimization algorithm is run so that the sum of the curves and noise fits the raw orientation histogram curve. In detail, the best solution to fit the synthetic curve on the original curve is obtained by minimizing the differences between the curve of the real data and the experimental composite curve by means of the *fminunc* (Find minimum of unconstrained multivariable) algorithm, which is based on the BFGS Quasi-Newton method (Fletcher 1970; Broyden 1970; Goldfarb 1970; Shanno 1970):

$$\text{Raw_histogram_orientation} - (\sum \text{histo_orientation}_i + \text{noise}) = 0 \quad \text{Eq. 6.1}$$

where the two terms are the orientation histogram of the dataset and the sum of the experimental curves, respectively.

Successively, the MATLAB routine calculates the intersections between each normal curve, corresponding to the limits of the orientation of each joint set, to classify them. Therefore, for each DS, a file with the coordinates of the polylines' nodes is created.

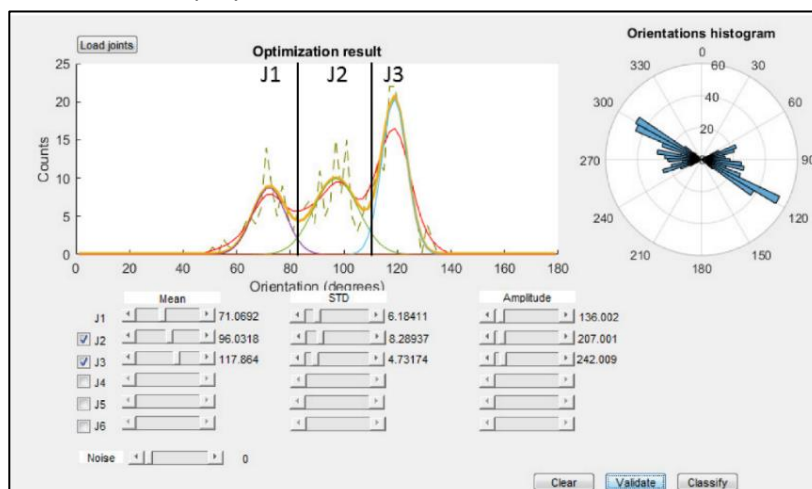


Figure 6.7: Step 1: Optimization process for the semi-automatic identification of the discontinuity sets forming the synthetic dataset by means of Gaussian composite curve fitting. The classification limits for each discontinuity set are represented by the black lines. The red and orange lines represent the smoothed curve and the estimation of the three joint sets, respectively; the purple, green, and blue curve represent J1, J2, and J3, respectively.

- Method 2: Hough transform

A second method to classify the discontinuity sets is based on the Hough transform, a technique introduced by Hough (1962) for machine analysis of bubble chamber photographs and later extended and adapted to image analysis and computer vision to detect shapes such as lines, circles, and ellipses in images (Rosenfeld 1969; Duda and Hart 1972; Leavers 1993; Mukhopadhyay and Chaudhuri 2015). Based on the Hough transform method, the MATLAB routine converts each joint in a new frame with the x and y axes corresponding to the orientation (θ) and distance from the origin (r) of each polyline, respectively (Figure 6.8). In this new frame, each joint is defined by a point, and joints with similar orientation are aligned on the vertical axis, allowing the identification of the main discontinuity sets (Figure 6.9).

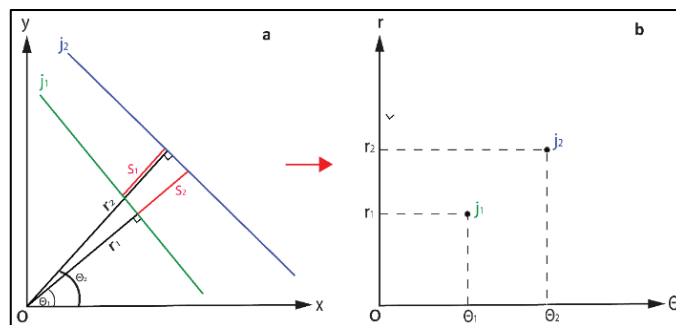


Figure 6.8: Conversion of discontinuity traces in the Hough frame. (a) representation of two discontinuity traces in the Cartesian reference frame, where r is the distance from the origin and θ is the angle orthogonal to the strike; (b) conversion into the Hough frame (θ, r): the lines are converted into points. The main discontinuity sets can be identified as points aligned on the r axis.

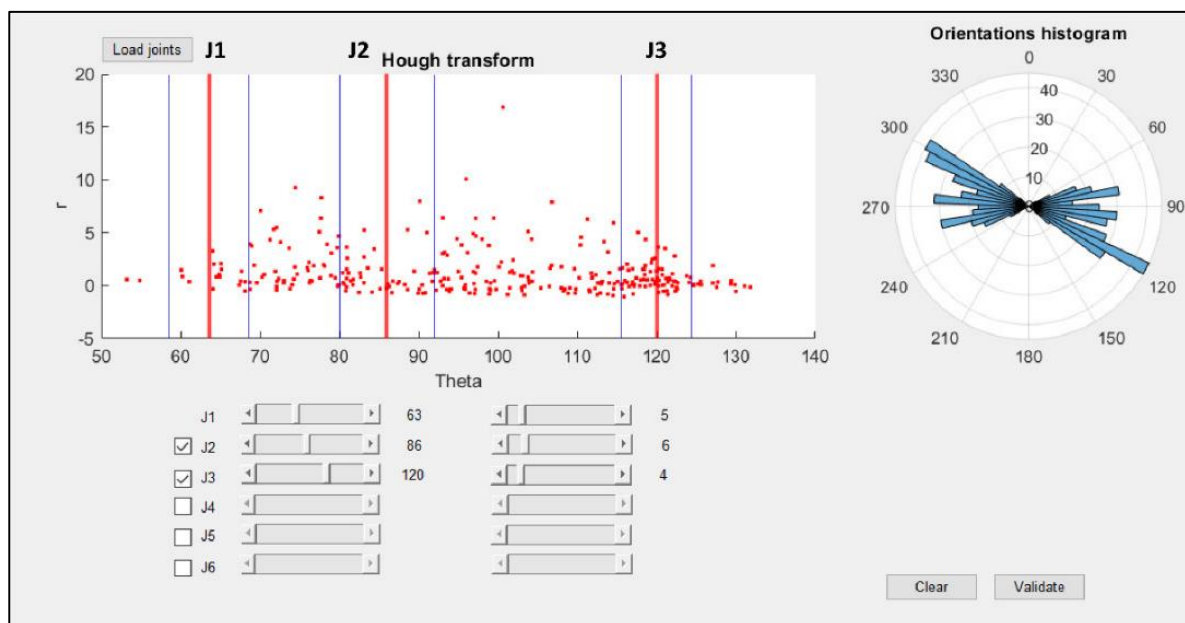


Figure 6.9: Application of the Hough transform for the classification into discontinuity sets.

Spacing

The normal spacing of the discontinuity set (i.e., distance between two adjacent discontinuities belonging to the same set measured along a sampling line orthogonal to the mean direction of the set)

can be calculated with two different methods according to their persistence. In a 2-D analysis, the discontinuity persistence, which is the areal extent or size of a discontinuity within a plane, can be expressed as the limit length ratio along a given line on a joint plane (Einstein et al. 1983):

$$K = \lim_{L_S \rightarrow x} \sum_i \frac{l_{s_i}}{L_S} \quad \text{Eq. 6.2}$$

where L_S is the length of a straight line segment S and l_{s_i} is the length of the i -th joint segment in S . In other words, persistent joints are represented by continuous traces, while non-persistent joints are formed by more segments separated by rock bridges.

- Spacing for non-persistent joints

After importing the file of one DS, the scanline method is applied to derive the normal spacing and frequency, with the assumption of non-persistent discontinuities. One or more scanlines can be plotted according to the user's setting. Specifically, one linear scanline can be automatically plotted in the middle of the frame orthogonal to the mean strike of the discontinuity set. To find the best scanline, the routine plots several randomly oriented scanlines and selects the one intersecting the highest number of joints. Alternatively, the user can pick the two endpoints or pick one endpoint and set the mean strike of the scanline directly on the trace map. In addition, a series of scanlines parallel to the reference one can be traced, with the possibility to choose the number of samples and the Δx – Δy interval. Considering the spatial variation of the strike of the traces, even if belonging to the same discontinuity set, Terzaghi's correction (1965) is applied to each line intersecting the scanline to avoid orientation bias:

$$S = \frac{S_{app}}{\sin \theta} \quad \text{Eq. 6.3}$$

where S , S_{app} , and θ are the corrected spacing, apparent spacing, and the minimum angle between the scanline and the mean strike of the discontinuity set. After the calculation of the apparent (not corrected) and normal spacings, the histogram and cumulative distributions of the spacings are plotted on the interface.

The normal spacing is then calculated as the mean distance of the intersections between the scanline and the traces (Figures 6.10 and 6.11). The mean fracture frequency is obtained as the inverse of the mean normal spacing.

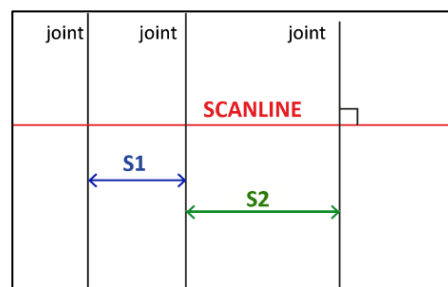


Figure 6.10: Normal set spacing calculated along a scanline (red) perpendicular to the mean direction of the joint set (black) (modified after Slob 2010).

- Spacing for persistent joints

The Hough transform method is applied to calculate the spacing of persistent joints, assuming infinite lengths (Figure 6.8). For each two adjacent joints, the spacing is calculated as the mean difference along the r axis. In the Cartesian frame, the mean spacing is given by:

$$S = \frac{S_2 + S_1}{2} = \frac{[r_2 - r_1 \cos(\theta_2 - \theta_1)] + [r_2 \cos(\theta_2 - \theta_1) - r_1]}{2} \quad \text{Eq. 6.4}$$

where S_2 and S_1 are the orthogonal distances between adjacent traces and θ_2 and θ_1 are the angles between the joints and the scanline.

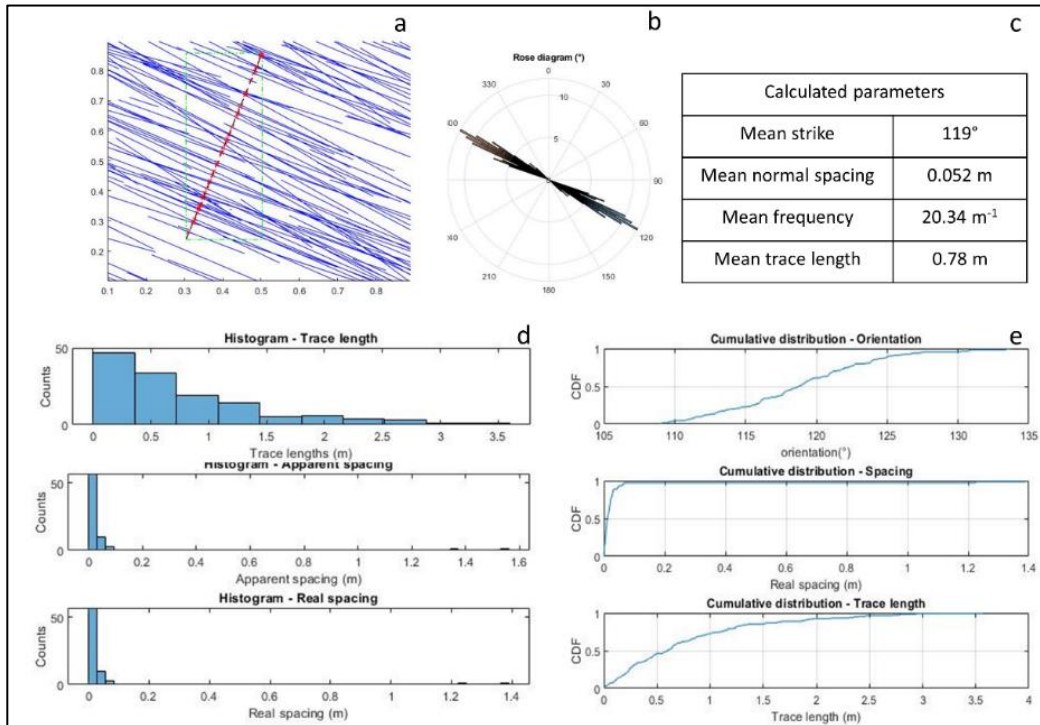


Figure 6.11: Step 3: linear scanline on JS3. (a) automatic generation of a linear scanline (black, dotted line) perpendicular to the mean strike of the discontinuity set; the discontinuities and their intersections with the scanline are, respectively, represented by the blue lines and the red crosses; (b) rose diagram of the JS; (c) table of the calculated parameters; (d) histograms of the calculated parameters; (e) cumulative distributions of the calculated parameters.

Trace Length

The mean trace length of the discontinuity set is obtained by calculating the mean length of the polylines in the dataset. In addition, the histogram and cumulative frequency of the trace lengths are plotted on the interface.

Persistence

The method proposed by Pahl (1981) is used to estimate the persistence of the discontinuity set by plotting a rectangular window on the trace map. The percentage of coverage area can be chosen by the user or drawn on the trace map. The discontinuities transecting the window n_2 (two intersections between the polyline and the window), contained in the window (n_0) (both endpoints are located in the window), and the total discontinuities (n_{tot}) are automatically counted, so that the mean persistence is calculated as:

$$\mu = \frac{w h}{w \cos \phi + h \sin \phi} \frac{n_{tot} + n_2 - n_0}{n_{tot} - n_2 + n_0} \quad \text{Eq. 6.5}$$

where w and h are, respectively, the length and height of the window and ϕ is the acute angle between the mean strike of the discontinuity set and the height of the window (Figure 6.12). The persistence is calculated in two steps:

1. over the entire dataset (Figure 6.13 a);
2. by dividing the dataset with a grid and calculating the persistence for each element of the grid (Figure 6.13 b,c).

The results of both methods are provided by the routine.

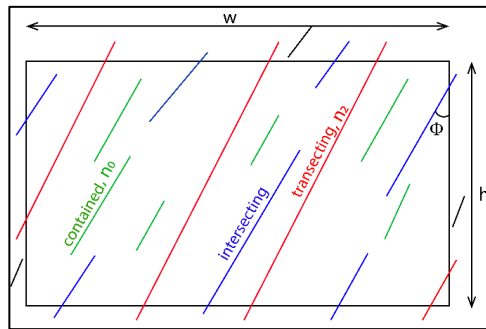


Figure 6.12: Method for persistence calculation (modified after Jaboyedoff et al. 1996).

6.2.6.2. Characterization of the Fracture Network

Intensity, Density, and Trace Length Estimators

Information on the fracture network is collected through the method proposed by Mauldon and Dershowitz (2000) by means of circular window sampling. A grid of circles is plotted on the polylines to compute the mean trace length P_{11} , the intensity P_{21} , and the density P_{20} estimators:

$$P_{11} = \frac{\pi r}{2} \frac{\bar{n}}{\bar{m}} \quad P_{21} = \frac{\bar{n}}{4r} \quad P_{20} = \frac{1}{2\pi} \frac{\Sigma m}{\Sigma r^2} \quad \text{Eq. 6.6}$$

where \bar{n} is the mean number of intersections between the polylines and the circles and m and \bar{m} are the total and mean number of endpoints of the polylines contained in the circles, respectively. The radii of the circles are automatically determined according to the number of circles covering the sampling area, which can be set by the user in the main interface of the routine. This method works if at least 2 circles are selected (i.e. not all the endpoints are located inside the circles).

Additionally, a persistence map can be plotted, with each pixel representing the persistence calculated in one circle.

Block Volume and Shape

Formulas illustrated by Palmstrøm (1996a,2001) are used to derive the block volume V_B , volumetric joint count J_v , and block shape factor β of the blocks delimited by discontinuities. As stated by Palmstrøm, rock blocks are formed from the intersection of at least three discontinuity sets with different directions. Since rock volumes cannot be determined by means of 2-D analyses from plan views, a third dimension is needed to apply this procedure. If only two joint sets are detected on the trace map, the third dimension can be represented by the bedding. If the rock mass is characterized by

more than three discontinuity sets, a rough estimation of the volumes can be achieved by considering the prevailing ones.

The block volume can be estimated from the mean spacings of the discontinuity sets:

$$V_B = \frac{S_1 S_2 S_3}{\sin \gamma_1 \sin \gamma_2 \sin \gamma_3} = \frac{S_1 S_2 S_3}{\sin \gamma_3} \quad \text{Eq. 6.7}$$

where S_1, S_2, S_3 are the mean spacings of the three discontinuity sets delimiting the rock volume, and $\gamma_1, \gamma_2, \gamma_3$ are the angles between the discontinuity sets. Since the method is applied to joint sets perpendicular to the strata ($\gamma_1 = \gamma_2 = 90^\circ$), only the angle between the two joint sets (γ_3) is taken into account.

For rock masses characterized by only one or two discontinuity sets, rock blocks can be formed when additional random joints cross the volume. In this case, the equivalent block volume can be calculated as:

$$V_B \approx 50 S_1^3 \text{ for only one joint set with mean spacing } S_1 \quad \text{Eq. 6.8}$$

$$V_B \approx 5 S_1 S_2 \text{ for two joint sets with mean spacing } S_1 \text{ and } S_2 \quad \text{Eq. 6.9}$$

The volumetric joint count is calculated as the number of joints per unit volume:

$$J_v = \sum \frac{1}{S_i} \quad \text{Eq. 6.10}$$

where S_i is the mean spacing of the i -th discontinuity set. The third dimension is needed to estimate J_v .

The parameters α_2 (medium spacing/smallest spacing) and α_3 (largest spacing/smallest spacing) are automatically calculated to determine the block shape factor β and to plot it on the chart shown by Palmstrøm (1996a) in order to classify the block shape:

$$\beta = \frac{(\alpha_2 + \alpha_2 \alpha_3 + \alpha_3)^3}{\alpha_2 \alpha_3^2} \quad \text{Eq. 6.11}$$

6.3. Results

6.3.1. Results of the Synthetic Dataset

The synthetic dataset was classified into three discontinuity sets by means of the Hough Transform and composite Gaussian curve fitting (Tables 5 and 6).

Table 6.5. Main parameters for the generation of the synthetic dataset and classification of the joint sets by means of Gaussian composite curve fitting.

Synthetic Dataset				Results of the Classification-Gaussian Fitting			
Name	Mean Strike	St. Deviation	N. of Joints	Name	Mean Strike	St. Deviation	Amplitude
J1	75°	10°	100	J1	71°	6°	136
J2	100°	7°	80	J2	96°	8°	207
J3	120°	5°	125	J3	118°	5°	242

Table 6.6. Results of the classification of the joint sets by means of Hough transform method.

Results of the Classification-Hough Transform			
Name	Mean Strike	Minimum Strike	Maximum Strike
J1	63°	53°	73°
J2	86°	44°	98°
J3	120°	112°	128°

Figures 6.11 and 6.13 illustrate, respectively, the results of the scanline and rectangular window sampling on the discontinuity set JS3 to calculate the mean orientation, normal spacing, trace length, and persistence.

The mean intensity, density, and trace length estimators of the synthetic dataset, calculated by means of circular windows, are 177.15 m^{-1} , 25.38 m^{-2} , and 1.14 m , respectively. A graphical representation of the results is given by means of intensity and density maps (Figure 6.14).

The block volume, volumetric joint count, and shape factor were calculated as 0.01 m^3 , 33.81 m^{-1} , and 40.58 , according to the mean strike and normal set spacings. Moderately flat blocks were identified on the diagram in Figure 6.15.

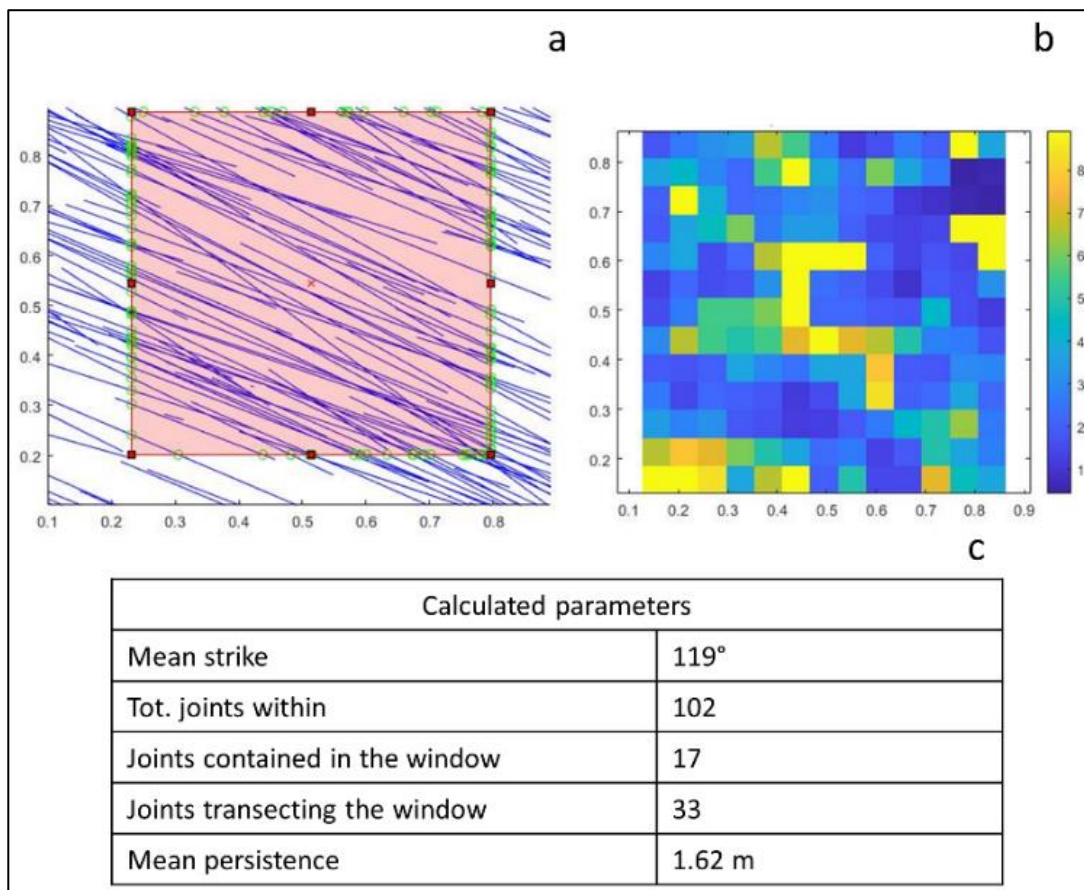


Figure 6.12: Step 3: persistence calculation for JS3. (a) persistence calculated over a rectangular window (colored in red). The intersection between the traces (blue) and the window are represented by the green circles; (b) persistence calculated for each element of the grid in which the window was subdivided; (c) results of the persistence calculation for the rectangular window.

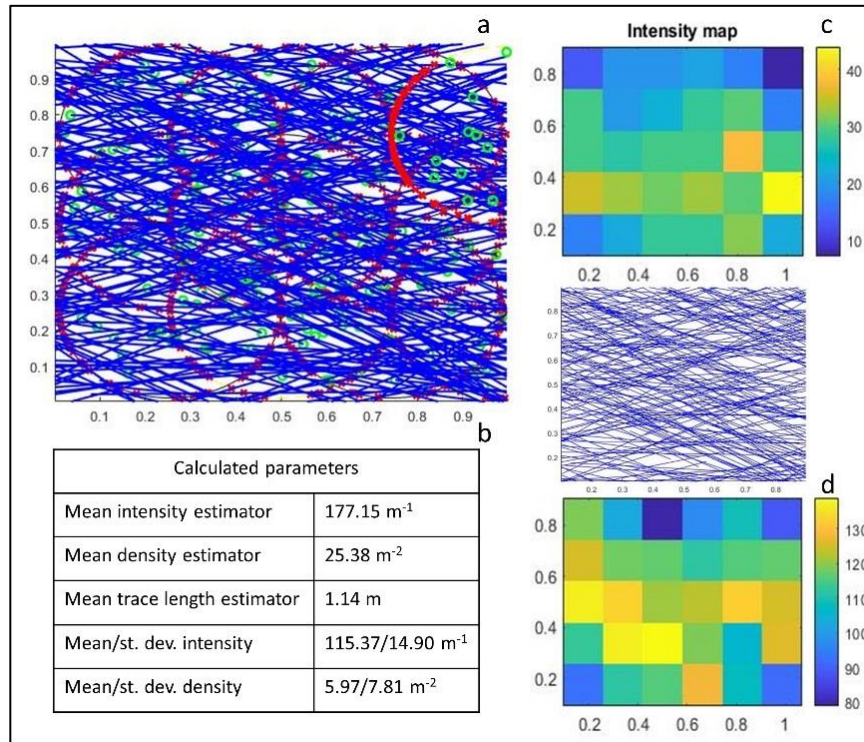


Figure 6.13: Step 4: generation of circular windows for the calculation of mean intensity, density, and trace length estimators of the whole dataset. (a) graphical representation of the circular windows, where the extremities of the traces transecting the circles are represented in green, and the traces intersecting the window (one intersection) are marked by the red circles. (b) Table of the calculated parameters; (c) intensity and (d) density maps of the dataset.

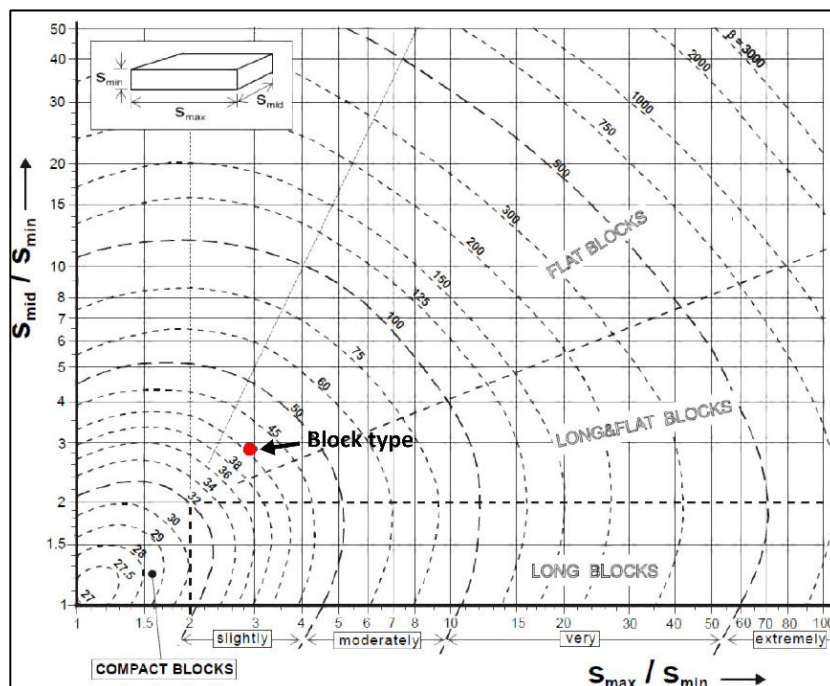


Figure 6.14: Step 4: semi-automatic estimation of block shape and volume of the experimental dataset (modified after Palmstrøm 1996 a).

6.3.2. Application to the Case Study

The results of the mean strike, spacing, trace lengths, and persistence, both for the MATLAB routine and field surveys, are shown in Figures 6.16 and 6.17. Three scanlines at different positions were traced on both the trace maps of JS1 and JS2 to investigate the effect of scanline positions on the estimation of the normal set spacing (Figure 6.18), as well as the fracture density and intensity maps (Figure 6.19). A sensitivity analysis was performed to estimate the effects of the sample size and number of circles to calculate the persistence, trace length intensity, trace intensity, and trace density (Figure 6.20). An equivalent block volume, equal to 0.03 m^3 , was obtained from the spacings of the two main discontinuity sets and the mean layer thickness (S_0 , calculated on exposed sub-vertical surfaces in the point cloud of the rock mass), using Equation (6.7). The reported volumetric joint count is 9.94 m^{-1} , while the block shape factor ($\beta = 28.98$) corresponds to a compact, slightly flat block shape, in agreement with field observations. The results of the MATLAB routine are reported in Table 6.7.

Moreover, the routine was applied on the trace maps of sectors A, B, D, and E to identify potential differences in the number of discontinuity sets, as well as their mean strikes. Figure 6.20 shows the differences between the mean joint sets detected in sector C and sector B.

The statistics of strike, spacing, and trace length of the joint sets extracted from the MATLAB routine (Figure 6.22) were used to generate a realistic Discrete Fracture Network model of the Calcare di Bari Fm along the cliff located at *Lama Monachile* site.

The data obtained from sector C were considered to be representative for the cliff after validation in the field (Figure 6.2). It is remarked that, since this chapter deals with 2-D analyses from data collected from orthophotos, the DFN model includes only the sub-vertical joint sets characterized by means of the MATLAB routine. A more advanced and realistic DFN model, which is out of the scope of this chapter, can be generated by integrating the results reported above with data collected on the field or on point clouds, especially concerning the bedding surfaces.

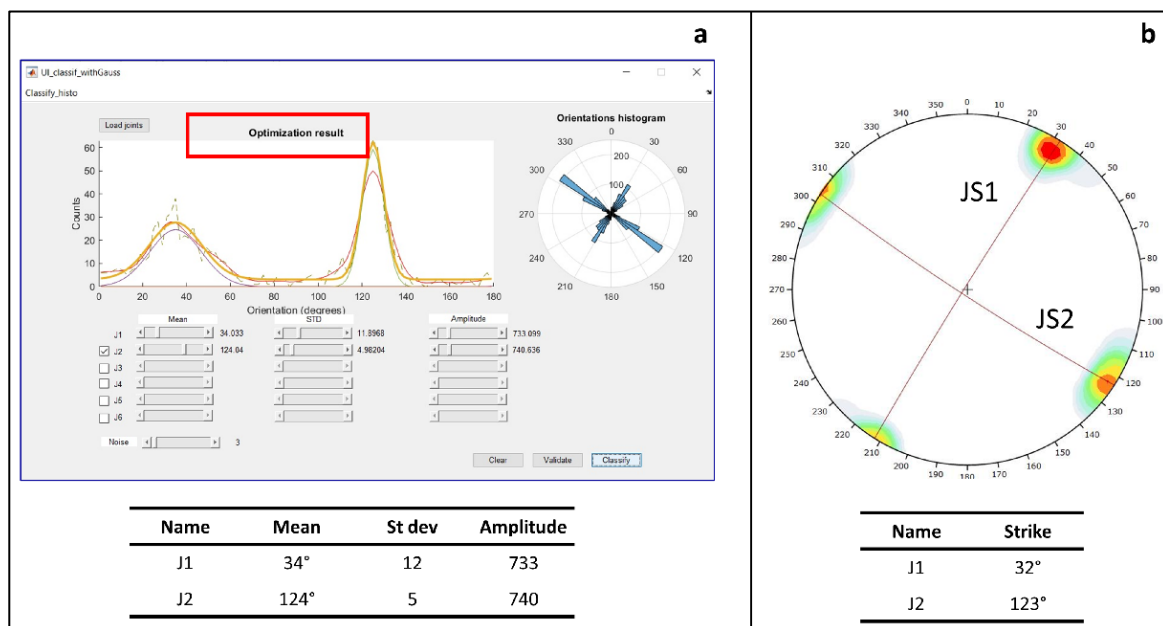


Figure 6.15: Results of the semi-automatic classification of the traces into joint sets (a) and of the data obtained from on-site geostructural and geomechanical surveys (b).

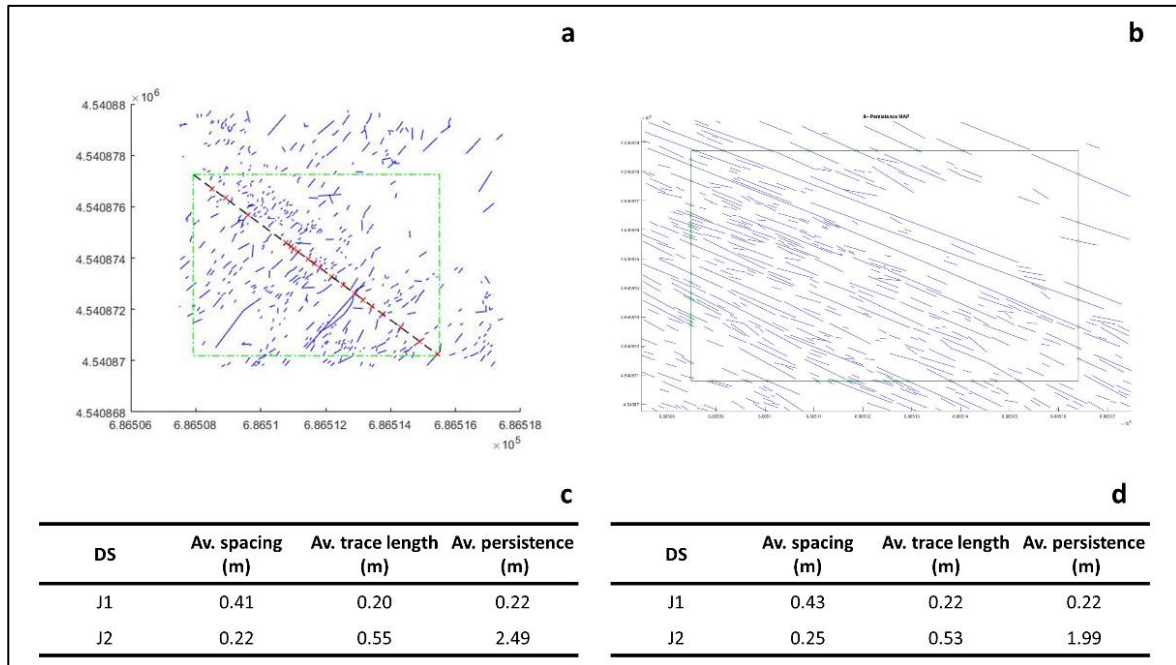


Figure 6.16: Results of the linear scanline and persistence methods. (a) Graphical representation of the scanline generated perpendicularly to J1; (b) graphical representation of the rectangular window generated for the calculation of the persistence of J2; (c) table of the parameters calculated with the MATLAB routine for J1 and J2; (d) table of the parameters measured in the field by means of conventional geostructural and geomechanical surveys.

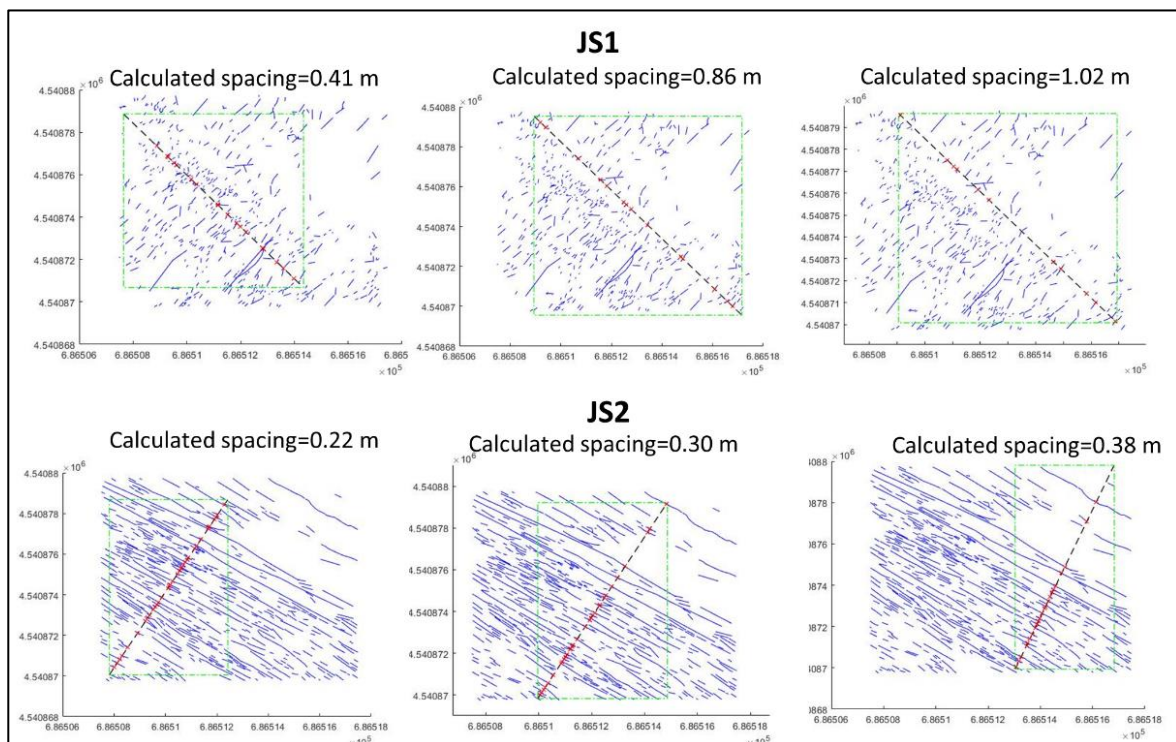


Figure 6.17: Normal set spacings calculated with different scanline locations.

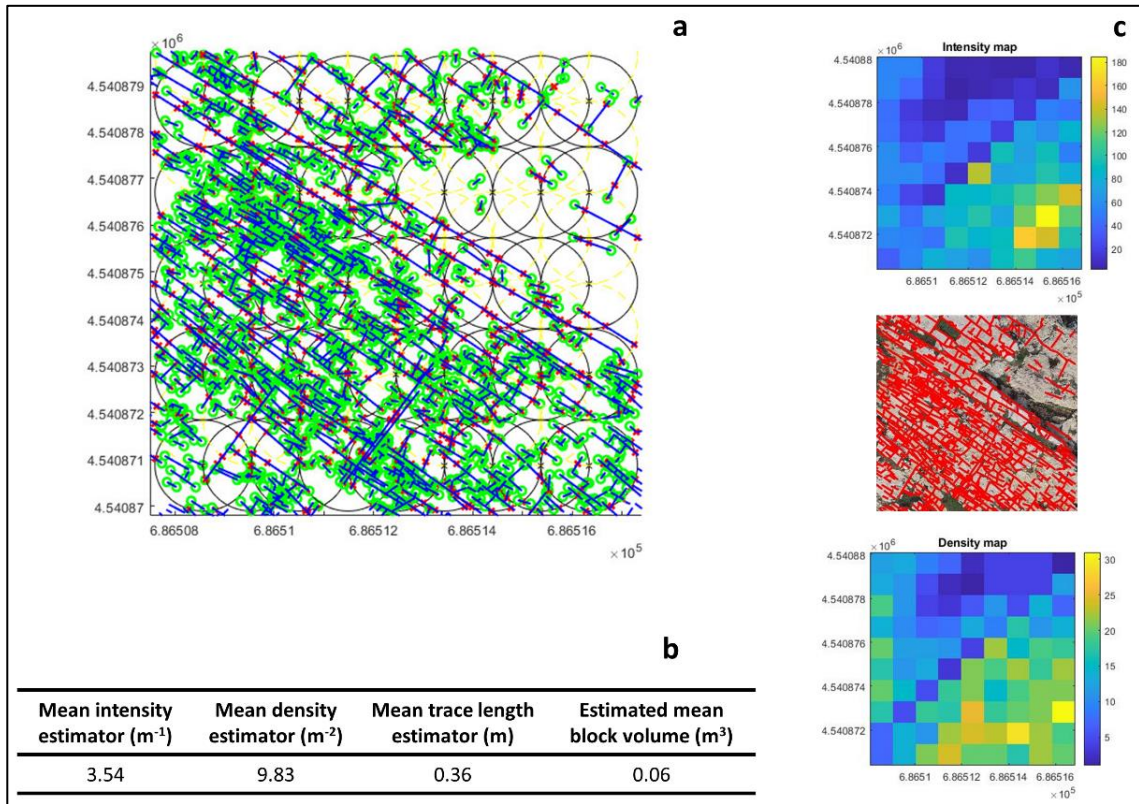


Figure 6.18: Evaluation of the jointing degree of the study area. (a) Graphical representation of the circular windows' method; (b) resuming table of the calculated mean intensity, density, and trace length estimators and block volume; (c) intensity and density maps of the analyzed area.

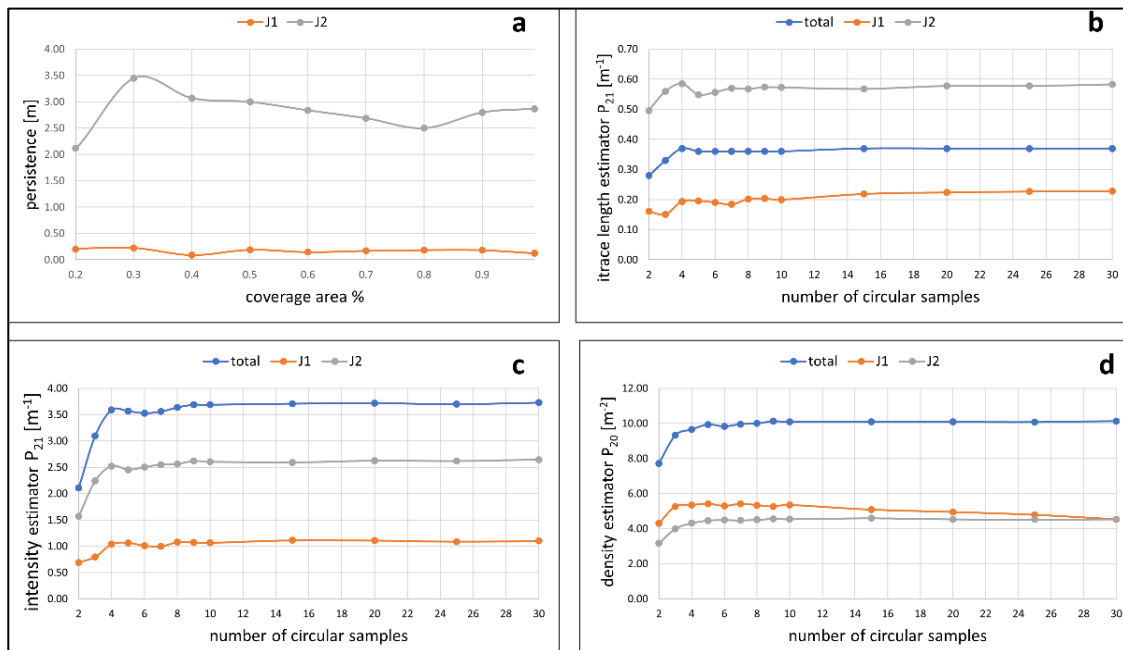


Figure 6.19: Sensitivity analysis to estimate the effects of the sample size and number of circles to calculate the persistence (a), trace length intensity (b), trace intensity (c), and trace density (d).

Table 6.7. Characterization of the discontinuity sets and of the jointed area with the MATLAB routine.

Characterization of Discontinuity Sets						
Identified DS	Strike			Normal Spacing (m)	Mean Trace Length (m)	Mean Persistence (m)
	Mean Strike (°)	St. Dev. (°)	Amplitude			
J1	34	12	733	0.41	0.20	0.22
J2	124	5	740	0.24	0.55	2.49
Characterization of the Joint Network						
Intensity Estimator $P_{21} (m^{-1})$	Density Estimator $P_{20} (m^{-2})$	Trace Length Estimator (m)	Volumetric Joint Count $J_v (m^{-1})$	Block Volume $V_B (m^3)$	Block Shape Factor β	Block Shape
3.54	9.83	0.36	9.94	0.06	28.98	compact

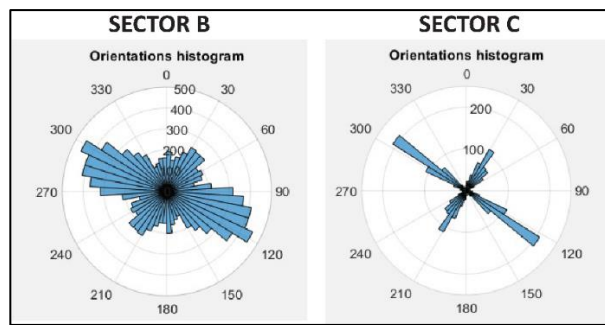


Figure 6.20. Rose plot of sector B (left) and sector C (right).

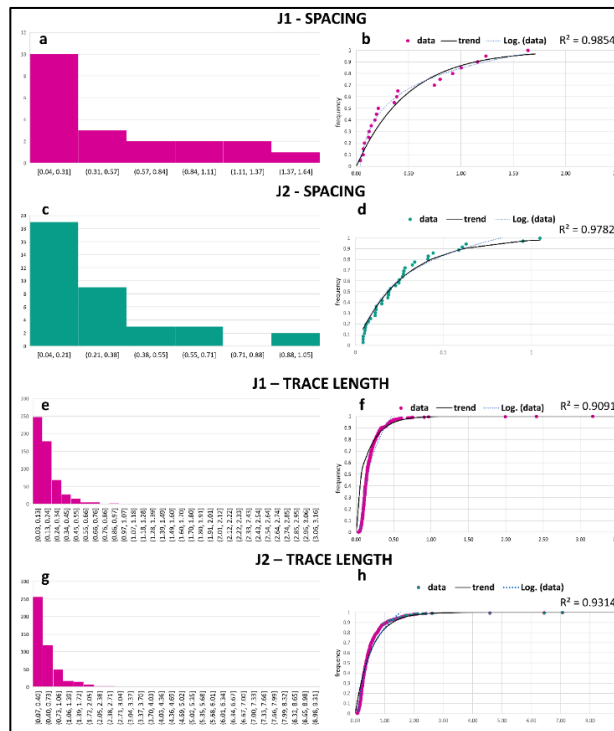


Figure 6.21: Histograms and cumulative frequencies of the spacing (a–d) and trace length (e–h) of the main joint sets for the generation of the Discrete Fracture Network Model.

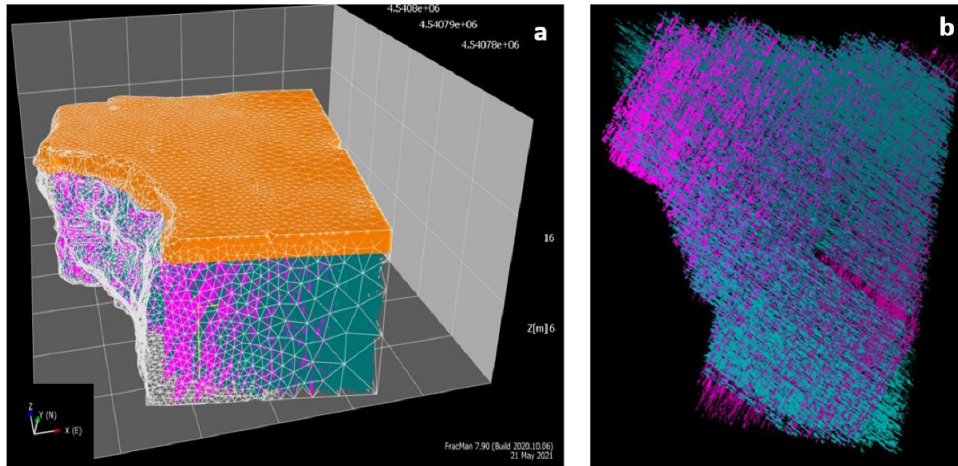


Figure 6.22: (a) DFN model created with the software FracMan for a sector of the rock cliff at *Lama Monachile* site, located at a distance of about 90 m from the study area. The fracture generation was limited to the Calcare di Bari Fm., which was the object of a specific geosurvey. (b) Top view of the discontinuities generated in the DFN model of the Calcare di Bari Fm. at *Lama Monachile* site. The joint sets were generated using the results of the quantitative analysis of the discontinuities carried out at *Pietra Piatta* site. J1 and J2 are, respectively, colored in magenta and green.

6.4. Discussion

With regards to the synthetic dataset, the Gaussian fitting method recognized 3/3 discontinuity sets, with a difference of 2° for the strike of each discontinuity set and up to 1° for the standard deviation (Figure 6.7). On the contrary, some difficulties were found for the classification by means of the Hough transform method, because discontinuities with too similar orientations create unprecise clusters in the theta-r diagram (Figure 6.9). It was found out that the histogram fitting method for classification is reliable for a high number of traces (at least 50), since it is based on statistic procedures, regardless of the orientations of the discontinuity sets. The Hough transform method is recommended for lower numbers of discontinuities, provided that the mean strikes of the sets are not too close (Figure 6.23).

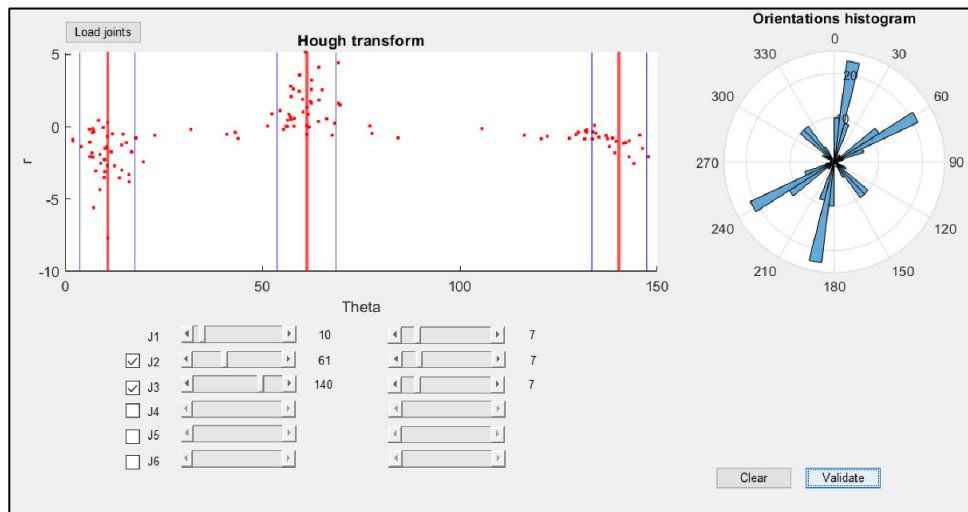


Figure 6.23: Correct classification by means of the Hough transform for three synthetic discontinuity sets with not too close orientations. The mean strike used for generating the synthetic dataset were 10°, 60°, and 140°.

Based on these observations, the traces of the study site were processed with the Gaussian fitting method and achieved good results with respect to the geosstructural-geomechanical analysis carried out on the study site. The mean strikes of the discontinuity sets J1 and J2 obtained from the MATLAB routine were 34° and 124° . These results were in agreement with the data collected by means of field surveys (32° and 123° for J1 and J2, respectively). The same standard deviation value of the strike of J2 was found both for the MATLAB routine and for the on-site surveys, while a difference of about 4° was detected for J1. The standard deviations differed 4.2° for J1 and 0° for J2. This difference can be related to a major dispersion of the poles of the discontinuities, which was not detected in the field because of the lower number of sampled discontinuities (50).

With regards to the spacing estimations, the mean values were 6 cm (J1) and 2 cm (J2), higher than the data measured in the field. Several tests were carried out in order to obtain results in agreement with the field observations because the calculated mean spacing can vary significantly with the position and strike of the scanline (Figure 6.18). In this perspective, it must be remarked that it is fundamental to use a proper dataset as input: unmapped traces in the orthophoto or objects/vegetation covering the joints could determine fewer intersections between the traces and the scanline, leading to an overestimation of the spacing. In addition, the possibility to apply linear samples in different locations of the dataset may help to understand the spatial variability of the calculated parameter, to identify potential changes of the stress field, or to detect sectors with different geomechanical behavior.

It is remarkable that, in agreement with field observations, both the spacing and trace lengths of J1 and J2 followed an exponential negative distribution, indicated by very good R-Squared values (in the range of 0.91–0.98, Figure 6.22), as found by many authors (Priest and Hudson 1976; Baecher and Lanney 1978; Wallis and King 1980; Priest 1993) for a variety of rock masses.

A difference of 0.5 m was found in the estimation of the mean persistence of J2. It is believed that this difference is attributable to the different sampling methods for its estimation. Indeed, the persistence of discontinuities is one of the most difficult parameters to estimate in the field (ISRM 1988) and, during the conventional geosstructural surveys, this property was roughly approximated from the trace lengths, according to Priest (1993). However, this approach can lead to size and censoring bias (Cruden 1977; Priest and Hudson 1981), thus undersampling smaller discontinuities and censoring surfaces, which extend beyond the sampling area. Indeed, since the traces belonging to J1 were not truncated or censored because both the majority of their terminations fell within the area sampled in the field, no difference was found with respect to the results of the MATLAB routine. Based on these observations, it is believed that the results of the MATLAB routine are more reliable because the estimation of the persistence by means of Pahl's method (1981) takes into account the number of discontinuities transecting and contained in the sampling window, thus avoiding censoring bias. However, care should be taken when choosing the size of the coverage area. As pointed out by Priest (1993), this method is not suitable when all the discontinuities transect the window (the persistence would be infinite) and when no discontinuities are contained in the window (the persistence would be zero). For this reason, the sampling window should be chosen so that at least one trace is located inside it. In addition, it was observed how the persistence varied with different dimensions of the sampling area (Figure 6.20a): Although two datasets are not enough to identify potential mathematical relations, it is evident that significantly different results were obtained by changing the area covered by the sampling window, especially for long traces (e.g., J2 curve in Figure 6.20a). As a matter of

fact, Priest and Hudson (1981) observed that persistence can vary up to more than 50% of the real value by changing the rectangular sampling window location and size.

The additional parameters calculated from the routine such as mean intensity, density, and trace length estimators give useful information for the identification of more fractured zones, represented by the yellow pixels in Figure 6.19c. Moreover, the fracture abundance of one discontinuity set constituted by non-parallel, subparallel, or non-persistent traces can be expressed by means of fracture intensity (Mauldon et al. 2001). In fact, the estimation of fracture abundance for non-parallel traces by means of spacing is rather unclear because the distance is not unique. With regards to the length, intensity, and density estimators, sensitivity analyses pointed out that more accurate results can be achieved by choosing about 6–8 circles: A minor number would give unreliable results, while a larger number could cause unnecessary long computational times (Figures 6.12 b,d).

Concerning the block volume, this method relies on the assumption that the blocks are determined by the totally persistent discontinuities; therefore, the block volume could be underestimated. More precise results can be obtained directly from measurements on 3-D point clouds, with respect to 2-D analyses.

The script for the semi-automatic identification of discontinuity sets can be used in different zones of an orthophoto to identify potential deformation zones or changes of the stress field. Figure 6.21 depicts a shear deformation zone in sector B detected from two additional joint sets (with mean strikes N–S and E–W) and higher standard deviations of the strike of J1 and J2 with respect to sector C, which are the result of non-linear shear structures.

The presented approach helps to calculate the geometrical parameters of the discontinuity sets affecting a rock mass in a less time-consuming, more precise, and safer manner compared to the conventional geosstructural and geomechanical surveys. However, a complete characterization of rock masses also requires information on roughness, wall strength, aperture, filling, and seepage of the discontinuities that cannot be estimated from 2-D analyses. The determination of wall strength, nature of filling, and seepage requires direct measurements at the site, while only centimetric apertures could be measured on high-resolution remote sensing products (Gigli and Casagli 2011). In addition, recent advances in the literature proposed methods to determine the roughness/undulation of discontinuities from point clouds (Gigli and Casagli 2011; Oppikofer et al. 2011; Tatone and Grasselli 2013; Li et al. 2019).

In this perspective, the MATLAB routine can contribute to identify the main discontinuity sets from discontinuity traces in low-relief rock masses characterized by discontinuities perpendicular to the strata and combined with point clouds, to localize accessible and representative surfaces in order to measure the non-geometrical properties, as well as to collect information not visible from 2-D images, by means of conventional techniques. Finally, the combination of geometrical and non-geometrical properties of discontinuities and point clouds or meshes can be used to create discrete models for quantitative stability analyses in rock masses by means of discontinuum approaches. It is specified that interactions among individual fractures or discontinuity sets (fracture topology) need to be defined to characterize rock mass permeability, especially when dealing with fault damage zones and reservoir modelling (Smith 1980; Smith et al. 1990; Taylor and Dietvorst 1991; Knai and Knipe 1998; Fisher and Knipe 2001; Wiprut and Zoback 2002; Jolley et al. 2007; Martinelli et al. 2020). In this perspective, the MATLAB routine developed could be improved through the characterization of fracture nodes and terminations (Manzocchi 2002; Saevik and Nixon 2017) to define the network connectivity and its influence on the rock mass physics (Zimmerman and Main 2004; Laubach et al. 2018).

6.5. Conclusions

This study illustrated a new MATLAB tool for 2-D semi-automatic analyses of discontinuities from high-resolution orthophotos obtained by means of remote sensing techniques, aimed at characterizing rock masses. Although similar tools were presented in the literature (Gigli and Casagli 2011; Healy et al. 2017), they are not publicly available or do not provide a complete description of discontinuities for rock mass characterization. Therefore, the routine was compiled by adapting and updating the standard methods (i.e., scanline, rectangular, and circular window sampling) for a complete and detailed analysis of discontinuity traces, which is preferable to 3-D point cloud analyses for low-relief rock masses or man-made excavations, in a user-friendly digital environment.

The code was initially built on a synthetic dataset and successively tested and validated on a case study by comparing the results of the conventional geosstructural and geomechanical surveys carried out in the same area. The routine was developed in the form of consecutive steps, which can be singularly run depending on the objective of the analysis. In addition, the calculations do not require high-performance computers but can be run on standard laptops in a few seconds.

A new feature allows the semi-automatic identification and classification of the mean discontinuity sets in a Graphic User Interface, by fitting Gaussians curves on the strike histograms of the traces or by using the Hough transform, according to the number and approximate orientation of the discontinuity sets. In addition, the normal spacing of the discontinuity sets can be calculated both for persistent and non-persistent joints. The procedure for the classification and characterization of the discontinuity sets, as well as the estimation of the jointing degree of the analyzed area, can be easily repeated in different parts of an orthophoto to identify potential changes of the mean discontinuity sets, implicating modifications in the stress field, which can be further investigated on site for structural analyses.

Future developments may concern the improvement of the unit block volume calculation through direct measurements on the areas delimited by discontinuities rather than from spacing and orientation of the main discontinuity sets. Moreover, an automatic-semiautomatic method for drawing the discontinuities on orthophotos could exceptionally decrease the time required for data pre-processing.

Eventually, future research topics could deal with the conversion of the proposed Hough Transform method in the 3-D space to detect discontinuity surfaces from point clouds or triangulated surfaces. The results could be compared with the methods available in the literature to validate the technique's reliability or identify potential discrepancies (Wang and AlRegib 2014; Leng et al. 2016; Vera et al. 2018). In addition, the Gaussian fitting method could be implemented to have 3-D histograms of the orientations (x = dip, y = dip direction, z = frequency) and a composite Gaussian surface instead of a curve, to detect discontinuity planes from 3-D models. Finally, discontinuity sets' spacings could be calculated both from the 3-D Hough Transform Method and from the 3-D Gaussian fitting method and compared with each other.

Supplementary Materials: The QDC-2-D routine and the instruction file are available online in the GitHub public repository at: <https://github.com/charlottewolff/-QDC-2-D>, accessed on 5 December 2021.

PART III

INTEGRATION OF REMOTE SENSING
AND CONVENTIONAL SURVEYS FOR
STABILITY ANALYSES

Chapter 7 Multidisciplinary approach for stability analyses of rock masses: integration of field surveys, remote sensing techniques and numerical modelling

Abstract: This chapter aims to present a methodological approach to perform advanced three-dimensional analysis of rock slopes by combining conventional geostructural and geomechanical surveys with remote sensing techniques supported by Unmanned Aerial Vehicle (UAV) systems. The proposed methodology is divided in four main steps: 1) conventional geostructural and geomechanical surveys and physical and mechanical characterization of the rock materials; 2) remote sensing surveys, processing and interpretation for the 2-D and 3-D quantitative characterization of the discontinuity sets; 3) validation by means of field-inspection and set-up of the geomechanical model; 4) stability assessment by means 3-D and 2-D numerical modelling, the latter optimized through the stochastic generation of discontinuity sets by means of Discrete Fracture Network (DFN) techniques. The final section discusses the implementation of discontinuities in Finite Element Method (FEM) models through the use of equivalent models with reduced deformations and strength properties and explicit interfaces, by comparing the failure mechanisms. Moreover, different surface processes detected in the field are simulated using both approaches, and the differences are commented. Further improvements of the methodology are reported in the conclusion section.

7.1. Introduction

Rock slope failures in urban areas represent a high risk for human lives and infrastructures, and in some cases are capable to damage the cultural, natural and archaeological heritage of protected sites, as reported by many researchers (e.g. Matsuoka and Sakai 1999; Carreño and Kalafatovich 2006; Borgatti et al. 2006; Wei et al. 2014; Cafiso and Cappadonia 2019; Garduño - Monroy et al. 2020). These examples clearly show that advanced methodologies for landslide susceptibility assessment are needed in our society, especially in poor countries and in places of historical importance, to carry out hazard mapping, aimed at developing the most proper plan mitigation actions and prevention measures.

In the last decades, remote sensing techniques such as terrestrial or airborne *Light Detection and Ranging* (LiDAR), terrestrial and *Unmanned Aerial Vehicle* (UAV) *Structure from Motion* were combined with conventional field surveys to achieve a comprehensive geostructural and geomechanical characterization of the investigated area. The integration of remote sensing techniques is related to the possibility to acquire data of large extent areas in reasonably short time and safe conditions, as well as to create permanent databases (Feng and Röshoff 2004; Haneberg and Findley 2006; Jaboiedoff et al. 2008; Sturzenegger and Stead 2009).

Many researches illustrate how remote sensing techniques can be used for rock slope investigations, with particular emphasis on the generation of 3-D models and on the detection of discontinuities and

potential unstable areas (Lemy and Hadjigeorgiou 2003; Feng and Röshoff 2004; Stead et al. 2004; Abellán et al. 2006; Coggan et al. 2007; Jaboyedoff et al. 2008; Runquiu and Xiujun 2008; Haneberg 2008; Armesto et al. 2009; Ferrero et al. 2009; Mah et al. 2011; Salvini and M. 2013; Santo et al. 2013; Salvini et al. 2013; Gauthier and Hutchinson 2015; Francioni et al. 2015; Donati et al. 2017). The state of the art on the potential applications, advantages and limitations of several remote sensing technologies for rock slope characterization was reported by various authors (Slob and Hack 2004; Westoby et al. 2012; Tofani et al. 2013; Abellán et al. 2014; Abellan et al. 2016; Cawood et al. 2017; Stead et al. 2019).

In addition, several interesting studies were addressed to the semi-automatic and automatic extraction of the discontinuities of jointed rock masses from point clouds (Buyer and Schubert, 2016; Ferrero et al., 2009; García-Sellés et al., 2011; Gigli and Casagli, 2011; 2007; Olariu et al., 2008; Pagano et al., 2020; Palma et al., 2017; Riquelme et al., 2014) or triangulated surfaces (Lato and Vöge, 2012; Li et al., 2016; Slob et al., 2005; Vöge et al., 2013) and to the quantitative characterization of the discontinuity sets, as well as block size and shape estimation (Gigli and Casagli 2011; Sturzenegger et al. 2011; Oppikofer et al. 2011; Riquelme et al. 2015, 2018; Buyer and Schubert 2017, 2018; Kong et al. 2020, 2021). A detailed review of these techniques was proposed by Battulwar and co-workers (Battulwar et al. 2021).

If, on the one hand, the products of remote sensing techniques have been addressed to very targeted studies (i.e. calculation of joints spacing or roughness), on the other hand they have been used in broader contexts for a variety of engineering geology applications. Indeed, the use of Digital Elevation Models (DOMs) as input in numerical modelling software, combined with data collected on the field and in a geotechnical laboratory, would be a great step towards more realistic three-dimensional analyses, and this is still rarely explored. As a matter of fact, early numerical methods to assess rock mass stability are based on conceptual models which do not explicitly implement information collected using remote sensing techniques (Krahn and Morgenstern 1976; Radbruch-Hall et al. 1976; Kalkani and Piteau 1976; Hart 1993; Carranza-Torres et al. 1997; Sitar and MacLaughlin 1997; Bye and Bell 2001; Guadagno et al. 2003; Eberhardt et al. 2005; Gischig et al. 2011, to mention a few).

Despite conceptual models allow the definition of the stability conditions of the investigated area, as well as the identification of the processes which can trigger future failures or the interventions which can stabilize on-going failures, better accuracy can be accomplished by introducing geometrical elements collected using drones or laser scanners. For instance, overhanging volumes or caves (e.g. karst caves in carbonate rock masses), where failures may occur, can be easily modelled using the derived point clouds or triangulated surfaces.

This shortcoming has been pointed out in a few recent studies, which hence were dedicated to the combination of conventional techniques and DOMs to carry out advanced 3-D stability analyses. For instance, some methods to carry out kinematic analyses and detect rockfalls source areas, taking advantage of point clouds, were proposed in the literature (Francioni et al. 2015; Menegoni et al. 2021). Further, other studies optimized deterministic limit-equilibrium analyses with terrestrial digital photogrammetry and laser scanning (Ferrero et al. 2009; Gigli et al. 2011; Brideau et al. 2011; Salvini and Francioni 2013; Salvini et al. 2013; Martino and Mazzanti 2014).

In the last decade, point clouds and meshes were introduced in the most advanced 3-D numerical modelling techniques to study rock mass stability by means of different approaches.

At present, there is no standard procedure for the modelling of rock slopes (Jing and Hudson 2002; Jing 2003; Nikolic et al. 2016). On the one hand, rock masses are schematized as continuum models

(Francioni et al. 2015; Mancini et al. 2017; Fazio et al. 2019, to mention a few), where, eventually, the contribute of joints is taken into account by reducing the rock mass properties (Dershowitz et al. 2004; Hoek 2007). Recent continuum-based FEM softwares are able to introduce a few discontinuities in the form of interface elements, as proposed by some authors (Bfer, 1985; Fazio et al., 2019; Goodman et al., 1968; Jamshid et al., 1973). It is specified that, in this case, the continuity of the model is preserved, hence the detachment of blocks is not allowed, given the fundamental condition of displacements compatibility at element nodes (Jing 2003; Hammah et al. 2008). On the other hand, discontinuum-based techniques discretize the domain into blocks connected by discontinuities and solve the equations of motion through continuous detection and treatment of the contacts between blocks (Corkum and Martin 2002; Ghirotti and Genevois 2007; Brideau et al. 2011; Firpo et al. 2011; Kalenchuk et al. 2011; Boon et al. 2014; Francioni et al. 2014; Spreafico et al. 2016; Montiel et al. 2020). For these models, large displacements such as rotation, fracture opening and complete detachment are allowed (Jing 2003).

More complex hybrid approaches combine continuum and discontinuum techniques to model the transition from continuum to discontinuum conditions by explicitly simulating fracture and fragmentation processes (Munjiza et al. 1995; Munjiza and John 2002; Coggan et al. 2003; Eberhardt et al. 2004; Stead et al. 2004a, b, 2006; Fabian et al. 2007; Vyazmensky et al. 2010; Lisjak and Grasselli 2014; Bonilla-Sierra et al. 2015; Lollino and Andriani 2017).

In most cases, the discontinuities of numerical models are represented by means of deterministic approaches through the implementation of segments or planar surfaces respectively for 2-D and 3-D applications. However, for moderately jointed rock masses the detection of discontinuities, whether by means of field surveys or with the help of remote sensing technologies, might be quite challenging and time-consuming, with the drawback of applying simplifications. In addition, the discontinuities are generally assumed as persistent, though it is well known that failures in rock masses are caused by the interaction of non-persistent discontinuities that propagate through coalescence, according to a step-path mechanism (Lajtai 1969; Jennings 1970; Sjöberg 1996; Goodman and Kieffer 2000; Diederichs 2003; Kemeny 2006; Frayssines and Hantz 2006; Brideau et al. 2009; Zhang et al. 2017). It is clear that randomly located, non-persistent discontinuities play a key role in rock slope stability and should be considered when dealing with numerical modelling, although this aspect is quite challenging (Wasantha et al. 2014; Fan et al. 2015). In this perspective, some pioneering researches proposed the use of Discrete Fracture Network (DFN) models (Merrien-Soukatchoff et al. 2012; Scholtès and Donzé 2012; Lisjak and Grasselli 2014; Havaej et al. 2016; Salvini et al. 2017; Lei et al. 2017; Montiel et al. 2020) to stochastically generate more realistic discontinuity sets, based on the probabilistic distribution of variables such as orientation, persistence and spatial location of the discontinuities. However, stability analyses by coupling DFN approaches and continuum, discontinuum or hybrid techniques are limited to a few researches (Elmo 2006; Elmo and Stead 2010; Mas Ivars et al. 2011; Merrien-Soukatchoff et al. 2012; Havaej et al. 2016; Montiel et al. 2020; Zhang et al. 2020) and further investigations need to be carried out.

This chapter deals with the combination of the studies reported in the previous sections to achieve more realistic stability analyses, fully exploiting the potentiality of remote sensing techniques. A complete procedure for advanced 3-D stability analyses in rock slopes, based on the integration of laboratory investigation, conventional and remote sensing geostructural and geomechanical analyses, to produce advanced geomechanical models is proposed. Since, as stated above, there is not a unique solution to model jointed rock masses, different numerical modelling approaches were tested.

The procedure, developed on an appropriate case study, is based on four main steps: 1) conventional geostructural and geomechanical surveys and physical and mechanical characterization of the rock materials; 2) remote sensing surveys, processing and interpretation for the 2-D and 3-D quantitative characterization of the discontinuity sets; 3) validation by means of field-inspection and set-up of the geomechanical model; 4) stability assessment by means of 3-D numerical modelling. During the last step, the role of surface processes acting on the site were investigated by means of 2-D models. Both continuum-based and discontinuum-based FEM approaches were tested to observe the effects of the chosen method on the resulting factor of safety (FS) and failure mechanisms. In addition, the results of each method were compared to the field observations and to those from the DOM to assess their reliability. It is pointed out that the reported method is a preliminary stability assessment, through which the continuum approach was used to evaluate the global-scale stability of the case study, considering that the site is characterized by non-persistent discontinuity sets, modelled by means of a DFN approach. Alternative methods (i.e. coupled DFN-discontinuous/hybrid approaches) may be taken into account for future specific researches aimed at comparing the results with those obtained through this study.

7.2. Methodology overview

The proposed methodology is developed according to the following procedure:

a. Conventional geological, geostructural and geomechanical field surveys

They aim at the identification of the rock materials and at the characterization of their physical and mechanical properties by means of microscopy inspection and laboratory tests carried out on representative samples. The effects of saturation and weathering on the mechanical strength of the rock materials can also be evaluated at the laboratory scale to analyze potential disturbances of rock slopes in marine environments. Focus is given to the quantitative analysis of the discontinuities which play a key role in the stability of discontinuous rock masses (Cardia et al., 2021; Goodman, 1976; Hudson and Harrison, 2000; Jaboyedoff et al., 2009; Kainthola et al., 2015; Priest, 1993). Both the intact rock and the discontinuities are taken into account to classify the rock mass for engineering applications, according to the most appropriate system. Moreover, the typical occurred, on-going and potential failure mechanisms are identified in the field.

b. Application of remote sensing techniques

Advanced techniques such as airborne/terrestrial LiDAR or digital photogrammetry can be used to generate high-resolution georeferenced point clouds and triangulated surfaces to obtain a Digital Outcrop Model (DOM) which can be easily consulted for further investigations and to measure surfaces, areas and volumes. Several bi-dimensional and three-dimensional procedures for the quantitative analysis of the discontinuity sets can be applied to achieve an advanced and comprehensive characterization of the rock mass. The choice of the method for the geostructural and geomechanical analysis from DOMs depends on several factors, like accessibility, weather conditions and financial and time availability (Stead et al., 2019).

c. Validation and generation of the geomechanical model

The results of the remote sensing techniques are validated by means of direct comparison with the data collected by means of conventional field surveys. Moreover, both datasets are combined to produce a detailed geomechanical model of the rock mass.

d. Preliminary identification of the main kinematics

Field observations and geometric information from point clouds or triangulated meshes are used to carry out preliminary kinematic analyses to identify the potential failure mechanisms.

e. Detection of the typical instability mechanisms

The results of kinematic analyses are validated or discarded based on field observations and remote sensing interpretation. Simultaneously, the main processes contributing to the rock slope instability are outlined to assemble a conceptual model of the case study for further investigations by means of numerical modelling.

f. Numerical modelling

Three-dimensional and bi-dimensional numerical techniques are performed to assess the global-scale stability of the rock slope, using an advanced geomechanical model built through the integration of quantitative on-site observations and remote sensing interpretation. Thanks to the opportunity of using complex constitutive laws and to easily re-calibrate the model, the geological processes acting on the case study can be investigated to detect the critical conditions which can cause failure.

Detailed information on the methodology carried out for each section are reported in the sections below.

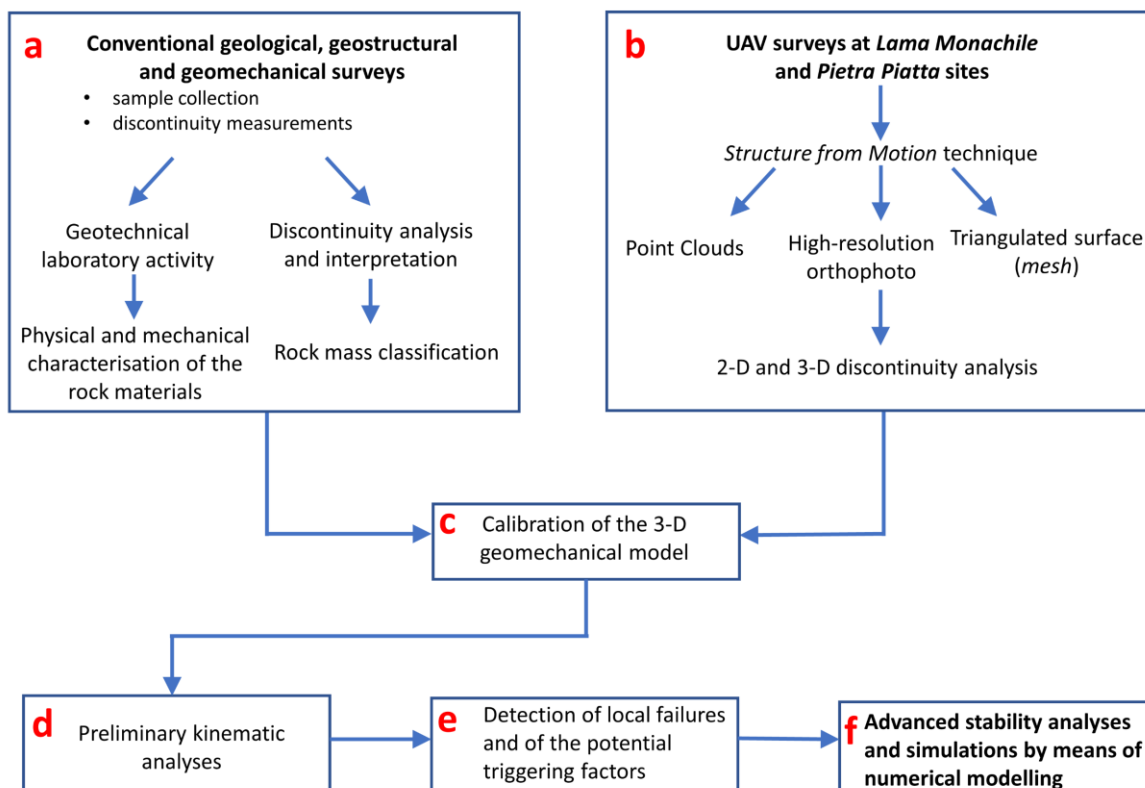


Figure 7.1: Workflow of the proposed methodology applied on the study site.

7.3. Case study: Polignano a Mare (southern Italy)

7.3.1. Geological and morphologic setting

The study area is located in the municipality of Polignano a Mare, on the Adriatic side of the Apulian coast (SE Italy). From a geologic standpoint, the site belongs to the eastern part of Murge plateau, an emerged part of the Apulian foreland, made up of a 3 km-thick Cretaceous succession related to a wide carbonate platform, unconformably overlain by Quaternary deposits of shallow agitated marine waters (Ricchetti et al. 1988; Tropeano and Sabato 2000). The Cretaceous formation cropping out at the study site is constituted by whitish to greyish, well-stratified limestones and dolostones belonging to the Calcare di Bari Fm., whilst the Plio-Pleistocene deposits are formed by massive yellowish calcarenites associated to the Calcarenite di Gravina Fm. Due to carbonate nature of the rock masses, karst processes represent the main morphological agent in the Murge, with most of the landforms having a karst origin (Sauro 1991; Parise 2011).

The Adriatic Apulian coast develops through a series of marine terraces subparallel to the coastline, linked by small scarps, which develop from about 150 m a.s.l. until reaching the sea. The main drainage network is represented by slightly incised flat-bottomed karst valleys, locally named *lame*, which are typically dry except during intense rainfall events (Parise 2003; Parise et al. 2013). These morphostructures are the result of the superimposition of regional uplift and glacio-eustatic sea-level changes, started from the middle Pleistocene, but have also been explained as related to sapping (Ciaranfi et al. 1988; Mastronuzzi and Sansò 2002).

In the study area, the prevailing morphology is constituted by platforms, promontories and embayments covered by coastal erosion deposits (*pocket beaches*). It is to these structures that the study sites belong (Figure 7.4): the *Pietra Piatta* site (“flat stone” translated from Italian) is an about 6000 m² low-relief platform developing from 10 m a.s.l. to the current coastline and *Lama Monachile* site is one of the mentioned karst valleys cutting a 20 m high sub-vertical cliff and reaching the sea as well. While in the first area the Calcare di Bari Fm. only is visible (due to erosional processes the Quaternary deposits crop out in the inner zone), at the second site the succession of limestones and dolostones overlain by the Calcarenite di Gravina Fm. is cropping out. The base of the cliff is covered by loose materials of variable grain size forming a *pocket beach* that attracts many tourists throughout the year.

Notches, karst conduits and caves, which are well visible along the cliff, reduce rock mass strength and represent a serious hazard for stability (Parise 2010, 2015; Gutiérrez 2010; Gutiérrez et al. 2014). In addition, bedding surfaces and joints are widespread in the Calcare di Bari Fm., causing evident anisotropy. As a matter of fact, several niches along the sub-vertical walls and boulders occasionally visible below the sea level indicate local failures and even small-size potential instabilities, which cannot be excluded, can seriously endanger people’s safety, especially considering the high density of tourists in the beach for large part of the year. Moreover, the old town of Polignano a Mare is partially built and carved on the weaker calcarenites, which are highly susceptible to chemical and mechanical degradation (Calcaterra and Parise 2010), therefore potential instabilities can damage buildings of architectural and historical relevance. The situation is even farther complicated by diffuse presence of karst features, such as caves of variable size, conduits and voids, which certainly cause an additional decrease in the resistance of the carbonate rock mass, also favouring the flow of water within it (Andriani and Parise 2015, 2017). To all of this, human actions along the coast must be added, which

often result in accelerating the cliff retreat processes, as observed along the whole Apulian coastline (Delle Rose and Parise 2004; Andriani and Walsh 2007; Pellicani et al. 2015; Lollino et al. 2021). Despite the landslide risk is larger for *Lama Monachile* site for the mentioned factors, geostructural and geomechanical surveys were performed also at *Pietra Piatta* site, which might be less interesting from a tourist point of view, but is essential for quantitative discontinuity characterization, as the lack of Quaternary deposits, which cover the top of the sub-vertical cliff, allows to map discontinuity traces affecting the intensely jointed limestones and dolostones.

7.3.2. Physical and mechanical characterization of the rock materials

The studied outcrop is constituted by a 20 m thick carbonate succession made up of calcarenites belonging to the Calcarenite di Gravina Fm., unconformably overlying the limestones and dolostones of the Calcare di Bari Fm.

Petrographic examination with transmitted light was performed on thin sections of representative samples, using optical polarizing microscopy. The Calcare di Bari Fm., which at *Lama Monachile* site is formed by sub-horizontal thin to thick bedded layers (0.05 – 1 m), for a total thickness of 15 m, is constituted by two lithofacies which alternate in the carbonate succession. The first facies is represented by whitish-greyish micritic limestones (mudstone-wackstone) made up of bioclasts, such as benthic foraminifera and peloids, dispersed in a micritic matrix (Figure 7.2a-b). This facies shows a partial dolomitization process associated to magnesium-rich waters. The second facies is constituted by grey-light brown dolostones (crystalline dolomite) in which rhombohedral dolomite crystals totally obliterated the original texture of the limestones (Figure 7.2b-c). The Calcarenite di Gravina Fm. overlies the Cretaceous bedrock through an angular erosional unconformity and reaches a total thickness of about 8 meters at the main profile of reference, although the upper boundary is not well visible because of the buildings located at the top of the cliff. It is made up of poorly cemented, yellowish-greyish coarse to medium-grained calcarenites (grainstone) with fragments of lamellibranchs, brachiopods, gastropods, serpulids, calcareous algae and benthic foraminifera (Figure 7.2e-f).

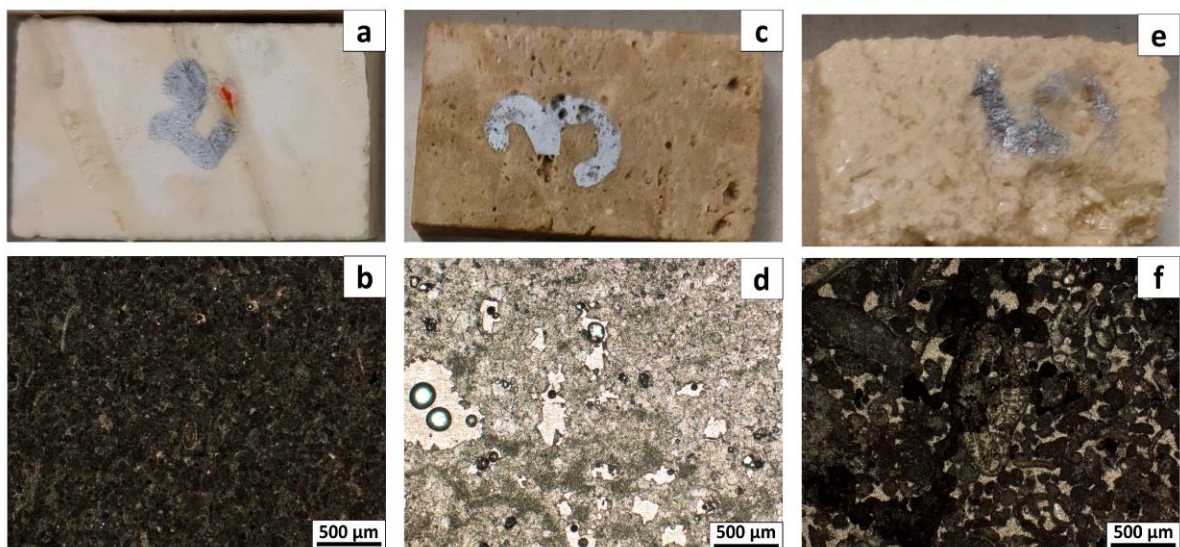


Figure 7.2: Polished slabs (above) and thin sections microphotographs (below) in plane-polarized light of the lithofacies cropping out at *Lama Monachile* site: (a-b) Calcare di Bari Fm.- mudstone-wackstone facies; (c-d) Calcare di Bari Fm. - crystalline dolomite facies; (e-f) Calcarenite di Gravina Fm. - grainstone.

Albeit the three lithofacies are characterized by a similar chemico-mineralogical composition (carbonate-rich), they were classified in three different lithotechnical units, distinguished on the basis of specific physical and mechanical properties, related to different depositional fabric and diagenetic processes. In detail, the first unit is represented by Plio-Pleistocene transgressive deposits of the Calcare di Gravina Fm., while two lithotechnical units, corresponding to the whitish limestone and the greyish dolostone facies, constitute the Calcare di Bari Fm. Heavy physical and chemical weathering, which is visible in the form of voids and cavities caused by karst processes, salt crystallization, wetting and drying cycles and biological activity affects all lithotechnical units in a heterogeneous way (Fookes et al. 1988; Zezza and Macrì 1995; Price 1995; Andriani and Walsh 2007; Andriani and Pellegrini 2014; Andriani et al. 2015). As a matter of fact, the rock mass strength decay is evident in the calcarenites, which is subjected to microcracking, dissolution of the fine cementation and granular disaggregation (Andriani and Walsh 2007), as demonstrated by several failed blocks on the shore bottom. It has to be recalled that the calcarenite rocks, widely cropping out in many sectors of Apulia, are heavily interested by development of karst caves and landforms (Parise 2011). On the other hand, notches and sea caves are present in the Calcare di Bari Fm. as a combination of wave undercutting and chemical solution, especially in the salt and fresh water mixing area (Delle Rose and Parise 2004). In addition, the dolomitic facies, even though less interested by dissolution with respect to the limestones, shows too evidence of minor karst features.

Aimed at defining the mechanical behaviour of the materials cropping out at *Lama Monachile* site, representative rock samples were collected in the field for further investigation. Due to difficult logistics, calcarenite rock samples belonging to the same lithofacies were collected in an open-pit quarry at a distance of about 1500 m, while rock blocks of the Calcare di Bari Fm. were sampled in accessible areas at the bottom of the cliff.

Following the standard procedures outlined by ISRM (ISRM 1979a; Ulusay 2015), laboratory measurements and tests were carried out on 35 samples to determine the dry density, total porosity (n), water adsorption (w_a), degree of saturation (S_r), *Brazilian* tensile strength (σ_t) and uniaxial compressive strength (σ_c) of the rock materials, respectively on disk (diameter=60 mm, height=30 mm) and cylindrical (diameter=60 mm, height=140mm) samples (Table 7.1). At the study site, aerosol particles transported by the marine spray tend to deposit in the pores and cavities of the exposed rock materials, where salt crystallization causes stresses within the pores, disaggregation and crumbling of the surfaces (Blanchard and Woodcock 1980; Amoroso and Fassina 1983; Zezza and Macrì 1995; Torfs and van Grieken 1997). Being rock mass degradation particularly intense in the more porous Calcare di Gravina Fm (Andriani and Walsh 2002), tests on saturated samples were carried out to investigate any variations in the mechanical behaviour of the calcarenite units. Water adsorption and degree of saturation were calculated after the immersion and suspension of the specimens in distilled water at 20°C for 48 hours and the successive saturation under vacuum (80 kPa), without removing the specimens from the water basket, following the procedure established by Andriani and Walsh (2002). Specific gravity (G_s) values of 2.70, 2.70 and 2.74 were assumed respectively for the calcarenites, limestones and dolostones on the basis of their chemical composition.

The Calcare di Gravina unit has a dry density ranging between 1.48 and 1.72 Mg/m³, with a mean value of 1.60 Mg/m³ and a saturated density ranging between 1.88 and 2.06 Mg/m³, with a mean value of 1.97 Mg/m³. The porosity, water adsorption and degree of saturation are in the range 36-56%, 23-90%, 74-100%, respectively. With regard to the mechanical properties, the *Brazilian* tensile strength is in the range 0.54-0.96 MPa in dry conditions and 0.41-0.83 MPa under saturated

conditions. The uniaxial compressive strength minimum and maximum values are 3.71 and 5.44 MPa in dry conditions, 0.91 and 3.12 MPa under saturated conditions. As shown in Figure 7.3, the indirect tensile strength of the calcarenite unit under saturation can decrease up to the 50% with respect to the dry conditions; the same behaviour was observed for the uniaxial compressive strength tests. Based on its uniaxial compressive strength in dry conditions, the calcarenite lithotechnical unit can be classified as very weak according to the ISRM classification system (ISRM 1979b) and soft-very soft according to Bieniawski's system (1989, 1993).

Table 7.1: Physical and mechanical properties of the rock materials cropping out in the study area.

Property		Calcarenite di Gravina			Calcare di Bari micritic facies			Calcare di Bari dolomitic facies		
		Min	Max	Mean	Min	Max	Mean	Min	Max	Mean
Specific gravity, G_s				2.70			2.70			2.74
Dry density (Mg/m^3)		1.48	1.72	1.60	2.44	2.52	2.47	2.47	2.72	2.62
Sat. density (Mg/m^3)		1.88	2.06	1.97	2.49	2.57	2.52	2.52	2.73	2.64
Porosity, n (%)		36.13	45.16	40.75	6.81	11.48	9.03	0.68	9.74	4.47
water absorption, w_o (%)		18.29	29.69	23.06	1.00	4.79	2.69	0.21	1.96	1.03
Degree of saturation, S_r %		73.91	99.77	89.98	36.06	99.84	70.90	49.74	89.61	70.84
Brazilian tensile strength, σ_t (MPa)	dry	0.54	0.96	0.75	5.20	7.31	6.52	9.48	12.04	10.76
	sat	0.41	0.83	0.64						
Uniaxial compressive strength, σ_n (MPa)	dry	3.71	5.44	4.26	36.40	51.17	45.66	84.28	89.15	86.72
	sat.	0.91	3.12	2.18						

Concerning the limestones, dry density ranges between 2.44 and 2.52 Mg/m^3 , whereas the saturated density is between 2.49 and 2.57 Mg/m^3 . Porosity is in the range 7-11%, water absorption is 1-5% and degree of saturation is 36-100%. *Brazilian* tensile strength and uniaxial compressive strength in dry conditions are in the range 5.20-7.31 MPa and 36.40-51.17 MPa, respectively. On the basis of the uniaxial compressive strength in dry conditions, the micritic facies of the Calcare di Bari Fm. can be classified as moderately strong and low-moderately strong according to Bieniawski (1989, 1993) and the ISRM (1979b) classification systems, respectively.

The dolostones have a dry density of 2.47-2.62 Mg/m^3 and a saturated density of 2.52-2.64 Mg/m^3 . The porosity, water absorption and degree of saturation are 0-10%, 0-2% and 50-90%. *Brazilian* tensile strength and uniaxial tensile strength in dry conditions are 9.48-12.04 MPa and 84.28-89.15 MPa, respectively. The dolomitic facies of the Calcare di Bari Fm. cropping out at Polignano a Mare can be classified as of medium strength according to Bieniawski (1989, 1993) and to the ISRM (1979b) systems.

It must be noted that the above used geomechanical classification systems tend to overrate the behaviour of rock masses interested by karst processes, since the features related to dissolution, such as caves and karst conduits are not taken into account in the attribution of the classes, as pointed out by Andriani and Parise (2015, 2017).

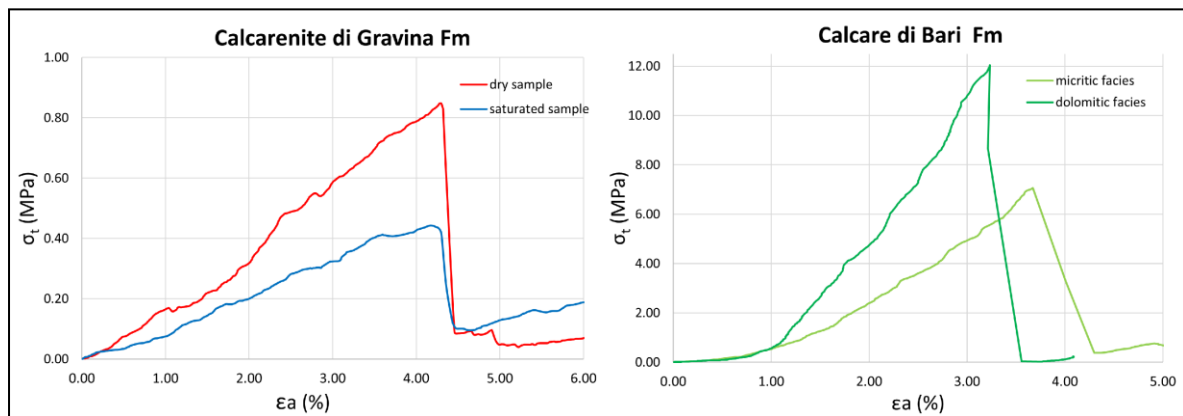


Figure 7.3: Representative *Brazilian* tensile strength stress-strain curves of the litotechnical units; **(a)** Calcarenite di Gravina Fm. samples in dry and saturated conditions; **(b)** micritic and dolomitic facies of the Calcare di Bari Fm in dry conditions.

7.3.3. Conventional geostructural and geomechanical surveys

Direct geostructural and geomechanical surveys were carried out along the steep scarps and sub-horizontal terraces of the study site according to the ISRM standards (ISRM 1988) to build a realistic geomechanical model. Aim of this procedure was to estimate the rock mass jointing conditions, with particular focus on the discontinuities, which play a key role in the mechanical behavior of rock masses (Goodman 1976; Hoek and Bray 1981; Kulatilake and Wu 1984a; Priest 1993; Zhang and Einstein 1998; Hudson and Harrison 2000). Due to scarce accessibility along the cliff at *Lama Monachile* site, additional information was collected on the low-relief rock mass at *Pietra Piatta* site (after validation of its representativeness) to have enough data to perform statistical analyses. The main joint sets were identified on the study area by visual inspection, according to their orientation. Successively, 10 m scanlines and 100 m² square windows (Kulatilake and Wu 1984c; Priest 1993) were marked on representative sectors of both the cliff and low-relief area, to perform quantitative analyses. For each discontinuity intersecting the scanline or partially located in the window, the orientation, spacing, persistence, aperture, water conditions and filling were collected. Large-scale roughness and wall strength were measured with a Barton Comb profilometer and a Schmidt Hammer sclerometer. The poles of the measured discontinuities were reported in the Dips software (Rocscience 2021g) by means of Schmidt equi-areal projections (southern hemisphere) to get statistical information of the attitude of the discontinuity sets, using Fischer concentration contour lines.

Three main discontinuity sets, related to the tectonic and geomorphologic evolution of the area, were identified on the Calcare di Bari Fm. by means of stereographic projections (Figure 7.11). The bedding S0 is constituted by sub-horizontal surfaces, whilst the joint sets J1 and J2, which are sub-vertical and orthogonal to each other, are respectively associated to the anti-apenninic and apenninic structural domains (Doglioni 1991; Festa 1999; Scrocca 2010; Di Bucci et al. 2011), according to their attitude (Table 7.2, bottom).

Table 7.2: Properties of the intact rock (top) and of the discontinuity sets (bottom) of the Calcare di Bari Fm. The weight % represents the percentage of the poles of the considered set over the total.

AVERAGE PROPERTIES OF THE INTACT ROCK												
Facies	Specific gravity G_s	Dry density (Mg/m ³)	Sat. density (Mg/m ³)	Porosity n (%)	water absorption w_a (%)	Degree of saturation S_r %	Brazilian tensile strength σ_t (MPa)	Uniaxial compressive strength σ_n (MPa)				
micr.	2.70	2.47	2.52	9.03	2.69	70.90	6.52	45.66				
dolom.	2.74	2.62	2.64	4.47	1.03	70.84	10.76	86.72				
DISCONTINUITY SETS												
DS	Type	Mean Dip dir. °	Mean dip °	Fisher's K	Weight %	Spacing (m)	Persistence (m)	Aperture (mm)	Water conditions	Filling	JRC	Compressive strength (MPa)
J1	Joint	122	88	141	50	0.12-1.00	0.22	Up to 0.5	Damp	Generally absent	V-VII	47
J2	Joint	33	84	126	20	0.08-0.30	1.99	Up to 0.5	Damp	Generally absent	V-VII	49
S0	Bedding	224	5	402	30	0.05-1	>20	Up to 0.5	Damp	Generally absent	VIII	50

The joint set J1 strikes between 15 and 45°, with a mean direction of 32° and is constituted by sub-vertical fractures (80-90°). The spacing ranges between 0.12 and 1.00 m, with a modal value of 0.43 m. The joints are closed (up to 0.5 mm) and non-persistent (about 0.22 m). No free water was detected, the infilling is generally absent, especially close to the cliff edge, but in some areas soil and calcite were detected. The mean Joint Roughness Coefficient JRC and compressive strength obtained from the Joint Compressive Strength JCS are 9 and 47 MPa, respectively. The joint set J2 has sub-vertical fractures (80-90°) with strike in the range of 118-135° (mean value=123°) and higher persistence (about 2 m). The joint spacing ranges between 0.08 and 0.30 m, with a modal value of 0.25 m (see also Fig. 6.3). The joints have no free water and infilling and, in places, present infilling of residual materials of karst dissolution, a JRC of V-VII and a compressive strength of 49 MPa. The area of the cliff in which the limestone and dolostones belonging to the Calcare di Bari Fm. crop out appears intensely fractured and weathered. More in detail, karren, karst voids, cracking and flaking caused by wetting-drying cycles and by crystallization processes are visible in the spray zone (Blanchard and Woodcock 1980; Zezza and Macri 1995). With regards to the stratification, the bedding surfaces dip towards different directions due to the presence of rotated blocks and gentle folds, thus ranging between NNW and NNE, always with inclinations lower than 10°.

The three outlined discontinuity sets, which are perpendicular to each other, delimit potentially unstable rock blocks. Following Palmstrøm's method (1996a, 2001), the volumetric joint count J_v (number of joints per unit volume), block volume V_b and block shape factor β were calculated as 9.83 m⁻³, 30 dm³ and 28.52. According to the J_v value, the rock mass was classified as *strongly jointed* and is formed by moderately large, compact-moderately flat blocks with right-angled shapes. The contribute of the joints to the rock mass strength was estimated through the jointing parameter JP, which in

turn depends on the block volume and joint condition factor (jC). The latter was calculated on the basis of the joint roughness, length and alteration factors. A joint roughness factor jR equal to 1.5 was calculated considering the waviness and smoothness of the discontinuities, which are planar and slightly rough at the large and small scale, respectively. The joint asperity factor Ja=1.0 and the joint length and continuity factor jL=1.5 were calculated from specific tables depending on the alteration conditions and trace lengths of the discontinuities (Figure 7.4). A joint condition factor jC equal to 3 was determined based on the parameters reported above. Finally, a Rock Mass Index (RMi) equal to 5.66 was obtained by reducing the uniaxial compressive strength of the intact rock by means of the jointing parameter, which was calculated according to the block volume and the joint condition factor (JP=0.12):

$$RMi = \sigma_c * JP \quad \text{Eq. 7.1}$$

According to Palmstrøm's system, the rock mass can be classified as *strong*. Moreover, a classification based on the GSI system (Marinos and Hoek 2000; Hoek and Brown 2019) was carried out following Marinos's system (2017) specifically proposed for carbonate rock masses. According to the rock mass structure (type A) and to the joint conditions (good-fair), a GSI range of 55-65 was assigned to the Calcare di Bari Fm.

As concern the calcarenite unit, cropping out at the top of the cliff, direct measurements on the discontinuity sets could not be performed because of the lack of accessible and safe areas. In addition, human interventions such as excavations and building structures, and heavy weathering as well, made the data collection even more uncertain. For this reason, a qualitative characterization of the discontinuity sets on the Calcarenite di Gravina Fm. was performed by means of visual inspection from the bottom of the cliff, but further investigation by means of remote sensing techniques was planned to achieve more reliable results (Figure 7.5). At this stage, moderately wide discontinuities (up to 10 mm), dipping in the range 75-85°, with no free water and infilling of reprecipitated calcite and residual materials (red soils) were detected. They are widely spaced (1-3 m), low persistent (up to 2.5 m), undulated (JRC= IV-VI) joints mostly dipping toward SSW; however, some joints dipping toward NNE to ENW were observed, too. The calcarenite units have a massive structure and no bedding planes were identified. The effects of weathering processes are more evident in the Calcarenite di Gravina Fm. which, although characterized by medium-large pores, is weaker than the Calcare di Bari Fm. and thus more susceptible to decay (Andriani and Walsh 2007). Since open discontinuities are evident in the calcarenite unit and can control potential instabilities, its strength properties were scaled using the GSI classification system: GSI=55-65 (see also section 7.3.8).

TABLE 5 RATINGS OF THE JOINT ROUGHNESS FACTOR (jR)

small scale smoothness ¹⁾ of joint surface	large scale waviness ²⁾ of joint plane				
	planar	slightly undulating	strongly undulating	stepped	interlocking (large scale)
very rough	3	4	6	7.5	9
rough	2	3	4	5	6
slightly rough	1.5	2	3	4	4.5
smooth	1	1.5	2	2.5	3
polished	0.75	1	1.5	2	2.5
slickensided ³⁾	0.6 - 1.5	1 - 2	1.5 - 3	2 - 4	2.5 - 5
For irregular joints a rating of jR = 5 is suggested					

¹⁾ For filled joints: jR = 1

³⁾ For slickensided joints the highest value is used for marked striations.

TABLE 6 RATINGS OF THE JOINT ALTERATION FACTOR (jA).

A. CONTACT BETWEEN THE TWO ROCK WALL SURFACES			
TERM	DESCRIPTION	jA	
Clean joints			
-Healed or welded joints	Softening, impermeable filling (quartz, epidote etc.)	0.75	
-Fresh rock walls	No coating or filling on joint surface, except of staining	1	
-Alteration of joint wall:			
1 grade more altered	One class higher alteration than the intact rock	2	
2 grades more altered	Two classes higher alteration than the intact rock	4	
Coating or thin filling			
-Sand, silt, calcite, etc.	Coating of friction materials without clay	3	
-Clay, chlorite, talc, etc.	Coating of softening and cohesive minerals	4	
B. FILLED JOINTS, PARTLY OR NO JOINT WALL CONTACT			
TYPE OF FILLING MATERIAL	DESCRIPTION OF FILLING MATERIAL	Partly wall contact thin filling (< 5 mm ²⁾ jA	No wall contact thick filling jA
-Sand, silt, calcite, etc.	Friction materials without clay	4	8
-Compacted clay	"Hard" clayey material	6	10
-Soft clay	Medium to low over-consolidation of filling	8	12
-Swelling clay	The material shows clear swelling properties	8 - 12	12 - 20

²⁾ Based on joint thickness division in the RMR system (Bieniawski, 1973)

TABLE 7 RATINGS OF THE JOINT SIZE AND CONTINUITY FACTOR (jL).

JOINT LENGTH	TERM	TYPE	jL	
			continuous joints	discontinuous joints ¹⁾
< 0.5 m	very short	bedding/foliation partings	3	6
0.1 - 1.0 m	short/small	joint	2	4
1 - 10 m	medium	joint	1	2
10 - 30 m	long/large	joint	0.75	1.5
> 30 m	very long/large	(filled) joint, seam ²⁾ or shear ²⁾	0.5	1

¹⁾ Often a singularity, and should in these cases be treated separately. ²⁾ Discontinuous joints end in massive rock

Figure 7.4: Joint roughness factor (jR), joint alteration factor (jA) and size and continuity factor (jL) estimated from reference tables (after Palmstrøm 1996a, available at https://www.rockmass.net/ap/51_Palmstrom_on_RMi_in_rock_engineering.pdf)

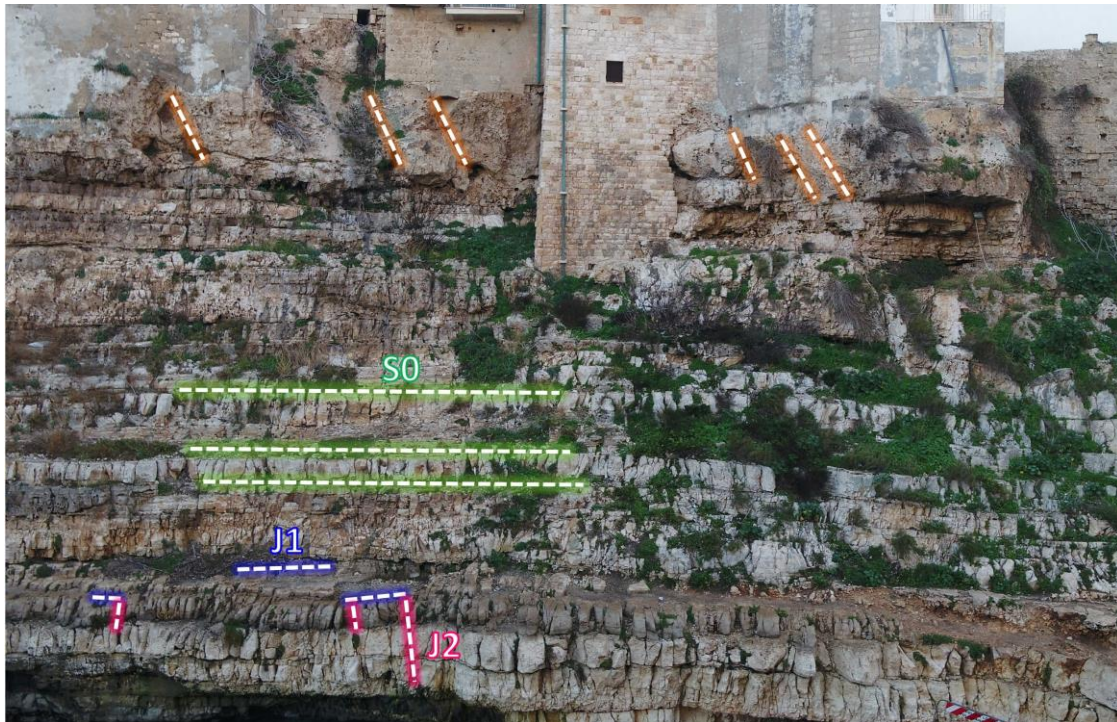


Figure 7.5: Main discontinuities detected during the field surveys in the Calcarene di Gravina Fm at *Lama Monachile* site (with orange outline). The main orientation of the discontinuity set could not be measured in the point clouds because of the surface roughness and of the lack of appropriate planes where to collect the data. The main discontinuity sets identified in the Calcare di Bari Fm. are highlighted in blue (J1), magenta (J2) and green (S0).

7.3.4. UAV surveys

The Unmanned Aerial Vehicle surveys were carried out on both *Lama Monachile* and *Pietra Piatta* sites by means of a quadcopter platform DJI Inspire 2, equipped with a 20.8-megapixel resolution camera, an integrated Global Navigation Satellite System (GNSS) and a remote flight controller (Figure 7.6). With regards to the sub-vertical cliff, 130 frontal photos with side and frontal overlap of 75% and 85% were taken at horizontal distance of 18 m from the cliff. On the other hand, 248 photos were acquired by means of nadir photogrammetry at *Pietra Piatta* site setting frontal and side overlap of 75%; 3 Ground Control Points were positioned on the terrain and their coordinates were measured by means of a differential Global Positioning System (dGPS) to georeference the point cloud during the processing stage. The camera locations, image overlap, position and estimated error of the GCPs in both the surveyed zones are illustrated in Figure 7.7.

Both datasets were processed by means of *Structure from Motion* technique using *Agisoft Metashape* software (Agisoft 2020), according to the workflow described by Westoby (2012) and Carrivick and co-workers (Carrivick et al. 2016). Five Ground Control Points evenly distributed in the study area were picked on the photos of *Lama Monachile* site to georeference the 3D model in a global reference system. The coordinates were assigned by picking the same points from a point cloud previously acquired by means of Terrestrial Laser Scanning technique georeferenced using a dGPS. With regards to the model of the flat area, the coordinates of the 3 GCPs were inserted as input in the software. After keypoints detection and matching by means of Scale Invariant Feature Transform

(SIFT) algorithm (Snavely et al. 2008), the collinearity equations (Mikhail et al. 2001) were automatically solved for each point and for each photograph by means of least-square bundle adjustment (Brown 1976; Triggs et al. 1999; Snavely et al. 2008; Fonstad et al. 2013; Lucieer et al. 2013). At this stage, a sparse point cloud located in a 3D environment was generated from each dataset. Successively, dense point clouds were obtained using Multi-View-Stereo (MVS) algorithms.

The dense point cloud of *Lama Monachile* site (more than 52 million points) was sub-sampled (minimum distance between points of 1 cm) and segmented using the CloudCompare software. The resulting point cloud consists of about 22 million points, with density of 5244 points/m² and mean point distance of 1.3 cm (Figure 7.8). To correct *doming shape deformations* caused by the camera lens distortion on elongated zones (James and Robson 2014; Eltner et al. 2016), the UAV point cloud was further aligned on the TLS point cloud, characterized by higher accuracy and resolution (Riquelme et al. 2017; Petrie and Toth 2018; Stead et al. 2019). More in detail, the two point clouds were split in smaller sub-areas and aligned at couples using the *Iterative Closest Point* (ICP) algorithm (Besl and McKay 1992), using the laser scanner point cloud as reference, until reducing the Root Mean Square Error (RMSE) between the two datasets to 79 mm. A final triangulated surface (*mesh*) made up of about 6.5 million polygons was generated by means of the Poisson Surface Reconstruction (Kazhdan and Hoppe 2013).

Concerning the 3D scene of *Pietra Piatta* site, the 3 GCPs were considered sufficient to produce a correctly georeferenced point cloud (about 100 million points, 12896 points/m²) because no deformations were detected, and the GPS system integrated in the UAV instrument provided reliable coordinates (in contrast with the photos acquired at *Lama Monachile* site, where the site conditions caused a loss of the GPS signal) (Figure 7.9). Aimed at accurately mapping the discontinuity traces, a high-resolution orthophoto (4.71 mm pixel size) of the *Pietra Piatta* site was obtained after generating an about 10 million facets triangulated surface.



Figure 7.6: Areas investigated by means of UAV techniques and conventional geomechanical-geostructural surveys.

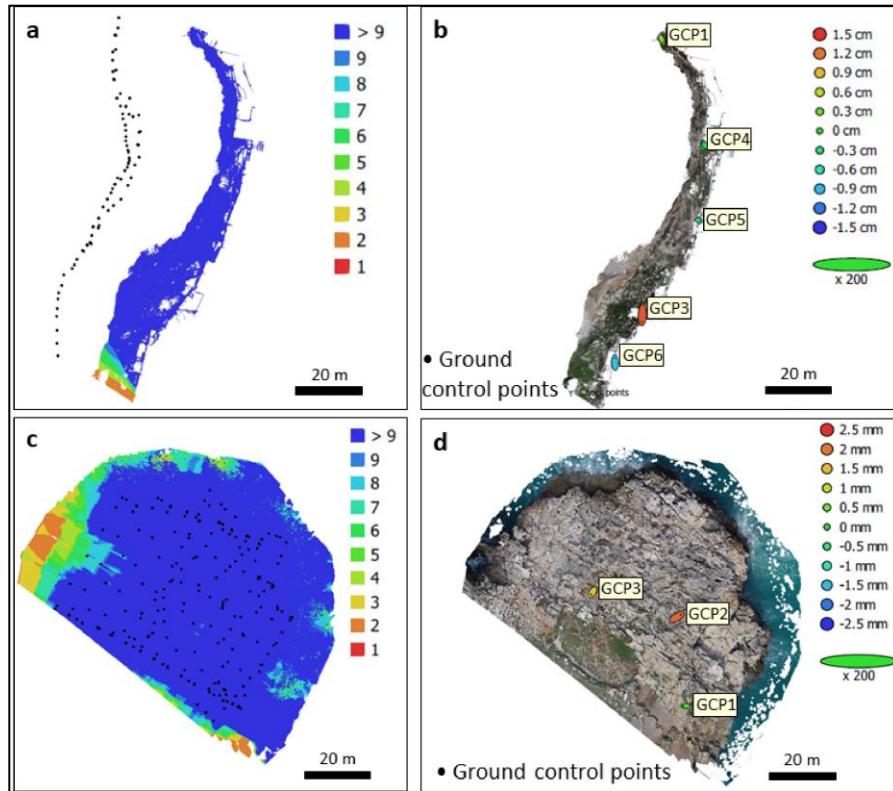


Figure 7.7: Details of the UAV surveys carried out at Polignano a Mare and of the point clouds obtained during the SfM technique with the software Agisoft Metashape: (a) camera locations and image overlap at *Lama Monachile* site; (b) top view of the raw point cloud, Ground Control Points and error estimations at *Lama Monachile* site; (c) camera locations and image overlap at *Pietra Piatta* site; (d) top view of the raw point cloud, Ground Control Points and error estimations at *Pietra Piatta* site.

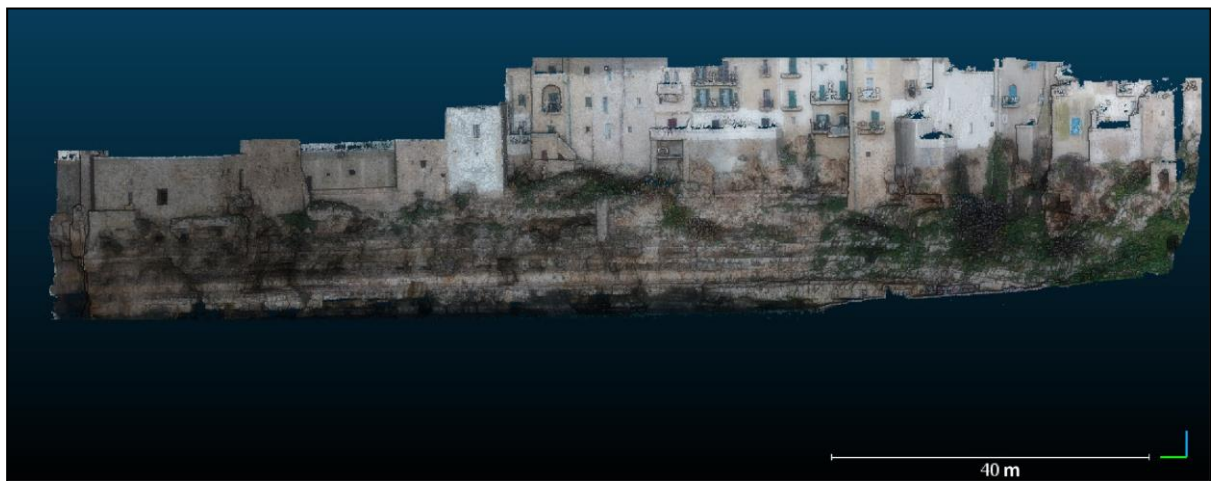


Figure 7.8: Final point cloud of *Lama Monachile* site after the subsampling and cleaning process, 29,922,815 points, mean surface density = 3377 points/m².

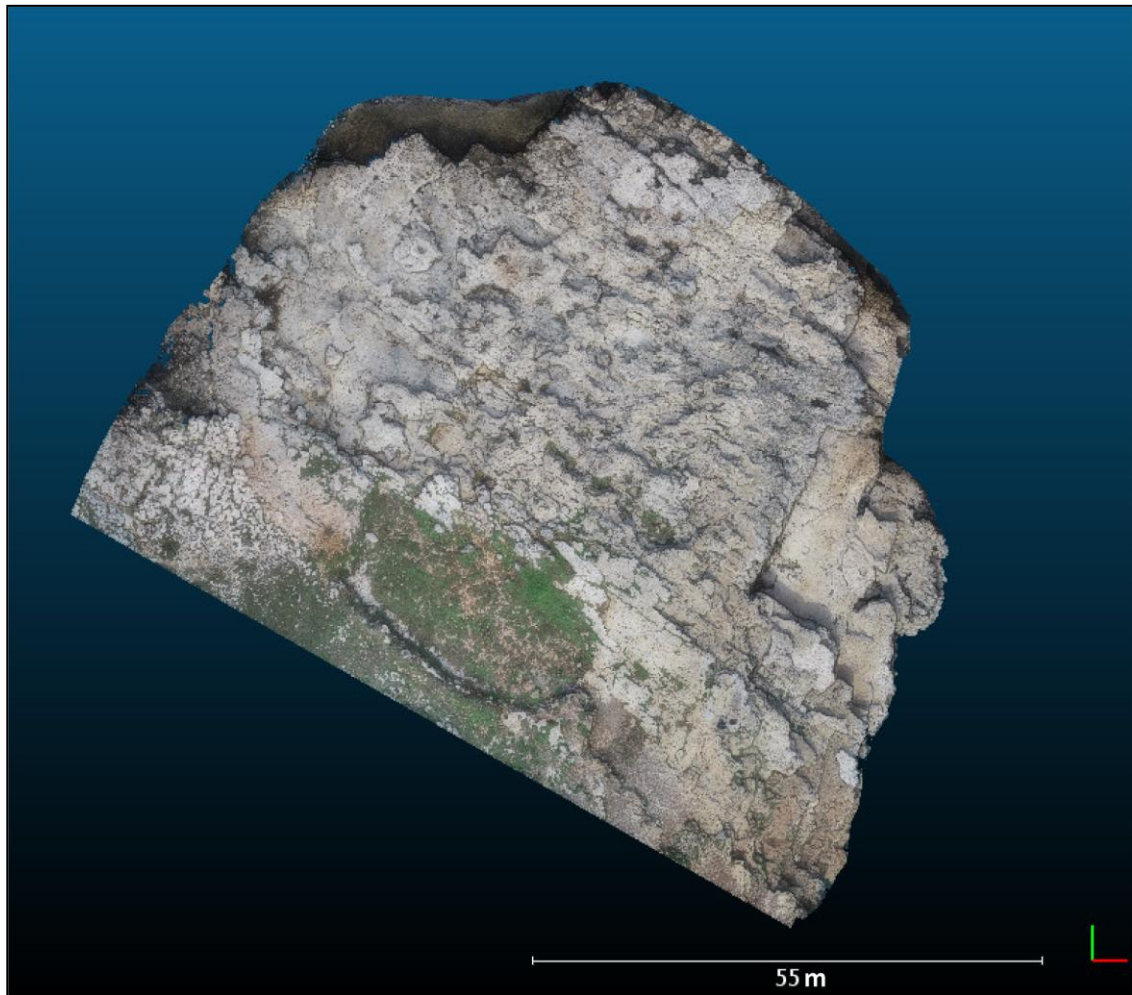


Figure 7.9: Final point cloud of *Pietra Piatta* site after the cleaning process, 22,155,255 points, mean surface density = 12896 points/m². The point cloud was not subsampled in order to generate a high resolution orthophoto for the geostructural and geomechanical analysis of a representative area of the rock mass.

7.3.5. Geostructural analysis from orthophotos/point clouds

The discontinuity sets characterising the rock mass were investigated from 2-D and 3-D datasets. In a first phase, the point clouds of *Lama Monachile* and *Pietra Piatta* sites were analyzed using *Coltop3D* software (Terranum 2021) to semi-automatically extract the discontinuity sets by means of the Jaboyedoff and co-workers' approach (Jaboyedoff et al. 2007). After computing the normal to each point, the software automatically calculates the dip direction/dip by means of eigenvalue analysis of the covariance matrix of a local neighbourhood and provides a point cloud coloured by means of Hue Saturation Intensity (HSI) colour scale. The modified point cloud is coloured so that the dip direction and dip of the poles are respectively represented by the hue and saturation values and allows the user to identify the main discontinuity sets according to their orientation. Since both investigated areas are characterized by sub-vertical rough surfaces, the interpretation of the HSI rendering was not immediate, as some areas of the same discontinuity plane, locally dipping toward opposite sides, were represented by colours located in the opposite side of the stereonet. For this reason, the meshes generated during the SfM process were analyzed by means of *Lime* software (Virtual Outcrop Geology Group 2021) which colors the surfaces according to their strike (Figure 7.10).

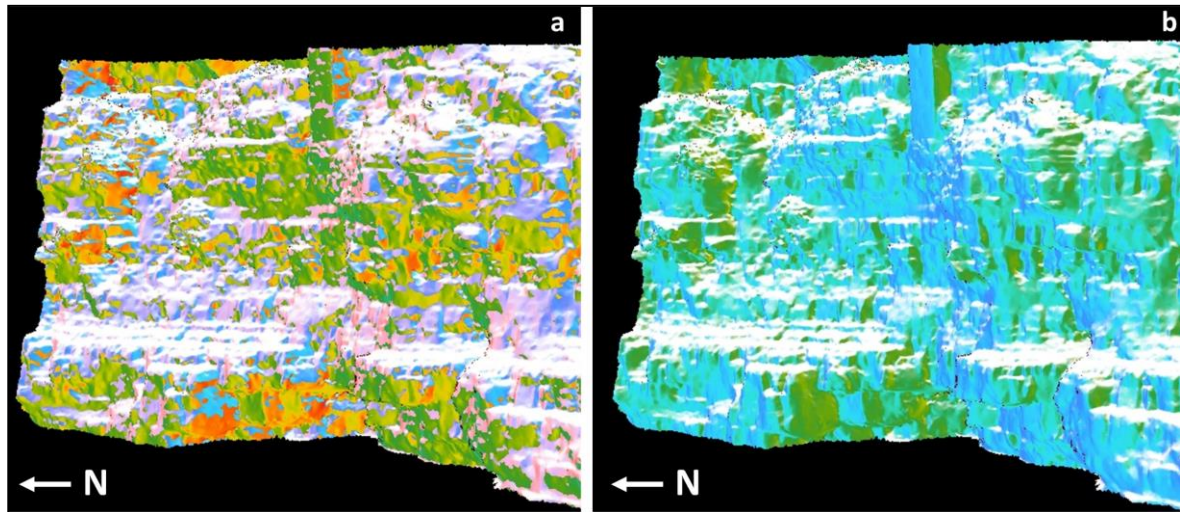


Figure 7.10: Mesh of a sector of *Lama Monachile* site visualised by means of *Lime* software (VOG Group, 2021). (a) the identification of sub-vertical discontinuity sets using the dip direction/dip rendering is challenging because rough surfaces are represented by “spots” with different colours; (b) the interpretation of the discontinuity sets is facilitated using the strike rendering.

In addition, the sub-vertical cliff is characterized by flat surfaces (terraces) and steep steps, therefore few planar surfaces could be detected on the point cloud due to their scarce exposition. For this reason, a smaller area of the point cloud where joint sets could be detected as planes (instead of traces), was segmented and used for this analysis. These steps allowed the identification of the main discontinuity sets within the point cloud with *Coltop3D*. After mapping a few polygons considered representative for a discontinuity set, the parallel planes (with a user-defined tolerance of 30°) were automatically extracted. Later, the coordinates and dip direction/dip of the points belonging to each discontinuity set were imported in CloudCompare and the respective point clouds were overlapped on the original point cloud to validate the results (Figure 7.11).

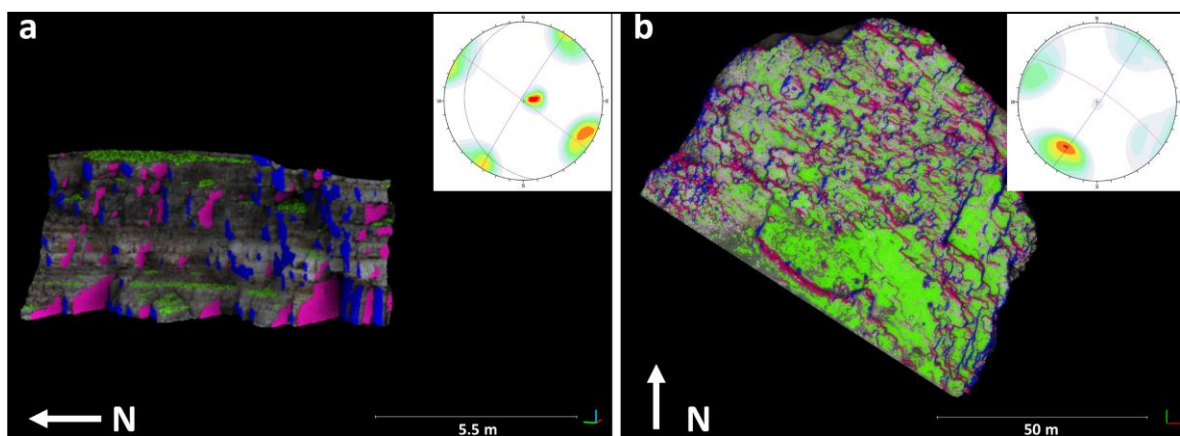


Figure 7.11: Semi-automatic identification of the main discontinuity sets at *Lama Monachile* (a) and *Pietra Piatta* (b) sites with *Coltop3D* software.

In a second phase, quantitative analyses of the discontinuity sets were performed using the high-resolution orthophoto of *Pietra Piatta* site generated by means of SfM technique. As a matter of fact,

it is evident that not all planes belonging to the discontinuity sets were extracted from the point clouds because several discontinuities are visible in the form of traces. Fracture undersampling can strongly influence the results of quantitative analyses. Therefore, a specific MATLAB routine was developed to semi-automatically identify and characterize the sub-vertical joint sets from trace maps and ran it on more than 1000 traces manually drawn on a representative area of the rock mass (Loitine et al. 2021). For each joint set, the MATLAB routine provided the mean strike, spacing, trace length and persistence. The joint network was characterized by means of intensity, density and trace length estimators (Mauldon 1998; Mauldon and Dershowitz 2000; Mauldon et al. 2001) and the volumetric joint count, block volume, block shape factor and block shape were provided by the routine as well.

Three main discontinuity sets, represented by the sub-horizontal bedding and two orthogonal joint sets, were extracted both from the 3-D and 2-D analysis. At a final stage, the results of the discontinuity characterization were validated by means of comparison with the results of the conventional geosstructural and geomechanical surveys (Figure 7.12, Table 7.3). During this phase, an issue regarding the identification of the bedding from point clouds emerged. As shown in Figure 7.11a, not all the bedding surfaces were detected because most of them are present in the form of traces along the sub-vertical steps. Because only the joint sets could be mapped on the orthophoto, the MATLAB routine was not applied to the stratification. With regard to *Pietra Piatta* site, in addition to the outlined problem, the sub-horizontal bedding surfaces were merged with points belonging to the topography (Figure 7.11b). Based on these observations, the data acquired by means of field surveys were considered to be more representative and more reliable, and they were therefore selected for the analyses reported in the next sections.

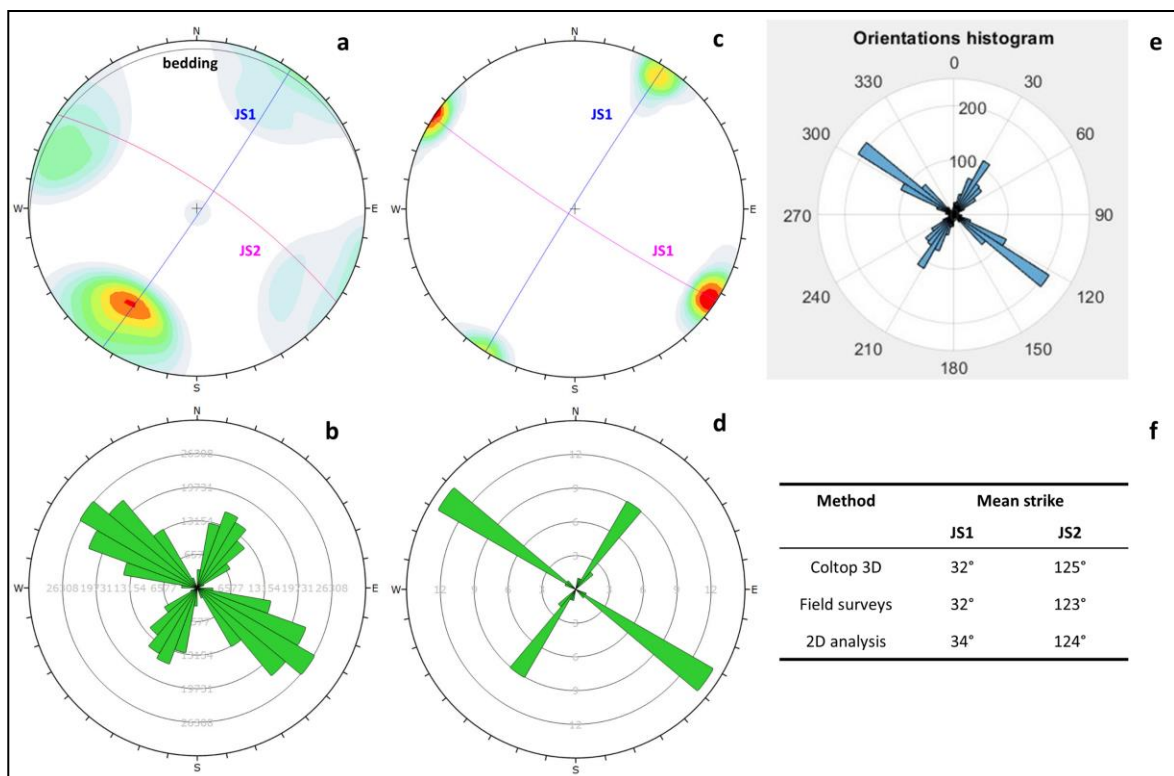


Figure 7.12: Orientation of the main joint sets identified at *Pietra Piatta* site by means of different methods, lower-hemisphere Schmidt equal-angle stereographic projections. (a) best-fit great circles and contour plot of

the poles of the main discontinuity sets identified with *Coltop 3D*; (b) rose plot of the main discontinuity sets identified with *Coltop 3D*; (c) best-fit great circles and contour plot of the poles of the main discontinuity sets identified by means of conventional geosstructural-geomechanical surveys; (d) rose plot of the main discontinuity sets identified by means of conventional geosstructural-geomechanical surveys; (e) rose plot of the main discontinuity sets identified by performing the 2D analysis with the developed MATLAB routine; (f) summary table of the orientations of the main discontinuity sets estimated with the different methods. Note that the bedding was not compared because a characterization through the MATLAB routine was not possible.

Table 7.3: Validation of the discontinuity characterization from the point clouds and orthophoto by means of comparison with the results of the conventional geomechanical and geosstructural surveys.

Dataset	Strike °	Spacing (m)	Trace length (m)	Persistence (m)
JOINT SET J1				
Point cloud	32			
Orthophoto	34	0.41	0.20	0.22
Conventional surveys	32	0.43	0.22	0.22
JOINT SET J2				
Point cloud	125			
Orthophoto	124	0.22	0.55	2.49
Conventional surveys	123	0.25	0.53	1.99
JOINTING NETWORK				
Block volume	Volumetric joint Count J_v (m^{-1})	Block volume V_b (dm^3)	Block shape factor β	Block shape
Orthophoto	9.94	60	28.98	compact
Conventional surveys	9.83	30	28.52	Compact- moderately flat

With regards to the block volume V_b , its estimation was obtained from the mean orientation and spacing of the joint sets and stratification. However, larger volumes were observed from both field investigations and point cloud inspections. As a matter of fact, the joint sets and bedding spacings are distributed according to exponential negative and normal distributions, respectively, therefore the minimum and maximum values can be considerably different from the mean. In addition, persistent sub-vertical discontinuities occasionally cut more layers, leading to the failure of rock blocks larger than those estimated by means of the V_b parameter. To achieve a more reliable assessment of the block volumes, 50 failed blocks were approximately measured by identifying the failure surfaces in the point clouds and assuming different shapes (Figure 7.13a). More precisely, the volumes were calculated assuming triangular and rectangular prisms as shapes. The maximum calculated volumes for triangular and rectangular prismatic shapes are about 4 and 8 m^3 , respectively (Table 7.4). The calculated block volumes follow an inverse power law distribution (Figure 7.13d). The mean value is more than 10 times larger than V_b (calculated for tabular blocks) because larger blocks were identified in the point clouds and, at the same time, very small blocks might have been undersampled. Since the described technique is based on direct measurements carried out on the point clouds, the corresponding results are considered to be more accurate with respect to Palmstøm's method. Therefore, based on measurements performed on failed blocks, the most common potential failures that are expected in the case study involve volumes ranging between a few dm^3 and about $10m^3$. However,

larger instabilities determined by very persistent discontinuities (*i.e.* tension cracks) are not excluded. As a matter of fact, some potential instabilities involving large volumes formed by several blocks were detected in the field (Figure 7.15) and may indicate more dangerous scenarios. This analysis should be integrated with measurements carried out on larger failed blocks, which are probably located below the sea level and might have been dismantled during the impact or over time. Alternatively, the method proposed in Section 4.3.5 could be used to compare point clouds generated from historical photographs covering a large period of time.

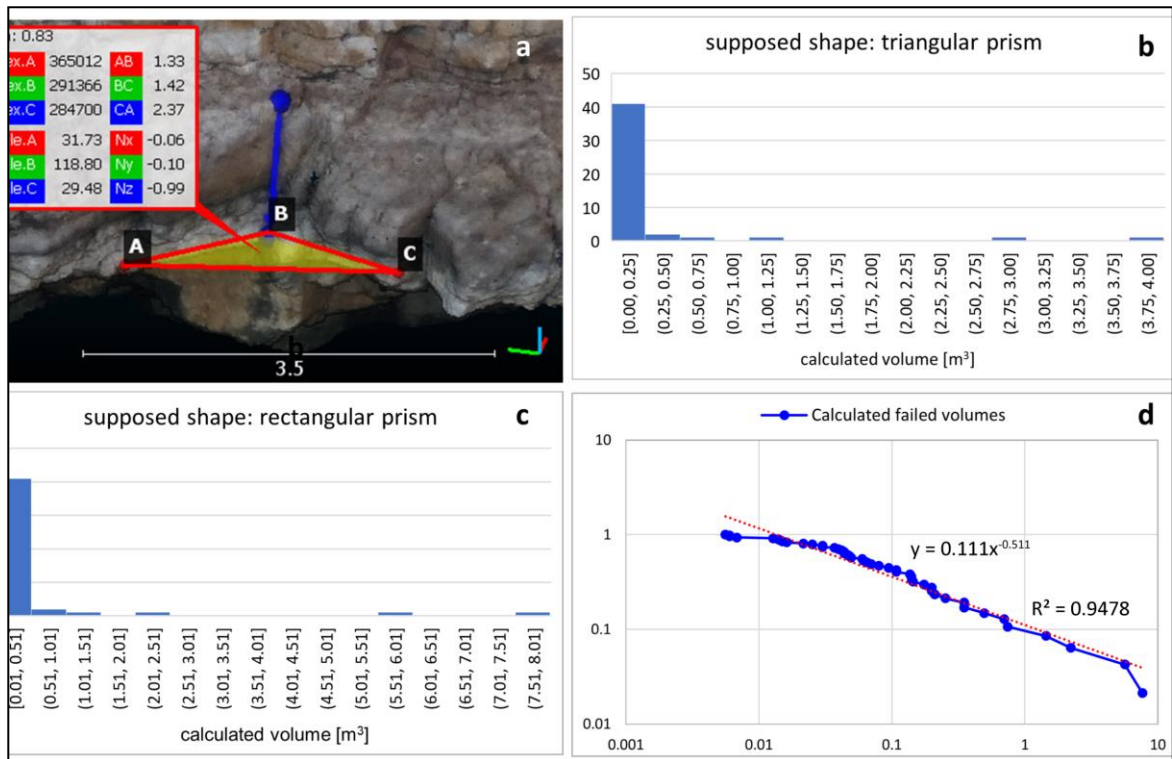


Figure 7.13: Volume estimation of failed blocks. (a) estimation from point clouds by measuring area and height from visible niches; (b) histogram of 50 volumes calculated for triangular prism shapes; (c) histogram of 50 volumes calculated for rectangular prism shapes; (d) log-log chart showing that the calculated block volumes for both shapes follow an inverse power law.

Table 7.4: Minimum, maximum and mean values of the 50 failed blocks analyzes in the point cloud, by assuming the shape of triangular and rectangular prisms.

Calculated volume (m ³)	Hypothesized shape of the failed blocks	
	Triangular prism	Rectangular prism
Minimum	0.00	0.01
Maximum	3.82	7.64
Mean	0.24	0.48

7.3.6. Kinematic analyses

Kinematic analyses were performed using the Dips software (Rocscience 2021g) to identify the main structurally controlled failure mechanisms of the rock mass, based on the geometrical relationships between the discontinuities and the topography. The coastal stretch of the study site was subdivided into 7 sectors according to the slope orientation (Figure 7.14). For each sector, the results of the quantitative analyses of the fracture traces were reported in the software to generate the joint sets. Data on the bedding surfaces collected by means of conventional surveys were added as well. Successively, the slope dip direction/dip, friction angle and later limits were defined for each sector to assess the probability of mechanisms such as planar slides, wedge slides and direct topple by means of Goodman and Shi's approach (1985).

Kinematic tests against planar sliding, wedge sliding and direct toppling were carried out in different sectors of *Lama Monachile* site using *Dips* software and simulating the three main discontinuity sets described in the sections above (Figure 7.14). Flexural toppling was exempted from the analysis because it is incompatible with the site conditions, as no continuous sub-vertical columns are present in the study site. A basic friction angle ϕ of 40° was determined from the linearization of the Hoek-Brown failure envelope by assuming $GSI=50$, $m_i=9$ and $D=0$. As shown in Table 7.5, the results of the kinematic analyses show that the most probable failure mechanisms are represented by wedge sliding and toppling mechanisms. The stereonets of the tests for planar sliding, wedge sliding and direct toppling carried out for each sector are reported in the supplementary materials. In detail, about 67% of the intersections among the inserted discontinuities are compatible with wedge slide failures within the overall slope, which can occur along the intersection line between two discontinuities (J1 vs J2), or along one plane with the most favourable orientation. About 37-50% of the intersections, depending on the sector, are compatible with toppling mechanisms defined by Hudson and Harrison (2000). These failure modes are related to the presence of two joint sets (J1 vs J2) whose sub-vertical intersection line dips into the slope and sub-horizontal bedding surfaces (S0) acting as releasing planes. The majority of the intersection lines fall outside the lateral limits thus determining oblique-type toppling, except for sector F, in which direct toppling is favoured. In addition, combined sliding-toppling failures can occur simultaneously according to the "base plane" type, especially for sectors G, D and F. Planar sliding can rarely take place in sectors A-F, in which the percentage of probability is less than 5%. However, the kinematic tests performed in sector G indicated that about 31% of the discontinuities can lead to planar slides.

It is pointed out that, at present, the available softwares for kinematic analyses are limited to uniform slope morphologies. With regards to the *Lama Monachile* site, instability mechanisms observed in the field such as failure of overhanging blocks and progressive bending and detachment of the karst cave roofs could not be taken into account during the kinematic analyses. Future improvements may concern the application of the methodology proposed by some authors in order to carry out kinematic analyses on 3-D models (DOMs) and detect susceptibility indexes for specific failure modes (Matasci et al. 2018; Menegoni et al. 2021). Moreover, these preliminary tests do not consider the physical and mechanical properties of the rock materials (except for the friction angle). For these reasons, more advanced investigations were carried out by means of numerical modelling.



Figure 7.14: Subdivision of the study area in 7 sectors, according to the local orientation of the slope, in order to perform the kinematic analyses.

Table 7.5: Results of the kinematic analysis performed in the different sectors at *Lama Monachile* site. About 66 % of the intersections of the discontinuities are compatible with wedge sliding failures (mainly along the intersection lines between JS1 and JS2 in sectors A, B, C, E and along one plane in sectors D,F,G), about 43 % of the intersections could lead to toppling mechanisms (mostly oblique, except for sector F in which direct toppling is favoured) and 3 % of the discontinuities could produce planar slides. The local orientation of the slope in sector G increases the probability of planar slides (31.37 %) compared to the other zones. In addition, some discontinuities could represent release surfaces for combined toppling and planar sliding mechanisms (“base plane” section of the toppling test, especially for sectors G, D, F). Note: the graphical representations of the kinematic analyses are reported in the supplementary materials (Figures S7.1-7).

SECTOR	SLOPE ORIENTATION		FAILURE MECHANISM							
			PLANAR SLIDE	WEDGE SLIDE			TOPPLING			
	Dip direction	Dip	Total %	Both planes %	One plane %	Total %	Direct %	Oblique %	Total %	Base plane %
A	94	90	1.85	52.16	14.41	66.57	4.37	37.56	41.93	2.21
B	120	90	2.95	53.15	13.33	66.48	13.05	37.56	50.61	10.33
C	97	90	1.85	52.47	14.12	66.59	6.38	37.56	43.94	3.69
D	241	90	5.17	24.07	42.40	66.47	0.46	37.56	38.02	21.03
E	109	90	2.21	52.80	13.72	66.52	12.70	37.56	50.26	7.01
F	181	90	4.80	29.79	36.68	66.47	38.25	0.00	38.25	16.97
G	230	90	31.37	23.67	43.14	66.81	0.85	37.56	38.41	46.86
Average total along the slope			7.17	Average total along the slope		66.56	Average total along the slope			43.06

7.3.7. Instability mechanisms

Instability processes in the study area are related to planar and wedge slides, topples, rockfalls and partial roof collapse of the caves (Figures 7.15-17), as typically occurs for rock failures in karst areas with vertical to sub-vertical cliffs (Parise et al. 2015a). Planar slides take place along sub-vertical discontinuities parallel to the coastline and dipping outside the slope, with the bedding surfaces, locally slightly dipping seawards, acting as release planes (e.g. Figure 7.15 d). Wedge slides occur along the intersection line, dipping seawards, of two discontinuities, typically belonging to joint sets J1 and J2 (e.g. Figures 7.15 a,c,e), whilst toppling mechanisms are determined by the rotation of blocks detached from sub-vertical discontinuities dipping inland. The sub-vertical fractures responsible for planar slides and topples are related to the joint sets and, in more severe cases, to release tensional cracks developed parallel to the coastline and characterized by larger apertures. In some cases, tension cracks delimit the back part of blocks involved in wedge slides. Rockfalls are common on the overhanging sectors of the rock mass, lying above notches formed by chemical and mechanical degradation of the rock materials and/or above karst conduits and caves. In detail, these features are located at the sea level (notch) and along the contact between the Calcarene di Gravina Fm. and the Calcare di Bari Fm (karst features) (e.g. Figures 7.15 b,f, Figure 7.16 b). In the first case, rockfalls are caused by the failure of blocks due to wave undercutting and to the corrosive and erosive wave action, especially in correspondence of karstified levels and along the discontinuity sets. A typical mechanism occurring just above the sea level is associated to the fall of tabular blocks formed by the intersection of the two joint sets along the overhanging levels (Figure 7.16 c, Figure 7.17 d). In the second case, calcarenite overhanging blocks lose support from the underlying levels characterized by a series of karst conduits and caves.

As concerns these latter, partial or total collapse of the cave roofs under flexural stress are caused by the joint sets cutting through the laminations of the Calcare di Bari Fm. at steep angles. Snap-through, crushing, sliding and diagonal cracking mechanisms are compatible with the observed cave failures (Diederichs and Kaiser 1999a, b; Andriani 2015) (Figure 16a, Figs. 17e,f).

It is remarked that failed blocks identified in the field belong to only one formation, as they are characterized by different mechanical behaviour. Indeed, heavy physical and mechanical weathering along the coastline causing strength loss acts on the two units with different degrees. Weathering processes are significant in the Calcarene di Gravina Fm., in which progressive microcracking, dissolution of the fine cementation and salt crystallization determine granular disaggregation (Andriani and Pellegrini 2014). On the other hand, the less porous and more cemented limestones and dolostones belonging to the Calcare di Bari Fm. are less susceptible to weathering processes, even if strongly jointed and affected by karst.

Cliff retreat in the study site is represented by episodic and localized failures that, even if involving small volumes (see section 5.3.5), can represent a serious risk considering the presence of people, especially during the busy summer season. Moreover, it cannot be excluded that cyclic daily and annual thermal variations might contribute to rock mass degradation and induce deformation along the discontinuities. Hence, the cumulative effects of slight but repeated thermal perturbations may cause failure of rock blocks in the long-term (Tsesarsky and Hatzor 2009; Villarraga et al. 2018; Marmoni et al. 2020). In addition to the mentioned factors, cyclic wave action at the sea level and seismic activity could trigger future failures. Polignano a Mare locality is characterized by low seismicity and the earthquakes recorded so far took place in the neighbouring seismogenetic zones (Gargano, Basilicata, Calabria, central-southern Apennines, Albania, Greece), therefore seismic actions represent a minor

hazard for coastal landslides. As reported by Andriani and Walsh (2007), attention should be paid to sea storms, which caused major retreat events in the surrounding area. The study area is characterized by a typical Mediterranean climate with dry summers, mild winters and low precipitations. However, the prevailing winds, with particular reference to those coming from N, NNW and NNW, can cause intense storms (Maracchione et al. 2001), with broken waves that can reach the houses located at 20 m a.s.l. Even minor events prolonged over time can lead to a considerable strength reduction, as long-lasting cyclic loads caused by wave action can generate crack initiation and propagation (Brossard and Duperret 2004; Adams et al. 2005; Sunamura 2015). Unquestionably, the presence of joints and karst features within the rock mass reduce even more its resistance against wave assault.

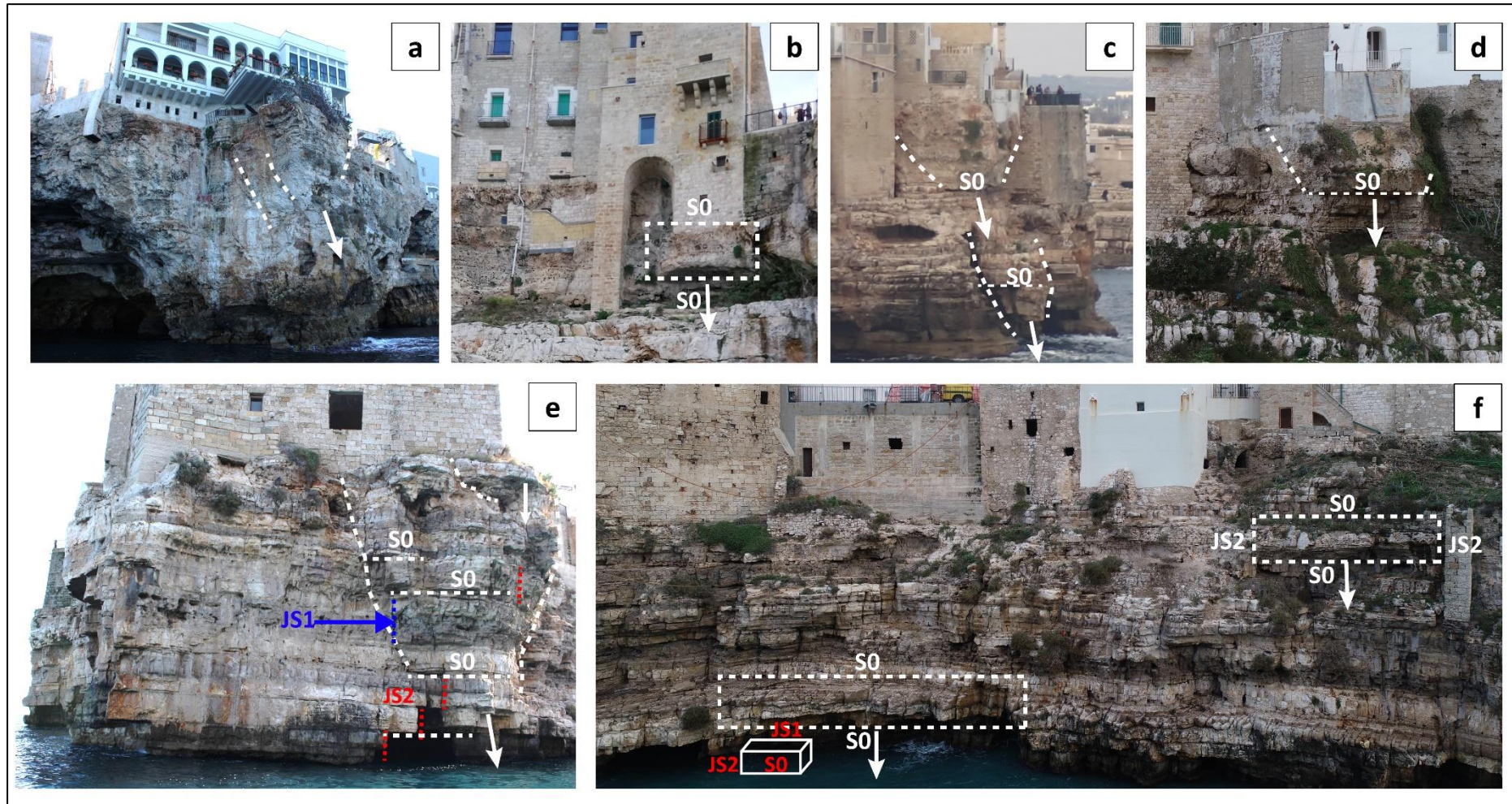


Figure 7.15: Examples of failures at Lama Monachile site: (a, c, e) wedge slide of the largest potential failure detected, approximate volume of 815 m³ (measured on the UAV point cloud by means of Poisson Surface Reconstruction); (b, f) falls of overhanging blocks; (d) planar slide.

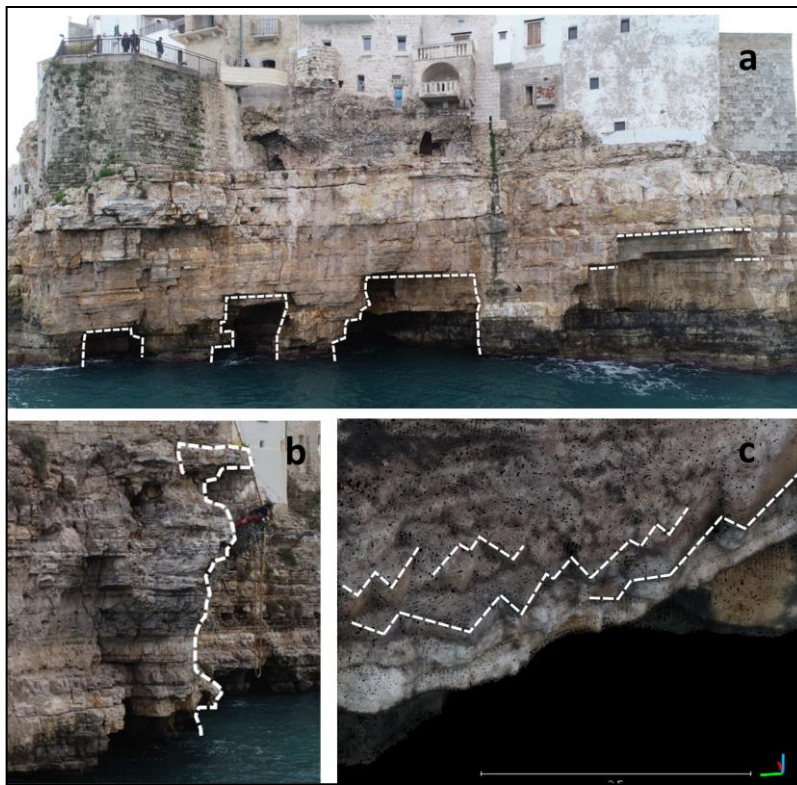


Figure 7.16: Other examples of failures at *Lama Monachile* site: (a) partial collapse of the cave roof; (b) potential instabilities of overhanging blocks which may fall, slide or topple along sub-vertical fractures; (c) failures of tabular blocks determined by the intersections of JS1 and JS2 detected in the point cloud.

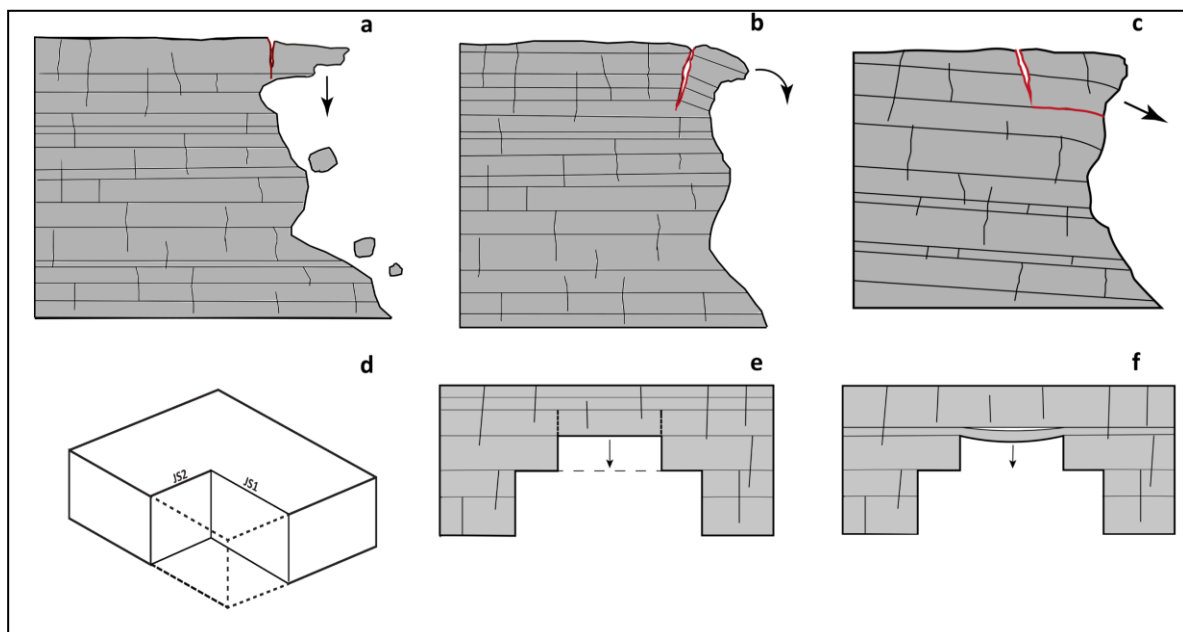


Figure 7.17: Sketches of the main failure modes occurring in the study area: (a) rockfall determined by the detachment of overhanging blocks from sub-vertical fractures and/or tension cracks; (b) topple of blocks from sub-vertical fractures and/or tension cracks; (c) planar slide of blocks delimited by sub-vertical discontinuities

and bedding surfaces gently dipping towards the sea; (d) failure of blocks generated by the intersection of two perpendicular discontinuity sets, they occur in the form of falls (overhanging blocks) or slides (intersection line dipping seaward); (e) partial detachment of the roof in the karst caves, favoured by the intersection between subvertical joints and bedding; (f) progressive roof bending and breakdown in the karst caves.

7.3.8. Finite Element Method analyses

7.3.8.1. Three-dimensional model

Objectives

The results of field and remote sensing surveys, quantitative discontinuity characterization and physical and mechanical characterization of the rock materials were combined for a preliminary global scale assessment of the cliff stability at *Lama Monachile* site. Three-dimensional numerical stability analyses were carried out by means of a Finite Element Method approach using RS3 software (Rocscience 2021c). This software allows the generation of advanced 3-D models through the combination of data collected by means of remote sensing techniques (i.e. point clouds or meshes), field surveys and laboratory tests. Thanks to the user-friendly interface, it is possible to easily implement discontinuities, water levels, loads, and excavations in the geometric model, and to build high-resolution meshes. However, it must be specified that a good compromise between the objectives of the analyses and the model set-up needs to be reached, especially if the computation is carried out by means of standard computers. Further specifications on RS3 can be found at: <https://www.roscience.com/help/rs3/overview/technical-specifications>).

In a first phase, tests performed at a small scale allowed the identification of the areas of the rock cliff more prone to failure, for further investigation. A Digital Terrain Model derived from 1-m resolution LiDAR data (retrieved from www.sitpuglia.it) of a larger area was set as geometric model. The analysis carried out setting a simple elastic constitutive model allowed to identify the critical area of the higher-resolution point cloud of *Lama Monachile* site (Figure 7.18).

Model set-up

- Geometric model

The geometric domain of the area of interest was built by importing and simplifying the corresponding triangulated surface in RS3 and adding a volume below the sea level, according to the bathymetry of the area. Vertical and horizontal boundaries were set respectively at the sides and top-bottom of the rock slope to delimit the numerical domain. The Calcare di Bari Fm. and the Calcarenite di Gravina Fm. were delimited tracing a plane along the geologic contact.

- Water conditions, loads and restraints

A water table was added in correspondence of the present sea level, whilst the weight of the water column above the immersed volume was simulated by means of a ponded water load. In addition, the weight of the buildings located on the top of the cliff was reproduced using a 60 kPa (overestimated for precautionary purposes) uniform load on the top surface of the model. The restraints were assigned according to the site conditions.

It is specified that the abovementioned elements were assigned through a chronological multi-stage procedure to obtain a more realistic model.

- Lithotechnical characterization

To evaluate the effects of joints implementation in FEM methods, the physical and mechanical properties of the rock materials were set following two approaches:

a. Continuum-equivalent approach: the equivalent Mohr-Coulomb parameters of the rock mass were evaluated through the linearization of the generalised Hoek-Brown failure criterion (Hoek and Brown 1980, 2019; Hoek et al. 2002; Marinou 2017) using the GSI values defined for the lithotechnical units, according to the site conditions (Table 7.6). The Calcarenite di Gravina Fm. was assumed to behave as an elastic-perfectly plastic medium, with cohesion $c'=100$ kPa, friction angle $\phi=33^\circ$ and tensile strength $\sigma_t=100$ kPa. The Calcare di Bari Fm. was considered as an elastic-perfectly plastic medium, with cohesion $c'=418$ kPa, friction angle $\phi'=54^\circ$ and tensile strength $\sigma_t=418$ kPa.

b. Anisotropic approach: the rock mass was considered as formed by an anisotropic matrix (intact rock) affected by lower strength properties along the discontinuity sets. A jointed Mohr Coulomb strength criterion (Rocscience 2021c) was set by using the equivalent Mohr-Coulomb parameters of the intact rock (GSI=100) and adding the discontinuity sets according to the mean orientations defined in section 5.3.5 (Table 7.7). With regards to the Calcarenite di Gravina Fm., the intact rock was characterized by $c'=200$ kPa, $\phi'=33^\circ$ and $\sigma_t=200$ kPa, whilst two sub-vertical joint sets were implemented assigning a Mohr-Coulomb failure criterion, with $c'=50$ kPa, $\phi'=35^\circ$ and $\sigma_t=50$ kPa. It is specified that the cohesion and tensile strength of the discontinuities were related to the presence of rock bridges. Since the percentage of rock bridges could not be defined in the field, a sensitivity analysis was later carried out to evaluate the factor of safety for different rock bridges percentages. The friction angle was estimated by adding the joint roughness contribute to the base friction angle, obtained from reference tables (Barton and Choubey 1977).

Concerning the Calcare di Bari Fm., $c'=6700$ kPa, $\phi'=54^\circ$ and $\sigma_t=6700$ kPa were assigned to the intact rock. Following the same procedure, three discontinuity sets (2 sub-vertical joint sets and bedding) with $c'=1675$ kPa, $\phi'=45^\circ$ and $\sigma_t=1675$ kPa were added.

As regards the physical properties of the rock materials, the data in Table 7.1 were used. It is specified that, for the sake of simplicity and for precautionary purposes, the properties of the micritic limestones were assigned to the Calcare di Bari Fm. The physical and mechanical properties of the Calcarenite di Gravina in wet conditions were used to take into account the effect of marine spray and wave splashing, considering the higher porosity.

Table 7.6: Geotechnical parametrization of the continuum approach. Equivalent Mohr-Coulomb parameters obtained for each lithotechnical unit through the linearization of the generalized Hoek-Brown failure criterion.

Lithotechnical unit	INPUT							OUTPUT		
	σ_c [kPa]	GSI	m_i	D	E_i [kPa]	Unit weight [kN/m ³]	Slope height [m]	Cohesion C' [kPa]	Friction angle ϕ' [°]	Tensile strength σ_t [kPa]
Calcarenite di Gravina Fm.	218000	65	8	0	2050	19	20	100	33	100
Calcere di Bari Fm.	45000	50	9	0	19800	25	20	418	54	418

Table 7.7: Geotechnical parametrization of the anisotropic approach. Equivalent Mohr-Coulomb parameters obtained for each lithotechnical unit through the linearization of the generalized Hoek-Brown failure criterion.

Lithotechnical unit	INPUT							OUTPUT		
	σ_c [kPa]	GSI	m_i	D	E_i [kPa]	Unit weight [kN/m ³]	Slope height [m]	Cohesion C' [kPa]	Friction angle ϕ' [°]	Tensile strength σ_t [kPa]
Calcarenite di Gravina Fm.	218000	100	8	0	2050	19	20	200	33	200
Calcere di Bari Fm.	45000	100	9	0	19800	25	20	6700	54	6700

Mesh generation

For both the models, a three-dimensional mesh formed by about 1,800,000 4-nodes tetrahedral elements was generated. In order to successfully carry out the stability analyses at acceptable times with a standard computer, the average element size was set to 0.40 m in the target area and to 2.7 m in the adjacent zones (Figure 7.18).

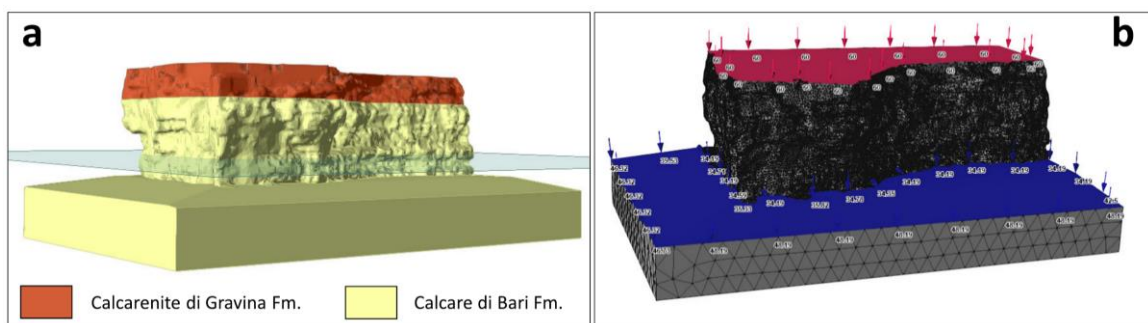


Figure 7.18: Geomechanical model (a) and discretised mesh (b) built for the 3-D FEM analyses.

Computation

For both model a and model b, two types of simulations were performed:

1. In a first phase, the initial stress state was calculated by means of a gravity loading procedure. In a second phase, an elastic-perfectly plastic behaviour was assumed for the lithofacies. Lastly, after the models converged, the Shear Strength Reduction (SSR) method (Matsui and San 1992; Griffiths and Lane 1999; Dawson et al. 1999; Hammah and Yacoub 2006; Hammah et al. 2007) was carried out through the progressive reduction of the rock mass strength properties to calculate the factor of safety (FS) of the cliff and to simulate the cliff failure, aimed at observing the potential unstable areas, as well as the failure mechanisms.
2. Sensitivity analyses for the intact rock properties were performed keeping the friction angle fixed and setting the cohesion and tensile strength in the range of 100-10 % of the initial values, to simulate different weathering degrees and to identify the entity of mechanical strength loss for which failure occurs. Sensitivity analyses were additionally carried out on model b to observe the relationship between the factor of safety and the properties of the joints introduced in the form of anisotropic surfaces. The cohesion and friction angle of the joints were set in the range 1-100 % of the intact rock properties.

Results and interpretation

1. At a first stage, the initial gravity loading and plastic calculation resulted in convergence of both models. The values of the FS calculated by means of the SSR method are 2.70 and 4.70 for the continuum-equivalent and anisotropic models, respectively. However, it is outlined that the values reported here and in the sections below are indicative as the FS depends on the combination of many factors (i.e. initial conditions and loading sequence imposed to the model, presence of very small localized failures causing the non-convergence of the model). When failure occurs, the maximum shear strain is localized at the interface between the lithotecnical units, at the base of the cliff and along indented surfaces, for both models (Figure 7.19a, Figure 7.20a). Note that Figures 7.19-22 are reported in larger size in the Supplementary Materials. The larger total displacements are concentrated in the protruding areas of the Calcarene di Gravina Fm. and in correspondence of building structures at the top of the cliff, both for the continuum-equivalent model and the anisotropic one (Figure 7.19b, Figure 7.20b). In addition, a potential unstable area was found on a cave roof in the Calcare di Bari Fm. (Figure 7.19b, Figure 7.20b, right). More in-depth, analyses were carried out along sections I-I' and II-II' to detect potential differences of the failure mechanisms between the two approaches. Although the distribution of the total displacements appears the same for the two models (Figure 7.21, Figure 7.22), a difference was found for the yielded elements. In other words, for the continuum equivalent model the yielded elements are located at the edges of the calcarenite unit and along the contact with the limestone unit (Figure 7.21, right). Yielded elements are also distributed in the overhanging zones and at the base of the cliff. As regards the anisotropic model, the yielded elements are limited to the calcarenite unit and involve larger zones (Figure 7.22, right).

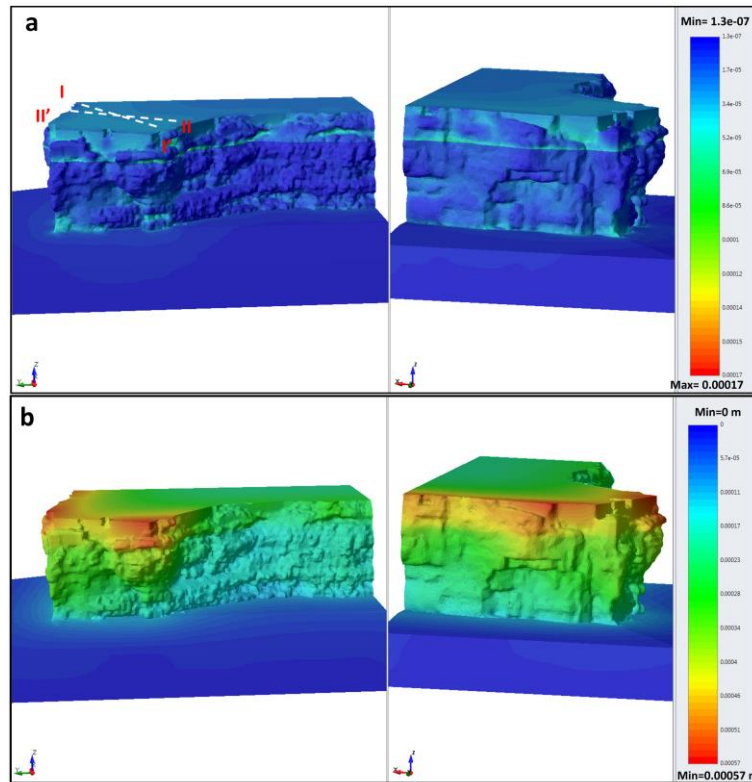


Figure 7.19: Maximum shear strain (a) and total displacements (b) of the continuum-equivalent model (model a); FS=2.70.

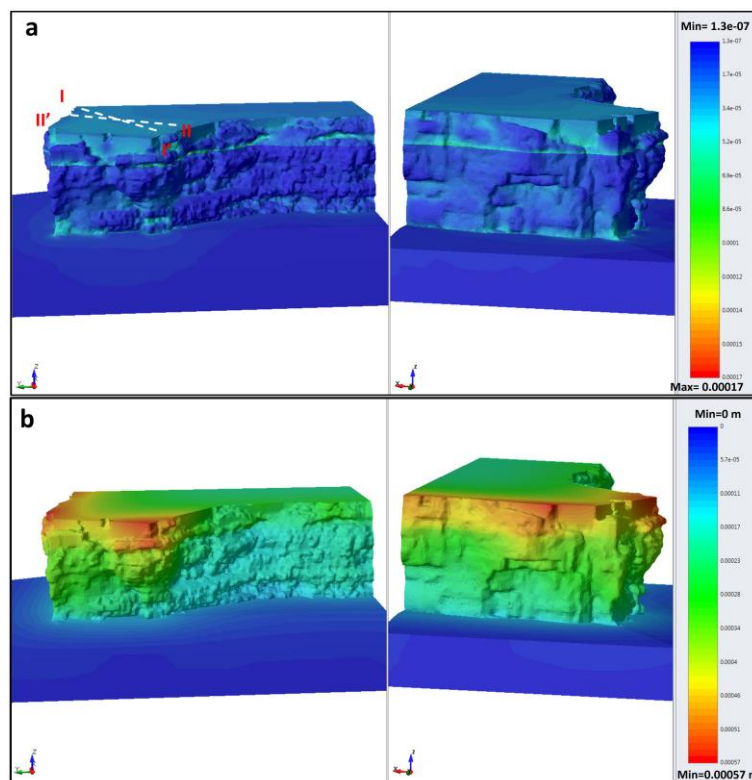


Figure 7.20: Maximum shear strain (a) and total displacements (b) of the anisotropic model (model b); FS=4.70.

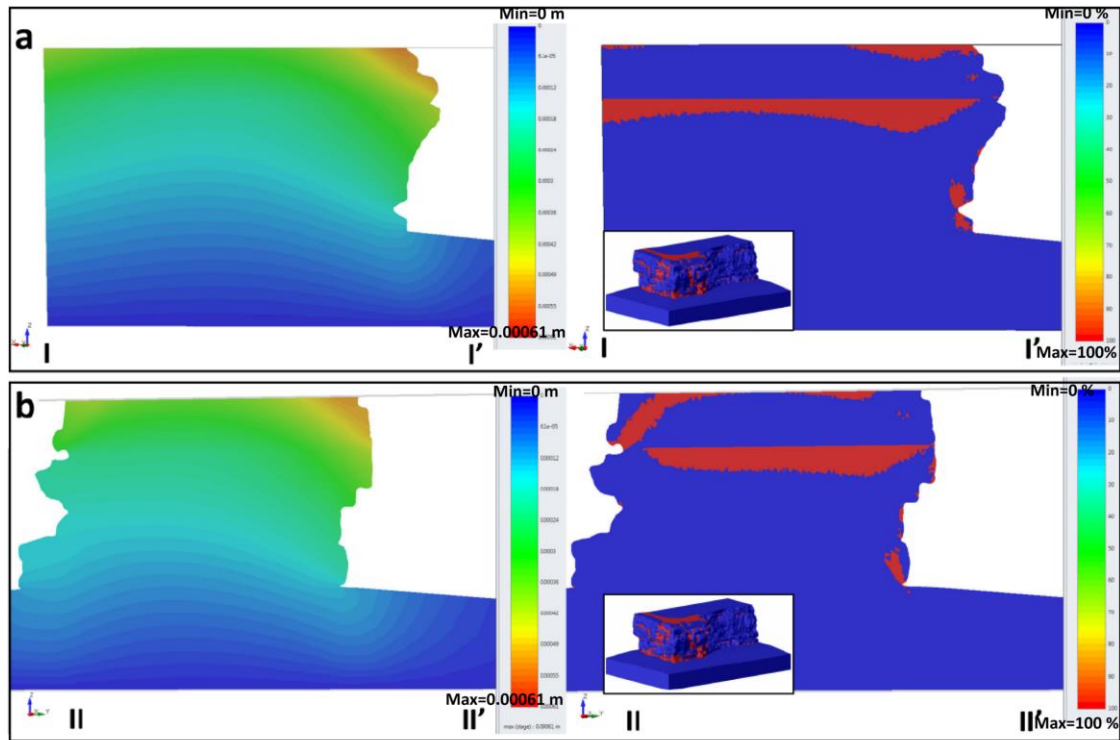


Figure 7.21: Cross sections I-I' (a) and II-II' (b) of the continuum-equivalent model (model a); left: total displacements; right: yielded elements.

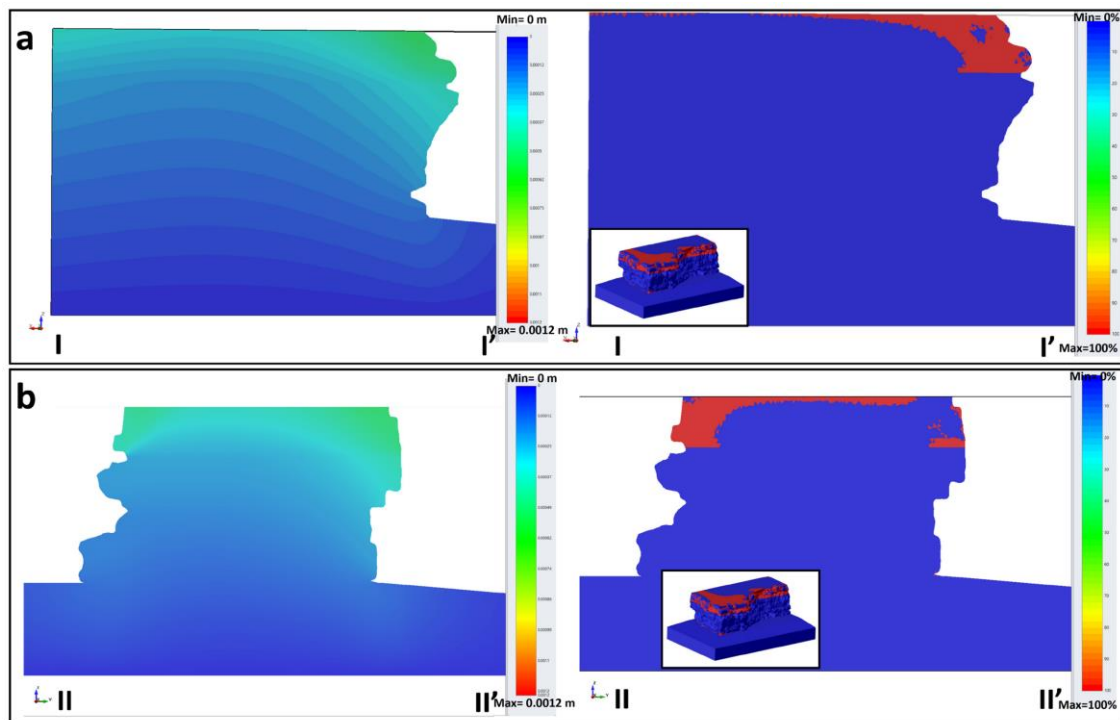


Figure 7.22: Cross sections I-I' (a) and II-II' (b) of the anisotropic model (model b); left: total displacements; right: yielded elements.

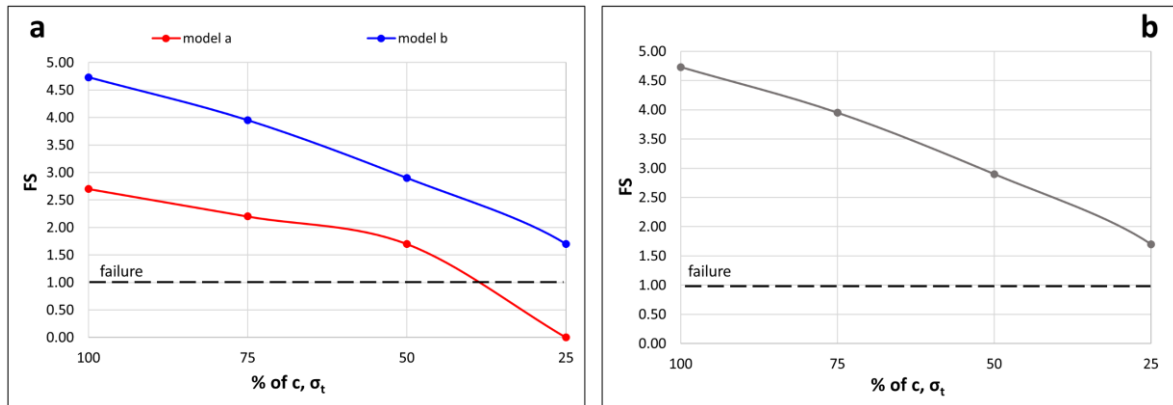


Figure 7.23: Sensitivity analyses. (a) FS in function of the cohesion c and tensile strength σ_t of the intact rock (in the range 25-100% of the assigned initial values); the red and blue curves represent respectively the continuum-equivalent and anisotropic models. (b) FS of the anisotropic model in function of the cohesion c and tensile strength σ_t of the joints implemented in the model (in the range 25-100% of the intact rock). It is specified that further reduction of c and σ_t caused non-convergence of the models for both sensitivity analyses.

2. Sensitivity analyses performed on the continuum-equivalent and the anisotropic models illustrate how FS decreases as the cohesion and tensile strength of the rock materials are reduced. For the continuum-equivalent model, failure occurs when c' and σ_t are less than 40% with respect to the initial assigned values, whilst the anisotropic model converged even with a 75% reduction of the strength properties (Figure 7.23a). Moreover, the sensitivity analysis carried out changing the joints strength properties of the initial anisotropic model ($c', \sigma_t = 100\%$) point out that the cliff is stable until the discontinuities have cohesion and tensile strength values larger than 25% with respect to the intact rock (Figure 7.23b). This means that, for the case study, approach b converges if the implemented anisotropies correspond to non-persistent discontinuities, with at least 25% of their size formed by rock bridges. Indeed, the non-persistence of the discontinuities was confirmed by the conventional geotechnical and geomechanical surveys, as well as by the 2-D quantitative characterization.

7.3.8.2. Two-dimensional model

Objectives

Further analyses were performed to investigate different geological processes that might originate the rock slope failure. Due to the computational limits when dealing with complex 3-D models and to the necessity of conducting a significant number of simulations, a bi-dimensional FEM approach was adopted by means of RS2 software (Rocscience 2021a), which is the 2-D equivalent of RS3 (the technical specifications can be found at: <https://www.rocscience.com/help/rs2/overview/technical-specifications>). Being located in the most critical zones, sections I-I' and II-II' were used to perform this study, also in the perspective to achieve more detailed results through a finer mesh. A first model was generated according to the continuum-equivalent approach showed in section 5.3.8.1. Later on, a second model was obtained by introducing a joint network in both Calcare di Bari and Calcarenite di Gravina formations. It is specified that the discontinuity sets were implemented as interfaces and not as anisotropic zones, as in the 3-D model. The simulations were carried out on both models, to

compare the results and observe the effects of joints implementation in traditional continuum or continuum-equivalent FEM models.

Model set-up and mesh generation

The geometric model was built importing the two sections in RS2 software and adding the water conditions, loads and restraints as in the 3-D model.

- Continuum-equivalent model

The Calcarene di Gravina Fm. and the Calcare di Bari Fm. were assumed as elastic-perfectly plastic Mohr-Coulomb materials, with $c'=100$ kPa, $\sigma_t=100$ kPa, $\phi'=33^\circ$ for the calcarenite unit and $c'=418$ kPa, $\sigma_t=418$ kPa, $\phi'=54^\circ$ for the limestone unit. As in the 3-D model, these data were obtained through the linearization of the generalised Hoek-Brown criterion for the estimation of the rock mass equivalent Mohr-Coulomb parameters. About 16,000 and 18,000 six-node triangular elements were created during the discretisation and mesh generation for section I-I' and section II-II', respectively.

- Jointed model: in this case, the lithotechnical units were considered as elastic-perfectly plastic Mohr-Coulomb media with GSI=100. For the Calcarene di Gravina Fm. $c'=200$, $\phi'=33^\circ$ and $\sigma_t=200$ kPa, whilst for the Calcare di Bari Fm. $c'=6700$ kPa, $\phi'=54^\circ$ and $\sigma_t=6700$ kPa. Two joint networks, made up of discontinuities according to the definition proposed by Goodman and Shi (1985) were introduced in the lithotechnical units in the form of interfaces (mesh-less elements), preserving numerical continuity between the adjacent sectors. With regards to the Calcarene di Gravina Fm., a sub-vertical joint set was introduced based on qualitative observations in the field and on point clouds inspection (see Figure 7.5). Two sub-vertical joint sets and the bedding surfaces were introduced in the Calcare di Bari Fm. More in detail, since the analyzed sections are not parallel to the mean strike of the sub-vertical joint sets, both of them were supposed to intersect the model. The distributions obtained from the 2-D quantitative analyses of the discontinuity traces (section 5.3.5) were used to generate the sub-vertical joint sets by means of Discrete Fracture Network (DFN) approach (Dershowitz and Einstein 1988; Merrien-Soukatchoff et al. 2012; Havaej et al. 2016; Montiel et al. 2020). The results of digital scanlines along the bedding surfaces of the rock mass were used to produce the bedding surfaces.

This approach allowed a more realistic representation of the discontinuity sets by taking into account the sets mean spacing, trace length and persistence. With regards to the persistence, this work refers to the definition proposed by Einstein and co-workers and Hudson and Priest (Einstein et al. 1983; Hudson and Priest 1983). In detail, in the bi-dimensional space, the discontinuity persistence can be expressed as the limit length ratio along a given line on a joint plane:

$$K = \lim_{L_s \rightarrow x} \sum_i \frac{l_{s_i}}{L_s}$$

where L_s is the length of a straight line segment S and l_{s_i} is the length of the i -th joint segment in S . In other words, persistent joints are represented by continuous traces (Figure 7.23a), whilst non-persistent joints are either intermittent (Figure 7.24b) or made up of separate segments (Figure 7.24c) (Hudson and Priest 1983). In both cases, the shear strength of non-persistent discontinuities is related to the rock bridges located between the discontinuity segments (Figure 7.24d). Based on field observation and quantitative discontinuity analyses, the sub-vertical joint

sets of the numerical model were considered as non-persistent, both for the Calcarenite di Gravina Fm. and Calcare di Bari Fm, although with different rock bridges percentages. Conversely, persistent discontinuities were attributed to the bedding surfaces of the Calcare di Bari Fm.

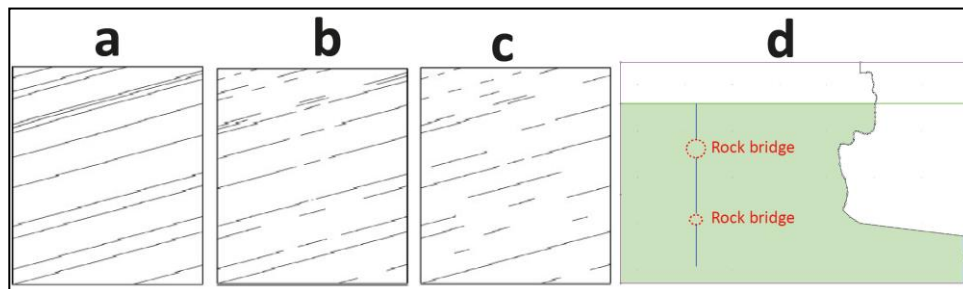


Figure 7.24: Persistence definition used in this study. (a) persistent discontinuities; (b) intermittent discontinuities; (c) separate non-persistent discontinuities (after Riquelme et al. 2018); (d) modelling of non-persistent discontinuities: the tensile strength σ_t and cohesion c along a discontinuity is related to σ_t and c' of the intact rock in correspondence of the rock bridges (modified after Riquelme et al. 2018).

The strength properties of the joints were assigned according to the Mohr-Coulomb failure criterion. Specifically, for all the discontinuity segments, the cohesion and tensile strength were set to zero, while a friction angle of 35° and 45° were assigned to those belonging to the calcarenite and limestone units, respectively, according to the procedure illustrated in the paragraph above. The discretized meshes are made up of about 29,800 for section I-I' and about 30,000 for section II-II'.

The final models are shown in Figure 7.25.

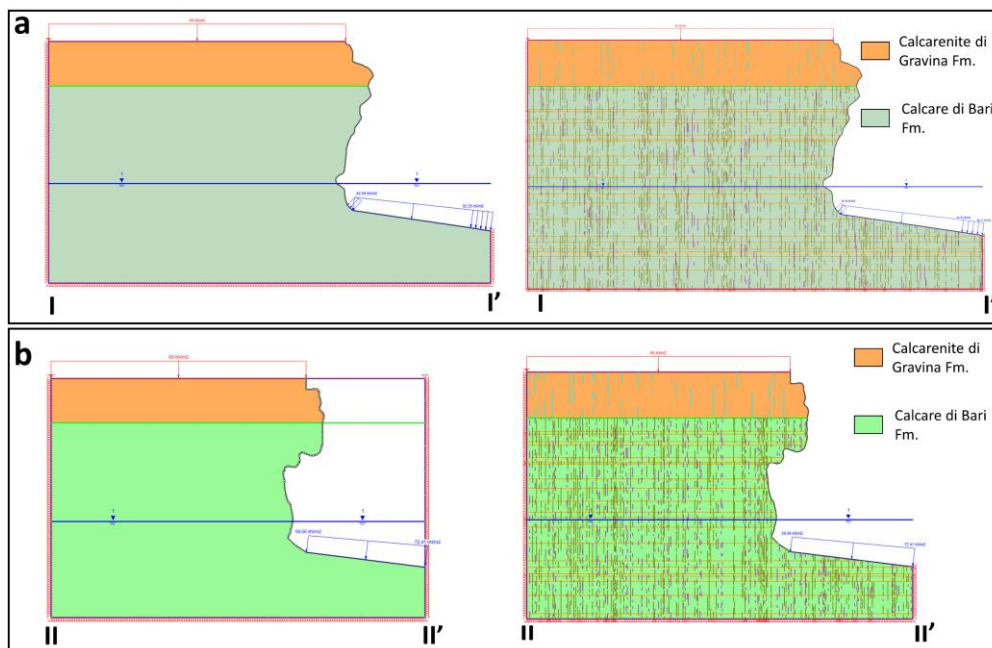


Figure 7.25: Model set-up of section I-I' (a) and section II-II' (b). To the left, continuum-equivalent model; to the right, jointed model.

Simulations and computation

For each model, the following simulations were carried out:

1. At a first stage, the gravity loading and plastic computation were run for each section. The SSR method was carried out through the progressive reduction of the rock materials strength properties to determine the FS and the failure mechanisms. Moreover, a sensitivity analysis was carried out to point out the effects of rock mechanical degradation (lowering the cohesion and tensile strength of the rock materials in the range 40-100% of the initial values) on the slope stability using both approaches.
2. Several excavations were simulated at the cliff foot on the continuum-equivalent and the jointed models to investigate the role of sea erosion in the cliff stability, and to assess any difference between the approaches used. The tests were executed by changing the horizontal erosion depth of the notch, until reaching the critical conditions (FS close to 1). Later on, keeping an erosion depth for which both models converged, the rock materials strength was gradually reduced in terms of cohesion and tensile strength, until reaching incipient failure. This simulation was done to observe the effects of different environmental weathering degrees on the stability of the cliff, modelled through the continuum-equivalent and the jointed models.
3. Tension cracks were implemented by adding vertical joints in the form of interfaces and re-meshing the initial models (without erosion notch). The distance between the tension crack and the external border of the model (towards the sea) was progressively reduced to detect the threshold beyond which failure occurs. Moreover, at critical distance, the rock materials strength properties were reduced until reaching non-convergence of the models, to observe the effects of rock degradation on the cliff affected by a tension crack. Finally, the combined action of tension crack development and sea erosion were examined by keeping the tension crack at a fixed distance (though stability was preserved) and deepening the marine erosion notch, until producing incipient failure.

Results and interpretation

- The FS values of section I-I' are 2.93 for the continuum-equivalent model and 6.83 for the jointed model. These results are in agreement with the theory proposed by Tsesarsky and Hatzor (2009), developed by means of generalized rigid body analyses and numerical discontinuous deformation analyses. According to this theory, overhanging slopes with eccentricity ratio $e = B/L > 0.4$, where B and L are respectively the base and the top surface lengths, are in stable conditions. As a matter of fact, the minimum eccentricity ratio e for section I-I' is 0.89, hence ensuring the stability according to the mentioned theory. When non-convergence is obtained by means of SSR technique, the failure of the continuum-equivalent model occurs through a sliding surface developed from the toe to the top of the cliff (Figure 7.26 a1-c1). Note that Figures 7.26-31 are reported in larger size in the Supplementary Materials. In addition, the external volume just below the buildings, delimited by a surface dipping towards the slope, tends to topple. The yielded elements are localized along these surfaces and mostly in the Calcarene di Gravina Fm. It has to be specified that the displacements shown in the figures are exaggerated to better visualise the movements and deformations, but the continuity condition is preserved, as a fundamental assumption of the Finite Element Methods (Jing 2003; Hammah et al. 2008). In other words, detachments of individual blocks are not allowed in these simulations. As concerns the jointed model, a rotational slide is limited to

the Calcarenite di Gravina Fm., whilst rock blocks delimited by the discontinuity sets are prone to sliding and toppling processes in the Calcare di Bari Fm. (Figure 7.26 a2-c2). The yielded joints contributing to the cliff instability are illustrated in Figure 7.26 c2.

- For section II-II', the FS values are 1.33 and 4.14 respectively for the continuum-equivalent and the jointed models. Also in this case, the results are in agreement with the theory proposed by Tsesarsky and Hatzor ($e=0.87$). When failure is achieved, a shear band from the base of an overhanging block to the top of the cliff forms in the continuum-equivalent model (Figure 7.26 d1-f1). At the small scale, the volume of the slope delimited by this shear band is prone to sliding. However, the load exerted from the buildings located on the top causes a smaller wedge failure and the toppling of the block located on the external edge of the model. As for section I-I', the yielded elements are concentrated in the calcarenite unit. Although similar mechanisms characterize the jointed model, localized failures occur in the form of slides and topples in the same volume (Figure 7.26 d2-f2).

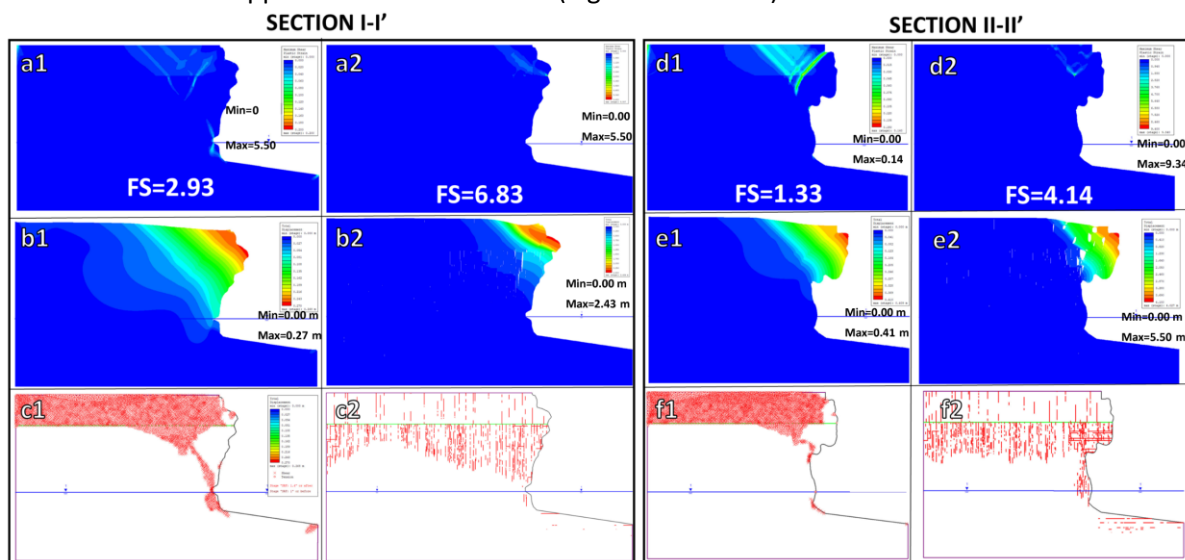


Figure 7.26: Critical failure mechanisms of sections I-I' and II-II' for the continuum-equivalent model (left) and the jointed model (right) produced by means of the SSR method. (a, d) maximum shear strain; (b, e) total displacements with deformation contours; (c1, f1) yielded elements for shear and tension; (c2, f2) yielded joints. Note that the displacements are exaggerated for visualisation purposes. For both sections, the failure mechanism of the continuum-equivalent model is represented by the sliding of the area dipping towards the sea and a slight toppling of the sector on the edge. For the jointed models, failure involves rock blocks delimited by the discontinuity sets. While rotational movements affect the Calcarenite di Gravina Fm., slides and topples affect the Calcare di Bari Fm.

The results of the sensitivity analyses performed on the jointed model by reducing the cohesion and tensile strength of the rock materials show that, despite a rock mechanical degradation of 60%, both sections are in stable conditions. On the contrary, using the continuum-equivalent model, a strength reduction of 60% and 45% can cause the failure of section I-I' and II-II', respectively (Figure 7.27). However, the mechanical properties of the joints implemented in the jointed model were not changed. This is a limitation which can be improved for future studies, because chemical alteration and mechanical degradation, especially at the sea level, are more likely to reduce the discontinuities strength properties.

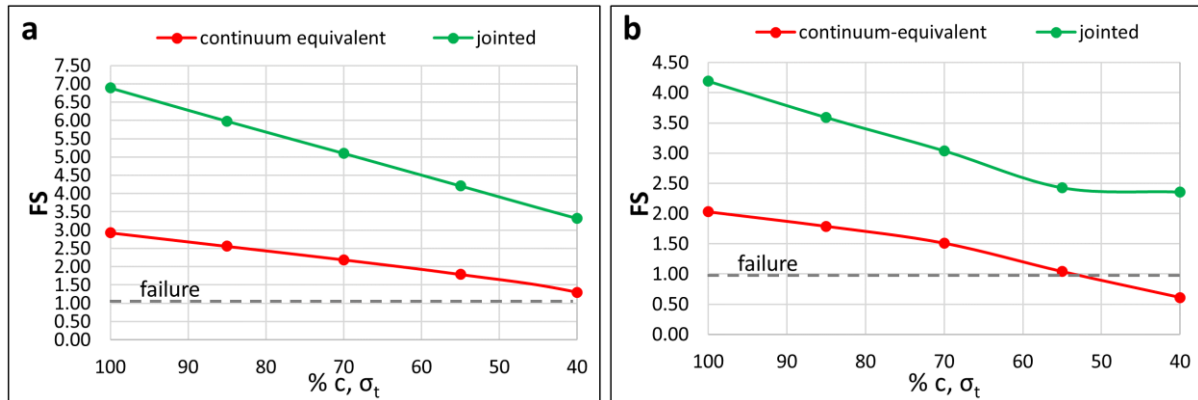


Figure 7.27: Sensitivity analyses showing the FS in function of the cohesion c' and tensile strength σ_t of the intact rock (in the range 40-100% of the assigned initial values) of section I-I' (a) and section II-II' (b). The red and green curves represent the continuum-equivalent and the jointed models, respectively.

Effects of marine erosion and tension crack formation

Section I-I'

- A significant marine erosion depth is required to produce the cliff failure using the continuum-equivalent approach (about 5 m, Figures 7.28 a1,3). Conversely, according to the results of the jointed model, an erosion depth of 1.5 m would be enough to cause the failure (Figures 7.28 a2,4). Whilst the failure of the former model involves the volume delimited by a shear surface developing from the notch to the top of the cliff, the latter is characterized by rotation of the sector just above the notch, with slides and topples of smaller rock blocks. With an erosion depth of 1 m for both models, strength reductions of 50% and 25% are needed, respectively, for the continuum-equivalent and the jointed model to produce the cliff failure.

The results of these tests point out that, despite the jointed model has a high FS, the failure is achieved much earlier than in the continuum-equivalent model (considering that the marine erosion notch deepens with time), and involves smaller volumes. At the same time, small degrees of weathering have a major impact on the cliff stability of the jointed model with respect to the continuum-equivalent one. It is outstanding that the parametric analyses show that the continuum-equivalent model is more susceptible to rock mechanical degradation than the jointed model. This contradiction can be due to the fact that, at critical conditions, the implemented joint sets play a key role on the cliff stability. In addition, any further deepening of the marine notch interacts with the sub-vertical joints and the bedding, causing the partial detachment of rock blocks.

- When a slightly cemented ($c'=10$ kPa, $\sigma_t=10$ kPa) tension crack develops parallel to the slope, the cliff stability is preserved when its distance from the external border is larger than about 4 m, for both models (Figure 7.29 a1-4). A shear surface develops from the toe of the cliff towards the tension crack, causing the rotation of the delimited volume. The continuum-equivalent model illustrates a flexural toppling mechanism (Figure 7.29 a3), whilst the bedding surfaces of the jointed model contribute to the simultaneous sliding of the volume (Figure 7.29 a4). In critical conditions, a reduction of 25% of the mechanical properties of the rock materials can cause the cliff failure of the jointed model (Figure 7.29 b1-2). The level of strength reduction for the continuum-equivalent approach is 50% (Figure 7.29 b3-4). Moreover, in critical conditions, the continuum-equivalent model indicates failure with a less intense marine erosion process compared the jointed model

(0.5 m against 1.0 m) (Figure 7.29 c1-4). It has to be noted that the instability occurred by introducing the tension cracks is in agreement with the theory proposed by Tsesarsky and Hatzor (2009), as the eccentricity ratio of the overhanging zone (average eccentricity=0.44 for simulations a1-c4) is very near to the threshold established by the authors (i.e. 0.40).

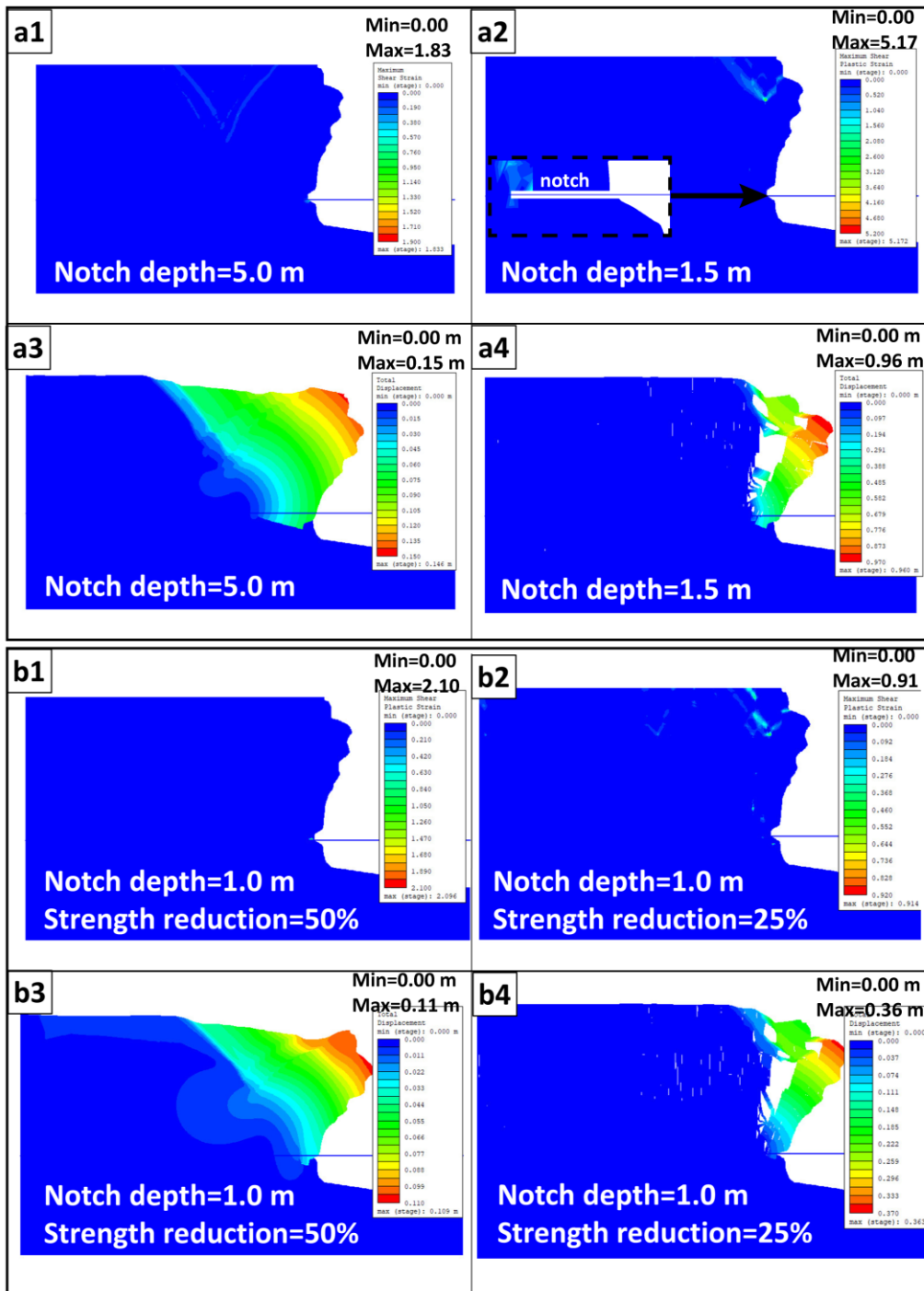


Figure 7.28: Critical failure mechanisms of section I-I' produced simulating marine erosion. Note: due to software rendering, the notch is only visible with extensive zoom. It is specified that, for all the following images, the morphology is similar to that illustrated in Figure a2, although with different notch depth. Top window: sea erosion process; (a1-2) maximum shear strain of the continuum-equivalent (a1) and the jointed models (a2);

(a3-4) total displacements and deformation contours of the continuum-equivalent (a3) and the jointed models (a4). Small erosion depths (>1.5 m) can cause the failure of the jointed model. The contours of the continuum-equivalent model indicate a composite movement (sliding and toppling) of a larger area compared to the jointed model, which in turns is characterized by the failure of smaller blocks defined by the discontinuity sets. Bottom window: combination of sea erosion and weathering processes; (b1-2) maximum shear strain of the continuum-equivalent (b1) and the jointed models (b2); (b3-4) total displacements and deformation contours of the continuum-equivalent (a3) and the jointed models (b4). Although the kinematics are similar to the previous simulation, for an erosion depth of 0.50 m, a small degree of weathering (25% strength reduction) can cause the rock slope failure for the jointed model. Both for the continuum-equivalent and continuum approach, the erosion process favours the toppling of the sector located just above the notch.

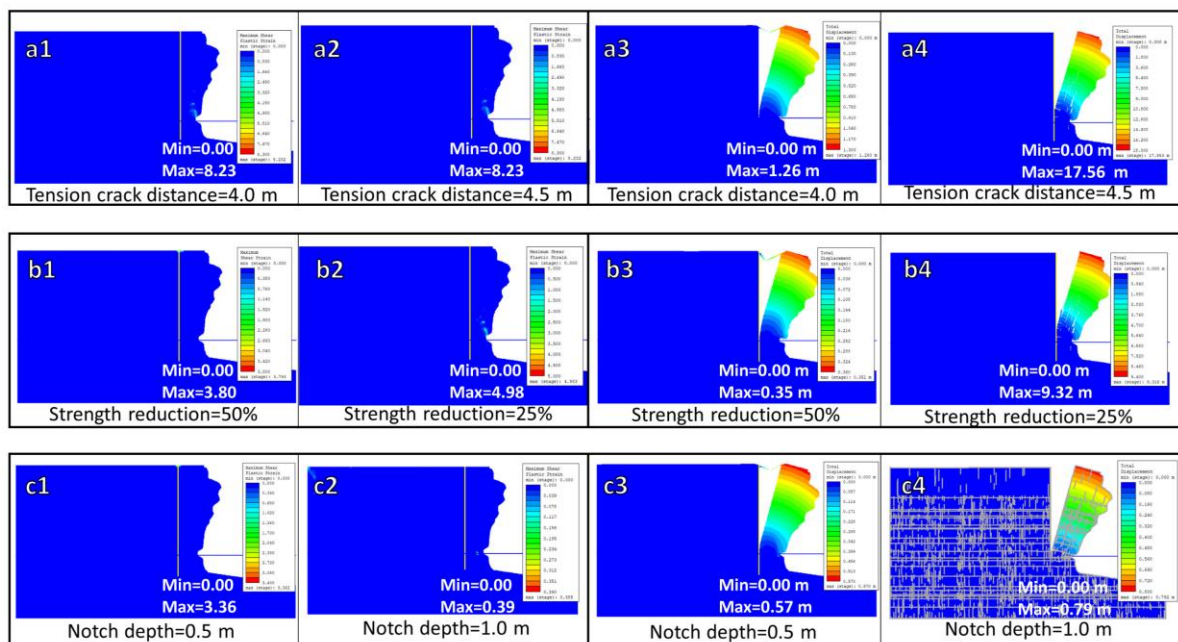


Figure 7.29: Critical failure mechanisms of section I-I' produced introducing a slightly cemented tension crack. To the left (a1, a2, b1, b2, c1, c2), maximum shear strain. To the right (a3, a4, b3, b4, c3, c4), total displacements with deformation contours. (a1-4) minim external edge-tension crack distance, beyond which failure occurs. (b1-4) with a tension crack located at 4.0 m from the external edge, failure occurs with a 50% and 25% reduction (in terms of cohesion and tensile strength of the rock materials), for the continuum-equivalent and jointed models, respectively. (c1-4) with the same tension crack, failure is also achieved when marine erosion develops, with a notch depth of 0.5 and 1.0 m respectively for the continuum-equivalent and for the jointed models. For all the simulations, flexural toppling characterizes the continuum-equivalent model. As regards the jointed model, a volume just above the sea notch is subjected to composite toppling and sliding, using a bedding surface as base plane.

Section II-II'

- As in section I-I', a very small erosion depth (0.5 m) can cause the cliff failure of the jointed model, whilst the continuum-equivalent approach shows that the cliff is stable even with an erosion depth of 5 m Figure 7.30 a1,3). The failure mechanism of the continuum-equivalent model is represented by the sliding along a surface extending from the notch to the top of the cliff. As concerns the jointed model, localized failures in correspondence of the notch caused non-convergence of the analysis (Figure 7.30 a2,4).

The jointed model appears less sensitive to the strength reduction of the mechanical properties of the rock materials, compared to the continuum-equivalent model (75% vs 25%). This result is not consistent with that of section I-I'. A possible explanation is that the initial continuum-equivalent model (without erosion and strength reduction) is close to failure (FS=1.33), so that any rock mechanical degradation causes non-convergence.

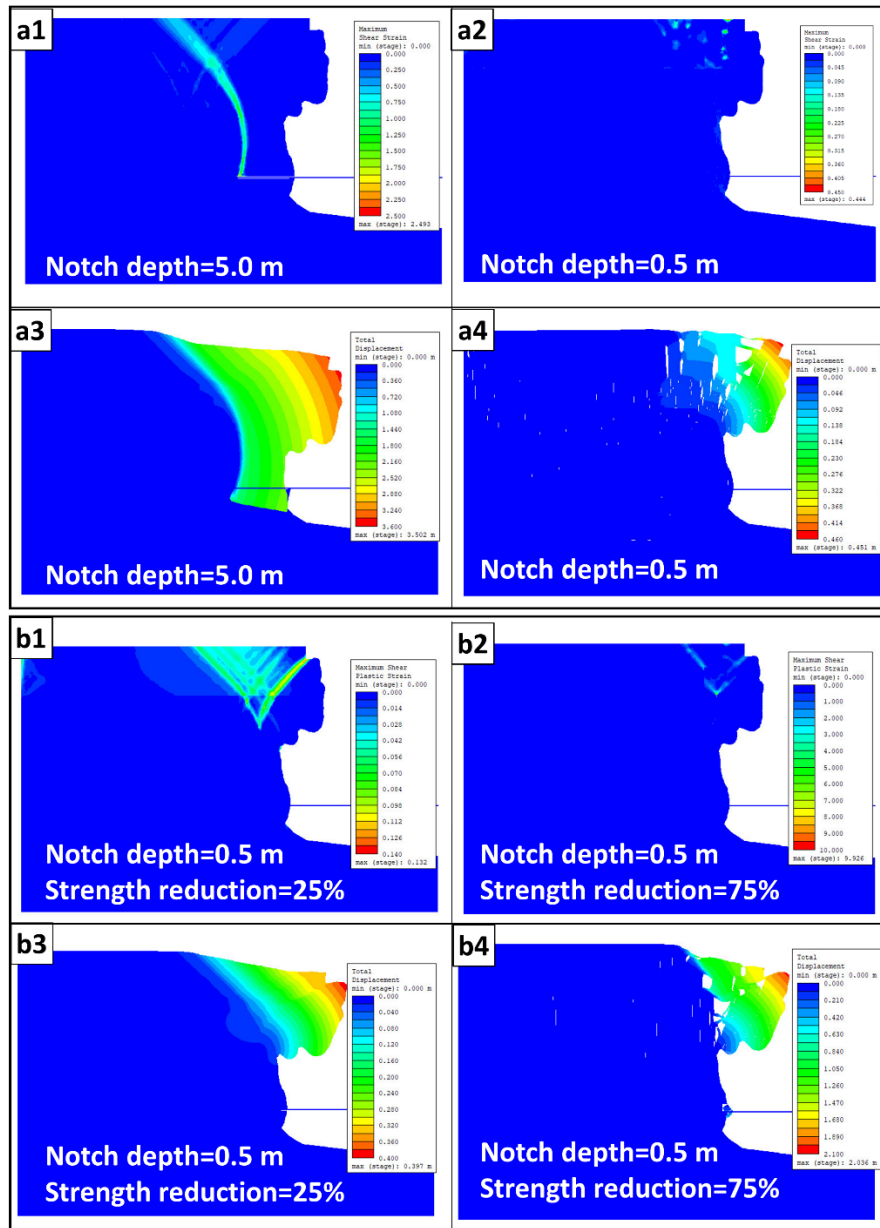


Figure 7.30: Critical failure mechanisms of section II-II' produced simulating marine erosion. Top window: sea erosion process; (a1-2) maximum shear strain of the continuum-equivalent (a1) and the jointed models (a2); (a3-4) total displacements and deformation contours of the continuum-equivalent (a3) and the jointed models (a4). For the continuum-equivalent model, a failure surface develops from the notch at the base of the cliff foot to the top. Conversely, the jointed model is characterized by the failure of rock blocks at the erosion notch (a2). A non-realistic sea erosion depth (>5 m) is required to have the continuum-equivalent models failed, whilst less intense processes (erosion depth >0.5 m) can produce the failure of the jointed models.

- As for section I-I', the critical distance of a slightly cemented tension crack needed to preserve cliff stability is similar for the continuum-equivalent and the jointed models (about 5 m) (Figure 7.31 a1-4). For the continuum-equivalent model, shear structures concentrate at mid-height of the slope and cause the flexural toppling of the volume above (Figure 7.31 a1,a3). As regards the jointed model, the presence of the tension crack favours the partial detachment of the external sector at the top of the cliff, whose strain is also determined by the weight of the buildings located above (Figure 7.31 a2,a4). In addition, localized failures within the same volume occur along the discontinuity systems.

In critical conditions (tension crack located at 5.5 m from the edge), the percentage of mechanical degradation which can cause non-convergence is the same for both models (75%) (Figure 7.31 b1-4). In addition, the same notch deepening (about 0.50 m) with a tension crack located at critical distance causes the cliff failure, using either the continuum-equivalent approach or the jointed one (Figure 7.31 c1-4).

As regards the kinematics of the continuum-equivalent model, weathering processes cause a major effect with respect to the tension crack, because failure occurs through a surface independent from the tension crack (Figure 7.31 b3). The notch deepening results in a larger height of the failed volume (Figure 7.31 c3). The failure mechanisms of the jointed model with the tension crack, whether isolated or coupled with the weathering or the erosion notch, are similar (Figure 7.31 a4, b4, c4). However, local failures at the notch were detected (Figure 7.31 c4). This is in agreement with the failures observed by means of field and point clouds observations, through which portions of strata detached from the bedding surfaces were observed at the present sea level. Also in this case, the eccentricity ratio in critical conditions is close to that proposed by Tsersarsky and Hatzor (2009). As a matter of fact, the mean eccentricity ratio for simulations a1-c4 is equal to 0.44, whilst the value proposed by the authors is 0.40.

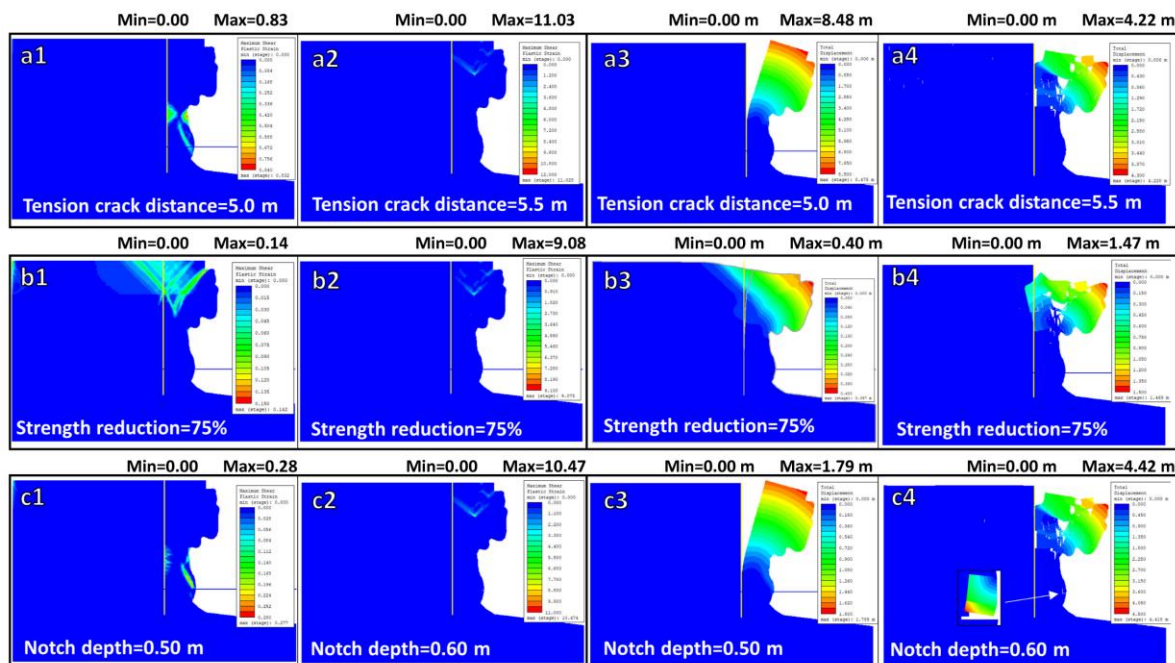


Figure 7.31: Critical failure mechanisms of section II-II' with a slightly cemented tension crack. To the left (a1, a2, b1, b2, c1, c2), maximum shear strain. To the right (a3, a4, b3, b4, c3, c4), total displacements with

deformation contours. **(a1-4)** minim external edge-tension crack distance, beyond which failure occurs. **(b1-4)** with a tension crack located at 5.5 m from the external edge, failure occurs with a 75% strength reduction for both models. **(c1-4)** with the same tension crack, failure occurs for both models with an erosion depth of about 0.5 m. As concerns the continuum-equivalent model, a volume detached from the tension crack topples towards the sea. The deepening of the marine erosion notch slightly increases the height of the failed block. When the strength properties are reduced of 75%, the failure is caused by sliding and rotational surfaces in the upper part of the cliff. As regards the jointed model, a rock mass portion delimited by the tension crack is subjected to toppling and localized failures of rock blocks in the external area. The 75% strength reduction causes the failure of a wedge on the top of the model **(b4)**, probably because of the load exerted by the buildings. The marine erosion process produces also small failures in correspondence of the notch **(c4)**.

7.3.8.3. Remarks

Despite the numerical analyses were carried out using two different systems (3-D and 2-D), some interesting results emerged. Both techniques indicate that the case study is currently in stable conditions, with a minimum FS value of 2.03 (2-D analysis, section II-II', continuum-equivalent approach). In general, the mechanical degradation of the rock materials as consequence of environmental weathering processes can expose the overhanging areas of the weaker Calcare di Gravina Fm., as well as the karst caves roofs and indented zones, to local failures (i.e. Figures. 7.19-22). It is remarked that the critical degree of weathering beyond which failure occurs can be quite different, depending on the approach used (i.e. continuum equivalent or anisotropic/jointed).

As concerns the failure mechanisms, both 3-D and the 2-D continuum equivalent models indicate that, despite the yield is mostly concentrated in the calcarenite units, the failure surfaces develop from the foot of the cliff, in correspondence of the sea notch, to the top (Figure 7.21, Figure 7.26 a1-c1, d1-f1). Contrarily, the 3-D anisotropic model and the 2-D jointed model show that the rock mass degradation causes small-size local failures of the overhanging areas (Figure 7.22, Figure 26 a2-c2, d2-f2). However, whilst the 3-D model detected instabilities only in the calcarenite unit, the 2-D model highlighted mobilisation also in the upper part of the Calcare di Bari Fm. With regard to the 3-D model, it is specified that the presence of soft rocks on the top of the cliff might have caused a localized concentration of displacements and strains and masked smaller values in the Calcare di Bari Fm. Another possible explanation for this discrepancy is that the strength reduction factor used during the SSR phase of the 3-D model reduced the Calcare di Gravina mechanical properties until reaching a critical condition, contrarily to the Calcare di Bari Fm. that, even if characterized by anisotropy along the discontinuity sets, did not fail. On the contrary, the degradation of the rock materials of the 2-D model caused an incompatibility with the strength properties of the joint networks (structural interfaces) in both formations, producing local failures in the upper part of the limestone unit. Based on these observations, it is believed that the failure mechanisms depicted through the continuum-equivalent models may occur at the global scale and over long terms. More in detail, the failure mechanism observed for section I-I' is in agreement with field observations and point clouds inspection, through which the progressive sliding of the same multi-block sector was recognized, as also demonstrated by cracks in the overlying building (Figure 7.15e). According to the geostructural and geomechanical surveys, localized failures through the mobilisation of rock blocks delimited by the discontinuity systems and the topography are more frequent. As a matter of fact, several blocks of well-defined shape (i.e. tabular blocks) were found at the base of the cliff and on the shore bottom. Moreover, the marine erosion action, weathering processes (i.e. salt crystallization, marine spray, rainfall water infiltration, wind erosion, etc.) and the formation of tension cracks parallel to the cliff

are more likely to interact with the discontinuity systems and to determine failures even with little processes, as outlined in section 7.3.8.2. As final remark, it must be specified that uniform weathering processes were considered in all the simulations (as a current limitation of the FEM methods), but a larger effect is expected along the discontinuity systems, especially at the sea level.

7.4. Conclusion

In this chapter an exhaustive procedure for hazard assessment in rock slopes was presented, as well as its application to a case study. This methodology includes both conventional field surveys and the application of UAV systems to carry out comprehensive geostructural and geomechanical analyses. Particular focus was given to the quantitative characterization of the discontinuity sets that affect the case study, with meticulous analyses carried out both in 2-D and 3-D to detect the number of discontinuity sets and their mean orientation, spacing, trace length, and persistence, as well as to define the probabilistic distributions of the mentioned properties. It is stressed that the results were validated by means of specific field surveys and that, despite the data obtained from point clouds were in agreement, the data derived from 2-D analyses were considered more appropriate. As a matter of fact, the investigated rock mass is constituted by sub-horizontal and sub-vertical surfaces (i.e. marine, alluvial and anthropogenic terraces), therefore some discontinuities were subsampled during the point cloud processing, as many of them are visible only in the form of traces. However, 3-D data allowed a better estimation of the failed volumes and of the probabilistic distribution compared to the 2-D analyses. It must be remarked that the physical and mechanical characterization of the rock materials and of the discontinuities is essential to understand the rock mass mechanical behaviour and to assemble a comprehensive geomechanical model. For this reason, specific laboratory tests were carried out, both under dry and wet conditions, considering that the case study is a cliff subjected to marine spray processes. As a matter of fact, a 50% tensile and uniaxial compressive strength reduction was detected for the Calcarenite di Gravina Fm. In favour of safety, the physical and mechanical properties of the calcarenite unit in wet conditions were assigned to the geomechanical model. However, since the mechanical properties of the discontinuities were deduced from the literature, future improvements may involve the execution of mechanical tests on the discontinuities, although the sampling in the field would be quite challenging, considering low accessibility and law restrictions. Artificial discontinuities and specific correlations could be alternatively used.

The geomechanical model allowed a preliminary assessment of the failure mechanisms by means of kinematic analyses individually carried out on different sectors of the surveyed area. The results were compared with those of field surveys and remote sensing investigations and the typical failure mechanisms of the case study were defined.

Later on, advanced 3-D and 2-D FEM analyses were carried out to study the site stability at the global scale, and to simulate the effect of surface processes observed both in the field and on the DOMs (i.e. weathering, tension cracks, marine erosion at the sea level). At this stage, a comparative analysis between continuum-based and discontinuum (anisotropic and jointed models respectively for the 3-D and 2-D analyses) approaches was presented, to observe the effects of the choice of the method when dealing with numerical methods. The data collected by analysing the discontinuity traces were fully exploited using the 2-D DFN approach, to achieve a more realistic model of the study site. As concern the failure mechanisms, which were better represented through the 2-D analyses, the continuum-based technique depicted the sliding and rotation towards the sea of a larger sector of the rock mass with respect to the discontinuum method, which showed smaller failures of volumes

delimited by the discontinuity sets. Both mechanisms are in agreement with field observations: global-scale failures may occur in long times, whilst smaller instabilities attributable to the failure of rock bridges connecting the discontinuities, and in correspondence of the karst caves, are more probable in the near future.

It must be remarked that the FEM method, which was used to study the effect of non-persistent joints and because of software availability, does not allow complete detachment of rock blocks. However, the failure mechanisms may involve isolated rock blocks, as locally observed in the field. As a matter of fact, several discontinuities were found to be under yielding condition during the simulations (e.g. Figure 7.26 c2, f2) and may play a key role on the mechanical behaviour of the rock mass. Hence, a further specific approach could be addressed to the application of DEM aimed at considering also the constitutive laws for joints and intact blocks, the forces between blocks and the motion law of each block. An interesting research topic could deal with the comparison of the results shown by Tsesarsky and Hatzor (2009) for a similar case study (dolostone succession with bedding and sub-vertical joint sets). By direct comparison of DDA (Discontinuous Deformation Analysis) and FEM models, the authors found out that the two approaches indicated the same failure mechanisms and displacements of the slope face when no joints were implemented in the DDA analysis. When the joints were added to the DDA simulation, the authors observed that the displacements were one order of magnitude larger with respect to the FEM analysis, but the mode of failures were the same.

Moreover, non-uniform weathering and cyclic loads (i.e. earthquakes and sea storms) could be simulated to have a detailed overview of the study site and optimize the proposed methodology. Crackmeters might be installed in the open discontinuities to investigate the role of cyclic and annual thermal variations, and to eventually integrate them in the numerical models. Finally, the processes simulated, as well as the discontinuity sets in the form of joint networks, could be implemented in a 3-D environment though, in this context, progresses in academic-software development and computing technologies should be accomplished.

7.5. Supplementary materials

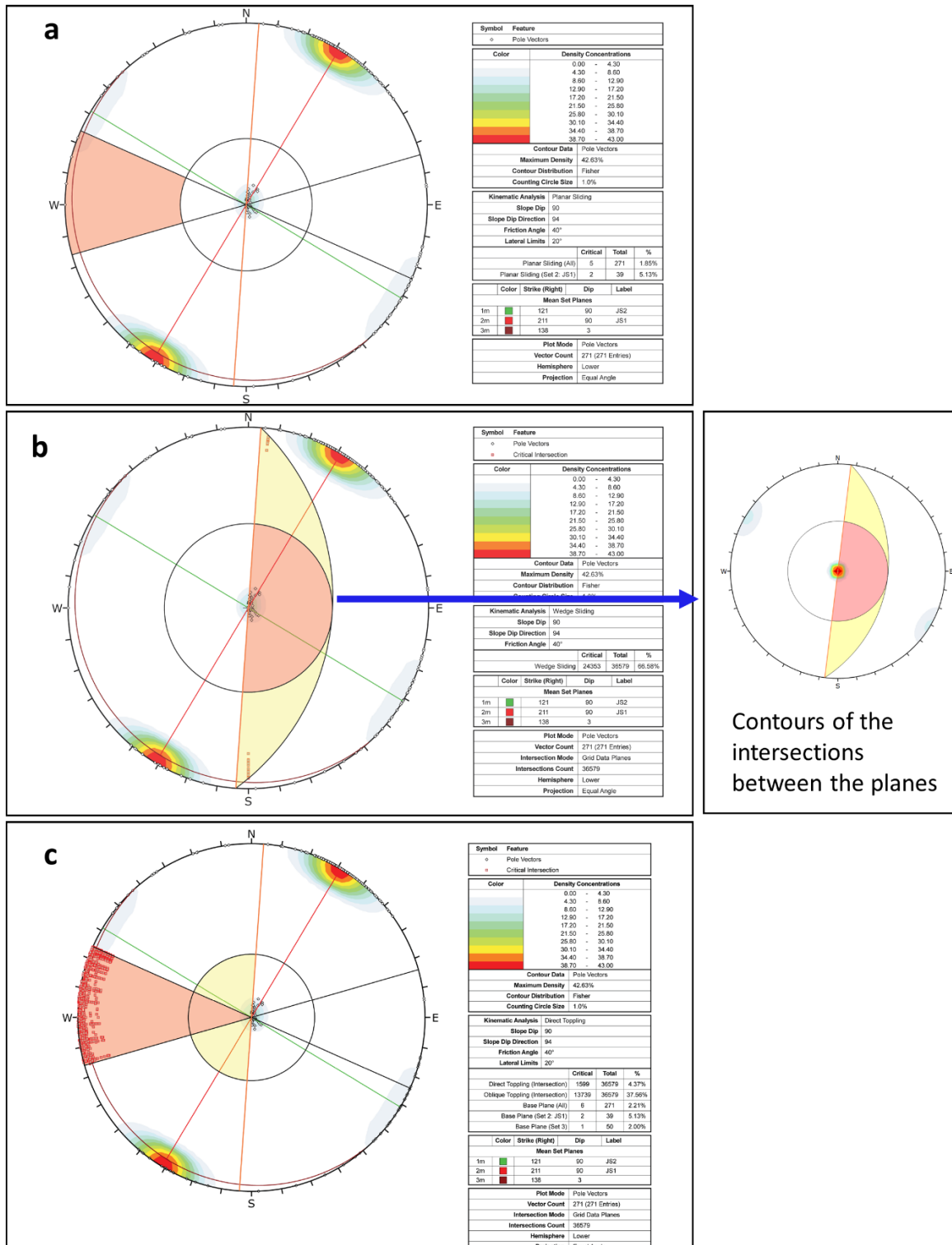


Figure S7.1: Kinematic tests for planar sliding (a), wedge sliding (b) and direct toppling (c) for Sector A. Important note for the wedge sliding test (also for the figures below): most of the intersections between the planes belonging to JS1 and JS2 are located exactly at the centre of the stereonet and are overlapped. It might appear that no critical intersections are located inside the critical area, however it is just a visualization defect of the used software and the results reported in the table should be considered.

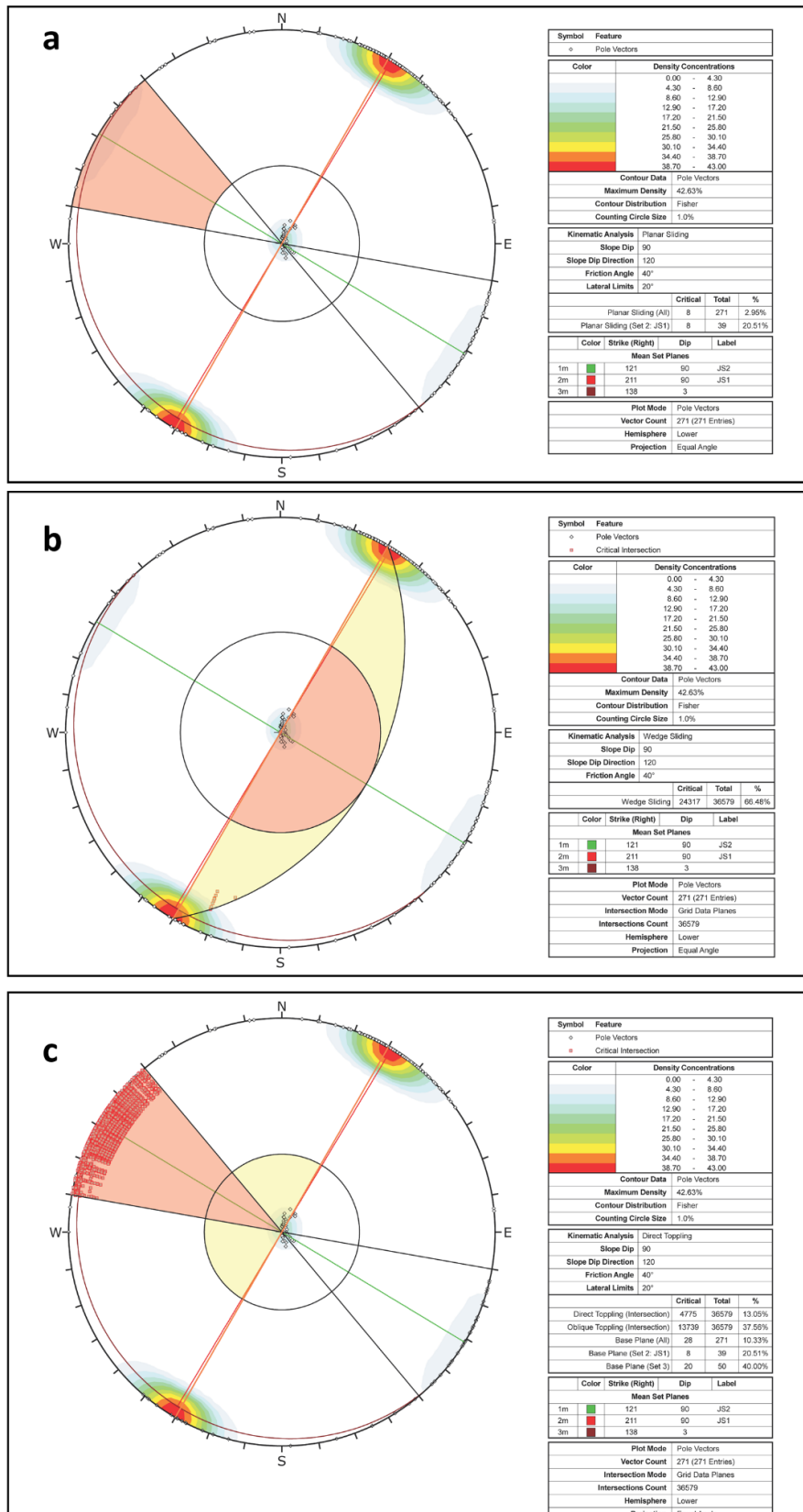


Figure S7.2: Kinematic tests for planar sliding (a), wedge sliding (b) and direct toppling (c) for Sector B.

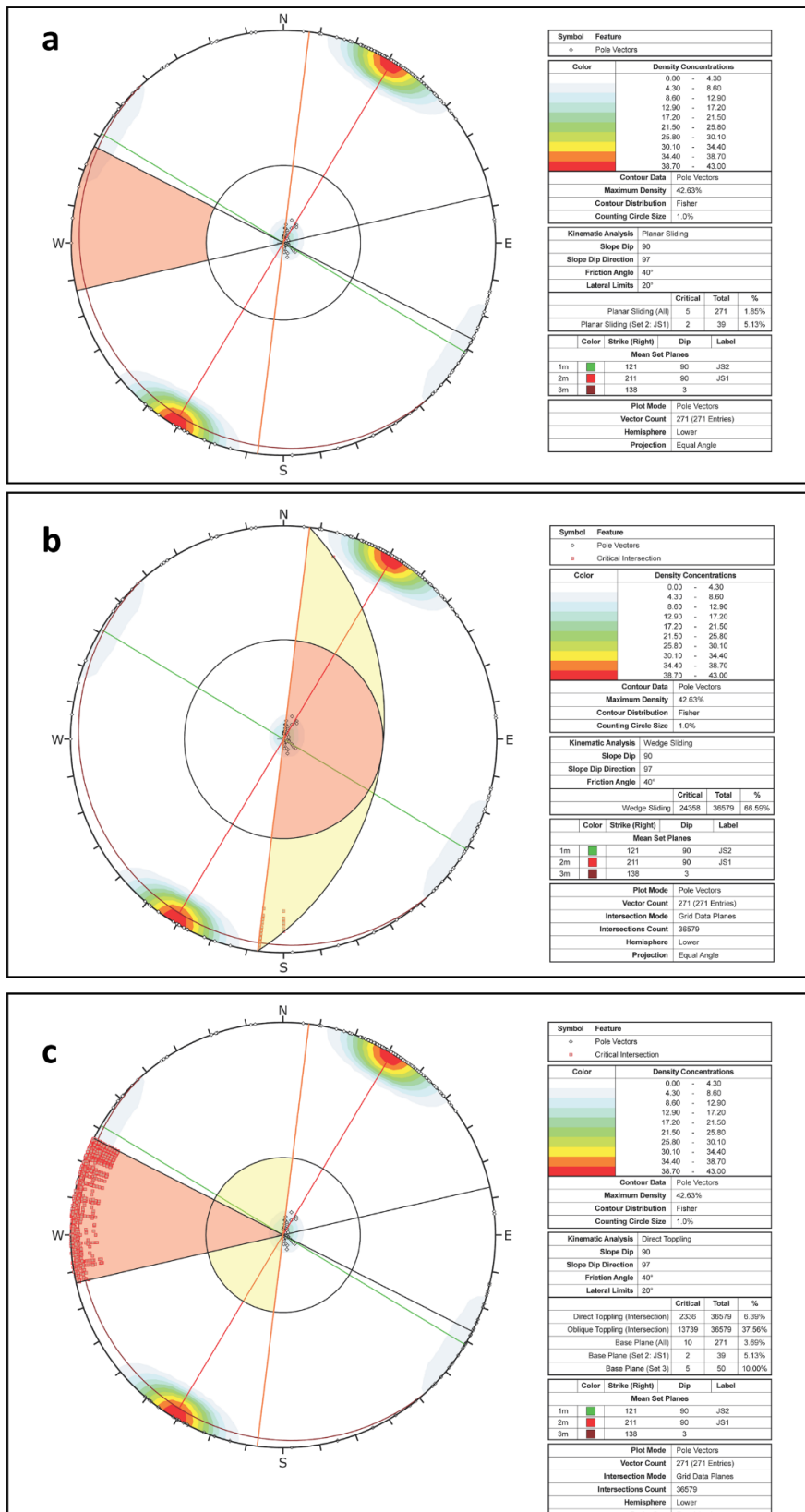


Figure S7.3: Kinematic tests for planar sliding (a), wedge sliding (b) and direct toppling (c) for Sector C.

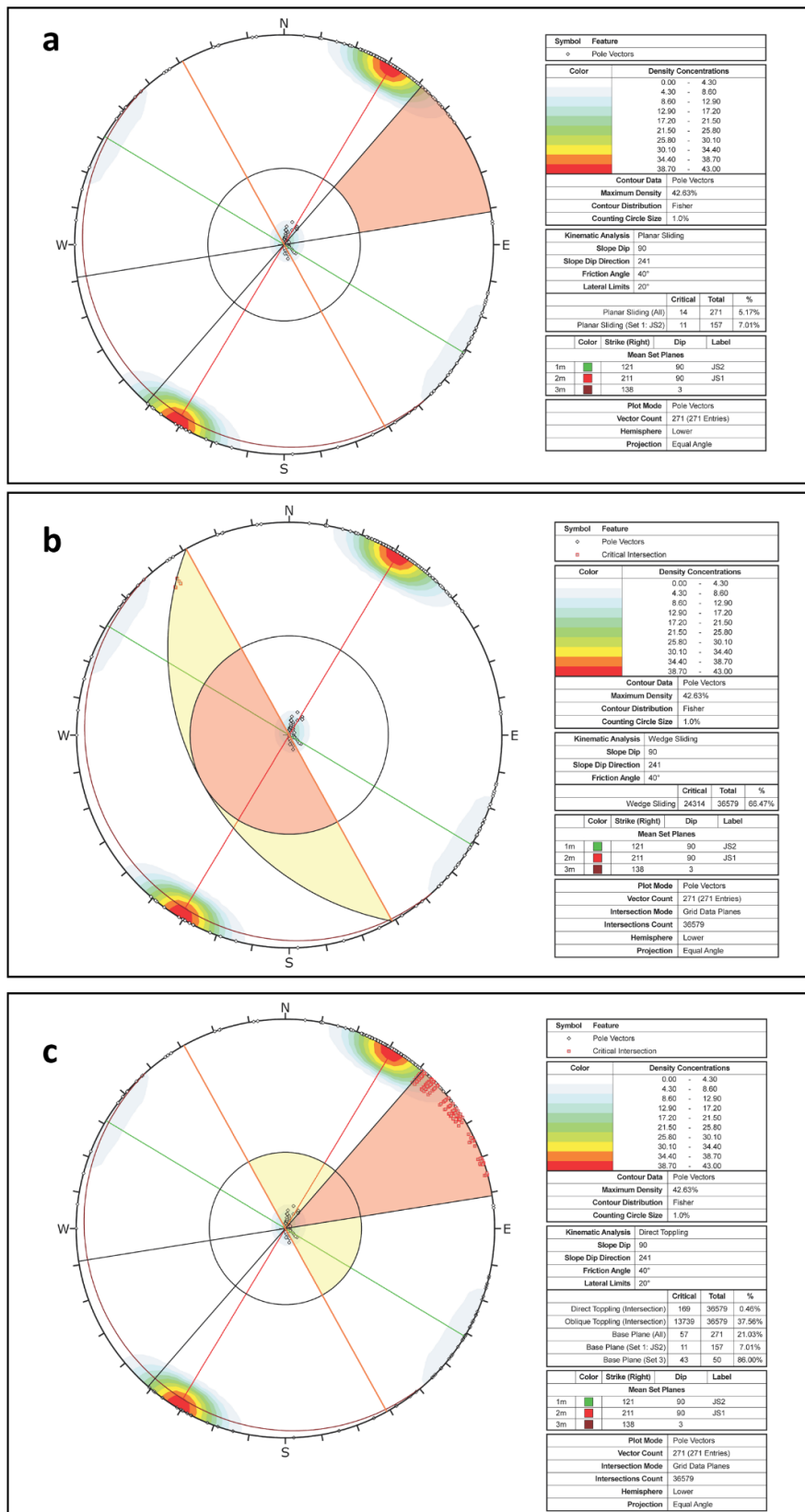


Figure S7.4: Kinematic tests for planar sliding (a), wedge sliding (b) and direct toppling (c) for Sector D.

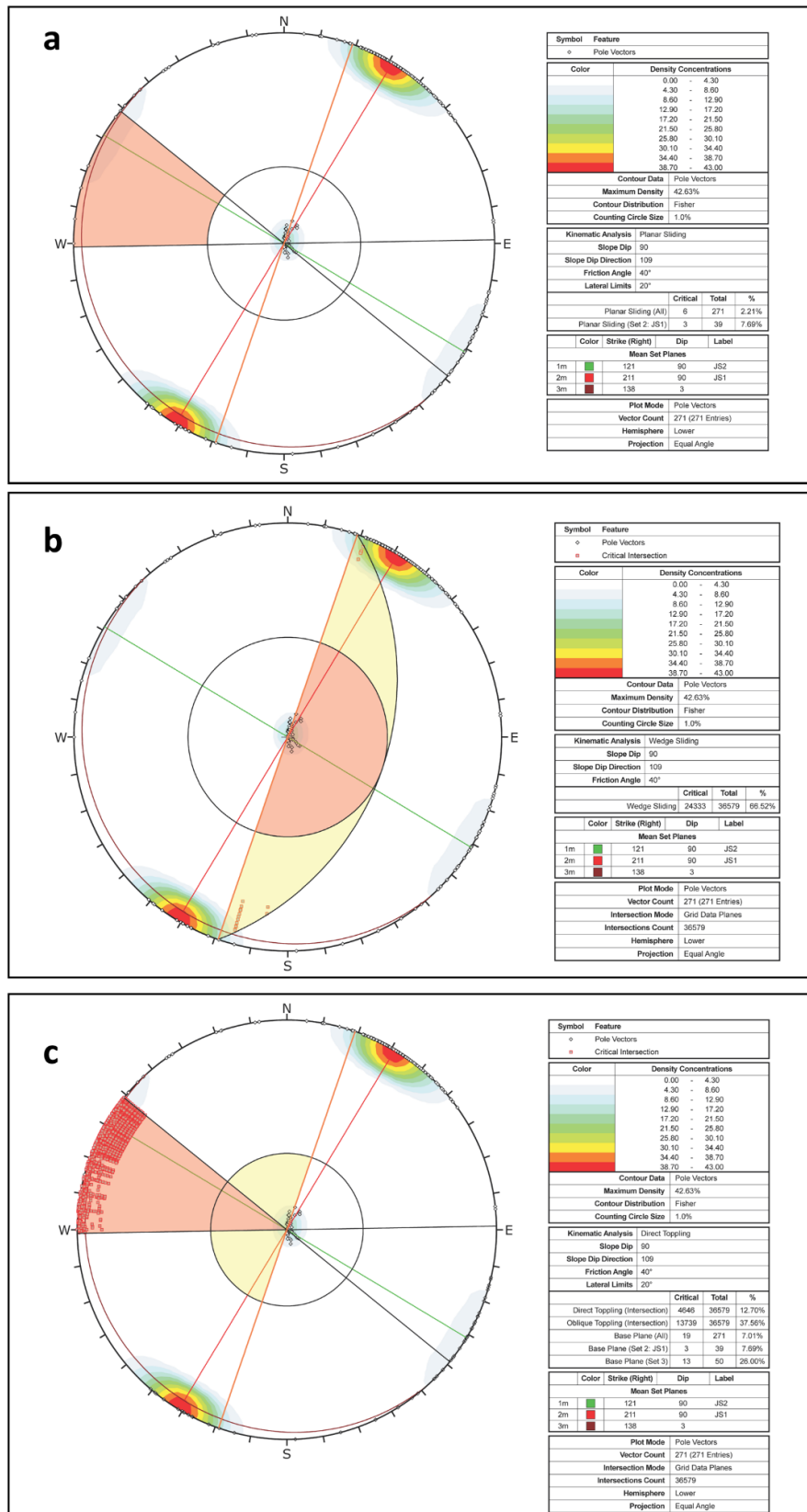


Figure S7.5: Kinematic tests for planar sliding (a), wedge sliding (b) and direct toppling (c) for Sector E.

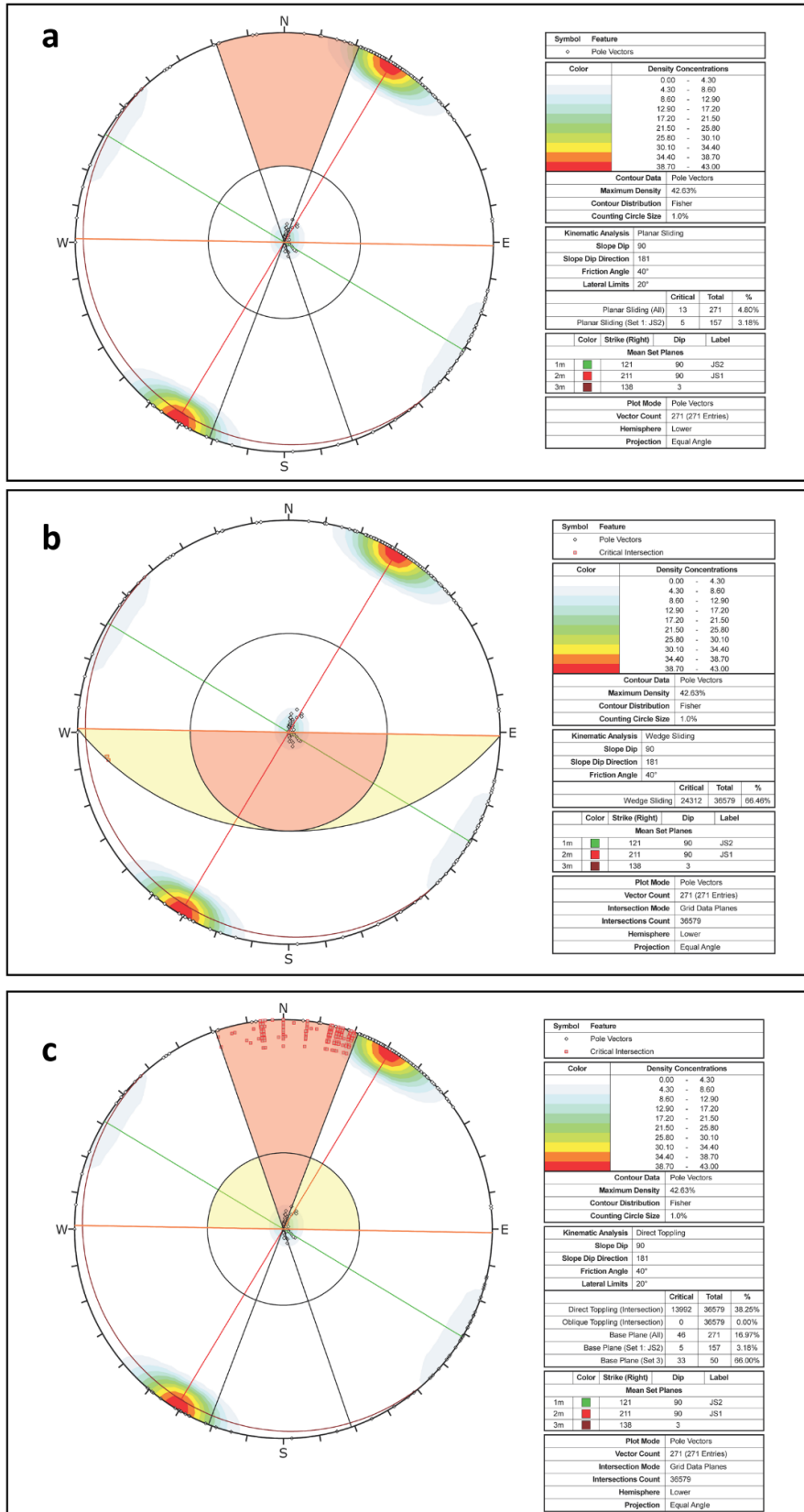


Figure S7.6: Kinematic tests for planar sliding (a), wedge sliding (b) and direct toppling (c) for Sector F.

Multidisciplinary approach for stability analyses of rock masses: integration of field surveys, remote sensing techniques and numerical modelling

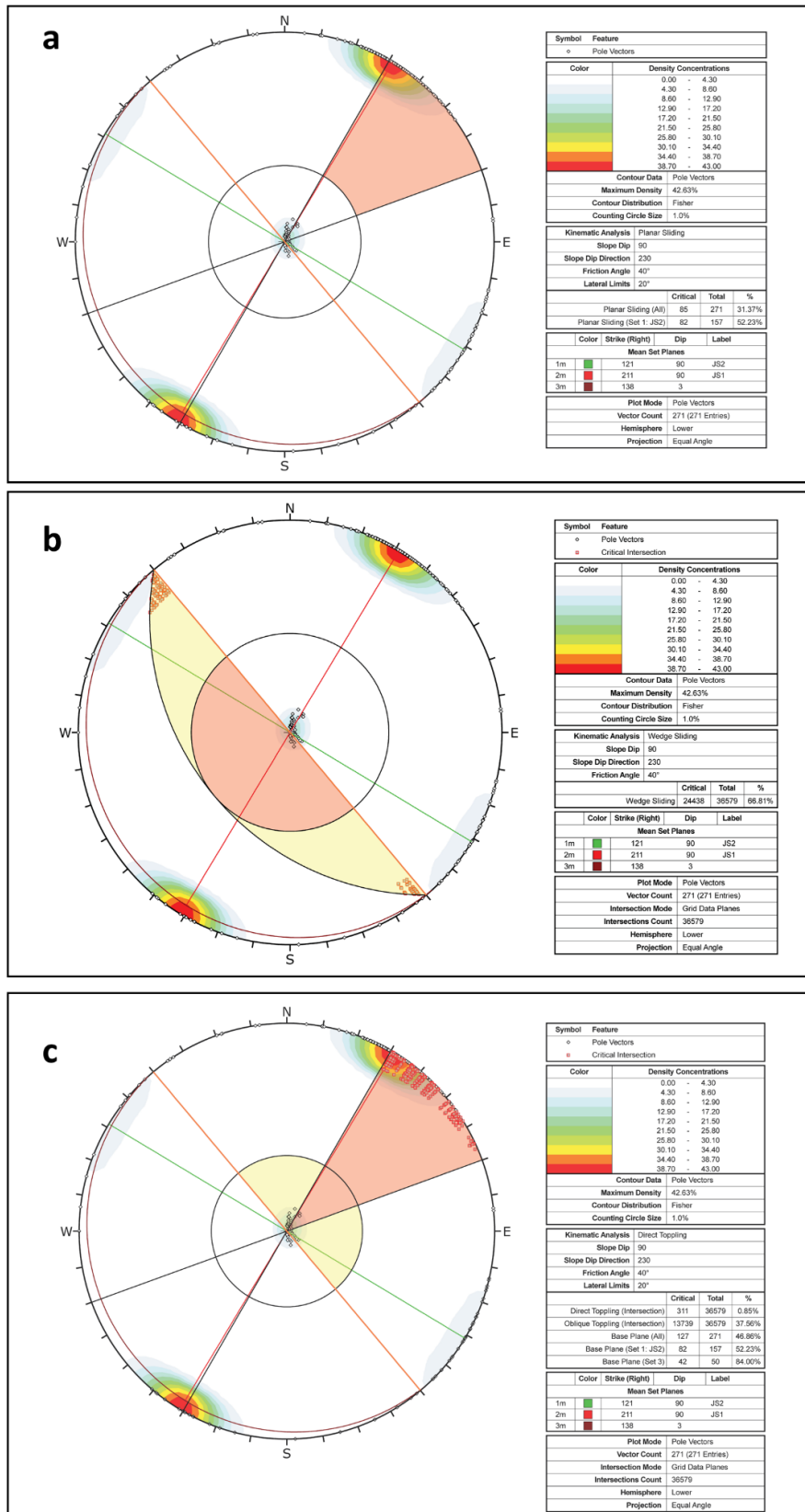
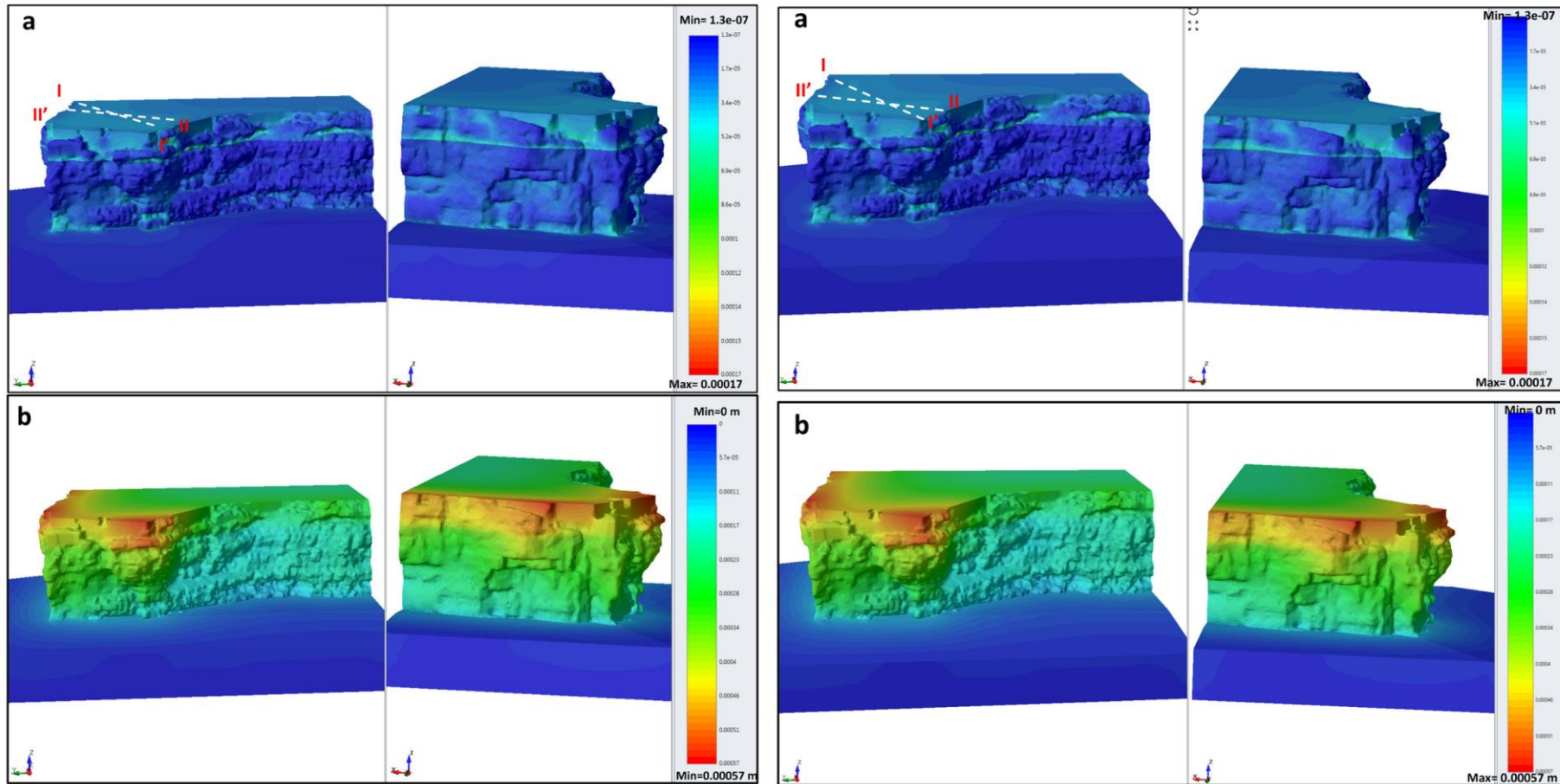


Figure S7.7: Kinematic tests for planar sliding (a), wedge sliding (b) and direct toppling (c) for Sector G.

Model A – continuum-equivalent approach

Model B – anisotropic approach



Figures S7.19 (left) and S7.20 (right): Maximum shear strain (a) and total displacements (b) of the continuum-equivalent model (left, FS=2.70) and of the anisotropic model (right, FS=4.70).

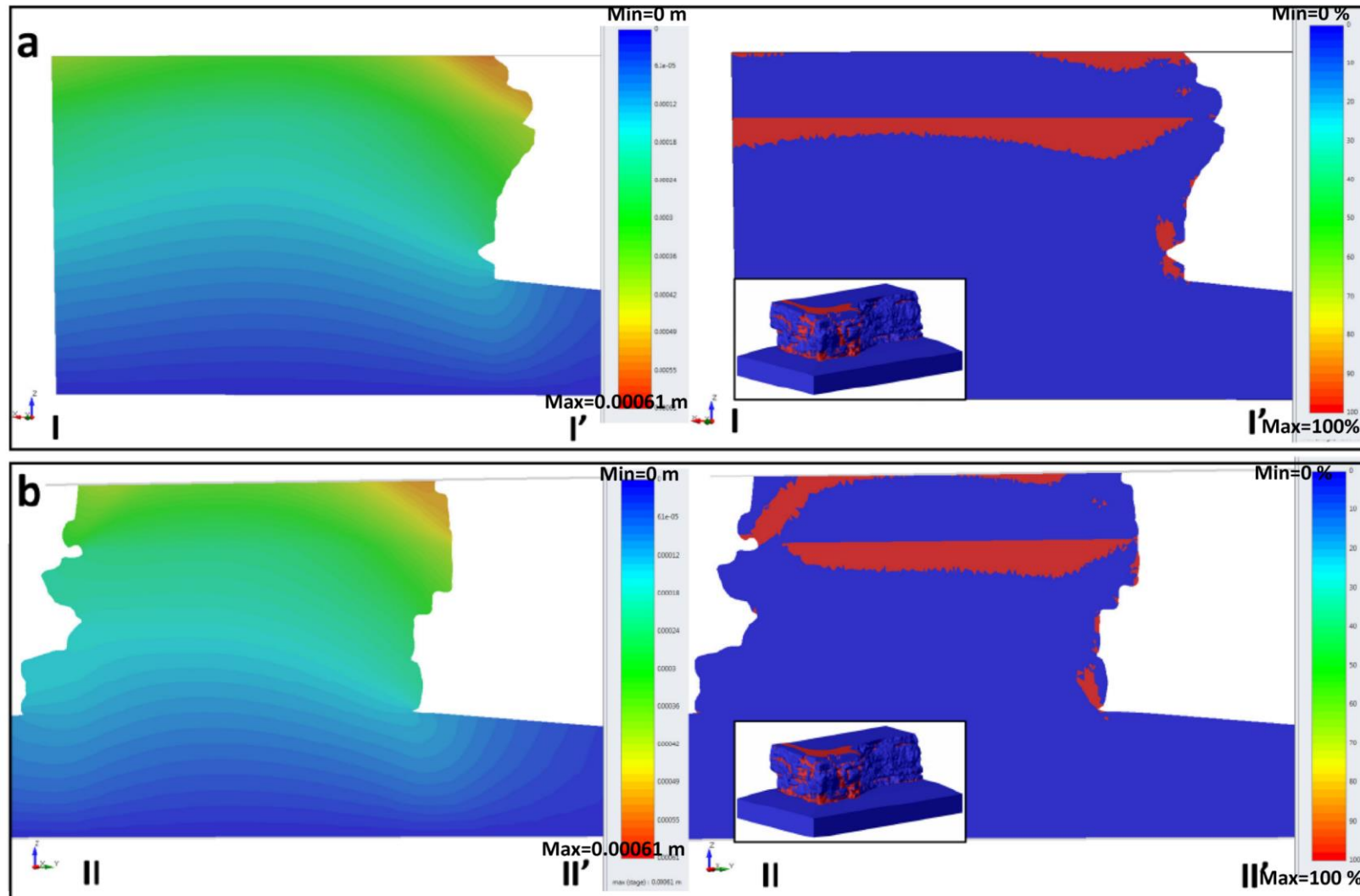


Figure S7.21: Cross sections I-I'(a) and II-II'(b) of the continuum-equivalent model (model a); left: total displacements; right: yielded elements.

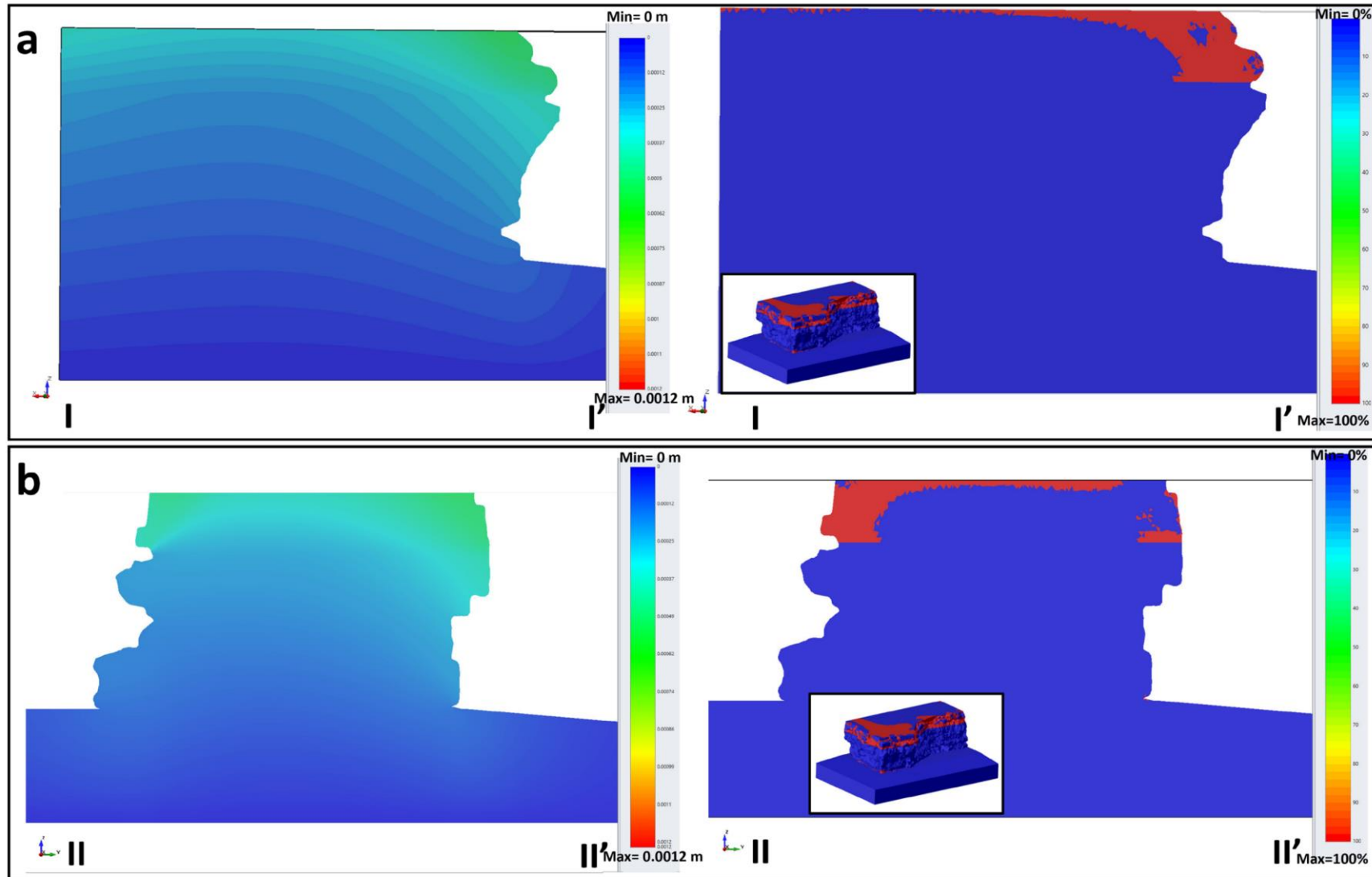


Figure S7.22: Cross sections I-I' (a) and II-II' (b) of the anisotropic model (model b); left: total displacements; right: yielded elements.

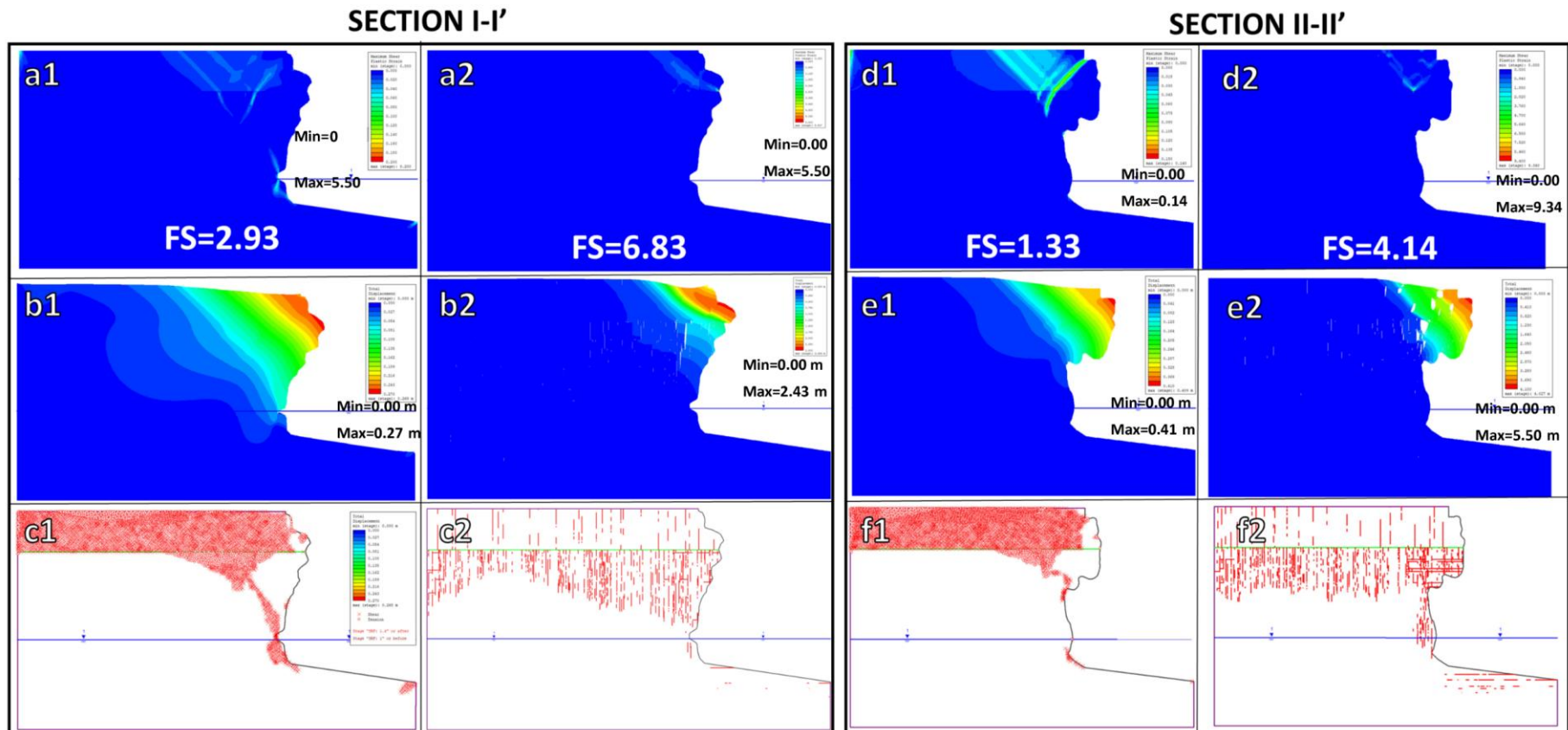


Figure S7.26: Critical failure mechanisms of sections I-I' and II-II' for the continuum-equivalent model (left) and the jointed model (right) produced by means of the SSR method. (a, d) maximum shear strain; (b, e) total displacements with deformation contours; (c1, f1) yielded elements for shear and tension; (c2, f2) yielded joints. Note that the displacements are exaggerated for visualisation purposes. For both sections, the failure mechanism of the continuum-equivalent model is represented by the sliding of the area dipping towards the sea and a slight toppling of the sector on the edge. For the jointed models, failure involves rock blocks delimited by the discontinuity sets. While rotational movements affect the Calcarene di Gravina Fm., slides and topples affect the Calcare di Bari Fm.

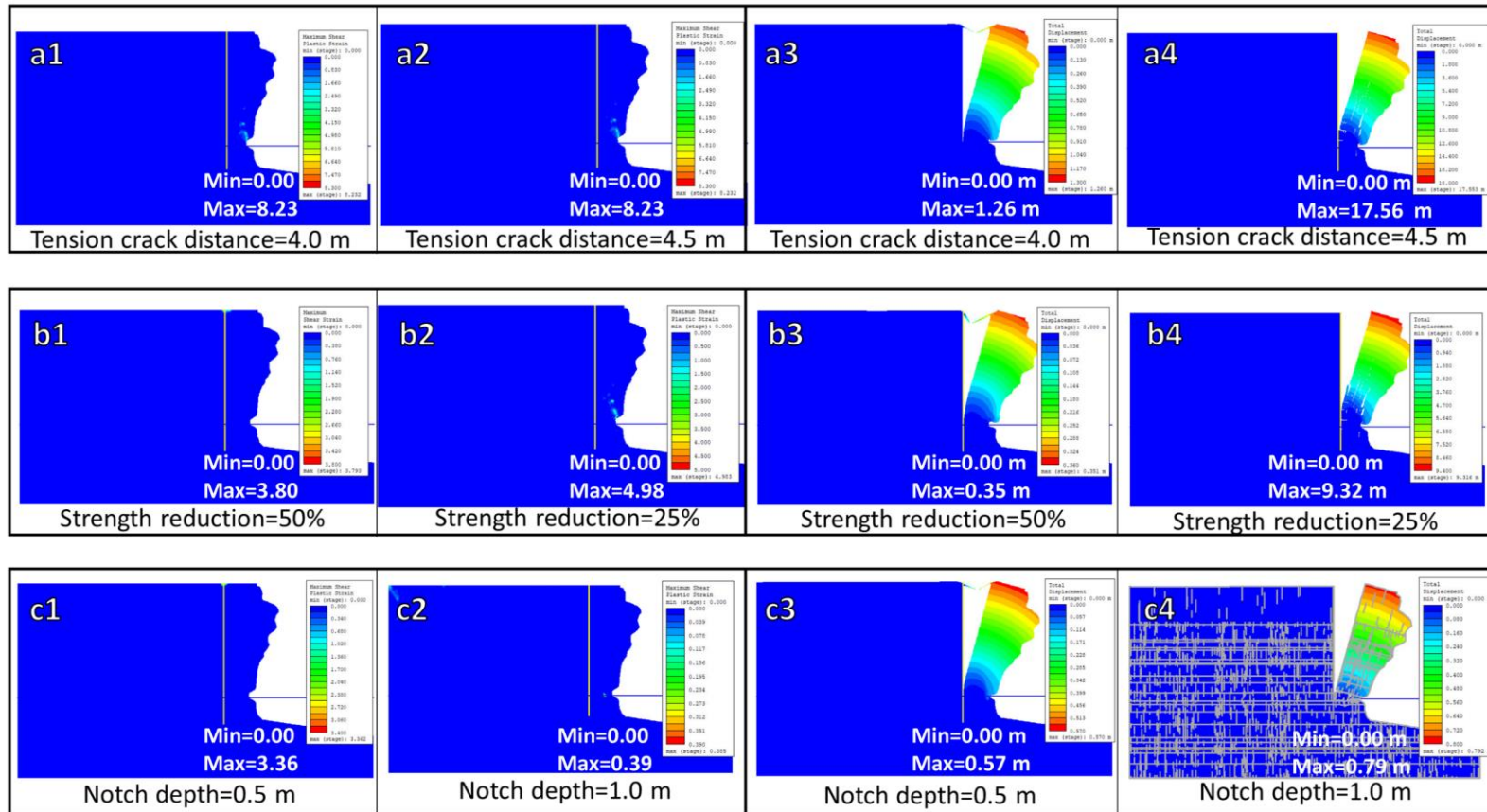


Figure S7.29: Critical failure mechanisms of section I-I' produced introducing a slightly cemented tension crack. To the left (a1, a2, b1, b2, c1, c2), maximum shear strain. To the right (a3, a4, b3, b4, c3, c4), total displacements with deformation contours. (a1-4) minim external edge-tension crack distance, beyond which failure occurs. (b1-4) With a tension crack located at 4.0 m from the external edge, failure occurs with a 50% and 25% reduction (in terms of cohesion and tensile strength of the rock materials), for the continuum-equivalent and jointed models, respectively. (c1-4) with the same tension crack, failure is also achieved when marine erosion develops, with a notch depth of 0.5 and 1.0 m respectively for the continuum-equivalent and for the jointed models. For all the simulations, flexural toppling characterizes the continuum-equivalent model. As regards the jointed model, a volume just above the sea notch is subjected to composite toppling and sliding, using a bedding surface as base plane.

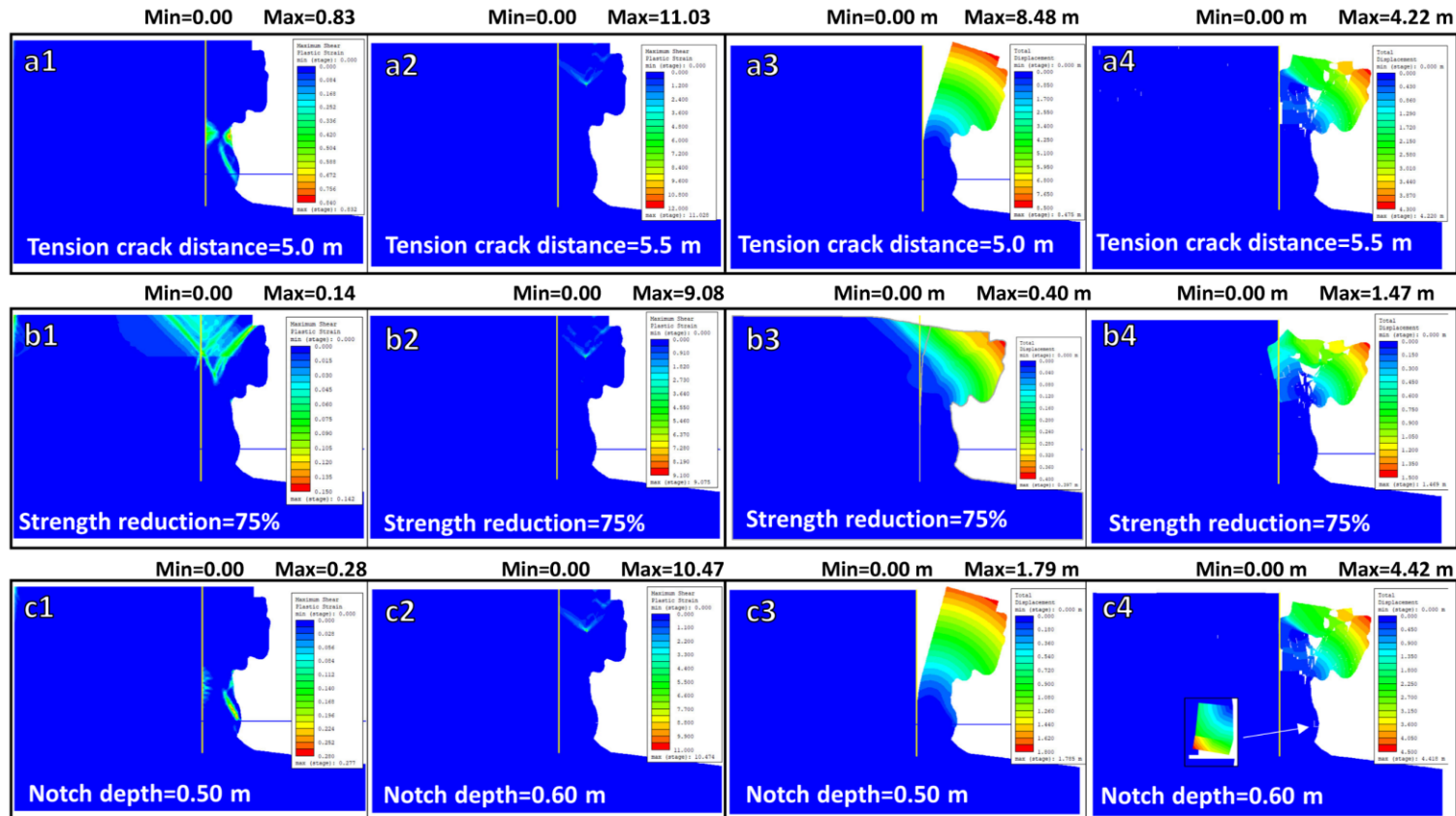


Figure S7.31: Critical failure mechanisms of section II-II' with a slightly cemented tension crack. To the left (**a1**, **a2**, **b1**, **b2**, **c1**, **c2**), maximum shear strain. To the right (**a3**, **a4**, **b3**, **b4**, **c3**, **c4**), total displacements with deformation contours. (**a1-4**) minim external edge-tension crack distance, beyond which failure occurs. (**b1-4**) with a tension crack located at 5.5 m from the external edge, failure occurs with a 75% strength reduction for both models. (**c1-4**) with the same tension crack, failure occurs for both models with an erosion depth of about 0.5 m. As concerns the continuum-equivalent model, a volume detached from the tension crack topples towards the sea. The deepening of the marine erosion notch slightly increases the height of the failed block. When the strength properties are reduced of 75%, the failure is caused by sliding and rotational surfaces in the upper part of the cliff. As regards the jointed model, a rock mass portion delimited by the tension crack is subjected to toppling and localized failures of rock blocks in the external area. The 75% strength reduction causes the failure of a wedge on the top of the model (**b4**), probably because of the load exerted by the buildings. The marine erosion process produces also small failures in correspondence of the notch (**c4**).

Chapter 8 Conclusion and future perspectives

The research undertaken so far allowed the achievement of new findings on the applicability and combination of remote sensing techniques and the conventional geostructural and geomechanical surveys for rock mass stability analyses. In this chapter, the research questions and objectives posed in Chapter 2 are answered in light of the outcomes emerged throughout this manuscript.

- 1. From a practical standpoint, is there any difference among TLS, traditional photogrammetry and UAV techniques, in terms of accuracy, site conditions, required time and economical resources?**
- 2. Does the choice of the survey technique influence the results of rock slope characterization and monitoring from point clouds or triangulated surfaces?**
- 3. Moreover, when dealing with the extraction and characterization of discontinuity sets from point clouds, regardless of the survey technique, does the chosen method provide different results with respect to the others proposed in the literature?**

These questions were addressed in Chapter 5. The mentioned remote sensing techniques were used to generate point clouds of a complex case study, characterized by limited accessibility, Mediterranean vegetation, irregular surfaces related to weathering and karst dissolution of the rock materials (e.g. discontinuities, dissolution voids and caves), marine, alluvial and anthropogenic terraces, human interventions, dynamic disturbance, and low GPS signal.

As concern the accuracy of the datasets, it was found out that, in these complex conditions, the Structure from Motion technique may suffer of misalignment issues and “distortions” related to doming deformations (James and Robson 2014), which cannot be solved if it is not possible to place on the field a sufficient number of Ground Control Points. This problem can be solved for UAV point clouds by carrying out a fine registration process, using laser scanner point clouds as reference. However, during this study, it was observed that some problems of deformation remained unsolved for the terrestrial SfM point cloud. The three types of remote sensing techniques, if carried out correctly, are able to provide similar accuracies on simple geometries (e.g. building walls). However, TLS and UAV techniques are more reliable when dealing with complex geometries like weathered and karstified surfaces or discontinuities. Terrestrial SfM may provide the same accuracy level if professional cameras and lenses are used, in order to have denser point clouds. As regard the required time, it is believed that the three techniques are comparable: if on the one hand UAV and manual-based photos can be done in a few minutes (provided that the analyzed area is limited) as stated by Rosser and co-workers, on the other hand they require longer processing and computing phases compared to the TLS technique (Rosser et al. 2005). With regard to the economic resources, it is specified that, as outlined by Stead and co-workers (Stead et al. 2019), laser scanner instruments are quite expensive, hence other techniques may be alternatively used, if the accuracy is not of primary importance.

When dealing with rock slope characterization, with particular reference to the discontinuity extraction, this study illustrated that the choice of the acquisition technique does not particularly influence the results. More in detail, all the discontinuity sets of the case study were extracted in the three types of point clouds by means of a semi-automatic approach. However, the percentage of poles of each discontinuity set can vary according to the analyzed point cloud, especially if they are affected by occlusions (shadow zones). By direct comparison with field-surveys, it is specified that UAV point clouds, if correctly georeferenced, are more reliable to establish the weight of the discontinuity sets, as they provide a full coverage of the area. Alternatively, occlusion problems in laser scanner point clouds can be solved using more than one scan position, if accessibility is ensured. A special remark is given for the use of more automated techniques for discontinuity extraction: not well-defined geometries might cause an incorrect classification of the poles into discontinuity sets, as observed in Section 4.4.3. In these circumstances, UAV systems may be a good solution because the results can be validated using RGB point clouds, high resolution photos or texturized meshes.

Rockfall source areas and human slope modifications can be detected by means of multi-temporal acquisitions using UAV systems or TLS techniques, which are more accurate compared to terrestrial SfM. The choice of the survey tool depends on the aim of the study: while laser scanners provide accurate estimations of the failed volumes and have lower detection thresholds, UAV systems allow the inspection of larger areas with minor efforts. In addition, UAV systems may be fundamental to monitor rock slopes characterized by intense vegetation in Mediterranean sites because shrubs and bushes are difficult to recognize in the low-resolution photos taken from laser scanners.

Finally, it must be remarked that each method has its advantages and limitations, and that a comprehensive rock slope characterization would be ideally achieved by coupling two of the three described methods (TLS + SfM) and, above all, by validating the results with traditional field surveys, which remain irreplaceable to collect information on the mechanical behaviour of the rock mass.

The findings of this part of the research represent an innovative contribution for the literature because, to the writer's knowledge, no quantitative comparative analyses have been proposed so far. Future developments may concern the use of laser scanners supported by inertial systems to extend the comparison carried out in this study with UAV systems along the coastline, focusing on the detection of rockfalls and on the deformations at the centimetric scale.

4. Is the IRT technique useful for rock mass characterization at a relatively large scale for sites characterized by lithological units with similar diffusivity, mild climate, dense vegetation and anthropogenic disturbances?

5. Are other survey techniques needed to interpret the thermal response of rock masses?

The research activity conducted to assess the applicability of the IRT technique for rock slope characterization provided interesting results. The same case study was used to test this technique, taking advantage of the complex site conditions. At a first glance, the results of the 24 hours monitoring were difficult to interpret because the lateral and vertical heterogeneity of the rock materials (in terms of colour, fracture frequency and porosity) resulted in warm and cold anomalies diffused within the thermograms. As a matter of fact, other remote sensing techniques are needed as support for the IRT method to detect discontinuities, voids and rock mass properties. The methodological approach reported in Chapter 5 illustrates how IRT techniques can be coupled with UAV systems to detect discontinuities and voids in rock masses, as well as to correlate the temperature profiles at the air-rock interface with the topography, the lithology and the jointing degree of the rock mass. A

remarkable result is that lithofacies characterized by primary porosity are easily detectable in thermograms acquired during the heating phase in the form of warm areas, because the air circulating within the pore systems causes a rise in temperature. This aspect is unique because weathered and karstified rocks with different types of porosity and similar colour (as in the case study) are not easy to discriminate in point clouds or high-resolution photos. Hence, IRT surveys coupled with UAV systems may be of paramount support to derive rock mass properties in inaccessible areas. As concern the contribute given to the literature, it is specified that the detection of discontinuities from IRT techniques was proposed by many authors (Squarzone et al. 2008; Liu et al. 2011; Teza et al. 2012; Baroñ et al. 2012; Gigli et al. 2013; Gero et al. 2013; Frodella et al. 2014, 2015, 2017b, a; Mineo et al. 2015a, b; Pappalardo et al. 2016; Fiorucci et al. 2018; Pappalardo and Mineo 2019; Mineo and Pappalardo 2019; Guerin et al. 2019; Grechi et al. 2021; Loche et al. 2021). However, the application of InfraRed Thermography to indirectly obtain information on the topography, lithology, jointing degree, and Geological Strength Index of inaccessible zones by means of profiles correlations seems to be novel, as well as the detection of lithofacies of similar color but with different pore connectivity. Future researches could involve mounting a thermal camera on UAV systems to explore the three-dimensional rock mass thermal behaviour, focusing on small-scale discontinuities and on the karst caves visible along the coastline.

6. 2-D discontinuity characterization

As outlined in Chapter 6, large part of this thesis was dedicated to the development of a publicly available digital tool for the quantitative characterization of discontinuity traces drawn on orthophotos generated by means of SfM techniques. As a matter of fact, several methods for the rock slope characterization from Digital Outcrop Models were proposed in the literature (specific references are reported in the mentioned chapter), but the traditional 2-D analyses, which are more appropriate for sub-vertical or sub-horizontal outcrops, lack of an update in a digital environment. Despite a few publications deal with this topic (3GSM; CREALP; Gigli and Casagli 2011; Healy et al. 2017), this contribution is novel in the current literature because it provides a comprehensive discontinuity analysis, specifically aimed at rock mass characterization, with the peculiarity of semi-automatically extracting the discontinuity sets from discontinuity traces by means of two methods. Since the proposed tool was validated only on a synthetic dataset and at the case study, more applications should be performed in the future. As stated in Chapter 6, future developments may involve the conversion of the proposed routine in the 3-D space and the comparison with the methods currently available in the literature for discontinuity analysis from point clouds.

7. How can the data obtained by means of remote sensing techniques and conventional geostructural and geomechanical surveys be optimally combined to perform sophisticated rock slope stability analyses?

The third part of this PhD thesis was devoted to the combination of conventional geostructural and geomechanical surveys, remote sensing techniques, and laboratory tests to produce advanced 3-D geomechanical models to perform sophisticated stability analyses. 2-D and 3-D simulations by means of Finite Element Method (FEM) were performed to assess the stability conditions of the case study, and to evaluate the effects of surface processes observed in the field and on the point clouds. In the current literature and in professional works stability analyses, FEM methods are widely used because

of their flexibility in modelling different configurations and processes (Hammah et al. 2008). However, when dealing with jointed rock masses, the models are set up using equivalent strength properties (continuum approach) for adding interfaces (discontinuum approach), depending on the joint frequency (Goodman et al. 1968; Ghaboussi et al. 1973; Beer 1985; Dershowitz et al. 2004). In this study, both methods were used and compared, though ensuring numerical continuity as a fundamental assumption of the FEM techniques, to identify the main differences. Given the presence of a large number of discontinuities, the discontinuum-based method was improved by adding joint networks by means of a stochastic approach (Discrete Fracture Network method - DFN), using the results of the quantitative discontinuity analysis. This application represents an innovative contribution to the literature, as joints generation through DFN techniques have been used for Distinct Element Methods or hybrid approaches so far (Elmo 2006; Elmo and Stead 2010; Ivars et al. 2011; Merrien-Soukatchoff et al. 2012; Havaej et al. 2016; Montiel et al. 2020; Zhang et al. 2020).

By direct comparison with field and point clouds inspection, it was found out that the failure mechanisms provided by the two approaches occur simultaneously at the study site: whilst the failure of large sectors behaving as continuum media occurs over long times, smaller volumes delimited by the discontinuity sets are prone to failure in the short time. It must be remarked that the main goal of this PhD was to develop a methodology for rock mass stability analyses through the combination of remote sensing and traditional field surveys, with focus on the characterization of the parameters needed to set-up sophisticated 3-D geomechanical models. The data collected throughout this research were combined to perform a preliminary stability analysis of the case study, to validate the proposed methodology and to assess the effects of joints implementation (specifically characterized) in numerical models. However, further investigations should be performed by means of coupled Distinct Element Methods (DEM)-DFN approaches or the most advanced hybrid techniques to investigate structurally-controlled or more complex failure mechanisms. Furthermore, dynamic analyses simulating earthquakes or sea storms would allow a full understanding of the rock mass stability in varied scenarios. These outlines represent an interesting standpoint for specific studies which, based on the experience faced during this PhD, would require a time-consuming trial-error procedure. In this perspective, this manuscript is concluded with a statement made by one of the most expert numerical modelling researchers: *“Rock mechanics modelling and rock engineering design are both a science and an art. They rest on a scientific foundation but require empirical judgements supported by accumulated experiences through long-term practices”* (Jing 2003).

References

- 3-Dflow 3-DF Zephyr 2018. Software available at: <https://www.3-Dflow.net/it/software-di-fotogrammetria-3-Df-zephyr/>.
- Abellán, A.; Calvet, J.; Vilaplana, J.M.; Blanchard, J. Detection and Spatial Prediction of Rockfalls by Means of Terrestrial Laser Scanner Monitoring. *Geomorphology* **2010**, *119*, 162–171.
- Abellan, A.; Derron, M.H.; Jaboyedoff, M. Use of 3D Point Clouds in Geohazards. Special Issue: Current Challenges and Future Trends. *Remote Sensing* **2016**, *8*(2):130.
- Abellán, A.; Jaboyedoff, M.; Oppikofer, T.; Vilaplana, J.M. Detection of Millimetric Deformation Using a Terrestrial Laser Scanner: Experiment and Application to a Rockfall Event. *Nat. Hazards Earth Syst. Sci.* **2009**, *9*, 365–372.
- Abellán, A.; Oppikofer, T.; Jaboyedoff, M.; Rosser, N.J.; Lim, M.; Lato, M.J. Terrestrial Laser Scanning of Rock Slope Instabilities. *Earth Surface Processes and Landforms* **2014**, *39*, 80–97.
- Abellán, A.; Vilaplana, J.M.; Calvet, J.; García-Sellés, D.; Asensio, E. Natural Hazards and Earth System Sciences Rockfall Monitoring by Terrestrial Laser Scanning-Case Study of the Basaltic Rock Face at Castellfollit de La Roca (Catalonia, Spain). *Hazards Earth Syst. Sci.* **2011**, *11*, 829–841.
- Abellán, A.; Vilaplana, J.M.; Martínez, J. Application of a Long-Range Terrestrial Laser Scanner to a Detailed Rockfall Study at Vall de Núria (Eastern Pyrenees, Spain). *Engineering Geology* **2006**, *88*, 136–148.
- Adachi, T.; Ohnishi, Z.; Arai, K. Investigation of Toppling Slope Failure at Route 305 in Japan. In *Proceedings of the 7th ISRM Congress*; **1991**.
- Adams, P.N.; Storlazzi, C.D.; Anderson, R.S. Nearshore Wave-Induced Cyclical Flexing of Sea Cliffs. *Journal of Geophysical Research: Earth Surface*, **2005**, 110.F2.
- Adhikary, D.P.; Dyskin, A. v; Jewell, R.J.; Stewart, D.P. A Study of the Mechanism of Flexural Toppling Failure of Rock Slopes. *Rock Mechanics and Rock Engineering* **1997**, *30*, 75–93.
- Admassu, Y.; Shakoor, A. DIPANALYST: A Computer Program for Quantitative Kinematic Analysis of Rock Slope Failures. *Computers & Geosciences* **2013**, *54*, 196–202.
- Adorno, V.; Barnobi, L.; la Rosa, F.; Leotta, A.; Paratore, M. Contributo della tecnologia laser scanner e termografia R nella caratterizzazione geomeccanica di un costone roccioso. In *Proceedings of the Atti 13a Conferenza Nazionale ASITA, Bari, Italy, 1–4 December 2009*.
- Agisoft Agisoft Metashape. *User Manual: Professional Edition, Version 1.6* 2020, 160.
- Agisoft LLC, Agisoft Metashape Professional Software, Version 1.6 2020, 160. St. Petersburg, Russia. Available online: <https://www.agisoft.com/downloads/installer/> (accessed on 12 October 2021).
- Agisoft. General Image Capture Tips. 2020. Available online: https://Agisoft.Freshdesk.Com/Support/Solutions/Articles/3100_0149337-General-Image-Capture-Tips (accessed on 11 October 2021).
- Alejano, L.R. Considerations on Failure Mechanisms of Rock Slopes Involving Toppling. *IOP Conference Series: Earth and Environmental Science* **2021**, *833*, 012004.
- Alejano, L.R.; Veiga, M.; Pérez-Rey, I.; Castro-Filgueira, U.; Arzúa, J.; Castro-Caicedo, Á.J. Analysis of a Complex Slope Failure in a Granodiorite Quarry Bench. *Bulletin of Engineering Geology and the Environment* **2019**, *78*, 1209–1224.
- Amoroso, G.G.; Fassina, V. *Stone Decay and Conservation: Atmospheric Pollution, Cleaning, Consolidation and Protection*; Amsterdam; New York : Elsevier, **1983**, 453 pp, ISBN 13: 9780444421463.
- Anderson, K.; Westoby, M.J.; James, M.R. Low-Budget Topographic Surveying Comes of Age: Structure from Motion Photogrammetry in Geography and the Geosciences. *Progress in Physical Geography: Earth and Environment*. **2019**;43(2):163-173.

- Andersson, J.; Shapiro, A.M.; Bear, J. A Stochastic Model of a Fractured Rock Conditioned by Measured Information. *Water Resources Research* **1984**, *20*, 79–88.
- Andriani, G.; Parise, M.; Diprizio, G. Uncertainties in the Application of Rock Mass Classification and Geomechanical Models for Engineering Design in Carbonate Rocks. In *Engineering Geology for Society and Territory, 5. Urban Geology, Sustainable Planning and Landscape Exploitation*; Lollino, G., Manconi, A., Guzzetti, F., Culshaw, M., Bobrowsky, P., Luino, F., Eds.; S., Eds.; Springer: Berlin, Germany, **2015**; pp. 545–548 ISBN 978-3-319-09048-1.
- Andriani, G.; Pellegrini, V. Qualitative Assessment of the Cliff Instability Susceptibility at a given Scale with a New Multidirectional Method. *International Journal of Geology* **2014**, *8*, 73–80.
- Andriani, G.; Walsh, N. Fabric, Porosity and Water Permeability of Calcarenes from Apulia (SE Italy) Used as Building and Ornamental Stone. *Bulletin of Engineering Geology and the Environment* **2003**, *62*, 77–84.
- Andriani, G.F. Sulla Valutazione Della Stabilità Di Cavità Sotterranee in Ammassi Roccosi Stratificati. *Geologia e Territorio*, volume 1, 23–32 **2015**, 23–32.
- Andriani, G.F.; Loiotine, L. Multidisciplinary Approach for Assessment of the Factors Affecting Geohazard in Karst Valley: The Case Study of Gravina Di Petruscio (Apulia, South Italy). *Environmental Earth Sciences* **2020**, *79*, 458.
- Andriani, G.F.; Parise, M. Applying Rock Mass Classifications to Carbonate Rocks for Engineering Purposes with a New Approach Using the Rock Engineering System. *Journal of Rock Mechanics and Geotechnical Engineering* **2017**, *9*, 364–369.
- Andriani, G.F.; Parise, M. On the Applicability of Geomechanical Models for Carbonate Rock Masses Interested by Karst Processes. *Environmental Earth Sciences* **2015**, *74*, 7813–7821.
- Andriani, G.F.; Pastore, N.; Giasi, C.I.; Parise, M. Hydraulic Properties of Unsaturated Calcarenes by Means of a New Integrated Approach. *Journal of Hydrology* **2021**, *602*, 126730.
- Andriani, G.F.; Walsh, N. Physical Properties and Textural Parameters of Calcarene Rocks: Qualitative and Quantitative Evaluations. *Engineering Geology* **2002**, *67*, 5–15.
- Andriani, G.F.; Walsh, N. Rocky Coast Geomorphology and Erosional Processes: A Case Study along the Murgia Coastline South of Bari, Apulia - SE Italy. *Geomorphology* **2007**, *87*, 224–238.
- Argnani, A.; Favalli, P.; Frugoni, F.; Gasperini, M.; Ligi, M.; Marani, M.; Mattiotti, G.; Mele, G. Foreland Deformational Pattern in the Southern Adriatic Sea. *Annals of Geophysics*, **1993**, 36.2.
- Armesto, J.; Ordóñez, C.; Alejano, L.; Arias, P. Terrestrial Laser Scanning Used to Determine the Geometry of a Granite Boulder for Stability Analysis Purposes. *Geomorphology* **2009**, *106*, 271–277.
- Attewell, P.B.; Farmer, I.W. Principles of Engineering Geology; Springer Science & Business Media, **2012**.
- Baczynski, N.R.P. STEPSIM4 Step-Path Method for Slope Risks. In *Proceedings of the ISRM International Symposium*; **2000**.
- Baecher, G.; Lanney, N.A. Trace Length Biases in Joint Surveys. 19th U.S. *Symposium on Rock Mechanics* **1978**, *1*, 56–65.
- Baecher, G.B. Statistical Analysis of Rock Mass Fracturing. *Journal of the International Association for Mathematical Geology* **1983** *15:2* 1983, *15*, 329–348.
- Bahrani, N.; Kaiser, P.K.; Valley, B. Distinct Element Method Simulation of an Analogue for a Highly Interlocked, Non-Persistently Jointed Rockmass. *International Journal of Rock Mechanics and Mining Sciences* **2014**, *71*, 117–130.
- Baltsavias, E.P. Airborne Laser Scanning: Basic Relations and Formulas. *ISPRS Journal of Photogrammetry and Remote Sensing* **1999**, *54*, 199–214.
- Barla, G.; Barla, M. Continuum and Discontinuum Modelling in Tunnel Engineering. *Rud. Geol. Naft. Zb.* **2000**, *12*, 45–57.
- Baroň, I.; Bečkovský, D.; Míča, L. Application of Infrared Thermography for Mapping Open Fractures in Deep-Seated Rockslides and Unstable Cliffs. *Landslides* **2012** *11(1)*, 15–27.

- Barton, N. Some New Q-Value Correlations to Assist in Site Characterization and Tunnel Design. *International Journal of Rock Mechanics and Mining Sciences* **2002**, 39, 185–216.
- Barton, N.; Choubey, V. The Shear Strength of Rock Joints in Theory and Practice. *Rock mechanics* **1977** 10:1, 10, 1–54.
- Barton, N.; Lien, R.; Lunde, J. Engineering Classification of Rock Masses for the Design of Tunnel Support. *Rock Mech. Felsmech. Mécanique Des Roches* **1974**, 6, 189–236.
- Bassa, C.M.; Oyanguren, P.R.; Philippon, R.G.; Lois, M.F.-P. The Toppling of Large Blocks on the Northeast Slope of the Meirama Mine. In: *ISRM Regional Symposium - EUROCK 2014*, Vigo, Spain, May **2014**.
- Battulwar, R.; Zare-Naghadehi, M.; Emami, E.; Sattarvand, J. A State-of-the-Art Review of Automated Extraction of Rock Mass Discontinuity Characteristics Using Three-Dimensional Surface Models. *Journal of Rock Mechanics and Geotechnical Engineering*, **2021**, 920-936, 13(4).
- Bay, H.; Ess, A.; Tuytelaars, T.; van Gool, L. Speeded-Up Robust Features (SURF). *Computer Vision and Image Understanding* **2008**, 110, 346–359.
- Beardsley, P.A.; Zisserman, A.; Murray, D.W. Sequential Updating of Projective and Affine Structure from Motion. *International Journal of Computer Vision* **1997** 23:3, 23, 235–259.
- Benjamin, J.; Rosser, N.J.; Brain, M.J. Rockfall Detection and Volumetric Characterization Using LiDAR. In: *Landslides and Engineered Slopes. Experience, Theory and Practice*, **2018**, CRC Press.
- Bentley PLAXIS 3-D 2013. Software available online at <https://www.virtuosity.com/product/plaxis-3-D/>.
- Bernatchez, P.; Dubois, J.-M.M. Seasonal Quantification of Coastal Processes and Cliff Erosion on Fine Sediment Shorelines in a Cold Temperate Climate, North Shore of the St. Lawrence Maritime Estuary, Québec. *J. Coast. Res.* **2008**, 24, 169.
- Besl, P.J.; McKay, N.D. A Method for Registration of 3-D Shapes. *IEEE Transactions on Pattern Analysis and Machine Intelligence* **1992**, 14, 239–256.
- Bevan, D.J.; Brook, M.S.; Tunncliffe, J.; Richards, N.P. Use of UAV Mounted / Structure-from-Motion (SfM) Data Capture for Engineering Geological Landslide Mapping. *Proc. 20th NZGS Geotechnical Symposium* **2017**, 1–8.
- Bfer, G. An Isoparametric Joint/Interface Element for Finite Element Analysis. *International Journal for Numerical Methods in Engineering* **1985**, 21, 585–600.
- Bieniawski, Z. Rock Mass Classification in Rock Engineering. In *Proceedings of the Symposium on Exploration for Rock Engineering* (ed. ZT Bieniawski); **1976**; pp. 97–106.
- Bieniawski, Z.T. Classification of Rock Masses for Engineering: The RMR System and Future Trends. *Comprehensive rock engineering. Vol. 3* **1993**, 553–573.
- Bieniawski, Z.T. Engineering Classification of Jointed Rock Masses. *Civ Eng S Afr* **1973**, 15, 335–343.
- Bieniawski, Z.T. *Engineering Rock Mass Classifications*; John Wiley and Sons: Chichester, UK, **1989**; ISBN 978-0-471-60172-2.
- Bieniawski, Z.T. *The Geomechanics Classification in Rock Engineering Applications*; *ISRM Congress*: Montreux, Switzerland, **1979**.
- Bird, E.C.F. *Coastal Geomorphology: An Introduction*; John Wiley & Sons, **2011**.
- Bishop, A.W. The Use of the Slip Circle in the Stability Analysis of Slopes. *Geotechnique* **1955**, 5, 7–17.
- Bitenc, M.; Kieffer, D.S.; Khoshelham, K. Range Versus Surface Denoising of Terrestrial Laser Scanning Data for Rock Discontinuity Roughness Estimation. *Rock Mechanics and Rock Engineering* **2019**, 52, 3103–3117, doi:10.1007/s00603-019-01755-2.
- Bjerrum, L. The Third Terzaghi Lectures; Progressive Failure in Slopes of Overconsolidated Plastic Clay and Clay Shales. *Journal of the Soil Mechanics and Foundations Division* **1967**, 93, 1–49.
- Blanchard, D.C.; Woodcock, A.H. The Production, Concentration, and Vertical Distribution of the Sea-Salt Aerosol. *Annals of the New York Academy of Sciences* **1980**, 338, 330–347.
- Blyth, F.G.H.; De Freitas, M.H. *A Geology for Engineers*; CRC Press, **2017**.

- Bobet, A. Numerical Methods in Geomechanics. *The Arabian Journal for Science and Engineering* **2010**, 35, 27–48.
- Bobet, A.; Fakhimi, A.; Johnson, S.; Morris, J.; Tonon, F.; Yeung, M.R. Numerical Models in Discontinuous Media: Review of Advances for Rock Mechanics Applications. *Journal of Geotechnical and Geoenvironmental Engineering* **2009**, 135, 1547–1561.
- Boehler, W.; Boehler, W.; Marbs, A. Investigating Laser Scanner Accuracy. Proceedings of *XIXTH CIPA Symposium* **2003**.
- Böhme, M.; Hermanns, R.L.; Oppikofer, T.; Fischer, L.; Bunkholt, H.S.S.; Eiken, T.; Pedrazzini, A.; Derron, M.-H.; Jaboyedoff, M.; Blikra, L.H.; et al. Analyzing Complex Rock Slope Deformation at Stampa, Western Norway, by Integrating Geomorphology, Kinematics and Numerical Modeling. *Engineering Geology* **2013**, 154, 116–130.
- Bonacci, O.; Ljubenkovic, I.; Roje-Bonacci, T. Karst Flash Floods: An Example from the Dinaric Karst (Croatia). *Natural Hazards and Earth System Sciences* **2006**, 6, 195–203.
- Bonilla-Sierra, V.; Scholtès, L.; Donze, F.; Elmoultie, M. Rock Slope Stability Analysis Using Photogrammetric Data and DFN–DEM Modelling. *Acta Geotechnica* **2015**.
- Bonneau, D.; DiFrancesco, P.-M.; Hutchinson, D.J. Surface Reconstruction for Three-Dimensional Rockfall Volumetric Analysis. *ISPRS International Journal of Geo-Information* **2019**, Vol. 8, Page 548, 8, 548.
- Boon, C.W.; Houlsby, G.T.; Utili, S. New Insights into the 1963 Vajont Slide Using 2-D and 3-D Distinct-Element Method Analyses. *Geotechnique* **2014**, 64, 800–816.
- Borgatti, L.; Corsini, A.; Barbieri, M.; Sartini, G.; Truffelli, G.; Caputo, G.; Puglisi, C. Large Reactivated Landslides in Weak Rock Masses: A Case Study from the Northern Apennines (Italy). *Landslides* **2006**, 3, 115–124.
- Boufama, B.; Mohr, R.; Veillon, F.; Boufama, B.; Mohr, R.; Veillon, F. Euclidean Constraints for Uncalibrated Reconstruction. *4th International Conference on Computer Vision (ICCV '93)*, May 1993, Berlin, Germany.
- Bramson, M.A. Introduction. Infrared radiation. A handbook for applications. Optical Physics and Engineering, **1968**.
- Bremer, M.; Sass, O. Combining Airborne and Terrestrial Laser Scanning for Quantifying Erosion and Deposition by a Debris Flow Event. *Geomorphology* **2012**, 138, 49–60.
- Brideau, M.-A.; Pedrazzini, A.; Stead, D.; Froese, C.; Jaboyedoff, M.; van Zeyl, D. Three-Dimensional Slope Stability Analysis of South Peak, Crowsnest Pass, Alberta, Canada. *Landslides* **2011**, 8, 139–158.
- Brideau, M.A.; Yan, M.; Stead, D. The Role of Tectonic Damage and Brittle Rock Fracture in the Development of Large Rock Slope Failures. *Geomorphology* **2009**, 103, 30–49.
- Brodu, N.; Lague, D. 3-D Terrestrial Lidar Data Classification of Complex Natural Scenes Using a Multi-Scale Dimensionality Criterion: Applications in Geomorphology. *ISPRS J. Photogramm. Remote Sens.* **2012**, 68, 121–134.
- Brossard, J.; Duperret, A. Coastal Chalk Cliff Erosion: Experimental Investigation on the Role of Marine Factors. Geological Society, London, *Engineering Geology Special Publications* **2004**, 20, 109–120.
- Brown, D.C. The Bundle Method--Progress and Prospects. *International Archives of Photogrammetry* **1976**, 21, 1–33.
- Bruno, G.; Del Gaudio, V.; Mascia, U.; Ruina, G. Numerical Analysis of Morphology in Relation to Coastline Variations and Karstic Phenomena in the Southeastern Murge (Apulia, Italy). *Geomorphology* **1995**, 12, 313–322.
- Buckley, S.J.; Howell, J.A.; Enge, H.D.; Kurz, T.H. Terrestrial Laser Scanning in Geology: Data Acquisition, Processing and Accuracy Considerations. *Journal of the Geological Society* **2008**, 165, 625–638.
- Buyer, A.; Schubert, W. Calculation the Spacing of Discontinuities from 3D Point Clouds. In *Procedia Engineering*; **2017**; Vol. 191, pp. 270–278.
- Buyer, A.; Schubert, W. Extraction of Discontinuity Orientations in Point Clouds. In Proceedings of the *ISRM International Symposium—EUROCK 2016*, International Society for Rock Mechanics. Ürgüp, Turkey, 29 August **2016**; pp. 1133–1137.

- Buyer, A.; Schubert, W. Joint Trace Detection in Digital Images. In Proceedings of *the 10th Asian Rock Mechanics Symposium*, Singapore, 29 October **2018**.
- Bye, A.R.; Bell, F.G. Stability Assessment and Slope Design at Sandsloot Open Pit, South Africa. *International Journal of Rock Mechanics and Mining Sciences* **2001**, *38*, 449–466.
- Cafiso, F.; Cappadonia, C. Landslide Inventory and Rockfall Risk Assessment of a Strategic Urban Area (Palermo, Sicily). *Rendiconti Online della Società Geologica Italiana* **2019**, *48*, 96–105.
- Calcaterra D. & Parise M. (Eds.). Weathering as a predisposing factor to slope movements. Geological Society of London, *Engineering Geology Special Publication* **2010** no. 23, 233 pp.
- Calonder, M.; Lepetit, V.; Strecha, C.; Fua, P. BRIEF: Binary Robust Independent Elementary Features. Lecture Notes in Computer Science (including subseries Lecture Notes in Artificial Intelligence and Lecture Notes in Bioinformatics) **2010**, 6314 LNCS, 778–792.
- Cardia, S.; Palma, B.; Parise, M. The Iterative Pole Density Estimation, a New Approach to Assess the Stability of Rock Masses from 3D Point Clouds. In Proceedings of the 90th Congr. Società Geologica Italiana “Geology
- Carranza-Torres, C.; Fairhurst, C.; Lorig, L. Insights on the Stability of Large Excavations from Analytical and Numerical Models. *Felsbau* **1997**, *15*, 54–63.
- Carrea, D.; Abellan, A.; Derron, M.-H.; Gauvin, N.; Jaboyedoff, M. Using 3-D Surface Datasets to Understand Landslide Evolution: From Analogue Models to Real Case Study. *Landslides and Engineered Slopes: Protecting Society through Improved Understanding*, edited by: Eberhardt, E., Froese, C., and Turner, K., London: CRC Press, **2012**, 575–579.
- Carrea, D.; Abellan, A.; Derron, M.-H.; Jaboyedoff, M. Automatic Rockfalls Volume Estimation Based on Terrestrial Terrestrial Laser Scanning Data. In: *Engineering Geology for Society and Territory-Volume 2*. Springer, Cham, **2015**. p. 425–428.
- Carrea, D.; Abellan, A.; Humair, F.; Matasci, B.; Derron, M.H.; Jaboyedoff, M. Correction of Terrestrial LiDAR Intensity Channel Using Oren–Nayar Reflectance Model: An Application to Lithological Differentiation. *ISPRS Journal of Photogrammetry and Remote Sensing* **2016**, *113*, 17–29.
- Carreño, C.R.; Kalafatovich, C.S. The Alcamayo and Cedrobamba Catastrophic Debris Flow (January, March and April 2004) in Machupicchu Area-Peru. *Landslides* **2006**, *3*, 79–83.
- Carrivick, J.L.; Smith, M.W.; Quincey, D.J. Structure from Motion in the Geosciences. *Structure from Motion in the Geosciences*. John Wiley & Sons, **2016**.
- Casagli, N.; Frodella, W.; Morelli, S.; Tofani, V.; Ciampalini, A.; Intrieri, E.; Raspini, F.; Rossi, G.; Tanteri, L.; Lu, P. Spaceborne, UAV and ground-based remote sensing techniques for landslide mapping, monitoring and early warning. *Geoenviro. Disasters* **2017**, *4*, 1–23.
- Casnedi, R.; Crescenti, U.; Tonna, M. Evoluzione Della Avanfossa Adriatica Meridionale Nel Plio-Pleistocene, Sulla Base Di Dati Di Sottosuolo. *Mem. Soc. Geol. It.* **1982**, *24*, 243–260.
- Castedo, R.; Murphy, W.; Lawrence, J.; Paredes, C. A New Process-Response Coastal Recession Model of Soft Rock Cliffs. *Geomorphology* **2012**, *177–178*, 128–143.
- Cawood, A.J.; Bond, C.E.; Howell, J.A.; Butler, R.W.H.; Totake, Y. LiDAR, UAV or Compass-Clinometer? Accuracy, Coverage and the Effects on Structural Models. *Journal of Structural Geology* **2017**, *98*, 67–82.
- Cherubini, C.; Pastore, N.; Rapti, D.; Giasi, C.I. Numerical Modeling of Flow and Transport in the Bari Industrial Area by Means of Rough Walled Parallel Plate and Random Walk Models. *Hydrology and Earth System Sciences* **2018**, *22*, 5211–5225.
- Chicco, J.M.; Vacha, D.; Mandrone, G. Thermo-physical and geo-mechanical characterization of faulted carbonate rock masses (Valdieri, Italy). *Remote Sens.* **2019**, *11*, 179.
- Chigira, M.; Duan, F.; Yagi, H.; Furuya, T. Using an Airborne Laser Scanner for the Identification of Shallow Landslides and Susceptibility Assessment in an Area of Ignimbrite Overlain by Permeable Pyroclastics. *Landslides* **2004**, *1*, 203–209.
- Chowdhury, R.N.; A-Grivas, D. Probabilistic Model of Progressive Failure of Slopes. *Journal of the Geotechnical Engineering Division* **1982**, *108*, 803–819.

References

- Ciaranfi, N.; Ghisetti, F.; Guida, M.; Iaccarino, G.; Lambiase, S.; Pieri, P.; Rapisardi, L.; Ricchetti, G.; Torre, M.; Tortorici, L.; Vezzani, L. Carta neotettonica dell'Italia meridionale. *Prog. Fin. Geod. Pub*, 515, 1-62; **1983**.
- Ciaranfi, N.; Pieri, P.; Ricchetti, G. Note alla carta geologica delle Murge e del Salento (Puglia centromeridionale). *Memorie della Società Geologica Italiana*, **1988**, 41: 449-460.
- Ciaranfi, N.; Pieri, P.; Ricchetti, G. Note Alla Carta Geologica Delle Murge e Del Salento (Puglia Centromeridionale). *Memorie della Società Geologica Italiana* **1988**, 41, 449–460.
- Clapuyt, F.; Vanacker, V.; Oost, K. Reproducibility of UAV-Based Earth Topography Reconstructions Based on Structure-from-Motion Algorithms. *Geomorphology* **2016**, 260, 4–15.
- Coggan, J.; Wetherelt, A.; Gwynn, X.; Flynn, Z.N. Comparison of Hand-Mapping With Remote Data Capture Systems For Effective Rock Mass Characterization.; In: *11th Congress of the International Society for Rock Mechanics*, Lisbon, Portugal, **2007**.
- Coggan, J.S.; Pine, R.J.; Stead, D.; Rance, J.M. Numerical Modelling of Brittle Rock Failure Using a Combined Finite-Discrete Element Approach: Implications For Rock Engineering Design 2003. In *10th ISRM Congress*, Sandton, South Africa, September **2003**.
- Coggan, J.S.; Stead, D.; Eyre, J.M. Evaluation of Techniques for Quarry Slope Stability Assessment. Transactions of the Institution of Mining and Metallurgy. Section B. *Applied Earth Science* **1998**, 107.
- Corkum, A.G.; Martin, C.D. Discrete Element Analysis of the Effect of a Toe Berm on a Large Rockslide. In Proceedings of the *55th Canadian Geotechnical Conference*., Niagara Falls. Canadian Geotechnical Society, Toronto; **2002**; pp. 633–640.
- Costa, M.; Coggan, J.S.; Eyre, J.M. Numerical Modelling of Slope Behaviour of Delabole Slate Quarry (Cornwall, UK). *International Journal of Surface Mining, Reclamation and Environment* **1999**, 13, 11–18.
- Cotecchia, V. Le Acque Sotterranee e l'intrusione Marina in Puglia: Dalla Ricerca All'emergenza Nella Salvaguardia Della Risorsa. Memorie Descrittive della Carta Geologica d'Italia. *ISPRA Serv. Geologico d'Italia*, Vol. 92, **2014**.
- Cotecchia, V.; Dauru, M.; Limoni, P.P. Osservazioni Sull'evoluzione Dell'intrusione Marina Degli Acquiferi Carbonatici Costieri Della Puglia. In Proceedings of the Workshop "Il degrado qualitativo delle acque sotterranee in Puglia"; **2001**.
- Cotecchia, V.; Grassi, D.; Polemio, M. Carbonate Aquifers in Apulia and Seawater Intrusion. *G Geol Appl* 1: 219-231 2005. *Giornale di Geologia Applicata* 1 219–231, **2005**.
- Cotecchia, V.; Polemio, M. L'inquinamento e Il Sovrasfruttamento Delle Risorse Idriche Sotterranee Pugliesi. In Proceedings of the VI Workshop del Progetto Strategico "Clima, Ambiente e Territorio nel Mezzogiorno"(December 13 1995); **1997**.
- Cotecchia, V.; Tadolini, T.; Tulipano, L. Sea Water Intrusion in the Planning of Groundwater Resources Protection and Utilization in the Apulia Region (Southern Italy). *Geologia Applicata e Idrogeologia* **1983**, 18, 367–382.
- Cruden, D.; Martin, D. Before the Frank Slide. *Canadian Geotechnical Journal* **2007**, 44, 765–780.
- Cruden, D.M. Describing the Size of Discontinuities. *International Journal of Rock Mechanics and Mining Sciences & Geomechanics Abstracts* **1977**, 14, 133–137.
- Cruden, D.M. The Shapes of Cold, High Mountains in Sedimentary Rocks. *Geomorphology* **2003**, 55, 249–261.
- Damjanac, B.; Cundall, P. Application of Distinct Element Methods to Simulation of Hydraulic Fracturing in Naturally Fractured Reservoirs. *Computers and Geotechnics* **2016**, 71, 283–294.
- Danzi, M.; Di Crescenzo, G.; Ramondini, M.; Santo, A. Use of Unmanned Aerial Vehicles (UAVs) for Photogrammetric Surveys in Rockfall Instability Studies. *Rendiconti on line Società Geologica Italiana* **2013**, 24.
- Dawson, E.M.; Roth, W.H.; Drescher, A. Slope Stability Analysis by Strength Reduction. *Géotechnique* **1999**, 49, 835–840.
- De Alteriis, G; Aiello, G. Stratigraphy and Tectonics Offshore of Puglia (Italy, Southern Adriatic Sea). *Marine Geology* **1993**, 113, 233–253.
- Dearman, W.R. Engineering Geological Mapping. Elsevier, **1991**.

- Deere, D.U. Technical Description of Rock Cores for Engineering Purposes. *Rock Mechanics and Engineering Geology*, **1964**, 1.1: 17-22.
- Del Prete, S.; Iovine, G.; Parise, M.; Santo, A. Origin and Distribution of Different Types of Sinkholes in the Plain Areas of Southern Italy. *Geodinamica Acta* **2010**, 23 (1/3), 113–127.
- Delle Rose, M.; Parise, M. Slope Instability along the Adriatic Coast of Salento, Southern Italy. *Proceedings of IX International Symposium on Landslides* 28 June-2 July **2004**, Rio de Janeiro, Brazil, 1, 399–404.
- Deng, N.-F.; Qiao, L.; Li, Q.; Hao, J.-W.; Wu, S. A method to predict rock fracture with infrared thermography based on heat diffusion analysis. *Geofluids* **2021**, 1–13.
- Derron, M.-H.; Jaboyedoff, M.; Pedrazzini, A.; Michoud, C.; Villemin, T. Remote Sensing and Monitoring Techniques for the Characterization of Rock Mass Deformation and Change Detection. In *Rockfall Engineering*; **2011**; pp. 615–629 ISBN 9781848212565.
- Dershowitz, W.; Pointe, P.R. Ia; Doe, T.W. Advances in Discrete Fracture Network Modeling. In *Proceedings of the US EPA/NGWA fractured rock conference*, **2004**, Portland (pp. 882-894).
- Dershowitz, W.S.; Einstein, H.H. Characterizing Rock Joint Geometry with Joint System Models. *Rock mechanics and rock engineering* **1988**, 21, 21–51.
- Dershowitz, W.S.; Herda, H.H. Interpretation of Fracture Spacing and Intensity 1992. *Proc 33rd US Symposium on Rock Mechanics*, Santa Fe, 3–5 June **1992** P757–766.
- Dershowitz, W.S.; Lee, G.; Geier, J.; Hitchcock, S.; La Pointe, P. FRACMAN - Interactive Discrete Feature Data Analysis, Geometric Modeling, and Exploration Simulation. User Documentation, V. 2.4. Golder Associates Inc, Seattle **1994**.
- Dewitt, D.P.; Nutter, G.D. *Theory and Practice of Radiation Thermometry*. John Wiley & Sons **1988**.
- Di Bucci, D.; Caputo, R.; Mastronuzzi, G.; Fracassi, U.; Selleri, G.; Sansò, P. Quantitative Analysis of Extensional Joints in the Southern Adriatic Foreland (Italy), and the Active Tectonics of the Apulia Region. *Journal of Geodynamics* **2011**, 51, 141–155.
- Di Francesco, P.-M.; Bonneau, D.; Hutchinson, D.J. The Implications of M3C2 Projection Diameter on 3-D Semi-Automated Rockfall Extraction from Sequential Terrestrial Laser Scanning Point Clouds. *Remote Sensing* **2020**, Vol. 12, Page 1885 2020, 12, 1885.
- Diederichs, M.S. Rock Fracture and Collapse Under Low Confinement Conditions. *Rock Mechanics and Rock Engineering* **2003**, 36, 339–381.
- Diederichs, M.S.; Kaiser, P.K. Stability of Large Excavations in Laminated Hard Rock Masses: The Voussoir Analogue Revisited. *International Journal of Rock Mechanics and Mining Sciences* **1999a**, 36, 97–117.
- Diederichs, M.S.; Kaiser, P.K. Tensile Strength and Abutment Relaxation as Failure Control Mechanisms in Underground Excavations. *International Journal of Rock Mechanics and Mining Sciences* **1999b**, 36, 69–96.
- Dietrich, W.E.; Bellugi, D.; De Asua, R.R. Validation of the Shallow Landslide Model, SHALSTAB, for Forest Management. *Water science and Application*, **2001**, 2: 195-227.
- Dini, M.; Mastronuzzi, G.; Sansò, P. The Effects of Relative Sea Level Changes on the Coastal Morphology of Southern Apulia (Italy) during the Holocene. *Geomorphology, Human Activity and Global Environmental Change* **2000**, 43–65.
- Discontinuity Set Extractor. 2020. Software. Available online: <https://sourceforge.net/projects/discontinuity-set-extractor/> (accessed on 12 August 2021).
- Doglion, C. A Proposal for the Kinematic Modelling of W-Dipping Subductions - Possible Applications to the Tyrrhenian-Apennines System. *Terra Nova* **1991**, 3, 423–434.
- Doglion, C.; Mongelli, F.; Pieri, P. The Puglia Uplift (SE Italy): An Anomaly in the Foreland of the Apenninic Subduction Due to Buckling of a Thick Continental Lithosphere. *Tectonics* **1994**, 13, 1309–1321.
- Doglion, C.; Tropeano, M.; Mongelli, F.; Pieri, P. Middle-Late Pleistocene Uplift of Puglia: An “Anomaly” in the Apenninic Foreland. *Memorie Società Geologica Italiana* **1996**, 51, 101–117.

- Donati, D.; Stead, D.; Brideau, M.-A.; Ghirotti, M. A Remote Sensing Approach for the Derivation of Numerical Modelling Input Data: Insights from the Hope Slide, Canada. In Proceedings of the *ISRM AfriRock 2017 - Rock Mechanics for Africa*; Cape Town, South Africa, October 3 **2017**; pp. 861–878.
- Doorn, A.J. van; Koenderink, J.J. Affine Structure from Motion. *JOSA A*, Vol. 8, Issue 2, pp. 377–385 **1991**.
- Duncan, A.C. A Review of Cartesian Coordinate Construction from a Sphere, for Generation of Two Dimensional Geological Net Projections. *Computers & Geosciences* **1981**, 7, 367–385.
- Duncan, J.M. State of the Art: Limit Equilibrium and Finite-Element Analysis of Slopes. *Journal of Geotechnical Engineering* **1996**, 122, 577–596.
- Eberhardt, E.; Stead, D.; Coggan, J.S. Numerical Analysis of Initiation and Progressive Failure in Natural Rock Slopes—the 1991 Randa Rockslide. *International Journal of Rock Mechanics and Mining Sciences* **2004**, 41, 69–87.
- Eberhardt, E.; Stead, D.; Loew, S. Progressive Failure, Rock Mass Fatigue and Early Warning Applied to Deep-Seated Rock Slope Failures. In: Landslides and Engineered Slopes. In: *ISRM Progressive Rock Failure Conference*, Ascona, Switzerland, June **2017**.
- Eberhardt, E.; Thuro, K.; Luginbuehl, M. Slope Instability Mechanisms in Dipping Interbedded Conglomerates and Weathered Marls—the 1999 Rufi Landslide, Switzerland. *Engineering Geology* **2005**, 77, 35–56.
- Edelbro, C. Rock Mass Strength: A Review. **2003**. Technical Report, Luleå University of Technology, Luleå.
- Einstein, H.H.; Baecher, G.B. Probabilistic and Statistical Methods in Engineering Geology. *Rock Mechanics and Rock Engineering* **1983** 16:1 1983, 16, 39–72.
- Einstein, H.H.; Baecher, G.B.; Veneziano, D. Risk Analysis for Rock Slopes in Open Pit Mines; USBM Technical Report J0275015; Department of Civil Engineering, Massachusetts Institute of Technology, **1979**.
- Einstein, H.H.; Veneziano, D.; Baecher, G.B.; O’reilly, K.J. The Effect of Discontinuity Persistence on Rock Slope Stability. In *Proceedings of the International journal of rock mechanics and mining sciences & geomechanics abstracts*; **1983**; Vol. 20, pp. 227–236.
- Elmo, D. Evaluation of a Hybrid FEM/DEM Approach for Determination of Rock Mass Strength Using a Combination of Discontinuity Mapping and Fracture Mechanics Modelling, with Particular Emphasis on Modelling of Jointed Pillars. Ph.D. Thesis. Camborne School of Mines, **2006**.
- Elmo, D.; Stead, D. An Integrated Numerical Modelling–Discrete Fracture Network Approach Applied to the Characterization of Rock Mass Strength of Naturally Fractured Pillars. *Rock Mechanics and Rock Engineering* **2010**, 43, 3–19,
- Eltner, A.; Kaiser, A.; Castillo, C.; Rock, G.; Neugirg, F.; Abellán, A. Image-Based Surface Reconstruction in Geomorphometry—Merits, Limits and Developments. *Earth Surface Dynamics* **2016**, 4, 359–389.
- Eltner, A.; Sofia, G. Structure from Motion Photogrammetric Technique. In *Developments in Earth Surface Processes*; **2020**; Vol. 23, pp. 1–24 ISBN 9780444641779.
- Ester, M.; Kriegel, H.-P.; Sander, J.; Xu, X. A Density-Based Algorithm for Discovering Clusters in Large Spatial Databases with Noise. In Proceedings of the *Second International Conference on Knowledge Discovery and Data Mining*, Portland, OR, USA, 2 August **1996**; Volume 96, pp. 226–231.
- Fabian, D.; Peter, C.; Daniel, B.; Torsten, G. Evaluation of Damage-Induced Permeability Using a Three-Dimensional Adaptive Continuum/Discontinuum Code (AC/DC). *Physics and Chemistry of the Earth, Parts A/B/C* **2007**, 32, 681–690.
- Fan, X.; Kulatilake, P.H.S.W.; Chen, X. Mechanical Behavior of Rock-like Jointed Blocks with Multi-Non-Persistent Joints under Uniaxial Loading: A Particle Mechanics Approach. *Engineering Geology* **2015**, 190, 17–32.
- Fardin, N.; Feng, Q.; Stephansson, O. Application of a New in Situ 3-D Laser Scanner to Study the Scale Effect on the Rock Joint Surface Roughness. *Int. J. Rock Mech. Min. Sci.* **2004**, 41, 329–335.
- Favale, F., Sauro, U. Le Grotte Di Polignano; Le Grotte di Polignano: studi in memoria di Franco Orofino. *Federazione speleologica pugliese*, **1994**.
- Favalli, M.; Fornaciai, A.; Isola, I.; Tarquini, S.; Nannipieri, L. Multiview 3-D Reconstruction in Geosciences. *Computers & Geosciences* **2012**, 44, 168–176.

- Fazio, N.L.; Perrotti, M.; Andriani, G.F.; Mancini, F.; Rossi, P.; Castagnetti, C.; Lollino, P. A New Methodological Approach to Assess the Stability of Discontinuous Rocky Cliffs Using In-Situ Surveys Supported by UAV-Based Techniques and 3-D Finite Element Model: A Case Study. *Engineering Geology* **2019**, *260*, 105205.
- Fellenius, W. Calculations of the Stability of Earth Dams. In Proceedings of the *Second Congress of Large Dams*. **1936**; pp. 4:445-53.
- Feng, Q.; Sjögren, P.; Stephansson, O.; Jing, L. Measuring Fracture Orientation at Exposed Rock Faces by Using a Non-Reflector Total Station. *Engineering Geology* **2001**, *59*, 133–146.
- Feng, Q.H.; Röshoff, K. In-Situ Mapping and Documentation of Rock Faces Using a Full-Coverage 3d Laser Scanning Technique. *International Journal of Rock Mechanics and Mining Sciences* **2004**, *41*, 139–144.
- Fernández, O. Obtaining a Best Fitting Plane through 3-D Georeferenced Data. *Journal of Structural Geology* **2005**, *27*, 855–858.
- Ferrero, A.M.; Forlani, G.; Roncella, R.; Voyat, H.I. Advanced Geostructural Survey Methods Applied to Rock Mass Characterization. *Rock. Mech. Rock. Eng.* **2009**, *42*, 631–665.
- Festa, V. Cretaceous Structural Features of the Murge Area (Apulian Foreland, Southern Italy). *Eclogae Geologicae Helvetiae* **2003**, *96*, 11–22.
- Festa, V. *L'Avampaese Apulo Nel Quadro Dell'evoluzione Dell'Appennino Meridionale: La Deformazione Della Piattaforma Carbonatica Apula Nel Settore Murgiano (Puglia, Italia Meridionale)*; **1999**, PhD thesis, University of Bari, Italy.
- Fiorucci, M.; Marmoni, G.M.; Martino, S.; Mazzanti, P. Thermal Response of Jointed Rock Masses Inferred from Infrared Thermographic Surveying (Acuto Test-Site, Italy). *Sensors* **2018**, (7), 2221.
- Firpo, G.; Salvini, R.; Francioni, M.; Ranjith, P.G. Use of Digital Terrestrial Photogrammetry in Rocky Slope Stability Analysis by Distinct Elements Numerical Methods. *International Journal of Rock Mechanics and Mining Sciences* **2011**, *48*, 1045–1054.
- Fischler, M.A.; Bolles, R.C. Random Sample Consensus: A Paradigm for Model Fitting with Applications to Image Analysis and Automated Cartography. *Communications of the ACM* **1981**, *24*, 381–395.
- FLIR Tools Thermal Analysis and Reporting (Desktop) | Teledyne FLIR Available online: <https://www.flir.com/products/flir-tools/> (accessed on 6 July 2021).
- FLIR. User's manual FLIR T6xx series. **2014**. Available online: https://flir.custhelp.com/app/account/fl_download_manuals (date accessed: 11/12/2021).
- Fonstad, M.A.; Dietrich, J.T.; Courville, B.C.; Jensen, J.L.; Carbonneau, P.E. Topographic Structure from Motion: A New Development in Photogrammetric Measurement. *Earth Surface Processes and Landforms* **2013**, *38*, 421–430.
- Fookes, P.G. Geology for Engineers: The Geological Model, Prediction and Performance. *Q. J. Eng. Geol.* **1997**, *30*, 293–424.
- Fookes, P.G.; Denness, B. Observational Studies on Fissure Patterns in Cretaceous Sediments of South-East England. *Geotechnique*, **1969**, *19.4*: 453-477.
- Fookes, P.G.; Gourley, C.S.; Ohikere, C. Rock Weathering in Engineering Time. *Quarterly Journal of Engineering Geology and Hydrogeology* **1988**, *21*, 33–57.
- Ford, D.; Williams, P. Karst Hydrogeology and Geomorphology. *Karst Hydrogeol. Geomorphol.* **2013**, 1–562.
- Förstner, W. A Feature Based Correspondence Algorithm for Image Matching. *ISPRS ComIII, Rovaniemi* **1986**, 150–166.
- Francioni, M.; Salvini, R.; Stead, D.; Giovannini, R.; Riccucci, S.; Vanneschi, C.; Gullì, D. An Integrated Remote Sensing-GIS Approach for the Analysis of an Open Pit in the Carrara Marble District, Italy: Slope Stability Assessment through Kinematic and Numerical Methods. *Computers and Geotechnics* **2015**, *67*, 46–63.
- Francioni, M.; Salvini, R.; Stead, D.; Litrico, S. A Case Study Integrating Remote Sensing and Distinct Element Analysis to Quarry Slope Stability Assessment in the Monte Altissimo Area, Italy. *Engineering Geology* **2014**, *183*, 290–302.

References

- Franklin, J.A.; Maerz, N.H.; Bennett, C.P. Rock Mass Characterization Using Photoanalysis. *Int. J. Min. Geol. Eng.* **1988**, *6*, 97–112.
- Fraser, C.; Cronk, S. A Hybrid Measurement Approach for Close-Range Photogrammetry. *ISPRS Journal of Photogrammetry and Remote Sensing* **2009**, *64*, 328–333.
- Frayssines, M.; Hantz, D. Failure Mechanisms and Triggering Factors in Calcareous Cliffs of the Subalpine Ranges (French Alps). *Engineering Geology* **2006**, *86*, 256–270.
- Frodella, W.; Fidolini, F.; Morelli, S.; Pazzi, V. Application of Infrared Thermography for Landslide Mapping: The Rotolon DSGDS Case Study. *Rendiconti Online Società Geologica Italiana* **2015**, *35*, 144–147.
- Frodella, W.; Gigli, G.; Morelli, S.; Lombardi, L.; Casagli, N. Landslide Mapping and Characterization through Infrared Thermography (IRT): Suggestions for a Methodological Approach from Some Case Studies. *Remote Sensing* **2017a**, *9*, 1281.
- Frodella, W.; Morelli, S.; Gigli, G.; Casagli, N. Contribution of Infrared Thermography to the Slope Instability Characterization. In: Proceedings of world landslide forum, 2-6 June **2014**, Beijing, China, p. 144-147.
- Frodella, W.; Morelli, S.; Pazzi, V. InfraRed Thermographic Surveys for Landslide Mapping and Characterization: The Rotolon DSGSD (Northern Italy) Case Study. *Italian Journal of Engineering Geology and Environment, Special Issue* **2017b**, *1*.
- Furukawa, Y.; Ponce, J. Carved Visual Hulls for Image-Based Modeling. *International Journal of Computer Vision* **2008**, *81*, 53–67.
- García-Sellés, D.; Falivene, O.; Arbués, P.; Gratacos, O.; Tavani, S.; Muñoz, J.A. Supervised Identification and Reconstruction of Near-Planar Geological Surfaces from Terrestrial Laser Scanning. *Comput. Geosci.* **2011**, *37*, 1584–1594.
- Garduño-Monroy, V.H.; Macías, J.L.; Morelli, S.; Figueroa-Soto, A.; Ruiz-Figueroa, A.; Robles-Camacho, J.; Veronica, P. Landslide Impact on the Archaeological Site of Mitla, Oaxaca. *Geoarchaeology* **2020**, *35*, 644–658.
- Gaussorgues, G. *Infrared Thermography*; Springer Netherlands: London, UK, **1994**.
- Gauthier, D.; Hutchinson, D.J. On the Precision, Accuracy, and Utility of Oblique Aerial Photogrammetry (OAP) for Rock Slope Monitoring and Assessment. In Proceedings of the *68th Canadian geotechnical conference, GeoQuebec*; **2015**.
- Gentile, P.; Iaia, C.; Liso, I.; Parise, M. Eventi Alluvionali Nell’ambiente Carsico Pugliese. *Geologia dell’ambiente*, suppl. n. 1/2020 **2020**, 56–63.
- Gero, M.; Suarez, F.; González Nicieza, C.; Álvarez-Fernández, M.I. Infrared Thermography Methodology Applied to Detect Localized Rockfalls in Self-Supporting Underground Mines. In: *EUROCK 2013 – The 2013 ISRM International Symposium – Rock Mechanics for Resources, Energy, and Environment*, Wroclaw-Poland, Volume: **2013** Taylor & Francis Group, London, ISBN 978-1-138-00080-3.
- Ghirotti, M.; Genevois, R. A Complex Rock Slope Failure Investigated by Means of Numerical Modelling Based on Laser Scanner Technique. In *Proceedings of the 1st Canada-US Rock Mechanics Symposium - Rock Mechanics Meeting Society’s Challenges and Demands*; **2007**; Vol. 2, pp. 917–924 ISBN 9780429107566.
- Giani, G.P. *Rock Slope Stability Analysis*; CRC Press, **1992**.
- Gigli, G., Morelli, S., Fornera, S., Casagli, N. Terrestrial laser scanner and geomechanical surveys for the rapid evaluation of rock fall susceptibility scenarios. *Landslides* **2014**, *11*, 1–14.
- Gigli, G.; Casagli, N. Extraction of Rock Mass Structural Data from High Resolution Laser Scanning Products. *Landslide Science and Practice: Spatial Analysis and Modelling* **2013**, *3*, 89–94.
- Gigli, G.; Casagli, N. Semi-Automatic Extraction of Rock Mass Structural Data from High Resolution LIDAR Point Clouds. *International Journal of Rock Mechanics and Mining Sciences* **2011**, *48*, 187–198.
- Gigli, G.; Fanti, R.; Canuti, P.; Casagli, N. Integration of Advanced Monitoring and Numerical Modeling Techniques for the Complete Risk Scenario Analysis of Rockslides: The Case of Mt. Beni (Florence, Italy). *Engineering Geology* **2011**, *120*, 48–59.

- Gigli, G.; Frodella, W.; Garfagnoli, F.; Morelli, S.; Mugnai, F.; Menna, F.; Casagli, N. 3-D Geomechanical Rock Mass Characterization for the Evaluation of Rockslide Susceptibility Scenarios. *Landslides* **2013**, *11*, 131–140.
- Gillespie, P.A.; Johnston, J.D.; Loriga, M.A.; McCaffrey, K.J.W.; Walsh, J.J.; Watterson, J. Influence of Layering on Vein Systematics in Line Samples. *Geological Society, London, Special Publications* **1999**, *155*, 35–56, doi:10.1144/GSL.SP.1999.155.01.05.
- Gischig, V.; Amann, F.; Moore, J.R.; Loew, S.; Eisenbeiss, H.; Stempfhuber, W. Composite Rock Slope Kinematics at the Current Randa Instability, Switzerland, Based on Remote Sensing and Numerical Modeling. *Engineering Geology* **2011**, *118*, 37–53.
- Golder Associates FracMan7-Interactive Discrete Feature, Data Analysis, Geometric Modeling and Exploration Simulation; **2018**. Available online: <https://www.golder.com/fracman/>.
- Goodman, R.E. *Methods of Geological Engineering in Discontinuous Rocks*; West Pub. Co.: St. Paul, MN, USA, **1976**; ISBN 0829900667.
- Goodman, R.E. The Resolution of Stresses in Rock Using Stereographic Projection. *International Journal of Rock Mechanics and Mining Sciences & Geomechanics Abstracts* **1964**, *1*, 93–103.
- Goodman, R.E.; Bray, J.W. Toppling of Rock Slopes. In: Proc. *Speciality Conference on Rock Engineering for Foundation and Slopes*. ASCE, **1976**. p. 201-234.
- Goodman, R.E.; Kieffer, D.S. Behavior of Rock in Slopes. *Journal of Geotechnical and Geoenvironmental Engineering* **2000**, *126*, 675–684.
- Goodman, R.E.; Shi, G. *Block Theory and Its Application to Rock Engineering*. **1985**, Prentice Hall, Englewood Cliffs, NJ.
- Goodman, R.E.; Taylor Robert, L.; Brekke Tor, L. A Model for the Mechanics of Jointed Rock. *Journal of the Soil Mechanics and Foundations Division* **1968**, *94*, 637–659.
- Grassi, D.; Micheletti, A. Sul Progressivo Abbassamento Della Superficie Della Falda Carsica e Sulle Interferenze Idrologiche Tra Pozzi Osservati Nell'interland Di Bari. *Geologia Applicata e Idrogeologia* **1972**, *7*, 183–205.
- Grechi, G.; Fiorucci, M.; Marmoni, G.M.; Martino, S. 3D Thermal Monitoring of Jointed Rock Masses through Infrared Thermography and Photogrammetry. *Remote Sensing* **2021**, *13* (5), 957.
- Griffiths, D. v.; Lane, P.A. Slope Stability Analysis by Finite Elements. *Géotechnique* **1999**, *49*, 387–403.
- Guadagno, F.; Martino, S.; Scarascia Mugnozza, G. Influence of Man-Made Cuts on the Stability of Pyroclastic Covers (Campania, Southern Italy): A Numerical Modelling Approach. *Environmental Geology* **2003** *43*:4 2003, *43*, 371–384.
- Guerin, A.; Abellán, A.; Matasci, B.; Jaboyedoff, M.; Derron, M.H.; Ravel, L. Brief Communication: 3-D Reconstruction of a Collapsed Rock Pillar from Web-Retrieved Images and Terrestrial Lidar Data-the 2005 Event of the West Face of the Drus (Mont Blanc Massif). *Nat. Hazards Earth Syst. Sci.* **2017**, *17*, 1207–1220.
- Guerin, A.; Jaboyedoff, M.; Collins, B.D.; Derron, M.-H.; Stock, G.M.; Matasci, B.; Boesiger, M.; Lefevre, C.; Podladchikov, Y.Y. Detection of Rock Bridges by Infrared Thermal Imaging and Modeling. *Scientific Reports* **2019** *9*:1 2019, *9*, 1–19.
- Guerin, A.; Stock, G.M.; Radue, M.J.; Jaboyedoff, M.; Collins, B.D.; Matasci, B.; Avdievitch, N.; Derron, M.H. Quantifying 40 years of Rockfall Activity in Yosemite Valley with Historical Structure-from-Motion Photogrammetry and Terrestrial Laser Scanning. *Geomorphology* **2020**, *356*, 107069.
- Gutiérrez, F. Hazards Associated with Karst. *Geomorphological Hazards and Disaster Prevention* **2010**, 161–176.
- Gutiérrez, F.; Parise, M.; De Waele, J.; Jourde, H. A Review on Natural and Human-Induced Geohazards and Impacts in Karst. *Earth-Science Reviews* **2014**, *138*, 61–88.
- Habib, A. Accuracy, Quality Assurance, and Quality Control of LiDAR Data. In *Topographic Laser Ranging and Scanning*; CRC Press, **2018**; pp. 269–294 ISBN 9781315219561.
- Hammah, R.; Yacoub, T. Investigating the Performance of the Shear Strength Reduction (Ssr) Method on the Analysis of Reinforced Slopes. *59th Canadian Geotechnical and 7th Joint IAHCNC and CGS Groundwater Speciality Conferences* **2006**.

References

- Hammah, R.E.; Yacoub, T.; Corkum, B.; Curran, J.H. The Practical Modelling of Discontinuous Rock Masses with Finite Element Analysis. In *The 42nd US Rock Mechanics Symposium (USRMS)*, 29 June-2 July **2008**, San Francisco, California.
- Hammah, R.E.; Yacoub, T.; Corkum, B.; Wibowo, F.; Curran, J.H. Analysis of Blocky Rock Slopes With Finite Element Shear Strength Reduction Analysis In *1st Canada - U.S. Rock Mechanics Symposium*, Vancouver, Canada, May **2007**.
- Hammah, R.E.; Yacoub, T.E.; Corkum, B.C.; Curran, J.H. The Shear Strength Reduction Method for the Generalized Hoek-Brown Criterion. In Proceedings of the Alaska Rocks 2005, *The 40th US Symposium on Rock Mechanics (USRMS)*; **2005**.
- Haneberg W.C.; Findley, D. Digital Outcrop Characterization for 3-D Structural Mapping and Rock Slope Design Along Interstate 90 Near Snoqualmie Pass. In: Proceedings, *57th annual highway geology symposium*, Breckenridge, Colorado. **2006**.
- Haneberg, W.C. Directional Roughness Profiles From Three-Dimensional Photogrammetric Or Laser Scanner Point Clouds. In: *1st Canada - U.S. Rock Mechanics Symposium*, Vancouver, Canada, May **2007**.
- Haneberg, W.C. Using Close Range Terrestrial Digital Photogrammetry for 3-D Rock Slope Modeling and Discontinuity Mapping in the United States. *Bulletin of Engineering Geology and the Environment* **2008**, *67*, 457–469.
- Haneberg, W.C.; Cole, W.F.; Kasali, G. High-Resolution Lidar-Based Landslide Hazard Mapping and Modeling, UCSF Parnassus Campus, San Francisco, USA. *Bulletin of Engineering Geology and the Environment* **2009** *68:2* 2009, *68*, 263–276.
- Hantz, D.; Vengeon, J.M.; Dussauge-Peisser, C. An Historical, Geomechanical and Probabilistic Approach to Rock-Fall Hazard Assessment. *Natural Hazards and Earth System Science* **2003**, *3*, 693–701.
- Harris, C.; Stephens, M. A Combined Corner and Edge Detector. In Proc. Of *Fourth Alvey Vision Conference* **1988**, 147-151.
- Harrison, J.P. Fuzzy Objective Functions Applied to the Analysis of Discontinuity Orientation Data. In Proceedings of the Rock Characterization: ISRM Symposium, Eurock '92; Hudson, J.A., Ed.; Chester, UK, **1992**; pp. 25–30.
- Hart, R.D. An Introduction to Distinct Element Modeling for Rock Engineering. In *Analysis and Design Methods*; Elsevier, **1993**; pp. 245–261.
- Havaej, M.; Stead, D.; Coggan, J.; Emo, D. Application of Discrete Fracture Networks (DFN) in the Stability Analysis of Delabole Slate Quarry, Cornwall, UK. In Proceedings of the *50th US Rock Mechanics/Geomechanics Symposium*; **2016**.
- Herda, H.H.W. Strike Standard Deviation for Shallow-Dipping Rock Fracture Sets. *Rock Mechanics and Rock Engineering* **1999**, *32*, 241–255.
- Hills, E.S. Elements of Structural Geology. Springer Science & Business Media, **2012**.
- Hoek, E. Practical Rock Engineering. **2007**, North Vancouver, BC, Canada.
- Hoek, E.; Bray, J. Rock Slope Engineering; CRC Press: Boca Raton, FL, USA, **1981**.
- Hoek, E.; Brown, E.T. Practical Estimates of Rock Mass Strength. *International Journal of Rock Mechanics and Mining Sciences* **1997**, *34*, 1165–1186.
- Hoek, E.; Brown, E.T. The Hoek–Brown Failure Criterion and GSI – 2018 Edition. *Journal of Rock Mechanics and Geotechnical Engineering* **2019**, *11*, 445–463.
- Hoek, E.; Brown, E.T. Underground Excavations in Rock. **1980**, CRC Press, 527 pp.
- Hoek, E.; Carranza-Torres, C.; Corkum, B.; others Hoek-Brown Failure Criterion-2002 Edition. Proceedings of *NARMS-Tac* **2002**, *1*, 267–273.
- Hoek, E.; Grabinsky, M.W.; Diederichs, M.S. Numerical Modelling for Underground Excavation Design. Institution of Mining and Metallurgy Transactions. Section A. Mining Industry **1991**, 100.

- Hoek, E.; Marinos, P. Predicting Tunnel Squeezing Problems in Weak Heterogeneous Rock Masses Predicting Tunnel Squeezing Problems in Weak Heterogeneous Rock Masses. Part 1: Estimating Rock Mass Strength. *Tunnels and Tunnelling International Part* **2000**, *1*.
- Holst, G.C. *Common Sense Approach to Thermal Imaging*. Washington: SPIE Optical Engineering Press, **2000**.
- Howell, J.R.; Mengüç, M.P.; Daun, K.J.; Siegel, R. *Thermal Radiation Heat Transfer*; **2021**; ISBN 9780367347079.
- Hudson, J.; Harrison, J. *Engineering Rock Mechanics: An Introduction to the Principles*; Elsevier: Amsterdam, The Netherlands, **2000**.
- Hudson, J.; Harrison, J. *Engineering Rock Mechanics: An Introduction to Principles (2nd ed.)*. Pergamon. **2000**.
- Hudson, J.A.; Priest, S.D. Discontinuities and Rock Mass Geometry. *International Journal of Rock Mechanics and Mining Sciences & Geomechanics Abstracts* **1979**, *16*, 339–362.
- Hudson, J.A.; Priest, S.D. Discontinuity Frequency in Rock Masses. *International Journal of Rock Mechanics and Mining Sciences & Geomechanics Abstracts* **1983**, *20*, 73–89.
- Hudson, R.D. *Infrared System Engineering, Vol.1*. New York: Wiley-Interscience **1969**.
- Humair, F.; Pedrazzini, A.; Epard, J.L.; Froese, C.R.; Jaboyedoff, M. Structural Characterization of Turtle Mountain Anticline (Alberta, Canada) and Impact on Rock Slope Failure. *Tectonophysics* **2013**, *605*, 133–148.
- Hungr, O. CLARA-W User's Manual 2001. Available online: <https://www.yumpu.com/en/document/view/7769571/users-manual-clara-w-o-hungr-geotechnical-research-inc>
- Hungr, O.; Evans, S.G. The Occurrence and Classification of Massive Rock Slope Failure. *Felsbau* **2004**, *22*, 16–23.
- Hungr, O.; Leroueil, S.; Picarelli, L. The Varnes Classification of Landslide Types, an Update. *Landslides* **2014**, *11*, 167–194.
- Hutchison, B.; Dugan, K.; Coulthard, M. Analysis Of Flexural Toppling At Australian Bulk Minerals Savage River Mine. *ISRM International Symposium*, Melbourne, Australia, November **2000**.
- Incropera, F.P. *Introduction to Heat Transfer*. John Wiley & Sons, 960 pages, **2007**.
- Ingensand, H. Metrological Aspects in Terrestrial Laser-Scanning Technology. 2006. In: *Proceedings of the 3rd IAG/12th FIG symposium*, Baden, Austria. **2006**.
- ISRM Rock Characterization, Testing and Monitoring; Brown, E.R., Ed.; Pergamon Press: Oxford, **1981**.
- ISRM Suggest Methods for Determining Water Content, Porosity, Density, Absorption and Related Properties and Swelling and Slake-Durability Index Properties. In: *International Journal of Rock Mechanics and Mining Science & Geomechanics Abstracts* **1979a**, *16*, 141-156.
- ISRM Suggested Methods for Determining the Uniaxial Compressive Strength and Deformability of Rock Materials. *International Journal of Rock Mechanics and Mining Sciences & Geomechanics Abstracts* **1979b**, *16*, 137.
- ISRM Suggested Methods for the Quantitative Description of Discontinuities in Rock Masses. *International Journal of Rock Mechanics and Mining Sciences & Geomechanics Abstracts* **1978**, *15*, 319–368.
- ISRM Suggested Methods for the Quantitative Description of Discontinuities in Rock Masses. *International Journal of Rock Mechanics and Mining Sciences & Geomechanical Abstracts* **1988**, *20*, 189–200.
- Itasca 3-DEC-Three-Dimensional Distinct Element Code. Ver.7.0. 2020. Available online: <https://www.itascacg.com/software/downloads/3-Dec>.
- Itasca FLAC3-D-Fast Lagrangian Analysis of Continua in Three Dimensions, Ver. 8.1. 2019. Available online: <https://www.itascacg.com/software/downloads/flac3-d>.
- Ivars, D.M.; Pierce, M.E.; Darcel, C.; Reyes-Montes, J.; Potyondy, D.O.; Paul Young, R.; Cundall, P.A. The Synthetic Rock Mass Approach for Jointed Rock Mass Modelling. *International Journal of Rock Mechanics and Mining Sciences* **2011**, *48*, 219–244.
- Jaboyedoff, M.; Abellan, A.; Carrea, D.; Derron, M.-H.; Matasci, B.; Michoud, C. Mapping and Monitoring of Landslides Using LIDAR. In: *Natural Hazards*. CRC Press, **2018**. p. 397-420.

- Jaboyedoff, M.; Baillifard, F.; Hantz, D.; Heindenreich, B.; Mazzocolla, D. Terminologie= Terminologia. Prévention des mouvements de versants et des instabilités de falaises: Confrontation des méthodes d'étude des éboulements dans l'arc alpin Report number: Programme INTERREG II C - "FALAISES", Méditerranée Occidentale et Alpes Latines, **2001**.
- Jaboyedoff, M.; Couture, R.; Locat, P. Structural Analysis of Turtle Mountain (Alberta) Using Digital Elevation Model: Toward a Progressive Failure. *Geomorphology* **2009**, *103*, 5–16.
- Jaboyedoff, M.; Derron, M.-H. Landslide Analysis Using Laser Scanners. In *Developments in Earth Surface Processes*; Elsevier, **2020**; Vol. 23, pp. 207–230.
- Jaboyedoff, M.; Metzger, R.; Oppikofer, T.; Couture, R.; Derron, M.; Locat, J.; Turmel, D. New Insight Techniques to Analyze Rock-Slope Relief Using DEM and 3-D-Imaging Cloud Points. In *Rock Mechanics: Meeting Society's Challenges and Demands*; Taylor & Francis: London, UK, **2007**; pp. 61–68.
- Jaboyedoff, M.; Oppikofer, T.; Abellán, A.; Derron, M.H.; Loye, A.; Metzger, R.; Pedrazzini, A. Use of LIDAR in Landslide Investigations: A Review. *Natural Hazards* **2012**, *61*, 5–28.
- Jaboyedoff, M.; Oppikofer, T.; Minoia, R.; Locat, J.; Turmel, D. Terrestrial Lidar Investigation of the 2004 Rockslide along Petit Champlain Street, Québec City (Quebec, Canada). In: *4th Canadian Conference on Geohazards: From Causes to Management*. Presse de l'Université Laval, **2008**. p. 295-301.
- James, M.R.; Robson, S. Mitigating Systematic Error in Topographic Models Derived from UAV and Ground-Based Image Networks. *Earth Surface Processes and Landforms* **2014**, *39*, 1413–1420.
- James, M.R.; Robson, S. Straightforward Reconstruction of 3-D Surfaces and Topography with a Camera: Accuracy and Geoscience Application. *J. Geophys. Res. Earth Surf.* **2012**, *117*, 1–17.
- Jamshid, G.; L, W.E.; Jeremy, I. Finite Element for Rock Joints and Interfaces. *Journal of the Soil Mechanics and Foundations Division* **1973**, *99*, 833–848.
- Janbu, N. Slope Stability Computations. *Embankment-Dam Eng* **1973**, 47–86.
- Javernick, L.; Brasington, J.; Caruso, B. Modeling the Topography of Shallow Braided Rivers Using Structure-from-Motion Photogrammetry. *Geomorphology* **2014**, *213*, 166–182.
- Jennings, J.E. A Mathematical Theory for the Calculation of the Stability of Slopes in Open Cast Mines. In *Proceedings of the Planning Open Pit Mines*, Johannesburg; **1970**; Vol. 21, pp. 87–102.
- Jensen, J.R. Remote Sensing of the Environment An Earth Perspective. Upper Saddle River, N.J.: Pearson Prentice Hall, **2007**.
- Jimenez-Rodriguez, R.; Sitar, N. A Spectral Method for Clustering of Rock Discontinuity Sets. *International Journal of Rock Mechanics and Mining Sciences* **2006**, *43*, 1052–1061.
- Jing, L. A Review of Techniques, Advances and Outstanding Issues in Numerical Modelling for Rock Mechanics and Rock Engineering. *Int. J. Rock Mech. Min. Sci.* **2003**, *40*, 283–353.
- Jing, L.; Hudson, J.A. Numerical Methods in Rock Mechanics. *International Journal of Rock Mechanics and Mining Sciences* **2002**, *39*, 409–427.
- John, K.W. Engineering Analyses of Three-Dimensional Stability Problems Utilizing the Reference Hemisphere. *International Society of Rock Mechanics*, Proceedings **1970**.
- Jones, R.R.; Kokkalas, S.; McCaffrey, K.J.W. Quantitative Analysis and Visualization of Nonplanar Fault Surfaces Using Terrestrial Laser Scanning (LIDAR)—The Arkitsa Fault, Central Greece, as a Case Study LIDAR Analysis and Visualization of Nonplanar Faults at Arkitsa, Greece. *Geosphere* **2009**, *5*, 465–482.
- Junique, T.; Vazquez, P.; Thomachot-Schneider, C.; Hassoun, I.; Jean-Baptiste, M.; Géraud, Y. The use of infrared thermography on the measurement of microstructural changes of reservoir rocks induced by temperature. *Appl. Sci.* **2021**, *11*, 559.
- Kainthola, A.; Singh, P.K.; Singh, T.N. Stability Investigation of Road Cut Slope in Basaltic Rockmass, Mahabaleshwar, India. *Geoscience Frontiers* **2015**, *6*, 837–845.
- Kalenchuk, K.S.; Diederichs, M.S.; Hutchinson, D.J. Three-Dimensional Numerical Simulations of the Downie Slide to Test the Influence of Shear Surface Geometry and Heterogeneous Shear Zone Stiffness. *Computational Geosciences* **2011** *16:1* 2011, *16*, 21–38.

- Kalkani, E.C.; Piteau, D.R. Finite Element Analysis of Toppling Failure at Hell's Gate Bluffs, British Columbia. *Environmental and Engineering Geoscience* **1976**, XIII, 315–327.
- Kalkani, E.C.; von Frese, R.R.B. Computer Construction of Equal-Angle Fabric Diagrams and Program Comparisons. *Computers & Geosciences* **1980**, 6, 279–288.
- Kamerman, G. Laser Radar (Chapter 1). In *The infrared and electro-optical systems handbook*; Fox CS, Ed.; Ann Arbor, Michigan, **1993**; pp. 1–76.
- Kazhdan, M.; Hoppe, H. Screened Poisson Surface Reconstruction. *ACM Transactions on Graphics* **2013**, 32(3), 1–13.
- Kemeny, J. The Time-Dependent Reduction of Sliding Cohesion Due to Rock Bridges along Discontinuities: A Fracture Mechanics Approach. *Rock Mechanics and Rock Engineering* **2003**, 36, 27–38.
- Kemeny, J.; Turner, K.; Norton, B. LIDAR for Rock Mass Characterization: Hardware, Software, Accuracy and Best-Practices. *Laser and photogrammetric methods for rock face characterization* **2006**, 49–62.
- Kirchhoff, G. I. On the Relation between the Radiating and Absorbing Powers of Different Bodies for Light and Heat. *The London, Edinburgh, and Dublin Philosophical Magazine and Journal of Science* **1860**, 20, 1–21.
- Kogure, T.; Aoki, H.; Maekado, A.; Hirose, T.; Matsukura, Y. Effect of the Development of Notches and Tension Cracks on Instability of Limestone Coastal Cliffs in the Ryukyus, Japan. *Geomorphology* **2006**, 80, 236–244.
- Kong, D.; Saroglou, C.; Wu, F.; Sha, P.; Li, B. Development and Application of UAV-SfM Photogrammetry for Quantitative Characterization of Rock Mass Discontinuities. *International Journal of Rock Mechanics and Mining Sciences* **2021**, 141, 104729.
- Kong, D.; Wu, F.; Saroglou, C. Automatic Identification and Characterization of Discontinuities in Rock Masses from 3D Point Clouds. *Engineering Geology* **2020**, 265, 105442.
- Krahn, J.; Morgenstern, N.R. Mechanics of the Frank Slide. In *Proceedings of the Rock Engineering for Foundations & Slopes*; **1976**; pp. 309–332.
- Kromer, R.; Hutchinson, D.; Lato, M.; Gauthier, D.; Edwards, T. Identifying Rock Slope Failure Precursors Using LiDAR for Transportation Corridor Hazard Management. *Engineering Geology* **2015**, 195.
- Kromer, R.A.; Abellán, A.; Hutchinson, D.J.; Lato, M.; Chanut, M.A.; Dubois, L.; Jaboyedoff, M. Automated Terrestrial Laser Scanning with Near-Real-Time Change Detection - Monitoring of the Séchilienne Landslide. *Earth Surface Dynamics* **2017**, 5, 293–310.
- Kulatilake, P.; Ucpirti, H.; Wang, S.; Radberg, G.; Stephansson, O. Use of the Distinct Element Method to Perform Stress Analysis in Rock with Non-Persistent Joints and to Study the Effect of Joint Geometry Parameters on the Strength and Deformability of Rock Masses. *Rock Mechanics and Rock Engineering* **1992**, 25, 253–274.
- Kulatilake, P.H.S.W. Application of Probability and Statistics in Joint Network Modeling in Three Dimensions. In *Proceedings of the Conf. on Probabilistic Methods in Geotech. Eng.*; Lamberra, Australia, **1993**; pp. 63–87.
- Kulatilake, P.H.S.W. Bivariate Normal Distribution Fitting on Discontinuity Orientation Clusters. *Mathematical Geology* **1986** 18:2 1986, 18, 181–195.
- Kulatilake, P.H.S.W. Fitting Fisher Distributions to Discontinuity Orientation Data. *Journal of Geological Education* **1985**, 33, 266–269.
- Kulatilake, P.H.S.W.; Wu, T.H. Estimation of Mean Trace Length of Discontinuities. *Rock Mechanics and Rock Engineering* **1984a** 17:4 1984, 17, 215–232.
- Kulatilake, P.H.S.W.; Wu, T.H. Sampling Bias on Orientation of Discontinuities. *Rock Mechanics and Rock Engineering* **1984b**, 17, 243–253.
- Kulatilake, P.H.S.W.; Wu, T.H. The Density of Discontinuity Traces in Sampling Windows. *International Journal of Rock Mechanics and Mining Sciences & Geomechanics Abstracts* **1984c**, 21, 345–347.
- La Pointe, P.R.; Hudson, J.A. Characterization and Interpretation of Rock Mass Joint Patterns. *Geological Society of America*, **1985**.
- Lajtai, E.Z. Strength of Discontinuous Rocks in Direct Shear. *Géotechnique* **1969**, 19, 218–233.

- Large, A.R.G.; Heritage, G.L. Laser Scanning for the Environmental Sciences. *Laser Scanning for the Environmental Sciences* **2009**, 1–278.
- Lato, M.; Diederichs, M.S.; Hutchinson, D.J.; Harrap, R. Optimization of LiDAR Scanning and Processing for Automated Structural Evaluation of Discontinuities in Rockmasses. *International Journal of Rock Mechanics and Mining Sciences* **2009**, 46, 194–199.
- Lato, M.; Hutchinson, D.; Gauthier, D.; Edwards, T.; Ondercin, M. Comparison of Airborne Laser Scanning, Terrestrial Laser Scanning, and Terrestrial Photogrammetry for Mapping Differential Slope Change in Mountainous Terrain. *Canadian Geotechnical Journal* **2014**, 52, 1–12.
- Lato, M.; Kemeny, J.; Harrap, R.M.; Bevan, G. Rock Bench: Establishing a Common Repository and Standards for Assessing Rockmass Characteristics Using LiDAR and Photogrammetry. *Computers and Geosciences* **2013**, 50, 106–114.
- Lato, M.J.; Vöge, M. Automated Mapping of Rock Discontinuities in 3D Lidar and Photogrammetry Models. *International Journal of Rock Mechanics and Mining Sciences* **2012**, 54, 150–158.
- Lavecchia, G.; Boncio, P.; Creati, N.; Brozzetti, F. Some Aspects Of The Italian Geology Not Fitting With A Subduction Scenario. *Journal of The Virtual Explorer* **2003**, 10, 1-14.
- Lawn, B. Fracture of Brittle Solids. Cambridge solid state science series, **1993**.
- Lei, Q.; Latham, J.P.; Tsang, C.F. The Use of Discrete Fracture Networks for Modelling Coupled Geomechanical and Hydrological Behaviour of Fractured Rocks. *Computers and Geotechnics* **2017**, 85, 151–176.
- Lemy, F.; Hadjigeorgiou, J. Discontinuity Trace Map Construction Using Photographs of Rock Exposures. *International Journal of Rock Mechanics and Mining Sciences* **2003**, 40, 903–917.
- Li, J.; Li, E.; Chen, Y.; Xu, L.; Zhang, Y. Bundled Depth-Map Merging for Multi-View Stereo. In: *2010 IEEE Computer Society Conference on Computer Vision and Pattern Recognition*. IEEE, **2010**. p. 2769–2776.
- Li, X.; Chen, J.; Zhu, H. A New Method for Automated Discontinuity Trace Mapping on Rock Mass 3D Surface Model. *Computers and Geosciences* **2016**, 89, 118–131.
- Li, X.; Chen, Z.; Chen, J.; Zhu, H. Automatic Characterization of Rock Mass Discontinuities Using 3-D Point Clouds. *Engineering Geology* **2019**, 259, 105131.
- Lichti, D.D. Error Modelling, Calibration and Analysis of an AM–CW Terrestrial Laser Scanner System. *ISPRS Journal of Photogrammetry and Remote Sensing* **2007**, 61, 307–324.
- LIDAR-Generated Digital Elevation Models. *Rock Mech. Rock Eng.* **2015**, 48, 1589–1604.
- Lim, M.; Petley, D.N.; Rosser, N.J.; Allison, R.J.; Long, A.J.; Pybus, D. Combined Digital Photogrammetry and Time-of-Flight Laser Scanning for Monitoring Cliff Evolution. *Photogrammetric Record* **2005**, 20, 109–129.
- Lisjak, A.; Grasselli, G. A Review of Discrete Modeling Techniques for Fracturing Processes in Discontinuous Rock Masses. *J. Rock Mech. Geotech. Eng.* **2014**, 6, 301–314.
- Liso, I.S.; Chieco, M.; Fiore, A.; Pisano, L.; Parise, M. Underground Geosites and Caving Speleotourism: Some Considerations, From a Case Study in Southern Italy. *Geoheritage* **2020**, 12, 1–12.
- Liso, I.S.; Parise, M. Apulian Karst Springs: A Review. *Journal of Environmental Science and Engineering Technology* **2020**, 8, 63–83.
- Liu, G.; Klette, R.; Rosenhahn, B. Collinearity and Coplanarity Constraints for Structure from Motion. In: *Pacific-Rim Symposium on Image and Video Technology*. Springer, Berlin, Heidelberg, **2006**. p. 13-23.
- Liu, Q.; Liu, Q.; Pan, Y.; Peng, X.; Deng, P.; Huang, K. Experimental study on rock indentation using infrared thermography and acoustic emission techniques. *J. Geophys. Eng.* **2018**, 15, 1864–1877.
- Liu, S.; Xu, Z.; Wu, L.; Ma, B.; Liu, X. Infrared Imaging Detection of Hidden Danger in Mine Engineering. In: *Progress in Electromagnetics Research Symposium 12-16 September* **2011**, Suzhou, China, 125.
- Loche, M.; Scaringi, G.; Blahůt, J.; Melis, M.T.; Funedda, A.; Da Pelo, S.; Erbi, I.; Deiana, G.; Meloni, M.A.; Cocco, F. An Infrared Thermography Approach to Evaluate the Strength of a Rock Cliff. *Remote Sensing* **2021**, 13(7), 1265.

- Loiotine, L.; Andriani, G.F.; Jaboyedoff, M.; Parise, M.; Derron, M.-H. Comparison of remote sensing techniques for geostructural analysis and cliff monitoring in coastal areas of high tourist attraction: The case study of Polignano a Mare (Southern Italy). *Remote Sens.* **2021a**, *13*, 5045.
- Loiotine, L.; Wolff, C.; Wyser, E.; Andriani, G.F.; Derron, M.-H.; Jaboyedoff, M.; Parise, M. QDC-2D: A Semi-Automatic Tool for 2D Analysis of Discontinuities for Rock Mass Characterization. *Remote Sensing* **2021b**, *13*, 5086.
- Lollino, P.; Andriani, G.F. Role of Brittle Behaviour of Soft Calcarenes Under Low Confinement: Laboratory Observations and Numerical Investigation. *Rock Mechanics and Rock Engineering* **2017** 50:7 2017, 50, 1863–1882.
- Lollino, P.; Martimucci, V.; Parise, M. Geological Survey and Numerical Modeling of the Potential Failure Mechanisms of Underground Caves. *Geosystem Engineering* **2013**, *16* (1), 100–112.
- Londe, P.; Vigier, G.; Vormeringer, R. Stability of Rock Slopes, A Three-Dimensional Study. *Journal of the Soil Mechanics and Foundations Division* **1969**, *95*, 235–262.
- Long, J.C.S.; Remer, J.S.; Wilson, C.R.; Witherspoon, P.A. Porous Media Equivalents for Networks of Discontinuous Fractures. *Water resources research* **1982**, *18*, 645–658.
- Lorig, L.; Varona, P. Numerical Analysis. In *Rock Slope Engineering: Fourth Edition*; CRC Press, **2004**; pp. 218–244 ISBN 9781482265125.
- Lowe, D.G. Distinctive Image Features from Scale-Invariant Keypoints. *International Journal of Computer Vision* **2004** 60:2 2004, 60, 91–110.
- Loye, A.; Jaboyedoff, M.; Isaac Theule, J.; Liébault, F. Headwater Sediment Dynamics in a Debris Flow Catchment Constrained by High-Resolution Topographic Surveys. *Earth Surface Dynamics* **2016**, *4*, 489–513.
- Loye, A.; Pedrazzini, A.; Theule, J.I.; Jaboyedoff, M.; Liébault, F.; Metzger, R. Influence of Bedrock Structures on the Spatial Pattern of Erosional Landforms in Small Alpine Catchments. *Earth Surface Processes and Landforms* **2012**, *37*, 1407–1423.
- Lucieer, A.; De Jong, S.M.; Turner, D. Mapping Landslide Displacements Using Structure from Motion (SfM) and Image Correlation of Multi-Temporal UAV Photography. *Progress in physical geography*, **2014**, *38*.1: 97–116.
- Mah, J.; Samson, C.; McKinnon, S.D. 3D Laser Imaging for Joint Orientation Analysis. *International Journal of Rock Mechanics and Mining Sciences* **2011**, *48*, 932–941.
- Mahtab, M.A.; Yegulalp, T.M. Similarity Test For Grouping Orientation Data In Rock Mechanics. In *The 25th US Symposium on Rock Mechanics (USRMS)*, **1984**.
- Mancini, F.; Castagnetti, C.; Rossi, P.; Dubbini, M.; Fazio, N.L.; Perrotti, M.; Lollino, P. An Integrated Procedure to Assess the Stability of Coastal Rocky Cliffs: From UAV Close-Range Photogrammetry to Geomechanical Finite Element Modeling. *Remote Sensing* **2017**, *9*, 1235.
- Maracchione, M.I.; Mastronuzzi, G.; Sansò, P.; Sergio, A.; Walsh, N. Approccio Semi-Quantitativo Alla Dinamica Delle Coste Rocciose: L'area Campione Fra Monopoli e Mola Di Bari (Puglia Adriatica). *Studi costieri* **2001**, *4*, 4–17.
- Marinos, P. V. New Proposed GSI Classification Charts for Weak or Complex Rock Masses. *Bulletin of the Geological Society of Greece* **2017**, *43*, 1248.
- Marinos, P.; Hoek, E. GSI-A Geologically Friendly Tool for Rock Mass Strength Estimation. In *Proceedings of the International Conference on Geotechnical and Geological Engineering (GeoEng2000)*, Melbourne, Australia, 19–24 November **2000**; pp. 1422–1446.
- Marinos, V. New proposed GSI classification charts for weak or complex rock masses. *Bull. Geol. Soc. Greece* **2017**, *43*, 1248.
- Markland, J.T. A Useful Technique For Estimating the Stability of Rock Slopes When the Rigid Wedge Slide Type of Failure Is Expected; Rock mechanics research report; Imperial College of Science & Technology, **1972**.
- Marmoni, G.M.; Fiorucci, M.; Grechi, G.; Martino, S. Modelling of Thermo-Mechanical Effects in a Rock Quarry Wall Induced by near-Surface Temperature Fluctuations. *International Journal of Rock Mechanics and Mining Sciences* **2020**, *134*, 104440.

- Martin, D.C. Deformation of Open Pit Mine Slopes by Deep Seated Toppling. *International Journal of Surface Mining, Reclamation and Environment*, **1990**, 4.4: 153-164.
- Martino, S.; Mazzanti, P. Integrating Geomechanical Surveys and Remote Sensing for Sea Cliff Slope Stability Analysis: The Mt. Pucci Case Study (Italy). *Nat. Hazards Earth Syst. Sci.* **2014**, 14, 831–848.
- Martinotti, M.E, Pisano, L., Marchesini, I., Rossi, M., Peruccacci, S., Brunetti M.T., Melillo, M., Amoruso, G., Loiacono, P., Vennari, C., Vessia, G., Trabace, M., Parise, M., Guzzetti, F. Landslides, Floods and Sinkholes in a Karst Environment: The 1-6 September 2014 Gargano Event, Southern Italy. *Natural Hazards and Earth System Sciences* **2017**, 17, 467–480.
- Mas Ivars, D.; Pierce, M.E.; Darcel, C.; Reyes-Montes, J.; Potyondy, D.O.; Paul Young, R.; Cundall, P.A. The Synthetic Rock Mass Approach for Jointed Rock Mass Modelling. *International Journal of Rock Mechanics and Mining Sciences* **2011**, 48, 219–244.
- Mastronuzzi, G.; Sansò, P. Pleistocene Sea-Level Changes, Sapping Processes and Development of Valley Networks in the Apulia Region (Southern Italy). *Geomorphology* **2002**, 46, 19–34.
- Matasci, B.; Carrea, D.; Jaboyedoff, M.; Pedrazzini, A.; Stock, G.; Oppikofer, T. Structural Characterization of Rockfall Sources in Yosemite Valley from Remote Sensing Data: Toward More Accurate Susceptibility Assessment; In: Proceedings of the 14th ISSMGE Pan-American conference. **2011**.
- Matasci, B.; Stock, G.M.; Jaboyedoff, M.; Carrea, D.; Collins, B.D.; Guérin, A.; Matasci, G.; Ravelin, L. Assessing Rockfall Susceptibility in Steep and Overhanging Slopes Using Three-Dimensional Analysis of Failure Mechanisms. *Landslides* **2018**, 15, 859–878.
- Matsui, T.; San, K.-C. Finite Element Slope Stability Analysis by Shear Strength Reduction Technique. *Soils and Foundations* **1992**, 32, 59–70.
- Matsuoka, N.; Sakai, H. Rockfall Activity from an Alpine Cliff during Thawing Periods. *Geomorphology* **1999**, 28.
- Matthews, N. A. Aerial and Close-Range Photogrammetric Technology. Technical Note 428 **2008**, 42.
- Mauldon, M. Estimating Mean Fracture Trace Length and Density from Observations in Convex Windows. *Rock Mechanics and Rock Engineering* **1998** 31:4 1998, 31, 201–216.
- Mauldon, M.; Dershowitz, W.S. A Multi-Dimensional System of Fracture Abundance Measures. *Geological Society of America Abstracts with Programs* **2000**, 3, A474.
- Mauldon, M.; Dunne, W.M.; Rohrbaugh, M.B. Circular Scanlines and Circular Windows: New Tools for Characterizing the Geometry of Fracture Traces. *Journal of Structural Geology* **2001**, 23, 247–258.
- Mavrouli, O.; Corominas, J.; Jaboyedoff, M. Size distribution for potentially unstable rock masses and in situ rock blocks using LIDAR-generated digital elevation models. *Rock mechanics and rock engineering*, **2015**, 48.4: 1589-1604.
- Menegoni, N.; Giordan, D.; Perotti, C. An Open-Source Algorithm for 3D ROck Slope Kinematic Analysis (ROKA). *Applied Sciences* **2021**, 11, 1698.
- Merrien-Soukatchoff, V.; Korini, T.; Thoraval, A. Use of an Integrated Discrete Fracture Network Code for Stochastic Stability Analyses of Fractured Rock Masses. *Rock Mechanics and Rock Engineering* **2012**, 45, 159–181.
- Michoud, C.; Derron, M.-H.; Horton, P.; Jaboyedoff, M.; Baillifard, F.-J.; Alexandre, L.; Nicolet, P.; Pedrazzini, A.; Queyrel, A. Rockfall Hazard and Risk Assessments along Roads at a Regional Scale: Example in Swiss Alps. *Natural hazards and earth system sciences* **2012**, 12, 615–629.
- Mikhail, E.M.; Bethel, J.S.; McGlone, J.C. Introduction to Modern Photogrammetry. New York **2001**, 19.
- Milanovic, P. The Environmental Impacts of Human Activities and Engineering Constructions in Karst Regions. *Episodes* **2002**, 25, 13–21.
- Miller, S.M. A Statistical Method to Evaluate Homogeneity of Structural Populations. *Journal of the International Association for Mathematical Geology* **1983** 15:2, 15, 317–328.
- Mindszenty, A.; D’Argenio, B.; Aiello, G. Lithospheric Bulges Recorded by Regional Unconformities. The Case of Mesozoic-Tertiary Apulia. *Tectonophysics* **1995**, 252, 137–161.

- Mineo, S.; Calcaterra, D.; Zampelli, S.P.; Pappalardo, G. Application of Infrared Thermography for the Survey of Intensely Jointed Rock Slopes. *Rendiconti Online Società Geologica Italiana* **2015a**, *35*, 212–215.
- Mineo, S.; Caliò, D.; Pappalardo, G. UAV-based photogrammetry and infrared thermography applied to rock mass survey for geomechanical purposes. *Remote Sens.* **2022**, *14*, 473.
- Mineo, S.; Pappalardo, G. InfraRed Thermography Presented as an Innovative and Non-Destructive Solution to Quantify Rock Porosity in Laboratory. *International Journal of Rock Mechanics and Mining Sciences* **2019**, *115*, 99–110.
- Mineo, S.; Pappalardo, G. Rock emissivity measurement for infrared thermography engineering geological applications. *Appl. Sci.* **2021**, *11*, 3773.
- Mineo, S.; Pappalardo, G.; Rapisarda, F.; Cubito, A.; di Maria, G. Integrated geostructural, seismic and infrared thermography surveys for the study of an unstable rock slope in the Peloritani Chain (NE Sicily). *Eng. Geol.* **2015b**, *195*, 225–235.
- Miroshnikova, L.S. Engineering-Geologic Models as an Effective Method of Schematization of Rock Masses for Purposes of Hydrotechnical Construction. *Hydrotech. Constr.* **1999**, *33*, 603–612.
- Modest, M.F. Radiative Heat Transfer. Radiative Heat Transfer. Elsevier, **2013**.
- Mohtarami, E.; Jafari, A.; Amini, M. Stability Analysis of Slopes against Combined Circular–Toppling Failure. *International Journal of Rock Mechanics and Mining Sciences* **2014**, *67*, 43–56.
- Monchau, J.-P. Mesure d'émissivité Pour La Thermographie Infrarouge Appliquée Au Diagnostic Quantitatif Des Structures. **2013**. PhD Thesis. Paris Est.
- Mongillo, M.A.; Wood, C.P.; Mongillo, M.A.; Wood, C.P. Thermal Infrared Mapping of White Island Volcano, New Zealand. *JVGR* **1995**, *69*, 59–71.
- Monserrat, O.; Crosetto, M. Deformation Measurement Using Terrestrial Laser Scanning Data and Least Squares 3-D Surface Matching. *ISPRS Journal of Photogrammetry and Remote Sensing* **2008**, *63*, 142–154.
- Montiel, E.; Varona, P.; Fernandez, C.; Espinoza, Z. Use of Discrete Fracture Networks in 3D Numerical Modelling for Stability Analysis in Open Pits. In Proceedings of the *2020 International Symposium on Slope Stability in Open Pit Mining and Civil Engineering*; Australian Centre for Geomechanics, Perth, May 12 **2020**; pp. 913–926.
- Morgenstern, N.R.; Price, V.E. The Analysis of the Stability of General Slip Surfaces. *Geotechnique* **1965**, *15*, 79–93.
- Mossa, M. The Floods in Bari: What History Should Have Taught. *Journal of Hydraulic Research* **2007**, *45*, 579–594.
- Moxham, R.M.; Crandell, D.R.; Marlatt, W. Thermal Features at Mount Rainier, Washington, as Revealed by Infrared Surveys. US Geological Survey Professional Paper, **1965**, 93-100.
- Munjiza, A.; John, N. Mesh Size Sensitivity of the Combined FEM/DEM Fracture and Fragmentation Algorithms. *Engineering Fracture Mechanics - ENG FRACTURE MECH* **2002**, *69*, 281–295.
- Munjiza, A.; Owen, D.R.J.; Bicanic, N. A Combined Finite-discrete Element Method in Transient Dynamics of Fracturing Solids. *Engineering Computations* **1995**, *12*, 145–174.
- Neumann, A.C. Biological Erosion of Limestone Coasts. In *Geomorphology. Encyclopedia of Earth Science.*; Springer Berlin Heidelberg: Berlin, Heidelberg, **1997**; pp. 75–81 ISBN 978-3-540-31060-0.
- Nikolic, M.; roje-Bonacci, T.; Ibrahimbegovic, A. Overview of the Numerical Methods for the Modelling of Rock Mechanics Problems. *Tehnicki Vjesnik-technical Gazette* **2016**, *23*, 627–637.
- Odling, N.E.; Gillespie, P.; Bourguine, B.; Castaing, C.; Chiles, J.P.; Christensen, N.P.; Fillion, E.; Genter, A.; Olsen, C.; Thrane, L.; et al. Variations in Fracture System Geometry and Their Implications for Fluid Flow in Fractures Hydrocarbon Reservoirs. *Petroleum Geoscience* **1999**, *5*, 373–384, doi:10.1144/petgeo.5.4.373.
- Ohnishi, Y.; Nishiyama, S.; Yano, T.; Matsuyama, H.; Amano, K. A Study of the Application of Digital Photogrammetry to Slope Monitoring Systems. *International Journal of Rock Mechanics and Mining Sciences* **2006**, *43*, 756–766.

- Okay, U.; Telling, J.; Glennie, C.; Dietrich, W. Airborne Lidar Change Detection: An Overview of Earth Sciences Applications. *Earth-Science Reviews* **2019**, *198*, 102929.
- Olariu, M.I.; Ferguson, J.F.; Aiken, C.L.V.; Xu, X. Outcrop Fracture Characterization Using Terrestrial Laser Scanners: Deep-Water Jackfork Sandstone at Big Rock Quarry, Arkansas. *Geosphere* **2008**, *4*, 247–259.
- Olsen, M.J.; Wartman, J.; McAlister, M.; Mahmoudabadi, H.; O'Banion, M.S.; Dunham, L.; Cunningham, K. To Fill or Not to Fill: Sensitivity Analysis of the Influence of Resolution and Hole Filling on Point Cloud Surface Modeling and Individual Rockfall Event Detection. *Remote Sensing* **2015**, Vol. 7, Pages 12103-12134.
- Oppikofer, T. Detection, Analysis and Monitoring of Slope Movements by High-Resolution Digital Elevation Models. PhD Thesis. Université de Lausanne, Faculté des géosciences et de l'environnement, **2013**.
- Oppikofer, T.; Bunkholt, H.S.S.; Fischer, L.; Saintot, A.; Hermanns, R.L.; Longchamp, C.; Derron, M.-H.; Jaboyedoff, M. Investigation and Monitoring of Rock Slope Instabilities in Norway by Terrestrial Laser Scanning. Taylor Francis Group, London, **2012**, 1235-1241.
- Oppikofer, T.; Jaboyedoff, M.; Blikra, L.; Derron, M.H.; Metzger, R. Characterization and Monitoring of the Åknes Rockslide Using Terrestrial Laser Scanning. *Natural Hazards and Earth System Science* **2009**, *9*, 1003–1019.
- Oppikofer, T.; Jaboyedoff, M.; Keusen, H.-R. Collapse at the Eastern Eiger Flank in the Swiss Alps. *Nature Geoscience* **2008** *1*:8, *1*, 531–535.
- Oppikofer, T.; Jaboyedoff, M.; Pedrazzini, A.; Derron, M.H.; Blikra, L.H. Detailed DEM Analysis of a Rockslide Scar to Characterize the Basal Sliding Surface of Active Rockslides. *Journal of Geophysical Research: Earth Surface* **2011**, *116*, 2016.
- Optech ILRIS-3-D Intelligent Laser Ranging and Imaging System from Optech. Available at <http://www.optech.ca/IL3-Dprodline-Ilr3-Dhtm> 2009.
- Pagano, M.; Palma, B.; Ruocco, A.; Parise, M. Discontinuity Characterization of Rock Masses through Terrestrial Laser Scanner and Unmanned Aerial Vehicle Techniques Aimed at Slope Stability Assessment. *Applied Sciences (Switzerland)* **2020**, *10*, 2960.
- Pahl, P.J. Estimating the Mean Length of Discontinuity Traces. *International Journal of Rock Mechanics and Mining Sciences & Geomechanics Abstracts* **1981**, *18*, 221–228.
- Palma, B.; Parise, M.; Ruocco, A. Geo-Mechanical Characterization of Carbonate Rock Masses by Means of Laser Scanner Technique. *IOP Conference Series: Earth and Environmental Science* **2017**, *95*, 062007.
- Palmer, A.N. Cave geology and speleogenesis over the past 65 years: Role of the National Speleological Society in advancing the science. *J. Cave Karst Stud.* **2017**, *69*, 3–12.
- Palmstrøm, A. Characterizing Rock Masses by the RMI for Use in Practical Rock Engineering: Part 1: The Development of the Rock Mass Index (RMI). *Tunnelling and Underground Space Technology* **1996b**, *11*, 175–188.
- Palmstrøm, A. Measurement and Characterization of Rock Mass Jointing. In *In situ characterization of rocks*; AA Bøllkema publishers, **2001**; pp. 49–97.
- Palmstrøm, A. Rmi - A System for Characterizing Rock Mass Strength for Use in Rock Engineering. *Journal of Rock Mechanics and Tunnelling Technology* **1996a**, *1*, 69–108.
- Pappalardo, G.; Mineo, S. Study of Jointed and Weathered Rock Slopes Through the Innovative Approach of InfraRed Thermography. *Landslides: Theory, Practice and Modelling*, **2019**, 85-103.
- Pappalardo, G.; Mineo, S.; Angrisani, A.C.; Di Martire, D.; Calcaterra, D. Combining field data with infrared thermography and DInSAR surveys to evaluate the activity of landslides: The case study of Randazzo Landslide (NE Sicily). *Landslides* **2018**, *15*, 2173–2193.
- Pappalardo, G.; Mineo, S.; Imposa, S.; Grassi, S.; Leotta, A.; la Rosa, F.; Salerno, D. A quick combined approach for the characterization of a cliff during a post-rockfall emergency. *Landslides* **2020**, *17*, 1063–1081.
- Pappalardo, G.; Mineo, S.; Zampelli, S.P.; Cubito, A.; Calcaterra, D. InfraRed Thermography Proposed for the Estimation of the Cooling Rate Index in the Remote Survey of Rock Masses. *International Journal of Rock Mechanics and Mining Sciences* **2016**, *83*, 182–196.

- Parise, M. A Procedure for Evaluating the Susceptibility to Natural and Anthropogenic Sinkholes. *Georisk: Assessment and Management of Risk for Engineered Systems and Geohazards* **2015**, 9(4), 272–285.
- Parise, M. Flood History in the Karst Environment of Castellana-Grotte (Apulia, Southern Italy). *Natural Hazards and Earth System Science* **2003**, 3, 593–604.
- Parise, M. Geomorphology of the Canale Di Pirro Karst Polje (Apulia, Southern Italy). *Z. Fur Geomorphol.* **2006**, 147, 143–158.
- Parise, M. Hazards in karst. In: Bonacci O. (Ed.), Proceedings International Interdisciplinary Scientific Conference “Sustainability of the karst environment. Dinaric karst and other karst regions”, Plitvice Lakes (Croatia), 23–26 September 2009, IHP-UNESCO, Series on Groundwater **2010**, no. 2, p. 155–162.
- Parise, M. Surface and Subsurface Karst Geomorphology in the Murge (Apulia, Southern Italy). Surface and subsurface karst geomorphology in the Murge (Apulia, southern Italy). *Acta Carsologica* **2011**, 40, 79–93.
- Parise, M., Federico, A., Delle Rose, M., Sammarco, M. Karst terminology in Apulia (southern Italy). *Acta Carsologica* **2003**, 32 (2), 65–82.
- Parise, M.; Benedetto, L.; Chieco, M.; Fiore, A.; Lacarbonara, M.; Liso, I.; Masciopinto, C.; Pisano, L.; Riccio, A.; Vurro, M. First Outcomes of a Project Dedicated to Monitoring Groundwater Resources in Apulia, Southern Italy. In: Bertrand C., Denimal S., Steinmann M., Renard P. (eds) *Eurokarst* **2018**, Besançon. Advances in Karst Science. Springer, Cham.
- Parise, M.; Closson, D.; Gutiérrez, F.; Stevanović, Z. Anticipating and Managing Engineering Problems in the Complex Karst Environment. *Environ. Earth Sci.* **2015a**, 74, 7823–7835.
- Parise, M.; De Pasquale, P.; Martimucci, V.; Meuli, V.; Pentimone, N.; Pepe, P. Grotta Della Rondinella a Polignano a Mare: Un Progetto Di Ricerca Della Federazione Speleologica Pugliese. In Proceedings of the Atti del XXI Congresso Nazionale di Speleologia “Diffusione delle conoscenze”; EUT Edizioni Università di Trieste, **2013**; pp. 437–448.
- Parise, M.; Ravbar, N.N.; Živanović, V.; Mikszewski, A.; Kresic, N.; Mádl-Szo”nyi, J.; Kukuric, N.; Kukuric, N. Hazards in Karst and Managing Water Resources Quality. In *Karst Aquifers—Characterization and Engineering; Professional Practice in Earth Sciences; Stevanović, Z., Ed.; Springer: Cham, Switzerland*, **2015b**.
- Patton, F.D. Multiple Modes of Shear Failure In *Rock*. *1st ISRM Congress*, Lisbon, Portugal, September **1966**.
- Pedrazzini, A.; Oppikofer, T.; Jaboyedoff, M.; Güell i Pons, M.; Chantry, R.; Stampfli, E. Assessment of Rockslide and Rockfall Problems in an Active Quarry: Case Study of the Arvel Quarry (Western Switzerland); **2010**; ISBN 9780415586542.
- Pesci, A.; Teza, G.; Bonali, E. Terrestrial Laser Scanner Resolution: Numerical Simulations and Experiments on Spatial Sampling Optimization. *Remote Sensing* **2011**, Vol. 3, Pages 167–184 2011, 3, 167–184.
- Petrie, G.; Toth, C.K. Introduction to Laser Ranging, Profiling, and Scanning. In *Topographic laser ranging and scanning*; CRC Press, **2018**; pp. 1–28.
- Phillips, F.C. The Use of Stereographic Projection in Structural Geology. *Soil Science* **1955**, 79.
- Pieri, P.; Festa, V.; Moretti, M.; Tropeano, M. Quaternary Tectonic Activity of the Murge Area (Apulian Foreland -Southern Italy). *Annals of Geophysics* **1997**, 40.
- Pieri, P.; Sabato, L.; Spalluto, L.; Tropeano, M. Note Illustrative Della Carta Geologica d’Italia Alla Scala 1:50.000 Foglio 438 - BARI; **2012**; ISBN 2035-8008.
- Pilkey, O.H.; Davis, T.W. An Analysis of Coastal Recession Models: North Carolina Coast. In *Sea-Level Fluctuations and Coastal Evolution; SEPM (Society for Sedimentary Geology)*, **1987**; pp. 59–68.
- Piteau, D.R. Characterizing and Extrapolating Rock Joint Properties in Engineering Practice. In: *Geomechanics—Progress in Theory and Its Effects on Practice*. Springer, Vienna, 1973. p. 5–31.
- Pix4DMapper Pix4D SA 2017. Software available online: <https://www.pix4d.com/download-software>.
- Pollyea, R.M.; Fairley, J.P. Estimating Surface Roughness of Terrestrial Laser Scan Data Using Orthogonal Distance Regression. *Geology* **2011**, 39, 623–626.
- Prendes-Gero, M.-B.; Suárez-Domínguez, F.J.; González-Nicieza, C.; Álvarez-Fernández, M.I. Infrared thermography methodology applied to detect localized rockfalls in self-supporting underground mines. In

References

- Proceedings of the EUROCK 2013—The 2013 ISRM International Symposium—Rock Mechanics for Resources, Energy, and Environment, Wroclaw, Poland, 23–26 September 2013.
- Price, D.G. Weathering and Weathering Processes. *Quarterly Journal of Engineering Geology and Hydrogeology* **1995**, *28*, 243–252.
- Price, N.J. Fault and Joint Development: In Brittle and Semi-Brittle Rock; Elsevier, **2016**.
- Priest, S.D. Discontinuity Analysis for Rock Engineering; Chapman & Hall: London, UK, **1993**.
- Priest, S.D.; Hudson, J.A. Discontinuity Spacings in Rock. *International Journal of Rock Mechanics and Mining Sciences & Geomechanics Abstracts* **1976**, *13*, 135–148.
- Priest, S.D.; Hudson, J.A. Estimation of Discontinuity Spacing and Trace Length Using Scanline Surveys. *International Journal of Rock Mechanics and Mining Sciences & Geomechanics Abstracts* **1981**, *18*, 183–197.
- Pringle, J.K.; Howell, J.A.; Hodgetts, D.; Westerman, A.R.; Hodgson, D.M. *Virtual Outcrop Models of Petroleum Reservoir Analogues: A Review of the Current State-of-the-Art*. *First Break* **2006**, *24*, 33–42.
- Prokop, A.; Panholzer, H. Assessing the Capability of Terrestrial Laser Scanning for Monitoring Slow Moving Landslides. *Natural Hazards and Earth System Science* **2009**, *9*, 1921–1928.
- Rabatel, A.; Deline, P.; Jaillet, S.; Ravel, L. Rock Falls in High-Alpine Rock Walls Quantified by Terrestrial Lidar Measurements: A Case Study in the Mont Blanc Area. *Geophysical Research Letters* **2008**, *35*.
- Radbruch-Hall, D.H.; Varnes, D.J.; Savage, W.Z. Gravitational Spreading of Steep-Sided Ridges (“Sackung”) in Western United States. *Bulletin of the International Association of Engineering Geology* **1976**, *13*, 23–35.
- Read, John.; Stacey, P. Guidelines for Open Pit Slope Design. **2009**. CRC Press, 510 pages.
- Rees, W.G. Physical Principles of Remote Sensing. **2012**, Cambridge University Press.
- Remondino, F.; El-Hakim, S. Image-Based 3-D Modelling: A Review. *The photogrammetric record* **2006**, *21*, 269–291.
- Rengers, N. Influence of Surface Roughness on The Friction Properties of Rock Planes. *International Society of Rock Mechanics, Proceedings* **1970**, *1*.
- Reshetyuk, Y. Self-Calibration and Direct Georeferencing in Terrestrial Laser Scanning. PhD Thesis. KTH, **2009**.
- Ricchetti, G. Contributo Alla Conoscenza Strutturale Della Fossa Bradanica e Delle Murge. *Bollettino Società Geologica Italiana*, **1980**, *99*(4), 421-430.
- Ricchetti, G.; Ciaranfi, N.; Luperto-Sinni, E.; Mongelli, F.; Pieri, P. Geodinamica Ed Evoluzione Sedimentaria e Tettonica Dell'avampaese Apulo. *Mem. Soc. Geol. It.* **1988**, *41*, 57–82.
- Ricchetti, G.; Mongelli, F. Flessione e Campo Gravimetrico Della Micropiastra Apula. *Italian Journal of Geosciences* **1980**, *99*, 431–436.
- RIEGL. RIEGLVZ-400 Terrestrial Laser Scanner, Summary Specification Sheets. 2017. Available online: http://www.riegl.com/uploads/Tx_pxriegl/downloads/10_DataSheet_VZ-400_2017-06-14.Pdf 2017 (accessed on 11 April 2021).
- Rinker, J.N. Airborne Infrared Thermal Detection of Caves and Crevasses. *Photogrammetric Engineering and Remote Sensing* **1975**, *41*, 1391–1400.
- Riquelme, A.; Cano, M.; Tomás, R.; Abellán, A. Identification of Rock Slope Discontinuity Sets from Laser Scanner and Photogrammetric Point Clouds: A Comparative Analysis. *Procedia Engineering* **2017**, *191*, 838–845.
- Riquelme, A.; Tomás, R.; Cano, M.; Pastor, J.L.; Abellán, A. Automatic Mapping of Discontinuity Persistence on Rock Masses Using 3-D Point Clouds. *Rock Mech. Rock Eng.* **2018**, *51*, 3005–3028.
- Riquelme, A.; Tomás, R.; Cano, M.; Pastor, J.L.; Abellán, A. Automatic Mapping of Discontinuity Persistence on Rock Masses Using 3D Point Clouds. *Rock Mechanics and Rock Engineering* **2018**, *51*, 3005–3028.
- Riquelme, A.J.; Abellán, A.; Tomás, R. Discontinuity Spacing Analysis in Rock Masses Using 3-D Point Clouds. *Eng. Geol.* **2015**, *195*, 185–195.

- Riquelme, A.J.; Abellán, A.; Tomás, R.; Jaboyedoff, M. A New Approach for Semi-Automatic Rock Mass Joints Recognition from 3D Point Clouds. *Computers and Geosciences* **2014**, *68*, 38–52.
- Riquelme, A.J.; Tomás, R.; Abellán, A. Characterization of Rock Slopes through Slope Mass Rating Using 3-D Point Clouds. *Int. J. Rock Mech. Min. Sci.* **2016**, *84*, 165–176.
- Rives, T.; Razack, M.; Petit, J.P.; Rawnsley, K.D. Joint Spacing: Analogue and Numerical Simulations. *Journal of Structural Geology* **1992**, *14*, 925–937.
- Robertson, E.C. Thermal Properties of Rocks. US Department of the Interior: Geological Survey **1988**, 88–441.
- Rocscience 2021a. RS2 (11.012). Available at: <https://www.rocscience.com/software/rs2>.
- Rocscience 2021b. RS3 User Guide. Available at: www.rocscience.com.
- Rocscience 2021c. RS3 - Version 4.020. Available at: <https://www.rocscience.com/software/rs3>
- Rocscience 2021d. Slide3 Version 3.016. <https://www.rocscience.com/software/slide3>.
- Rocscience 2021e. RocPlane (Version 4.009). Available at: <https://www.rocscience.com/software/roplane>.
- Rocscience 2021f. Swedge (Version 7.014). <https://www.rocscience.com/software/swedge>.
- Rocscience 2021g. Dips - version 8.015. Available at: <https://www.rocscience.com/software/dips>.
- Rodriguez, A.; Laio, A. Clustering by Fast Search and Find of Density Peaks. *Science* **2014**, *344*, 1492–1496.
- Romana, M. New Adjustment Ratings for Application of Bieniawski Classification to Slopes. In Proceedings of the *International Symposium on the Role of Rock Mechanics, International Society for Rock Mechanics*; Zacatecas, Mexico, **1985**; pp. 49–53.
- Roncella, R.; Re, C.; Forlani, G. Performance Evaluation of a Structure and Motion Strategy in Architecture and Cultural Heritage. *Int. Archives of Photogrammetry, Remote Sensing and Spatial Information Sciences* **2011**, *38*.
- Rosen, P.S. Erosion Susceptibility of the Virginia Chesapeake Bay Shoreline. *Mar. Geol.* **1980**, *34*, 45–59.
- Rosnell, T.; Honkavaara, E. Point Cloud Generation from Aerial Image Data Acquired by a Quadcopter Type Micro Unmanned Aerial Vehicle and a Digital Still Camera. *Sensors* **2012**, *12*, 453–480. [PubMed](#)
- Rosser, N.J.; Petley, D.N.; Lim, M.; Dunning, S.A.; Allison, R.J. Terrestrial Laser Scanning for Monitoring the Process of Hard Rock Coastal Cliff Erosion. *Q. J. Eng. Geol. Hydrogeol.* **2005**, *38*, 363–375.
- Roy, A.; Perfect, E.; Dunne, W.M.; Odling, N.; Kim, J.-W. Lacunarity Analysis of Fracture Networks: Evidence for Scale-Dependent Clustering. *Journal of Structural Geology* **2010**, *32*, 1444–1449.
- Royán, M.J.; Abellán, A.; Jaboyedoff, M.; Vilaplana, J.; Calvet, J. Spatio-Temporal Analysis of Rockfall Pre-Failure Deformation Using Terrestrial LiDAR. *Landslides* **2013**, *11*, 1–13.
- Rudnicki, J. Origin of the Collapse-Solution Breccia and Its Importance in Phreatic System of Karst Circulation. *Boll. Sc. Polon. Sc.* **1973**, *21*, 225–232.
- Rudnicki, J. Origin of the Collapse-Solution Breccia and Its Importance in Phreatic System of Karst Circulation. *Bull. Acad. Polon. Sci.* **1973**, *21*, 225–232.
- Rudnicki, J. Processi Carsici Sotterranei in Area Costiera (in Base All'esempio Della Puglia, Italia Meridionale). *Grotte e Dintorni* **2003**, *5*, 5–34.
- Ruggles, S.; Clark, J.; Franke, K.W.; Wolfe, D.; Reimschuessel, B.; Martin, R.A.; Okeson, T.J.; Hedengren, J.D. Comparison of Sfm Computer Vision Point Clouds of a Landslide Derived from Multiple Small Uav Platforms and Sensors to a Tls-Based Model. *J. Unmanned Veh. Syst.* **2016**, *4*, 246–265.
- Runqiu, H.; Xiujun, D. Application of Three-Dimensional Laser Scanning and Surveying in Geological Investigation of High Rock Slope. *Journal of China University of Geosciences* **2008**, *19*, 184–190.
- Sagaseta, C. On the Modes of Instability of a Rigid Block on an Inclined Plane. *Rock Mechanics and Rock Engineering* **1986** *19*:4 1986, *19*, 261–266.
- Salvini, R.; Francioni, M. Geomatics for Slope Stability and Rock Fall Runout Analysis: A Case Study along the Alta Tambura Road in the Apuan Alps (Tuscany, Italy). *Italian Journal of Engineering Geology and Environment*, **2013**, 481–492.

References

- Salvini, R.; Francioni, M.; Riccucci, S.; Bonciani, F.; Callegari, I. Photogrammetry and Laser Scanning for Analyzing Slope Stability and Rock Fall Runout along the Domodossola-Iselle Railway, the Italian Alps. *Geomorphology* **2013**, *185*, 110–122.
- Salvini, R.; Mastrorocco, G.; Seddaiu, M.; Rossi, D.; Vanneschi, C. The Use of an Unmanned Aerial Vehicle for Fracture Mapping within a Marble Quarry (Carrara, Italy): Photogrammetry and Discrete Fracture Network Modelling. *Geomatics, Natural Hazards and Risk* **2017**, *8*, 34–52.
- Santo, A.; M., D.; di Crescenzo, G.; Ramondini, M.; A, S. Use of Unmanned Aerial Vehicles (UAVs) for Photogrammetric Surveys in Rockfall Instability Studies. *rendiconti on line società geologica italiana* **2013**, *24*.
- Sarma, S.K. Stability Analysis of Embankments and Slopes. *Géotechnique* **1973**, *23*, 423–433.
- Sartori, M.; Baillifard, F.; Jaboyedoff, M.; Rouiller, J.D. Kinematics of the 1991 Randa Rockslides (Valais, Switzerland). *Natural Hazards and Earth System Science* **2003**, *3*, 423–433.
- Sauro, U. A Polygonal Karst in Alte Murge (Puglia, Southern Italy). *Zeitschrift fur Geomorphologie* **1991**, *35*, 207–223.
- Scavia, C. A Method for the Study of Crack Propagation in Rock Structures. *Géotechnique*, **1995**, *45.3*: 447-463.
- Scholtès, L.; Donzé, F.V. Modelling Progressive Failure in Fractured Rock Masses Using a 3-D Discrete Element Method. *International Journal of Rock Mechanics and Mining Sciences* **2012**, *52*, 18–30.
- Schowengerdt, R.A. Remote sensing: models and methods for image processing. Elsevier, **2006**.
- Scrocca, D. Southern Apennines: Structural Setting and Tectonic Evolution. *Journal of the Virtual Explorer* **2010**, *36*.
- Sella, M.; Turci, C.; Riva, A. Sintesi geopetrolifera della Fossa Bradanica (Avanfossa della Catena Appenninica meridionale). *Memorie della Società Geologica Italiana*, **1988**, *41*: 87-107.
- Shanley, R.J.; Mahtab, M.A. Delineation and Analysis of Clusters in Orientation Data. *Journal of the International Association for Mathematical Geology* **1976**, *8*, 9–23.
- Shannon, H.; Sigda, J.; van Dam, R.; Hendrickx, J.; Mclemore, V. Thermal Camera Imaging of Rock Piles at the Questa Molybdenum Mine, Questa, New Mexico. 22nd American Society of Mining and Reclamation Annual National Conference June 18-25, **2005** Breckenridge, Colorado.
- Sharma, V.M.; Saxena, K.R.; Woods, R.D. Distinct Element Modelling in Geomechanics; A.A. Balkema, **1999**; ISBN 978-9054107750.
- Shashua, A. Projective Structure from Uncalibrated Images: Structure From Motion and Recognition. *Transactions on Pattern Analysis and Machine Intelligence*, **1994**, *16.8*: 778-790.
- Sitar, N.; MacLaughlin, M.M. Kinematics and Discontinuous Deformation Analysis of Landslide Movement. In Proceedings of the *2nd Panamerican Symp. on Landslides*, Rio de Janeiro; **1997**.
- Sjöberg, J. Large Scale Slope Stability in Open Pit Mining: A Review. Technical report / Luleå University of Technology; **1996**:10.
- Slob, S.; Hack, H.R.G.K.; Feng, Q.; Roshoff, K.; Turner, A.K. Fracture Mapping Using 3-D Laser Scanning Techniques. In Proceedings of the *11th ISRM Congress*, Lisbon, Portugal, 9 July **2007**.
- Slob, S.; Hack, R. 3-D Terrestrial Laser Scanning as a New Field Measurement and Monitoring Technique. In *Engineering Geology for Infrastructure Planning in Europe*; Hack, R., Azzam, R., Charlier, R., Eds.; Lecture Notes in Earth Sciences; Springer: Berlin/Heidelberg, Germany, **2004**; Volume 104.
- Slob, S.; van Knapen, B.; Hack, R.; Turner, K.; Kemeny, J. Method for Automated Discontinuity Analysis of Rock Slopes with Three-Dimensional Laser Scanning. *Transp. Res. Rec. J. Transp. Res. Board* **2005**, *1913*, 187–194.
- Smith, M.W.; Carrivick, J.L.; Quincey, D.J. Structure from Motion Photogrammetry in Physical Geography. *Progress in Physical Geography*, **2016**, *40.2*: 247-275.
- Snavely, N.; Seitz, S.M.; Szeliski, R. Modeling the World from Internet Photo Collections. *International Journal of Computer Vision* **2008**, *80*, 189–210.

- Spampinato, L.; Calvari, S.; Oppenheimer, C.; Boschi, E. Volcano Surveillance Using Infrared Cameras. *Earth-Science Reviews* **2011**, *106*, 63–91.
- Spencer, E. A Method of Analysis of the Stability of Embankments Assuming Parallel Inter-Slice Forces. *Geotechnique* **1967**, *17*, 11–26.
- Spetsakis, M.; Aloimonos, J.Y. A Multi-Frame Approach to Visual Motion Perception. *International Journal of Computer Vision* **1991**, *6*, 245–255.
- Spreafico, M.C.; Francioni, M.; Cervi, F.; Stead, D.; Bitelli, G.; Ghirotti, M.; Girelli, V.A.; Lucente, C.C.; Tini, M.A.; Borgatti, L. Back Analysis of the 2014 San Leo Landslide Using Combined Terrestrial Laser Scanning and 3-D Distinct Element Modelling. *Rock Mechanics and Rock Engineering* **2016**, *49*, 2235–2251.
- Squarzone, C.; Galgaro, A.; Teza, G.; Acosta, C.A.T.; Pernito, M.A.; Bucceri, N. Terrestrial Laser Scanner and Infrared Thermography in Rock Fall Prone Slope Analysis. *Geophysical Research Abstracts* **2008**, *10*, 2008–09254.
- Stacey, T.R.; Xianbin, Y.; Armstrong, R.; Keyter, G.J. New Slope Stability Considerations for Deep Open Pit Mines. *Journal of the Southern African Institute of Mining and Metallurgy* **2003**, *103*, 373–389.
- Staub, I.; Fredriksson, A.; Outters, N. Strategy for a Rock Mechanics Site Descriptive Model. Development and testing of the theoretical approach. Swedish Nuclear Fuel and Waste Management Co., **2002**.
- Stavropoulou, M.; Exadaktylos, G.; Saratsis, G. A Combined Three-Dimensional Geological-Geostatistical-Numerical Model of Underground Excavations in Rock. *Rock Mech. Rock Eng.* **2007**, *40*, 213–243.
- Stead, D.; Coggan, J.; Eberhardt, E. Modelling of Complex Rock Slope Failure Mechanisms Using a Hybrid Finite-/Discrete-Element Code. *Landslides: evaluation and stabilization* **2004**, 1067–1072.
- Stead, D.; Donati, D.; Wolter, A.; Sturzenegger, M. Application of Remote Sensing to the Investigation of Rock Slopes: Experience Gained and Lessons Learned. *ISPRS Int. J. Geo-Inf.* **2019**, *8*, 296.
- Stead, D.; Eberhardt, E.; Coggan, J.S. Developments in the Characterization of Complex Rock Slope Deformation and Failure Using Numerical Modelling Techniques. *Engineering Geology* **2006**, *83*, 217–235.
- Stead, D.; Jaboyedoff, M.; Coggan, J. Invited Keynote Presentation and Paper, Rock Mass Characterization and Geomechanical Modelling of Landslides. *Landslide and engineering slopes* **2012**, *1*, 83–100.
- Stead, D.; Wolter, A. A Critical Review of Rock Slope Failure Mechanisms: The Importance of Structural Geology. *Journal of Structural Geology* **2015**, *74*, 1–23.
- Steidtmann, E. The Evolution of Limestone and Dolomite. *J. Geol.* **1911**, *19*, 323–345.
- Stimpson, B. A Rapid Field Method for Recording Joint Roughness Profiles. *International Journal of Rock Mechanics and Mining Sciences & Geomechanics Abstracts* **1982**, *19*, 345–346.
- Stock, G.M.; Bawden, G.W.; Green, J.K.; Hanson, E.; Downing, G.; Collins, B.D.; Bond, S.; Leslar, M. High-Resolution Three-Dimensional Imaging and Analysis of Rock Falls in Yosemite Valley, California. *Geosphere* **2011**, *7*, 573–581.
- Strecha, C.; Bronstein, A.M.; Bronstein, M.M.; Fua, P. LDAHash: Improved Matching with Smaller Descriptors. *IEEE Transactions on Pattern Analysis and Machine Intelligence* **2012**, *34*, 66–78.
- Sturzenegger, M.; Stead, D. Close-Range Terrestrial Digital Photogrammetry and Terrestrial Laser Scanning for Discontinuity Characterization on Rock Cuts. *Eng. Geol.* **2009**, *106*, 163–182.
- Sturzenegger, M.; Stead, D. Close-Range Terrestrial Digital Photogrammetry and Terrestrial Laser Scanning for Discontinuity Characterization on Rock Cuts. *Engineering Geology* **2009**, *106*, 163–182.
- Sturzenegger, M.; Stead, D.; Elmo, D. Terrestrial Remote Sensing-Based Estimation of Mean Trace Length, Trace Intensity and Block Size/Shape. *Eng. Geol.* **2011**, *119*, 96–111.
- Sunamura, T. Rocky Coast Processes: With Special Reference to the Recession of Soft Rock Cliffs. Proceedings of the Japan Academy Series B: *Physical and Biological Sciences* **2015**, *91*, 481–500.
- Sunamura, T. Rocky Coast Processes: With Special Reference to the Recession of Soft Rock Cliffs. *Proceedings of the Japan Academy Series B: Physical and Biological Sciences* **2015**, *91*, 481–500.
- Sunamura, T. The Geomorphology of Rocky Coasts; Wiley, Ed.; Chichester, UK, **1992**.

References

- Szeliski, R.; Kang, S.B. Recovering 3-D Shape and Motion from Image Streams Using Nonlinear Least Squares. *Journal of Visual Communication and Image Representation* **1994**, *5*, 10–28.
- Terranum, Coltop3-D. 2020. Software. Available online: <https://www.terranum.ch> (accessed on 20 November 2021).
- Terranum, Coltop3-D. 2020. Software. Available online: <https://www.terranum.ch> (accessed on 20 November 2021).
- Terzaghi, R.D. Sources of Error in Joint Surveys. *Geotechnique* **1965**, *15*, 287–304, doi:10.1680/geot.1965.15.3.287.
- Teza, G.; Galgaro, A.; Zaltron, N.; Genevois, R. Terrestrial Laser Scanner to detect landslide displacement fields: A new approach. *Int. J. Remote Sens.* **2007**, *28*, 3425–3446.
- Teza, G.; Marcato, G.; Castelli, E.; Galgaro, A. IRTROCK: A MATLAB Toolbox for Contactless Recognition of Surface and Shallow Weakness of a Rock Cliff by Infrared Thermography. *Computers & Geosciences* **2012**, *45*, 109–118.
- Tofani, V.; Segoni, S.; Agostini, A.; Catani, F.; Casagli, N. Technical Note: Use of Remote Sensing for Landslide Studies in Europe. *Nat. Hazards Earth Syst. Sci.* **2013**, *13*, 299–309.
- Torfs, K.; van Grieken, R. Chemical Relations between Atmospheric Aerosols, Deposition and Stone Decay Layers on Historic Buildings at the Mediterranean Coast. *Atmospheric Environment* **1997**, *31*, 2179–2192.
- Travelletti, J.; Oppikofer, T.; Delacourt, C.; Malet, J.-P.; Jaboyedoff, M. Monitoring Landslide Displacements during a Controlled Rain Experiment Using a Long-Range Terrestrial Laser Scanning (TLS). *The International Archives of the Photogrammetry, Remote Sensing and Spatial Information Sciences* **2008**, *37*.
- Trenhaile, A.S. Modeling Cohesive Clay Coast Evolution and Response to Climate Change. *Mar. Geol.* **2010**, *277*, 11–20.
- Trenhaile, A.S. *The Geomorphology of Rock Coasts; Oxford Research Studies in Geography*; Clarendon Press: Oxford, UK, **1987**; ISBN 9780198232797.
- Triggs, B.; McLauchlan, P.F.; Hartley, R.I.; Fitzgibbon, A.W. Bundle Adjustment — A Modern Synthesis. Lecture Notes in Computer Science (including subseries Lecture Notes in Artificial Intelligence and Lecture Notes in Bioinformatics) **1999**, *1883*, 298–372.
- Tropeano, M.; Sabato, L. Response of Plio-Pleistocene Mixed Bioclastic-Lithoclastic Temperate-Water Carbonate Systems to Forced Regressions: The Calcarene Di Gravina Formation, Puglia, SE Italy. *Geological Society Special Publication* **2000**, *172*, 217–243.
- Tsesarsky, M.; Hatzor, Y.H. Kinematics of Overhanging Slopes in Discontinuous Rock. *Journal of Geotechnical and Geoenvironmental Engineering* **2009**, *135*, 1122–1129,
- Tsesarsky, M.; Hatzor, Y.H. Kinematics of Overhanging Slopes in Discontinuous Rock. *Journal of Geotechnical and Geoenvironmental Engineering* **2009**, *135*, 1122–1129.
- Turner, D.; Lucieer, A.; Watson, C. An Automated Technique for Generating Georectified Mosaics from Ultra-High Resolution Unmanned Aerial Vehicle (UAV) Imagery, Based on Structure from Motion (SfM) Point Clouds. *Remote Sensing* **2012**, Vol. 4, Pages 1392-1410 2012, *4*, 1392–1410.
- Ulusay, R. *The ISRM Suggested Methods for Rock Characterization, Testing and Monitoring: 2007-2014; 2015*; ISBN 978-3-319-07712-3.
- Usamentiaga, R.; Venegas, P.; Guerediaga, J.; Vega, L.; Molleda, J.; Bulnes, F.G. Infrared Thermography for Temperature Measurement and Non-Destructive Testing. *Sensors (Switzerland)* **2014**, *14* (7), 12305–12348.
- Van Riel, S. Exploring the Use of 3-D GIS as an Analytical Tool in Archaeological Excavation Practice. Thesis in Archaeology - Lund University **2016**.
- Vanneschi, C.; Eyre, M.; Francioni, M.; Coggan, J. The Use of Remote Sensing Techniques for Monitoring and Characterization of Slope Instability. *Procedia Engineering* **2017**, *191*, 150–157.
- Vavilov, V.; Burleigh, D. *Infrared thermography and thermal nondestructive testing*. Springer, **2020**.

- Vennari, C.; Casarano, D.; Marchesini, I.; Salvati, P.; Parise, M.; Lollino, P. LAND-DeFeND 1.1 Un Geodatabase Di Eventi Geo-Idrologici per Attività Di Protezione Civile Nella Regione Puglia. In *Geologia dell'Ambiente*, suppl. n. 1/2020, ISSN 1591-5352; **2020**; pp. 156–160.
- Viero, A.; Teza, G.; Massironi, M.; Jaboyedoff, M.; Galgaro, A. Laser Scanning-Based Recognition of Rotational Movements on a Deep Seated Gravitational Instability: The Cinque Torri Case (North-Eastern Italian Alps). *Geomorphology* **2010**, *122*, 191–204.
- Villaescusa, E. A Review and Analysis of Rock Discontinuity Mapping Methods. In: Proc. *6th ANZ Conf. on Geomechanics*. **1992**. p. 274-279.
- Villarraga, C.J.; Gasc-Barbier, M.; Vaunat, J.; Darrozes, J. The Effect of Thermal Cycles on Limestone Mechanical Degradation. *International Journal of Rock Mechanics and Mining Sciences* **2018**, *109*, 115–123.
- Voegtle, T.; Schwab, I.; Landes, T. Influences of Different Materials on the Measurement of a Terrestrial Laser Scanner (TLS). Proc. of the *XXI Congress, the International Society for Photogrammetry and Remote Sensing*, ISPRS2008 **2008**, 37.
- VOG Group Lime **2021**. Virtual Outcrop Geology Group, NORCE Norwegian Research Centre. <https://virtual-outcrop.com/lime>.
- Vöge, M.; Lato, M.J.; Diederichs, M.S. Automated Rockmass Discontinuity Mapping from 3-Dimensional Surface Data. *Engineering Geology* **2013**, *164*, 155–162.
- Vyazmensky, A.; Stead, D.; Elmo, D.; Moss, A.; Vyazmensky, A.; Stead, D.; Elmo, D.; Moss, A. Numerical Analysis of Block Caving-Induced Instability in Large Open Pit Slopes: A Finite Element/Discrete Element Approach. *Rock mechanics and rock engineering*, **2010**, *43*, 21–39.
- Walkden, M.; Dickson, M. Equilibrium Erosion of Soft Rock Shores with a Shallow or Absent Beach under Increased Sea Level Rise. *Mar. Geol.* **2008**, *251*, 75–84.
- Wallis, R.F.; King, M.S. Discontinuity Spacings in a Crystalline Rock. *International Journal of Rock Mechanics and Mining Sciences & Geomechanics Abstracts* **1980**, *17*, 63–66.
- Waltham, T. The Engineering Classification of Karst with Respect to the Role and Influence of Caves. *Int. J. Speleol.* **2002**, *31*, 19–35.
- Waltham, T.; Bell, F.; Culshaw, M. Rock Failure in Collapse and Caprock Sinkholes. In *Sinkholes and Subsidence*; Springer Berlin Heidelberg, **2005**; pp. 49–84.
- Wang, Q.; Tan, Y.; Mei, Z. Computational Methods of Acquisition and Processing of 3-D Point Cloud Data for Construction Applications. *Archives of Computational Methods in Engineering* **2019** *27:2* 2019, *27*, 479–499.
- Warburton, P.M. A Stereological Interpretation of Joint Trace Data. *International Journal of Rock Mechanics and Mining Sciences & Geomechanics Abstracts* **1980**, *17*, 181–190.
- Wasantha, P.L.P.; Ranjith, P.G.; Xu, T.; Zhao, J.; Yan, Y.L. A New Parameter to Describe the Persistency of Non-Persistent Joints. *Engineering Geology* **2014**, *181*, 71–77.
- Wehr, A.; Lohr, U. Airborne Laser Scanning—an Introduction and Overview. *ISPRS Journal of Photogrammetry and Remote Sensing* **1999**, *54*, 68–82.
- Wei, L.-W.; Chen, H.; Lee, C.-F.; Huang, W.-K.; Lin, M.-L.; Chi, C.-C.; Lin, H.-H. The Mechanism of Rockfall Disaster: A Case Study from Badouzi, Keelung, in Northern Taiwan. *Engineering Geology* **2014**, *183*, 116–126.
- Westoby, M.J.; Brasington, J.; Glasser, N.F.; Hambrey, M.J.; Reynolds, J.M. “Structure-from-Motion” Photogrammetry: A Low-Cost, Effective Tool for Geoscience Applications. *Geomorphology* **2012**, *179*, 300–314.
- Wichmann, V.; Strauhai, T.; Fey, C.; Perzmaier, S. Derivation of Space-Resolved Normal Joint Spacing and in Situ Block Size Distribution Data from Terrestrial LIDAR Point Clouds in a Rugged Alpine Relief (Kühtai, Austria). *Bulletin of Engineering Geology and the Environment* **2018**, *78*, 6, 4465–4478.
- Williams, J.; Rosser, N.; Hardy, R.; Brain, M.; Afana, A. Optimising 4-D Surface Change Detection: An Approach for Capturing Rockfall Magnitude-Frequency. *Earth Surface Dynamics* **2018**, *6*, 101–119.
- Windsor, C.R. Rock Reinforcement Systems. *International journal of rock mechanics and mining sciences* **1997**, *34*, 919–951.

References

- Wolfe, W.L.; Zissis, G.J.; Environmental Research Institute of Michigan. Infrared Information and Analysis Center. United States. Office of Naval Research.; Environmental Research Institute of Michigan. The Infrared Handbook. **1985**.
- Wu, J.H.; Lin, H.M.; Lee, D.H.; Fang, S.C. Integrity assessment of rock mass behind the shotcreted slope using thermography. *Eng. Geol.* **2005**, *80*, 164–173.
- Wyllie, D.C. Foundations on Rock; 2nd ed.; Taylor & Francis: London, UK, **1999**; ISBN 9780367865757.
- Wyllie, D.C. Rock Slope Engineering: Civil Applications. 5th Edition; CRC Press LLC, **2017**.
- Xu, C.; Dowd, P. A New Computer Code for Discrete Fracture Network Modelling. *Computers & Geosciences* **2010**, *36*, 292–301.
- Xu, T.; Xu, L.; Yang, B.; Li, X.; Yao, J. Terrestrial Laser Scanning Intensity Correction by Piecewise Fitting and Overlap-Driven Adjustment. *Remote Sensing* **2017**, Vol. 9, Page 1090, 9, 1090.
- Zeza, F.; Macrì, F. Marine Aerosol and Stone Decay. *Science of The Total Environment* **1995**, *167*, 123–143.
- Zhang, L. Engineering Properties of Rocks: Second Edition. Engineering Properties of Rocks: Second Edition, Elsevier, **2016**, 1–378.
- Zhang, L.; Ding, X. Variance of Non-Parametric Rock Fracture Mean Trace Length Estimator. *International Journal of Rock Mechanics and Mining Sciences* **2010**, *47*, 1222–1228.
- Zhang, L.; Einstein, H.H. Estimating the Mean Trace Length of Rock Discontinuities. *Rock Mechanics and Rock Engineering* **1998** *31*:4, 31, 217–235.
- Zhang, W.; Wang, J.; Xu, P.; Lou, J.; Shan, B.; Wang, F.; Cao, C.; Chen, X.; Que, J. Stability Evaluation and Potential Failure Process of Rock Slopes Characterized by Non-Persistent Fractures. *Natural Hazards and Earth System Sciences* **2020**, *20*, 2921–2935.
- Zhang, W.; Zhao, Q.; Chen, J.; Huang, R.; Yuan, X. Determining the Critical Slip Surface of a Fractured Rock Slope Considering Preexisting Fractures and Statistical Methodology. *Landslides* **2017**, *14*, 1253–1263.
- Zhu, F.; Stephansson, O.; Wang, Y. Stability Investigation and Reinforcement for Slope at Daye Open Pit Mine, China. In Proceedings of the *ISRM International Symposium-EUROCK 96*; **1996**.
- Zienkiewicz, O.C.; Humpheson, C.; Lewis, R.W. Associated and Non-Associated Visco-Plasticity and Plasticity in Soil Mechanics. *Geotechnique* **1975**, *25*, 671–689.

Publication list

Articles on international journals

- Loiotine L.**, Andriani G. F., Derron, M.-H., Parise M., Jaboyedoff M. (2022). Evaluation of InfraRed Thermography Supported by UAV and Field Surveys for Rock Mass Characterization in Complex Settings. *Geosciences*, 12(3), 116.
- Diprizio G., Andriani G.F., **Loiotine L.**, Liso I.S., Parise M. (2021). An integrated approach to elaborate 3-D geological and geotechnical models: a case study from the Daunian sub-apennine (Apulia, southern Italy). *Italian Journal of Engineering Geology and Environment*, Special Issue 2021 - AIGA - VII National Congress - Lecco 2021.
- Jaboyedoff M., Choanji T., Derron M.-H., Fei L., Gutierrez A., Fei L., **Loiotine L.**, Noel F., Sun C., Wyser E., Wolff C. (2021). Introducing Uncertainty in Risk Calculation Along Road Using Simple Stochastic Approach. *Geosciences* 2021, 11, 143.
- Loiotine L.**, Andriani G. F., Jaboyedoff M., Parise M., Derron M.-H. (2021). Comparison of Remote Sensing Techniques for Geostructural Analysis and Cliff Monitoring in Coastal Areas of High Tourist Attraction: The Case Study of Polignano a Mare (Southern Italy). *Remote Sensing*, 13(24), 5045.
- Loiotine L.**, Wolff C., Wyser E., Andriani G. F., Derron, M.-H., Jaboyedoff M., Parise M. (2021). QDC-2-D: A Semi-Automatic Tool for 2-D Analysis of Discontinuities for Rock Mass Characterization. *Remote Sensing*, 13(24), 5086
- Andriani, G. F., and **Loiotine, L.** (2020). Multidisciplinary approach for assessment of the factors affecting geohazard in karst valley: the case study of Gravina di Petruscio (Apulia, South Italy). *Environmental Earth Sciences*, 79(19), 458.
- Liso I.S., **Loiotine L.**, Andriani G.F., Parise M. (2019). Apulian caves as natural hydrogeological laboratories. *Italian Journal of Engineering Geology and Environment*, Special Issue 1, 67-72.
- Loiotine L.**, Liso I.S., Parise M., Andriani G.F. (2019). Optimization of geostructural surveys in rock mass stability analyses using Remote Sensing techniques. *Italian Journal of Engineering Geology and Environment*. Apulian caves as natural hydrogeological laboratories. *Italian Journal of Engineering Geology and Environment*, Special Issue 1, 73-78.

Proceedings and abstracts

- Loiotine L.**, Andriani G. F., Derron, M.-H., Jaboyedoff M., Parise M. (2022). The neglected role of karst features in rock mass characterization and stability assessment. In: *EGU General Assembly 2022 – Austria, Vienna + online, 23-27 May 2022*.
- Andriani, G. F., Diprizio, G., Liso, I. S., **Loiotine, L.**, and Parise, M. (2021). Geoengineering problems and solutions in the Murge karst (Apulia, SE Italy). In: *EGU General Assembly 2021 – Online, 19-30 April 2021*.
- Choanji, T., Wolff, C., Fei, L., **Loiotine, L.**, Gutierrez, A., Sun, C., Derron, M.-H., Carrea, D., and Jaboyedoff, M. (2021). Cross-Bedding and Structural Mapping for Rockfall Assessment of a Tunnel using Hi-Resolution LiDAR (Fribourg, Switzerland). In: *EGU General Assembly 2021 – Online, 19-30 April 2021*.

- Loiotine L.**, La Salandra M., Andriani G.F., Apicella E., Jaboyedoff M., Parise M., Derron M-H. (2021). Implementation of InfraRed Thermographic surveys in complex coastal areas: the case study of Polignano a Mare (southern Italy). In: EGU General Assembly 201 – Online, 19-30 April 2021.
- Loiotine L.**, Liso I.S., Parise M., Diprizio G., Andriani G.F. (2020). Stability problems concerning the relationships between soft rock properties and anthropization levels: a case study from Apulia (south Italy). In: 7° Congresso Nazionale della Associazione Italiana Di Geologia Applicata E Ambientale (A.I.G.A.) 2021.
- Wyser E., **Loiotine L.**, Wolff C., Andriani G.F., Jaboyedoff M., Parise M. (2021). 2-D quantitative analysis of fractures from high-resolution photos for the geomechanical characterization of rock masses. In: EGU General Assembly 2021 – Online, 19-30 April 2021.
- Liso I.S., **Loiotine L.**, Andriani G.F., Parise M. (2019). Apulian caves as natural hydrogeological laboratories. In: XI Convegno Nazionale dei Giovani Ricercatori in Geologia Applicata, September 2019, Matera.
- Loiotine L.** (2019). Optimization of slope stability analyses in carbonate rock masses by means of Remote Sensing Techniques. Presented at scientific seminar: Research Focus in Applied Geology, Department of Earth and Environmental Sciences, University of Bari (Italy), 17 May 2019.
- Loiotine L.**, Liso I.S., Parise M., Andriani G.F. (2019). Optimization of geostructural surveys in rock mass stability analyses using Remote Sensing techniques. In: XI Convegno Nazionale dei Giovani Ricercatori in Geologia Applicata, September 2019, Matera.
- Andriani G.F., Diprizio G., Liso I.S., **Loiotine L.**, Parise M. (2020). Dynamic soil characterization of structurally complex formations by means of laboratory testing. 1st Mediterranean Symposium on Landslides, 7-9 June 2021, Naples.
- Loiotine L.**, La Salandra M., Andriani G.F, Barracane G., Derron M-H., Jaboyedoff M., Marsico A., Parise M. (2020). Geomechanical characterization of rock masses by means of remote sensing techniques. In: EGU General Assembly 2020 - Online, 4-8 May 2020, Session NH3.2 Rockfalls, rockslides and rock avalanches and in: Post EGU General Assembly 2020 - Zoom seminar - 14 May 2020.